

**Analysis of the Higgs boson decay in the
 $H \rightarrow \tau_{\text{had}}\tau_{\text{had}}$ channel and CP properties
with $\sqrt{s} = 13$ TeV collisions at the ATLAS
detector**

Dissertation
zur
Erlangung des Doktorgrades (Dr. rer. nat.)
der
Mathematisch-Naturwissenschaftlichen Fakultät
der
Rheinischen Friedrich-Wilhelms-Universität Bonn

von
Stephanie P. Y. Yuen
aus
Brooklyn, New York, Vereinigte Staaten von Amerika

Bonn, November 2018

Dieser Forschungsbericht wurde als Dissertation von der Mathematisch-Naturwissenschaftlichen Fakultät der Universität Bonn angenommen und ist auf dem Hochschulschriftenserver der ULB Bonn http://hss.ulb.uni-bonn.de/diss_online elektronisch publiziert.

1. Gutachter: Prof. Dr. Jochen Christian Dingfelder

2. Gutachterin: Prof. Dr. Klaus Desch

Tag der Promotion: 15. Juli 2019

Erscheinungsjahr: 2019

Zusammenfassung

In 2012 wurde das Higgs-Boson, das letzte unentdeckte Teilchen des Standardmodells der Teilchenphysik (SM), von den ATLAS und CMS Kollaborationen am CERN in einiger seiner bosonischen Zerfälle entdeckt. Die Entdeckung ist ein wichtiger Schritt zum Verständnis der Natur der elektroschwachen Symmetriebrechung. Nachfolgende Studien der Spinquantenzahl, Parität, und Kupplung des Higgs-Bosons sind zentral um die Kompatibilität zwischen dem entdeckten Higgs-Boson und dem SM Higgs-Boson zu prüfen. Die Themen der Dissertation sind Untersuchungen der Higgsanalyse und der Ladungs-Parität (CP) in Zerfällen in Paare hadronisch zerfallender Tau-Leptonen. Die verwendeten Datensätze werden gesammelt in 2015 und 2016 mit Protonen-Protonen Kollisionen an LHC, wobei einer integrierten Luminosität von 3.21 fb^{-1} beziehungsweise 32.9 fb^{-1} entsprechen.

In der Physik des Higgs-Bosons sind die fermionischen Zerfallsmodi wichtig weil sie direkten Zugang zu den Yukawa-Kupplungen des Higgs-Bosons bieten. In der präsentierten Untersuchung der Higgszerfall zu Tau-Leptonen wird die Signalextraktion über einen Vergleich der erwarteten Signal- und Untergrundmassenverteilung zu den beobachteten Daten durchgeführt. Ein Überschuss wird mit einer Signalsignifikanz von 1.52σ gemessen, was einer Signalstärke relativ zur Standardmodellerwartung von $\mu = 0.62_{-0.24}^{+0.25}(\text{stat})_{-0.31}^{+0.36}(\text{syst}) = 0.62_{-0.40}^{+0.44}$ entspricht.

Nachfolgende Studien der CP -Bestandteile werden im selben Zerfallskanal durchgeführt, wobei die Analyse der Higgsanalyse als Grundlage dient. Obwohl CP -Messungen in den bosonischen Zerfallsmodi Abweichungen von der CP -Quantenzahlen des SM Higgs-Bosons ausgeschlossen haben, die fermionischen Zerfallsmodi bieten gesonderte Informationen zu den CP Eigenschaften. Wenn es Zeichen von CP -Mischung in den fermionischen Sektor gibt, könnte das Higgs-Boson ein CP -Verletzungskandidat sein und die Asymmetrie zwischen Materie und Antimaterie im Universum erklären. Die Sensitivität auf die Higgs- CP Eigenschaften wird extrahiert über einen Vergleich der erwarteten Signal- und Untergrundverteilung zu den beobachteten Daten wobei CP -sensitive Observablen genutzt werden. Die Signalextraktion wird mit Toy-Experimenten getestet. Zusätzlich werden Limitierungen der Messung untersucht, von denen die wichtigste die Hauptbehinderung die beschränkte integrierte Luminosität ist. Ein CP -Mischungswinkel von 10° wird gemessen mit einer Unsicherheit von 18.3° wenn der Wirkungsquerschnitt des Higgs-Bosons fest ist und 27.5° wenn der frei ist. Der Messwert ist konsistent mit der Standardmodellserwartung von $\phi_\tau = 0^\circ$.

Abstract

In 2012, the last undiscovered particle predicted by the Standard Model of particle physics (SM), the Higgs boson, was discovered by the ATLAS and CMS collaborations in a number of its bosonic decay channels. This has been an important step in understanding the nature of electroweak symmetry breaking. Subsequent studies of the Higgs boson spin, parity, and coupling properties are vital in confirming whether the discovered Higgs boson is compatible with the SM Higgs boson. The topics of this dissertation are the analyses of the Higgs decay to a pair of hadronically decaying tau leptons and the Higgs charge-parity (\mathcal{CP}) properties in the same decay channel using datasets collected during 2015 and 2016 from proton-proton collisions at the LHC, corresponding to integrated luminosities of 3.21 fb^{-1} and 32.9 fb^{-1} , respectively.

In Higgs physics, the fermionic decay channels are important because they provide direct access to the Higgs boson Yukawa couplings. In the presented analysis of the Higgs decay to tau leptons ($H \rightarrow \tau\tau$), the signal extraction is performed by comparing the expected signal and background distributions to the observed di-tau mass distribution in data. An excess of signal events beyond the expected background yield is measured with an observed significance of 1.52σ , corresponding to a signal strength relative to the SM prediction of $\mu = 0.62_{-0.24}^{+0.25}(\text{stat})_{-0.31}^{+0.36}(\text{syst}) = 0.62_{-0.40}^{+0.44}$.

Subsequent studies of Higgs \mathcal{CP} properties are performed in the same decay channel using the $H \rightarrow \tau\tau$ analysis as the basis. While \mathcal{CP} measurements in the bosonic decay channels have excluded deviations from SM Higgs boson \mathcal{CP} quantum numbers, the fermionic decay channels provide unique \mathcal{CP} information. If there are signs of \mathcal{CP} mixing in the fermionic sector, the Higgs boson can possibly explain the matter-antimatter asymmetry in the universe. The Higgs \mathcal{CP} sensitivity is extracted by comparing the expected signal and background distributions to the observed data distribution constructed from experimental observables sensitive to Higgs \mathcal{CP} mixing. Studies are performed to validate the signal extraction with toy experiments and to identify the main hindrance of the analysis, which is the limited integrated luminosity. A \mathcal{CP} mixing angle of 10° is measured with an uncertainty of 18.3° for the case where the Higgs boson cross section is fixed to the SM prediction and an uncertainty of 27.5° where it is fitted. It is consistent with the SM prediction of $\phi_\tau = 0^\circ$.

Contents

1	Introduction	1
2	Theory	3
2.1	The Standard Model of particle physics	3
2.1.1	Symmetries of the Standard Model	3
2.1.2	Quantum chromodynamics	4
2.1.3	Quantum electrodynamics	10
2.1.4	The weak interaction and electroweak unification	11
2.1.5	Spontaneous symmetry breaking and the Higgs mechanism	14
2.1.6	The Higgs boson production and decay modes	17
2.1.7	Higgs boson CP properties	22
2.2	Physics with tau leptons	24
2.2.1	Tau lepton polarization	24
2.3	Higgs CP studies with tau leptons	29
2.4	Shortcomings of the Standard Model	32
2.5	Theories beyond the Standard Model	33
3	The LHC and the ATLAS detector	35
3.1	The Large Hadron Collider accelerator system	35
3.1.1	The LHC parameters	36
3.1.2	LHC results in Run-I and Run-II	39
3.2	The ATLAS detector	39
3.2.1	The coordinate system	42
3.2.2	The inner detector	42
3.2.3	The calorimeter system	45
3.2.4	The trigger system	49
4	Object reconstruction	51
4.1	Track and vertex reconstruction	51
4.2	Jet reconstruction	51
4.3	Missing transverse energy reconstruction	53
4.4	Hadronic tau decays at ATLAS	54
4.4.1	Tau reconstruction	54
4.4.2	Tau identification	55
4.4.3	Performance of the tau reconstruction and identification	57
4.4.4	The tau trigger	57
4.5	The tau particle flow reconstruction	61
4.5.1	Data and simulated samples	61

4.5.2	Concept and method	62
4.5.3	Subtraction of π^\pm energy deposits	62
4.5.4	Identification of neutral pions	65
4.5.5	π^0 cluster separation using photon hits	67
4.5.6	Final tau decay mode classification	69
4.5.7	Tau four-momentum reconstruction	71
4.5.8	Performance of the tau particle flow algorithm	72
4.5.9	Outlook	74
5	$H \rightarrow \tau\tau$ analysis in the $\tau_{\text{had}}\tau_{\text{had}}$ final state	75
5.1	$H \rightarrow \tau\tau$ final states	77
5.2	Signal processes	77
5.3	Background processes	79
5.4	Data and simulated samples	80
5.4.1	Data	80
5.4.2	Simulated samples	80
5.5	Di-tau invariant mass reconstruction	83
5.6	Event selection and categorization	86
5.6.1	Selection of physics objects	86
5.6.2	Event preselection	88
5.6.3	Event categorization	91
5.7	Background model	94
5.7.1	Estimation of the $Z \rightarrow \tau\tau$ background	97
5.7.2	Estimation of the fake- τ background	99
5.8	Systematic Uncertainties	116
5.8.1	Experimental uncertainties	116
5.8.2	Theoretical uncertainties	121
5.9	Fit model and signal extraction	121
5.9.1	The likelihood function	122
5.9.2	Hypothesis testing	123
5.9.3	Expected sensitivity	124
5.10	Results	128
5.11	Conclusion	131
6	Higgs CP analysis in the $H \rightarrow \tau_{\text{had}}\tau_{\text{had}}$ channel	135
6.1	CP -sensitive observables	135
6.1.1	Impact parameter method	136
6.1.2	ρ method	138
6.1.3	Combined $IP\rho$ method	139
6.2	Signal and background processes	139
6.3	Data and simulated samples	140
6.4	Event selection and categorization	141
6.5	Background model	142
6.5.1	Estimation of the $Z \rightarrow \tau\tau$ background	142
6.5.2	Estimation of the fake- τ background	144
6.5.3	Background model validation	150

6.6	Systematic uncertainties	150
6.6.1	Systematic uncertainties on the fake- τ background estimation	151
6.6.2	Systematic uncertainties on the $Z \rightarrow \tau\tau$ background estimation	152
6.6.3	Systematic uncertainties from the substructure reconstruction	153
6.7	Fit model and sensitivity estimate	154
6.7.1	Toy experiments	154
6.8	Sensitivity projection	156
6.9	Addition of a_1 decay modes with machine learning	158
6.9.1	The ρa_1 method	158
6.9.2	The $a_1 a_1$ method	160
6.9.3	Boosted decision trees for the ρa_1 and $a_1 a_1$ decay modes	161
6.10	Results	164
6.11	Conclusion	165
7	Conclusion	171
	Bibliography	173
A	Relevant algebra of the unitary group $U(n)$ and special unitary group $SU(n)$	183
B	Relevant Properties of the ATLAS Detector	185
B.1	Segmentation of the Calorimeters at ATLAS	185
B.2	Amount of Material in the ATLAS Detector	186
C	Variables Used for the π^0-ID	187
D	Properties of the simulated single π^\pm sample used for developments of the tau particle flow algorithm	189
E	Cross section values of background and signal processes in the $H \rightarrow \tau\tau$ analyses	191
F	Changes to the $H \rightarrow \tau_{\text{had}}\tau_{\text{had}}$ preselection in Run-II	193
G	Composition of the SS and nOS control regions	195
H	Validation of the Background Modeling in the $H \rightarrow \tau\tau$ analysis	197
I	Supplemental information on the final fit to the $m_{\text{MMC}}^{\tau\tau}$ distribution in the couplings analysis	203
I.1	Binning of the $m_{\text{MMC}}^{\tau\tau}$ discriminant in the statistical interpretation	203
I.2	Definitions of nuisance parameters	203
I.3	Prefit impact of each nuisance parameter in each signal category	207
J	Studies concerning the flavor composition of the jet energy scale nuisance parameter in the couplings analysis	211
K	Validation of the Background Modeling in the Higgs CP analysis	213
K.1	VBF category	213
K.2	Boosted tight category	215

K.3 Boosted loose category	218
L Supplemental information on the final fit to the φ_{CP}^* observables in the Higgs CP analysis	221
L.1 Definitions of nuisance parameters specific to the Higgs CP analysis	221
L.2 Prefit impact of each nuisance parameter in each Higgs CP signal category	222
List of Figures	239
List of Tables	243

Introduction

The idea that matter is composed of elementary particles dates back, at least, to the 6th century BC. This concept has since changed substantially, culminating in modern particle physics described by the Standard Model (SM). The SM has successfully predicted the existence of all known elementary particles, including the Higgs boson, the last hitherto missing SM component discovered in 2012 at the Large Hadron Collider (LHC) by the ATLAS and CMS collaborations [1]. The LHC is at the energy frontier of particle physics, testing the predictions of the SM, such as the conjectured properties of the Higgs boson, as well as searching for new particles predicted by theories beyond the SM that address unresolved questions of physics.

In 2015, the LHC began its second run of collision data-taking at center-of-mass energies of $\sqrt{s} = 13$ TeV, following a successful first run from 2010 to 2012 at $\sqrt{s} = 7$ TeV and 8 TeV. With this first run of data-taking, the LHC has been at the energy frontier of particle physics, accessing the TeV energy region and achieving discoveries of the Higgs boson in its bosonic decay channels, as well as observations of, for example, quark-gluon plasma and the rare $B_s \rightarrow \mu^+ \mu^-$ decay [1–3]. With the new dataset at an increased energy scale, physicists are able to better investigate pressing fundamental questions. For example, observations and discoveries of the Higgs Yukawa coupling to fermions have been achieved by the ATLAS collaboration independently, including the Higgs boson in its decay to a pair of tau leptons and its decay to a pair of b quarks, as well as its production in association with top quarks [4–6]. With this new dataset, there are, so far, no signs of new physics beyond the SM.

Tau leptons play an important role in the physics goals of the LHC. Measurements of the Higgs boson decaying to a di-tau pair are important tests of the coupling of the SM Higgs boson to elementary fermions since the di-tau decay channel has the highest sensitivity among channels directly probing the Higgs Yukawa couplings. In addition, tau leptons contain unique information about the charge-parity (CP) properties of the Higgs boson. If CP violation exists in the Higgs sector, the Higgs boson may be a candidate for an explanation of the physics of the early universe (particularly baryogenesis, the process responsible for the asymmetry between matter and antimatter).

In this dissertation, a measurement of the Higgs boson decaying to a pair tau leptons, which decay to one or more hadrons and accompanying neutrinos, is presented. This decay channel suffers from the overwhelming production of hadronic jets at the LHC that can mimic the hadronic tau decay signature. In order to suppress this multijet background, the analysis targets events characteristic of the vector boson fusion and gluon-gluon fusion production processes of the Higgs boson, where a Higgs boson with high transverse momentum is accompanied by

one or two highly energetic jets. Even after the selection of these events, though, the multijet background makes up about half of the events expected in data, so a robust estimate of its expected contribution and kinematic distributions are of crucial importance. Methods are introduced in this dissertation that improve the multijet background modeling by using a sizable control region in data that has never before been used for background estimation in this decay channel.

This analysis is also the basis for the analysis of Higgs CP mixing properties in the same decay channel. Subsequent studies of the Higgs boson spin and parity properties are vital in confirming whether the Higgs boson observed at the LHC is compatible with the SM Higgs boson. Although deviations from the CP quantum numbers predicted by the SM have been constrained in the bosonic decay channels, fermions contain unique information on Higgs CP properties. Of the known fermions, the tau lepton is one of the few fermions whose spin is experimentally accessible at the LHC. This dissertation uses tau polarization to probe the transverse tau spin correlations in which Higgs CP mixing properties are encoded. At the LHC, these transverse spin correlations can be inferred from the acoplanarity angle between the tau decay planes since tau leptons decay in the LHC beam pipe with a momentum direction that cannot be accurately measured, due to the presence of neutrinos. Thus, the methods developed for the construction of the acoplanarity angle require the identification of the tau decay mode and the reconstruction of each tau decay product (except for the neutrinos). Studies are performed in this dissertation to improve the tau reconstruction using a particle flow approach in which measurements from different components of the ATLAS detector are combined to reconstruct the individual tau decay products.

The dissertation is structured according to the following chapters:

- Chapter 2 provides the theoretical background and motivation for the presented analyses. First, the SM of particle physics is introduced. Then, detailed sections follow focusing on tau polarization and its application in Higgs CP studies.
- Chapter 3 describes the LHC and the ATLAS detector. A description of the tracking system and the calorimeter of the ATLAS detector is provided in more detail since they are the most important detector components for the presented studies.
- Chapter 4 gives an overview of the reconstruction and identification of relevant physics objects, with an emphasis on hadronically decaying tau leptons at ATLAS. The results of these algorithms are used in one of the analyses presented in this dissertation.
- Chapter 5 presents the analysis of the Higgs boson decay to a pair of hadronically decaying tau leptons using data from ATLAS. It is the basis for the analysis in the next chapter.
- Chapter 6 delineates the analysis of Higgs CP properties in the same Higgs boson decay channel using data from ATLAS.
- Finally, the dissertation is concluded by the conclusion in Chapter 7.

Throughout the chapters, SI units and space-time coordinates, where $c = 1$, are used, unless otherwise noted.

Theory

In the following chapter, the theoretical background for the dissertation is discussed. First, the Standard Model of particle physics (SM) is detailed in Section 2.1, with the Higgs boson introduced in Section 2.1.6. Then, the physics of tau leptons is described in Section 2.2, with an emphasis on tau polarization. Next, Higgs \mathcal{CP} measurements with tau leptons are discussed in Section 2.3. Finally, the chapter is concluded with the shortcomings of the SM in Section 2.4, which can be addressed by theories beyond the SM presented in Section 2.5.

2.1 The Standard Model of particle physics

Symmetry principles play an important role in fundamental physics. In Einstein’s theory of general relativity, for example, the predictive power of symmetry is utilized in the requirement of invariance under general coordinate transformations [7]. In Noether’s theorem, continuous symmetries of action correspond to conserved quantities [8]. The conservation of energy, for example, corresponds to time invariance, and the conservation of parity corresponds to invariance under reflections in space. In nuclear physics, symmetry of the quantum number, isospin, is related to the amazingly similar masses of the proton and the neutron [9]. Going to even more elementary levels in particle physics, gauge symmetries dictate the quantum field theories underlying the SM that describe the universe at its most fundamental level. The SM predicts many physical quantities that are in good agreement with experimental data and explains a wide range of physical phenomena. The gauge symmetries of the SM are described next.

2.1.1 Symmetries of the Standard Model

The SM provides a unified framework describing all known elementary particles and forces, with the exception of gravity, which is described by the theory of general relativity. Tables 2.1, 2.2, and 2.3 provide an overview of the half-integer spin fermions, whose interactions are mediated by integer spin bosons. The fermions are empirical input to the theory, with the force-mediating bosons arising from symmetry principles imposed on the SM gauge groups. The following gauge groups construct the non-Abelian gauge theory of the SM:

$$\mathcal{G} = \text{SU}(2)_L \otimes \text{U}(1)_Y \otimes \text{SU}(3)_C \xrightarrow{\text{SSB}} \text{U}(1)'_{\text{QED}} \otimes \text{SU}(3)'_C, \quad (2.1)$$

where the subscripts denote the conserved quantum number under local symmetry transformations of that gauge group.¹ These gauge transformations connect states that cannot be physically distinguished. Each of the conserved quantum numbers is explained in detail in the next sections. The quantum number L refers to left-handed fields, while Y refers to the charge of the unitary group $U(1)$, called hypercharge, and C refers to color charge. The latter part of Equation 2.1 represents the SM after spontaneous symmetry breaking (SSB) to the quantum electrodynamic (QED) subgroup in order to give mass to the known particles.

The fermions are separated into quark and lepton groups based on their behavior under these symmetries. The electroweak (EW) interaction of leptons corresponds to the local $SU(2)_L \otimes U(1)_Y$ symmetry, while the strong interaction of quarks corresponds to the local $SU(3)_C$ symmetry of the three colors for the six quarks. These two theories are differentiated by the fact that particles participate in EW interactions since they carry weak charge, while quarks also participate in the strong interaction since they, in addition, carry non-zero color charge. The theory of strong interactions is described in Section 2.1.2, and the unified theory for electroweak interactions is presented in Sections 2.1.3 and 2.1.4. Then, the absence of mass terms in the EW sector for the known particles, which would make the renormalizable SM nonrenormalizable, is addressed by the Higgs mechanism of SSB in Section 2.1.5. These sections are brief summaries based on [10–15] and present the important theoretical background relevant to this dissertation.

Force	Mediating particle	Mass of Mediating Particle	Relative strength	Range (m)
Weak	W^\pm bosons	80.385 ± 0.015 GeV	10^{-5}	10^{-18}
	Z boson	91.188 ± 0.002 GeV		
Electromagnetic	Photon, γ	Massless	10^{-2}	∞
Strong	Gluon, g	Massless	1	10^{-15}

Table 2.1: The fundamental forces mediated by integer-spin bosons. Relative strength is described by the ratio to the strong coupling evaluated at the EW scale. Numbers are from [16].

2.1.2 Quantum chromodynamics

Quantum chromodynamics (QCD) is the non-Abelian quantum field theory describing the strong interaction between quarks and gluons that binds them to colorless hadrons. The strong interaction is ~ 100 times stronger than the electromagnetic interaction at the scale of the square of the Z boson mass, m_Z^2 , and very short-ranged (see Table 2.1) [16]. The underlying symmetry in QCD requiring local gauge invariance implies the existence of a gauge field mediated by bosons (gluons) that couple to spin- $\frac{1}{2}$ Dirac fermions (quarks). Quarks do not interact with each other directly but rather via gluons, while gluons are predicted to self-interact. This self-interaction is responsible for the special features of QCD, including asymptotic freedom and color confinement. By the end of the section, it is shown that the QCD Lagrangian form and the features of QCD arise from the symmetry of the $SU(3)_C$ group. (The relevant algebra of this group is listed in Appendix A.)

¹ Under local transformations of these symmetry groups, the physical content of the theory remains unchanged, but the transformation can be different for each space-time point, whereas a global transformation acts on any space-time point in the same way, independent of the space coordinate.

	Generation			Quantum numbers			
	I	II	III	Q	T	T_3	Y
Leptons	$L_{L_1} = \begin{pmatrix} e \\ \nu_e \end{pmatrix}_L$	$L_{L_2} = \begin{pmatrix} \mu \\ \nu_\mu \end{pmatrix}_L$	$L_{L_3} = \begin{pmatrix} \tau \\ \nu_\tau \end{pmatrix}_L$	-1 0	1/2	$\begin{pmatrix} 1/2 \\ -1/2 \end{pmatrix}$	-1
	$E_{R_1} = (e)_R$	$E_{R_2} = (\mu)_R$	$E_{R_3} = (\tau)_R$	-1	0	0	-2
Quarks	$Q_{L_1} = \begin{pmatrix} u \\ d \end{pmatrix}_L$	$Q_{L_2} = \begin{pmatrix} c \\ s \end{pmatrix}_L$	$Q_{L_3} = \begin{pmatrix} t \\ b \end{pmatrix}_L$	2/3 -1/3	1/2	$\begin{pmatrix} 1/2 \\ -1/2 \end{pmatrix}$	+1/3
	$U_{R_1} = (u)_R$	$U_{R_2} = (c)_R$	$U_{R_3} = (t)_R$	2/3	0	0	+4/3
	$D_{R_1} = (d)_R$	$D_{R_2} = (s)_R$	$D_{R_3} = (b)_R$	-1/3	0	0	-2/3

Table 2.2: The spin- $\frac{1}{2}$ fermions and their properties. The left-handed fermions are doublets, while the right-handed fermions are singlets. For each fermion, there exists an antiparticle with the same mass but opposite quantum numbers. The relevant quantum numbers shown are charge (Q), weak isospin (T), third component of the weak isospin (T_3), and hypercharge (Y). Masses are shown in Table 2.3.

Generation	I	II	III
m_e	0.511(13) MeV	m_μ 105.7(24) MeV	m_τ 1.7777 \pm 0.16 GeV
m_{ν_e}	< 2.2 eV	m_{ν_μ} < 0.17 MeV	m_{ν_τ} < 15.5 MeV
m_u	2.3 $^{+0.7}_{-0.5}$ MeV	m_c 1.29 $^{+0.05}_{-0.11}$ GeV	m_t 173.07 \pm 0.4 GeV
m_d	4.8 $^{+0.5}_{-0.3}$ MeV	m_s 95 $^{+5}_{-5}$ MeV	m_b 4.18 $^{+0.04}_{-0.03}$ GeV

Table 2.3: The masses of the spin- $\frac{1}{2}$ fermions. Masses are from [16].

Quarks are spin- $\frac{1}{2}$ fermions described by Dirac spinors, $u(k, \lambda)$. For a free fermion, the wave function is expressed as $\psi_{k,\lambda}(x) = u(k, \lambda)e^{-i(Et - \vec{x}\cdot\vec{k})}$, where the latter term is a plane wave with 4-momentum $k^\mu = (E, \vec{k})$ and polarization λ . The quark (antiquark) fields consist of

$$\overset{(-)}{\psi}_{fi} = \begin{cases} f = u, d, s, c, b, t & N_f = 6 \text{ (flavor index)} \\ i = 1, 2, 3 & N_c = 3 \text{ (color index, labeled red, green, and blue)} \end{cases}. \quad (2.2)$$

If a quark does not interact with other fields, the free Lagrangian is

$$\mathcal{L} = \bar{\psi}_i (i\gamma^\mu \partial_\mu - m) \psi_i \quad (2.3)$$

where γ^μ are the Dirac matrices and m is the free mass.² QCD arises from the non-Abelian $SU(3)_C$ local gauge symmetry requiring the free fermion Lagrangian in Equation 2.3 to remain invariant under unitary transformations:

$$\psi'(x) = U\psi(x), \quad U = e^{ig_S\alpha(x)\cdot\hat{\mathbf{T}}}, \quad (2.4)$$

in which g_S is a dimensionless coupling strength, $\alpha(x)$ are eight functions of the space-time coordinate x , $\hat{\mathbf{T}} = \frac{1}{2}\lambda$, and the λ matrices are the nine generators of the group and act on

² In reality, quarks are subject to confinement, as is discussed in Section 2.1.2.1.

the SU(3) color representations of the quarks. Of the nine, only eight are independent. To maintain gauge invariance, a gauge covariant derivative is used that introduces eight gluon fields corresponding to the eight SU(3) generators:

$$\partial_\mu \rightarrow D_\mu = \partial_\mu - ig_S A_\mu, \quad (2.5)$$

where $A_\mu(x) = \sum_{a=1}^8 T_a A_\mu^a(x)$ are the associated gluon potentials. The modified free quark Lagrangian is then invariant if the gauge potentials transform as $A_\mu \rightarrow U \left(A_\mu + \frac{i}{g_S} \partial^\mu \right) U^\dagger$. Gluons are predicted to be massless since a mass term $m_g A_\mu^a A_\mu^a$ would break the invariance.

Next, natural gauge-invariant terms are considered in the QCD Lagrangian. A kinetic term describing gluon dynamics is included in order for the gluon field to be a truly propagating field. This term uses the gluon field tensor defined as

$$\begin{aligned} G_{\mu\nu} \equiv G_{\mu\nu}^a T_a &= \partial_\mu A_\nu^a T_a - \partial_\nu A_\mu^a T_a - ig_S A_\mu^a A_\nu^b [T_a, T_b] \\ &= \left(\partial_\mu A_\nu^a - \partial_\nu A_\mu^a + g_S f_{abc} A_\mu^b A_\nu^c \right) T_a, \end{aligned} \quad (2.6)$$

where the last term arises from the commutation relation for the generators of the SU(3) symmetry (c.f. Equation A.1). In principle, there is another natural gauge-invariant and renormalizable term that can be added to the Lagrangian and which breaks \mathcal{CP} symmetry. This is known as the strong \mathcal{CP} problem since experiments do not indicate the existence of \mathcal{CP} violation in the QCD sector. It is further discussed in Section 2.4.

The final QCD Lagrangian, neglecting \mathcal{CP} violation and non-perturbative QCD, as written in [10], is

$$\begin{aligned} \mathcal{L}_{\text{QCD}} &= \sum_f \bar{\psi}_f (i\gamma^\mu D_\mu - m_f) \psi_f - \frac{1}{4} G_{\mu\nu}^a G_a^{\mu\nu} \\ &= \sum_f \bar{\psi}_f (i\gamma^\mu D_\mu - m_f) \psi_f - \frac{1}{4} (\partial^\mu G_a^\nu - \partial^\nu G_a^\mu) (\partial_\mu G_\nu^a - \partial_\nu G_\mu^a) \\ &\quad - g_S G_a^\mu \sum_f \bar{\psi}_f^\alpha \gamma_\mu \left(\frac{\lambda^a}{2} \right) \psi_f^\beta \\ &\quad + \frac{g_S}{2} f^{abc} (\partial^\mu G_a^\nu - \partial^\nu G_a^\mu) G_\mu^b G_\nu^c - \frac{g_S^2}{4} f^{abc} f_{ade} G_b^\mu G_c^\nu G_\mu^d G_\nu^e, \end{aligned} \quad (2.7)$$

$$(2.8)$$

where the terms are:

- The quark and gluon propagators in the first line of Equation 2.8.
- The $q\bar{q}g$ vertex in the second line of Equation 2.8 (see Figure 2.1(a)). It shows that quark β becomes quark α through emission of a gluon and that all interactions in QCD are proportional to the strong coupling constant, g_S , which is related to the running strong coupling constant, discussed in Section 2.1.2.2, by

$$\alpha_S = \frac{g_S^2}{4\pi}. \quad (2.9)$$

Gluons must carry color and anticolor charge in order for color to be conserved at the interaction vertex (one of red, green, or blue, and one of antired, antigreen, or antiblue).

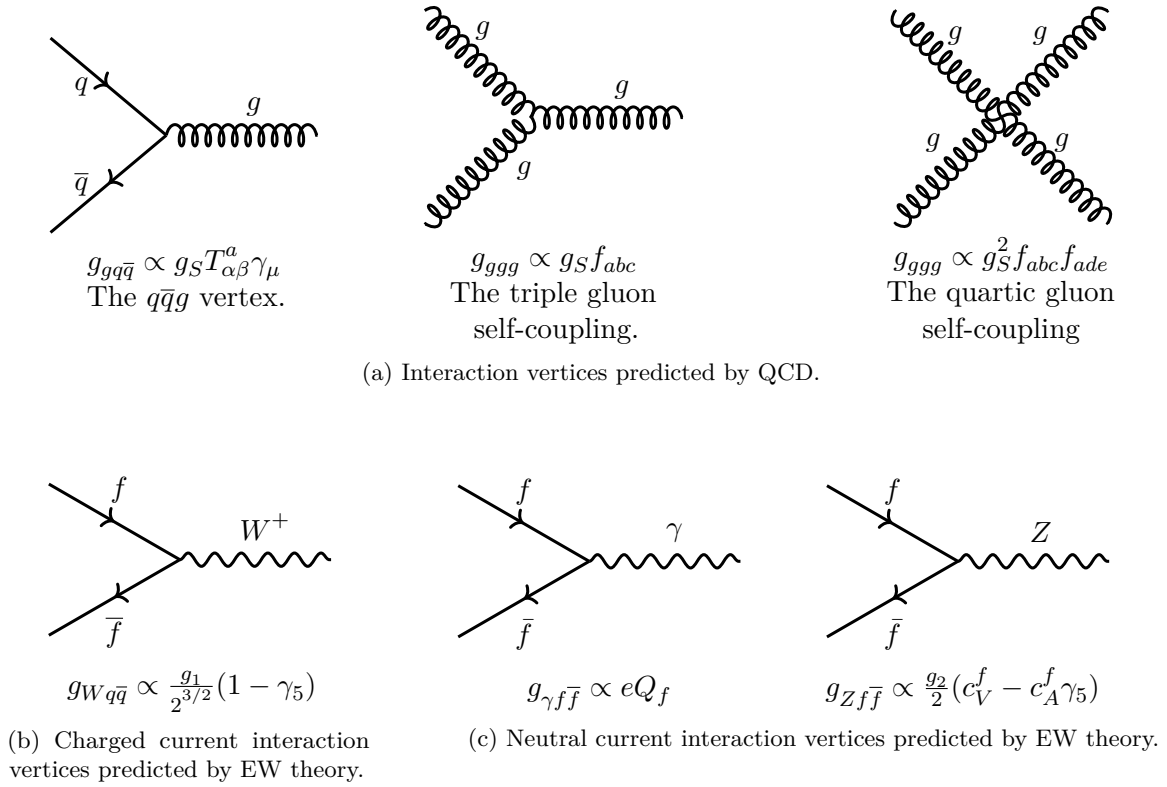


Figure 2.1: Leading-order interaction vertices predicted by the SM before spontaneous symmetry breaking. The coupling strength is shown below each diagram.

- The non-Abelian interactions of the triple and quartic self-couplings of gluons arising from the last line of Equation 2.8 (see Figure 2.1(a)). The consequences of self-interacting gluons give rise to asymptotic freedom at high energies, described later in Section 2.1.2.2.

The features of QCD are described in the next sections. The self-coupling nature of gluons that gives rise to the absence of observations of free quarks is described in Section 2.1.2.1. The running nature of the QCD coupling constant and QCD renormalization are discussed in Section 2.1.2.2, and factorization and parton distribution functions are presented in Section 2.1.2.3.

2.1.2.1 Color confinement

The lack of experimental evidence for the observation of free quarks is explained by the hypothesis of color confinement. Qualitatively, the self-interaction of gluons gives rise to confinement, since the interaction between quarks involves the exchange of virtual gluons. The color field between these quarks is squeezed into a tube. The energy stored in the color field is proportional to the separation of the quarks and is described by a potential

$$V(r) = -\frac{4}{3} \frac{\alpha_S}{r} + \kappa r \xrightarrow{r \rightarrow \infty} \kappa r, \quad (2.10)$$

where α_S is the running strong coupling constant later described in Section 2.1.2.2 and the energy density κ is experimentally determined to be ~ 1 GeV/fm [11]. Since the energy in the color field increases linearly with the distance between quarks, infinite energy is required to

separate two quarks.

Therefore, color confinement implies that quarks are always observed in bound, color-singlet states. Free quarks form bound, colorless hadrons (usually mesons with a $q\bar{q}$ pair and baryons with three quarks) in a process called hadronization or fragmentation. This process results in jets of hadrons seen in particle physics experiments, such as those later described in Sections 3 and Section 4.2. Another consequence of color confinement is that gluons are also bound to colorless states. Unlike the photon, they do not propagate over macroscopic distances.

2.1.2.2 The running strong coupling constant and renormalization

The strong coupling constant, α_S , is the only free parameter in the QCD Lagrangian. It can be measured in many different processes, including deep inelastic scattering, jet production rates in e^+e^- annihilation, and hadronic decays of the tau lepton. Its dependence on the squared momentum transfer, Q^2 , from different experiments is shown in Figure 2.2.

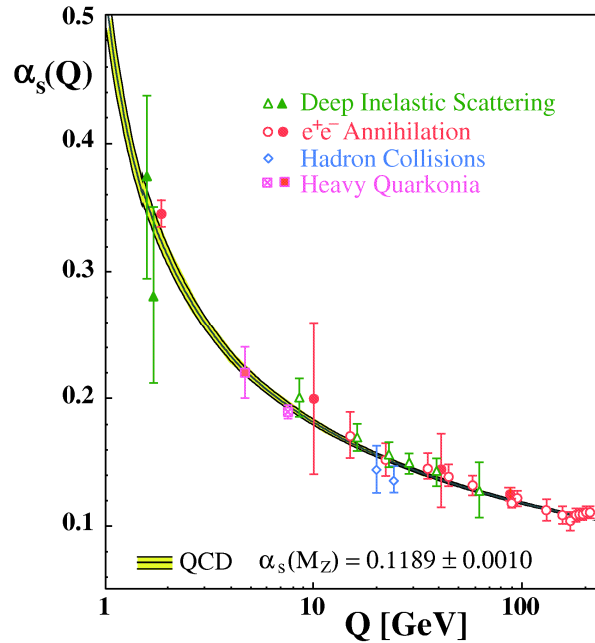


Figure 2.2: Summary of measurements of the strong coupling constant, α_S , as a function of the momentum transfer, Q , from different experiments. Taken from [17].

Due to the running nature of α_S , where α_S becomes small at high energies or small distances, high energy QCD processes can be calculated using perturbation theory, which allows one to calculate the total amplitude for a given process, \mathcal{M}_{fi} , by taking the sum of all individual amplitudes that give the final state, f , i.e.,

$$\mathcal{M}_{fi} \equiv \mathcal{M}_{\text{LO}} + \sum_n \mathcal{M}_{1,n} + \dots, \quad (2.11)$$

where \mathcal{M}_{LO} is matrix element of the lowest/leading order (LO) Feynman diagram, and n is the n^{th} order Feynman diagram [11]. The decreasing property of α_S at high energies is known as asymptotic freedom. These regimes with $|Q| > 100$ GeV, where Q is the momentum transfer

of a particular process, and $\alpha_S \sim 0.1$ are typical of interesting events at high energy collider experiments, such as those at the LHC described later in Section 3.

At low energy scales, $\alpha_S \sim \mathcal{O}(1)$ is large, and the sum $\sum_n \alpha_{S,n} \sigma_n$, where n is the QCD order, does not converge and becomes nonperturbative. This nonperturbative regime applies to bound hadronic states and the later stages of hadronization processes. Low energy QCD processes are, instead, calculated using a computationally intensive technique called lattice QCD, where quantum-mechanical calculations are performed on a discrete lattice of space-time points [18].

The running of the strong coupling constant is closely linked to QCD renormalization. The technique of renormalization is required because Feynman diagrams beyond the LO are divergent, and QCD is a renormalizable quantum field theory since the strong coupling constant is dimensionless. Ultraviolet (UV) divergences arise from the large momentum of the Feynman diagram loops that represent the amplitude. Infrared (IR) divergences come from a real or virtual particle that reaches zero momentum or a massless particle that radiates another massless particle. IR divergences are addressed by a factorization scale, which is discussed in Section 2.1.2.3. Renormalization takes care of the UV divergent terms by introducing a renormalization scale, μ_R , and absorbing them into a redefinition of fields or parameters. With the renormalization scheme dependence, α_S can be defined as a function of Q^2 as

$$\alpha_S(Q^2) = \frac{\alpha_S(\mu^2)}{1 + \beta \alpha_S(\mu^2) \ln \frac{Q^2}{\mu^2}}, \quad (2.12)$$

where $\beta = \frac{11N_c - 2N_f}{12\pi}$, and N_c (N_f) is the numbers of colors (flavors), previously defined in Equation 2.2 [16]. Since μ_R is a spurious parameter, it is fixed to a physically meaningful value. The strong coupling constant is typically quoted at the $Q = M_Z$ scale: $\alpha_S(m_Z^2) = 0.1184 \pm 0.0007$.

The α_S precision is important in physics at the LHC. For example, the cross section of the ggH production process for the Higgs boson (later described in Section 2.1.6) has a dependence of

$$\sigma_H \sim \alpha_S^2, \quad \frac{\delta \alpha_S \sigma_H}{\sigma_H} \sim 2 \frac{\delta \alpha_S}{\alpha_S}, \quad (2.13)$$

so a 2% error on α_S leads, at least, to a 4% error on the cross section. Uncertainties come from the experimental errors on the measurement of α_S and the fact that it is truncated at a fixed order in perturbation theory.

2.1.2.3 Factorization and parton distribution functions

As previously stated in Section 2.1.2.2, factorization addresses infrared divergences, where singularities come from long-distance physics that take place after the initial hard scattering. It turns perturbative QCD into a reliable calculation tool by isolating and absorbing long distance singularities into parton densities for the initial state and fragmentation functions for the final state. The partonic cross section can then be calculated using perturbation theory, with the nonperturbative parton distributions taken from experiment. The QCD factorization theorem states that they are universal and do not depend on the hard scattering process [19]. That is, they can be measured in one process and used for predictions in other processes, such as pp collisions at the LHC. An example of these parton distribution functions (PDFs) is shown in Figure 2.3. They are used, for example, in the calculation of the cross sections of important processes at

the LHC, such as the Higgs boson production cross sections shown later in Figure 2.7.

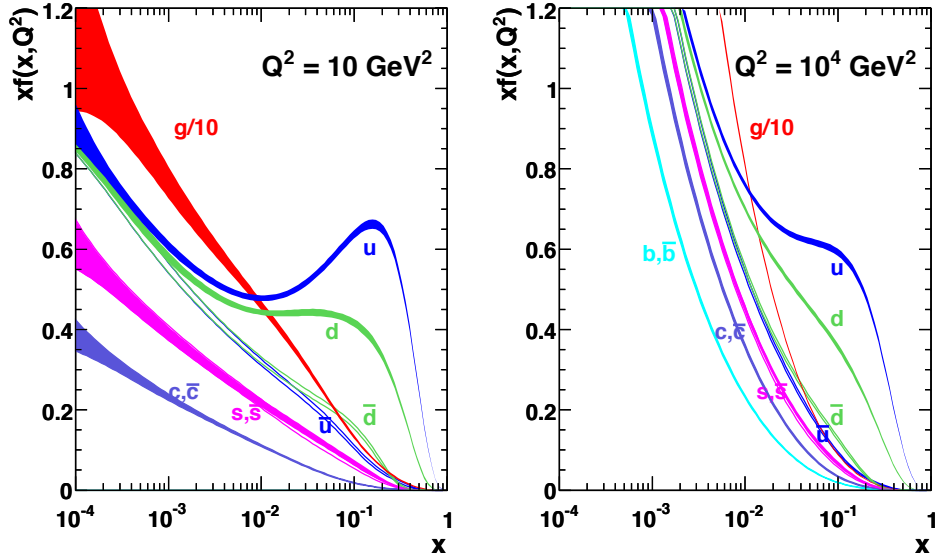


Figure 2.3: Martin-Stirling-Thorne-Watt (MSTW) parton distribution functions for two values of the squared momentum transfer, Q^2 [20].

2.1.3 Quantum electrodynamics

Quantum electrodynamics (QED) is an Abelian gauge theory describing the interactions of spin- $\frac{1}{2}$ Dirac leptons via the exchange of photons. Local transformations of the $U(1)_{\text{QED}}$ group in QED conserve the electric charge. The Lagrangian for a spin- $\frac{1}{2}$ electron/positron field is

$$\mathcal{L} = \bar{\psi} (i\gamma^\mu \partial_\mu - m) \psi \quad (2.14)$$

The physical quantities in the Lagrangian, charge density ($\bar{\psi}\psi$) and current ($\bar{\psi}\gamma^\mu\psi$), must remain invariant under a local $U(1)$ gauge transformation:

$$\psi'(x) = U\psi(x), \quad U = e^{iq\Lambda(x)}, \quad (2.15)$$

where $\Lambda(x)$ is a local phase and q is the parameter for the strength of the phase transformation, interpreted as the electric charge $q = -e$. To maintain gauge invariance, a gauge covariant derivative is introduced:

$$D_\mu = \partial_\mu - iqA_\mu, \quad (2.16)$$

where the vector field A_μ transforms as $A_\mu \rightarrow A_\mu + \partial_\mu\Lambda(x)$, with the condition that it conserves the current, and thus the electric charge. The photon is predicted to be massless since a mass term breaks the invariance. Experimentally, it is known to be $m_\gamma < 1 \times 10^{-18}$ eV [16].

Next, natural gauge-invariant terms are considered. A kinetic term is included for the

propagating A_μ field, yielding the QED Lagrangian

$$\mathcal{L}_{\text{QED}} = \bar{\psi} (i\gamma^\mu \partial_\mu - m) \psi + q\bar{\psi}\gamma^\mu A_\mu\psi - \frac{1}{4}F_{\mu\nu}F^{\mu\nu}, \quad (2.17)$$

where $F_{\mu\nu}F^{\mu\nu}$ is the EM field tensor with $F_{\mu\nu} = \partial_\mu A_\nu - \partial_\nu A_\mu$. Here, it can be seen that local gauge invariance has led to a potential term $q\bar{\psi}\gamma^\mu A_\mu\psi$ that describes the interaction between EM fields and matter. The corresponding interaction vertex is shown in Figure 2.1(c).

2.1.4 The weak interaction and electroweak unification

QED is unified with the theory of weak interactions in the electroweak theory described by the Glashow-Weinberg-Salam Model [21, 22]. In this section, the Lagrangian for the weak interactions is introduced, with EW unification shown afterward.

The weak interaction explains physical phenomena, such as the β decay, that involve a non-contact force with a finite range. The associated gauge-invariant Lagrangian density for this interaction is constructed from the $\text{SU}(2)_L \otimes \text{U}(1)_Y$ symmetry group. The relevant algebra is listed in Section A. Local transformations of the $\text{U}(1)_Y$ group conserve the weak hypercharge

$$Y_W = 2(Q - T_3), \quad (2.18)$$

which is a combination of the weak isospin, T , and the electric charge, Q , of a particle. The charge associated with the weak interaction is the weak isospin, T , whose third component, T_3 , is conserved in the weak interaction.

From a wealth of experimental evidence, such as the ^{60}Co decay in the Wu experiment, it is known that the weak interaction is parity violating, i.e.,

$$\hat{P}\psi(\vec{x}, t) \neq \psi(-\vec{x}, t), \quad (2.19)$$

where \hat{P} is the parity operator. If parity were conserved in the Wu experiment, for example, there would be equal rates for the production of electrons in directions along and opposite the ^{60}Co nuclear spin [23]. The weak interaction, therefore, distinguishes between the helicity states of particles, where helicity, h , relates the angular momentum component of a particle along its momentum:

$$h \equiv \frac{\vec{s} \cdot \vec{p}}{|\vec{s}||\vec{p}|}, \quad (2.20)$$

with eigenvalues of the helicity operator for a spin- $\frac{1}{2}$ particle equal to ± 1 , termed

- $h = -1$: Left-handed (LH), where the spin of the particle is opposite to its momentum direction.
- $h = +1$: Right-handed (RH): the spin of the particle is along its momentum direction.

However, since helicity is the scalar product of two vectors, it is not invariant under space rotations, nor is it Lorentz invariant for particles of nonzero mass. For example, if a lower-velocity particle were to accelerate past a second massive particle, the latter would appear to have had its helicity flipped. In the relativistic limit, the Dirac equation can be written for a massless fermion as $\gamma^\mu \partial_\mu \psi = \gamma^\mu \partial_\mu (\gamma_5 \psi) = 0$, with the properties $\gamma_5^2 = 1$ and $\{\gamma_5, \gamma_\mu\} = 0$ [24]. This

leads to the definition of the chirality operators that project the LH and RH chiral states, which are eigenfields of γ_5 , regardless of their mass:

$$P_L = \frac{1 - \gamma^5}{2}, \quad P_R = \frac{1 + \gamma^5}{2}, \quad \text{with } \psi = P_L\psi + P_R\psi = \psi_L + \psi_R. \quad (2.21)$$

This means that in the relativistic limit, the helicity state is the same as the chirality eigenstate. The theories in [25, 26] use the concept of chirality to address the experimental evidence and assert that the weak interaction has a chiral V-A structure, with the consequence that it preferably couples to LH particles and RH antiparticles. It is formulated such that only the LH chirality eigenstates of fermions, ψ_L , transform nontrivially under the weak isospin. LH fermions are doublets with $T_3 = \pm\frac{1}{2}$, while their RH counterparts are singlets with $T_3 = 0$ (c.f. Table 2.2).

As in QCD and QED, the starting point is the free Lagrangian, which, for the weak interaction, sums over the LH weak isodoublets and the RH weak isosinglets:

$$\mathcal{L} = \sum_{\psi_L} \bar{\psi}_L i\gamma^\mu \partial_\mu \psi_L + \sum_{\psi_R} \bar{\psi}_R i\gamma^\mu \partial_\mu \psi_R \quad (2.22)$$

It must remain invariant under local $SU(2)_L \otimes U(1)_Y$ transformations in the flavor space:

$$\psi'_L(x) = e^{iY_W\beta} U \psi_L(x), \quad U = e^{\frac{i}{2}\sigma_i\alpha^i}, \quad (i = 1, 2, 3), \quad (2.23)$$

$$\psi'_R(x) = e^{iY_W\beta} \psi_R(x), \quad (2.24)$$

where σ_i are the Pauli matrices and are related to the $SU(2)$ generators by $\sigma_i = 2T_a$, where $T_a = 0$ for the $SU(2)$ doublets, and $\alpha_i(x)$ and $\beta(x)$ are four gauge parameters. Invariance is maintained if the ordinary partial derivatives become the following covariant derivatives:

$$D_\mu \psi_R(x) = \left(\partial_\mu + \frac{i}{2} g_1 Y_W B_\mu(x) \right) \psi_R(x), \quad (2.25)$$

$$D_\mu \psi_L(x) = \left((\partial_\mu + \frac{i}{2} g_1 B_\mu(x)) + \frac{i}{2} g_2 \sigma_i \cdot \mathbf{W}_\mu(x) \right) \psi_L(x), \quad (2.26)$$

where g_1 and g_2 are the $U(1)_Y$ and $SU(2)_L$ coupling constants, respectively, Y_W is the weak hypercharge, and W_μ^a ($a = 1, 2, 3$) and B_μ are the weak isospin and weak hypercharge gauge fields, respectively. Here, it can be seen that local gauge invariance requires four gauge bosons: three from the $SU(2)$ symmetry (W_μ^a) and one from the $U(1)$ symmetry (B_μ). The transformation of these gauge fields is fixed by the requirement that $D_\mu \psi(x)$ transform the same way as the $\psi(x)$ fields. The kinetic term of the Lagrangian for these fields remains gauge invariant if the field strengths are defined as (c.f. Equation A.2):

$$B_{\mu\nu} = \partial_\mu B_\nu - \partial_\nu B_\mu \quad (2.27)$$

$$W_{\mu\nu}^a = \partial_\mu W_\nu^a - \partial_\nu W_\mu^a - g\epsilon^{ijk} W_\mu^j W_\nu^k. \quad (2.28)$$

The Lagrangian, without accounting for mass, as written in [14], is

$$\mathcal{L}_{\text{EW}} = \mathcal{L}_{\text{Gauge}} + \mathcal{L}_f \quad (2.29)$$

$$\begin{aligned} &= -\frac{1}{4}B_{\mu\nu}B^{\mu\nu} - \frac{1}{4}W_{\mu\nu}^a W_a^{\mu\nu} - \frac{1}{4}G_{\mu\nu}^a G_a^{\mu\nu} \\ &\quad + \bar{Q}_L i \not{D}_\mu Q_L + \bar{U}_R i \not{D}_\mu U_R + \bar{D}_R i \not{D}_\mu D_R + \bar{L}_L i \not{D}_\mu L_L + \bar{E}_R i \not{D}_\mu E_R, \end{aligned} \quad (2.30)$$

where $\not{D}_\mu = \gamma^\mu D_\mu$ and the isospin doublets (L_L, Q_L) and singlets (E_R, U_R, D_R) were previously presented in Table 2.2. The missing pieces in Equation 2.30 are the masses of the gauge bosons and fermions.³ Mass terms would break gauge invariance, and mass terms especially for the fermions would imply communication between the LH doublet and RH singlet fields. The masses are, instead, generated by an explicit breaking of the gauge symmetry, which is described in Section 2.1.5.

Of the four gauge fields, two of the linear combinations are the charged weak fields, whose quanta are the W^\pm bosons with unit charges $\pm e$:

$$\begin{aligned} W_\mu^+(x) &= \frac{1}{\sqrt{2}} \left(W_\mu^1(x) + iW_\mu^2(x) \right) \\ W_\mu^-(x) &= \frac{1}{\sqrt{2}} \left(W_\mu^1(x) - iW_\mu^2(x) \right) \end{aligned} \quad (2.31)$$

Their interaction vertices are shown in Figure 2.1(b), and the charged current shows that interaction strength is universal for quarks and leptons. The other two linear combinations are for the Z^0 boson and the photon, in which the A_μ photon field is incorporated for electroweak unification:

$$\begin{pmatrix} W_\mu^3 \\ B_\mu \end{pmatrix} = \begin{pmatrix} \cos \theta_W & \sin \theta_W \\ -\sin \theta_W & \cos \theta_W \end{pmatrix} \begin{pmatrix} Z_\mu \\ A_\mu \end{pmatrix}, \quad (2.32)$$

where θ_W is the weak mixing angle, also known as the Weinberg angle, and with the condition that the coupling constants of the W^3 , B , and photon fields be related and that the EM coupling strength is equivalent to e . This defines the relation $e = g_1 \sin \theta_W = g_2 \cos \theta_W$. The weak mixing angle is measured to be [16]:

$$\sin^2 \theta_W = 1 - \left(\frac{m_W}{m_Z} \right)^2 \approx 0.2223(21), \quad (2.33)$$

The strength of the weak interaction is historically defined by the Fermi coupling constant, G_F , which plays an important role in precision tests of the EW sector of the SM as it is used as input to all higher order corrections. It is defined as $G_F = \frac{\sqrt{2}g_2^2}{8m_W^2} = 1.66 \times 10^{-5} \text{ GeV}^2$ [16].

Unlike the W^\pm bosons, the Z boson has a B_μ part and violates parity, coupling to both LH and RH chiral components with different strengths. Using the projection operators to obtain the vector and axial-vector couplings, c_V and c_A , respectively, the vertex factor is $-i\frac{g_2}{2}\gamma_\mu(c_V - c_A\gamma_5)$, where c_V and c_A are

$$c_V = T_3 - Q \sin^2 \theta_W, \quad c_A = T_3 \quad (2.34)$$

and are defined from the Z boson currents. The values for each fermion type are listed in

³ A massless W^\pm would imply a long-range weak force, while the weak force is known to be very short, and the W and Z bosons are known to be massive [27]. The fermions are also known to have mass.

Table 2.4. The neutral current interaction vertices are shown in Figure 2.1(c).

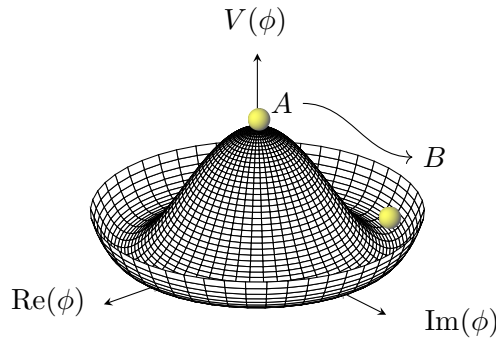
Fermion	T_3	Q	c_V	c_A
ν_e, ν_μ, ν_τ	0.5	0	0.5	0.5
e, μ, τ	-0.5	-1/2	$-\frac{1}{2} + 2 \sin^2 \theta_W = -0.0400$	-0.5
u, c, t	0.5	2/3	$\frac{1}{2} - \frac{4}{3} \sin^2 \theta_W = 0.193$	0.5
d, s, b	-0.5	1/3	$-\frac{1}{2} + \frac{2}{3} \sin^2 \theta_W = -0.347$	-0.5

 Table 2.4: Vector and axial-vector couplings of the fermions. A value of $\sin^2 \theta_W = 0.22$ from [16] is used (c.f. Equations 2.33 and 2.34).

The Higgs boson is not only needed to generate the masses of the fermions and W/Z bosons but also to address the WW scattering predicted by the EW Lagrangian, arising from the non-Abelian structure of the $SU(2)_L$ group. In these triple and quartic self-interactions among the gauge bosons, there is always a W pair present as the $SU(2)$ algebra does not generate a neutral vertex with only a photon or a Z boson. In the current form of the theory presented, the longitudinal vector boson scattering amplitudes at tree level grow with energy until unitarity is violated at the TeV scale ($\sigma(WW \rightarrow ZZ) \propto E^2$). The quantum mechanical sense of probability conservation in scattering amplitudes breaks down without the introduction of a scalar particle, such as the Higgs boson, that has the appropriate gauge couplings to exactly cancel the residual E^2 dependence.

2.1.5 Spontaneous symmetry breaking and the Higgs mechanism

In the following section, the Higgs-Brout-Englert-Guralnik-Hagen-Kibble mechanism of spontaneous symmetry breaking (SBB) is presented to give mass to the fermions and bosons, with the photon remaining massless, while maintaining the invariance of the $SU(2) \otimes U(1)$ gauge theory [28–32]. The gauge symmetries described in Sections 2.1.2, 2.1.3, and 2.1.4 are broken by a vacuum, triggering the SSB of the EW group to the QED subgroup (c.f., Equation 2.1), generating mass via the scalar Higgs boson.


 Figure 2.4: The Higgs potential for a complex scalar field described in Equation 2.36 for the $\mu^2 > 0$ case. The state A is the state before SSB, and B is the state after SSB when the Higgs fields acquires a vacuum expectation value.

In SSB, a complex scalar field composed of a weak isospin doublet, $\phi = \begin{pmatrix} \phi^+ \\ \phi^0 \end{pmatrix} = \frac{1}{\sqrt{2}} \begin{pmatrix} \phi_1 + i\phi_2 \\ \phi_3 + i\phi_4 \end{pmatrix}$, with a hypercharge of $Y_W = 1$, is introduced to Equation 2.30:

$$\mathcal{L}_{\text{SM}} = \mathcal{L}_{\text{Gauge}} + \mathcal{L}_f + \mathcal{L}_{\text{Higgs}} + \mathcal{L}_{\text{Yukawa}}, \quad (2.35)$$

with $\mathcal{L}_{\text{Yukawa}}$ the Yukawa term arising from the coupling of the scalar to fermions and $\mathcal{L}_{\text{Higgs}}$ a specific potential term that spontaneously breaks the symmetry:

$$\mathcal{L}_{\text{Higgs}} = \frac{1}{2} (\partial_\mu \phi)^\dagger (\partial^\mu \phi) - V(\phi), \quad V(\phi) = \frac{1}{2} \mu^2 \phi^\dagger \phi - \frac{1}{4} \lambda (\phi^\dagger \phi)^2, \quad (2.36)$$

with a ϕ^4 term describing self-interactions with intensity λ and $\lambda > 0$ such that Equation 2.36 has a finite minimum. Higher powers of ϕ are excluded since they would make the theory nonrenormalizable.

In the $\mu^2 > 0$ case, the minimum of the potential is where both fields are 0, in which case Equation 2.36 becomes a Lagrangian with a particle of mass μ . On the other hand, in the $\mu^2 < 0$ case, the potential has an infinite set of minima when $\nu^2 \equiv \frac{-\mu^2}{\lambda}$, where ν is the vacuum expectation value (VEV) of the scalar field (see Figure 2.4). A perturbation expansion is set up around the ground state as a polar decomposition and is transformed by the choice of the unitary gauge as

$$\phi(x) = \frac{1}{\sqrt{2}} \begin{pmatrix} \phi_1(x) + i\phi_2(x) \\ \nu + \eta(x) + i\phi_4(x) \end{pmatrix} \xrightarrow{\text{Unitary Gauge}} \frac{1}{\sqrt{2}} \begin{pmatrix} 0 \\ \nu + H(x) \end{pmatrix}, \quad (2.37)$$

where $\eta(x)$ and $\xi(x)$ are real fields, $H(x)$ is the Higgs field. The second component of $\phi(x)$ results from the choice of the unitary gauge to take care of the three massless Goldstone bosons arising from each broken symmetry, as predicted by the Goldstone theorem [33]. This is due to the choice of a direction ($\phi_3 = \nu$, $\phi_1 = \phi_2 = \phi_4 = 0$). With this unitary gauge, their degrees of freedom appear as the longitudinal polarization of the W^\pm and Z^0 bosons that acquire mass.

With this field, the $\text{SU}(2) \otimes \text{U}(1)$ invariance is maintained by defining the appropriate covariant derivatives (c.f. Equation 2.26) with the quantum numbers of the Higgs doublet designated to be $Y_W = 1$ and the lower component of the Higgs doublet to be neutral with a weak isospin of $T_3 = -\frac{1}{2}$. The $|D_\mu \phi|^2$ term in Equation 2.36 becomes

$$|D_\mu \phi|^2 = \frac{1}{2} (\partial_\mu H)^2 + \frac{1}{8} g_2^2 (\nu + H)^2 |W_\mu^1 + iW_\mu^2|^2 + \frac{1}{8} (\nu + H)^2 |g_2 W_\mu^3 - g_1 B_\mu|^2. \quad (2.38)$$

The new fields of the physical gauge bosons appear as $VV(\nu + H)^2$, where V is a vector boson. The masses of the bosons are determined by the ν^2 terms to be

$$M_W = \frac{1}{2} \nu g_2, \quad M_Z = \frac{1}{2} \nu \sqrt{g_2^2 + g_1^2}, \quad M_A = 0. \quad (2.39)$$

There is no term proportional to the A_μ term, so the photon remains massless. The VVH and $VVHH$ terms give rise to the triple and quartic couplings between the gauge bosons and one or two Higgs bosons (see Figure 2.5(c)). The Lagrangian also predicts self-interactions of the

Higgs boson, shown in Figure 2.5(b). The real scalar field is the Higgs boson with a mass of

$$m_H = \sqrt{2\lambda\nu^2}, \quad \nu = \sqrt{\frac{1}{\sqrt{2}G_F}} = 246.221 \text{ GeV}. \quad (2.40)$$

The masses of the fermions are generated by the Yukawa term in Equation 2.35 when the Higgs field acquires a VEV and spontaneously breaks SU(2) symmetry. The interaction vertex of the Higgs coupling to fermions is shown in Figure 2.5(a), and an important consequence of the Yukawa term is that the $Hf\bar{f}$ interaction is directly proportional to the mass of the fermion. The Yukawa Lagrangian for the down-type fermions, as written in [14], is

$$\mathcal{L}_{\text{Yukawa}_d} = -\lambda_e (\bar{L}_L \phi E_R + h.c.) - \lambda_d (\bar{Q}_L \phi D_R + h.c.), \quad (2.41)$$

where λ_e (λ_d) is the Yukawa constant for leptons (down-type quarks). The total hypercharge of each term is zero since the Higgs boson has a hypercharge of $Y_W(\phi) = 1$, while $Y_W(L_L) = -1$, $Y_W(E_R) = -2$, $Y_W(Q_L) = 1/3$, and $Y_W(D_R) = -2/3$ (c.f. Table 2.2). The SM does not generate neutrino masses since it does not contain right-handed neutrinos. They are, however, known to have mass from neutrino oscillation studies; this shortcoming of the SM is discussed in Section 2.4.

For up-type quarks with $Y_W(U_R) = 4/3$, a Yukawa term of form $Q_L \phi U_R$ is hypercharge-violating with $Y_W = -1/3 + 1 + 4/3 \neq 0$. An SU(2) property, though, is that the conjugate doublet transforms in the same way as the doublet [15]. Therefore the following conjugate Higgs

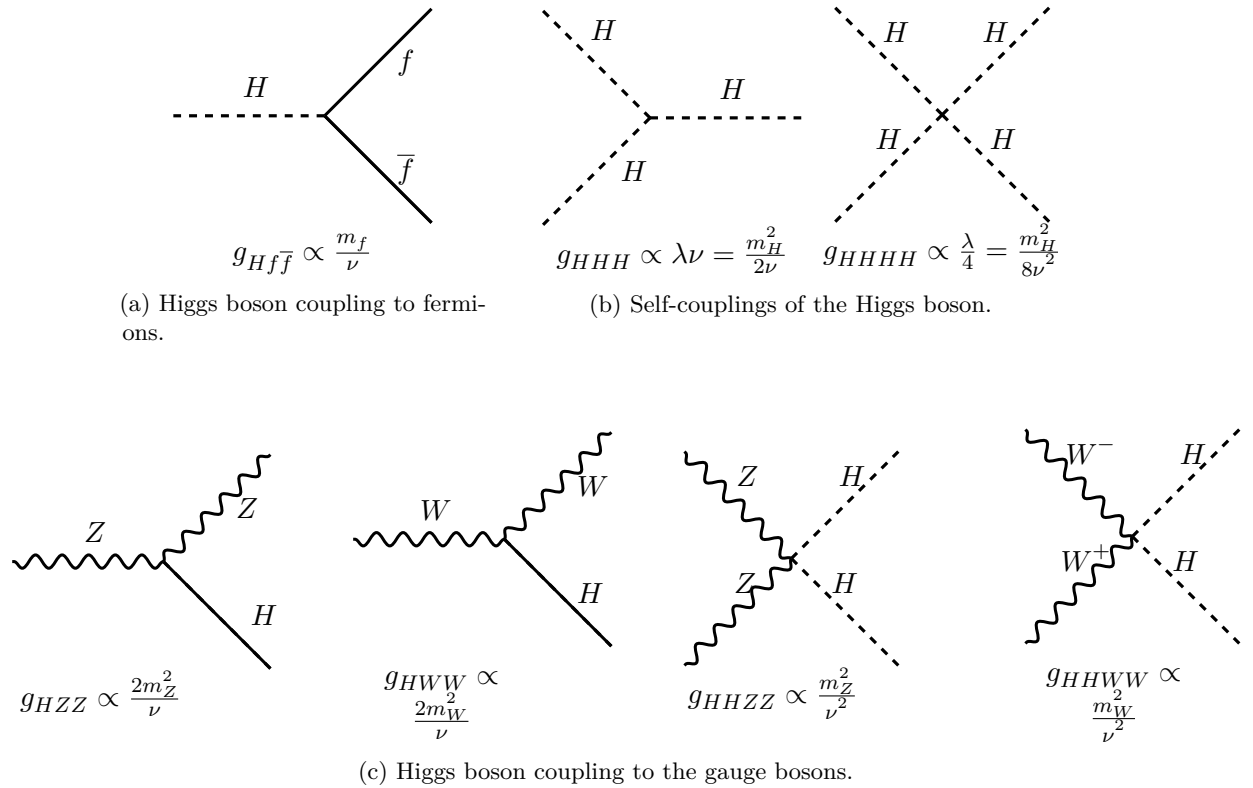


Figure 2.5: Higgs boson interaction vertices. The coupling strength is shown below each diagram.

doublet is used:

$$\tilde{\phi} = i\tau_2\phi^* = \begin{pmatrix} \phi^{0*} \\ -\phi^- \end{pmatrix} \rightarrow \begin{pmatrix} \nu + H(x) \\ 0 \end{pmatrix}, \quad Y(\tilde{\phi}) = -1$$

and the Yukawa Lagrangian for up-type quarks is

$$\mathcal{L}_{\text{Yukawa}_u} = -\lambda_u (\bar{Q}_L \tilde{\phi} D_R + h.c.). \quad (2.42)$$

This form adequately describes only one generation of quarks. To describe the three known generations, the Yukawa coupling in Equation 2.42 is written in terms of the quark mass matrices in the fermion generation space:

$$M_{i,j}^u = \lambda_{i,j}^u \frac{\nu}{\sqrt{2}}, \quad M_{i,j}^d = \lambda_{i,j}^d \frac{\nu}{\sqrt{2}}.$$

These matrices are not diagonal in the generation space, so the mass matrices need to be diagonalized in order to obtain the mass eigenstates. The up- and down-type Yukawa matrices are diagonalized separately with the unitary transformation matrices $V_{L,u}$, $V_{R,u}$, $V_{L,d}$, $V_{R,d}$ since up-type quarks acquire mass while neutrinos do not in the SM:

$$\text{diag}(m_u, m_c, m_t) = \frac{\nu}{\sqrt{2}} V_{L,u} \lambda^u V_{R,u}^\dagger \quad (2.43)$$

$$\text{diag}(m_d, m_s, m_b) = \frac{\nu}{\sqrt{2}} V_{L,d} \lambda^d V_{R,d}^\dagger \quad (2.44)$$

The charged current interaction now has a flavor structure encoded in the CKM matrix, with $V_{\text{CKM}} = V_{L,u} V_{L,d}^\dagger$ that connects the LH up-type quark of one generation to the LH down-type quark of another generation [34, 35]. This quark-mixing matrix is the source of \mathcal{CP} violation in the SM, which is further discussed in Section 2.1.7.

After SSB, the full SM Lagrangian in a compact form is

$$\mathcal{L}_{\text{SM}} = \underbrace{-\frac{1}{4} F_{\mu\nu} F^{\mu\nu}}_{\text{1st term}} + \underbrace{i\bar{\psi} \not{D} \psi}_{\text{2nd term}} + \underbrace{D_\mu \phi^\dagger D^\mu \phi - V(\phi)}_{\text{3rd term}} + \underbrace{\bar{\psi}_L \lambda \phi \psi_R + h.c.}_{\text{4th term}},$$

where the first term describes the force carriers, the second term the quarks and leptons, as well as their interactions, the third term the Higgs boson, and the fourth term the masses of the quarks and leptons.

2.1.6 The Higgs boson production and decay modes

The Higgs boson was the last undiscovered particle of the SM until its discovery by the ATLAS and CMS Collaborations at the LHC in 2012, about 50 years after it was first postulated [1]. The Higgs boson production processes at a hadron collider such as the LHC are discussed in Section 2.1.6.1. Then, its decay modes, through which its signal is identified at the LHC, are discussed in Section 2.1.6.2.

2.1.6.1 Higgs boson production

The Higgs boson is predicted to be produced through four main processes at the LHC: gluon-gluon fusion (ggH), vector boson fusion production (VBF), in association with a vector boson (VH), and in association with a heavy quark pair ($q\bar{q}H$). The analyses presented in Chapters 5 and 6 target the ggH and VBF processes. The LO Feynman diagrams for these processes are shown in Figure 2.6. The cross sections as a function of the center-of-mass energy are shown in Figure 2.7, with the cross sections at $\sqrt{s} = 7, 8, \text{ and } 13$ TeV listed in Table 2.5. Their calculations depend on QCD and EW corrections, as well as, the PDFs of the gluon(s) in the proton.

\sqrt{s}	Production cross section for $m_H = 125$ GeV [pb]					Total
	ggH	VBF	WH	ZH	$t\bar{t}H$	
7	$15.3^{+10\%}_{-10\%}$	$1.24^{+2\%}_{-2\%}$	$0.58^{+3\%}_{-3\%}$	$0.34^{+4\%}_{-4\%}$	$0.09^{+8\%}_{-14\%}$	17.5
8	$19.5^{+10\%}_{-11\%}$	$1.60^{+2\%}_{-2\%}$	$0.70^{+3\%}_{-3\%}$	$0.42^{+5\%}_{-5\%}$	$0.13^{+8\%}_{-8\%}$	22.3
13	$44.1^{+11\%}_{-11\%}$	$3.78^{+2\%}_{-2\%}$	$1.37^{+2\%}_{-2\%}$	$0.88^{+5\%}_{-5\%}$	$0.51^{+9\%}_{-13\%}$	50.6

Table 2.5: Higgs boson production cross sections at the LHC. Numbers from [16].

Gluon-gluon fusion At the LHC, ggH is the dominant production process. Since the gluon is massless, the Higgs boson is produced via a virtual loop of heavy fermions (usually top quarks, see Figure 2.6). At LO, the cross section is

$$\sigma_{\text{LO}}(gg \rightarrow H) \xrightarrow{m_t \rightarrow \infty} \frac{G_F \alpha_S^2}{288 \sqrt{2} \pi} \left| \sum_q F(\tau_q) \right|^2 \quad (2.45)$$

in the top quark mass limit ($m_t \rightarrow \infty$), where $F(q)$ is a form factor approaching 1 for $m_q \gg m_H/2$ and $\tau_q = \frac{m_H^2}{4m_q^2}$ [37]. Calculations with a finite top mass show the deviation using this limit to be less than 1% at NNLO [38]. The bottom quark loop has a 5–10% contribution to the cross section at NLO, and the other four light quarks are negligible at <1%.⁴

At LO, the Higgs boson is produced without transverse momentum. Higher order processes include qg and $q\bar{q}$ processes, additional virtual corrections, and the radiation of gluons in the final state that form jets, from which the Higgs boson recoils and balances the transverse momentum. The QCD corrections are calculated with NLO perturbation theory, with a k -factor of 1.8–2.0 [37, 39], where the k -factor relates the leading order and the next leading order:

$$k = \frac{\sigma_{\text{NLO}}}{\sigma_{\text{LO}}}, \quad (2.46)$$

The NNLO contributions are calculated in the top quark mass limit and increase the cross section by an additional $\sim 20\%$ [40]. The calculations have a significant renormalization scale dependence until N³LO is reached. The N³LO contributions correct the NNLO cross section by about 16% and reduce the scale dependence of the NNLO result [41]. EW contributions from radiated photons computed at NLO increase the cross section by $\sim 5\%$ [42].

⁴ The full bottom quark mass dependence is included in the calculation due to its relatively small mass.

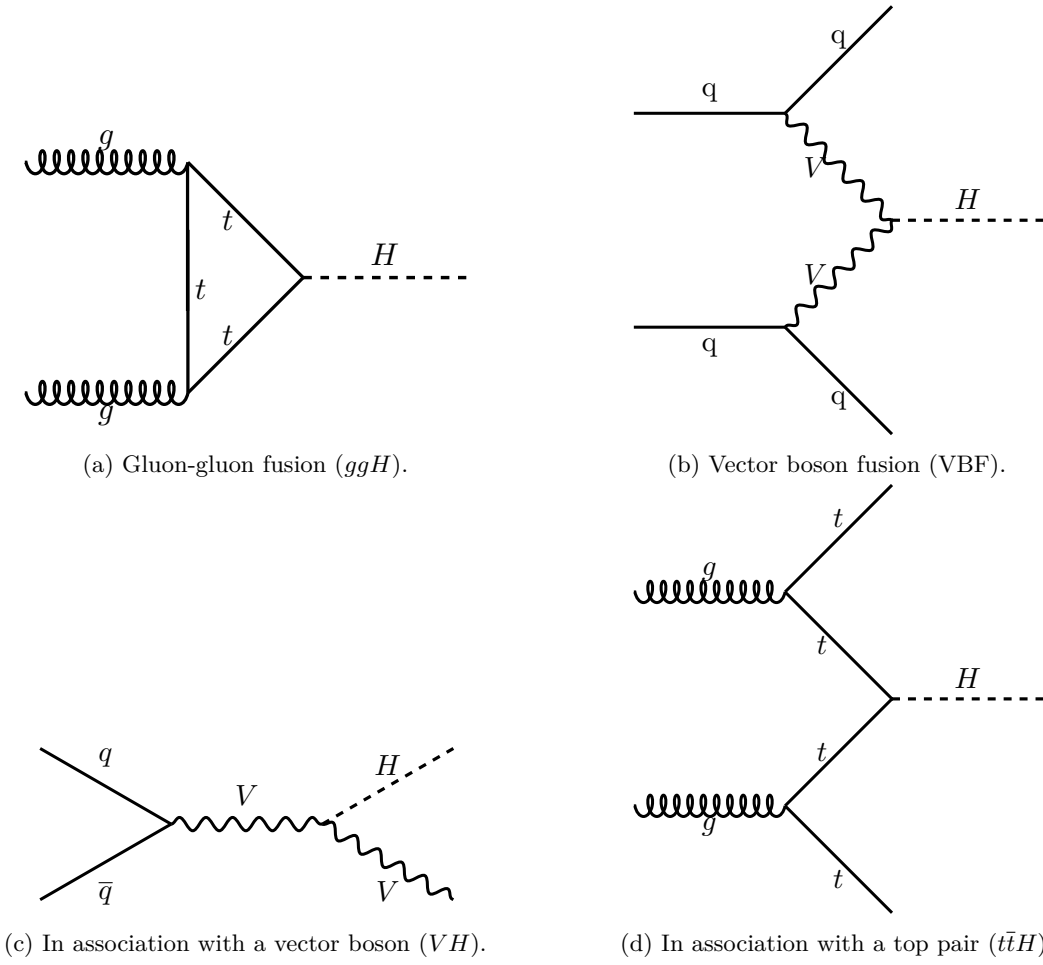
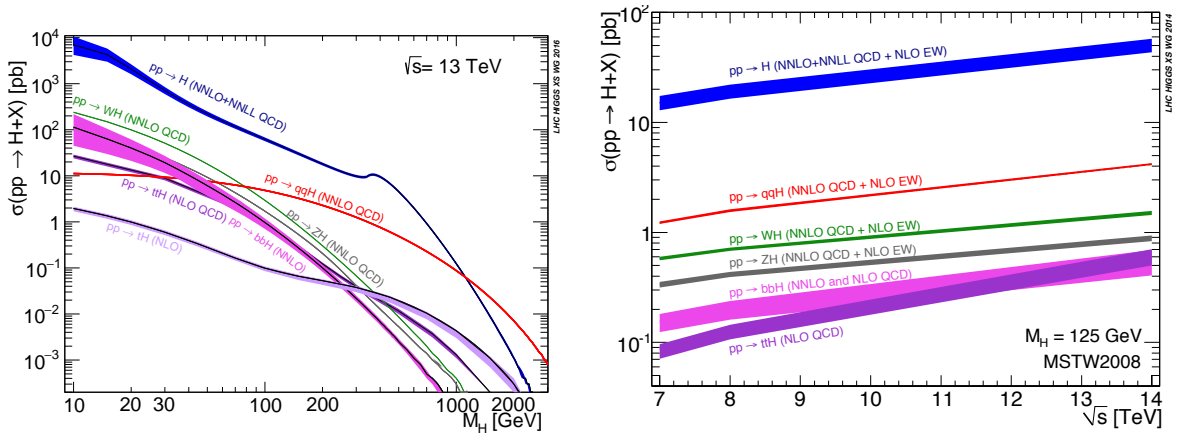


Figure 2.6: Feynman diagrams of the main Higgs boson production processes at the LHC.


 Figure 2.7: Cross sections of the Higgs boson production processes at $\sqrt{s} = 13$ TeV vs. the mass of the Higgs boson (left) and \sqrt{s} (right) based on SM-like couplings. EW corrections are not included. Taken from [36].

Due to the large contribution of higher orders to the ggH cross section and their unique experimental signature, Higgs boson couplings measurements, such as the one presented in this dissertation, search for Higgs bosons in production with one or two additional jets. A correct description of the Higgs boson p_T distribution is important for the event selection of additional jets in this dissertation. The differential ggH cross section as a function of the Higgs boson p_T depends on the top and bottom quark masses, with the top quark mass dominating at high p_T where the top quark mass limit becomes invalid [43, 44].

Vector boson fusion The VBF production process is the second most common at the LHC. Although its cross section is $\mathcal{O}(1)$ less than the ggH cross section, it has a distinct experimental signature. Its interference effects with the ggH process are below the percent level [45]. As can be seen in the LO diagram in Figure 2.6(b), the VBF Higgs production is accompanied by two outgoing quarks that hadronize to form high- p_T jets. The jets from the t -diagram are typically produced in opposite directions of the laboratory frame (high η and close to the incoming proton beams, with the Higgs boson in the center of the laboratory frame). This signature improves the sensitivity of analyses such as those described in Chapters 5 and 6. In addition, unlike the ggH process, the LO calculation does not need QCD corrections.

The NLO calculations approximate the cross section with the t - and u -diagrams (see Figure 2.6(b)) since the s -channel and the interferences are suppressed after VBF event selections. At NLO, EW corrections reduce the VBF cross section by 5%, while QCD corrections increase it by the same order [46]. The NNLO contributions increase the VBF cross section by less than 1% and reduce the theoretical uncertainties from 10–15% to 1–2% [47]. The PDF uncertainty has a $\sim 2\%$ impact on the cross section [48]. Since the incoming quarks are not connected by color fields, there is no additional gluon exchange between them in the t -channel, meaning QCD corrections around the Higgs boson (in the central laboratory frame) are negligible. This lack of hadronic activity, in addition to the accompanying jets, makes the VBF process distinguishable from SM processes.

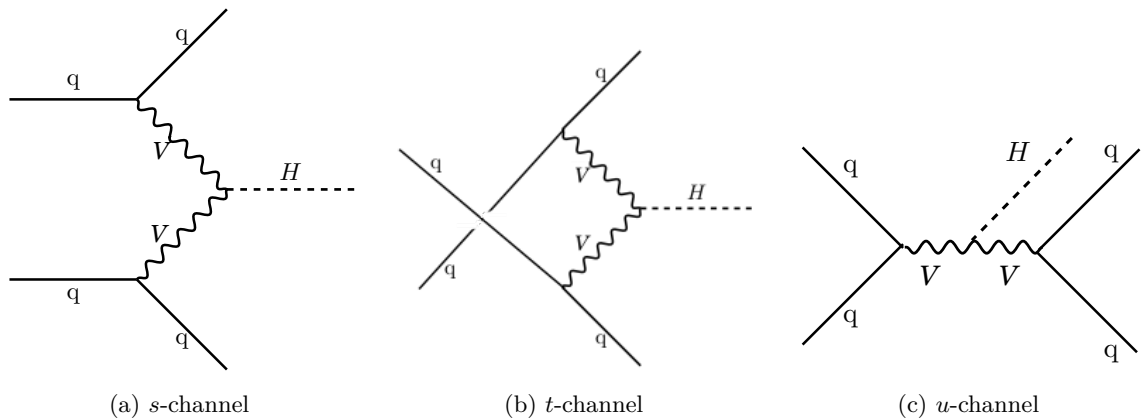


Figure 2.8: Feynman diagrams of the VBF production process. Topologies for s -, t -, and u -channel contributions to $qq \rightarrow qqH$ in LO are shown. The gap in the quark line of the t -channel diagram illustrates that crossing of the quark lines is not a four-fermion vertex.

Association with a vector boson The VH production process is the next most common at the LHC. Its cross section is calculated to NNLO accuracy for QCD corrections, with the NLO

increasing the LO cross section by 13–30% and the NNLO $-(1 \text{ to } 4)\%$, depending on the choices of μ_F and μ_R [49]. The EW corrections at NLO decrease the LO cross section by 5–10% [50].

Association with a heavy quark pair The $q\bar{q}H$ production process typically involves top quarks. Its cross section is $\mathcal{O}(2)$ lower than the ggH process, but it is important in probing the Higgs Yukawa coupling to top quarks. QCD corrections up to NLO are available and find a k -factor relating the LO and the NLO to be about 1.2 at the LHC [51].

2.1.6.2 Higgs boson decay

The Higgs boson can decay via $H \rightarrow f\bar{f}, V\bar{V}$ for kinematically allowed decay modes where $m_H > 2m_f, m_V$. It can, thus, decay to all known fermions except the top quark. For cases where the Higgs boson decays to a pair of W or Z bosons, one of the bosons is virtual since $m_H < 2m_W, 2m_Z$, i.e., $H \rightarrow WW^*$ and $H \rightarrow ZZ^*$. The branching ratio of the decay modes depends on the mass of its couplings to particle i , since the Higgs boson coupling is proportional to the mass. The total decay width of the Higgs boson is

$$\Gamma_{\text{total}} = \sum \Gamma_i, \quad \tau = \frac{1}{\Gamma_{\text{total}}}, \quad \text{BF}_i = \frac{\Gamma_i}{\Gamma_{\text{total}}}, \quad (2.47)$$

where τ is the particle lifetime, BF is the branching ratio to final state i (see Figure 2.9). In addition to the Higgs boson coupling properties, decay width measurements are also important because a wider decay width measured in experiment could, for instance, be a sign of dark matter candidates, where the Higgs boson decays to particles that are not detected [36].

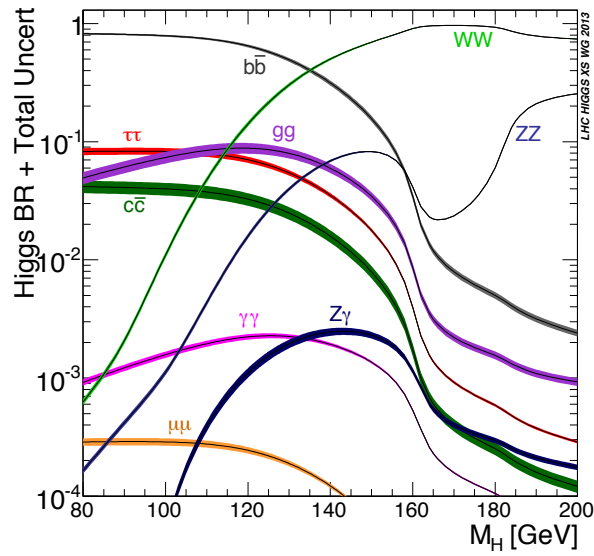


Figure 2.9: Branching ratios of the SM Higgs boson. Taken from [44].

The predicted Higgs boson branching ratios for the known decay channels are shown in Figure 2.9. The results from the Higgs boson discovery at the LHC in several of its decay channels are shown in Figure 2.10. They are consistent with the predicted Higgs boson coupling dependence on mass and the predicted Higgs boson mass of 125 GeV. This particular mass has important consequences in the SM since it determines the quartic coupling at the EW scale.

Of the bosonic decay channels, the $H \rightarrow \gamma\gamma$ channel is one of the most promising for Higgs boson studies at the LHC. The Higgs boson does not couple directly to photons, but rather through virtual loops occurring in second order perturbation theory. This means that the branching ratio of the two-photon channel is small. However, this channel provides a clear experimental signature with low background. In addition, the high di-photon invariant mass resolution provides a clear identification of the predicted Higgs mass signal. The $H \rightarrow ZZ^* \rightarrow 4\ell$ decay channel is also promising due to its distinctive signatures of four leptons. It has a smaller branching ratio than the $H \rightarrow WW^*$ because the latter has two times more degrees of freedom due to the ± 1 charges of the W^\pm boson. In addition, it has a larger phase space due to the smaller W boson mass.

Of the fermionic decay channels, the decay to two tau leptons has the highest sensitivity at the LHC. Although the b quarks are the heaviest of the known fermions to which the Higgs boson can decay, the $H \rightarrow b\bar{b}$ channel suffers from high background conditions. In addition, although the $H \rightarrow c\bar{c}$ branching fraction is higher than for tau leptons, Higgs boson decays to two c quarks are difficult to distinguish from QCD background. This is also the case for the experimentally hopeless Higgs boson decay channel to a pair of gluons. The last two Higgs boson decays to the other known leptons (a pair of muons and a pair of electrons) have the disadvantage of a low branching ratio but the advantage of better background conditions.

2.1.7 Higgs boson \mathcal{CP} properties

In addition to measurements of the Higgs boson decay width and coupling properties, tests of its spin and parity quantum numbers are vital in confirming that the discovered Higgs boson is consistent with the SM hypothesis. If it deviates, the Higgs boson can be a candidate for explaining the known matter-antimatter asymmetry of the universe. This is one of the outstanding questions of particle physics because the Big Bang produced equal amount of matter and antimatter [54]. Since this is not the case in the current universe, the laws of physics act differently for matter and antimatter and the prerequisite for this phenomenon is violation of \mathcal{CP} symmetry, or \mathcal{CP} violation. \mathcal{CP} symmetry is a composite of two fundamental symmetries:

- Charge conjugation (\mathcal{C}) symmetry: Symmetry between positive and negative charge.
- Parity (\mathcal{P}) symmetry: Symmetry of spatial coordinates previously discussed in Section 2.1.4 (see Equation 2.19).

\mathcal{CP} conjugation of a left-handed, negatively-charged particle transforms it into a right-handed, positively-charged particle. One source of \mathcal{CP} violation comes from the quark sector and involves the CKM matrix. \mathcal{CP} violation has been observed in this sector but can only account for a small portion of \mathcal{CP} violation [34, 35]. In principle, there are other sources of \mathcal{CP} violation:

- In the strong interaction, which is expected to be too small to account for the necessary \mathcal{CP} violation in the early universe. It is discussed in the strong \mathcal{CP} problem in Section 2.4 and has not been observed
- In the lepton sector involving the PMNS matrix [55]. \mathcal{CP} violation in this sector should be observed, but experimental tests are uncertain.

If experimental evidence of \mathcal{CP} violation in the lepton sector is found to be small, adding new particles or interactions to the SM can introduce new sources of \mathcal{CP} violation since \mathcal{CP} is not a

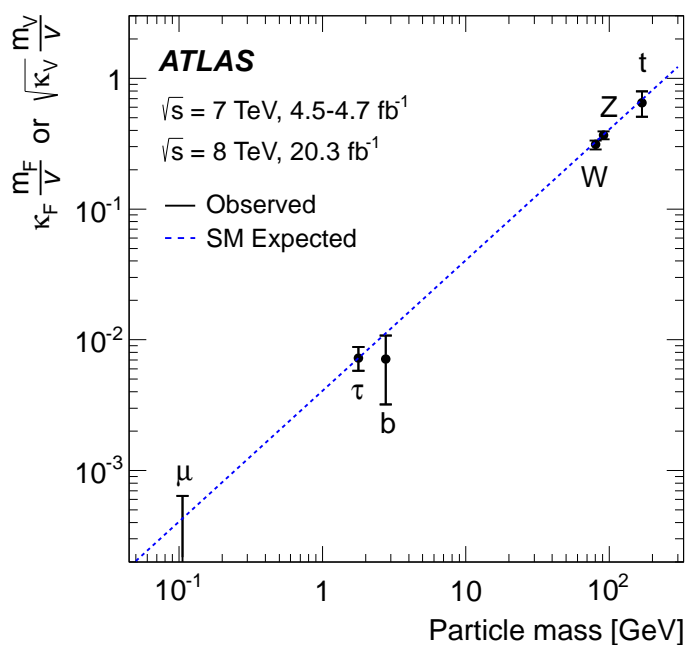
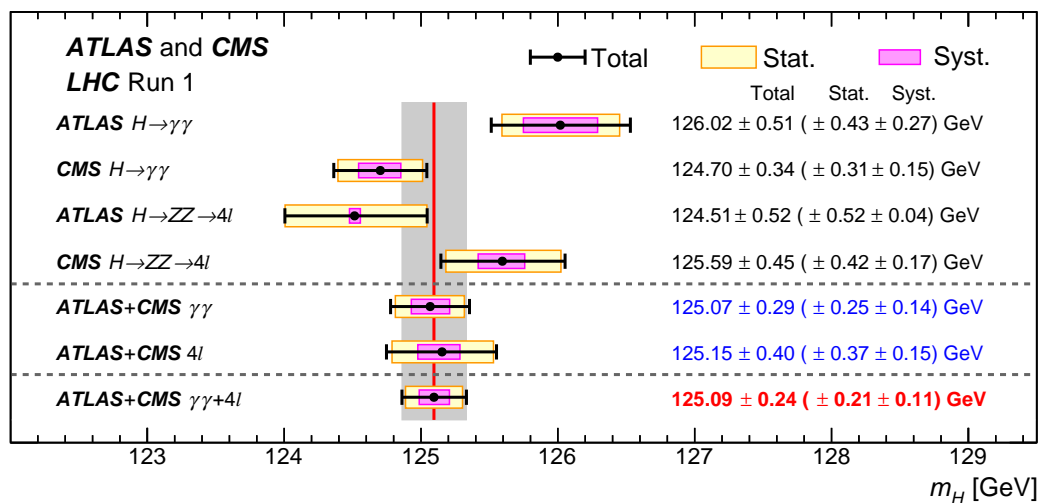


Figure 2.10: The measured Higgs boson mass (top) and coupling strength to the fermions and bosons (bottom). The dashed line shows the predicted mass dependence of the Higgs boson coupling. Taken from [52, 53].

symmetry of nature. This can happen, for example, in the Higgs sector, as is later discussed in Section 2.3 and Chapter 6.

So far, deviations from the SM Higgs boson with $\mathcal{C}P$ quantum numbers $J^P = 0^+$ have been excluded in the bosonic decay channels. The $J^P = 0^-, 1^+, 1^-,$ and 2^+ hypotheses have been rejected at the 99.974, 99.999, 99.997 and 99.989% confidence level, respectively [56, 57]. Studies of Higgs $\mathcal{C}P$ properties in fermionic decay channels are still in progress and provide unique information that the bosonic decay channels do not. This is due to the fact that, while $\mathcal{C}P$ -odd

Higgs bosons do not couple to gauge bosons at tree-level, they do couple to fermions at tree-level. The next sections describe the physics of tau leptons, especially their polarization, and their application in tests of Higgs \mathcal{CP} mixing. The analysis of Higgs \mathcal{CP} mixing with tau lepton decays is presented in Chapter 6.

2.2 Physics with tau leptons

In this section, a description of tau leptons is provided, with details on their polarization properties, followed by the application of tau polarization in Higgs \mathcal{CP} studies. Tau leptons play an important role in the physics agenda of the LHC. They are good probes for EW symmetry breaking since the Higgs boson couples proportionally to mass and tau leptons are the heaviest of the known leptons. In addition, many signatures of models beyond the Standard Model contain tau leptons in the final state. In particular, in the Minimal Supersymmetric Model (MSSM) described later in Section 2.5, tau leptons have an enhanced coupling to the MSSM Higgs boson over large regions of parameter space, while the couplings to vector bosons are suppressed. Tau leptons are also pertinent in polarization studies since they are the only known lepton whose polarization can be experimentally measured at the LHC. They are also excellent probes for Higgs \mathcal{CP} mixing because the fermionic decay channels of the Higgs boson exhibit \mathcal{CP} violating effects at tree level whereas \mathcal{CP} mixing in the bosonic decay channels can only occur via loops.

Tau leptons are the heaviest of the known leptons with a mass of 1777 ± 0.16 MeV [16, 58]. They are short-lived, with a mean lifetime of $(290.6 \pm 1.0) \times 10^{-15}$ s, and have a mean free path length of $87 \mu\text{m}$ [16]. Therefore, tau leptons typically decay in the beam pipe, before reaching the ATLAS detector and are reconstructed from their decay products.⁵ The tau lepton is the only lepton that can decay both leptonically and hadronically. Its decay modes and branching ratios are shown in Table 2.6.

2.2.1 Tau lepton polarization

The polarization states of the tau lepton are experimentally accessible via the decay product kinematics because the angular distributions of tau decay products are affected by the polarization of the tau lepton [59]. Such polarization measurements are important in measuring the spin of new $\tau^\pm \tau^\mp$ resonances, such as the Higgs boson, as previously discussed in Section 2.1.7. Tau polarization measurements are useful in other analyses as well. For example, they contain information on SUSY couplings. The average tau polarization in the $\tilde{\chi}_2^0 \rightarrow \tilde{\tau}_1 \tau \rightarrow \tau \tau \tilde{\chi}_1^0$ decay depends on the couplings between τ , $\tilde{\tau}_1$, and $\tilde{\chi}_j^0$, where a tilde denotes a superpartner in SUSY [60]. Moreover, polarization measurements can be used to discriminate against background processes in searches for charged MSSM Higgs bosons (described later in Section 2.5) because the main SM backgrounds have an opposite polarization from, for example, $H^- \rightarrow \tau_R^- \bar{\nu}_R$ decays.

In this section, polarization measurements of individual tau leptons in the simplest case of the $\tau \rightarrow \pi \nu_\tau$ decay are described, followed by the $\tau \rightarrow \rho \nu_\tau$ decay, which is more sensitive to tau polarization at the LHC. These two tau decay modes are used in the Higgs \mathcal{CP} studies of Chapter 6. This provides the theoretical motivation for the importance of correctly classifying

⁵ With the new inner B layer (IBL), discussed later in Section 3.2.2, bringing the detector closer to the beam pipe, it may be possible to detect tau leptons directly.

		τ Decay Mode	Branching Fraction (%)
Leptonic		$\tau^\pm \rightarrow e^\pm \begin{pmatrix} (-) \\ \nu_e \end{pmatrix} \begin{pmatrix} (-) \\ \nu_\tau \end{pmatrix}$	17.84 ± 0.04
		$\tau^\pm \rightarrow \mu^\pm \begin{pmatrix} (-) \\ \nu_\mu \end{pmatrix} \begin{pmatrix} (-) \\ \nu_\tau \end{pmatrix}$	17.41 ± 0.04
Hadronic	One-prong	$\tau^\pm \rightarrow \pi^\pm (\geq 0 \pi^0) \begin{pmatrix} (-) \\ \nu_\tau \end{pmatrix}$	49.46 ± 0.10
		$\tau^\pm \rightarrow \pi^\pm \begin{pmatrix} (-) \\ \nu_\tau \end{pmatrix}$	10.83 ± 0.06
		$\tau^\pm \rightarrow \rho^\pm (\rightarrow \pi^\pm \pi^0) \begin{pmatrix} (-) \\ \nu_\tau \end{pmatrix}$	25.52 ± 0.09
		$\tau^\pm \rightarrow a_1 (\rightarrow \pi^\pm 2\pi^0) \begin{pmatrix} (-) \\ \nu_\tau \end{pmatrix}$	9.30 ± 0.11
		$\tau^\pm \rightarrow \pi^\pm 3\pi^0 \begin{pmatrix} (-) \\ \nu_\tau \end{pmatrix}$	1.05 ± 0.07
		$\tau^\pm \rightarrow h^\pm 4\pi^0 \begin{pmatrix} (-) \\ \nu_\tau \end{pmatrix}$	0.11 ± 0.04
Hadronic	Three-prong	$\tau^\pm \rightarrow \pi^\pm \pi^\mp \pi^\pm (\geq 0\pi^0) \begin{pmatrix} (-) \\ \nu_\tau \end{pmatrix}$	14.57 ± 0.07
		$\tau^\pm \rightarrow \pi^\pm \pi^\mp \pi^\pm \begin{pmatrix} (-) \\ \nu_\tau \end{pmatrix}$	8.99 ± 0.06
		$\tau^\pm \rightarrow \pi^\pm \pi^\mp \pi^\pm \pi^0 \begin{pmatrix} (-) \\ \nu_\tau \end{pmatrix}$	2.70 ± 0.08

Table 2.6: Decay modes and branching ratios of the τ lepton. The h^\pm symbol denotes a π^\pm or a K^\pm . Branching ratios for tau decays involving K^0 , ω , and/or η are not included. Numbers from [16].

tau lepton decay modes using dedicated reconstruction algorithms, such as the one that was developed during the work presented in Section 4.5.

In the $\tau \rightarrow \pi\nu_\tau$ decay, the decay kinematics are dictated by conservation of angular momentum and the fixed chirality of the ν_τ . Figure 2.11 provides diagrams showing that the neutrino takes the spin of the tau lepton, since the pion is a pseudoscalar, spin-less meson. Thus, the neutrino is emitted opposite to the spin direction of the tau lepton in $\tau^- \rightarrow \pi^- \nu_\tau$ (and in the same direction of the spin of the tau lepton in $\tau^+ \rightarrow \pi^+ \bar{\nu}_\tau$).

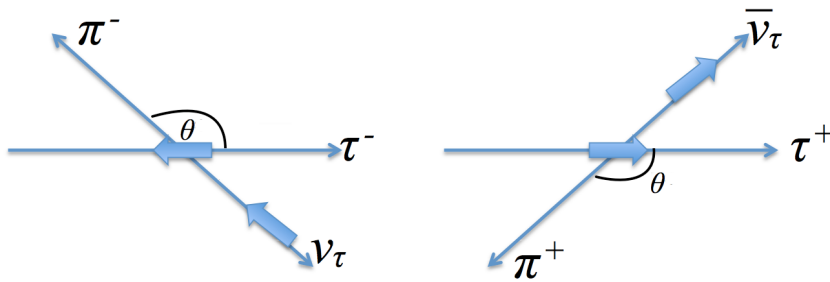


Figure 2.11: The decay $\tau \rightarrow \pi\nu_\tau$ in the rest frame of the τ (the thin horizontal arrow shows the flight direction of the tau in the lab frame) showing the preferred decay kinematics of the π and ν_τ decay products for a left handed τ^- (left) and a right-handed τ^+ (right). The other thin arrows show the directions of flight of the particles in the rest frame of the tau, and the thick arrows show the spin of the particles.

The distribution of the angle in the tau rest frame between the direction of the vector meson and the direction of the tau lepton's momentum, θ , depends on the polarization of the tau

lepton [60]:

$$\frac{1}{\Gamma_\tau} \frac{\Gamma_\pi}{d \cos \theta} \propto (1 + P_\tau \cos \theta) \quad (2.48)$$

where P_τ is the polarization of the tau lepton,

$$P_\tau = \frac{\sigma_R - \sigma_L}{\sigma_R + \sigma_L}, \quad (2.49)$$

and Γ is the decay width (c.f. Equation 2.47). A sample of purely RH (LH) tau leptons corresponds to $P_\tau = +1$ (-1). The angle, θ , depends on the kinematics of the decay:

$$\cos \theta = \frac{2x_h - 1 - a^2}{\beta(1 - a^2)}, \quad (2.50)$$

where $\beta = v/c \approx 1$ is the velocity of the tau lepton that is approximated to 1 for Z and H decays, and $x_h = E_h/E_\tau$ is the fraction of energy carried away by the hadron, h , which is the pion in this decay. The a factor is $a = m_h/m_\tau$, where m_h is the mass of the hadronic system. (Consequently, a can be ignored for the $\tau \rightarrow \pi\nu_\tau$ decay.) Equation 2.48 can be rewritten in terms of the decay kinematics to show that a RH (LH) tau leptons preferably decays to a hard (soft) pion:

$$\frac{1}{\Gamma_\tau} \frac{\Gamma_\pi}{dx_\pi} \propto 1 + P_\tau(2x_\pi - 1). \quad (2.51)$$

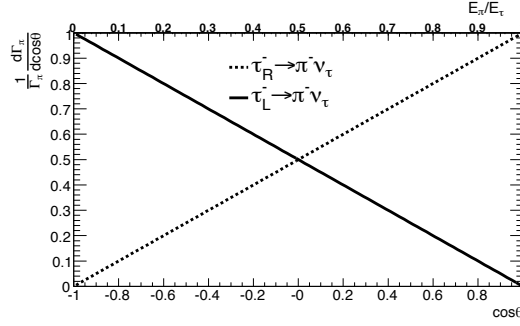
The distributions for LH and RH tau leptons are shown in Figure 2.12, where the linear dependence can be seen.

Unfortunately, the momentum direction of the tau lepton θ and the angle, θ , cannot be directly measured due to the presence of neutrinos in the tau decay. For the ρ decay case, however, helicity information is contained in the angle between the visible ρ decay products, which can be reconstructed. Tau polarization in the $\tau \rightarrow \rho\nu_\tau$ case is discussed next.

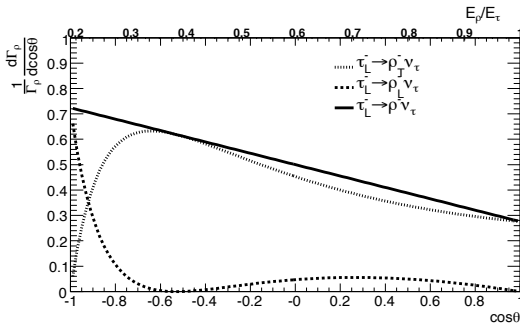
For the case of a tau lepton decaying into a vector meson, such as the ρ meson, that also carries spin, the situation is more complicated. For a tau lepton decaying through the ρ resonance, the ρ^\pm meson can be either longitudinally or transversely polarized due to conservation of angular momentum. The same spin possibilities exist for $\tau \rightarrow a_1\nu_\tau$ decays. Figure 2.13 shows the kinematics of the $\tau^- \rightarrow \rho^- \bar{\nu}_\tau$ decay in the rest frame of the tau lepton, which contain information on whether the ρ was longitudinally or transversely polarized. The angular distribution of the ρ^- decay products depends on the polarization of the tau lepton:

$$\begin{aligned} \frac{1}{\Gamma_\tau} \frac{\Gamma_T}{d \cos \theta} &\propto \frac{\frac{1}{2}m_\tau^2}{m_\tau^2 + 2m_\rho^2} (1 - P_\tau \cos \theta) \\ \frac{1}{\Gamma_\tau} \frac{\Gamma_L}{d \cos \theta} &\propto \frac{m_\rho^2}{m_\tau^2 + 2m_\rho^2} (1 + P_\tau \cos \theta), \end{aligned} \quad (2.52)$$

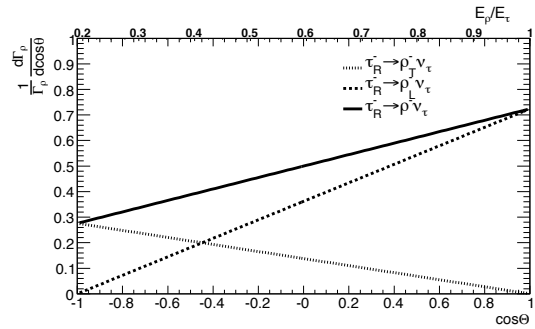
where the subscript T denotes the transverse vector meson state and L denotes the longitudinal vector meson state [61]. Compared to the $\tau \rightarrow \pi\nu_\tau$ case, this mixing of longitudinal and transverse polarized vector states leads to a loss of polarization sensitivity when the ρ meson polarization is not considered. Analogous to the $\tau \rightarrow \pi\nu_\tau$ case (c.f. Equation 2.51), the sum of Equations 2.52 can be rewritten in terms of the fraction of energy carried away by the vector



(a) Angular distribution of the angle between visible decay products (π^-) from the $\tau \rightarrow \pi \nu_\tau$ decay and the momentum direction of the tau lepton.



(b) Angular distribution of the visible decay products (ρ^-) from the $\tau^- \rightarrow \rho^- \nu_\tau$ decay and the momentum direction of the tau lepton.



(c) Angular distribution of the visible decay products (ρ^-) from the $\tau^+ \rightarrow \rho^+ \bar{\nu}_\tau$ decay and momentum direction of the tau lepton.

Figure 2.12: Angular distributions of the visible tau decay products (π^- in (a) and ρ^- in (b), (c)) and the momentum direction of the tau lepton for different tau polarization states. Taken from [61].

meson, x_ρ :

$$\frac{1}{\Gamma_\tau} \frac{d\Gamma}{dx_\rho} \propto \frac{1}{1-a^2} (1 + \alpha P_\tau \cos \theta), \quad \cos \theta = 1 + \alpha P_\tau \frac{2x_\rho - 1 - a^2}{1 - a^2}, \quad (2.53)$$

where $a = m_\rho/m_\tau$ [61]. The $\cos \theta$ distributions for transverse and longitudinal polarizations are shown in Figure 2.12, where the enhancement of hard longitudinally polarized and soft transversely polarized ρ states from a LH tau lepton is observed. If the transverse and longitudinal states are not distinguished, the sensitivity to P_τ is reduced by a factor of $\alpha = \frac{m_\tau^2 - 2m_\rho^2}{m_\tau^2 + 2m_\rho^2} \sim 1/2$. For the case of the decay via the a_1 , the factor almost vanishes.

Looking further at the visible decay products from the ρ meson, tau helicity information can be probed in the angle between the ρ direction of flight and its π^\pm decay product in the ρ rest frame, ψ [62]:

$$\cos \psi = \frac{m_\rho}{\sqrt{m_\rho^2 - 4m_\pi^2}} \frac{E_{\pi^\pm} - E_{\pi^0}}{|\vec{p}_{\pi^\pm} + \vec{p}_{\pi^0}|}. \quad (2.54)$$

This is because RH (LH) tau leptons produce more longitudinally (transversely) polarized ρ

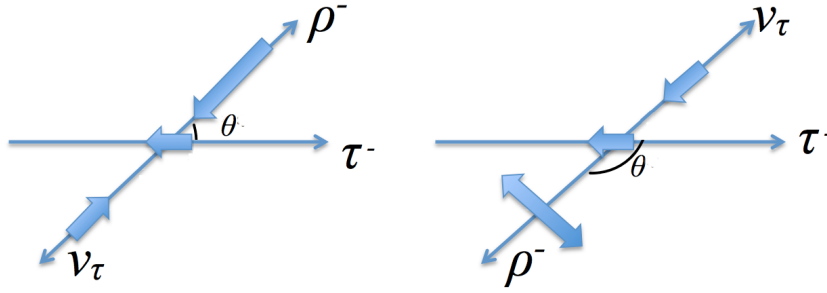


Figure 2.13: The $\tau^- \rightarrow \rho^- \bar{\nu}_\tau$ decay in the rest frame of the tau lepton for a longitudinally polarized ρ (left) and a transversely polarized ρ (right). The thin horizontal arrow shows the flight direction of the tau in the lab frame, the other thin arrows show the directions of flight of the tau decay products in the τ rest frame, and the thick arrows show the handedness of the particle.

mesons. From conservation of angular momentum, a longitudinally (transversely) polarized ρ meson preferably decays with angles of 0 or π ($\pi/2$). The spin of the ρ^\pm is transformed into orbital angular momentum in its decay into a π^\pm and a π^0 . When the spin of the ρ^- is perpendicular (parallel) to that of a left-handed τ^- lepton, the ρ^- is preferably emitted against (parallel to) the flight direction of the τ^- lepton. Thus, similarly, a boost of a transversely (longitudinally) polarized ρ in the tau lepton's direction of flight is suppressed (preferred) for left-handed tau leptons. These two cases can be distinguished by measuring the momenta of the π^\pm and the π^0 . If the two pions have similar momenta, then the ρ^- was transversely polarized. If the two pions have opposite momenta (one high, one low), then the ρ^- was longitudinally polarized. The angular distributions between the π^\pm and the ρ , in the rest frame of the ρ , separates these two polarization states [59].

It can be seen in Equation 2.54 that the angle, ψ , depends on the asymmetry in energies of the charged and neutral pions. It can be experimentally probed by dropping the term with m_ρ , which is difficult to reconstruct, and defining the observable Y :

$$Y_{\rho^\pm} = \frac{E_{\pi^\pm} - E_{\pi^0}}{E_{\pi^\pm} + E_{\pi^0}} \quad (2.55)$$

Another way to probe the helicity information contained in the ρ decay is to use polarimetric vectors, as is discussed in Section 2.3 [63].

In conclusion, for the ρ decay mode, tau polarization measurements can be performed using the visible decay products, while the $\tau \rightarrow \pi \nu_\tau$ decay relies also on the reconstruction of the neutrino four-momentum, which cannot be fully reconstructed at the LHC, as is discussed in Section 4. Moreover, with $m_\rho < m_{a_1}$, the ρ decay channel is more sensitive than the a_1 decay channel since polarization sensitivity depends on the boost of the vector meson emitted from the tau lepton in the tau rest frame. The angular distribution of the a_1 decay products is almost independent of the tau polarization.

Having shown that the preferred emission directions of the tau decay products encode the tau spin, the transverse spin correlations of a di-tau pair from a Higgs boson is discussed in the next section. This application of tau polarization allows one to probe possible \mathcal{CP} mixing in the Higgs sector.

2.3 Higgs \mathcal{CP} studies with tau leptons

As already discussed in Section 2.1.7, \mathcal{CP} violation can exist in the Higgs sector. The Lagrangian describing the fermion couplings of a Higgs boson, h , with variable \mathcal{CP} mixing hypotheses of a \mathcal{CP} -even component and a \mathcal{CP} -odd component is

$$\mathcal{L}_{hf\bar{f}} = - \sum_{f \in \text{fermions}} \frac{m_f}{v} h \bar{f} (a_f + i b_f \gamma_5) f, \quad (2.56)$$

where a_f and b_f are the reduced scalar and pseudoscalar Yukawa couplings, respectively. For the pure scalar SM Higgs, $a_f = 1$ and $b_f = 0$. For a pure pseudoscalar, $a_f = 0$ and $b_f \neq 0$. A mixed \mathcal{CP} Higgs boson has non-zero couplings, $a_f \neq 0$ and $b_f \neq 0$, leading to \mathcal{CP} violating effects in the $h \rightarrow f\bar{f}$ couplings for quarks and leptons at the Born level. However, for bosons, which are not \mathcal{CP} eigenstates, only the scalar $\mathcal{CP} = +1$ component of h couples to W^+W^- and ZZ bosons. If there is any pseudoscalar component for the boson pairs, it is small since it comes from loops.

Equation 2.56 can be rewritten for the coupling to tau leptons:

$$\begin{aligned} \mathcal{L}_{h\tau\bar{\tau}} &= - \left(\sqrt{2} G_F \right)^{\frac{1}{2}} m_\tau h (a_\tau \bar{\tau} \tau + b_\tau \bar{\tau} i \gamma_5 \tau) \\ &= -g_\tau h (\cos \phi_\tau \bar{\tau} \tau + \sin \phi_\tau \bar{\tau} i \gamma_5 \tau), \end{aligned} \quad (2.57)$$

where g_τ is the effective strength of the τ -Yukawa interaction

$$g_\tau = \left(\sqrt{2} G_F \right)^{\frac{1}{2}} m_\tau \sqrt{a_\tau^2 + b_\tau^2} \quad (2.58)$$

and ϕ_τ is the \mathcal{CP} mixing angle quantifying the degree of mixing between the scalar and pseudoscalar Higgs components that couple to tau leptons:

$$\tan \phi_\tau = \frac{b_\tau}{a_\tau}. \quad (2.59)$$

For a purely \mathcal{CP} -even Higgs boson predicted by the SM, $\phi_\tau = 0$ and $g_\tau = \left(\sqrt{2} G_F \right)^{\frac{1}{2}} m_\tau$, and $\phi_\tau \neq 0$ is a sign of new physics.

The transverse tau spin correlations from a Higgs boson, which are encoded in the angular distributions of the tau decay products, provide unique information on Higgs \mathcal{CP} properties. This can be seen when the decay width is parametrized to show its dependence on tau spin states:

$$\begin{aligned} \Gamma(h \rightarrow \tau^- \tau^+) &\sim 1 - s_z^+ s_z^- + \cos(2\phi_\tau) (\mathbf{s}_\perp^- \cdot \mathbf{s}_\perp^+) + \sin(2\phi_\tau) \left((\mathbf{s}_\perp^+ \times \mathbf{s}_\perp^-) \cdot \hat{\mathbf{k}}^- \right) \\ \Gamma(H(A) \rightarrow \tau^- \tau^+) &\sim 1 - s_z^+ s_z^- \quad (\text{---}) \quad s_\perp^+ s_\perp^-, \end{aligned} \quad (2.60)$$

where H (A) is the purely \mathcal{CP} -even, scalar (purely \mathcal{CP} -odd, pseudoscalar) Higgs boson, \hat{s}^\pm are the unit spin vectors of the τ^\pm lepton in the respective tau frames, and s_z^\pm (s_\perp^\pm) are the longitudinal (transverse) components of \hat{s}^\pm with respect to $\hat{\mathbf{k}}^-$ [64]. The probability for the configurations of longitudinal polarization of tau leptons depends on the origin of the tau pair and is the same for a scalar and pseudoscalar H and A boson, as listed in Table 2.7. The longitudinal tau polarization

in tau pair production from a Higgs boson are induced at higher-order EW corrections and are small [65]. On the other hand, the different transverse spin vector correlations for a SM H boson and a purely \mathcal{CP} -odd A boson lead to observably different tau decay kinematics. As shown in Figure 2.14, in the $\tau^\pm\tau^\mp$ Zero-Momentum-Frame (ZMF), the visible tau decay products from a scalar SM Higgs boson, H , (pseudoscalar Higgs boson, A) are preferably emitted antiparallel (parallel) to each other.

Origin	P_{τ^+}	P_{τ^-}	Probability
Neutral Higgs bosons: H, A	$P_{\tau^+} = +1$	$P_{\tau^+} = -1$	0.5
	$P_{\tau^+} = -1$	$P_{\tau^+} = +1$	0.5
Neutral vector boson: Z/γ^*	$P_{\tau^+} = +1$	$P_{\tau^+} = +1$	P_Z
	$P_{\tau^+} = -1$	$P_{\tau^+} = -1$	$1 - P_Z$

Table 2.7: Probability of the longitudinal polarization configurations of a tau lepton pair from different origins, where P_Z is the polarization of the Z boson and P_{τ^\pm} is the polarization of the tau lepton. Values from [66].

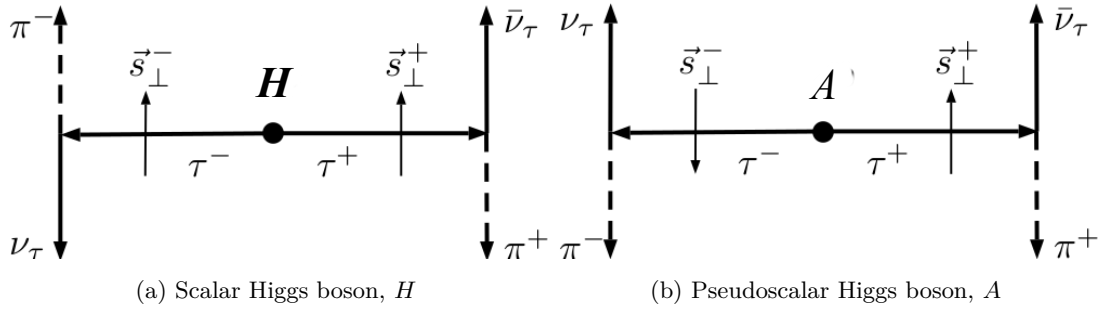


Figure 2.14: Angular correlations of the tau decay products from $H, A \rightarrow \tau\tau$. Taken from [67].

This spin dependence translates to correlations among the tau decay products. In the example of the $\tau^\pm \rightarrow \pi^\pm \nu_\tau$ mode, the angular correlation is

$$\frac{1}{\Gamma} \frac{d\Gamma(H(A) \rightarrow \pi^\pm \bar{\nu} \pi^\mp \nu)}{d\cos\theta_+^* d\cos\theta_-^* d\varphi^*} = \frac{1}{8\pi} (1 + \cos\theta_-^* \cos\theta_+^* \sin\theta_+^* \sin\theta_-^* \cos\varphi^*), \quad (2.61)$$

where θ_\pm^* are the polar angles between the π^\pm and the τ^- direction in the τ^\pm rest frames and φ^* is the relative azimuthal angle between the decay planes (see Figure 2.15).

The Higgs boson parity can be inferred from the asymmetry in the azimuthal angle after integrating over the polar angles:

$$\frac{1}{\Gamma} \frac{d\Gamma(H(A))}{d\varphi^*} = \frac{1}{2\pi} \left(1 \pm \frac{\pi^2}{16} \cos\varphi^* \right), \quad (2.62)$$

where the acoplanarity angle is

$$\varphi^* = \arccos(\vec{n}^+ \cdot \vec{n}^-) \quad \vec{n}^\pm = \frac{\vec{p}^{\pi^\pm} \times \vec{p}^{\tau^\mp}}{|\vec{p}^{\pi^\pm} \times \vec{p}^{\tau^\mp}|}. \quad (2.63)$$

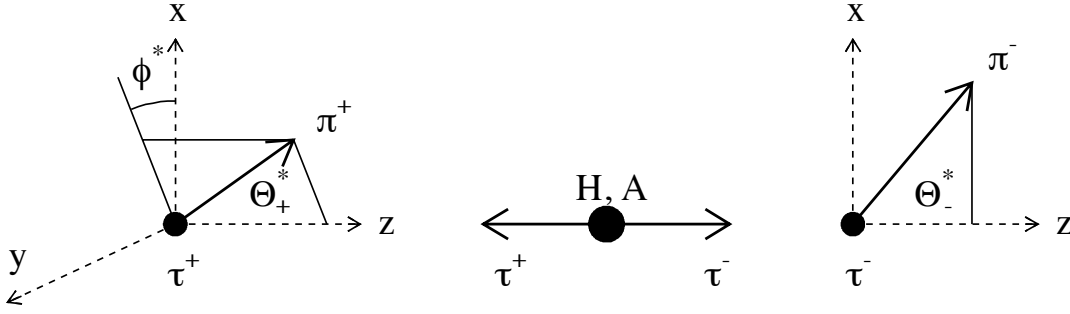


Figure 2.15: Schematic of the pion angles in the $\tau \rightarrow \pi\nu_\tau$ decay. The polar angles, θ_\pm^* , are defined in the τ^\pm rest frames with respect to the τ^\mp direction. The azimuthal angle ϕ^* remains unchanged under boosts along the τ^\pm axis. Taken from [68].

Experimental observables exploit the sign difference in the cosine dependence for a CP -even and a CP -odd Higgs boson. Since the rest frame of the tau lepton cannot be reconstructed at the LHC, as previously discussed in Section 2.2.1, an experimental method is developed for reconstructing this acoplanarity angle using the impact parameter of the tau lepton. This method is discussed in Section 6.1.1. The distribution of φ^* in Equation 2.63 showing the difference for a scalar and pseudoscalar Higgs boson is shown in Figure 2.16.

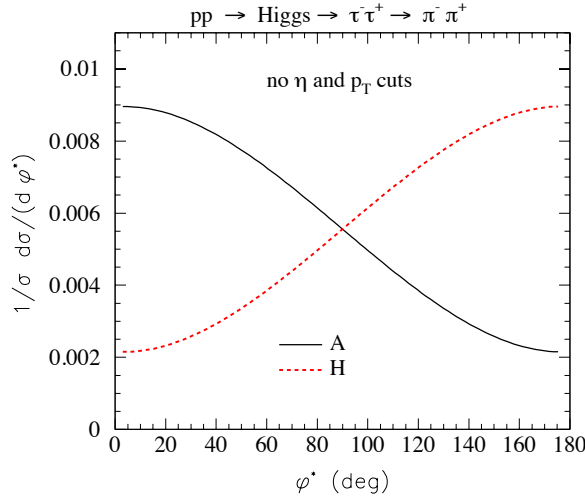


Figure 2.16: Distribution of the acoplanarity angle between the tau decay planes for a scalar and pseudoscalar Higgs boson (c.f. Equation 2.63). Taken from [69].

Compared to the $\tau \rightarrow \pi\nu_\tau$ decay, the $\tau \rightarrow \rho\nu_\tau$ decay is less sensitive because the angular

correlation term is reduced by a factor of $(m_\tau^2 - 2Q^2)^2 / (m_\tau^2 + 2Q^2)$ (c.f. Equation 2.61):

$$\frac{1}{\Gamma} \frac{d\Gamma(H(A) \rightarrow \rho^\pm \bar{\nu} \rho^\mp \nu)}{d \cos \theta_+^* d \cos \theta_-^* d \varphi^*} = \frac{1}{8\pi} \left(1 + \frac{(m_\tau^2 - 2Q^2)^2}{(m_\tau^2 + 2Q^2)} (\cos \theta_-^* \cos \theta_+^* \bar{} \sin \theta_+^* \sin \theta_-^* \cos \varphi^*) \right), \quad (2.64)$$

where Q^2 is the mass of the hadronic system, which can no longer be neglected compared to m_τ^2 [70, 71]. However, unlike in the $\tau \rightarrow \pi \nu_\tau$ decay, there exists experimentally accessible information in the ρ decay products, as previously discussed in Section 2.2.1. This information can be used to improve the polarimetric vector, as presented in [63, 71]:

$$h^i = \mathcal{N} \left(2(q \cdot N) q^i - q^2 N^i \right), \quad (2.65)$$

where \mathcal{N} is a normalization function, q is the difference between the four-momenta of the π^\pm and the π^0 , and N is for the four-momentum of the tau neutrino, all defined in the tau rest frame. In the tau lepton rest frame, the $q \cdot N$ term in Equation 2.65 can be exploited since the energies of the individual pions can, in principle, be measured:

$$q \cdot N = (E_{\pi^\pm} - E_{\pi^0}) m_\tau. \quad (2.66)$$

Thus, the difference between the π^\pm and π^0 energies provides additional information from which the tau helicity can be inferred. This feature is exploited in the method for reconstructing a \mathcal{CP} sensitive observable in the $\tau \rightarrow \rho \nu_\tau$ case presented in Section 6.1.2. The tau spin vector can also be inferred from the decay product distribution:

$$\Gamma(\tau \rightarrow X) \sim (1 + \vec{s} \cdot \vec{h}), \quad (2.67)$$

where it can be seen that the polarimetric vector, \vec{h} , gives the most likely tau spin direction, \vec{s} , for a given configuration, X , of its decay products [71].

In conclusion, Higgs \mathcal{CP} mixing can be probed in the $H \rightarrow \tau\tau$ channel, where both tau leptons decay hadronically, using the transverse tau spin correlations. Experimental observables sensitive to the mixing angle use applications of tau polarization described in this chapter. They also rely on the correct identification of the tau decay mode and the reconstruction of the individual tau decay products. The work performed in this dissertation improves an algorithm that performs this reconstruction and is presented in Section 4.5. The results from this algorithm are used for the \mathcal{CP} sensitive experimental observables in the Higgs \mathcal{CP} analysis described in Chapter 6.

2.4 Shortcomings of the Standard Model

The Standard Model is a theory that is in good agreement with numerous experimental results. However, it has several limitations. First, it does not include gravity. In addition, the Standard Model does not provide a candidate for the observed dark matter and energy in the universe, the former of which accounts for 84.5% of the total mass of the universe. Together, dark matter and dark energy constitute 95.1% of the mass-energy content [72]. The Standard Model cannot be an inclusive theory of particle physics if it can only explain the matter that makes up only a small fraction of the energy content of the universe.

In addition, the SM contains 19 free parameters:

- The fermion masses (9).
- The CKM mixing angles and phase (4).
- The SU(3), SU(2), and U(1) gauge coupling constants (3).
- The QCD vacuum angle (1).
- The Higgs vacuum expectation value (1).
- The Higgs boson mass (1).

This begs the questions of why the SM is dictated by this specific combination of small symmetry groups and this specific number of free parameters. The SM also predicts massless neutrinos, but neutrinos are known to oscillate, a phenomenon which requires neutrinos with nonzero mass. There are additional free parameters from the mixing angles and masses of the neutrinos.

In addition, there is no mechanism in the SM that explains the amount of asymmetry observed between matter and antimatter, as previously discussed in Section 2.1.7. In addition to this, the QCD Lagrangian contains a natural candidate for \mathcal{CP} violation, while no \mathcal{CP} violation has been observed in the QCD sector (c.f. Equation 2.8). Nevertheless, even if \mathcal{CP} violation existed in the QCD sector, it is expected to be small because the electric dipole moment of a neutron, for example, is expected to be $\sim 10^{-18} \cdot e \text{ m}$ while the current upper limit measured is $\mathcal{O}(9)$ smaller [73]. \mathcal{CP} violation in the QCD sector, thus, cannot describe the degree of \mathcal{CP} asymmetry observed in the universe. The amount of asymmetry can possibly be explained by \mathcal{CP} violation in the lepton sector in extended models with right-handed neutrinos, where \mathcal{CP} violating phases are intrinsic to the Majorana nature of neutrinos [74].⁶

Finally, aesthetic problems exist with the Standard Model. For one, it is not a Grand Unified Theory (GUT). For another, there are hierarchy problems where, for example, the coupling constants of the interactions described by the Standard Model do not coincide when extrapolated to higher energies (see Figure 2.17) [75]. In addition, at the Planck scale, the Higgs boson mass is comparable to the Planck mass ($\mathcal{O}(19)$ GeV). However, the Higgs boson mass is experimentally measured to be about 125 GeV [76].

2.5 Theories beyond the Standard Model

There are numerous theories that address one or more of the limitations of the Standard Model. These include models with extended gauge sector and Supersymmetry (SUSY). Attractive aspects of SUSY are that it provides a natural candidate for dark matter and that the fundamental forces can be unified when their coupling constants are extrapolated to the TeV scale. The Minimal Supersymmetric Standard Model (MSSM) is a minimal realization of the Higgs mechanism within supersymmetric extensions of the SM [77]. If it is realized, the LHC should discover five spin-0 Higgs bosons predicted from the Higgs mechanism operating on two Higgs doublets. The MSSM provides a stabilizing mechanism for the Higgs boson mass and fixes the discrepancy between running couplings of the SM forces using a renormalization group (c.f. Figure 2.17). It also provides a candidate for dark matter.

⁶ Majorana neutrinos satisfy the Majorana self-conjugate conditions requiring a fermion to be its own antiparticle.

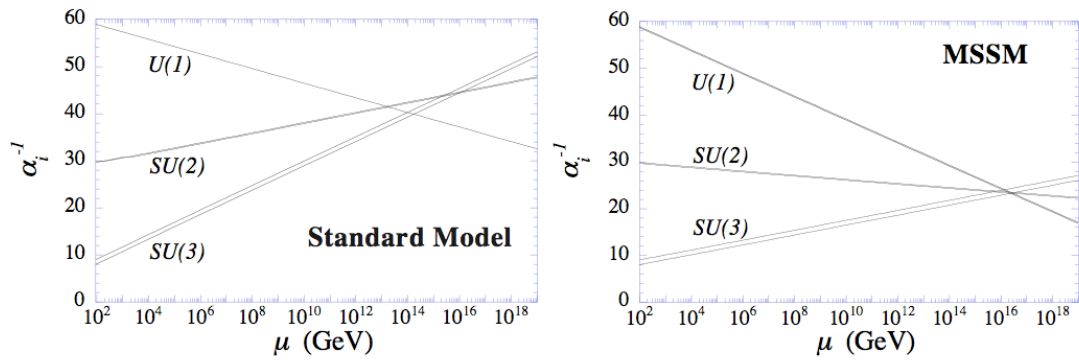


Figure 2.17: The discrepancy between gravity and the SM forces when extrapolated to high energies and their unification in the MSSM, described in Section 2.5. The y -axis corresponds to the reciprocal of the coupling strength, and the x -axis corresponds to the energy scale. Taken from [75].

Extra dimensions can also address the hierarchy problem concerning the weakness of the gravitational force compared to the EW force. The density of gravitational field lines fall more quickly if extra dimensions exist than they do in three-dimensional space. Extra dimensions can be revealed at the LHC, e.g., through the production of monojets [78].

The LHC and the ATLAS detector

An overview of the LHC (Large Hadron Collider) and the ATLAS (A Toroidal LHC Apparatus) detector is provided in the following chapter. The main components of the ATLAS detector are discussed, with more focus on the subcomponents related to the work presented in this dissertation: the tracking system, the calorimeters, and the trigger system.

3.1 The Large Hadron Collider accelerator system

The LHC is a circular particle accelerator that collides counter-propagating beams of protons or heavy ions. It is built 45 to 180 m underground, minimizing the detection of cosmic ray particles, at CERN (European Organization for Nuclear Physics) in Geneva, Switzerland, with a circumference of 27 km. In the proton-proton (pp) collisions at the LHC, each beam is designed to have 2808 bunches, with 1.15×10^{11} protons per bunch.

The proton beams at the LHC come from hydrogen atoms that have been stripped of their valence electrons by an electric field. These protons are then accelerated to an energy of 50 MeV by LINAC 2, the first accelerator of the acceleration chain (see Figure 3.1). The acceleration is performed using radio frequency cavities. Then, the Proton Synchrotron Booster accelerates them to 1.4 GeV, the Proton Synchrotron to 25 GeV, and the Super Proton Synchrotron to 450 GeV. Finally, the protons are transferred to the beam pipes of the LHC, the last element of the acceleration chain. The design center-of-mass energy of the LHC is $\sqrt{s} = 14$ TeV. At this energy, the protons travel about 3.1 m/s slower than the speed of light, c , with a Lorentz factor of about 6930. They can achieve a revolution frequency of $f = 11245.5$ Hz.

An 8.4 Tesla (T) magnetic field is required to deflect these beams of charged protons at a design energy of 7 TeV per beam. These strong magnetic fields are realized using superconducting magnets cooled to a temperature of 1.7 K using about 96 tons of superfluid helium-4. The beams are guided in the circular trajectory by 1232 superconducting dipole magnets and focused by 368 quadrupole magnets. Additional stronger quadrupole magnets are used at the interaction regions to maximize the chances of interaction.

The beams of protons travel clockwise and counter-clockwise, each in their own beam pipe, except for in the interaction regions, where the beams share the same pipe for approximately 130 m [79]. There are eight of these interaction points among the ring, where the beams are squeezed down to a cross section of about $16 \times 16 \mu\text{m}$ and brought to collide. Four of these interaction points are for acceleration purposes, beam cleaning, beam collimation, etc. The other four points are the detector locations of the major experiments at CERN, as shown in

analyzed in this dissertation is described.

	Units	Design	2010	2011	2012	2015	2016	2017
Center-of-mass energy, \sqrt{s}	[TeV]	14	7	7	8	13	13	13
Protons/bunch, n_p ($\times 10^{11}$)		1.15	1.0	1.3	1.5	1.1	1.1	1.15
Max. number of bunches, n_b		2808	368	1380	1380	2244	2076	2556
Bunch spacing	[ns]	25	150	50	50	25	25	25
Pileup, $\langle \mu \rangle$		20.0	3.50	9.00	20.7	13.4	25.1	37.8
Max. peak luminosity, \mathcal{L}_{\max}	[$\text{cm}^{-2}\text{s}^{-1}$]	1.00	0.021	0.35	0.77	0.51	1.01	2.06
Total luminosity recorded by ATLAS, \mathcal{L}_{int}	[fb^{-1}]	–	0.0450	5.08	21.3	3.90	35.6	46.9
\mathcal{L}_{int} used in the analyses in this dissertation [fb^{-1}]						3.21	32.9	–

Table 3.1: Parameters of pp collisions at the LHC from 2010 to 2017. Numbers are from [81–83]. See text for definitions of the parameters.

3.1.1.1 Center-of-mass energy

The first run at the LHC (Run-I) has seen center-of-mass energies of $\sqrt{s} = 2.76$, 7, and 8 TeV in 2010 (for one month), 2011, and 2012, respectively [82]. It broke a world record with an energy about 3.5 times higher than that achieved by a man-made accelerator. In the second run at the LHC (Run-II), a center-of-mass energy of 13 TeV was achieved, with a peak luminosity of $\mathcal{L} = 2.06 \times 10^{34} \text{ cm}^{-2} \text{ s}^{-1}$ (see Table 3.1 for more specifications). The higher center-of-mass energy makes it possible to study processes up to the TeV scale, at which several models beyond the SM (BSM) predict new particles. Figure 3.2 shows a comparison of the inclusive pp cross section ratios for several SM and BSM processes at 8 TeV compared to 13 TeV. The cross sections for new physics can increase by a factor of about 10–100 at 13 TeV.

3.1.1.2 Luminosity

The instantaneous luminosity describes the number of collisions per second. The corresponding integrated luminosity is $\mathcal{L}_{\text{int}} = \int dt \mathcal{L}$, with \mathcal{L} derived as

$$\mathcal{L} = \frac{f n_b n_p^2}{4\epsilon \beta^*}, \quad (3.1)$$

where f is the revolution frequency, n_b is the number of proton bunches, n_p is the number of protons per bunch, ϵ is the transverse emittance describing the degree to which the protons are confined to a small distance with similar momenta, and β^* is the amplitude function:

$$\beta^* = \frac{\pi \cdot \sigma^2}{\epsilon}, \quad (3.2)$$

where the cross sectional size of the bunch is given by σ . The β^* amplitude function is determined by the quadruple magnet arrangement and power. High luminosities are achieved with a high bunch population and a lower β^* , meaning the beam is squeezed. The luminosity integrated with respect to time determines the total number of events expected for a given process with a

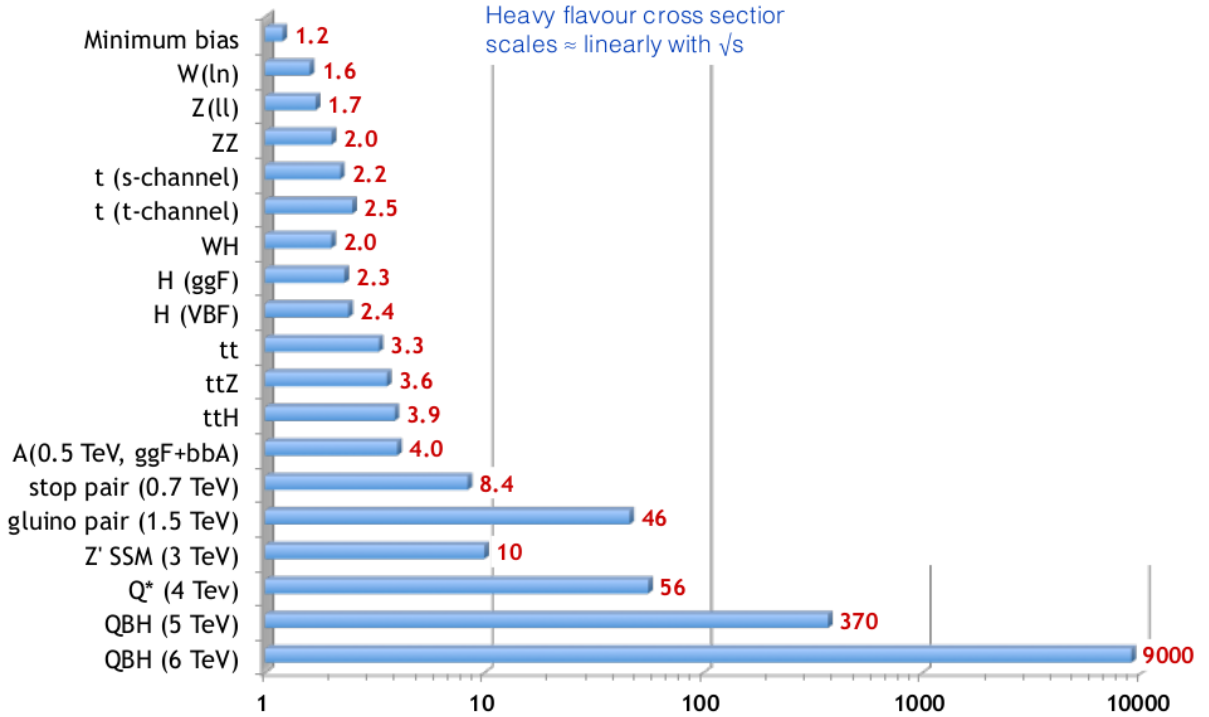


Figure 3.2: Ratio of the inclusive pp cross sections for selected physics processes at $\sqrt{s} = 8$ and 13 TeV. Taken from [84].

cross section σ_{process} :

$$n_{\text{process}} = \sigma_{\text{process}} \int dt \mathcal{L}. \quad (3.3)$$

3.1.1.3 Pileup and bunch spacing

At the LHC, a single crossing of proton bunches can result in several events, especially given that the proton-proton inelastic cross section is high, at about 69.1 ± 1.4 mb, where $1 \text{ mb} = 10^{-31} \text{ cm}^2$ [85]. This pileup of events is quantified by the average number of interactions per bunch crossing, $\langle \mu \rangle$, and has reached as high as $\langle \mu \rangle = 37.8$ in 2017. (Table 3.1 shows $\langle \mu \rangle$ for each year of operation at the LHC.) The ATLAS and CMS detectors are designed to select and record interesting and highly energetic events at this high pileup rate to a decent precision.

A schematic of an example pp collision is shown in Figure 3.3. The most important process from a pp collision at ATLAS is the hard scattering between two partons of the protons. Pileup comes from other protons in a bunch, while the collision of different bunches produces out-of-time pileup. The rest of the protons of the beam, or the beam remnant, that do not participate in a hard process or an underlying event continue along the beam axis.

In addition, the LHC collides many protons at a high rate, with short bunch spacings. In Run-I the LHC achieved about 1380 bunches per beam and a 50 ns bunch spacing, and in Run-II, it increased to 2556 bunches per beam with a 25 ns bunch spacing. The high frequency of interactions can result in out-of-time pileup, in addition to the [in-time] pileup described in the previous paragraph. In out-of-time pileup, additional interactions occur in bunch crossing

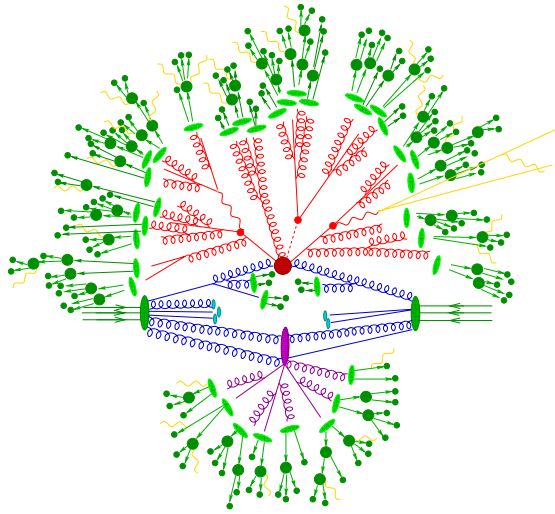


Figure 3.3: Schematic of a pp (incoming horizon green lines) collision, consisting of the hard scattering accompanied by hard gluon radiation (red), secondary interaction (purple), and the final state partons (light green) and hadron decays (dark green). Photon radiation (yellow) can occur at any stage. Taken from [86].

just before and after the collision of interest.

3.1.2 LHC results in Run-I and Run-II

The first collisions at the LHC began on November 2, 2009. From the Run-I dataset, a rich harvest of physics measurements and discoveries were achieved, including the discovery of the Higgs boson in many of its known decay channels, observations of quark-gluon plasma, particle-antiparticle mixing in the D meson system, and the rare $B_s \rightarrow \mu^+ \mu^-$ decay.

After Run-I, the LHC began its first long shutdown (LS1) in February 2013. LS1 lasted for about two years and was dedicated to the transition of the LHC's design energy to $\sqrt{s} = 13 - 14$ TeV. During LS1, a new inner detector component was also added to ATLAS to address the increased luminosity in Run-II. (It will be described later in Section 3.2.)

The Run-II dataset recorded by ATLAS from 2015 to 2016 contains an integrated luminosity of 39.5 fb^{-1} . Of this integrated luminosity delivered by the LHC, about 36.1 fb^{-1} of data passing the Good Run List (GRL)¹ are used in the physics analyses presented in this dissertation in Section 5 and Section 6. Recent results from the Run-II dataset include the independent $H \rightarrow \tau\tau$ discoveries by the ATLAS and CMS Collaborations, the observation of $t\bar{t}H$, and evidence for the $H \rightarrow b\bar{b}$ decay [4, 5, 87]. Future analyses will include the 2017 dataset from Run-II containing an integrated luminosity of 46.9 fb^{-1} .

3.2 The ATLAS detector

The ATLAS detector is designed for the following physics agenda:

- Discover the Higgs boson in its known decay channels and measure its properties.

¹ The GRL subjects each recorded event to certain data quality requirements.

- Search for signatures of new physics at the TeV scale.
- Perform precision measurements of the SM, e.g., QCD, electro-weak processes, flavor physics, and top-quark physics.

ATLAS is optimized to detect a wide range of known and hypothesized processes that result in many different final state particles: photons, electron, muons, tau leptons, jets from color-charged quarks and gluons that hadronize to form color-neutral particles (see Section 2.1.2.1), and missing transverse energy (MET or \cancel{E}_T) from minimally interacting or non-interacting particles. The reconstruction of these physics objects at ATLAS will be described in Chapter 4.

The ATLAS detector is 25 m high and 44 m long, weighing about 7000 tons. It is onion-layered with different principal subdetectors designed to detect a wide range of particles. A schematic is shown in Figure 3.4. From the beam pipe going outward, these subdetectors are:

- The inner detector: Measures the tracks of charged particles. It is enclosed in a 2 T magnetic field to bend the trajectory of charged particles, from which their charge and transverse momenta can be measured. The bending also separate charged and neutral particles. The tracks are matched together to reconstruct the vertex corresponding to the event origin and the secondary vertices in the case of some short-lived particles.
- The electromagnetic calorimeter (ECAL): A sampling calorimeter with alternating layers of active and absorbing material. It instigates the showers and measures the energy depositions of charged and neutral particles that create electromagnetic showers, the latter of which pass through the inner detector undetected. These particles are primarily electrons and photons, but hadrons can also start their showers in the ECAL.
- The hadron calorimeter (HCAL): A sampling calorimeter that measures the showers from jets and hadronically decaying tau leptons. These showers are initiated from nuclear interactions. The thickness of the HCAL is designed to contain the energy of the hadrons before they reach the outer muon chamber.
- The muon system: Detects tracks from muons, which traverse the inner layers of the detector without leaving significant energy depositions and continue on outward from the detector. The tracks from the muon chambers are matched to those in the inner detector to reject cosmic ray background. The muon tracks in the center part of the detector are deflected by the large barrel toroidal magnet, from which the ATLAS name is derived, and the muon tracks in the outer ends of ATLAS are bent by two endcap magnets at the ends of the barrel toroid.
- The trigger system: Reduces the data rate and selects interesting events that should be written to disk, given the high luminosity at the LHC. The online trigger system has been reoptimized for the Run-II scenario and consists of two levels: L1 and HLT (High Level Trigger) [88]. The L1 level makes a decision on an event in $\sim 2.5 \mu\text{s}$ based on information from a subset of detectors. It reduces the data rate from the LHC crossing rate of 30 MHz to $\sim 100 \text{ kHz}$. This is an increase from the rate of 75 kHz used in Run-I. It also seeds the region of interest used for HLT, which further reduces the data rate to $\sim 1 \text{ kHz}$ within a average processing time of $\sim 200 \text{ ms}$. This is in contrast to the lower 500 Hz used in Run-I.

The detector is enclosed in a magnetic system that bends particles around the various layers of subdetectors. This magnetic system is built to have a light and open structure to minimize

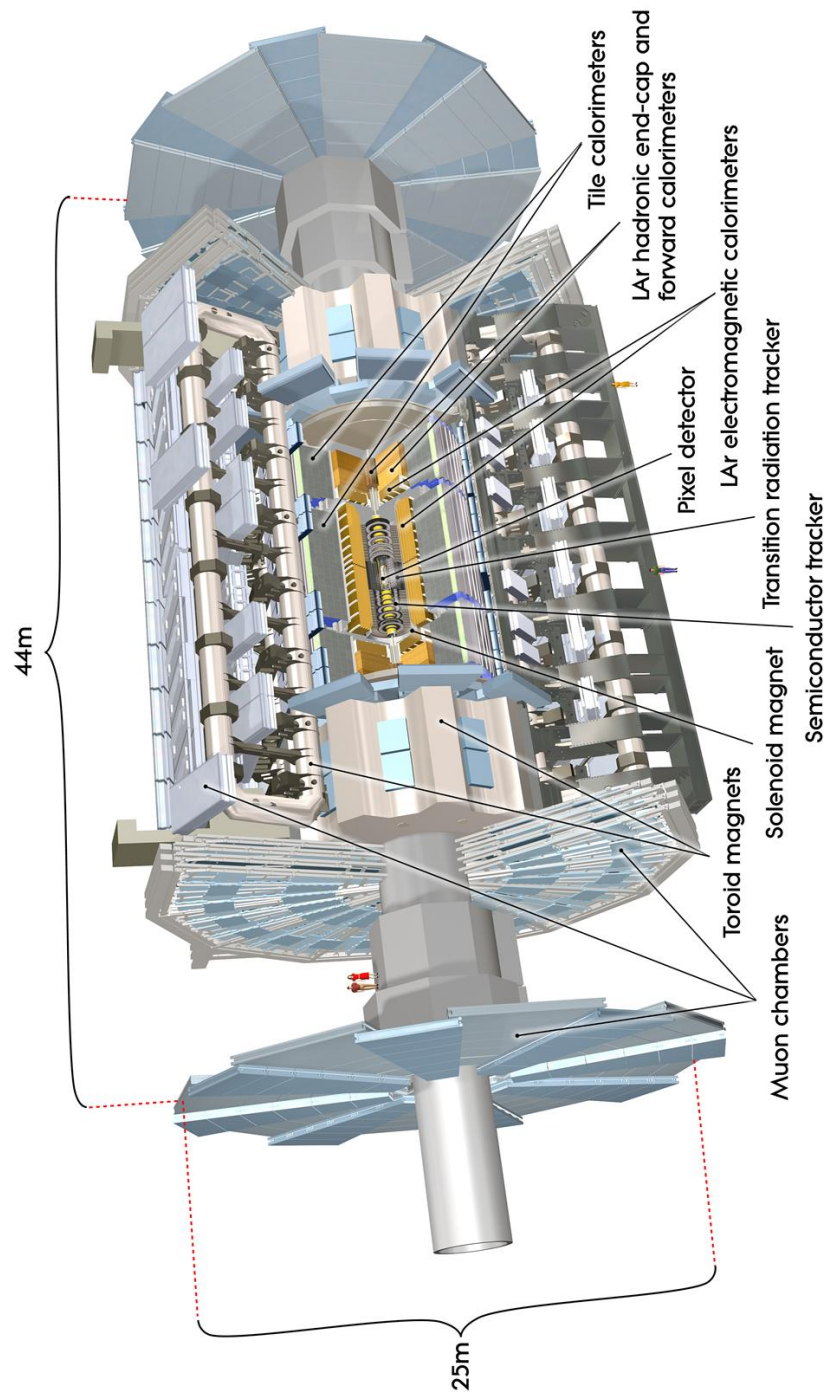


Figure 3.4: A cut-away schematic of the ATLAS detector showing the principal sub detectors. Taken from [79].

multiple scattering and consists of a barrel toroid, two endcap toroids, and one solenoid (see Figure 3.5). The central solenoid provides creates a 2 T magnetic field in the tracking chamber. The endcap toroids provide a magnetic field between 2 and 8 T and are located between the calorimeters and the muon system.

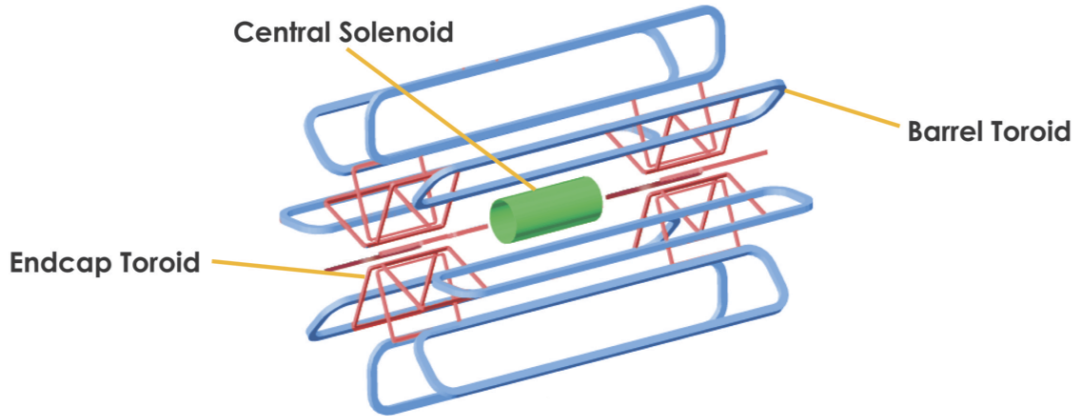


Figure 3.5: Schematic of the bare windings of the magnetic system: the 8 coils of the barrel toroid, the 2×8 coils of the endcap toroids, and the solenoid. Taken from [89].

This section will describe the coordinate system and the detector components relevant to the physics analyses in this dissertation in more depth: the inner detector, the calorimeter system, and the trigger system.

3.2.1 The coordinate system

ATLAS is a barrel-shaped detector that provides as much coverage of a collision emerging from the beam pipe as possible. Its coordinate system is right-handed, with the origin at the nominal interaction point. The z -axis is oriented in the longitudinal direction, pointing in the anti-clockwise direction along the beam. The transverse plane is along the xy -axis, where the x -axis points toward the center of the LHC and the y -axis points up, perpendicular to the xz -plane. The azimuthal angle, ϕ , is in the xy -plane, traversing around the beam pipe, and has a range of $[-\pi, \pi]$. The bending of charged particle from the magnetic system is in the ϕ direction. The polar angle, θ , is the angle with respect to the z -axis. It is translated to the pseudorapidity, η , for the following reasons: first, the pseudorapidity is roughly constant with respect to the η of relativistic particles and, second, differences in η are approximately invariant under boosts along the z -axis. The pseudorapidity is defined as

$$\eta = -\ln \left(\tan \left(\frac{\theta}{2} \right) \right). \quad (3.4)$$

Transverse quantities are defined in the xy -plane: transverse energy ($E_T = E \sin \theta$), transverse momentum ($p_T = |\vec{p}| \sin \theta$), MET (\cancel{E}_T , later defined in Equation 4.5). Distances between physics objects in the ATLAS detector are described by the radius of a cone in the $\eta - \phi$ space:

$$\Delta R = \sqrt{\Delta\eta^2 + \Delta\phi^2}. \quad (3.5)$$

3.2.2 The inner detector

The inner detector, or tracking chamber, lies at the innermost of the ATLAS detector and covers a length of 5.3 m with a diameter of 2.5 m. It reconstructs the tracks of charged particles by taking multiple measurements at several radii as particles move outward from the beam pipe. It

is also used to reconstruct primary and secondary vertices by matching tracks together. Given the high instantaneous luminosity in Run-II at the LHC, with about $\mathcal{O}(3)$ particles created per bunch crossing separated only by 25 ns, the detector must withstand radiation damage while performing efficiently in a high track density environment so that many tracks and vertices are recorded and reconstructed correctly. The parts of the inner detector consist of the pixel silicon detector (B layer), the silicon microstrip tracker (SCT), and the transition radiation tracker (TRT). An insertable B layer (IBL) was added to the pixel detector during LS1, moving the closest sensitive point of the detector to the interaction point from 5.05 cm to 3.27 cm [90]. A schematic of the layers is shown in Figure 3.6.

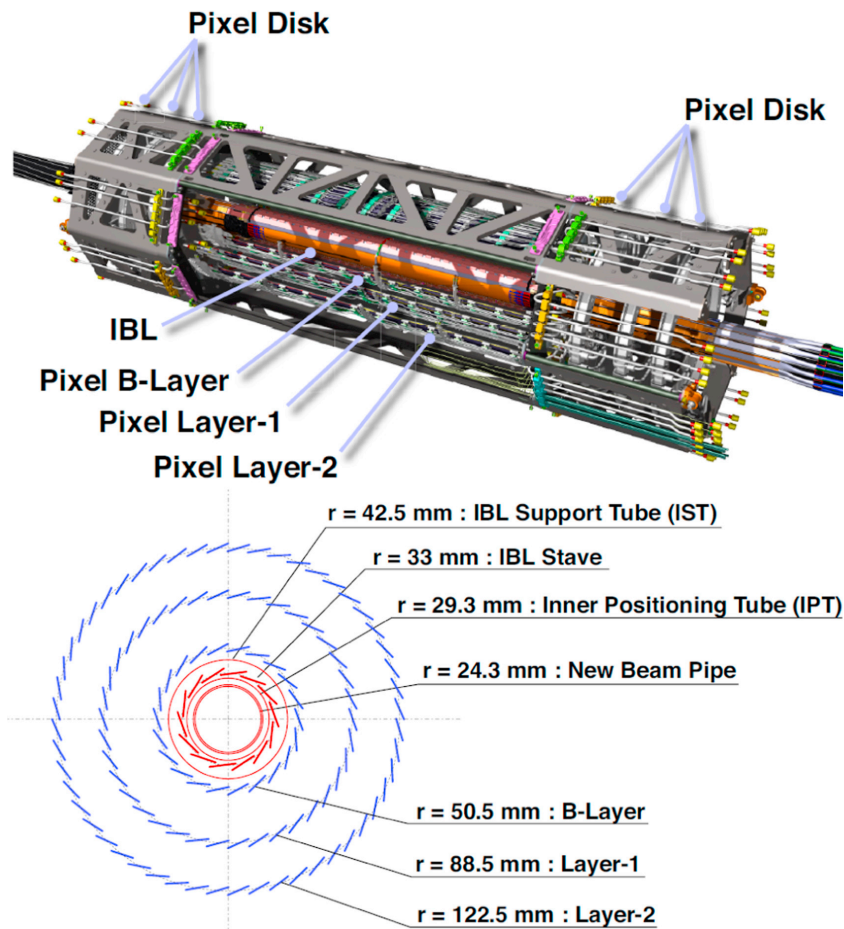


Figure 3.6: Cut-away schematic of each layer of the inner detector and their radial distance to the beam pipe. Taken from [91].

The silicon pixel detector is a high-granularity component of the inner detector with a matrix of modules that can measure particles in two dimensions. It is composed of 1744 modules, with 46080 silicon pixels per module, each with an area of $50 \mu\text{m} \times 400 \mu\text{m}$, and a thickness of $250 \mu\text{m}$, leading to about 80 million readout channels. A reverse bias voltage is applied to an n -doped silicon pixel that has a pn -junction at maximum depletion. The n -type side has extra electrons, and the p -type side has an excess of holes, which means a current can only pass through the pn -junction in one direction. A particle that passes through the depletion zone

creates electron hole pairs that drift toward the readout contacts of the silicon pixel. A charged particle's passage is indicated when a current higher than a certain threshold is measured.

The SCT uses silicon strips instead of pixels to record charged particles. It provides at least 4 measurements per track and consists of 4088 two-sided modules with over 6 million readout channels. These modules are distributed over 4 cylindrical layers in the barrel and 18 disks in the endcap. There are readout channels at every $80 \mu\text{m}$ of silicon that can record the passage of charged particles through the inner detector to an accuracy of $17 \mu\text{m}$ per layer.

The TRT is the outermost component of the inner detector. It consists of straw tubes (drift tube chambers) at a diameter of 4 mm with a gold-coated tungsten wire at their center to collect charges from ions created by a passing charged particle. There are about 50×10^3 straws in the barrel and 250×10^3 straws in the endcap. It can measure to an accuracy of 0.17 mm per hit, which is much lower than the pixel detector and the SCT. However, it provides many measurement points and provides information on the particle type, e.g., an electron vs. a pion. The electron identification comes from the fibers found between each straw tube, where Xenon gas is added to detect transition radiation photons, or X-rays, that created in a radiator between the straw tubes. The TRT can therefore operate with a high threshold for X-rays and a lower threshold for the passage of heavier charged particles, such as pions. This is an especially important feature in rejecting electrons that can be misidentified as tau leptons in the tau reconstruction later discussed in Section 4.

The momentum resolution of the tracking chamber is shown in Figure 3.7. For $0.25 < |\eta| < 0.5$, the relative transverse momentum resolution obtained with the inner detector for muons is parametrized as

$$\sigma_{1/p_T} = 0.34 \text{ TeV}^{-1} \left(1 \oplus \frac{44 \text{ GeV}}{p_T} \right), \quad (3.6)$$

where p_T is in GeV and \oplus denotes the square root of a sum in quadrature [79]. The resolution decreases with increasing p_T since higher p_T charged particles experience a lower deflection from the magnetic field. The resolution at low p_T is dominated by multiple scattering.

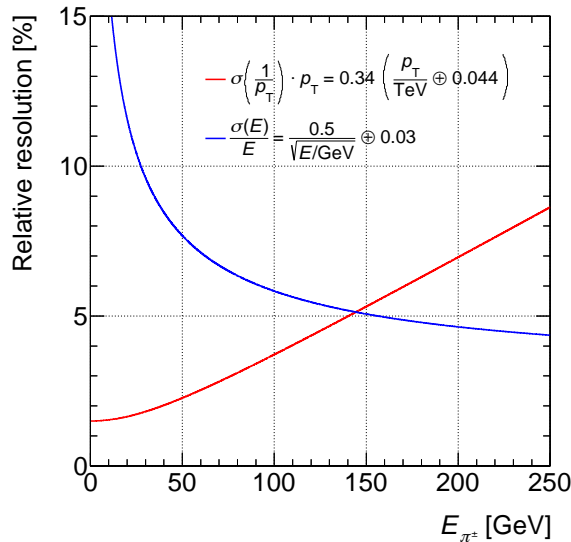


Figure 3.7: Energy and transverse momentum resolutions in the ATLAS calorimeter (blue) and tracking systems (red), respectively, for the central $|\eta|$ region. Taken from [92].

3.2.3 The calorimeter system

The ATLAS calorimeters measure energy depositions from neutral particles that do not leave signatures in the inner detector, in addition to energy depositions from charged particles. They are hermetic over a range of close to 4π , meaning they can be used to infer the presence of missing energy from neutrinos. In addition their energy resolution improves with particle energy.

The ATLAS calorimeters are segmented in depth for the identification of hadronic vs. electromagnetic showers. A schematic of the ATLAS calorimeter layers is shown in Figure 3.8. Since electromagnetic showers develop over shorter lengths than hadronic showers, the calorimeter system from the inner detector going outwards is configured with the ECAL in front of the HCAL. There is also a forward calorimeter (FCAL) that provides additional detector coverage at large $|\eta|$. The ECAL mostly measures electromagnetically interacting particles, while the HCAL samples the energy of hadrons. The forward calorimeter is located at large $|\eta|$ regions and is designed to detect high particle fluxes and debris from minimum bias events. The $|\eta|$ coverage of the ECAL and HCAL is further extended by using a barrel calorimeter with an endcap at each end. The calorimeter system can fully contain almost all known particles except for muons and neutrinos. The transition region between the two, sometimes referred to as the "crack", is not used in physics analyses since objects in this region have a poor energy and spatial resolution. The $|\eta|$ ranges for these different regions of the ECAL are listed in Table B.1.

The ATLAS calorimeters are sampling calorimeters made up of liquid argon (LAr) in the ECAL and some parts of the HCAL and plastic scintillating material in the other parts of the HCAL. These sampling calorimeters alternate between their absorber material to instigate a particle shower and a sampling material to measure the energy depositions from the particle shower. The sampling material consists of lead-stainless-steel in the ECAL, copper in the HCAL and the first layer of the FCAL, and tungsten in the hadron modules of the FCAL. The LAr is an active material, where electron-ion pairs are created when a particle enters or passes through the calorimeter. It flows in between the alternating absorbing plates. To maintain the liquid state of the LAr, the calorimeter is enclosed in a cryostat cooled to 89.3 K. The advantages of LAr are that it has stable response over time, is intrinsically hard against radiation, and has an intrinsic linear behavior.

The ionization by the LAr creates a cascade of secondary particles. The electrons and ions are accelerated toward the readout board by an electric field applied in the LAr barrel. The electrical currents are proportional to the energy deposited by these showers. They have a triangular readout signal that is amplified, shaped, and sampled 5 times every 25 ns. The rise time of the triangular signal is ~ 1 ns, and the drift time is $\mathcal{O}(2)$ ns [79]. This is larger than the time between the LHC bunch crossings (~ 25 ns). Therefore, only the beginning of the ionization signal is used in the readout. The spatial positions of the energy depositions in the calorimeters are obtained by the position of the readout channels. The readout board for the ECAL is very finely segmented to create a high granularity of cells, especially in η , as listed in Table B.1. Each ECAL cell is defined in η by etchings in the readout board, and for some parts of the ECAL, by grouping together adjacent readout boards in ϕ . The segmentation helps to measure the position and shape of the showers.

In general, sampling calorimeters perform worse than homogeneous calorimeters in energy resolution due to sampling fluctuations. However, their advantages are that they can reach sufficient interaction depths to contain showers and that their segmentation in the longitudinal direction is straightforward.

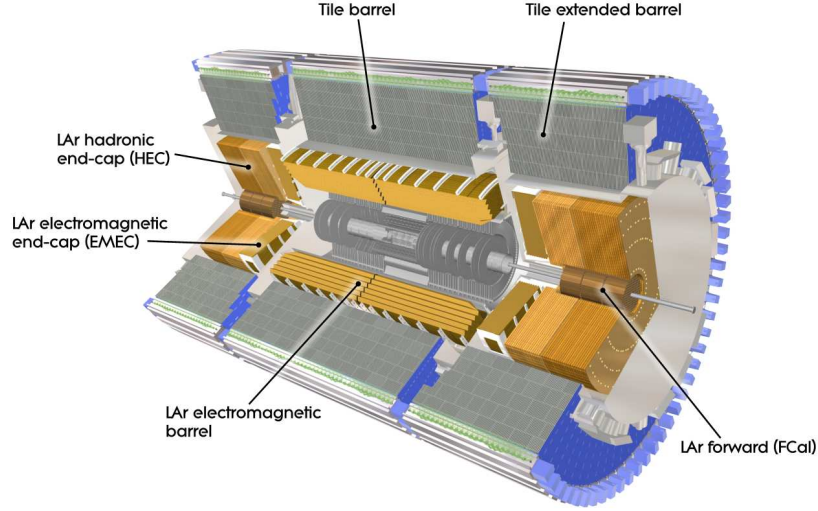


Figure 3.8: Cut-away schematic of the ATLAS calorimeter system. Taken from [79].

3.2.3.1 The electromagnetic calorimeter

The goal of the ECAL is to reconstruct mainly electrons and photons and contain their showers. The longitudinal thickness of the ECAL spans $\geq 26X_0$ radiation lengths and was optimized to completely contain electromagnetic showers and minimize the degradation in energy resolution for leakage into the later HCAL layers. This length is segmented into three ECAL layers, with a presampler at the front to correct for the energy lost before the particles enter the calorimeter. Going outward from the inner detector, the layers are ECAL1 (strip layer), ECAL2, and ECAL3 (see Figure 3.9). This segmentation helps in identifying the starting point of the shower and with the vertex matching of neutral particles since the shower axis can be reconstructed. These variables are used in, for example, the $H \rightarrow \gamma\gamma$ analysis [93]. The strip layer has a short longitudinal depth of $6X_0$ and the finest granularity of the ECAL layers, with a cell size of $\Delta\eta \times \Delta\phi = (0.003125 \times 0.098)$ in the barrel region. The pointing of each cell is directed to the center of the ATLAS detector. The high granularity is used to reconstruct energy deposits from multiple photons. This design was based on the need to reject neutral pions in the $H \rightarrow \gamma\gamma$ analysis [93]. The design is also used in the tau particle flow algorithm [94, 95]. ECAL2 is the thickest and contains most of energy from the EM shower. It has a coarser cell size of $\Delta\eta \times \Delta\phi = 0.025 \times 0.025$. The third layer contains the tails of the EM showers. Details on the lateral partitioning for each of the three layers in the barrel and endcap regions are given in Table B.1.

The benchmark channels for the design energy resolution of the ECAL are $H \rightarrow \gamma\gamma$ and $H \rightarrow ZZ \rightarrow eeee$. From [79], the relative energy resolution of the electromagnetic calorimeter after noise subtraction is parametrized as

$$\frac{\sigma(E)}{E} = \frac{a}{\sqrt{E}} \oplus b, \quad (3.7)$$

where E is in units of GeV. The parameters of the design energy resolution of the ECAL (barrel and endcap) are $a = 10\%$ and $b = 0.7\%$. From energy resolution studies using electron, muon, and pion beams with energies between 1 GeV and 250 GeV, these parameters are measured to

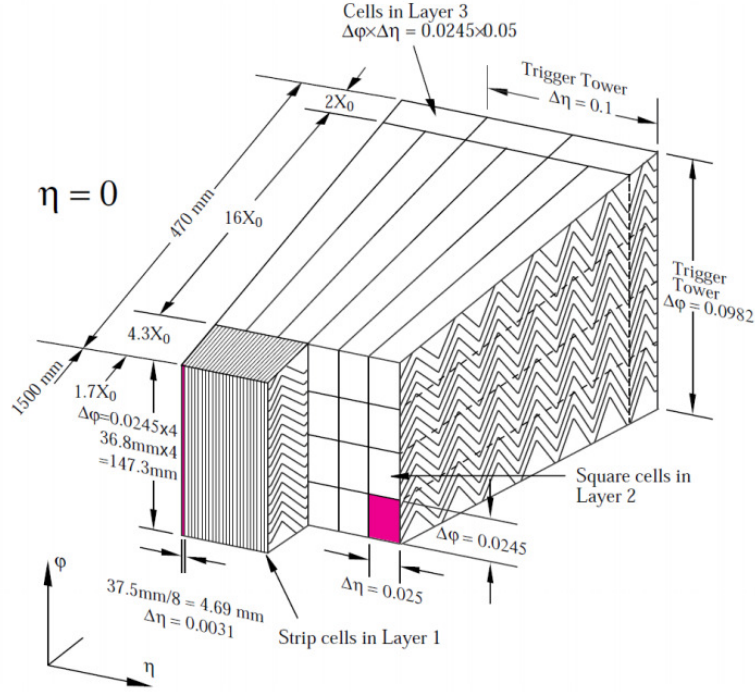


Figure 3.9: Schematic of a module of the ECAL barrel. Taken from [79].

be $a = 10.7\%$, $b = 0.5\%$ [79]. This equation shows that the energy resolution improves as energy increases, as shown in Figure 3.7.

The energy resolution depends on the fluctuations in shower developments, characterized by the first, stochastic term in Equation 3.7. Electromagnetic showers are statistical processes and depend on the number of particles in the shower that contribute to the ionization. They have an uncertainty proportional to \sqrt{E} . The most significant cause of shower fluctuations is the variation in depth of the first e^+e^- conversion pair from the photon or bremsstrahlung radiation from the electron. The stochastic term also has contributions from sampling fluctuations since the ECAL is a sampling calorimeter. The total track length, S , fluctuates as \sqrt{S} in the calorimeter. Thus, the measured energy has an error that scales as $\frac{\sigma}{E} \sim \frac{1}{\sqrt{E}}$ since $E \sim S$. In addition, the resolution scales with the thickness of the sampling layers. The second term is the constant term that comes from calibration errors, loss of energy in dead material, and leakage when the shower is not completely contained.

3.2.3.2 The hadron calorimeter

The next component moving outward from the ECAL is the HCAL. The HCAL is used to measure jet energies and angular directions, in addition to connecting the reconstructed jet energy to the parton from which it originated. It consists of a tile barrel and a tile extended barrel on each side. These components use organic scintillating tiles as the active material in the sampling calorimeter instead of LAr. Therefore, the signal formation in the HCAL barrel is different from in the ECAL barrel. The scintillation light from the interacting particle is emitted by the tiles of the HCAL. This light is guided by wavelength-shifting fibers toward photomultiplier tubes. Experimental measurements in the HCAL endcap using charged pion

beams yield a resolution of $a = (70.8 \pm 1.5)\%$ and $b = (5.8 \pm 0.2)\%$ (c.f. Equation 3.7). For the tile calorimeter, the energy resolution was measured to be $a = (56.4 \pm 0.4)\% \sqrt{\text{GeV}}$ and $b = (5.5 \pm 0.1)\%$ [79].

3.2.3.3 Clustering in the calorimeters

After the energy deposition in the cells of the calorimeter, the cells are grouped together into three-dimensional clusters using two clustering algorithms: the sliding window algorithm, used mainly for electrons and photons, and the topological clustering algorithm, used mainly for jets, hadronically decaying tau leptons, and MET [96]. These clusters help to make sense of the depositions and are used as input into particle reconstruction algorithms.

The sliding window algorithm uses a fixed rectangular window to search through the calorimeter cells. The fixed size of the window means that the clusters can be precisely calibrated. A cluster is formed if a local maximum is found in the $\eta - \phi$ space and the sum of the p_T found in the cells contained by the fixed window is above a certain threshold. The disadvantages of the sliding window algorithm are that it does not provide noise and pileup suppression and that it does not usually contain showers.

On the other hand, the topological clustering algorithm is efficient in suppressing noise and pileup, and each topocluster typically corresponds to one hadron. The clusters are seeded by cells with energy of $E_{\text{seed cell}} > 4(\sigma_{\text{electronic noise}} \oplus \sigma_{\text{pileup noise}})$. Neighboring cells are iteratively grouped with the seed cell if they pass an energy threshold of $E_{\text{neighbor cell}} > 2\sigma$. Then, the perimeter cells with $E_{\text{perimeter cell}} > 0\sigma$ are included. Next, the topocluster algorithm groups clusters together if they share a neighboring cell. Finally, a topocluster is divided by searching for local maxima within the cluster with $E_{\text{cell}} > 500 \text{ MeV}$. A reclustering is performed around the local maxima by grouping neighboring cells together, as before, but without an energy threshold applied. The clusters from these algorithms are then calibrated and used to reconstruct physics objects.

3.2.3.4 Calibration of the calorimeters

The calibration of the calorimeters is an important step for physics analyses using data from ATLAS. The energy response varies for the different components of the calorimeters, and not all of a particle's energy is deposited in the sensor material.

The first of the major calibration schemes for the reconstruction of jets and MET is the Local Hadron Calibration (LC) [97]. It is used to calibrate the signal measured by the detector to the particle level. This calibration of noise- and pileup-suppressed clusters corrects for energy deposited in cells outside of the cluster and for energy deposited in the dead material in front of and between the calorimeter modules. It is performed in the following steps: classification, hadronic weighting, out-of-cluster correction, and dead material correction.

First, a classification is performed that separates the electromagnetic and hadronic parts of clusters to determine the subclusters that should be calibrated to correct for hadronic activity. The different types of energy in a hadronic shower are shown in Figure 3.10. Unlike an EM shower, a hadronic shower only leaves energy depositions 75% of the time in its visible EM part and visible non-EM part. The invisible and escaped energies must be identified and corrected. This classification is performed using shower shape variables, such as the shower depth, and the energy density of the cells. A low calorimeter depth and a high average cell energy density denotes an EM shower. Second, the cells of the clusters classified as hadronic are weighted to

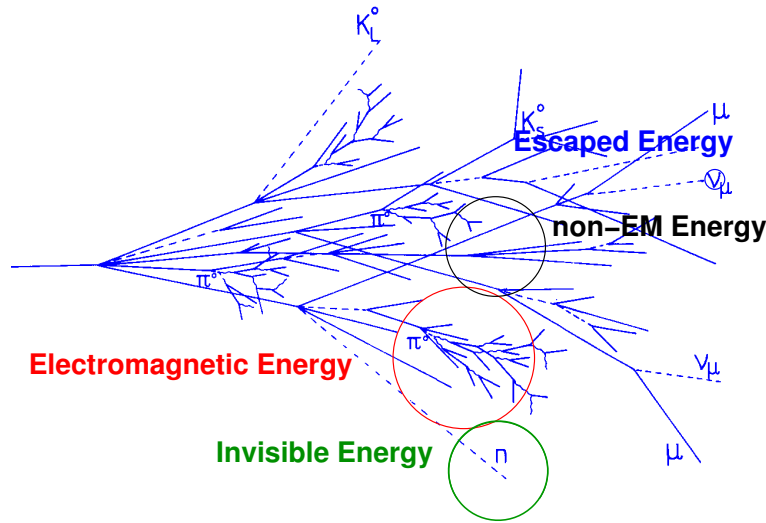


Figure 3.10: Schematic of a hadronic shower and the types of energy detected/undetected by the HCAL. Taken from [98].

account for invisible and escaped energy. The invisible energy comes from the breakup of nuclei and nuclear excitation, where energy is not deposited in the calorimeter, and accounts for about 25% of a hadronic shower. The escaped energy comes from neutrinos and accounts for about 2% of a hadronic shower. Third, the LC corrects for out-of-cluster effects, arising from cells discarded by the clustering algorithm when their energy is below the noise threshold. Finally, the LC corrects for energy lost outside of the active calorimeter material.

After the LC, the reconstructed jet energy in data is still lower than the jet energy scale expected in simulation. The LC cannot account for out-of-cone effects, such as where energy is lost by particles that never reach the calorimeter. The final jet calibration after the LC is described in Section 4.2.

3.2.4 The trigger system

ATLAS is not capable of recording all of the raw data at the production rates seen at the LHC. Therefore, a trigger system is used to reduce the large amount of uninteresting events, such as the vast majority of minimum-bias events, and maximize the acquisition efficiency of interesting events to pass a trigger requirement. The trigger system consists of an online trigger, which is used for quick reconstruction and decision making during data-taking, and an offline trigger, which is applied to recorded data in the ATLAS reconstruction software.

In Run-II, the trigger system is separated into the L1 and HLT trigger [88]. The L1 trigger uses reduced granularity information from the calorimeters to determine the region of interest (RoI) in which to search for electrons, photons, tau leptons, jets, and \cancel{E}_T (or MET). The calorimeter is grouped into trigger towers, an example schematic of which is shown in Figure 3.11. These towers are groups of cells with a typical granularity of $\Delta\eta \times \Delta\phi = 0.1 \times 0.1$. A schematic is shown in Figure 3.11. The candidate energy is calculated from the 2×2 core in the HCAL and the maximum of the four possible 2×1 sums in the RoI. L1 decides whether or not the event should be recorded, based on the trigger tower calculation, within a time frame of $2.5 \mu\text{s}$.

The RoI from L1 is used to seed a corresponding HLT trigger. An HLT trigger uses the full

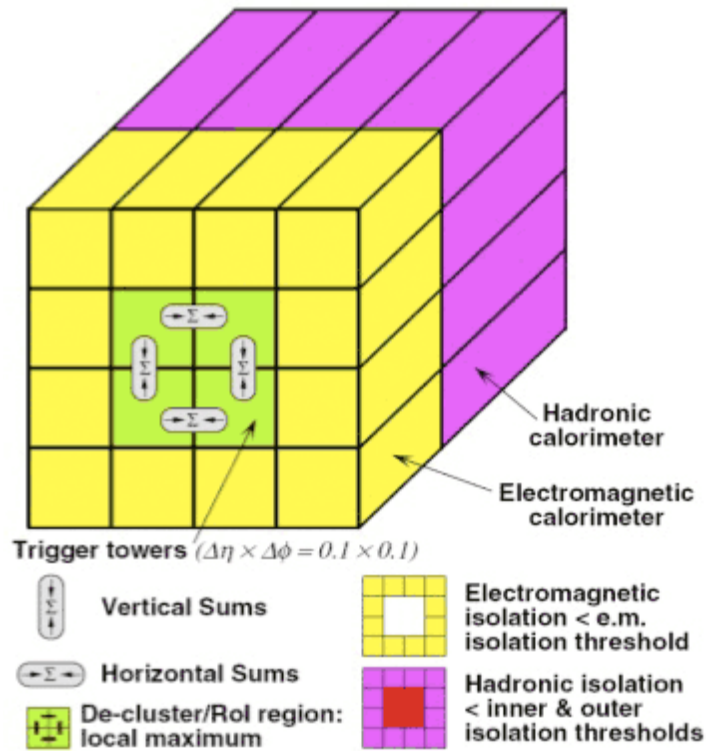


Figure 3.11: Schematic of an L1 trigger tower. Taken from [99].

granularity information in either the RoI or the whole event to reconstruct trigger identification variables that take too long to be reconstructed in the L1 trigger. At the highest instantaneous luminosities in Run-II so far, the HLT processing time for an event is about 235 ms [99]. In addition to the HLT trigger, some triggers may be prescaled, meaning only a certain percentage of randomly selected events are allowed to pass the trigger.

Specific triggers targeted for certain particles are used in the L1+HLT trigger system. The di-tau trigger targeting hadronically decaying tau leptons is used in this dissertation and is a combination of two trigger components, or trigger legs, to target each tau decay from, e.g., a Higgs boson. The tau triggers were reoptimized during LS1 to reduce the differences between the HLT tau triggers and the selections later made in physics analyses. This reduced the inefficiencies by over a factor of two. They are discussed in more detail in Section 4.4.4.

Object reconstruction

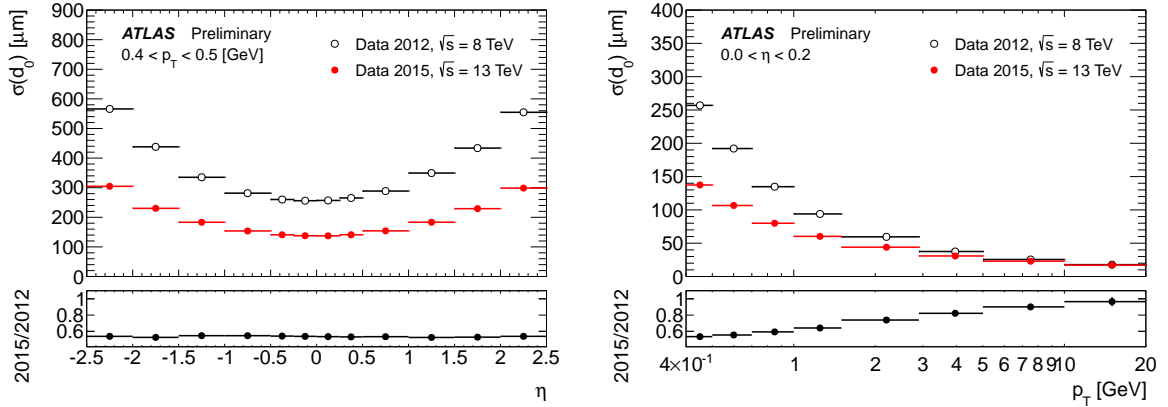
This chapter describes the reconstruction of physics objects relevant for the $H \rightarrow \tau\tau$ analyses: tracks and vertices, jets, missing transverse energy (MET or \cancel{E}_T), and tau leptons.

4.1 Track and vertex reconstruction

Tracks and vertices are used in the definition and reconstruction of higher-level physics objects and observables. Tracks are reconstructed from space points and clusters in the inner tracking detector [100]. They are characterized by its curvature, polar and azimuthal angles, and impact parameters. These impact parameters are $d_0(z_0)$, measuring the smallest distance to the vertex in the transverse (longitudinal) planes. They are defined with respect to the reconstructed primary vertex. This vertex is reconstructed by matching tracks together in a finding and a fitting algorithm [101]. First, the finding algorithm associates tracks to vertex candidates. Then, it reconstructs a vertex position and its corresponding error matrix. Since there are many vertices reconstructed from the bunches of protons the LHC collides, the vertex algorithm performs a χ^2 fit to the seed track and the tracks around it. Tracks that do not pass the fit are used as candidates for the next iteration of the fit until no tracks are left. The primary vertex is the vertex with the highest $\sum p_T^2$ of associated tracks. This vertex is especially important for a method using the impact parameter in the Higgs \mathcal{CP} analysis discussed in Section 6.1.1. The transverse impact parameter resolution, $\sigma(d_0)$, is improved in Run-II due to the introduction of the IBL. This is shown in the comparison in Figure 4.1, where the resolution is improved over the entire η range and, in particular, at low p_T .

4.2 Jet reconstruction

Jets from hadronizing quarks and gluons are present in pp collisions at the LHC, as previously discussed in Section 2.1.2.1. They are reconstructed from the infrared-safe (c.f. Section 2.1.2.1) anti- k_T algorithm. In this algorithm, the reconstructed jet will not change if a gluon is emitted between two partons because the algorithm is constructed such that soft jets are typically combined with hard jets. The method sequentially combines TopoClusters (previously described in Section 3.2.3.3) based on the distance from the beam pipe, d_{iB} , and the distance from other



(a) Transverse impact parameter resolution ($\sigma(d_0)$) as a function of the $|\eta|$ of the track in the $0.4 < p_T < 0.5$ region. (b) Transverse impact parameter resolution ($\sigma(d_0)$) as a function of the track p_T in the $0.0 < |\eta| < 0.2$ region.

Figure 4.1: The transverse impact parameter resolution measured from data with and without the IBL in 2012 and 2015 at $\sqrt{s} = 8$ and 13 TeV, respectively. Taken from [102].

TopoClusters, d_{ij} :

$$d_{ij} = \min(k_{ti}^{2p}, k_{tj}^{2p}) \frac{\Delta R_{ij}^2}{R^2}, \quad (4.1)$$

$$d_{iB} = k_{ti}^{2p}, \quad (4.2)$$

where R is the cone size set to 0.4, $\Delta R_{ij}^2 = (y_i - y_j)^2 + (\phi_i - \phi_j)^2$ is the distance between the i th and j th TopoCluster, k_{ti} , ϕ_i , and y_i are the p_T , azimuth, and rapidity of the i th particle, respectively, and p governs the relative power of the energy versus the geometrical ΔR scales [103]. If d_{iB} is the minimum of d_{iB}, d_{ij} , then the i th TopoCluster is reconstructed as a jet. If d_{ij} is the minimum, then the i th and j th TopoClusters are combined to form a new candidate for the anti- k_T algorithm.

Next, the anti- k_T jets are calibrated to relate the energy of a reconstructed jet to the energy of the parton from which it is initiated. This correction is the jet energy scale (JES) correction and is documented in [104]. The calibration is performed first at the parton level, which corrects for jets from different sources, such as from hadronization and initial and final state radiation. Then, the calibration is performed separately for different types of particles to account for different detector responses. For example, the calorimeter response is different between electromagnetic particles and hadronic particles. It also depends on the flavor composition. Finally, the final jet energy is determined after correcting for the following:

- The jet is corrected to point to its primary vertex instead of to its nominal interaction point.
- A pileup correction by removing pileup using an area-based subtraction.
- The biases from the $|\eta|$ position of the jets, arising from the gaps and transitions between calorimeter subdetectors, are corrected with an inter- $|\eta|$ calibration [105].
- The difference between data and simulation is applied to jets in data using an *in-situ*

calibration [105].

The jet energy resolution (JER) is determined in simulation the geometrical matching of particle-level jets to calorimeter jets. For a given particle-jet p_T , it is defined by the width of the response distribution, $(p_T^{\text{reco}} - p_T^{\text{particle}}) / p_T^{\text{reco}}$. In data, one of the ways for the determination of the JER uses the principle that two jets in dijet events at leading-order QCD are expected to have equal transverse momenta. A p_T -imbalance would arise from different calorimeter responses to jets, for example, in different calorimeter regions [106]. The asymmetry, \mathcal{A} , is used to probe the JER:

$$\sigma(\mathcal{A}) = \frac{\sqrt{\sigma(p_T^{\text{reference}})^2 + \sigma(p_T^{\text{probe}})^2}}{p_T^{\text{average}}}, \quad (4.3)$$

where $\sigma(p_T^{\text{reference}})$ and $\sigma(p_T^{\text{probe}})$ are the jet energy resolutions corresponding to the reference and probe jets. The principle of p_T -balance holds for $2 \rightarrow 2$ partonic events. In reality, it can be affected by, e.g., additional quark/gluon radiation outside of the jets. Therefore, a particle-level asymmetry is obtained from simulation to correct the measured asymmetry in Equation 4.3. The systematic uncertainty on the JER is taken to be the difference in JER between simulation and data. It arises from, e.g., the mismodeling of detector effects of physics in simulation. The mismodeling sources stem from uncertainties on, e.g., the calorimeter response, the particle-level correction to Equation 4.3, the JES calibration, the pileup subtraction, the veto of a third jet in dijet events, and the p_T - and η -dependence of the JER [104, 106]. To account for changes to the JER in Run-II from different detector conditions that may not be properly simulated, a smearing factor is applied as a scale factor to jets in simulation to increase the jet energy resolution to that measured in data, plus its error:

$$\sigma = \sqrt{(\sigma_{\text{data}} + \Delta\sigma_{\text{data}})^2 - \sigma_{\text{data}}^2}, \quad (4.4)$$

where σ_{data} is the jet resolution measured in data and $\Delta\sigma_{\text{data}}$ the corresponding uncertainty.

4.3 Missing transverse energy reconstruction

Neutral, weakly interacting particles, such as neutrinos, do not leave signatures in the ATLAS detector. Therefore, only the sum of the transverse momenta for all neutrinos, or \cancel{E}_T , can be measured. This is because the initial longitudinal momenta of the partons that participate in the hard scattering event is unknown in pp collisions. On the other hand, since there is no initial momentum in the transverse plane, momentum conservation yields the missing transverse momentum. It is calculated as the negative sum of all calibrated physics objects in an event and the soft term, which corresponds to all additional energy depositions and tracks not associated to any physics objects:

$$\cancel{E}_{x(y)} = \cancel{E}_{x(y)}^{\gamma} + \cancel{E}_{x(y)}^e + \cancel{E}_{x(y)}^{\mu} + \cancel{E}_{x(y)}^{\tau} + \cancel{E}_{x(y)}^{\text{jets}} + \cancel{E}_{x(y)}^{\text{soft term}}, \quad (4.5)$$

where x and y are the components of the transverse plane. The \cancel{E}_T resolution can be degraded by misreconstructed physics objects and detector resolution. The parametrization of this \cancel{E}_T resolution is relevant for the di-tau invariant mass reconstruction described in Section 5.5. Devoted uncertainties on the reconstruction of \cancel{E}_T are described in Section 5.8.1.2.

4.4 Hadronic tau decays at ATLAS

The properties of the tau lepton were previously presented in Section 2.2. This section discusses the algorithms for the reconstruction, identification, and calibration of hadronically decaying tau leptons. Unless otherwise noted, tau reconstruction refers to the reconstruction of tau leptons that decay hadronically, or τ_{had} . First, the reconstruction of jets as τ -jets is discussed, where τ -jets refer to jet candidates from hadronically tau decays. This is followed by the calibration of τ -jets. Then, the identification of τ -jets that are more likely to have come from a hadronically decaying tau lepton is detailed. τ -jets selected by the identification algorithm are called τ_{had} candidates. Finally, the section is concluded by a description of the tau trigger. The next chapter delineates the reconstruction of individual visible decay products from the τ_{had} candidate, which is an algorithm using particle flow methods.

4.4.1 Tau reconstruction

The tau reconstruction algorithm at ATLAS must reconstruct visible decays of the hadronically decaying tau candidate, henceforth called $\tau_{\text{had-vis}}$ decays, with a good 4-momentum resolution. This is important for physics analyses. For example, the $H \rightarrow \tau\tau$ couplings measurement presented in Chapter 5 makes use of the Higgs mass resolution to reject the $Z \rightarrow \tau\tau$ background, which has a mass peak that sits closely below the Higgs mass peak and which has a cross section about 600 times higher than the $H \rightarrow \tau\tau$ cross section. The reconstruction algorithm used in the Run-II data-taking at ATLAS is documented in [107–110]. This section provides a brief overview.

First, the tau reconstruction is seeded with LC-calibrated anti- k_T jets with a distance parameter of $R = 0.4$. Each jet must pass $p_T > 10$ GeV and $|\eta| < 2.5$. In addition, each jet must have a reconstructed primary vertex with at least three associated tracks. These tracks are associated to the τ -jet if they are found within a ΔR cone of radius 0.2 around the τ -jet direction, have a p_T of at least 1 GeV, and pass additional quality criteria, such as on the number of hits in the inner detector.

Next, the preliminary four-momentum of the τ -jets is determined. The three-momentum components of the τ -jet are designated by the barycenter of the topocluster calibrated at LC scale. Then, a jet vertex tagger (JVT) addresses cases where the tau lepton does not come from the designated primary vertex [111]. It takes all tau candidate tracks and selects the vertex with the highest fraction of the p_T sum. Next, the direction of the τ_{had} candidate is corrected using this selected vertex. The preliminary p_T of the $\tau_{\text{had-vis}}$ candidate is set as the total energy of all TopoClusters in $\Delta R < 0.2$. This energy is used for the calculation of $\tau_{\text{had, vis}}$ ID variables described in the next section and is the base value of the tau energy calibration that is described next.

A designated tau energy calibration corrects the τ -jet energy measured by the detector to the true visible energy. The tau energy scale (TES) adds corrections that are not addressed by the LC. It takes care of pileup subtraction and provides a response correction for effects such as tau decay products not reaching the calorimeter, tau decay products whose energy depositions do not result in TopoClusters due to low energy or deposition outside of the $\Delta R < 0.2$ tau cone, and different particle composition.

There are two TES options available in Run-II: calorimeter-only (Calo TES) and MVA TES, an machine-learning combination of the calorimeter TES and the substructure TES, where substructure refers to the use of particle flow methods that reconstruct the four-momenta of

the individual tau decay products, which are then summed in the constituent-based $\tau_{\text{had-vis}}$ momentum (described later in Section 4.5).¹ In the TES calibration, the Calo TES takes into account a pileup correction factor and a calibration function for the detector response. The advantage of including the substructure TES is that it uses calorimeter information combined with information from the tracker, which has better resolution for low- p_T charged pions (see Figure 3.7). This yields a more pileup robust TES. However, there are still large tails in the energy resolution. Combining the Calo TES and substructure TES in the MVA TES results in a better tail resolution and can further improve the energy resolution. The result is a p_T with a combined weighted average of the Calo and Substructure TES.

In addition, regardless of whether the tau p_T is based on calorimeter information or calibrated through the MVA method, the difference between the visible tau p_T in data and simulation needs to be measured. This TES *in situ* measurement is performed in $Z \rightarrow \tau_{\text{lep}}\tau_{\text{had}} \rightarrow \mu\tau_{\text{had}}|\nu\bar{\nu}$ events and is based on the fact that the reconstructed visible mass is sensitive to shifts in the TES for data and simulation.² The p_T correcting for the shift is

$$p_T(\alpha) = (1 + \alpha) \cdot p_{T, \text{calo/MVA}}, \quad (4.6)$$

where α is the shift factor to be determined. Systematic uncertainties on the TES are described in Section 5.8.1.1.

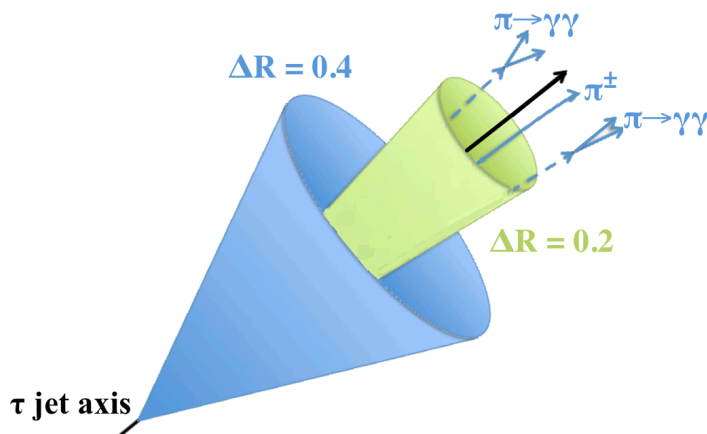


Figure 4.2: Schematic of the visible decay products of a $\tau^\pm \rightarrow a_1(\rightarrow \pi^\pm \pi^0 \pi^0) \nu_\tau$ decay in the isolation cone currently used at ATLAS. Tau decays are narrow and have a low multiplicity of particles.

4.4.2 Tau identification

The reconstruction and calibration of τ -jets does not provide discrimination against quark- and gluon-initiated jets that can be mistakenly reconstructed as τ_{had} candidates, which are called

¹ The particle flow method is described in the next section in more detail since it was part of the work of this dissertation.

² Other observables are also sensitive to shifts, including Upsilon, a polarization-sensitive observable later described in Section 6.1.2 and defined in Equation 6.8.

jet fakes. For this, the identification of hadronically decaying taus from the reconstructed τ -jets candidates is performed in a separate step. This $\tau_{\text{had, vis}}$ ID algorithm must identify tau decays efficiently while also achieving a good rejection of jets that can be misidentified as tau leptons. The jet production at ATLAS has a cross section many orders of magnitude higher than the cross section of EW interactions involving tau leptons. There are, however, key distinguishing features between jets and tau leptons that the tau identification algorithm uses. First, the decay products from a τ_{had} candidate are more collimated since they are produced with a boost. Second, tau decays also have a lower multiplicity of particles, typically one or three charged hadrons and up to two neutral hadrons (see Table 2.6 listing tau branching ratios). A schematic of a typical tau decay with collimated particles contained in its core cone ($\Delta R < 0.2$) is shown in Figure 4.2. The $\tau_{\text{had, vis}}$ ID algorithm uses discriminating variables that capitalize on these features in Boosted Decision Tree methods (BDT) [110, 112]. In this tau identification algorithm ($\tau_{\text{had, vis}}$ ID), BDTs are trained that exploit discriminating variables described in the next paragraph. They are trained on $Z/\gamma^* \rightarrow \tau\tau$ signal events and dijet background events selected from data, separately for 1- and 3-prong τ -jets. Based on the BDT output, τ_{had} candidates are selected for three working points based on the identification efficiency: 0.6, 0.55 and 0.45 for loose, medium, and tight 1-prong τ_{had} candidates and 0.5, 0.4 and 0.3 for 3-prong τ_{had} candidates [109]. The BDT requirement for the $\tau_{\text{had, vis}}$ ID workings points are optimized such that the efficiencies are stable as a function of p_T . Pileup corrections are applied so that the efficiencies are stable as a function of the average number of interactions, $\langle \mu \rangle$.

The identification variables in the $\tau_{\text{had, vis}}$ ID make use of key discriminating features between QCD and τ -jets:

- The associated tracks and the energy deposits in the calorimeter are more collimated for τ -jets. The multiplicity of particles is also lower for τ -jets (typically 0, 1, or 2 neutral pions).
- The longitudinal energy deposition, such as the sum of the p_T of the cluster energy deposited in the ECAL compared to the momentum of the tracks.
- The fraction of energy carried by the leading- p_T track is larger for τ -jets.
- The impact parameter with respect to the tau vertex, or the distance between the tau vertex and the decay product vector extended in the direction of the tau vertex, is non-negligible for τ -jets due to the decay length of the tau lepton.

The full list of variables is documented in [109]. Figure 4.3 shows an example of the signal and background distributions for a discriminating variable.

In addition, an electron rejection algorithm reduces the contribution from electron fakes, or electrons that can be misidentified as a one-prong τ_{had} candidate. Bremsstrahlung processes of the electron can even fake three-prong taus because there will be two additional tracks from the daughter electron and photon. The rejection of electrons faking tau leptons is performed using the likelihood discriminator developed for electron reconstruction and identification in Run-II [113]. The electron rejection is also aided by the TRT of the ATLAS detector (c.f. Section 3.2.2). The tau leptons that are matched to an electron candidate with a high electron likelihood score are rejected.

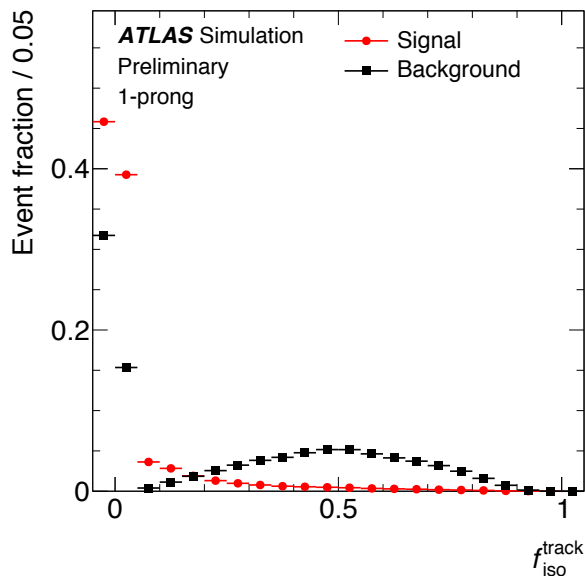


Figure 4.3: Example of a discriminating variable used in the $\tau_{\text{had, vis}}$ ID. The variable, $f_{\text{iso}}^{\text{track}}$, describes the scalar sum of the p_T of tracks associated to the τ_{had} candidate in the $0.2 < \Delta R < 0.4$ annulus divided by the sum of the p_T of all tracks associated with the τ_{had} candidate. Taken from [109].

4.4.3 Performance of the tau reconstruction and identification

The efficiency of the algorithms to correctly reconstruct and identify a true $\tau_{\text{had-vis}}$ candidate is shown in Figure 4.4. The reconstruction efficiency is the fraction of true one-prong (three-prong) hadronically decaying tau leptons that are reconstructed as one-track (three-track) τ_{had} candidates. The $\tau_{\text{had, vis}}$ ID efficiency is the fraction of true one-prong (three-prong) hadronically decaying tau leptons that are identified correctly as one-track (three-track) τ_{had} candidates passing the $\tau_{\text{had, vis}}$ ID selection. Since the efficiencies of the tau reconstruction and identification algorithms can be different in simulation and data, scale factors are derived to correct them to match efficiencies observed in data. These scale factors that are applied to simulation are defined as

$$\text{Scale Factor} = \frac{\epsilon_{\text{Data}}}{\epsilon_{\text{MC}}}. \quad (4.7)$$

They are derived from tag-and-probe analyses using $Z \rightarrow \tau\tau$, $W \rightarrow \tau\nu$, and $t\bar{t} \rightarrow \tau+\text{jets}$ events [114]. Systematic uncertainties on these scale factors are described in Section 5.8.1.1.

4.4.4 The tau trigger

Events in τ_{had} decays are selected for recording in the data acquisition stage by the tau trigger. This section describes the tau trigger components, or legs, that make up the di-tau trigger used in the physics analyses of this dissertation: the leading- and subleading- p_T τ_{had} trigger legs. Their corresponding selection requirements and ATLAS-internal nomenclature are summarized in Table 4.1.

The tau trigger is separated into two types: online and offline. The online trigger is used during data taking, and the offline trigger is used when processing the recorded data in the ATLAS reconstruction software. The online L1 tau trigger uses squares of 2×2 trigger towers

Trigger name	ATLAS-internal nomenclature	Online trigger selection
Leading- p_T τ_{had} trigger leg	ditau_tau0_HLT_tau35_medium1_tracktwo	$p_T(\tau_{\text{had}}) > 35$ GeV Pass medium BDT identification criteria.
Subleading- p_T τ_{had} trigger leg	ditau_tau1_HLT_tau25_medium1_tracktwo	$p_T(\tau_{\text{had}}) > 25$ GeV Pass medium BDT identification criteria.
2015 Di-tau trigger	HLT_tau35_medium1_tracktwo_tau25_ medium1_tracktwo_L1TAU20IM_2TAU12IM	Pass the leading- and subleading- p_T τ_{had} trigger legs.
2016 Di-tau trigger	HLT_tau35_medium1_tracktwo_tau25_ medium1_tracktwo	Pass the leading- and subleading- p_T τ_{had} trigger legs The leading- p_T L1 jet passes a threshold of $p_T > 25$ GeV.

Table 4.1: The tau trigger nomenclature and selection criteria at HLT [115]. (Refer to text for definitions of the selection criteria.)

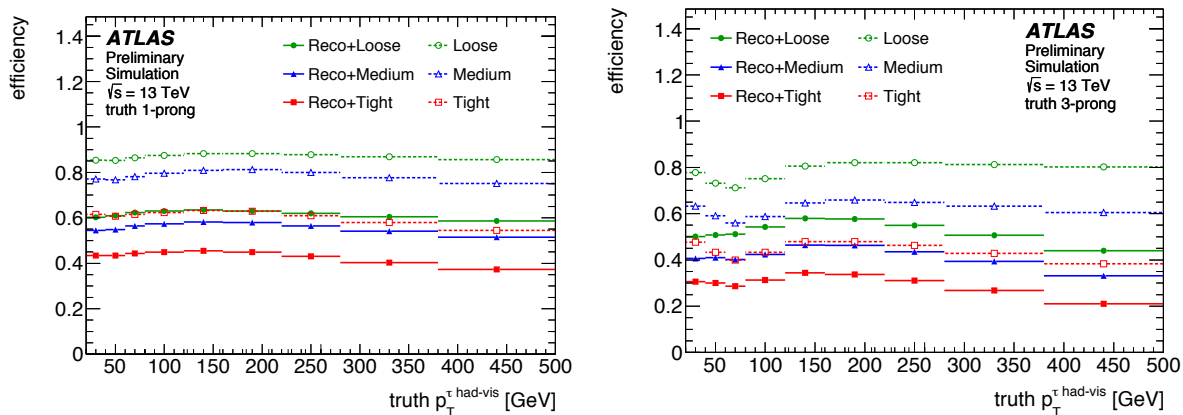


Figure 4.4: The $\tau_{\text{had,vis}}$ ID efficiency (open symbols) and combined $\tau_{\text{had,vis}}$ ID and reconstruction efficiencies (full symbols) for 1p (top left) and 3p (top right) $\tau_{\text{had,vis}}$ candidates vs. the p_T of the $\tau_{\text{had,vis}}$ candidate. Taken from [109].

in the calorimeter (see Section 3.2.4 where a trigger tower was previously defined), each with a granularity of $\Delta\eta \times \Delta\phi = 0.1 \times 0.1$. The visible E_T of the τ_{had} candidate is calculated as the sum of the E_T in the two highest E_T neighboring trigger towers in the ECAL and in the 2×2 towers in the HCAL. In addition, an EM isolation energy, $E_T^{\text{EM isolation}}$, is used and calculated to be the E_T found in the annulus from 0.2×0.2 to 0.4×0.4 in the ECAL. The quantity $E_T^{\text{EM isolation}}$ is used to maintain a high acceptance of signal while suppressing background and reducing trigger rates. A threshold of

$$E_T^{\text{EM isolation}} \leq \frac{E_T}{10} + 2 \text{ GeV} \quad (4.8)$$

is applied to τ_{had} candidates, up to 60 GeV. This requirement has a signal efficiency of 98%. The E_T reconstruction is much less accurate than that in the offline τ_{had} reconstruction algorithm. The coarsely granular cells in the L1 trigger tower are combined without the use of the TopoCluster algorithm and without specific τ_{had} candidate energy calibrations, which will be described in Section 4.4.1. This results in a significant loss of τ_{had} candidates with low visible E_T .

The HLT of the tau trigger is divided into three steps: calo-only preselection, track preselection, and offline-like selection (see Section 3.2.4 where HLT is defined). It is seeded by the RoI from the L1 trigger, as previously discussed in Section 3.2.4. In the calo-only preselection, a τ_{had} candidate is reconstructed with only calorimeter information using the full granularity of the calorimeter and the TopoCluster algorithm. It has a mean execution time of 8 ms. In the track preselection, tracking information is added in the reconstruction of the τ_{had} candidate. It uses a pattern recognition algorithm to search for the leading p_T track in a narrow ΔR cone around the visible τ_{had} candidate. Then, it associates additional possible tracks to the τ_{had} candidate. This is all completed within a mean execution time of 60 ms. In the offline-like selection, a BDT with τ_{had} identification variables is used to select τ_{had} candidates. On average, this step is executed within 22 ms.

The subleading- p_T τ_{had} trigger requires an isolated τ_{had} candidate with $E_T > 12$ GeV at L1 and $p_T > 25$ GeV at HLT passing the baseline medium BDT identification criteria (c.f. Table 4.1). This medium working point is defined to have a trigger efficiency of 96% for true one prong $\tau_{\text{had-vis}}$ candidates and 82% for three prong candidates. The analogous leading- p_T

τ_{had} trigger leg requires a p_T greater than 35 GeV at HLT. The efficiencies of the subleading- p_T τ_{had} trigger to select a true τ_{had} candidate is shown in Figures 4.5. The efficiency curves have a sharp turn-on at low p_T , a region in which τ_{had} candidates are rejected in analyses to ensure the trigger validity. The efficiencies at the plateaus are about 95% (85%) for τ_{had} candidates with one (three) tracks. The $H \rightarrow \tau\tau$ analyses presented in this dissertation use the 2015 and 20016

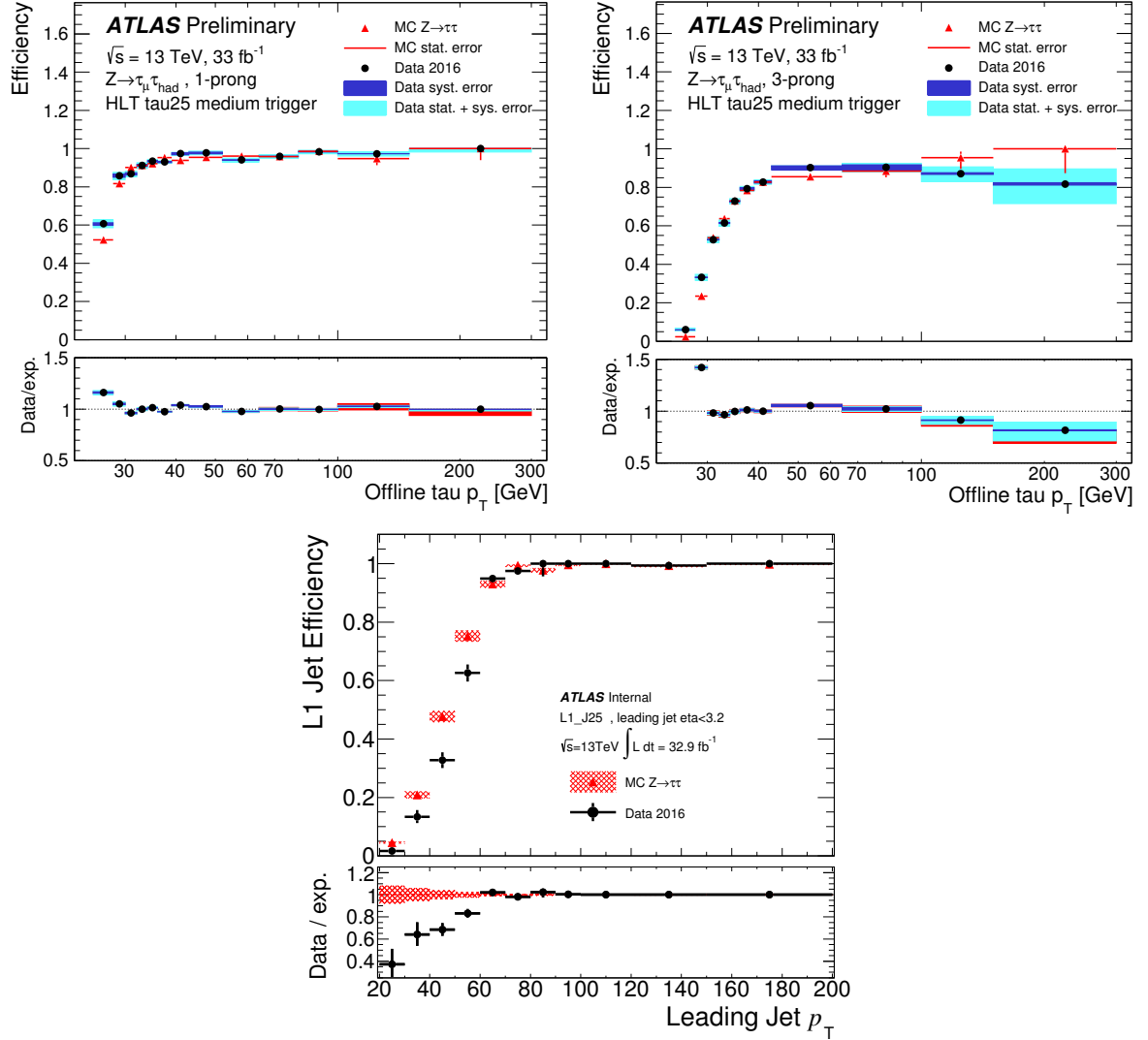


Figure 4.5: Efficiencies of the subleading- p_T τ_{had} trigger leg of the di-tau trigger for τ_{had} candidates with 1 track (top left) and 3 tracks (top right). (Refer to Table 4.1 where the trigger legs were previously defined.) The efficiency of the L1 jet requirement after requiring the L1 jet to be within $|\eta| < 3.2$ is shown in the bottom figure. Taken from [4, 115].

di-tau trigger with the leading- and subleading- p_T τ_{had} trigger legs (c.f. Table 4.1).

4.5 The tau particle flow reconstruction

In Run-II, the tau reconstruction at ATLAS uses a new particle flow algorithm that combines information from different detector components to reconstructs each individual decay product of a τ_{had} candidate. It is referred to in this dissertation as the *tau substructure* or *tau particle flow algorithm* [94]. The Run-I version of the tau reconstruction algorithm did not classify decay modes or reconstruct the four-momenta of each visible tau decay product [116], and efforts were made for the Run-II version since there are several advantages that come from correctly identifying the τ_{had} decay mode. First, correctly identifying the number of neutral pions in a τ_{had} decay improves the overall 4-momentum resolution of the tau lepton since it provides the neutral and charged energy components separately. Second, particle flow reconstruction is important for physics analyses that have been increasingly making use of tau polarization. The identification of charged and neutral pions from tau decays (π^0 -ID) is important in correctly identifying the tau decay mode, a classification which is important for polarization and Higgs CP measurements. The Higgs CP measurement presented in Section 6, in particular, uses results from this tau particle flow algorithm. Third, it can, to some degree, be used to suppress QCD jets mis-reconstructed as $\tau_{\text{had-vis}}$ candidates. It can also be used to improve the parametrization of the \cancel{E}_T resolution in the reconstruction of the di-tau invariant mass, as later described in Section 5.5.

4.5.1 Data and simulated samples

The simulated samples used for the tau particle flow results presented in this chapter are listed in Table 4.2. A summary of MC simulation is provided later in the first analysis chapter (Section 5.4.2). The development of the cluster level subtraction described in Section 4.5.3 is developed using a single π^\pm sample from PYTHIA 8.1 [117]. It is an artificial sample of simulated, single charged pions that originate from the center of the detector. The charged pions are generated from the center of the ATLAS detector. The energy and spatial distributions of this sample are shown in Appendix D. A $Z \rightarrow \tau\tau$ sample from PYTHIA 8.1 is also used in the tau particle flow development and later for the comparison of the performance of the tau particle flow applied to τ_{had} candidates in simulation and in data [117]. The PDF and underlying event (UE) tunes used for the simulation are the CTEQ6L1 PDF parametrization and the AU2 tune [118, 119]. A $Z \rightarrow \mu\mu$ sample from ALPGEN is used for the performance comparison on jets instead of tau leptons [120] [120]. The sample uses the CTEQ6L1 PDF parametrization and the PERUGIA UE tune [121]. The selection requirements for the $Z \rightarrow \tau\tau$ and $Z \rightarrow \mu\mu$ tag-and-probe analyses (described later in Section 4.5.8) are documented in [94].

Process	Generator	PDF	UE tune
Single π^\pm	PYTHIA 8.1	N/A	N/A
$Z \rightarrow \tau\tau$	PYTHIA 8.1	CTEQ6L1	AU2
$Z \rightarrow \mu\mu$	ALPGEN+PYTHIA 8	CTEQ6L1	PERUGIA

Table 4.2: Summary of the generators, PDFs, and UE tunes used for the simulated samples in the development and performance measurement of the tau particle flow algorithm.

4.5.2 Concept and method

The aim of the tau particle flow algorithm is to reconstruct each individual decay product of the τ_{had} candidate and classify τ_{had} candidate into the five dominant hadronic decay modes, listed in Table 4.3. The *ansatz* is to reconstruct the charged components of the τ_{had} decay, typically a charged pion or kaon and denoted as h^\pm . The charged components are reconstructed using the tracking system, which provides a better energy resolution than the calorimeter for the $p_T < 150$ GeV, as previously shown in Figure 3.7. Then, the neutral components of the τ_{had} decay (π^0) are reconstructed from energy deposits in the ECAL.

Decay mode	Decay mode nomenclature
h^\pm	1p0n
$h^\pm \pi^0$	1p1n
$h^\pm \geq 2\pi^0$	1pXn
$3h^\pm$	3p0n
$3h^\pm \geq 1\pi^0$	3pXn

Table 4.3: The decay modes classified by the tau particle flow algorithm (c.f. Table 2.6). Neutrinos are not listed. A charged hadron from a τ_{had} decay, h^\pm , is a charged pion or kaon.

This is realized in the tau particle flow algorithm as follows:

1. Estimate the charged component of the τ_{had} candidate (four-momenta of each charged hadron) using tracks (described in Section 4.5.3).
2. Estimate the neutral component of the τ_{had} candidate (four-momenta of each neutral pion) using the calorimeter, with contamination from charged pions energy deposits in the calorimeter removed (described in Section 4.5.4).
3. Identify energy deposits in the calorimeter from neutral pions using η -dependent p_T thresholds and a BDT (described in Section 4.5.4).
4. Identify multiple neutral pions that are reconstructed as one cluster (or merged neutral pions) using photon hits in the finely segmented strip layer of the ECAL (described in Section 4.5.5).
5. Classify each tau decay mode using global variables in BDTs (described in Section 4.5.6).

The algorithm performance is quantified by the percentage of correctly classified decay modes:

$$\text{Figure of merit} = \frac{\text{Total number of } \tau_{\text{had}} \text{ candidates whose decay mode is correctly reconstructed}}{\text{Total number of } \tau_{\text{had}} \text{ candidates reconstructed}}. \quad (4.9)$$

and the 4-momentum resolution of the τ_{had} candidate and its decay products.

4.5.3 Subtraction of π^\pm energy deposits

The crux of the tau particle flow reconstruction at the ATLAS detector lies in the fact that the tau lepton decays quickly, typically before reaching the inner detector, and the fact that the resulting charged and neutral pions showers overlap in certain layers of the calorimeters,

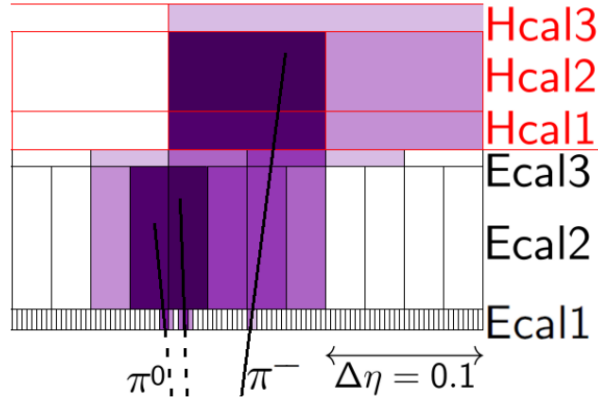


Figure 4.6: Schematic of the visible decay products of a $\tau^\pm \rightarrow \rho^\pm (\rightarrow \pi^\pm \pi^0) \nu_\tau$ decay in the ATLAS detector. A darker color indicates higher energy depositions. Taken from [122].

as shown in the schematic in Figure 4.6 of the signature of a τ_{had} decay in the ECAL of the ATLAS detector. This section discusses the disentanglement of the overlapping energy depositions.

Charged pions from a hadronically decaying tau lepton leave tracks in the inner detector and typically shower in the ECAL and the HCAL. The showering usually begins in the second layer of the ECAL (EM2), and the rest of the energy is deposited in the HCAL. Meanwhile, neutral pions deposit all of their energy in the ECAL, and the first two layers of the ECAL (EM1, 2) typically contains all of the energy from the neutral pion(s). For the purposes of the particle flow algorithm, the *HCAL* will henceforth refer to the third layer of the ECAL (EM3) grouped together with the HCAL, and *ECAL* will refer only to the first two layers of the ECAL. The mixture of depositions from both charged and neutral pions in the *ECAL* can then be disentangled using information from the π^\pm track(s) in the inner detector and the energy depositions in the *HCAL*:

$$E_{ECAL}^{\pi^\pm} = E_{\text{track}}^{\pi^\pm} - E_{\text{Cluster cells in HCAL}}^{\pi^\pm}. \quad (4.10)$$

Currently, the π^\pm tracks are the tracks found in the core region of the τ_{had} candidate. However, there may be other tracks that are misclassified as a charged pion, such as tracks from photon conversions, pileup, or underlying events. In future versions of the tau particle flow algorithm, it is possible to improve the association of tracks to charged pions to tag these background tracks [123].

After subtracting the contamination from the charged pion in the *ECAL* (described in Section 4.5.3.1), the remaining energy depositions are re-clustered using the TopoCluster algorithm, previously described in Section 3.2.3.3. The preliminary number of neutral pions is then predicted by counting the number of energy depositions identified as neutral pion clusters from the remaining depositions, as later explained in Section 4.5.4.

4.5.3.1 Redeveloped cluster level π^\pm subtraction

In previous versions of the π^\pm subtraction, the π^\pm energy depositions are subtracted out on a cell-by-cell level using average hadronic shower shapes measured in a simulated single π^\pm sample [95, 122, 124]. This version is referred to as the SSS for shower shape subtraction. This section discusses studies of a redeveloped method of π^\pm subtraction called the cluster level π^\pm

subtraction. Studies are performed in this dissertation to verify that simply removing the closest cluster to the π^\pm track, instead of cell-by-cell subtraction, achieves a compatible performance. A schematic of this concept is shown in Figure 4.7. The main difference is that $E_{ECAL}^{\pi^\pm}$ is calculated in a faster and simpler manner without loss of performance. The advantages of this development are:

- The π^\pm subtraction can be rerun more easily. This means that the $\tau_{\text{had-vis}}$ reconstruction algorithm does not have to be rerun if, for example, the definition of π^\pm tracks is changed, especially given the previously discussed new developments in correctly tagging π^\pm tracks.
- There is no need to parametrize the π^\pm shower shape, as was done in the SSS method using MC simulated π^\pm shapes. There is, therefore, less dependence on the accuracy of the MC.
- The reconstruction speed is increased, and the reclustering of the remaining energy deposits in the *ECAL* after the subtraction in principle becomes obsolete. The algorithm is now sufficiently fast to be utilized in the HLT if useful.

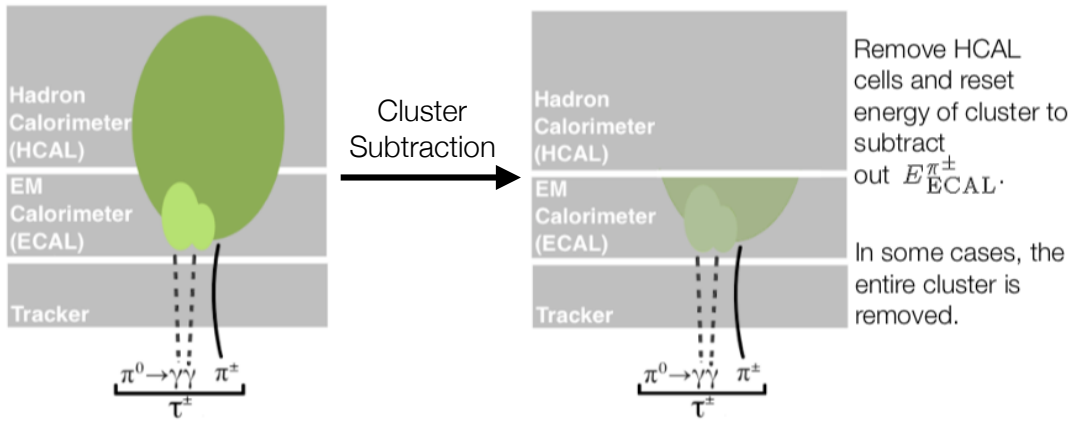


Figure 4.7: Schematic of the cluster level π^\pm subtraction.

To study the performance of this simplified method, the properties of the charged pion clusters are first studied on the simulated single π^\pm sample and the simulated $Z \rightarrow \tau\tau$ sample with pileup from Pythia 8.1 [117].

The procedure is to subtract the closest cluster to the π^\pm track and then set the energy of the closest cluster according to the following cases:

$$E'_{\text{leading cluster}} = \begin{cases} 0, & E_{ECAL}^{\pi^\pm} \geq E_{\text{closest cluster}} \\ E_{\text{leading cluster}} - E_{ECAL}^{\pi^\pm}, & E_{ECAL}^{\pi^\pm} < E_{\text{leading cluster}} \end{cases} \quad (4.11)$$

For the latter case, the η and ϕ of the scaled cluster remain the same. To verify the performance of this method, the fragmentation behavior of the charged pions is investigated in the single π^\pm sample. The simplified subtraction method should achieve the same performance as the SSS method, as measured by Equation 4.9. The p_T and spatial resolution of the reconstructed neutral pions and $\tau_{\text{had-vis}}$ are also used to check the performance.

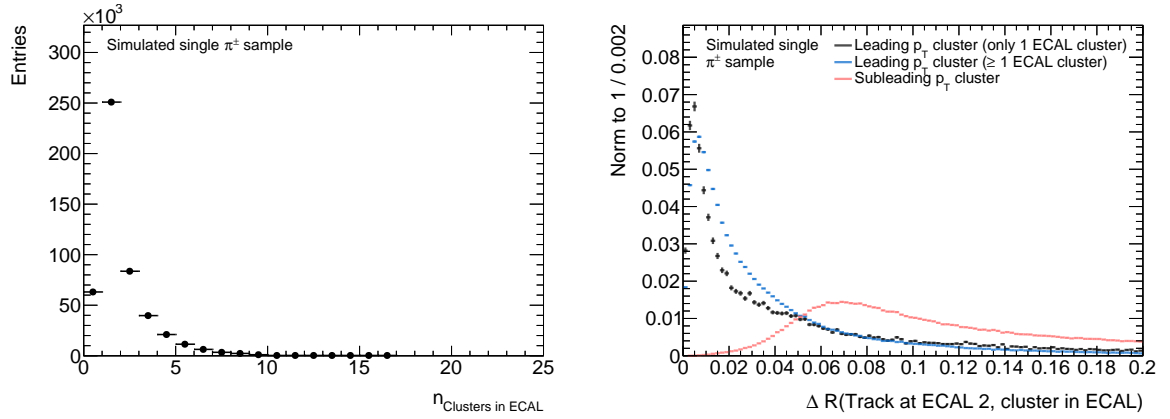
In practice, the cluster closest to the track is removed in the simplified π^\pm subtraction because it provides a better handle on the selection of the π^\pm cluster than removing, for example, the highest p_T cluster. Therefore, it is necessary to verify that the cluster closest to the track contains most of the π^\pm energy and that there is typically only one cluster created by the π^\pm in the *ECAL*. Figure 4.8(a) shows the number of clusters a single charged pion leaves in the *ECAL*. There is only one cluster in the *ECAL* about 45% of the time and more than one cluster in the *ECAL* about 35% of the time. In cases where there is more than one cluster reconstructed in the *ECAL* the leading p_T cluster is the closest cluster to the track about 95% of the time. Figure 4.8(b) shows that the π^\pm showers create clusters that are typically close to the track. For reference, the previous subtraction of the SSS method does not subtract cells further than $\Delta R = 0.05$ on average, due to the shape of the average hadronic showers. Having verified this, the p_T leftover in the *ECAL* after removing or scaling one cluster is checked. If only this leading- p_T cluster is subtracted in the *ECAL*, Figure 4.8(c) shows that the p_T of the π^\pm clusters that would be leftover in the *ECAL* is minimal, typically about 1 GeV. About 60% of the remaining clusters have $p_T > 1$ GeV. The clusters that are found at a distance of $\Delta R > 0.05$ therefore have negligible energy.

The subtraction of more than one cluster is also considered, and the performance gain from performing this in the simulated $Z \rightarrow \tau\tau$ sample is shown to be negligible. This can be seen in the width of the p_T resolution (RMS) for the $\tau_{\text{had-vis}}$ from the $Z \rightarrow \tau\tau$ sample in Figure 4.9, where the p_T resolution is the fractional difference between the generated and the reconstructed p_T . In order to avoid subtracting out potential π^0 clusters, only the closest cluster is removed or p_T -scaled.

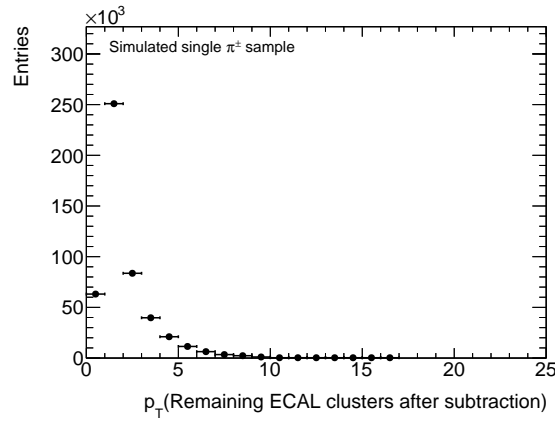
The performance on a $Z \rightarrow \tau\tau$ sample after the simplified π^\pm subtraction compared with the SSS method is shown to be similar in the next section in Figure 4.14. The performance achieved by the SSS method in the fraction of correct classified tau decay modes is only about 1% better than the cluster subtraction method presented here. This negligible degradation in performance is due to the fact that the π^0 showers are typically far enough away from the π^\pm clusters that a cell-by-cell level subtraction leaves the π^0 clusters unaffected. In addition, even when a π^0 cluster contains residual π^\pm showers, it is distinct enough that the π^0 -ID, described in the next section, can discriminate it from background π^0 clusters. Before showing the final performance of the simplified π^\pm subtraction, the π^0 -ID steps of the algorithm are first discussed since they are used in the results shown in this figure.

4.5.4 Identification of neutral pions

After the cluster level subtraction of the π^\pm cluster, neutral pions are identified in the remaining energy distribution. This step is known as the π^0 -ID. The remaining energy in the *ECAL* is reclustered, and an η -dependent p_T -requirement and a Boosted Decision Tree are used to either select or reject each π^0 candidate. This BDT is trained to identify signal π^0 clusters among background π^0 clusters caused by pileup, noise, and imperfect π^\pm subtraction. To reduce background, all π^0 cluster candidates are required to pass a preliminary energy threshold of 1.5 GeV. The remaining candidates are then classified as π^0 clusters or rejected as background clusters by exploiting cluster properties in the BDT. The properties used are detailed in Table C.1. They exploit, for example, the shape and depth of the cluster. Some kinematic quantities, such as the invariant mass of the π^0 cluster and the track, are not used in the BDT since they are employed in downstream analyses, such as the $\tau_{\text{had, vis}}$ ID and polarization studies. After the BDT, the final p_T and BDT requirements are determined based on the figure of merit in



(a) Number of clusters reconstructed in the *ECAL* from charged pion fragmentation. Only one cluster is found in the *ECAL* 45% of the time, and more than one cluster 35% of the time. (b) ΔR between the track (extrapolated to EM2) and the leading- p_T cluster in the *ECAL* for the single π^\pm sample.



(c) p_T of *ECAL* clusters leftover after the cluster level π^\pm subtraction in the simulated single π^\pm sample.

Figure 4.8: Behavior of charged pion showers in the *ECAL*.

Equation 4.9.

The BDT is trained and tested using the simulated $Z \rightarrow \tau\tau$ sample, which contains information on the original, generated particles. The π^0 cluster candidates as identified as signal if they are the closest cluster to the position of the generated π^0 . All other cluster candidates are classified as background. The separation achieved by the BDT between signal and background π^0 clusters is shown in the BDT output, which gives a score for each π^0 cluster based on how signal-like the π^0 cluster is (see Figure 4.10(a)). The performance of the BDT is quantified with a ROC curve, which shows the tradeoff between the efficiency of the BDT to identify true neutral pions and the BDT to reject background neutral pions (see Figure 4.10(b)). The area under the ROC curve (AUC) is a figure of merit used to measure the performance of the BDT. An AUC of 0.5 is equivalent to random guessing, and an AUC of 1.0 is equivalent to perfect performance. Since the classification is not perfect and an overlap exists between signal and background π^0 clusters in the BDT score output, the selection of signal-like π^0 clusters is performed using η -dependent p_T and BDT score criteria. They are optimized according to the percentage of

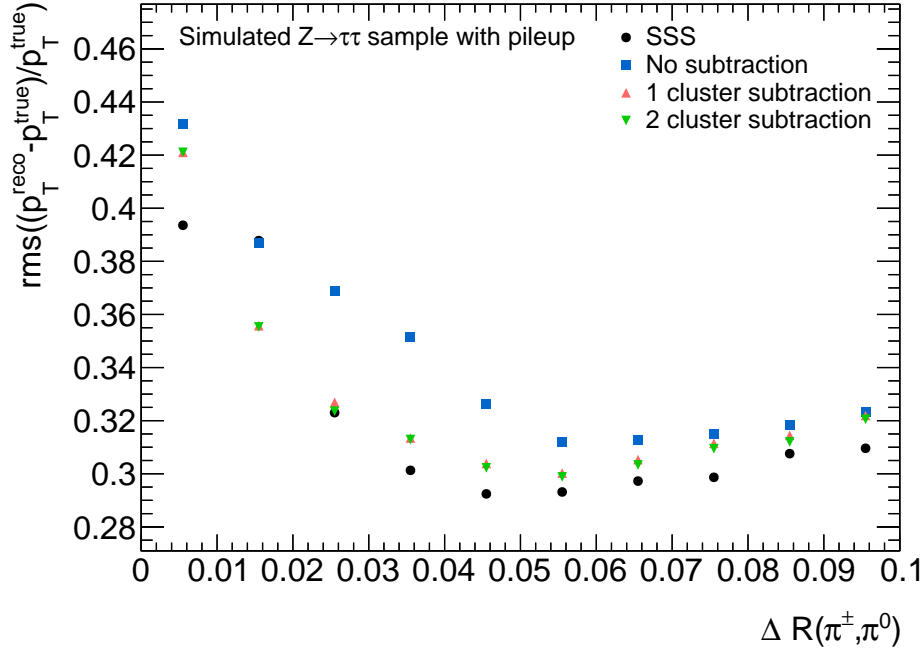


Figure 4.9: RMS of the p_T resolution for the $\tau_{\text{had-vis}}$ candidate after the different methods of subtraction in the simulated $Z \rightarrow \tau\tau$ sample with pileup.

correctly classified tau decay modes, previously defined in Equation 4.9. The optimized p_T threshold and BDT score selection for signal-like π^0 clusters are shown in Table 4.4.

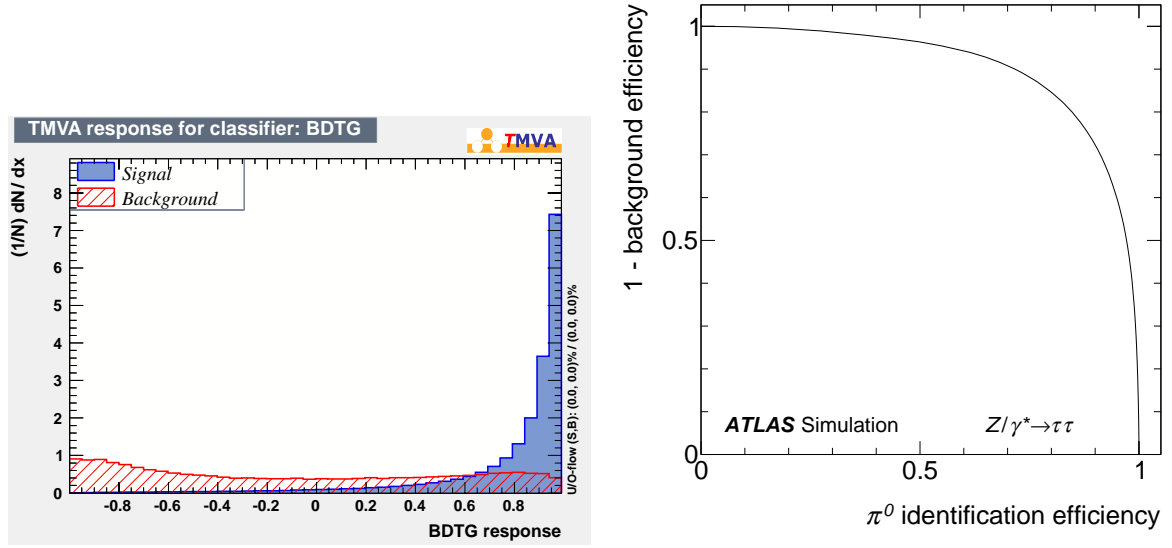
	$ \eta $ range	0.0–0.8	0.8–1.4	1.4–1.5	1.5–1.9	≥ 1.9
E_T cut for a π^0 cluster (MeV)		2100	2500	2700	2500	2200
BDT score cut for a π^0 cluster (1p)		0.47	0.45	0.55	0.46	0.44
BDT score cut for a π^0 cluster (3p)		0.61	0.60	0.71	0.69	0.52

Table 4.4: Optimized η -dependent requirements on the p_T and BDT score for an identified π^0 cluster.

4.5.5 π^0 cluster separation using photon hits

After having described the reconstruction and identification of π^0 clusters that pass the π^0 -ID, this section describes the use of the finely segmented *ECAL1* to further improve the tau particle flow algorithm. The π^0 clusters passing the π^0 -ID may contain more than one π^0 , especially if the neutral pions come from a highly boosted tau. I.e., the tau decay mode is classified as 1p1n instead of 1pXn.³ Such clusters are called merged π^0 clusters and, in a $Z \rightarrow \tau\tau$ sample with pileup, occur in about 50% of cases where a 1pXn τ_{had} candidate is wrongly classified as a 1p1n τ_{had} candidate [95, 122]. These merged π^0 clusters can be identified using photon hits

³ This misclassification degrades the 4-momentum resolution and can further degrade the sensitivity of downstream analyses, such as the Higgs \mathcal{CP} analysis that reconstructs \mathcal{CP} -sensitive observables based on the tau decay mode.



(a) BDT score distribution showing the separation between signal and background π^0 clusters used for the π^0 -ID. Taken from [125], which is the ATLAS internal documentation for [94].

(b) ROC curve showing the tradeoff between the signal efficiency and background rejection of the π^0 identification [94].

reconstructed in the *ECAL1* strip layer (previously shown in Figure 3.9, with segmentation listed in Table B.1). Figure 4.11 shows an event display of such photon hits reconstructed for the two photons from a π^0 in a simulated $Z \rightarrow \tau\tau$ decay.⁴ It shows that the cells of the finely granular strip layer are narrow enough that each photon from a π^0 can create its own local maximum, from which the photon hits are reconstructed. The details of the photon hit reconstruction, such as the η -dependent p_T thresholds for the center cell of a photon hit, are described in [94, 95].

The reconstruction efficiency of a photon hit is measured in a single π^0 sample, a sample that was previously described in [95]. The photons are reconstructed with almost 100% efficiency in Figure 4.12. This is consistent with the prediction of the probability of a photon from a π^0 to begin its shower in the strip layer:

$$P(\text{photon converts in strip layer}) = 1 - e^{-\frac{7}{9}N_{\text{rad}}}, \quad (4.12)$$

where $N_{\text{rad}} \approx 4.3$ is the number of radiation lengths of the strip layer for the barrel and end-cap, as shown in Figures B.2(a) and B.2(b) [79]. The radiation length is the mean path length after which the energy of a relativistic charged particle is reduced by a factor of $\frac{1}{e} = 0.368$. Considering the material in the strip layer, the probability of a photon to convert to an e^+e^- pair is approximately 96.5%.

The two photons from a π^0 can sometimes be so boosted that they create a single photon hit instead of two. This is shown in Figure 4.12 as the share probability, where it can be seen that the share probability increases with the p_T of the photon. Therefore, only three or more photon hits are required to identify a π^0 cluster as a merged π^0 cluster. A previously reconstructed 1p1n candidate is considered a 1pXn candidate if a merged π^0 cluster is identified. The performance of π^0 -ID and the decay mode classification after this photon hit counting to move wrongly classified 1p1n decay modes into the 1pXn category is shown in Figure 4.13. The figure of merit

⁴ The simulated $Z \rightarrow \tau\tau$ sample is from [117] and was previously described in [95].

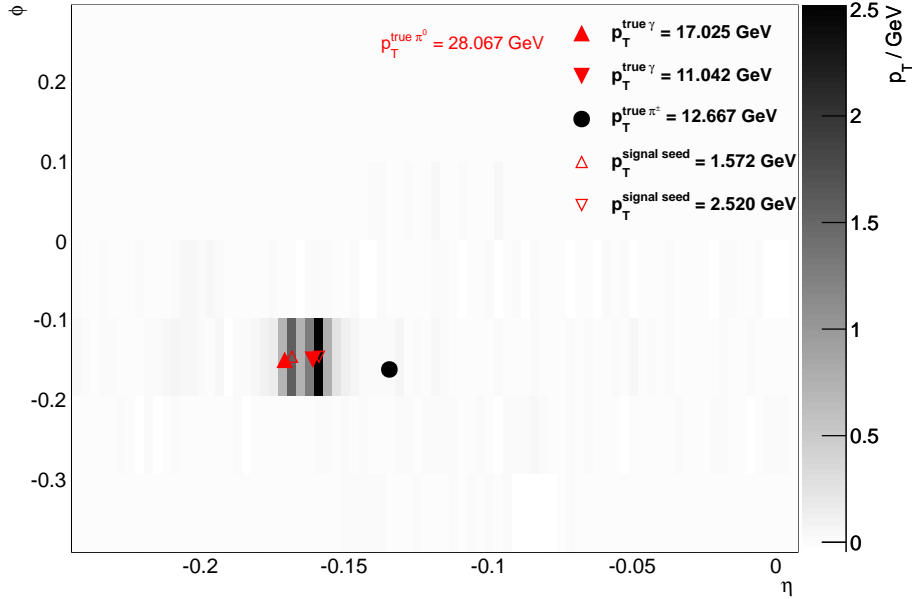


Figure 4.11: 2-D display of an MC $Z \rightarrow \tau\tau$ event in the strip layer. Each bin corresponds to one strip cell. The generated positions of the final state particles are overlaid on top of the cells, with their corresponding p_T shown in the legend. The position of the true photons are the filled red triangles, and the black circle is the generated position of the π^\pm [95].

value achieved is 70.9% of correctly classified tau decay modes (c.f. Equation 4.9). The η and ϕ resolution of the π^0 clusters after this reclassification are shown in Figure 4.14. In this figure, it can be seen that the SSS method does not perform significantly better than the cluster level cluster subtraction. All π^0 clusters after this reclassification using photon hits will be considered in the final decay mode classification, described in the next section, as a π^0 candidate.

4.5.6 Final tau decay mode classification

The decay mode classification after the π^0 -ID and photon hit counting can be further improved using a BDT method to differentiate between the following decay modes: 1p0n vs. 1p1n, 1p1n vs. 1pXn, and 3p0n vs. 3pXn. The final tau decay mode classification is performed as follows:

- The τ_{had} candidates with 1 or 3 associated tracks and 0 neutral pions identified are classified as 1p0n or 3p0n, respectively.
- The τ_{had} candidates with 1 associated track and ≥ 2 π^0 candidates are considered for re-classification in the 1p1n vs. 1pXn case.
- The τ_{had} candidates that were classified as 1p1n by the π^0 -ID but were migrated to 1pXn using photon hit counting are kept the same and do not enter any of the final decay mode classification tests.
- The decay mode of all remaining τ_{had} candidates with 1 or 3 associated tracks are re-evaluated in the 1p0n vs. 1p1n or 3p0n vs. 3pXn tests, respectively.

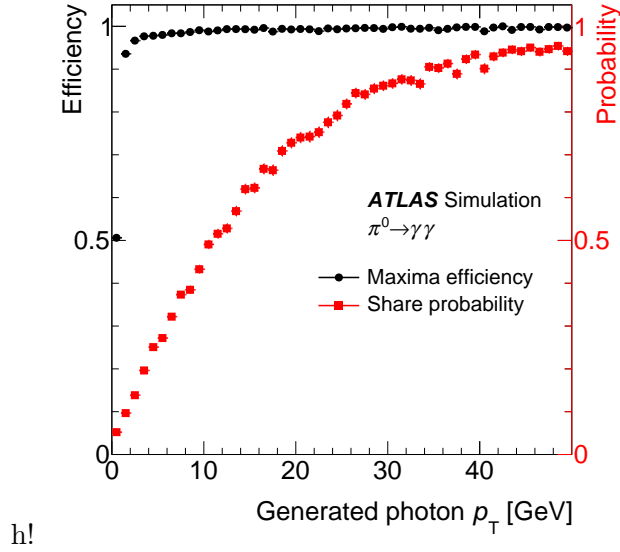


Figure 4.12: Reconstruction efficiency and share probability of photon hits in a simulated single π^0 sample [94].

		ATLAS Simulation				
		Tau Particle Flow (π^0 reconstruction)			Diagonal fraction: 70.9%	
					$Z/\gamma^* \rightarrow \tau\tau$	
Reconstructed decay mode	$3h^\pm \geq 1\pi^0$	0.2	2.5	3.5	11.0	55.3
	$3h^\pm$	0.2	0.6	0.4	86.8	41.5
	$h^\pm \geq 2\pi^0$	1.2	12.4	39.6	0.2	0.7
	$h^\pm \pi^0$	9.7	67.5	50.9	0.7	2.1
	h^\pm	88.6	16.9	5.6	1.4	0.5
		h^\pm	$h^\pm \pi^0$	$h^\pm \geq 2\pi^0$	$3h^\pm$	$3h^\pm \geq 1\pi^0$
		Generated decay mode				

Figure 4.13: Performance of the decay mode classification after the π^0 -ID and photon hit counting. Shown here is the matrix for the efficiency of correctly identifying a particular τ_{had} decay mode [94].

In each test, the BDT uses information about the kinematics of the tau decay products, the π^0 -ID BDT score, and the number of photon hits. A full list of BDT input variables can be found in [94]. The BDT training for each test is performed on a simulated $Z \rightarrow \tau\tau$ sample, and the input variables are chosen based on their ability to reject misidentified π^0 candidates, such as those from imperfect π^\pm subtraction, pileup, and underlying events. Background π^0 candidates, for example, usually have a low p_T and a low π^0 -ID BDT score.

The performance of each of these tests is shown in Figure 4.15(a). The figure of merit value achieved by the final decay mode classification is 74.7%, which shows an improvement compared

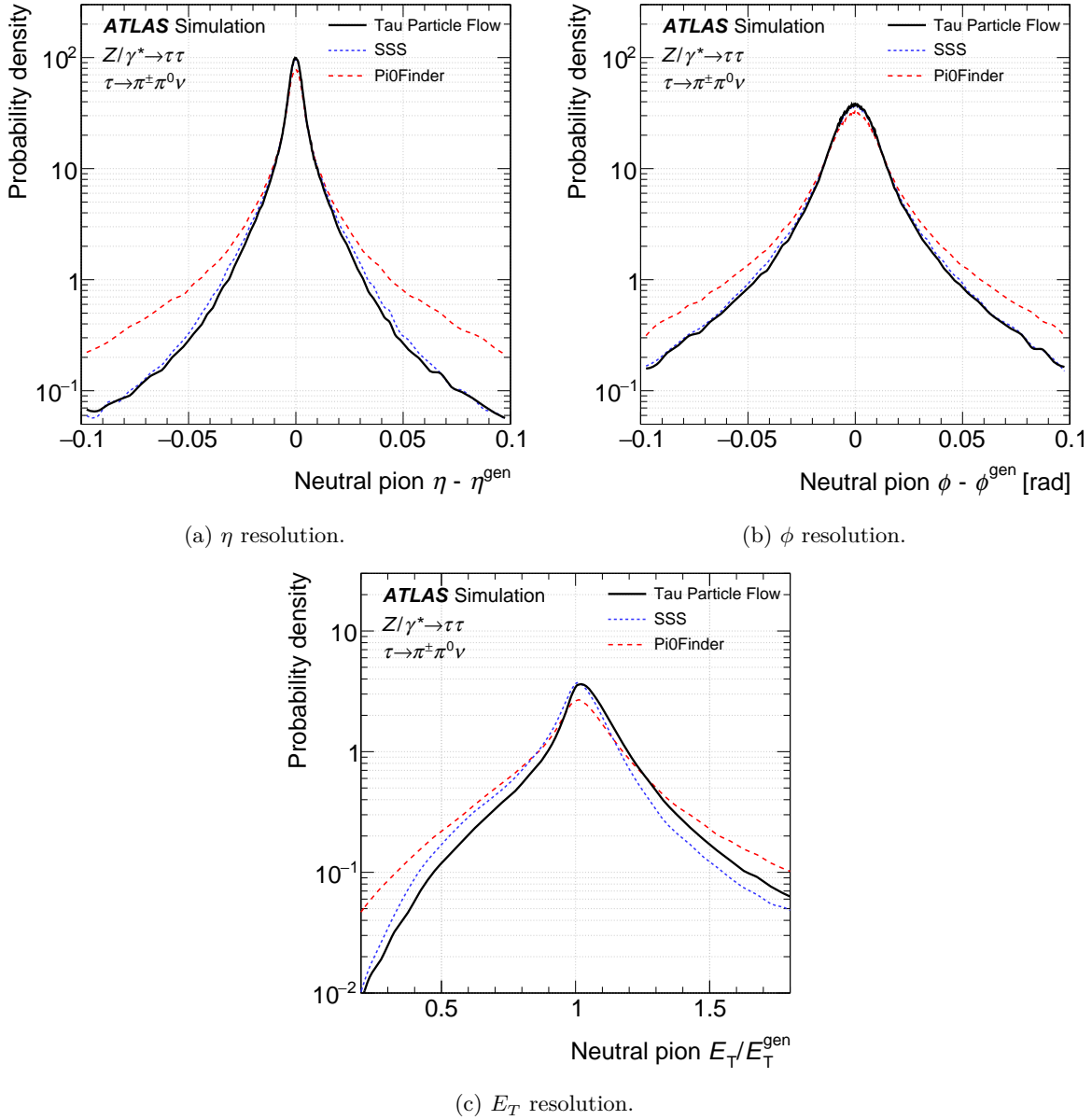
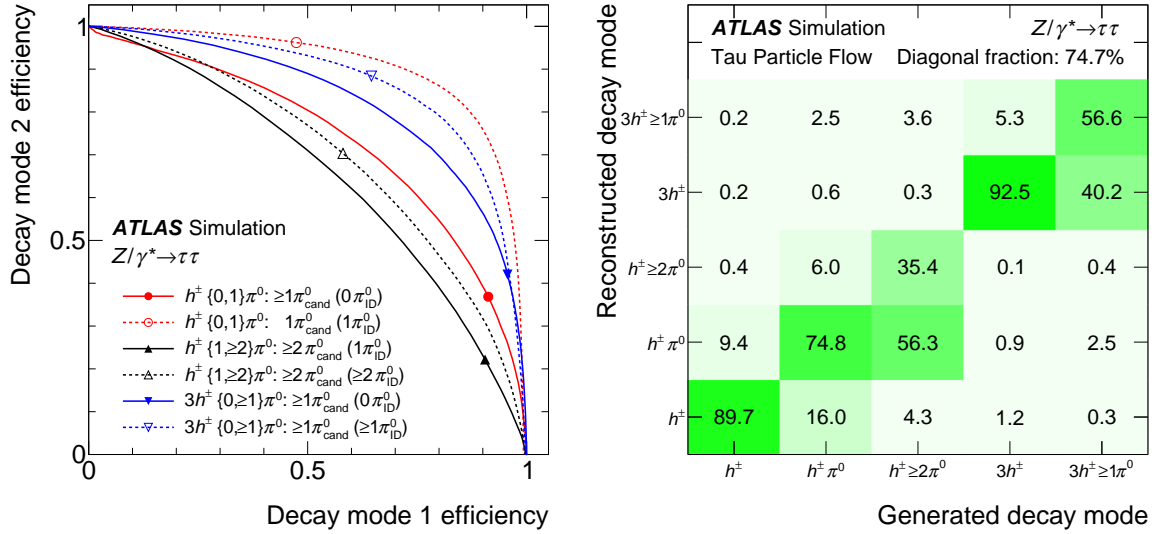


Figure 4.14: Energy and spatial resolution of reconstructed neutral pions achieved by the cluster level π^\pm subtraction discussed in this dissertation, labeled Tau Particle Flow. The old cell-by-cell level subtraction method is shown as SSS for "shower shape subtraction." The Pi0Finder shown in the figure is not discussed in this dissertation as it was an old algorithm from Run-I used for jet discrimination [94].

to 70.9% (see Figure 4.15(b) and c.f. Figure 4.13). The performance is stable against pileup.

4.5.7 Tau four-momentum reconstruction

Having reconstructed and identified the charged and neutral components of the τ_{had} decay, the τ_{had} four-momentum can be reconstructed using a constituent-based calculation by summing



(a) Performance of the BDTs to improve decay mode classification. (b) Efficiency matrix characterizing the decay mode classification after improvement with BDT tests.

Figure 4.15: Performance of the decay mode classification using BDT tests [94].

over the 4-momenta of the correct components:

$$\mathbf{p}_{\tau_{\text{had, vis}}} = \sum_i \mathbf{p}_{\text{track}_i} + \sum_j \mathbf{p}_{\pi^0 \text{ clusters}_j}. \quad (4.13)$$

Thus, the 4-momentum reconstruction relies heavily on the number of reconstructed π^0 clusters, and, therefore, on the tau decay mode classification. In addition, the $\tau_{\text{had-vis}}$ resolution is stable against pileup since the tau decay mode classification is stable against pileup. The classification efficiency is only degraded by $\sim 0.04\%$ per additional reconstructed vertex [94]. The 4-momentum resolution of the reconstructed $\tau_{\text{had-vis}}$ candidates in the simulated $Z \rightarrow \tau\tau$ sample is shown in Figure 4.16. It is shown in comparison to the Run-I version of the tau reconstruction that did not use particle flow, or Baseline [116]. It can be seen that particle flow significantly improves the core spatial resolution of the $\tau_{\text{had-vis}}$ candidate from 0.012 to 0.002 in η and from 0.02

The final particle flow energy calibration combines the constituent-based reconstruction with the baseline reconstruction, which performs better at high p_T .⁵ A calibration is applied in each decay mode as a function of the constituent-based E_T to address a π^0 energy bias where the number of neutral pions found in a cluster is not correct. This calibrated version of the $\tau_{\text{had-vis}}$ energy is shown in Figure 4.16 as the final tau particle flow performance in the solid black line. The resulting $\tau_{\text{had-vis}}$ energy performs well in all E_T regions.

4.5.8 Performance of the tau particle flow algorithm

Finally, the performance of the tau particle flow algorithm is measured in Run-I data. It is performed on true τ_{had} candidates and on jets that can be reconstructed as a τ_{had} candidate (or

⁵ This method is a predecessor of the MVA method described in Section 4.4.3.

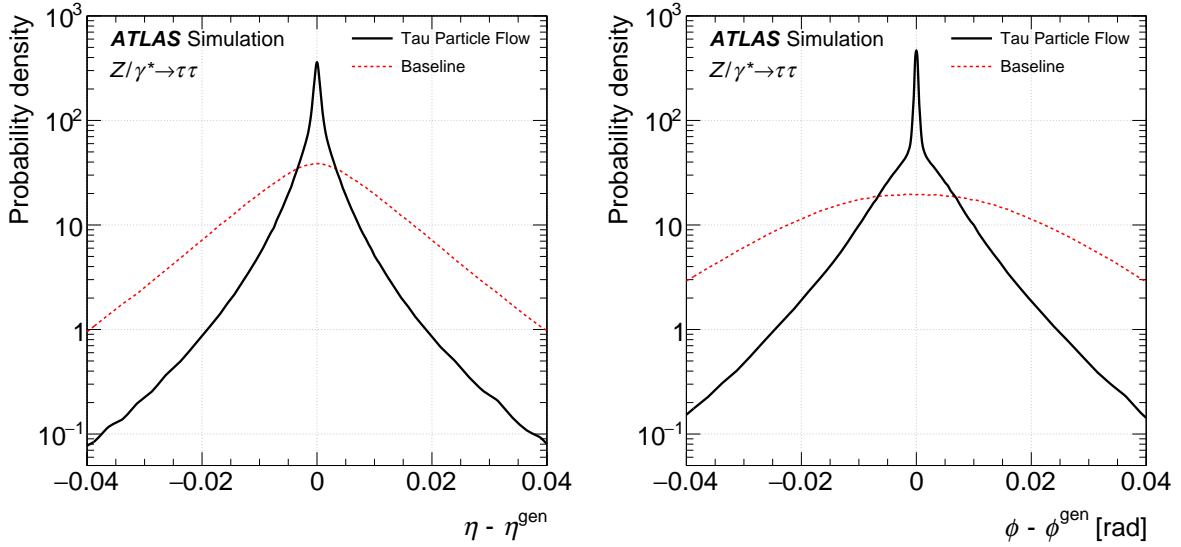
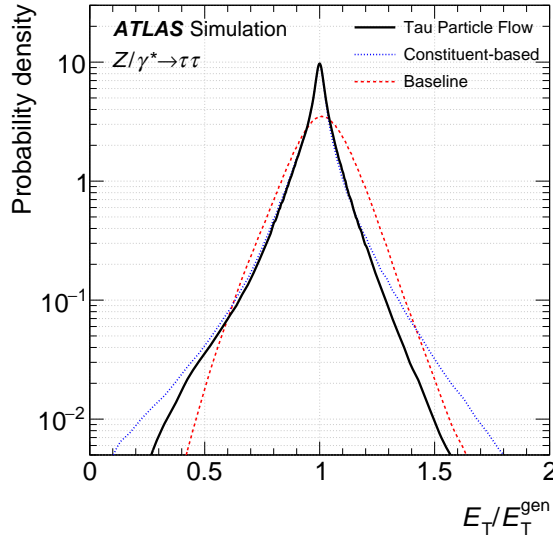
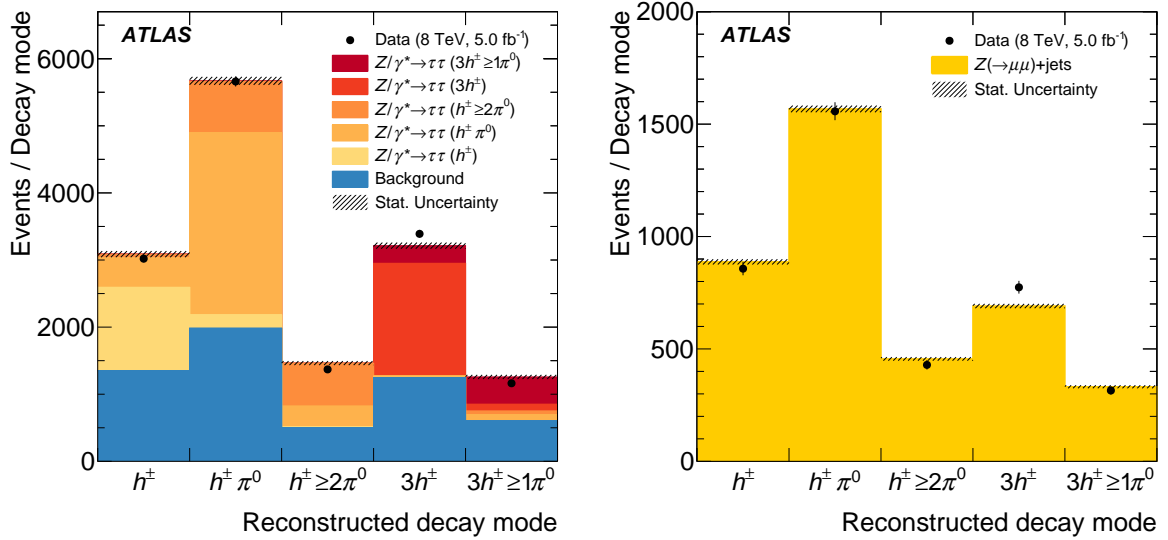
(a) η resolution.(b) ϕ resolution.(c) E_T resolution.

Figure 4.16: Energy and spatial resolution of reconstructed $\tau_{\text{had-vis}}$ candidates achieved by the Tau Particle Flow algorithm. It is shown in comparison to the performance of the $\tau_{\text{had-vis}}$ reconstruction algorithm used in Run-I, labeled Baseline, and the constituent-based calculation [94].

fake τ_{had} candidates). These τ -jets usually contain charged and neutral pions, so they can be used to study the modeling of the tau particle flow reconstruction.

Tag-and-probe analyses are used to select true (fake) τ_{had} candidate events in observed data involving $Z \rightarrow \tau\tau$ ($Z \rightarrow \mu\mu$) decays. In a $Z \rightarrow \tau\tau$ tag-and-probe analysis, one τ_{had} candidate is used as a tag and required to decay leptonically to a muon and accompanying neutrinos. This is due to the fact that muons are reconstructed with high purity and efficiency. Then, the other τ_{had} candidate in a possible $Z \rightarrow \tau\tau$ event is the probe and required to decay to hadrons and a neutrino. This probe is the τ_{had} candidate on which the tau particle flow performance

is measured. For fake τ_{had} candidates in the $Z \rightarrow \mu\mu$ tag-and-probe analysis, the muon pair in the $Z \rightarrow \mu\mu$ +jets events is required to have a mass close to the Z boson mass. The jet in these events is then used to measure the decay mode classification performance of the tau particle flow algorithm. Details on the selection used for these analyses are documented in [94]. The performance using these events is shown in Figure 4.17. It shows that tau particle flow reconstructed on simulated samples and on observed data performs similarly, especially for the important 1p0n and 1p1n modes. These decay modes are later used in reconstructing CP -sensitive observables in the Higgs CP analysis discussed in Section 6.



(a) Decay mode classification in the $Z \rightarrow \tau\tau$ tag-and-probe analysis.

(b) Decay mode classification in the $Z \rightarrow \mu\mu$ tag-and-probe analysis.

Figure 4.17: Performance of the decay mode classification at the reconstruction level on τ_{had} candidates in $Z \rightarrow \tau\tau$ events and on jets in $Z \rightarrow \mu\mu$ events [94].

4.5.9 Outlook

Possible improvements to the tau particle flow algorithm have been studied after the work described in this chapter. They include, for example, improving the matching of generated particles to their energy depositions in the detector using additional information. In addition, the association of tracks to charged pions can be improved using an algorithm for identifying background tracks from, for example, photon conversions.

The tau particle flow algorithm has been used in Run-II data-taking and is used in physics analyses. For example, the identification of individual decay products can improve the parametrizations used for the di-tau mass reconstruction algorithm (see Section 5.5). In addition, the Higgs CP analysis described in Chapter 6 uses the tau particle flow algorithm to reconstruct CP sensitive observables. Further studies are being performed on systematic uncertainties for the tau particle flow algorithm, as described in Section 6.6.

$H \rightarrow \tau\tau$ analysis in the $\tau_{\text{had}}\tau_{\text{had}}$ final state

In this chapter, the analysis of the Higgs boson decaying to a pair of hadronically decaying tau leptons, henceforth referred to as the $H \rightarrow \tau\tau$ analysis, is presented. Contributions to this analysis until June 2017 are presented. After this time, the work in this dissertation was focused on the analysis of Higgs CP properties in the same decay channel, henceforth referred to as the *Higgs CP analysis*.

In Higgs boson physics, searches of the Higgs boson decaying to a fermion pair are important because they provide direct access to the Higgs boson Yukawa coupling, which gives rise to the masses of the fermions, previously discussed in Chapter 2. At the LHC, the channel where the Higgs boson decays to two tau leptons ($H \rightarrow \tau\tau$), in particular, has the highest sensitivity among channels that probe the coupling of the Higgs boson to fermions (c.f. Figure 2.9).¹ In Run-I, the ATLAS and CMS collaborations reported the discovery of the Higgs boson decaying into a pair of tau leptons with a signal strength of $\mu_{\text{Measured}} = 1.11_{-0.22}^{+0.24}$, where

$$\mu \equiv \frac{(\sigma \cdot \Gamma_{H \rightarrow \tau\tau})_{\text{Measured}}}{(\sigma \cdot \Gamma_{H \rightarrow \tau\tau})_{\text{SM}}}, \quad (5.1)$$

in which measured refers to the combined result from the ATLAS and CMS analyses of recorded data, σ is the cross section of the Higgs boson production processes, and $\Gamma_{H \rightarrow \tau\tau}$ is the $H \rightarrow \tau\tau$ branching fraction. A value of $\mu = 1$ corresponds to a Higgs boson signal with a cross section as predicted by the SM and a value of $\mu = 0$ corresponds to the absence of signal. The result is shown in Figure 5.1.

In Run-II, with increased luminosity and a higher center-of-mass-energy, ATLAS aims to not only independently establish an $H \rightarrow \tau\tau$ discovery, but also to measure fiducial and differential $H \rightarrow \tau\tau$ cross sections with high precision. In 2017, the CMS Collaboration already published an independent discovery of the Higgs boson decaying to two tau leptons using Run-II data [87]. The ATLAS Collaboration recently published a measurement of the $H \rightarrow \tau\tau$ process using Run-II data in [4], with a supporting internal documentation in [126].

In addition to confirming the compatibility of the cross section of the observed Higgs boson with the Higgs Yukawa coupling to fermions predicted by the SM, this measurement is also a preparation for the analysis of Higgs boson CP properties in the $H \rightarrow \tau\tau$ channel. While CP studies in the bosonic decay channels of the Higgs boson already indicate the compatibility of

¹ Although $H \rightarrow b\bar{b}$ has a higher branching fraction, $H \rightarrow \tau\tau$ is more promising because it has better signal-to-background conditions.

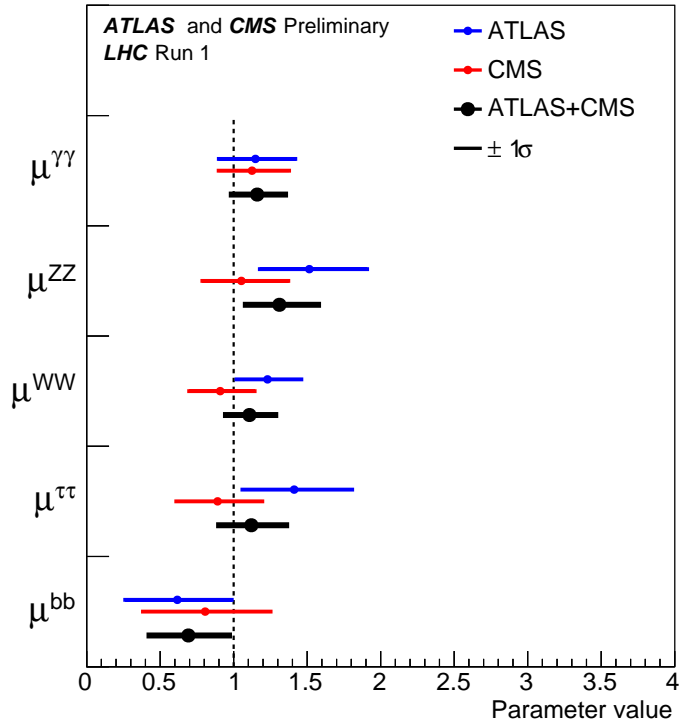


Figure 5.1: The best fit value of the Higgs boson signal strength, μ , in its known decay channels measured by the ATLAS and CMS Collaborations for the datasets from 2011 and 2012 at $\sqrt{s} = 7$ and 8 TeV, respectively. The individual and combined signal strengths are shown for the experiments. The error bars indicate the $\pm 1\sigma$ uncertainty. Taken from [1].

the Higgs boson's CP properties with those of the SM predictions [127], fermions provide unique information on Higgs CP properties. Chapter 6 describes a Higgs CP analysis in the $H \rightarrow \tau\tau$ channel.

This chapter describes the $H \rightarrow \tau\tau$ search in the final state where both tau leptons decay hadronically ($H \rightarrow \tau_{\text{had}}\tau_{\text{had}}$) as of June 2017, since the time spent during this dissertation thereafter was devoted to the Higgs CP analysis. The version presented uses an older data processing than that used in the public result of the $H \rightarrow \tau\tau$ search shown in [4] and an older version of the background estimation and certain systematic uncertainties.

Section 5.1 describes the $H \rightarrow \tau\tau$ final states. Sections 5.2 and 5.3 details the signal and relevant background processes in the $H \rightarrow \tau_{\text{had}}\tau_{\text{had}}$ decay channel. Section 5.4 lists the data and simulated samples used for the analysis. Section 5.5 presents the di-tau invariant mass reconstruction that is used as the discriminant variable for the final statistical interpretation. Section 5.6 outlines the selection of physics objects and events that targets the $H \rightarrow \tau_{\text{had}}\tau_{\text{had}}$ signal signature. Section 5.7 discusses the modeling of background contributions and studies performed to improve these methods. Section 5.8 delineates the uncertainties considered in the final statistical interpretation, discussed in Section 5.9. The final result is reported in Section 5.10.

5.1 $H \rightarrow \tau\tau$ final states

There are three possible final states in the $H \rightarrow \tau\tau$ analysis: $\tau_{\text{lep}}\tau_{\text{lep}}$, $\tau_{\text{lep}}\tau_{\text{had}}$, $\tau_{\text{had}}\tau_{\text{had}}$ (see Figure 2.6 and Figure 5.2). Each channel has its advantages and disadvantages. The $\tau_{\text{lep}}\tau_{\text{had}}$ channel is the most sensitive channel, profiting from the highest branching fraction (45.6%) and its distinctive experimental signature of a high p_T lepton (τ_{lep}) with a highly boosted jet (τ_{had}). The second most sensitive channel is the $\tau_{\text{had}}\tau_{\text{had}}$ channel, with a branching fraction of 41.9%. Although τ_{had} candidates suffer from high background stemming from quark- or gluon-initiated jets, the $\tau_{\text{had}}\tau_{\text{had}}$ channel profits from a better mass resolution. This is because the reconstructed \cancel{E}_T in a τ_{had} candidate only comes from the tau neutrino, whereas τ_{lep} candidates have two associated neutrinos, giving the di-tau mass reconstruction algorithm, discussed later in Section 5.5, more neutrino configurations to consider. The $\tau_{\text{lep}}\tau_{\text{lep}}$ channel profits from higher detection efficiency and high suppression of jets misidentified as leptons. However, it has the lowest sensitivity in the Higgs mass region, with a low branching fraction and a worse mass resolution due to the presence of four neutrinos.

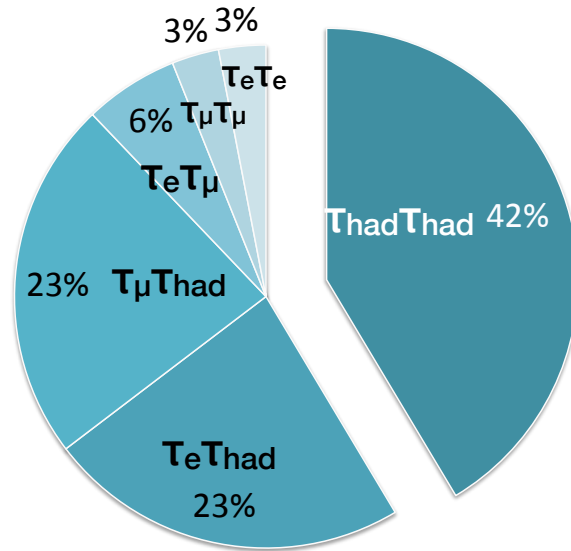


Figure 5.2: Final states and branching fractions of the $H \rightarrow \tau\tau$ decay channel. Percentages are calculated from [16].

This dissertation presents the analysis in the $\tau_{\text{had}}\tau_{\text{had}}$ channel on Run-II data. The precedent analysis in [1] performed on Run-I data is used as a baseline, and new methods are developed for Run-II. The measured signal strength in the $H \rightarrow \tau_{\text{had}}\tau_{\text{had}}$ channel in Run-I was $\mu = 2.0^{+0.9}_{-0.7}$ (c.f. Figure 5.3).

5.2 Signal processes

Unlike the bosonic decay channels, the $H \rightarrow \tau\tau$ analysis can be studied with various production processes. The signal considered in this $H \rightarrow \tau\tau$ analysis are produced by four main SM Higgs boson production mechanisms, as previously discussed in Section 2.1.6.1 (see the Feynman diagrams previously shown in Figure 2.7):

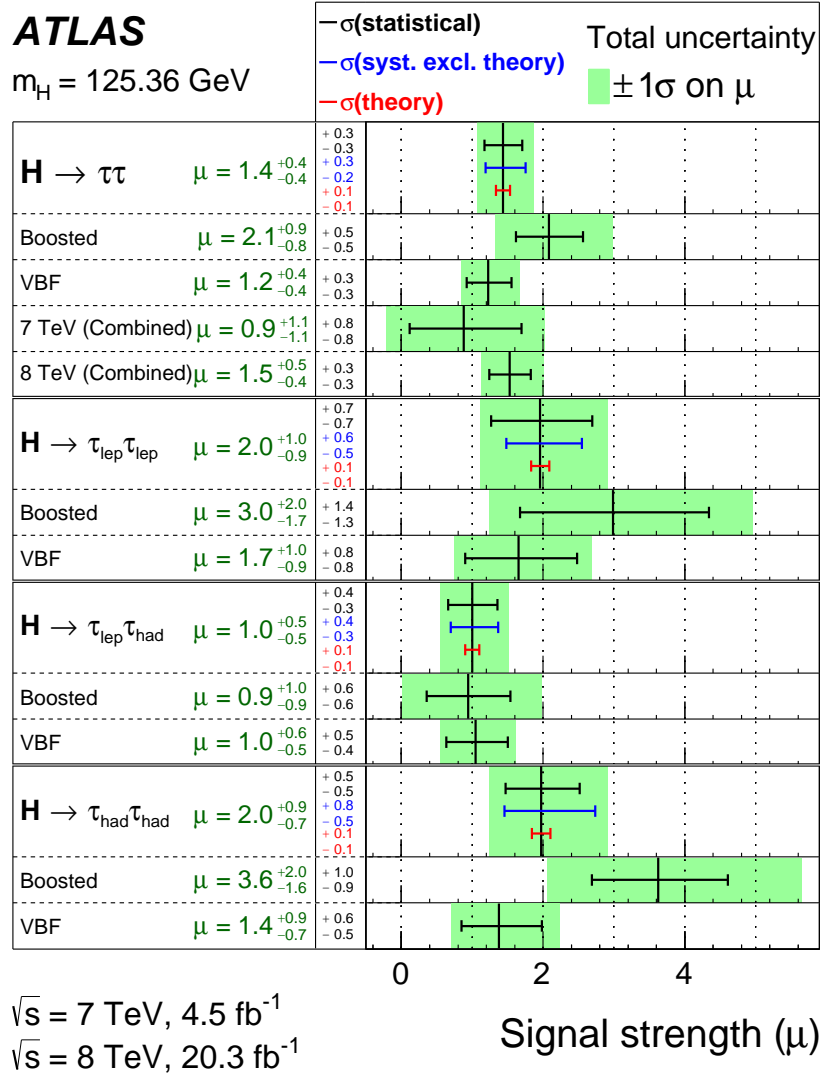


Figure 5.3: The best fit value of the Higgs boson signal strength, μ , in the individual $H \rightarrow \tau\tau$ decay channels for the full ATLAS datasets at $\sqrt{s} = 7, 8$ TeV. The error bars show the $\pm 1\sigma$ uncertainty for the total and individual contributions from the statistical, experimental, and theoretical uncertainties [128].

- ggH : Gluon-gluon fusion
- VBF: Vector boson fusion
- VH : Production in association with a vector boson (W or Z), or Higgstrahlung
- $t\bar{t}H$: Production in association with a $t\bar{t}$ pair

The most common Higgs boson production process at the LHC is via gluon-gluon fusion (c.f. Figure 2.6(a)). Although the Higgs boson does not couple to gluons, it can be produced at higher orders via a quark loop. From this heavy quark loop, there is typically an associated hard jet from a radiating gluon. Higher-order QCD corrections are important for this process since they correct for gluon radiation from the top loop. A highly boosted Higgs boson recoiling from

the hard jet is a distinctive signature that can be used to suppress the high QCD background in this production process.

The second most important production mechanism is the vector boson fusion process (c.f. Figure 2.6(b)). With two jets at leading order from electroweak vector boson fusion, the QCD corrections are less important than for the ggH production process. In these events, there is not only a highly boosted Higgs boson recoiling from the two hard jets, but also a distinctive configuration of the two hard jets, typically produced in the forward direction of the detector. This unique signature, with the \cancel{E}_T from the $\tau_{\text{had}}\tau_{\text{had}}$ decay pointing in between the two forward VBF jets, gives this category the highest signal sensitivity.

The other two main processes are production in association with a vector boson and production in association with a $t\bar{t}$ pair (c.f. Figures 2.6(c) and 2.6(d)). The VH process produces a non-negligible fraction of Higgs boson events but is not specifically studied in this analysis. Only the ggH and VBF production processes are targeted by the selection and categorization in this analysis, but production from VH and $t\bar{t}H$ is nevertheless considered to be signal if they pass the signal event selection.

5.3 Background processes

Background events in the $H \rightarrow \tau_{\text{had}}\tau_{\text{had}}$ analysis are produced by jets, leptons, and real τ_{had} candidates that can mimic the $H \rightarrow \tau\tau$ signal signature, i.e., pass the requirements on a signal-like event and fall into the signal region of this analysis. The LO Feynman diagrams of the main background processes for the VBF and ggH production processes are shown in Figure 5.4. The two dominant background contributions in the $\tau_{\text{had}}\tau_{\text{had}}$ channel come from multijet production (the production of at least two QCD jets misidentified as τ_{had} candidates) and QCD $Z \rightarrow \tau\tau$ +jets process. The former is also referred to as fake- τ background. The latter differentiates the QCD production process of the $Z \rightarrow \tau\tau$ background from the less commonly occurring electroweak (EWK) production process (see Figure 5.4 showing the two different production processes).

All other background processes contribute minimally and are grouped together as “Other”. They have at least one true electron or true hadronic tau decay matched to a reconstructed τ_{had} candidate. The Other background consists of diboson, W +jets, top quark(s), EWK production of $Z \rightarrow \tau\tau$ +jets, and $Z \rightarrow \ell\ell$. Diboson events can mimic signal events if a combination of W and Z bosons produce two jets misidentified as τ_{had} candidates and if an accompanying neutrino or object misreconstruction results in a nonnegligible \cancel{E}_T value. The W +jets background can mimic the signal when one true τ_{had} candidate is produced while the jets are misidentified as a τ_{had} candidate. The top quark background, which refers to $t\bar{t}$ and single top production (in the t - and s -production channels of the $q\bar{q} \rightarrow tq$ processes and in the W -associated top production) can also mimic the $H \rightarrow \tau_{\text{had}}\tau_{\text{had}}$ signal. The $t\bar{t}$ background can contain two τ_{had} candidates from the W bosons in top quark decays. The single top production can mimic the $H \rightarrow \tau_{\text{had}}\tau_{\text{had}}$ signal if, for example, the W boson from the top quark decay produces a true τ_{had} candidate, while a fake τ_{had} candidate is misidentified from background QCD jet(s). The EWK $Z \rightarrow \tau\tau$ +jets background can enter the signal region since two τ_{had} candidates are produced from a Z boson, whose mass is similar to that of the Higgs boson. Lastly, the $Z \rightarrow \ell\ell$ background can also enter the signal region if electrons are misidentified as τ_{had} candidates. In Run-I, the $Z \rightarrow \ell\ell$ background was not considered since it was shown to be negligible with the given data sample and cross section. In Run-II, it is added as a background due to potential

differences in the new likelihood-based electron veto developed for Run-II [113]. Since this background sits closely below the Higgs boson mass peak, even a few unaccounted events from $Z \rightarrow \ell\ell$ decays could be problematic in the $\tau_{\text{had}}\tau_{\text{had}}$ analysis. For abbreviation purposes in the future sections, all background not from the fake- τ background are called real- τ backgrounds.

5.4 Data and simulated samples

The following section describes the data and simulated samples used in the $H \rightarrow \tau\tau$ analysis.

5.4.1 Data

The analyzed data correspond to proton-proton collisions taken at the LHC in 2015 and 2016 at a center-of-mass energy of $\sqrt{s} = 13$ TeV. The data correspond to integrated luminosities of 3.21 fb^{-1} in the 2015 dataset and 32.9 fb^{-1} in the 2016 dataset. Events from these collisions are used if they pass data quality requirements for the Good Run List (GRL). For example, the GRL does not include data taken when the inner B-layer was defective.

Events are also required to pass the corresponding 2015 and 2016 di-tau triggers (c.f. Table 4.1). These triggers were previously described in Section 4.4.4. As previously explained, in response to the increased instantaneous luminosity during the 2016 data collection, the L1 trigger requirements are tightened. In order to maintain a high acceptance of signal, the p_T trigger thresholds on τ_{had} candidates remain the same, and an additional requirement is placed on the leading p_T L1 jet. The di-tau trigger requires events to have a leading L1 jet with $p_T > 25$ GeV. It is a significant difference from the $H \rightarrow \tau\tau$ analysis in the CMS collaboration, which uses a 0-jet category to constrain a number of their systematic uncertainties [87].

5.4.2 Simulated samples

Monte Carlo (MC) simulation samples for the $H \rightarrow \tau\tau$ signal and background processes are produced in pp collisions at a center-of-mass energy of 13 TeV as part of the MC15c production campaign using the ATLAS simulation infrastructure [129, 130]. The event generation starts with the matrix element calculation for the hard scattering and is followed by the parton shower and hadronization. Specific generators and their accuracies for each signal and background process are described in this section.

Each sample uses a parton distribution function (PDF²) as input to the event generator in order to describe the proton substructure. The PDF is correlated with tunings that are connected to the initial state radiation, thus affecting the reduction of initial beam energy before momentum transfer in the hard scattering process. The subsequent tau decays in these events are modeled by TAUOLA [71]. Each event is then processed through GEANT4 to simulate the ATLAS detector and trigger responses [131]. Afterward, they are weighted to match the pileup profile measured from Run-II data since they are produced with a different pileup profile. Then, the appropriate object selection efficiency is applied according to the ATLAS performance group recommendations. The specific generators, PDF parametrizations, and underlying event (UE) tunes for each process are summarized in Table 5.1. Their cross sections are listed in Table E.1.

² The capitalized abbreviation is used to differentiate parton distribution function (PDF) from probability distribution function (pdf).

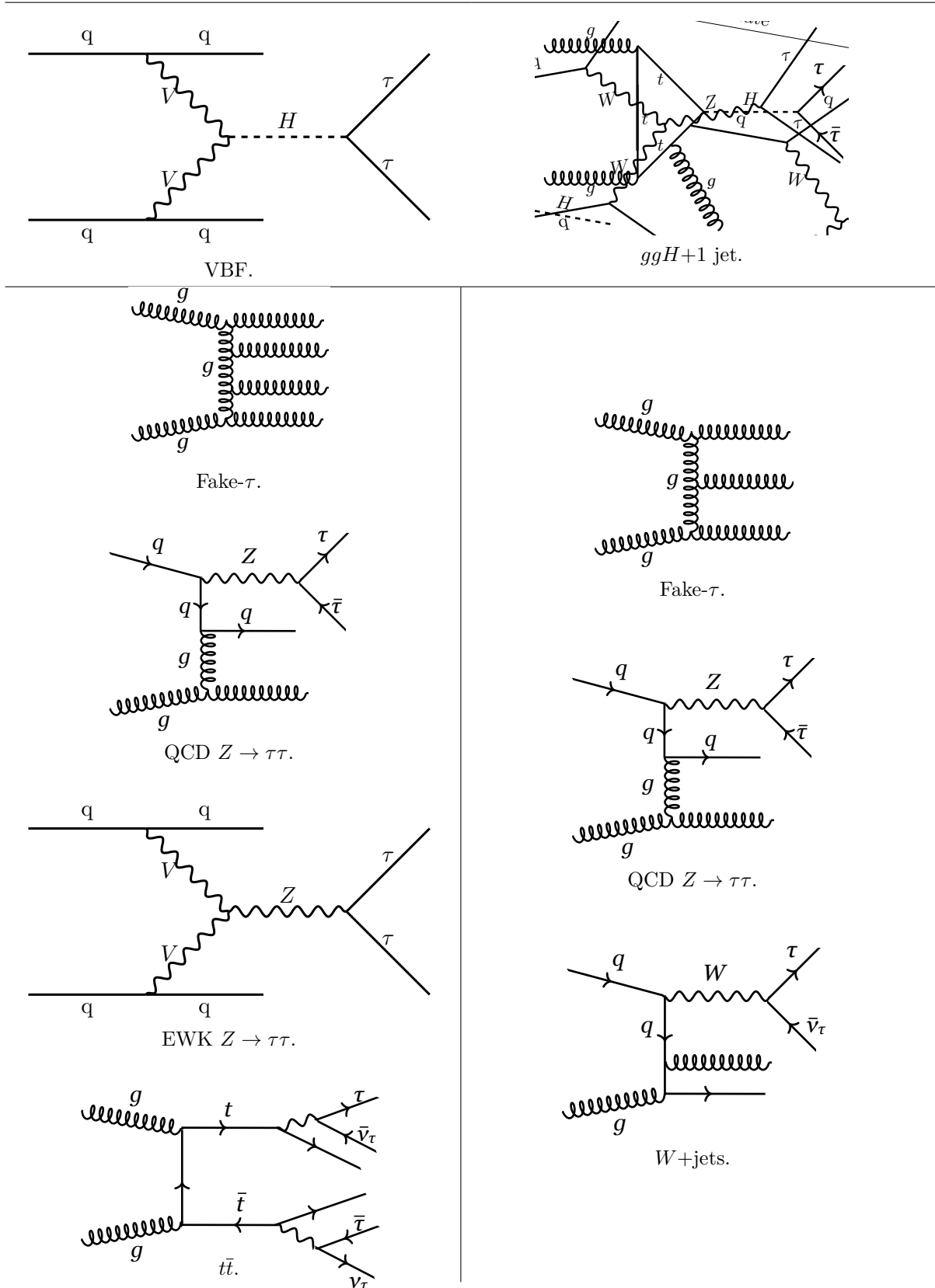


Figure 5.4: Example leading-order Feynman diagrams of the VBF (left) and ggH (right) signal processes with the corresponding main background processes below each diagram.

Process	Generator		PDF	UE tune	Order
	Matrix element	Parton shower			
ggH	POWHEG	PYTHIA 8	CT10	AZNLO	NNLO
VBF	POWHEG	PYTHIA 8	CT10	AZNLO	(N)NLO
WH	POWHEG	PYTHIA 8	NNPDF23LO	AZNLO	NNLO
ZH	POWHEG	PYTHIA 8	NNPDF23LO	AZNLO	NNLO
$t\bar{t}H$	AMCATNLO	HERWIG	CT10	A14	NLO
QCD $Z \rightarrow \tau\tau$		SHERPA	NNPDF30NNLO	SHERPA	NNLO
EWK $Z \rightarrow \tau\tau$		SHERPA	CT10	SHERPA	NNLO
$Z \rightarrow \ell\ell$		SHERPA	CT10	SHERPA	NNLO
Diboson		SHERPA	CT10	SHERPA	NNLO
W + jets	MADGRAPH	PYTHIA 8	N30NLO	–	NNLO
Top	POWHEG	PYTHIA 6	CT10	PERUGIA2012	NNLO+NNLL

Table 5.1: Summary of the generators, PDFs, and UE tunes used for the simulated samples.

5.4.2.1 Signal samples

The simulated signal samples are generated for a SM CP -even Higgs boson with a mass of 125 GeV. The ggH sample is generated at next-to-next-to-leading-order (NNLO) using POWHEG for the hard-scattering process (matrix element calculation) interfaced with PYTHIA 8 for the parton shower model [117, 132]. The VBF and VH modes are generated to NLO accuracy by POWHEG, interfaced with PYTHIA 8.186 for the parton shower [117]. The VBF and VH modes are normalized to their approximate NNLO QCD cross sections, with NLO electroweak corrections applied. The $t\bar{t}H$ mode is generated at NLO by AMCATNLO with the hard-scattering process interfaced from HERWIG [133–135].

The CT10 parametrization is used for the PDF of the ggH , VBF, and $t\bar{t}H$ production processes, while NNPDF23LO is used for the VH production processes [136]. The AZNLO tune is used for the UE for all production processes but the $t\bar{t}H$ process, where the A14 tune is used [137, 138]. Since the $\tau_{\text{had}}\tau_{\text{had}}$ search is designed to be model-dependent, the simulated signal samples are normalized to specific cross sections predicted by the SM (see Table E.1).

5.4.2.2 Background samples

This section describes the samples used for the fake- τ , $Z \rightarrow \tau\tau$, and other backgrounds. For the fake- τ background, a data-driven method using a control region in the data sample is employed since it is computationally infeasible to simulate enough events in the phase space where QCD multijet events pass the analysis selection criteria. Simulation of QCD jets is known to not describe the hadronization of jets or the misidentification rate of jets as τ_{had} candidates well.

The QCD $Z \rightarrow \tau\tau$ + jets background is the main irreducible background in the $\tau_{\text{had}}\tau_{\text{had}}$ channel. In the Run-I analysis, a data-driven embedding technique was employed to model the $Z \rightarrow \tau\tau$ background, where the muons from $Z \rightarrow \mu\mu$ events in data were replaced with τ decays, taking advantage of lepton universality. An embedding technique has not been fully developed in time for Run II, so three simulated $Z \rightarrow \tau\tau$ samples are considered: POWHEG+PYTHIA8, SHERPA 2.2, and MADGRAPH. Section 5.7.1 elaborates on the choice of the Sherpa sample to model the $Z \rightarrow \tau\tau$ background. This sample is used with the NNPDF30NNLO PDF set and the SHERPA tune [139].

The EWK $Z \rightarrow \tau\tau + \text{jets}$ sample, $Z \rightarrow \ell\ell$, and diboson samples are generated by SHERPA 2.2 for both hard scattering and parton showering. SHERPA calculates the hard scattering processes with a tree-level matrix-element generator, and the QCD parton cascades are described with a parton-shower model. The $W + \text{jets}$ sample is simulated with MADGRAPH for the hard scattering and PYTHIA 8 for the parton shower. The top sample ($t\bar{t}$, Wt , and single top) is generated by POWHEG, with the parton showering, hadronization, and underlying event modeled by PYTHIA 6.428 [140]. The UE tune for the top samples is from PERGUIA [121]. The samples are normalized according to the cross sections in Table E.1. Finally, all simulated samples are passed through the same reconstruction software that is used for data.

5.5 Di-tau invariant mass reconstruction

The $H \rightarrow \tau_{\text{had}}\tau_{\text{had}}$ analysis presented in this dissertation uses a di-tau invariant mass observable for the Higgs boson signal extraction (discussed later in Section 5.9) because it is a powerful observable that provides good discrimination between the Higgs boson and the dominant $Z \rightarrow \tau\tau$ background. It is important to reconstruct the di-tau invariant mass with as high a resolution as possible since the $Z \rightarrow \tau\tau$ background sits closely below the expected $H \rightarrow \tau\tau$ mass peak and has a higher cross section than that of the $H \rightarrow \tau\tau$ signal (about 600 times higher than for a 125 GeV Higgs boson, see Table E.1).

The di-tau invariant mass cannot be fully reconstructed at the ATLAS detector since neutrinos escape detection. However, assumptions can be made about the neutrinos from the tau decay. There are different possible partial mass observables that can be reconstructed from known quantities: MET (\cancel{E}_T) and the visible tau decay products. This section describes several relevant di-tau mass reconstruction options: the collinear mass approximation and the missing mass calculator (MMC).

The collinear mass approximation starts by reconstructing the visible di-tau invariant mass, which neglects the tau neutrinos and is calculated from the visible tau decay products:

$$m_{\text{vis}}^{\tau\tau} = \sqrt{\left(E_{\text{vis}}^{\tau_{\text{had},1}} + E_{\text{vis}}^{\tau_{\text{had},2}}\right)^2 - \left(\vec{p}_{\text{vis}}^{\tau_{\text{had},1}} + \vec{p}_{\text{vis}}^{\tau_{\text{had},2}}\right)^2}. \quad (5.2)$$

It then improves the visible di-tau invariant mass reconstruction by applying relevant assumptions on the neutrinos from the tau decay. Since the tau neutrinos should be emitted with a boost when coming from a heavy resonance decay ($m_{Z,H} \gg m_\tau$), they are expected to be approximately collinear to the direction of the respective τ_{had} candidate. Including the assumption that the neutrinos are the only source of \cancel{E}_T in the event, or $\cancel{E}_T = |\vec{p}_T^{\nu,1} + \vec{p}_T^{\nu,2}|$, the collinear mass is given as

$$m_{\text{collinear}}^{\tau\tau} = \frac{m_{\text{vis}}^{\tau\tau}}{\sqrt{x_1 x_2}}, \quad (5.3)$$

where x_i is the p_T fraction of the i^{th} visible tau decay product, or

$$x_i = \frac{p_T^i}{p_T^i + p_T^{\text{miss}}}. \quad (5.4)$$

This method, however, is still not ideal for $H \rightarrow \tau\tau$ searches since Equation 5.4 is not valid for all event topologies, such as cases where the tau leptons are not emitted with a boost from a high- p_T resonance.

As can be seen in Figure 5.5, the collinear mass approximation underestimates the Higgs boson mass, causing significant overlap with the Z boson mass peak. It performs well primarily in cases where the di-tau system is boosted. In the $H \rightarrow \tau\tau$ analysis, this exacerbates the decrease in signal sensitivity coming from the $Z \rightarrow \tau\tau$ background, whose collinear mass shoulder sits below the Higgs boson mass. The collinear mass distribution is also broadened by the large fraction of back-to-back events, which result in a worse \cancel{E}_T resolution.³

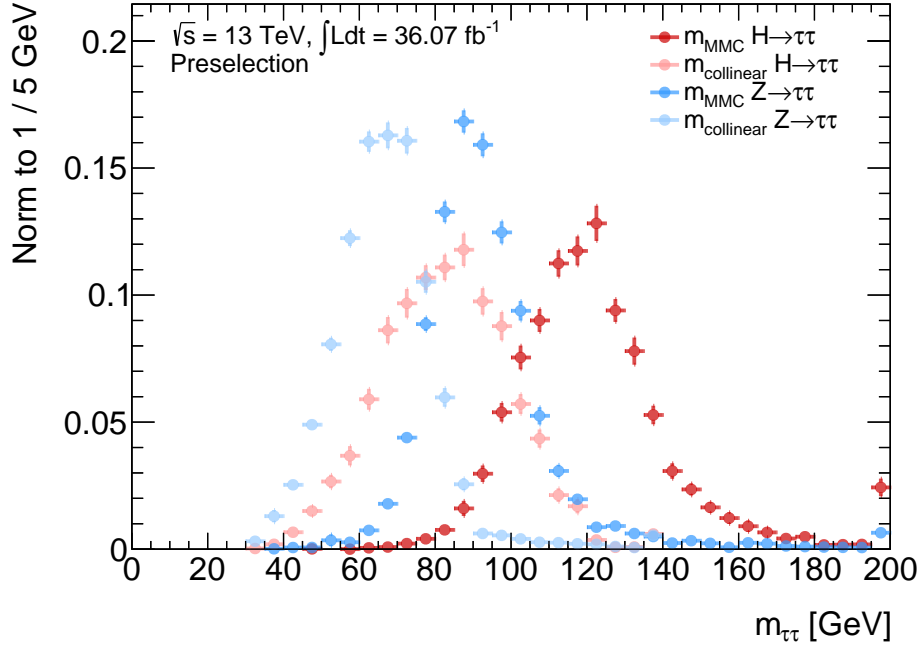


Figure 5.5: Comparison of the collinear mass approximation and MMC methods in the $H \rightarrow \tau_{\text{had}}\tau_{\text{had}}$ channel using the preselection region later described in Section 5.6. Only the statistical uncertainties are shown. The $H \rightarrow \tau_{\text{had}}\tau_{\text{had}}$ and QCD $Z \rightarrow \tau\tau$ +jets samples are used.

The missing mass calculator improves on the collinear mass approximation because it does not require the assumption that the tau neutrinos are collinear to the respective tau decay axis. Moreover, it is suitable for the di-tau decay configurations relevant in the $H \rightarrow \tau\tau$ decays and takes into account the finite \cancel{E}_T resolution. Assuming no other neutrinos are present in the event, the MMC guesses the most likely 3-vector components of the tau neutrinos (totaling six unknowns for the $\tau_{\text{had}}\tau_{\text{had}}$ final state). Since the measured quantities are the x - and y -components of the \cancel{E}_T and the invariant mass of each tau lepton, there are only four equations connecting the six unknowns:

³ Back-to-back events occur when the two decay products are emitted with an angle of about 180° with respect to each other in the laboratory frame.

$$\begin{aligned}
 \cancel{E}_{T,x} &= |\vec{p}_{\text{miss},1}| \sin \theta_{\text{miss},1} \cos \phi_{\text{miss},1} + |\vec{p}_{\text{miss},2}| \sin \theta_{\text{miss},2} \cos \phi_{\text{miss},2} \\
 \cancel{E}_{T,y} &= |\vec{p}_{\text{miss},1}| \sin \theta_{\text{miss},1} \sin \phi_{\text{miss},1} + |\vec{p}_{\text{miss},2}| \sin \theta_{\text{miss},2} \sin \phi_{\text{miss},2} \\
 m_{\tau,1}^2 &= m_{\text{miss},1}^2 + m_{\text{miss},2}^2 + 2 \sqrt{p_{\text{vis},1}^2 + m_{\text{vis},1}^2} \sqrt{p_{\text{miss},1}^2 + m_{\text{miss},1}^2} - 2p_{\text{vis},1}p_{\text{miss},1} \cos(\Delta R(\text{miss}_1, \text{vis}_1)) \\
 m_{\tau,2}^2 &= m_{\text{miss},2}^2 + m_{\text{miss},2}^2 + 2 \sqrt{p_{\text{vis},2}^2 + m_{\text{vis},2}^2} \sqrt{p_{\text{miss},2}^2 + m_{\text{miss},2}^2} - 2p_{\text{vis},2}p_{\text{miss},2} \cos(\Delta R(\text{miss}_2, \text{vis}_2)),
 \end{aligned}$$

where θ_i is the polar angle, ϕ is the azimuthal angle, “miss” denotes the invisible tau decay product, m_τ is the mass of the tau lepton (1.78 GeV), and the mass of the neutrino (not shown) is set to 0, thereby reducing the number of unknowns.

The unknown $\Delta R(\text{miss}_{1,2}, \text{vis}_{1,2})$ variables can be determined via a scan of the possible solutions in the $(\Delta R_1, \Delta R_2)$ plane. Although this system of equations is under-determined, the grid points in this plane are not all equally likely. The characteristics of a typical tau decay can be used to constrain the system by weighting each possible solution in the $(\Delta R_1, \Delta R_2)$ plane by a corresponding probability that characterizes a typical tau decay, or $\mathcal{P}_{\text{event}}$. Since the ΔR observable is strongly dependent on the number of tracks associated to the tau lepton and the tau momentum range, different ΔR distributions are used for 1- and 3-prong tau decays and tau p_T ranges. The event probability is then

$$\mathcal{P}_{\text{event}} = \mathcal{P}(\Delta R_1^{\text{vis,miss}}, p_{\tau,1}) \times \mathcal{P}(\Delta R_2^{\text{vis,miss}}, p_{\tau,2}). \quad (5.5)$$

The parameter space is scanned by a Markov chain, and the MMC mass is then the maximum of the possible weighted di-tau invariant masses from the scan in the $(\Delta R_1, \Delta R_2)$ plane. In this form, the fraction of events for which the MMC algorithm finds a physical solution, or the MMC reconstruction efficiency, is low. This is because the finite \cancel{E}_T resolution degrades the MMC resolution and MMC reconstruction efficiency.⁴ It breaks the assumption that the tau neutrinos are the only source of \cancel{E}_T in the event.

This can be addressed in the MMC algorithm since, unlike the collinear approximation, the MMC can take into account the poor \cancel{E}_T resolution. Each event can be weighted by an event probability that incorporates the \cancel{E}_T resolution, in addition to the ΔR probability density functions (pdf) of a typical tau decay. A scan is, thus, performed in a $(\Delta R_1, \Delta R_2, \cancel{E}_{T,x}, \cancel{E}_{T,y})$ plane with each grid point weighted to the corresponding event probability. The final MMC output used for the $m_{\text{MMC}}^{\tau\tau}$ observable in this analysis is obtained by maximizing the event likelihood that incorporates the event probability:

$$\mathcal{L} = -\log(\mathcal{P}_{\text{event}}) = -\log(\mathcal{P}(\Delta R_1, p_{\tau,1}) \times \mathcal{P}(\Delta R_2, p_{\tau,2}) \times \mathcal{P}(\Delta \cancel{E}_{T,x}) \times \mathcal{P}(\Delta \cancel{E}_{T,y})), \quad (5.6)$$

where the \cancel{E}_T resolution probability function is a function of $\Delta \cancel{E}_{T,x,y}$, the variations in the x - and y -directions of the \cancel{E}_T , and σ , the \cancel{E}_T resolution. It is given as

$$\mathcal{P}(\Delta \cancel{E}_{T,x,y}) = \exp\left(-\frac{\Delta \cancel{E}_{T,x,y}^2}{2\sigma^2}\right). \quad (5.7)$$

The $m_{\text{MMC}}^{\tau\tau}$ observable used in this dissertation comes from the MMC algorithm tuned for

⁴ The resolution of the tau momentum can also lead to mis-measurements of the \cancel{E}_T . However, this has a minimal effect on the MMC resolution and reconstruction efficiency and is, thus, not taken into account.

Run-I settings because an optimized Run-II version is not yet available. Improvements from a Run-II retuning include the re-parametrization of the \cancel{E}_T resolution, dependent on object and event selection [141]. They also include the use of tau substructure reconstruction, where the parametrization of the $(\Delta R_1, \Delta R_2)$ plane is based not only on the p_T of the tau lepton but also on the tau decay mode [142].

5.6 Event selection and categorization

In this section, the selection criteria, or cuts, placed on the relevant physics objects are presented: τ_{had} candidates, jets, MET, muons, and electrons. They select a Higgs-enriched signal region of the $\tau_{\text{had}}\tau_{\text{had}}$ analysis. Then, further event selection and categorization criteria are described. These are the first steps of the analysis, as shown in the analysis flow chart in Figure 5.6. The reconstruction of these objects of interest was previously described in Section 4. A summary of the selection criteria described in this section can be found in Tables 5.2 and 5.3. The event yield after each selection and for each category is shown in Table 5.4. The admixture of background and signal contributions found in each category is shown in Figure 5.7.

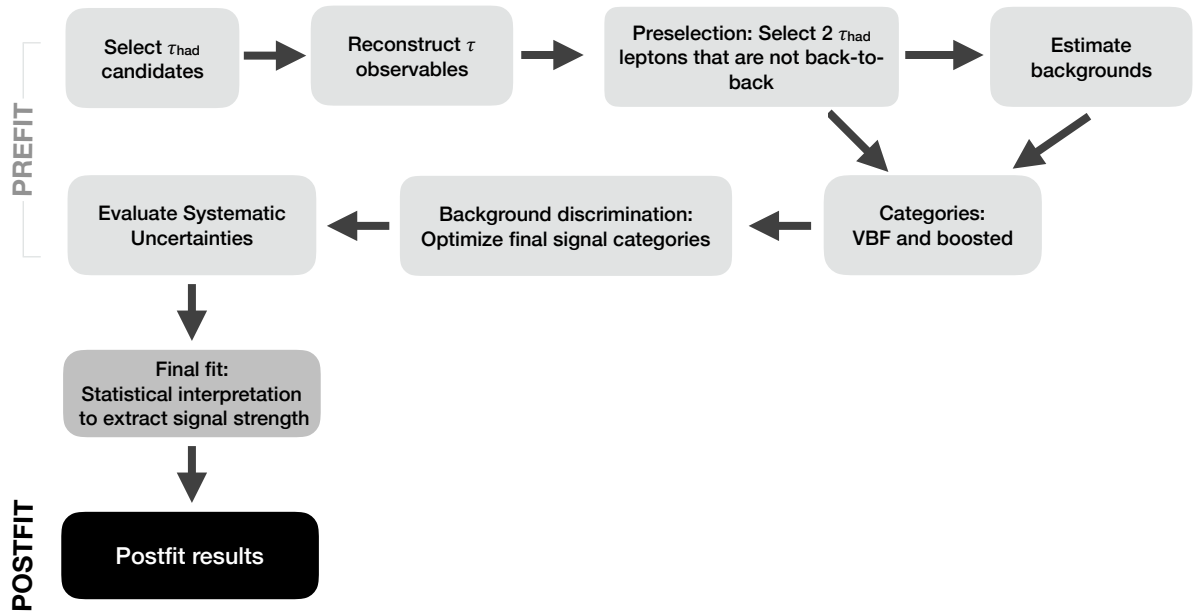


Figure 5.6: Flow chart showing each step of the analysis.

5.6.1 Selection of physics objects

Hadronically decaying tau leptons are the most important reconstructed physics object in this analysis. Each τ_{had} candidate should be matched to a tau trigger leg from the di-tau trigger ensuring the validity of tau trigger efficiency measurements for the event. The highest- p_T τ_{had} candidate, henceforth also referred to as the τ_0 candidate, should have a p_T greater than 40 GeV, and the second highest- p_T τ_{had} candidate, τ_1 , a p_T greater than 30 GeV. These thresholds reduce low p_T , nonresonant background and are based on the plateau of the tau trigger efficiency curve. Avoiding the turn-on region below the plateau of the trigger efficiency

curve prevents potential mismodeling in the analysis. The candidates must also be within the range of reconstruction of the ATLAS detector, $|\eta| < 2.5$, but not in the transition region between the barrel ECAL and the end cap ECAL, $1.37 < |\eta| < 1.52$, or crack, where there is extra detector material and a high rate of electrons misidentified as tau jets. Tau candidates are required to have one or three associated tracks within a cone of $\Delta R < 0.2$ around the τ -axis.

The τ_{had} candidates, at a minimum, also need to pass a level of τ identification that is tighter than the τ ID used at the trigger level. Since the trigger τ ID is less stringent than the offline (reconstruction-level) τ ID, the medium ID threshold used in both legs of the di-tau trigger approximately corresponds to an offline loose τ ID. The $\tau_{\text{had, vis}}$ ID working points are then optimized according to the S/\sqrt{B} figure of merit, where S is the number of signal events and B is the number of background events [143]. At the beginning of this analysis, the τ_{had} pair was required to pass at least the offline medium τ ID with at least one of the τ_{had} candidates passing the offline tight ID. This was an ID level taken from the Run-1 analysis, but this ID requirement was later re-optimized, to reduce the impact from the mismodeling of the $m_{\text{MMC}}^{\tau\tau}$ distribution. It was also reoptimized since, although the tau ID efficiency points stayed the same as in Run-1, the rejection rate in Run-II changed. Correction factors are applied on selected τ_{had} candidates from simulated samples to scale them to the same τ ID and trigger efficiencies observed in data. Lastly, selection criteria are placed on the collinear momentum fraction of the τ_{had} candidates, $0.1 < x_{0,1} < 1.4$, requiring the \cancel{E}_T from the ν_τ to be collinear to the respective τ -axis. The τ_{had} candidates that pass the tau object selection criteria are henceforth called τ_{had} decays.

Jets are important in selecting hadronizing quarks and gluons that come from the hard scattering process of the signal $H \rightarrow \tau\tau$ events in the ggH and VBF production modes. All jets must have $p_T > 20$ GeV and be found within $|\eta| < 4.5$. The leading p_T jet, in particular, is required to have $p_T > 70$ GeV and $|\eta| < 3.2$ to ensure that the event falls on the plateau of the trigger efficiency turn-on curves in p_T and $|\eta|$ for the L1 trigger jet (see Figure 4.5). In addition, the vertex tagger algorithm selects jets originating from the hard scattering process using tracks and vertices to minimize background jets from pileup events. Jets in the $|\eta| < 2.4$ region with $p_T < 50$ GeV have a $|\text{JVT}| > 0.59$ requirement. (JVT was previously explained in Section 4.4.1.) Jets with $p_T < 50$ GeV in the forward detector region, $|\eta| > 2.5$, are processed through the forward JVT algorithm, or fJVT [144], and are required to have $|\text{fJVT}| > 0.4$. No b -jet veto is applied on jets since the top background is minimal in the $\tau_{\text{had}}\tau_{\text{had}}$ channel.

The presence of \cancel{E}_T is a discriminating feature between QCD multijet production and hadronic tau decays since the latter have associated ν_τ particles. A requirement of $\cancel{E}_T > 20$ GeV is used.

Since the $H \rightarrow \tau_{\text{had}}\tau_{\text{had}}$ decay should not contain muons or electrons, henceforth also called leptons, a lepton veto is used. An event is vetoed if it contains a muon that passes the "loose" quality or an electron that passes the loose electron likelihood ID.

Additionally, all physics objects that pass the above selection are considered for overlap removal if they are found with a certain geometric distance in ΔR to another reconstructed physics object. The priority of which of the overlapping objects to retain is determined by the object reconstruction efficiency. Muons are of the highest priority, followed by electrons, τ_{had} candidates, and jets. The ΔR threshold depends on the types of overlapping objects, and the criteria for a muon in the case of overlap removal is loosened to loose ID and $p_T > 2$ GeV. If a jet is found within $\Delta R < 0.2$ to a medium τ_{had} candidate or a $\Delta R < 0.4$ of an electron or muon, the jet is removed. A τ_{had} candidate is removed if it is found within $\Delta R < 0.2$ to an electron or muon. Finally, an electron is removed if it is found within $\Delta R < 0.2$ to a muon.

5.6.2 Event preselection

After the physics object selection, the first event-level criteria, listed in Table 5.3, are placed at the preselection stage to increase the amount of Higgs-like events and reject backgrounds. The objective of the selection is to minimize the amount of contribution from the reducible fake- τ background and irreducible $Z \rightarrow \tau\tau$ background while maintaining high signal efficiency.

τ_{had}	Jet	\cancel{E}_T	Lepton
Trigger matched	$p_T > 20$ GeV	$\cancel{E}_T > 20$ GeV	Lepton veto
$ \eta < 2.5$, excluding $1.37 < \eta < 1.52$	$ \eta < 3.2$		
$p_T > 20$ GeV	$ \text{JVT} > 0.59$		
$ q = 1e$	$p_{T, \text{lead jet}}$		
Pass medium- $\tau_{\text{had, vis}}$ ID	is matched to the L1-trigger jet		
$0.1 < x_i < 1.4$	L1 trigger jet with $p_T > 70$ GeV		

Table 5.2: Object selection.

Of the possible τ_{had} candidates from the tau reconstruction algorithm, described in Section 4, the two highest- p_T tau candidates that pass the medium $\tau_{\text{had, vis}}$ ID are used to build the di-tau system in an event. These two τ_{had} candidates are required to come from the same vertex. These events should also contain at least one jet matched to the L1 trigger jet used in the di-tau trigger. There is no requirement on the maximum number of jets possible in the events to avoid additional theory uncertainties on the number of signal events.

Since the analysis searches for a τ_{had} pair from a neutral Higgs, they should have opposite signs. The event should contain exactly two τ_{had} candidates that satisfy the offline tight tau ID requirement. The exact requirement of no more than two avoids ambiguity on the application of tau ID scale factors to the τ_{had} candidates. This is a stricter requirement than the requirement in Run-I of the event to have exactly two medium-ID τ_{had} candidates and ≥ 1 tight τ_{had} candidate, where there was the disadvantage of the ambiguity in the application of the tight $\tau_{\text{had, vis}}$ ID scale factor. (Appendix F provides more details on the optimization of the selection in Run-II compared to Run-I.)

Requirements on the geometric configuration of the τ_{had} candidates are imposed to discriminate between Higgs-like τ_{had} -jet events and jets that come from random QCD processes. As opposed to τ_{had} candidates from the fake- τ background, τ_{had} candidates from a Higgs boson resonance are more boosted and are expected to be geometrically closer together. Therefore, the two τ_{had} candidates should have $\Delta\eta < 1.5$ and $\Delta R < 2.4$. To avoid τ_{had} candidates that overlap, resulting in poorly reconstructed tau jets, the minimum ΔR requirement is 0.8. This is slightly different than the ΔR selection made in [4], where the maximum ΔR requirement is loosened to $\Delta R < 2.8$ for a different background estimate strategy.

Additional topological requirements are placed on the \cancel{E}_T vector. Since the τ neutrinos are approximately collinear to their respective tau axes, the \cancel{E}_T vector typically points in between the τ_{had} candidates, produced with a boost from the Higgs, in the transverse plane. Due to the poor \cancel{E}_T resolution, cases where the \cancel{E}_T vector points close to one of the τ_{had} candidates are also selected, even if the \cancel{E}_T is not found in between the two τ_{had} candidates. That is, either the \cancel{E}_T vector should be in between the τ_{had} candidates, or the minimum of the $\Delta\phi$ between the \cancel{E}_T and the τ_{had} candidates should be less than $\frac{\pi}{4}$.

The percentage of $H \rightarrow \tau\tau$ signal events predicted to be obtained after the preselection

compared to background events is still small (about 1%). The next section describes how further selection criteria are placed to increase the signal fraction in the categories.

Preselection		
Two τ_{had} candidates from the same primary vertex		
Matched to the tau trigger objects selected by the di-tau trigger		
$q_{\tau_0} \cdot q_{\tau_1} < 1$		
$p_{T,\tau_0} > 40 \text{ GeV}$		
$p_{T,\tau_1} > 30 \text{ GeV}$		
$0.8 < \Delta R_{\tau\tau} < 2.4$		
$ \Delta\eta_{\tau\tau} < 1.5$		
Exactly two τ_{had} candidates passing the tight $\tau_{\text{had, vis}}$ ID requirement		
$\cancel{E}_T > 20 \text{ GeV}$		
$\min(\Delta\phi(\tau_0, \cancel{E}_T), \Delta\phi(\tau_1, \cancel{E}_T)) < \frac{\pi}{4}$ or \cancel{E}_T is between τ_0 and τ_1		
$p_{T,j_0} > 70 \text{ GeV}$		
$ \eta_j < 3.2$		
MMC algorithm has a physical solution		
$n_{\text{leptons}} = 0$		
Categories		
VBF		Boosted
At least two additional jets		Fail the VBF requirement
$p_{T,j_1} > 30 \text{ GeV}$		$p_{T, \text{resonance}} \geq 100 \text{ GeV}$
$m_{jj} > 400 \text{ GeV}$		
$\eta_{j_0} \cdot \eta_{j_1} < 0$		
$\min(\eta_{j_0}, \eta_{j_1}) < \eta_{\tau_0}, \eta_{\tau_1} < \max(\eta_{j_0}, \eta_{j_1})$		
$ \Delta\eta(\text{j,j}) > 3.0$		
VBF high ΔR tight		Boosted tight
$\Delta R(\tau, \tau) > 1.5$ or $p_{T, \text{resonance}} < 140$		$\Delta R(\tau, \tau) \leq 1.5$ and $p_{T, \text{resonance}} \geq 140 \text{ GeV}$
$m_{jj} > (-250 \cdot \Delta\eta(\text{j,j}) + 1550)$		
VBF high ΔR loose		Boosted loose
$\Delta R(\tau, \tau) > 1.5$ or $p_{T, \text{resonance}} < 140 \text{ GeV}$		$\Delta R(\tau, \tau) > 1.5$ or $p_{T, \text{resonance}} < 140 \text{ GeV}$
$m_{jj} < (-250 \cdot \Delta\eta(\text{j,j}) + 1550)$		
VBF low ΔR		
$\Delta R(\tau, \tau) \leq 1.5$		
$p_{T, \text{resonance}} \geq 140 \text{ GeV}$		

Table 5.3: Selection criteria for preselection and categories.

Region	Fake- τ	$Z \rightarrow \tau\tau$		Other		VBF	ggH	$ttH + VH$	Data	
Di-tau trigger	7 765 258.8 \pm 2 587.8	23 025.9 \pm 176.3	112 686.6 \pm 693.7	389 \pm 1	1 874.3 \pm 9	328.6 \pm 12.1	14 306 310 \pm 3 782.4			
L1 jet match	4 243 479.4 \pm 1 885.6	19 619.0 \pm 141.1	76 765.9 \pm 417.3	324.7 \pm 0.9	1 151.9 \pm 7	262 \pm 10.3	7 786 501 \pm 2 790.4			
L1 jet trigger	2 890 949.0 \pm 1 552.7	16 089.1 \pm 109.8	59 633.5 \pm 341.8	258.3 \pm 0.8	854.1 \pm 6.1	203.4 \pm 8.7	5 325 510 \pm 2 307.7			
$ q = 1$	2 866 755.4 \pm 1 537.1	14 600.0 \pm 104.8	36 928.9 \pm 263.9	213.9 \pm 0.8	708.3 \pm 5.5	156.9 \pm 7.6	2 426 450 \pm 1 557.7			
$n_{\text{track}} = 1, 3$	2 866 036.5 \pm 1 536.6	14 598.4 \pm 104.8	36 211.7 \pm 261.2	213.7 \pm 0.8	707.8 \pm 5.5	156.2 \pm 7.6	2 370 880 \pm 1 539.8			
$q_1 \cdot q_2 < 0$	2 857 427.2 \pm 1 531.4	14 443.1 \pm 104.3	27 757.7 \pm 228.9	208.9 \pm 0.7	695.2 \pm 5.4	135.7 \pm 7.2	1 420 165 \pm 1 191.7			
$p_T(\tau_0) > 40$ GeV	2 420 981.3 \pm 1 409.9	14 443.1 \pm 104.3	25 216.5 \pm 216.3	202.1 \pm 0.7	671.8 \pm 5.4	130.6 \pm 7.1	1 146 526 \pm 1 070.8			
$p_T(\tau_1) > 30$ GeV	1 683 623.9 \pm 1 175.9	14 443.1 \pm 104.3	19 617.6 \pm 186.6	171.5 \pm 0.7	563.4 \pm 4.9	106.5 \pm 6.3	729 510 \pm 854.1			
$\mathcal{E}_T > 20$ GeV	1 021 389.0 \pm 918.4	14 443.1 \pm 104.3	17 491 \pm 174.9	144.5 \pm 0.6	470 \pm 4.5	94.7 \pm 5.9	453 768 \pm 673.6			
$\Delta\eta < 1.5$	762 815.7 \pm 794.3	14 190.9 \pm 103.6	14 634.8 \pm 158.6	138.3 \pm 0.6	447.9 \pm 4.4	90.5 \pm 5.7	352 899 \pm 594.1			
$0.8 < \Delta R < 2.4$	361 409.4 \pm 473.4	15 895.1 \pm 115.9	8 409.5 \pm 112.3	112.0 \pm 0.5	364.9 \pm 3.8	64.9 \pm 4.7	227 742 \pm 477.2			
$0.1 < x_{0/1} < 1.4$	142 826.5 \pm 301.9	12 356.5 \pm 104.5	3 838.4 \pm 76.4	92.4 \pm 0.5	294.9 \pm 3.4	43.2 \pm 4	95 008 \pm 308.2			
Lepton veto	128 053.9 \pm 286.5	12 356.5 \pm 104.5	3 271.2 \pm 71.7	85.8 \pm 0.5	272.1 \pm 3.2	33.4 \pm 3.7	87 240 \pm 295.4			
$m_{\text{MMC}}^{\tau\tau}$ fit status	127 860.9 \pm 286.2	12 349.7 \pm 104.5	3 208.4 \pm 71.0	85.7 \pm 0.5	271.8 \pm 3.2	33.3 \pm 3.7	87 185 \pm 295.3			
≥ 1 Tight τ_{had} candidate	23 107.1 \pm 133.9	12 349.7 \pm 104.5	1 136.5 \pm 36.9	61.2 \pm 0.4	192.4 \pm 2.7	19.5 \pm 2.9	21 863 \pm 147.9			
2 Tight τ_{had} candidates	3 789.1 \pm 64.2	7 818.7 \pm 78	664.2 \pm 26.1	44 \pm 0.3	139.1 \pm 2.4	16.9 \pm 2.9	12 254 \pm 110.7			
VBF Low ΔR	19.6 \pm 4.9	127.2 \pm 6.5	19.6 \pm 3.0	11.3 \pm 0.2	5.1 \pm 0.4	0.8 \pm 0.6	158 \pm 12.6			
VBF High ΔR Tight	82.7 \pm 8.7	84.8 \pm 7.7	18.4 \pm 3.4	7.0 \pm 0.1	2.5 \pm 0.4	0 \pm 0.0	187 \pm 13.7			
VBF High ΔR Loose	49.5 \pm 6.8	50.7 \pm 4.9	9.0 \pm 2.7	1.7 \pm 0.1	1.4 \pm 0.2	0 \pm 0.0	100 \pm 10			
Boosted Tight	236.7 \pm 22.1	3 086.9 \pm 35.9	181.0 \pm 11.5	10.6 \pm 0.2	55.7 \pm 1.5	9.4 \pm 2.1	3 625 \pm 60.2			
Boosted Loose	1 692.6 \pm 42.8	2 887.7 \pm 46.1	329.4 \pm 20.7	9.4 \pm 0.2	49.4 \pm 1.4	6.5 \pm 1.9	4 832 \pm 69.5			

Table 5.4: Expected event yield of background and signal processes after each event selection, shown before the pre-fit background estimation in the top half. The bottom half shows the event yield after the pre-fit background estimation for and each signal category. The observed data yield is shown in the last column. Only the statistical uncertainties are shown.

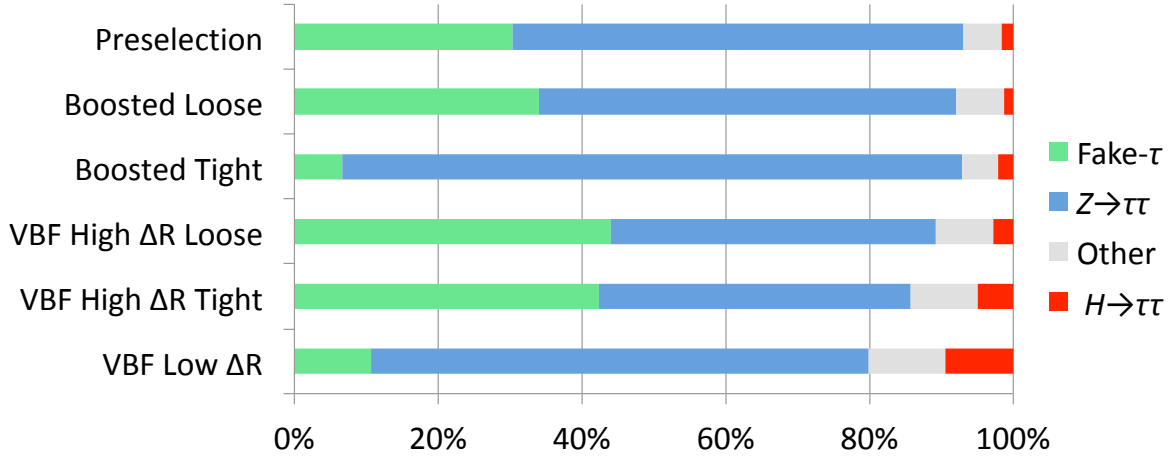


Figure 5.7: The admixture of background and signal contributions in each signal category.

5.6.3 Event categorization

After the preselection, additional criteria are imposed to increase the purity of signal using a categorization of events (see also Figure 5.6). This categorization is the strategy of the analysis presented in this dissertation. A multivariate (MVA) approach is also considered in [4]. Events are divided into orthogonal categories: the VBF category enriched with VBF-like events, the Boosted category with ggH -like events, and the Rest for discarded events that do not satisfy the VBF or ggH categorization criteria. The VBF and Boosted signal categories are further divided into orthogonal subcategories that are optimized for a SM 125 GeV Higgs boson according to the S/\sqrt{B} figure of merit. A summary of the categorization selection can be found in Table 5.3. These categories are used as the signal regions for the final statistical interpretation to extract the $H \rightarrow \tau\tau$ signal, described in Section 5.9 and henceforth referred to as the final fit.

In addition to increasing the signal-to-background fraction, the categorization also creates an admixture of background contribution and signal-to-background ratios in subcategories that helps to further constrain the fit parameters. Moreover, in certain categories, this categorization improves the resolution of the $m_{\text{MMC}}^{\tau\tau}$ observable, the discriminant used for the statistical interpretation of the observed signal strength, μ . The $m_{\text{MMC}}^{\tau\tau}$ resolution at the preselection level is poor due to the poor \cancel{E}_T resolution. Events at this stage are not required to come from a boosted Higgs boson resonance, so the \cancel{E}_T from the tau neutrinos of the di-tau resonance typically cancels out in the transverse plane. Figure 5.8 shows a schematic of the kinematic configuration. Going from preselection to the VBF and Boosted categories, the tau candidates become more boosted, and the two tau neutrinos, which are approximately collinear to their respective tau axes, also become more boosted. Since the tau neutrinos, then, are less likely to cancel each other out in the transverse plane, the larger \cancel{E}_T vector results in a higher \cancel{E}_T resolution, thus yielding a better mass resolution. This is important in the discrimination between the $H \rightarrow \tau\tau$ and the $Z \rightarrow \tau\tau$ background. Figure 5.9 presents the improvement in the $m_{\text{MMC}}^{\tau\tau}$ resolution going from preselection to the VBF and Boosted categories using the categorization criteria presented in the next sections (shown for the $H \rightarrow \tau\tau$ and $Z \rightarrow \tau\tau$ sample as examples). It can be seen that the $m_{\text{MMC}}^{\tau\tau}$ peak is slightly finer and higher in the Boosted category. The effect is also seen in the VBF category to a lesser degree. Because the categorization increases the signal sensitivity, the $m_{\text{MMC}}^{\tau\tau}$ distribution in the categories is blinded,

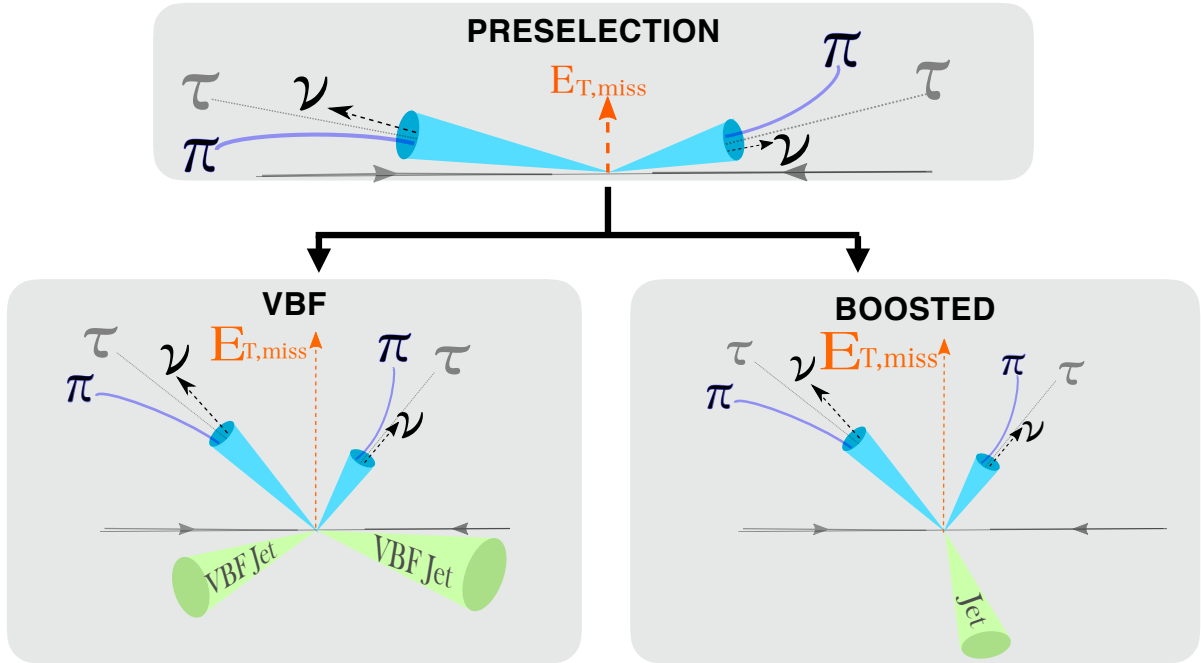
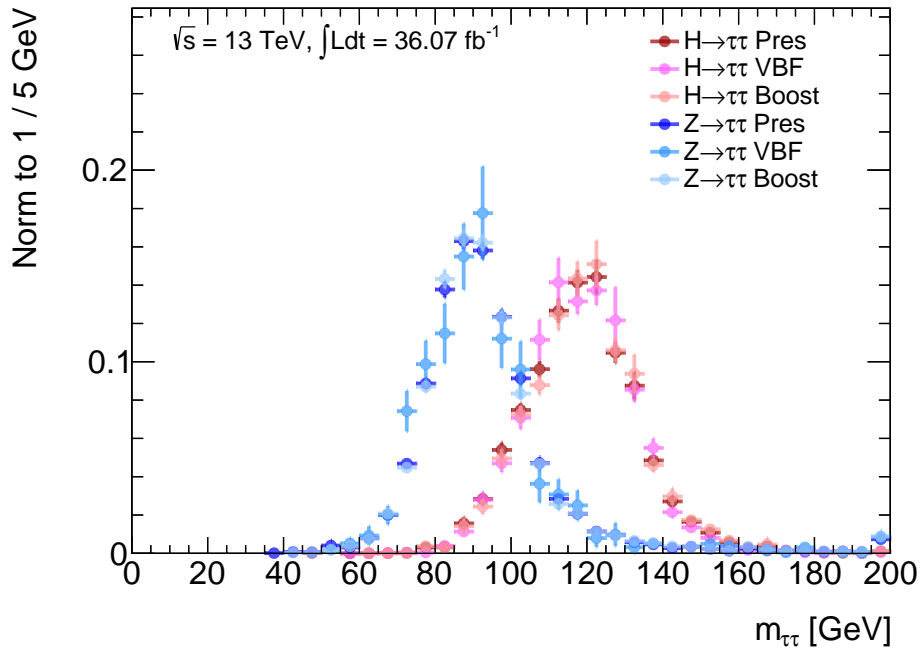


Figure 5.8: Schematic of the differences in kinematic configurations between preselection and the categories.

i.e., not shown for the signal window, $100 \text{ GeV} < m_{\text{MMC}}^{\tau\tau} < 150 \text{ GeV}$. The unblinding of the data is shown at the end of the analysis in Section 5.10.


 Figure 5.9: The improvement in the $m_{\text{MMC}}^{\tau\tau}$ resolution going from preselection to the VBF and Boosted categories, shown for the $H \rightarrow \tau\tau$ and $Z \rightarrow \tau\tau$ samples as examples.

5.6.3.1 VBF categories

Events passing the preselection criteria are first considered for the VBF category.⁵ The VBF production process is categorized by two high- p_T jets in the forward direction of the detector, or VBF tag jets, coming from the two outgoing quarks from the hard scattering process (see Figure 5.4 and Figure 5.8). VBF-like events are required to have a leading p_T jet with $p_T > 70$ GeV and a subleading p_T jet with $p_T > 30$ GeV. As previously discussed in Section 5.6.1, these p_T requirements are determined based on the turn-on region of the trigger efficiency in p_T to prevent potential mis-modeling in the analysis (see Figure 4.5). A selection of $\eta_{j_1} \cdot \eta_{j_2} < 0$ ensures that these two jets are emitted in opposite ends of the detector. The τ_{had} candidates should be in between the two VBF tag jets in η , i.e., $\min(|\eta_{j_1}|, |\eta_{j_2}|) < |\eta_{\tau_1}|, |\eta_{\tau_2}| < |\max(\eta_{j_1}, \eta_{j_2})|$. In addition, the VBF tag jets are required to have a separation of $|\Delta\eta_{j,j}| > 3.0$ to ensure that they are in the forward direction and a large invariant mass with $m_{j,j} > 400$ GeV, to target the two outgoing quarks from the hard scattering process and not low- p_T pileup interactions.

After the selection of VBF-like events, this inclusive VBF category is further subdivided into orthogonal categories: VBF low ΔR , VBF high ΔR tight, and VBF high ΔR loose. The VBF low ΔR category is the most sensitive of the exclusive VBF categories. It targets a high- p_T resonance, with

$$p_{T, \text{resonance}} = \left| p_T^{\tau_1, \text{vis}} + p_T^{\tau_2, \text{vis}} + \cancel{E}_T \right| \quad (5.8)$$

required to be at least 140 GeV and pass $\Delta R(\tau, \tau) \leq 1.5$. Although these two variables are highly correlated, selection cuts are imposed on both because, when combined, they can reject a phase space that is populated specifically by QCD multijet, as seen in Figure 5.10. Removing these events has an effect on the $m_{\text{MMC}}^{\tau\tau}$ distribution since this observable is not correctly reconstructed when the events do not come from a resonance like the Z or the Higgs.

Events that do not pass the VBF low ΔR selection are then considered for the VBF high ΔR categories. When these events are divided based on the characteristics of the VBF tag jets, two VBF high ΔR categories can be obtained with significantly opposite S/\sqrt{B} values, a difference that aids the final fit in constraining the event yields of the signal and background contributions. (See Figure 5.7 showing the different admixture of backgrounds in the categories.) As shown in Figure 5.11, events containing VBF tag jets with a high invariant mass, or $m_{j,j}$, or a high $\Delta\eta$ are more likely to come from a Higgs boson resonance. Therefore, events are divided into the VBF high ΔR tight and VBF high ΔR loose based on a diagonal criterion in $m_{j,j}$ and $\Delta\eta(j,j)$ of

$$m_{j,j} = -250 \cdot |\Delta\eta(j,j)| + 1550, \quad (5.9)$$

shown in Figure 5.11.

5.6.3.2 Boosted categories

Events that pass the preselection criteria but do not satisfy the VBF selection are considered for the Boosted category. This category targets ggH -like events that are accompanied by a jet from a radiating gluon, resulting in a high- p_T recoiling Higgs. Therefore, the di-tau resonance in the Boosted category is required to pass $p_{T, \text{resonance}} \geq 100$ GeV. Events passing these requirements are then further divided into orthogonal Boosted sub-categories based on $\Delta R_{\tau\tau}$ and the resonance p_T , observables which have a high separation power between resonant events

⁵ The categorization happens in this order for two reasons: the VBF category is more signal-sensitive, and the VBF category requires a minimum number of two additional jets whereas the Boosted category requires one.

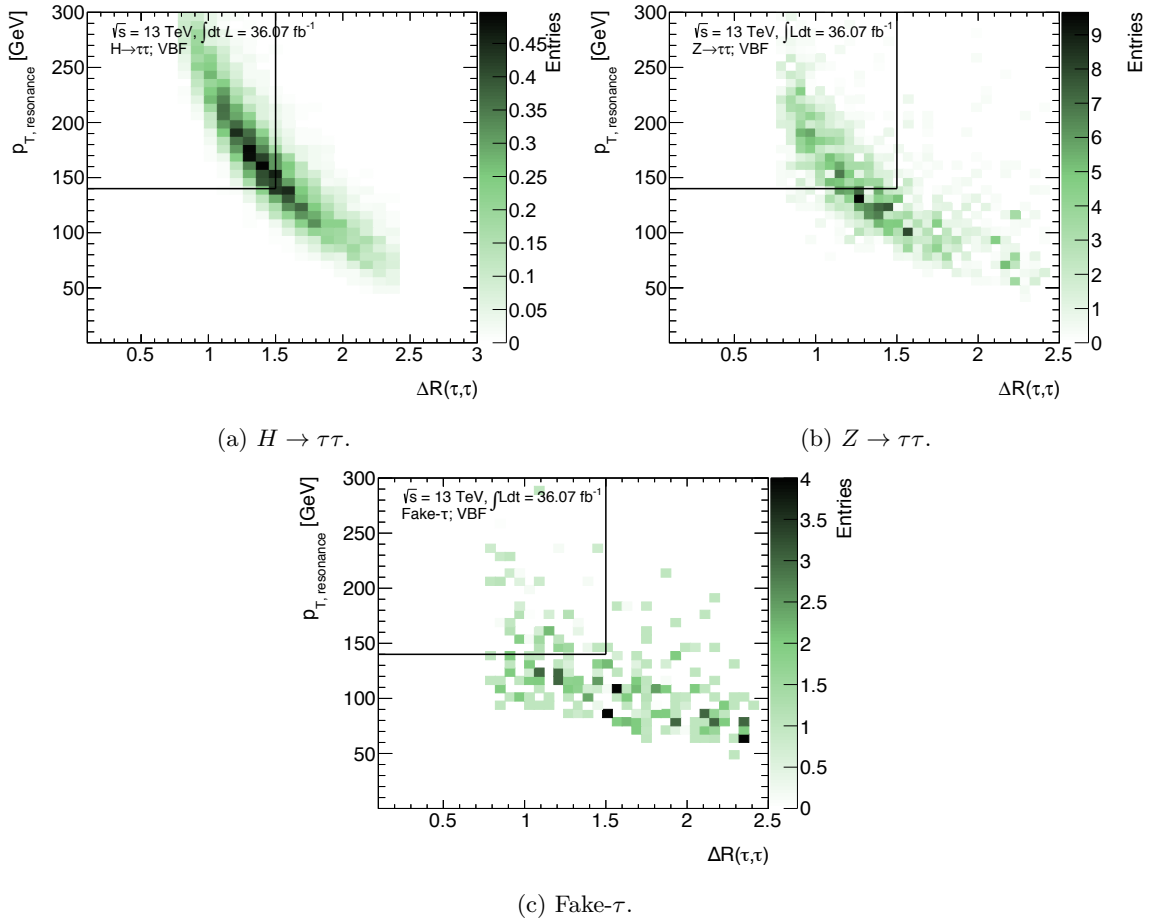


Figure 5.10: Categorization of the VBF region into the low and high ΔR VBF categories, shown for the $H \rightarrow \tau\tau$, $Z \rightarrow \tau\tau$, and fake- τ background processes.

and non-resonant background from QCD multijet, as shown in Figure 5.12. The Boosted tight category is the signal-enriched, high- p_T region and is divided from the Boosted loose category based on the same selection values as for the VBF high p_T categories: $\Delta R(\tau\tau) \leq 1.5$ and $p_{T, \text{resonance}} \geq 140$ GeV. As in the VBF categories, these Boosted categories have opposite signal-to-background ratios, which aids the final fit.

Events that do not pass the requirements for the inclusive VBF or Boosted categories are discarded and are not used for the signal region in the final fit. Although the VBF and Boosted categories are optimized to select VBF and ggH events, they contain contributions from VH events.

5.7 Background model

After the selection of events into the signal categories, the next step is the development of an accurate model of the event yield and observables for the expected background processes. This is important for the statistical interpretation of the observed data since the final statistical interpretation in the $H \rightarrow \tau\tau$ search tests the compatibility between the observed data and the expected signal and background contributions. Expected and observed refer to:

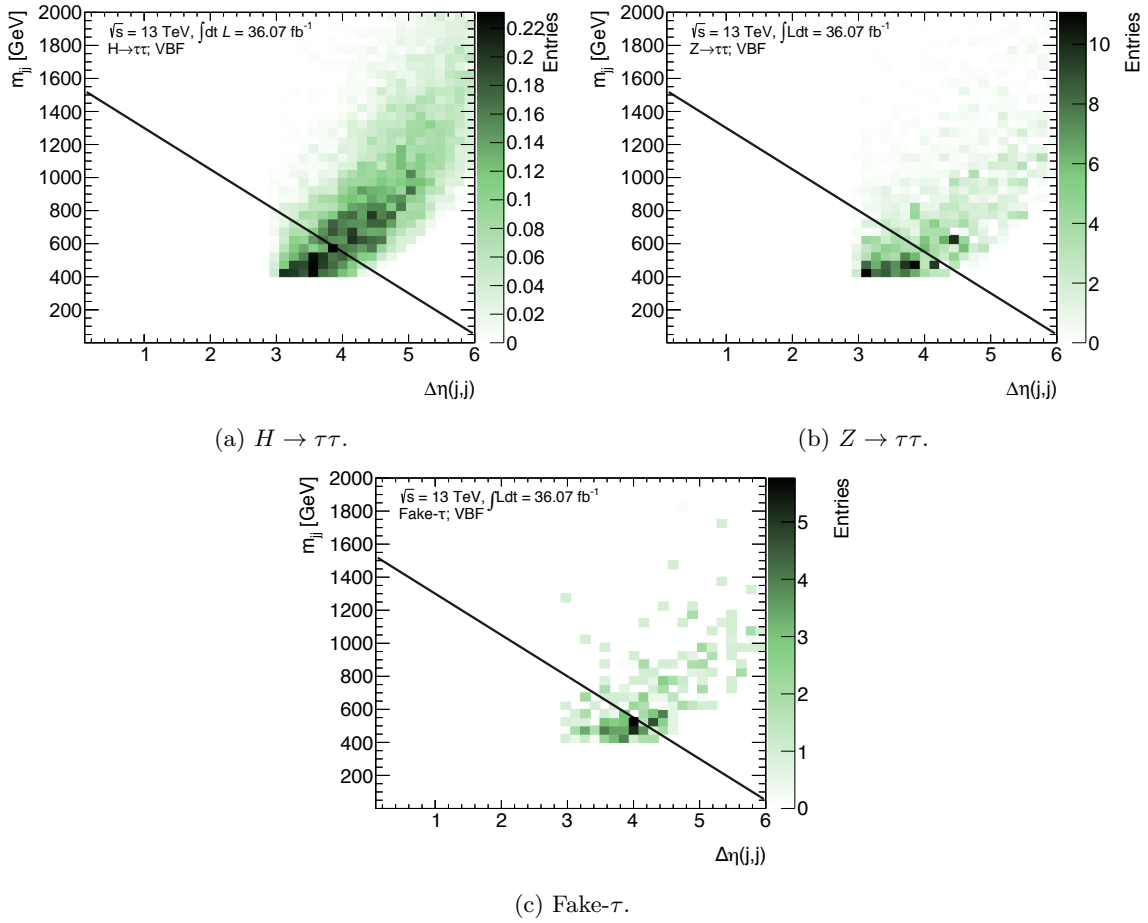


Figure 5.11: Categorization of the VBF High ΔR region into tight and loose categories, shown for the $H \rightarrow \tau\tau$, $Z \rightarrow \tau\tau$, and fake- τ background processes.

- The expected event yields and observables are those that one would expect to see if the same experiment were performed multiple times.
- The observed events are those seen in the data collected at the ATLAS detector, as described in Section 5.4.1.

The background model should predict the expected event yield to high precision. It should also robustly model physics observables well, especially those used in the event selection/categorization and the $m_{\text{MMC}}^{\tau\tau}$ variable used for the final statistical interpretation. These expected yields and observables should closely match those seen in the observed data.

A summary of the background estimation method is described in Table 5.5. This section describes the background estimation procedure for the dominant background contributions from the fake- τ and QCD $Z \rightarrow \tau\tau + \text{jets}$ processes. The shape and event yield of the fake- τ background are determined via a data-driven technique. The shape of the $Z \rightarrow \tau\tau$ background is determined from simulation while the event yield is determined from a fit to data. The other background processes, which have at least one true electron or τ_{had} candidate matched to a reconstructed τ_{had} candidate, contribute minimally and are predicted using simulation. This determination is at the so-called prefit level, i.e., before the final statistical interpretation to

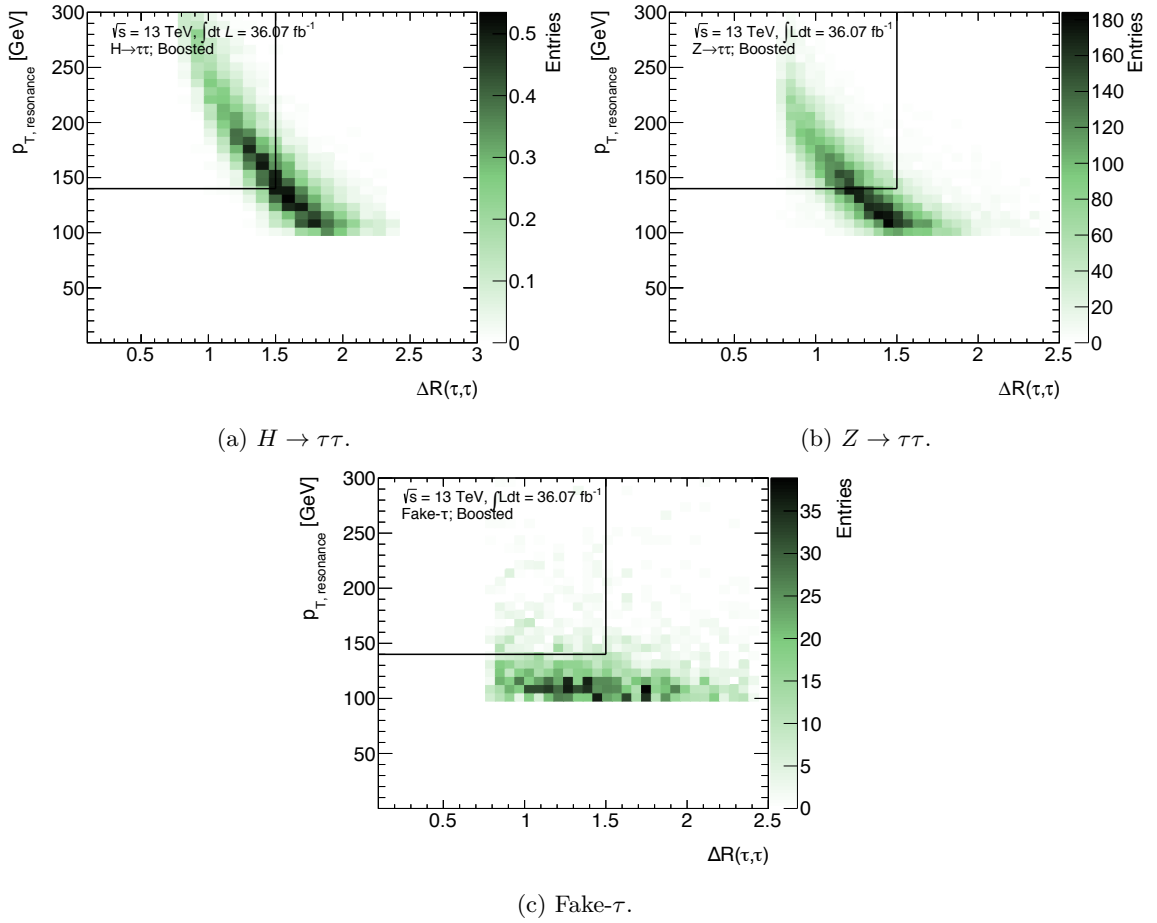


Figure 5.12: Categorization of the boosted region into the tight and loose boosted categories, shown for the $H \rightarrow \tau\tau$, $Z \rightarrow \tau\tau$, and fake- τ background processes.

extract the signal strength in the fit to the $m_{\text{MMC}}^{\tau\tau}$ distribution. The prefit background model is validated at the preselection level and in the signal categories with the data blinded in the $100 < m_{\text{MMC}}^{\tau\tau} < 150$ GeV region. It is then used to build the fit model for the final statistical interpretation to obtain the so-called postfit results, described later in Section 5.9. (See also a description of the analysis flow in Figure 5.6.)

Process	Template from	Prefit normalization from	Final fit normalization
Fake- τ	nOS Control Region	Fit to $\Delta\eta$	Floated (unconstrained)
$Z \rightarrow \tau\tau$	MC	Fit to $\Delta\eta$	Floated (unconstrained)
Other	MC	MC cross section	Fixed

Table 5.5: Summary of the background strategy.

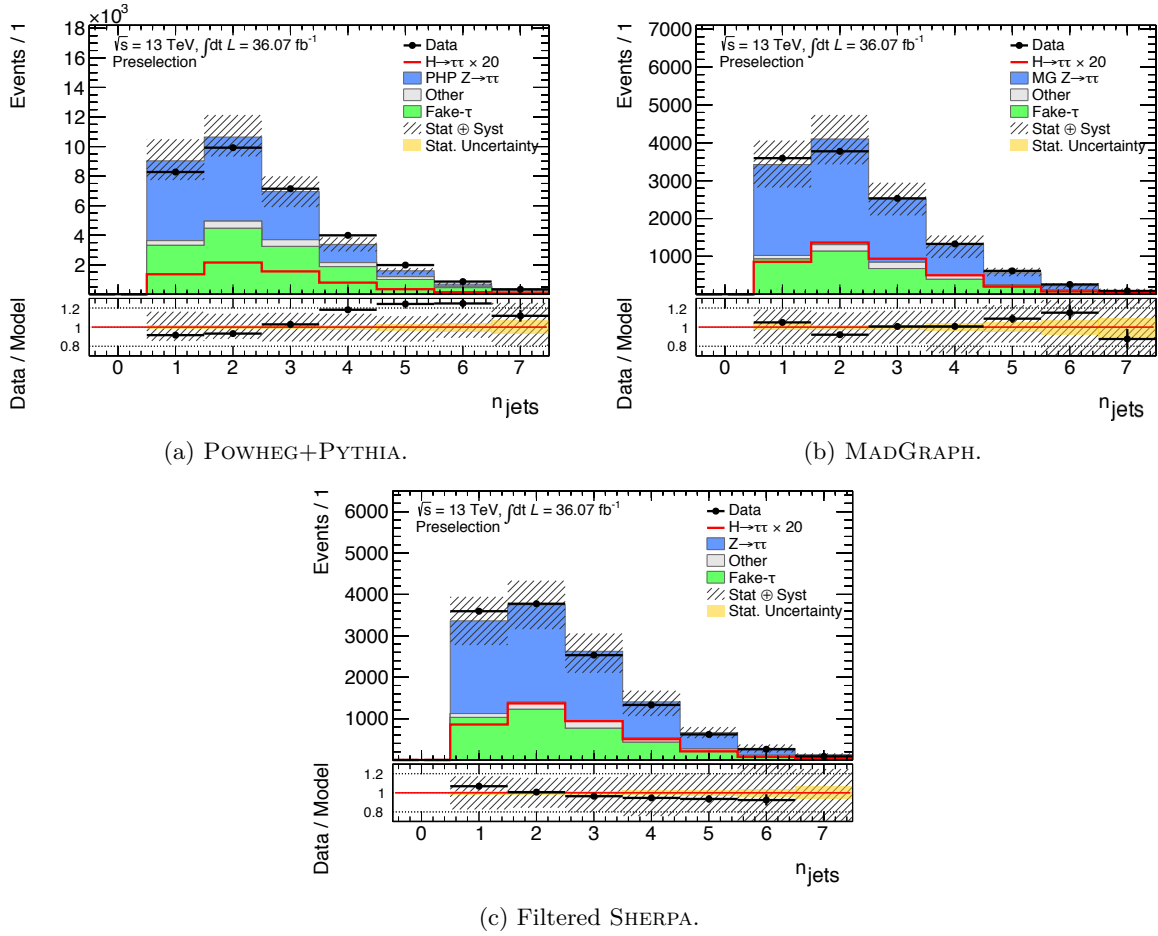


Figure 5.13: Modeling of the number of jets at preselection with the POWHEG+PYTHIA, MADGRAPH, and SHERPA $Z \rightarrow \tau\tau$ samples.

5.7.1 Estimation of the $Z \rightarrow \tau\tau$ background

The $Z \rightarrow \tau\tau$ background is the largest irreducible background in the $\tau_{\text{had}}\tau_{\text{had}}$ channel. Understanding and modeling the QCD $Z \rightarrow \tau\tau + \text{jets}$ background accurately is crucial. The most difficult feature of the QCD $Z \rightarrow \tau\tau + \text{jets}$ modeling is the production of associated jets. These associated jets impact the kinematic distributions of the $Z \rightarrow \tau\tau$ background, which is of high consequence in the $H \rightarrow \tau\tau$ analysis where the Higgs boson and $Z \rightarrow \tau\tau$ mass peaks sit close together. This feature is further exacerbated by the dilution of the di-tau mass resolution of both processes due to detector and reconstruction effects. It is particularly difficult to validate $Z \rightarrow \tau\tau$ simulation in the $\tau_{\text{had}}\tau_{\text{had}}$ final state because it is not possible to obtain a pure, high-statistics $Z \rightarrow \tau\tau$ control region in data that is representative of the general $\tau_{\text{had}}\tau_{\text{had}}$ phase space. The background results in the same final state as the signal.

The three available simulated samples have advantages and disadvantages. POWHEG+PYTHIA8 models the Drell-Yan process at NLO and models the $W/Z + 1$ jet processes well. However, it does not model other jets well, which is problematic for the categories in the $\tau_{\text{had}}\tau_{\text{had}}$ analysis that make use of additional jets in the hard scattering process. This can be seen in Figure 5.13 where there is an underestimation at $n_{\text{jets}} > 2$ and an overestimation at $n_{\text{jets}} \leq 2$. The SHERPA

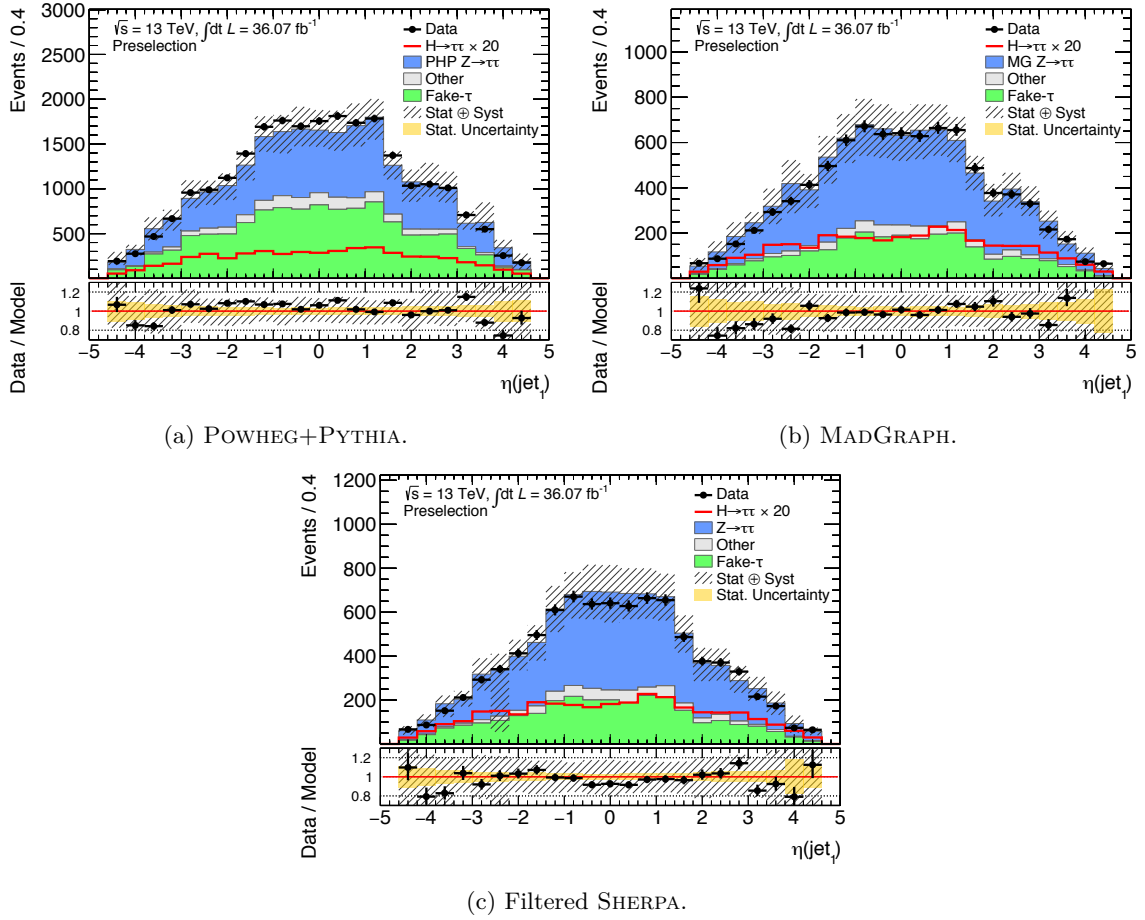


Figure 5.14: Modeling of the η of the subleading p_T jet at preselection with the POWHEG+PYTHIA, MADGRAPH, and SHERPA $Z \rightarrow \tau\tau$ samples.

2.2 sample, where SHERPA is used for the hard scattering and parton showering, profits from precise modeling of jet emission since it models $Z+n$ jets at matrix element and parton showering NLO. However, it starts to exhibit problems at $n_{\text{jets}} > 2$, as can be seen in the overestimation trend at $n_{\text{jets}} > 2$ in Figure 5.13(c), and also needs to be re-weighted according to truth jets. The SHERPA sample also has events with high weights that need to be removed. The MADGRAPH sample models $Z+n$ jets at LO only, and the LO PDF is problematic for the η modeling of the Z boson, as can be seen in the high $|\eta|$ regions in Figure 5.14(b). From modeling comparisons of the three generators, SHERPA 2.2 shows the best agreement with data, and a high-statistics filtered SHERPA $Z \rightarrow \tau\tau$ sample was produced for this analysis in order to reduce the statistical uncertainty from this background.

The shape of the $Z \rightarrow \tau\tau$ background is taken from the SHERPA sample. The event yield of the $Z \rightarrow \tau\tau$ background is determined from a fit to data. This fit is described in the next section. Systematic uncertainties on the $Z \rightarrow \tau\tau$ background estimation are described in Section 5.8.1.4.

5.7.2 Estimation of the fake- τ background

The fake- τ background consists of events where the two τ_{had} candidates stem from non-resonant production of QCD jets from hadronizing quarks and gluons. It is one of the major backgrounds in the $\tau_{\text{had}}\tau_{\text{had}}$ channel. Therefore, a robust fake- τ background estimate that models the data within reasonable uncertainty is important.

This background is estimated with a data-driven method since the use of simulation in the $H \rightarrow \tau_{\text{had}}\tau_{\text{had}}$ analysis is not ideal. The QCD multijet processes have a large cross section, which means the generation and simulation of the multijet are computationally expensive. The feasibility of an MC-filtered sample that is enriched with fake- τ events has been studied, but the filter efficiency is too low to produce a high-statistics sample that would populate the phase space of interest in the $\tau_{\text{had}}\tau_{\text{had}}$ channel.⁶ Simulated dijet samples do exist, but they are of limited size. In addition, the modeling of the detector performance for QCD jets is typically poor because hadronic showers are complicated. It is also difficult to model because of the non-perturbative QCD processes in hadronization, which are responsible for the number of particles in a jet.

A data-driven fake- τ background estimate is derived by reverting a signal region selection to reach an orthogonal control region in data. Control regions discussed in this dissertation are regions obtained by reversing the di-tau sign requirement and the tau identification:⁷

- The di-tau sign requirement can be reverted since this region should contain a low amount of $H \rightarrow \tau\tau$ and $Z \rightarrow \tau\tau$ contamination. Section 5.7.2.1 describes the method that utilizes this control region called the OS-nOS method, where OS means opposite-sign and nOS means not opposite-sign.
- The $\tau_{\text{had, vis}}$ ID requirements can also be reverted to obtain an anti- $\tau_{\text{had, vis}}$ ID for so-called fake-factor methods, which extrapolate that fake-enriched control region to the signal region using fake-factors. Fake-factor methods are, in general, better in statistically limited analyses that require a large control region. However, they have a disadvantage compared to the OS-nOS method since differences due to tau identification are typically larger than those due to di-tau sign requirements. Use of the anti- $\tau_{\text{had, vis}}$ ID control region for fake-factors was not feasible in the Run-I $\tau_{\text{had}}\tau_{\text{had}}$ analysis because the di-tau trigger requirements were too tight, making it difficult to select a statistically powerful anti-ID region enriched with fake- τ candidates. In Run-II, the di-tau trigger was loosened so that fake- τ estimate strategies using the anti-ID region could be explored. Sections 5.7.2.4 – 5.7.2.6 motivate and describe a method, called the matrix method, that utilizes the anti-ID region.

The resulting control regions are enriched with fake- τ background events and contain minimal contamination from signal and other background processes. They are also not significantly different from the signal region and do not significantly alter the $m_{\text{MMC}}^{\tau\tau}$ distribution.

⁶ Even if an MC-filtered fake- τ sample were not used as the nominal background estimate, it would be useful in validating the data-driven background estimation and in deriving systematic uncertainties on these data-driven methods.

⁷ Reversal of the other possible signal region requirements, described previously in Table 5.3, results in control regions with significantly different $m_{\text{MMC}}^{\tau\tau}$ distributions than the one found in the signal region. The inversion of the tau identification and the di-tau sign requirement have minimal impact on the kinematic properties of the selected events.

In the following sections (Sections 5.7.2.1 – 5.7.2.3), the OS-nOS method and its associated systematic uncertainties are first discussed. A mismodeling of data using a control region with this estimate is observed, motivating the development of the matrix method that uses another control region that is more similar to the signal region (Sections 5.7.2.4 – 5.7.2.7). The expected signal sensitivity of both methods is evaluated in Section 5.9, with the OS-nOS method performing better than the matrix method. The final results presented in this dissertation therefore use the OS-nOS method.

5.7.2.1 OS-nOS method

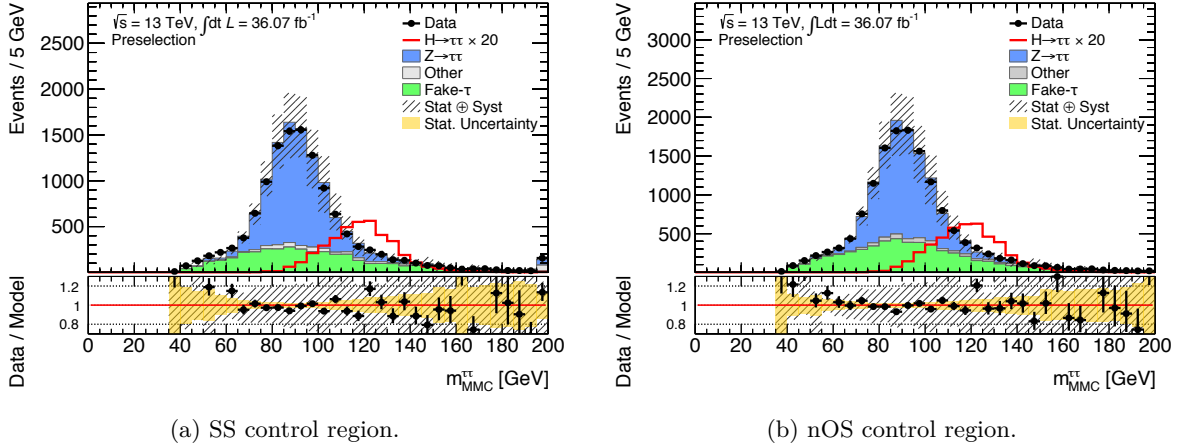
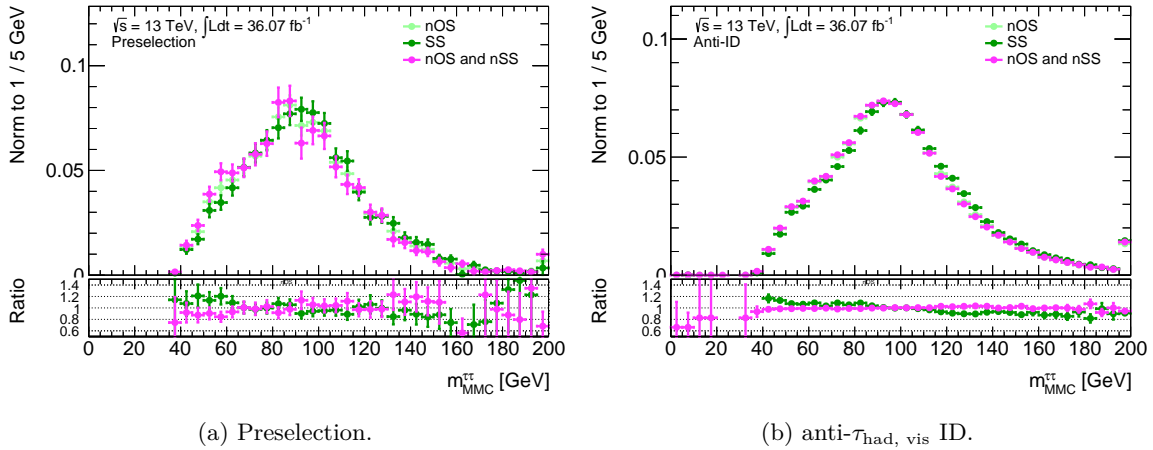
The OS-nOS method is a data-driven background estimate that uses a signal-depleted control region in data to determine the pre-fit event yield and template for the fake- τ background. Control regions can be obtained by reverting the OS requirement, keeping all other signal region criteria the same. The control regions considered in this section are the same sign (SS) and not opposite sign (nOS) control regions since they are signal-depleted regions that do not significantly affect kinematics and alter the $m_{\text{MMC}}^{\tau\tau}$ distribution. Their selection criteria are shown in Table 5.6. The motivation for the nOS control region is that it contains the additional orthogonal region of $q_{\tau,1} \cdot q_{\tau,2} = 0$ and was used in the $H \rightarrow \tau_{\text{had}}\tau_{\text{had}}$ analysis in Run-I [128].

Control Region	Di-tau sign requirement	Track requirement
Same Sign (SS)	$q_{\tau,1} \cdot q_{\tau,2} = 1$	$n_{\text{tracks}} = 1, 3$
Not Opposite Sign (nOS)	$q_{\tau,1} \cdot q_{\tau,2} \neq -1$	$n_{\text{tracks}} = 1, 2, 3$

Table 5.6: Selection requirements for the SS and nOS control regions, keeping all other signal region criteria the same.

Fake- τ background template in the OS-nOS method The fake- τ background template can be obtained from either the SS or nOS region, since they are both regions with di-tau sign reversals that are expected to be similar to the signal region, while profiting from a low contamination of background contribution from processes other than QCD multijet production (henceforth referred to as real- τ backgrounds). There is *a priori* no clear motivation to prefer either the SS or nOS region. After comparing the modeling of the data with both regions in Figure 5.15, however, the use of the SS control region reveals an underestimation of data in the low $m_{\text{MMC}}^{\tau\tau}$ region ($m_{\text{MMC}}^{\tau\tau} < 60$ GeV), while the use of the nOS region does not. The additional subset of 2-prong events not found in the SS region corrects the low $m_{\text{MMC}}^{\tau\tau}$ mismodeling.⁸ Figure 5.16 shows a linear trend in the $m_{\text{MMC}}^{\tau\tau}$ shape correction between the SS and nOS regions for the $m_{\text{MMC}}^{\tau\tau}$ observable. It also shows the subset of 2-prong events from the nOS region that are not found in the SS region (nOS and nSS). This subset fills up the underestimation at low $m_{\text{MMC}}^{\tau\tau}$. The linear trend can be seen more clearly in the anti- $\tau_{\text{had, vis}}$ ID region. It is useful to look at this region since there is less contamination from real- τ backgrounds (discussed in the next paragraph). The region is therefore less prone to uncertainties from the subtraction of real- τ background, as is discussed next.

⁸ The nOS control region is not as well understood as the SS region since there are no dedicated $\tau_{\text{had, vis}}$ ID scale factors for τ_{had} candidates with two tracks. By default, the scale factors derived for three-track τ_{had} candidates are applied on these two-track τ_{had} candidates.

Figure 5.15: Comparison of the $m_{MMC}^{\tau\tau}$ modeling with the SS and nOS control regions.Figure 5.16: Comparison of the $m_{MMC}^{\tau\tau}$ distribution in the SS and nOS regions with real- τ contribution subtracted, shown at the preselection (left) and anti- $\tau_{had, vis}$ ID level (right). The bottom ratios are calculated with respect to the nOS shape. The uncertainties include statistical uncertainties only.

The fake- τ background template obtained from the nOS control region contains contamination from processes that do not originate from multijet production. In order to avoid double-counting background events, any contamination from real- τ processes is subtracted in order to obtain the expected fake- τ background template. A low contamination is ideal since it implies smaller uncertainties in the subtraction.

Figure 5.17 shows the contamination that is subtracted from the nOS control region in order to obtain a fake- τ background template. The expected contamination from real- τ backgrounds, is small, at about 16% in the nOS region, as shown in Table 5.7. The nOS contamination is higher than the 6% of contamination found in the SS background. This is because about 57% of the nOS region is populated by events where at least one τ_{had} candidate contains exactly two tracks.

Table 5.7 also shows that almost all of the contamination in the nOS region comes from the $Z \rightarrow \tau\tau$ background. About 88% of this contamination arises from events where there is at least one τ_{had} candidates with exactly two tracks. This occurs when either two tracks are

merged or a conversion track passes as a tau track. (See Table G.1 in Appendix G showing the background composition of the nOS region based on the number of tracks.) The expected signal contamination in the SS and nOS regions is minimal at about 0.6%, as shown in Figure 5.17, and is not subtracted.⁹

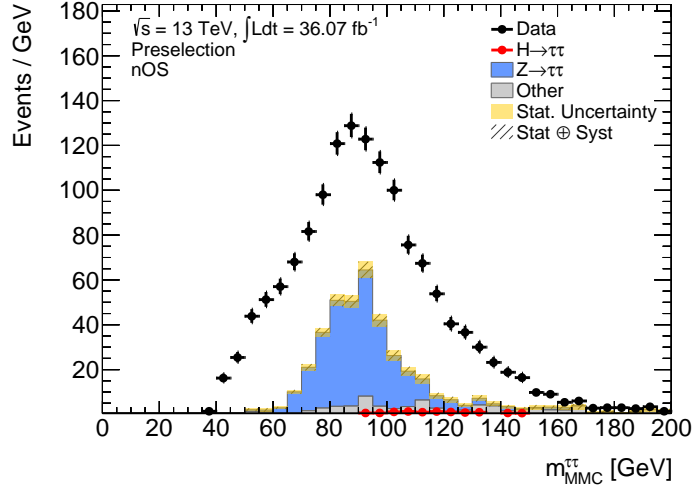


Figure 5.17: Contamination from signal and the $Z \rightarrow \tau\tau$ and other background processes in the nOS Control region. Shown at the preselection level. (See also Table 5.7 for the expected contamination in terms of percentage of the even yield in the nOS control region.)

Region	Di-tau sign	$Z \rightarrow \tau\tau$ and Other (%)	$H \rightarrow \tau\tau$ (%)
Preselection	nOS	16.0 ± 0.734	0.0967 ± 0.0311
Preselection	SS	5.94 ± 0.0130	0.0838 ± 0.0525
Anti- $\tau_{\text{had, vis}}$ ID	nOS	1.25 ± 0.0514	0.0132 ± 0.00295
Anti- $\tau_{\text{had, vis}}$ ID	SS	0.798 ± 0.0719	0.00203 ± 0.000027
Anti- $\tau_{\text{had, vis}}$ ID	OS	4.84 ± 0.164	0.0777 ± 0.00926

Table 5.7: Contamination from real- τ backgrounds ($Z \rightarrow \tau\tau$ and Other) in the SS and nOS control regions, shown as the percentage compared to the event yield in the respective control data region. The contamination from real- τ background in the nOS region is about 16% at preselection and about 1% in the anti- $\tau_{\text{had, vis}}$ ID region. The uncertainties take into account the fact that the samples are statistically independent.

Determination of the fake- τ background event yield in the OS-nOS method With the templates of the fake- τ and $Z \rightarrow \tau\tau$ backgrounds defined, the next step is to determine their expected event yields. To account for differences between the OS signal region and the nOS control region used for the fake- τ background template, an r_{QCD} factor is used to scale the nOS template to the event yield expected in OS data. For the $Z \rightarrow \tau\tau$ background, an r_Z factor is employed to scale the event yield predicted by MC to the expected event yield in data. The r_Z

⁹ This also avoids signal model dependencies in the subtraction.

factor accounts for possible deviations in the $\tau_{\text{had, vis}}$ ID scale factors and from MC prediction, especially since the tau trigger requires a high p_T underlying jet.

These r_{QCD} and r_Z factors are measured at the prefit level using a template fit to OS data:

$$N_{\text{Data, OS}} = N_{\text{Real-}\tau, \text{ OS}} + r_{\text{QCD}} \cdot (N_{\text{Data}} - N_{\text{Real-}\tau})_{\text{nOS}} \quad (5.10)$$

$$\begin{aligned} &= r_Z \cdot N_{Z \rightarrow \tau\tau, \text{ OS}} + \sum_{i \in \substack{\text{Other} \\ \text{real-}\tau \\ \text{backgrounds}}} N_{i, \text{ OS}} \\ &\quad + r_{\text{QCD}} \cdot \left(N_{\text{Data, nOS}} - r_Z \cdot N_{Z \rightarrow \tau\tau, \text{ nOS}} - \sum N_{i, \text{ nOS}} \right) \end{aligned} \quad (5.11)$$

where N refers to the event yield and other real- τ backgrounds are all real- τ backgrounds except the QCD $Z \rightarrow \tau\tau$ +jets background.

The prefit results are then used to validate the modeling of observables using this background strategy. The fitted r_{QCD} and r_Z values from the preselection level are applied in each of the signal categories (introduced earlier in Section 5.6.3). There are several reasons for this. First, the VBF categories, even when considered inclusively, are of limited size, meaning the fit procedure is more likely to find multiple minima. Additionally, the r_{QCD} and r_Z factors do not significantly differ at the preselection level and for the inclusive VBF/Boosted categories. Lastly, fit validation studies performed in this dissertation using a separate r_{QCD} factor each for the VBF and Boosted categories show that the sensitivity is similar when using one r_{QCD} for all categories. Since the additional complexity is unnecessary, using a single factor is used to aid the stability of the final fit. In the final statistical interpretation to obtain the postfit normalizations, the fake- τ and $Z \rightarrow \tau\tau$ normalizations are allowed to again float freely, where they are first given the prefit r_{QCD} and r_Z normalization factors as starting values.

The prefit procedure can be performed in variable distributions with at least two degrees of freedom, since there are two normalization factors to be determined. The templates should exhibit discriminating shape differences between the fake- τ and $Z \rightarrow \tau\tau$ background contributions. From fits to different di-tau observables, the normalization factors are found to be consistent. Therefore, the $\Delta\eta$ distribution is used, with an extension to $\Delta\eta < 2.0$ instead of the preselection requirement of $\Delta\eta < 1.5$, since the extra bins at $\Delta\eta > 1.5$ contain a high purity of fake- τ background that help to constrain the fit (see Figure 5.18). The prefit yields from a fit to $\Delta\eta$ model the other observables well, as is later shown in Figure 5.19. The extra $\Delta\eta$ range means that r_{QCD} and r_Z are not determined in the same region as that used for the signal regions, but these regions are similar enough to avoid potential mis-modeling effects. There is not a significant dependence of r_{QCD} and r_Z on the $\Delta\eta$ range.

The background estimation normalization factors are shown in Table 5.8, and the expected event yields are shown in Table 5.4. A value of r_{QCD} smaller than 1 implies that the fake- τ background template is statistically powerful and is modeled by a control region containing more events than that expected in the signal region. The $Z \rightarrow \tau\tau$ normalization is over 10 standard deviations away from 1 (considering only statistical uncertainties). The deviation may come from the exotic phase space used in the signal region since the tau trigger requires the leading- p_T jet to pass a 70 GeV threshold. This is related to the fact that the crux of the theoretical production for the QCD $Z \rightarrow \tau\tau$ +jets background lies in the rate of jet production associated with a Z boson, which impacts the kinematic variables. The deviation may also suggest that the $\tau_{\text{had, vis}}$ ID scale factors need to be re-evaluated.

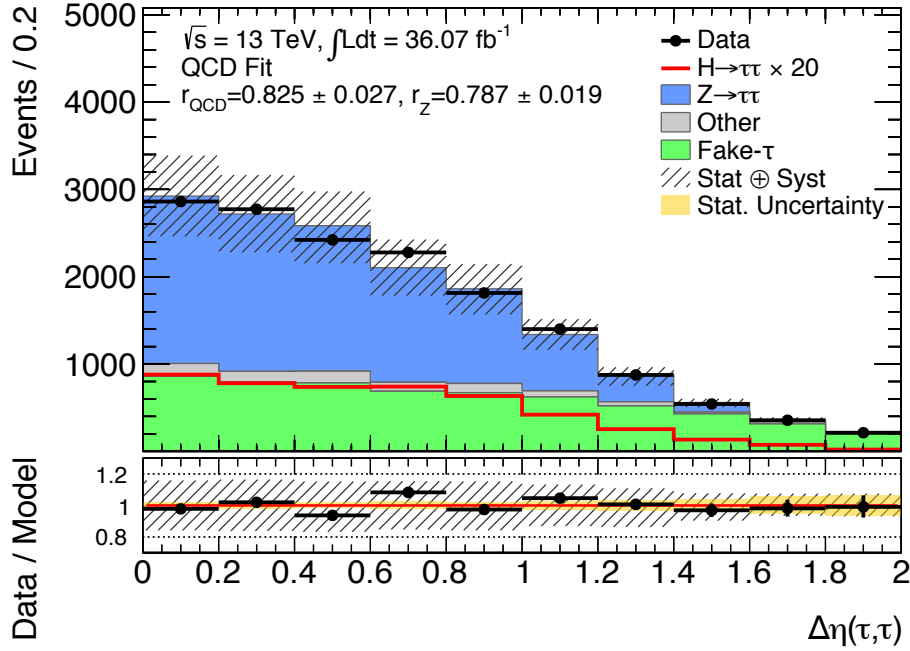


Figure 5.18: Fit to $\Delta\eta(\tau,\tau)$ in OS data to determine fake- τ and $Z \rightarrow \tau\tau$ background normalization factors. Systematic uncertainties include all systematic uncertainties except those related to the fake- τ background estimation.

Fit parameter	Value	Uncertainty
r_{QCD}	0.811	0.0303
r_Z	0.802	0.0189

Table 5.8: Normalization factors after the prefit background estimation (see Figure 5.18).

5.7.2.2 Background model validation

The background model is validated at the preselection level and in the signal categories with the data in the $100 < m_{\text{MMC}}^{\tau\tau} < 150$ GeV region blinded. At this level, the preselection region is signal-like but has a small percentage of $H \rightarrow \tau\tau$ events (less than 1%). The r_{QCD} and r_Z factors are defined such that the expected total yield of background events is equal to the total yield in data. Figure 5.19 shows the background validation for important variables, e.g., those used for the signal categorization. Further validation figures are shown in Appendix H. The next section describes the systematic uncertainties on the OS-nOS background estimate method. The slight mismodeling in some of the observables in Figure 5.19 are discussed in Section 5.7.2.4.

5.7.2.3 Systematic uncertainties for the OS-nOS background estimation

Uncertainties on the OS-nOS technique arise due to the following assumptions made in the method:

- The $m_{\text{MMC}}^{\tau\tau}$ shape of the fake- τ background contribution is the same in the nOS control

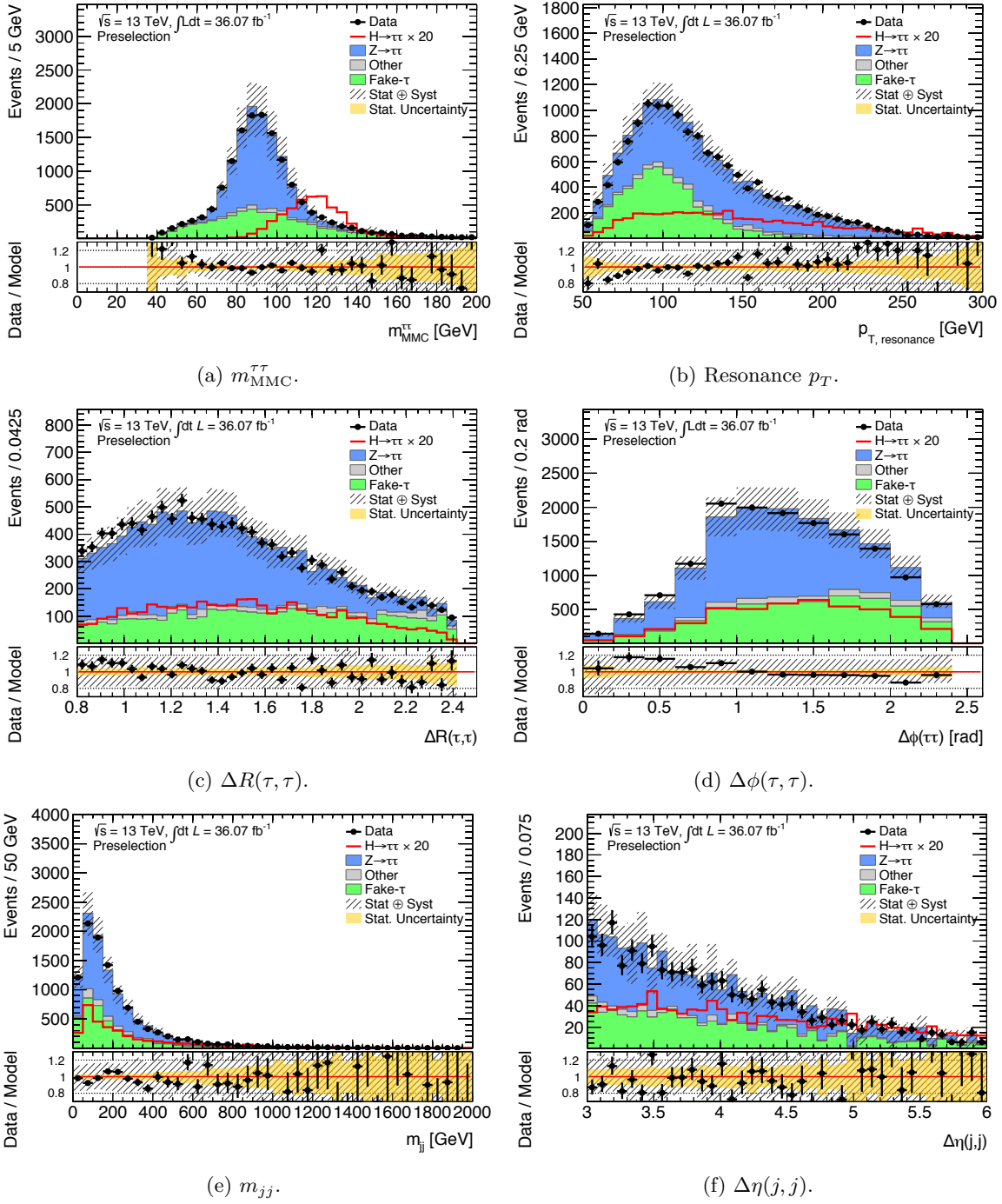


Figure 5.19: Validation of the OS-nOS background modeling. The systematic uncertainties include all uncertainties described later in Section 5.8 except for those concerning the fake- τ background estimation.

region and the OS signal regions.

- The subtraction of real- τ background contamination from the nOS control region is correct.
- The r_{QCD} and r_Z normalization factors determined at the preselection level can be used

in the VBF and Boosted categories.

- Scale factors that have been derived for three-prong τ_{had} candidates are applied on two-prong τ_{had} candidates.

Uncertainties arise from the usage of the nOS control region to model the fake- τ background in the OS region because of the potential differences concerning the QCD processes in the nOS region compared to the OS one. The nOS region is expected to contain more events with gluon-initiated jets while the OS should have more quark-initiated jets. This is because the quark charge is correlated with the reconstructed charge of the τ_{had} candidate. In addition, quarks have a different color charge than gluons. They produce narrower jets and are more likely to be reconstructed as τ_{had} candidates. Gluon-initiated jets, on the other hand, are more likely to be rejected by the $\tau_{\text{had, vis}}$ ID algorithm [145].

An uncertainty on the shape of the nOS fake- τ background template can be defined by performing a comparison of the nOS template in a control region that is orthogonal to the signal region. Shape uncertainties address bin-by-bin uncertainties and therefore prescribe a ± 1 standard deviation (σ) band on the nominal template. (Event yield uncertainties prescribe a $\pm 1\sigma$ with respect to the nominal event yield without changing the template.)

The ratio between the $m_{\text{MMC}}^{\tau\tau}$ distributions in control regions is used to define this nOS-OS extrapolation shape systematic uncertainty. There are several possible control regions for this shape systematic uncertainty. In this analysis, the ratio between the OS and nOS $m_{\text{MMC}}^{\tau\tau}$ distributions in the anti- $\tau_{\text{had, vis}}$ ID region is used. The motivation is that differences between the nOS and OS anti- $\tau_{\text{had, vis}}$ ID regions cover the differences between the nOS region and OS signal region, especially since the former regions are biased by requiring events to pass the tau trigger. The anti- $\tau_{\text{had, vis}}$ ID region can be defined to be as loose as possible, as defined in Table 5.9. This yields a statistically powerful region, but the tradeoff is that there are fewer signal-like τ_{had} candidates. Figure 5.20 shows the OS/nOS ratios at the different levels of anti- $\tau_{\text{had, vis}}$ ID listed in Table 5.9. The ratios are compatible with the statistical uncertainties, but results presented later in Section 5.7.2.6 show that the loosest anti- $\tau_{\text{had, vis}}$ ID region is not similar enough to the signal region. When using the tight anti- $\tau_{\text{had, vis}}$ ID region, there is a background contribution seen at the low $m_{\text{MMC}}^{\tau\tau}$ region that is not present in the loosest anti- $\tau_{\text{had, vis}}$ ID region. Therefore, the extrapolation systematic uses the tight anti- $\tau_{\text{had, vis}}$ ID region.

This nOS-OS extrapolation shape comparison is an improvement to the systematic uncertainty used in [128], where the ratio between the $m_{\text{MMC}}^{\tau\tau}$ distributions in the nOS and the SS control regions was used. The motivation was that it is a good estimate for the difference in the quark-gluon fraction since the nOS region has more gluon-initiated jets than the SS region. The caveat of this estimate is that it assumes that the differences between the nOS and SS regions cover the differences between the nOS and OS regions.

For each VBF category, the extrapolation shape systematic uncertainty is extracted from the inclusive VBF region due to the limited sample size. For each Boosted category, the extrapolation systematic uncertainty is extracted from the respective boosted category. The new extrapolation systematic assumes that the $\tau_{\text{had, vis}}$ ID is not correlated with charge requirement. This is verified in Figure 5.20, where the shape comparisons are performed at different anti- $\tau_{\text{had, vis}}$ ID levels. It shows that the ratios are consistent at the different anti- $\tau_{\text{had, vis}}$ ID levels.

In addition to the fake- τ extrapolation systematic uncertainty, a fake- τ contamination systematic uncertainty is defined for the potential uncertainties in the real- τ background subtraction from the nOS control region. This is also a shape systematic uncertainty and is evaluated by

Anti- $\tau_{\text{had, vis}}$ ID region	Selection
Tight	The leading p_T τ_{had} candidate passes the tight $\tau_{\text{had, vis}}$ ID working point and the subleading p_T τ_{had} candidate passes the medium $\tau_{\text{had, vis}}$ ID working point.
Medium	Exactly 1 τ_{had} candidate passes the tight $\tau_{\text{had, vis}}$ ID working point and both τ_{had} candidates pass the medium $\tau_{\text{had, vis}}$ ID working point.
Loose	Exactly 1 τ_{had} candidate passes the tight $\tau_{\text{had, vis}}$ ID working point and ≥ 1 τ_{had} candidates pass the medium $\tau_{\text{had, vis}}$ ID working point.
Loosest	Exactly 1 τ_{had} candidate passes the tight $\tau_{\text{had, vis}}$ ID working point and ≥ 1 τ_{had} candidates pass the loose $\tau_{\text{had, vis}}$ ID working point.

Table 5.9: The anti- $\tau_{\text{had, vis}}$ ID levels where at least one τ_{had} candidate is required to fail the tight $\tau_{\text{had, vis}}$ ID working point.

varying the real- τ contamination in the nOS control region by 1σ of the statistical uncertainty (see Figure 5.17 for the 1σ statistical uncertainty on the real- τ contamination). For each VBF category, the contamination shape systematic uncertainty is extracted from the inclusive VBF region due to limited statistics. For each Boosted category, the contamination systematic uncertainty is respected from the respective boosted category:

To address the fact that one r_{QCD} normalization factor is used for the fake- τ background in all categories, the expected results of the final fit are compared between an r_{QCD} from preselection and a separate r_{QCD} for the inclusive Boost and VBF categories. The validation shows that the expected signal sensitivity is not significantly impacted by the use of separate r_{QCD} factors. Therefore, one r_{QCD} normalization factor is used in the final fit, since this improves the fit stability.

5.7.2.4 Shortcomings of the OS-nOS background estimate

The OS-nOS method presented in the previous sections requires a certain configuration to model the data in the signal region well: the use of the nOS control region as opposed to the SS control region, a $\tau_{\text{had, vis}}$ ID working point stipulating that both τ_{had} candidates pass the tight requirement, and a floating r_Z normalization. The motivation as to why this particular configuration models the data better than another configuration suggests that the OS-nOS method has shortcomings.

For example, when using a looser $\tau_{\text{had, vis}}$ ID working point requiring at least one tight τ_{had} candidate instead of two, there is a significant underestimation of data in the low $m_{\text{MMC}}^{\tau\tau}$ region of $m_{\text{MMC}}^{\tau\tau} < 60$ GeV (see Figure 5.21(a)).¹⁰ Minimizing the fake- τ background contribution with a tighter $\tau_{\text{had, vis}}$ ID working point minimizes its impact on the mismodeling. In addition, when fixing the $Z \rightarrow \tau\tau$ normalization to the MC prediction instead of allowing it to float at the prefit level, there is a similar underestimation of data at the low $m_{\text{MMC}}^{\tau\tau}$ region (see Figure 5.21(b)). It raises the question of why the r_Z normalization factor needs to be scaled down by about 20% from the MC prediction. The mismodeling is also seen in the visible mass distribution, which

¹⁰ The difference in the signal sensitivity between the two signal region criteria is minimal.

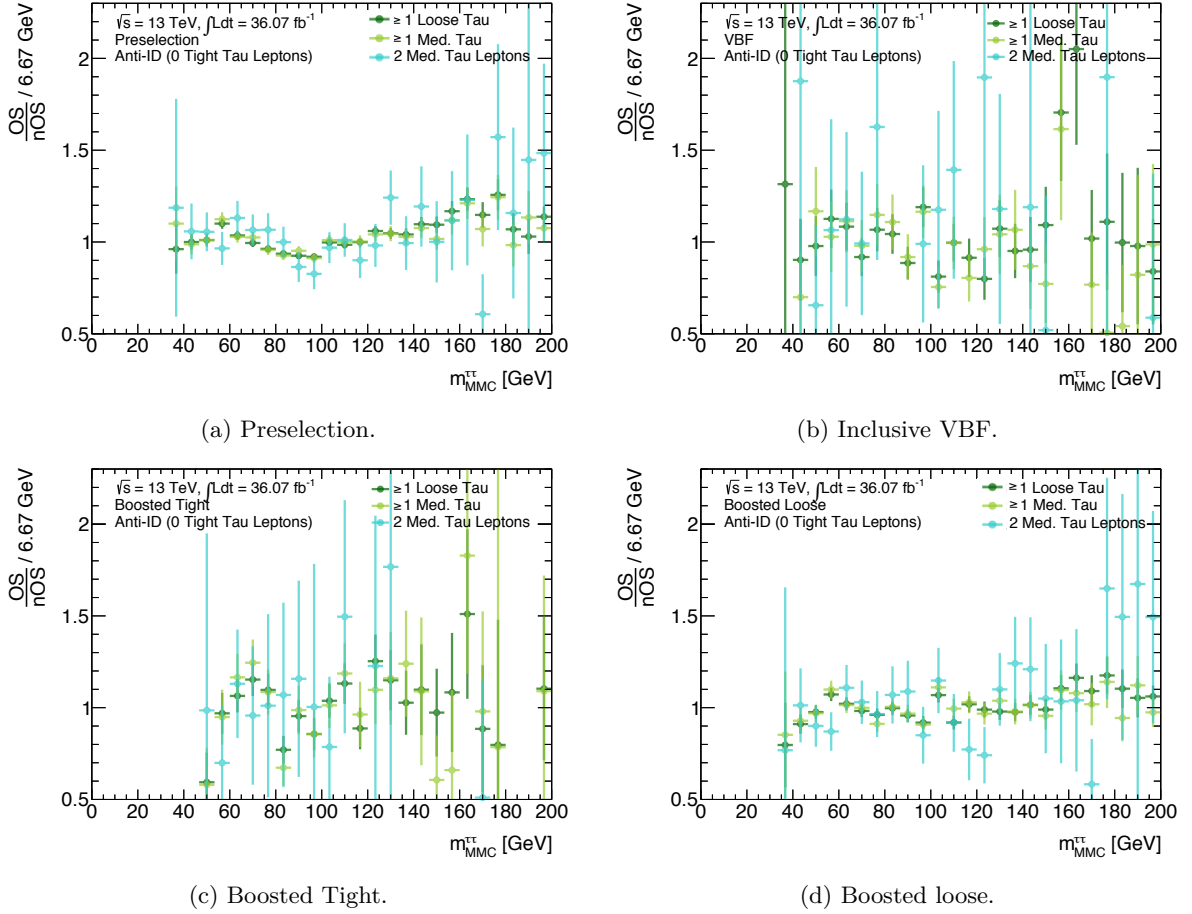


Figure 5.20: Comparison of the OS and nOS templates in the anti- $\tau_{\text{had, vis}}$ ID region at different $\tau_{\text{had, vis}}$ ID working points.

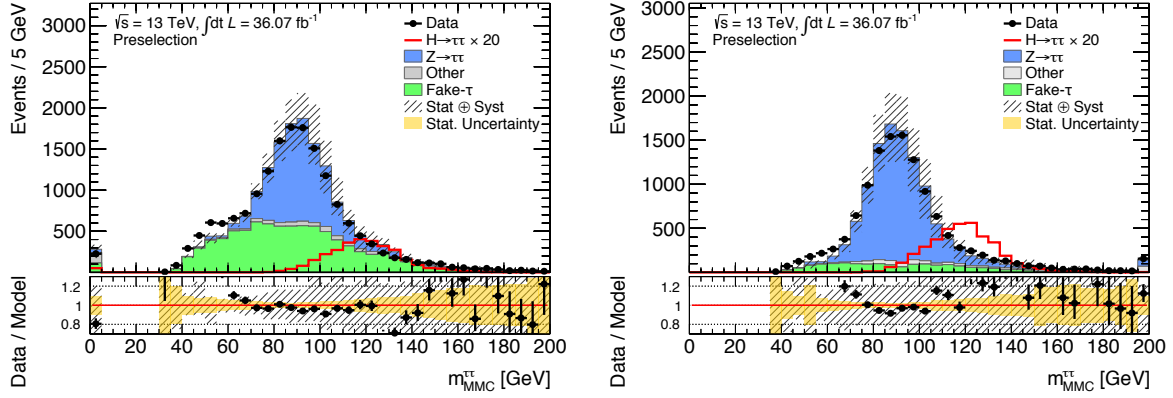
suggests that the origin of the problem does not come from the MMC algorithm. In studies performed in work of this dissertation, the mismodeling also does not show a dependence on pileup, number τ_{had} tracks, or π^0 multiplicity.

It is not feasible to simply remove the low $m_{\text{MMC}}^{\tau\tau}$ region since the constraint on the fake- τ background normalization in the final fit comes mainly from the low $m_{\text{MMC}}^{\tau\tau}$ region. In addition, a mismodeling shows a clear problem in the analysis that should be understood and not avoided. For example, with the background model configuration presented in the previous sections, background model validation in Figure 5.19 shows a mis-modeling of other important observables. The $\Delta R(\tau, \tau)$ distribution is underestimated in the low ΔR region, arising from an underestimation of the $\Delta\phi(\tau, \tau)$ observable in the low $\Delta\phi$ region. Although the mismodeling is covered by the combined statistical and systematic uncertainties, it is particularly problematic for the event categorization, which uses $\Delta R(\tau, \tau)$ to select the final signal categories.

To address this, a background model using the OS anti- $\tau_{\text{had, vis}}$ ID control region, called the matrix method, is developed, which fixes the low $m_{\text{MMC}}^{\tau\tau}$ deficit. One of the motivations for the use of the OS anti- $\tau_{\text{had, vis}}$ ID control region is the fact that there is clearly a process in the OS region that is not in the nOS preselection region. When correcting the nOS template with the fake- τ extrapolation region from the anti- $\tau_{\text{had, vis}}$ ID region though, the fake- τ extrapolation

ratio scales the low $m_{\text{MMC}}^{\tau\tau}$ shoulder higher.

This method is described later in Section 5.7.2.6. First, a projection study described in Section 5.7.2.5 is performed to quantify the gain in signal sensitivity from using the anti- $\tau_{\text{had, vis}}$ ID region.



(a) Background estimation requiring ≥ 1 τ_{had} candidate passing the tight $\tau_{\text{had, vis}}$ ID working point instead of 2.

(b) Background estimation with r_Z fixed.

Figure 5.21: Different configurations of the background model revealing an underestimate of the low $m_{\text{MMC}}^{\tau\tau}$ region. Shown on the left is the preselection region requiring at least one tight τ_{had} candidate while allowing the other τ_{had} candidate to at least pass the medium working point (instead of two tight τ_{had} candidates). Shown on the right is the background model requiring two tight τ_{had} candidates where the normalization of the $Z \rightarrow \tau\tau$ background is fixed to that predicted by simulation, i.e., $r_Z = 1.0$.

5.7.2.5 Improving the background estimate with fake factors

Since a systematic bias is expected in the OS-nOS method, an alternative method is presented in the following section. Based on the fake- τ extrapolation shape systematic uncertainties, it can be seen that scaling the nOS shape by the OS/nOS ratio from the anti- $\tau_{\text{had, vis}}$ ID control region increases the low $m_{\text{MMC}}^{\tau\tau}$ shoulder. It suggests that there is a process in the OS region that is not present in the nOS region. Therefore, this alternative method utilizes the OS anti- $\tau_{\text{had, vis}}$ ID control region instead of the nOS control region. Before pursuing this method, however, it is important to first investigate whether such a method is worth investigating and what the possible gains are besides the correction of the mismodeling in a few bins of the $m_{\text{MMC}}^{\tau\tau}$ distribution. This can be quantified with a projection of the reduction in uncertainties by using the anti- $\tau_{\text{had, vis}}$ ID control region compared to the nOS control region.

The uncertainty on the nOS template used in the OS-nOS fake- τ background estimation comes from the combined statistical and systematic uncertainties,

$$\sigma_{\text{total}} = \sqrt{\sigma_{\text{stat}}^2 + \sigma_{\text{sys}}^2}, \quad (5.12)$$

where, for the purposes of this study, the statistical and systematic uncertainties are assumed to be uncorrelated.¹¹

¹¹ This assumption is not fully accurate since the systematic uncertainty bands on the fake- τ template are taken

It is possible to reduce the impact from the statistical uncertainty on the total uncertainty by moving to a method using fake factors, where the sample size is increased by using a larger control region from the anti- $\tau_{\text{had, vis}}$ ID region. In this method, fake factors are used to extrapolate a fake-enriched control region in data to the signal region. In Run-II the τ_{had} trigger was loosened (compared to the Run-I trigger) to be able to define a statistically powerful anti- $\tau_{\text{had, vis}}$ ID region. Table 5.10 shows the relative sizes of the control regions used in the OS-nOS and fake factor methods. It shows that the loosest anti-ID OS region can be over three times more statistically powerful than the nOS region.

Anti- $\tau_{\text{had, vis}}$ ID region	Preselection	Inclusive VBF	Inclusive Boosted
Two τ_{had} candidates pass medium $\tau_{\text{had, vis}}$ ID	2.37 ± 0.0581	1.97 ± 0.0244	2.30 ± 0.00838
≥ 1 τ_{had} candidate pass medium $\tau_{\text{had, vis}}$ ID	2.87 ± 0.0221	2.84 ± 0.0111	2.75 ± 0.00324
≥ 1 τ_{had} candidate pass loose $\tau_{\text{had, vis}}$ ID	3.07 ± 0.0343	2.82 ± 0.0164	2.92 ± 0.00514
Two τ_{had} candidates pass loose $\tau_{\text{had, vis}}$ ID	3.26 ± 0.0180	3.29 ± 0.0957	3.14 ± 0.00273

Table 5.10: Relative size of the fake- τ background in the nOS control region compared to the OS region ($n_{\text{nOS}}/n_{\text{OS}}$) in the anti- $\tau_{\text{had, vis}}$ ID region: no τ_{had} candidates passing the tight $\tau_{\text{had, vis}}$ ID working point, keeping all other preselection (left), inclusive VBF (middle), or inclusive Boosted (right) criteria the same.

Knowing the decrease in the statistical uncertainty by using a fake factor method and the performance of the OS-nOS method, it is possible to predict the largest possible increase in systematic uncertainty from the fake factor method in order to perform at least as well as the OS-nOS strategy. This study uses results and methods from the fit model that are later described in Section 5.9. For the purposes of this section, the postfit μ (where μ was previously defined in Equation 5.1) and its uncertainty refer to the signal strength and its respective uncertainty fitted in the statistical interpretation when all statistical and systematic uncertainties are taken into account, as is detailed in Section 5.9. Table 5.11 shows the postfit μ and its statistical and systematic uncertainties on the OS-nOS method when the statistical and/or systematic uncertainties from the fake- τ background are turned on/off. It shows that a fake factor method can have as much as 25% larger systematic uncertainties than the OS-nOS method and still achieve similar performance (c.f. the systematic uncertainty of 0.164 compared to 0.130 in Table 5.11).

5.7.2.6 Matrix method background estimate

Having estimated the gain in sensitivity that can be achieved by using the anti- $\tau_{\text{had, vis}}$ ID region in a fake factor style method, this section describes the matrix method background estimation that uses the anti- $\tau_{\text{had, vis}}$ ID region. As previously mentioned, a fake factor method extrapolates a fake-enriched control region in data to the signal region. The extrapolation is performed in the so-called matrix method, or MM.

from control regions of limited size. However, performing the final fit with the statistical and/or systematic uncertainties on the fake- τ background turned on and off and calculating the impact from the uncertainties by adding the statistical and systematic impact separately yields an impact similar (on the order of $\frac{1}{100}$) to subtracting separately the difference in quadrature between the fit with and without both the statistical and systematic uncertainties.

Uncertainties from fake- τ background		Postfit μ	Uncertainty
Systematic uncertainties	Statistical uncertainties		
On	Off	1.00	0.439
Off	On	1.00	0.437
On	On	1.00	0.456
Off	Off	1.00	0.418
Impact from statistical uncertainties in the OS-nOS method			0.124
Impact from systematic uncertainties in the OS-nOS method			0.130
Impact from (stat. \oplus sys.) uncertainties in the OS-nOS method			0.179
Predicted stat. impact by using the anti- $\tau_{\text{had, vis}}$ ID region			0.0713
Maximum sys. impact to achieve same performance using the anti- $\tau_{\text{had, vis}}$ ID region			0.164

Table 5.11: Projection of the maximum possible impact from fake factors to achieve the same performance as the OS-nOS method. The postfit μ (c.f. Equation 5.1) and its uncertainty refer to the signal strength and its respective uncertainty fitted in the statistical interpretation, as detailed in Section 5.9. The impact from the statistical and/or systematic uncertainties are calculated using Equation 5.12, and the predicted statistical impact by using the anti- $\tau_{\text{had, vis}}$ ID region is determined by scaling the OS-nOS statistical impact down by \sqrt{n} , where n is the maximum possible increase in the number of events shown in Table 5.10.

The MM uses two levels of event selection: loose and tight (a subset of loose).¹² The loose criteria select the anti-ID control region that is transferred to the signal region to model the fake- τ background. The tight selection corresponds to the same selection used for the signal region. The two regions can be related to determine the background from fake di-tau events that is expected to be found in the signal region. The unknown fake- τ template in the signal region can be solved with the following equation:

$$\begin{pmatrix} N_{\text{Tight}} \\ N_{\text{Loose}} \end{pmatrix} = \begin{pmatrix} e & f \\ 1 & 1 \end{pmatrix} \begin{pmatrix} N_{\text{Real}} \\ N_{\text{Fake}} \end{pmatrix}, \quad (5.13)$$

where

- N_{Loose} refers to events passing the loose selection. In this case, the loose selection requires the leading p_T τ_{had} candidate to pass the tight $\tau_{\text{had, vis}}$ ID and the sub-leading τ_{had} candidate to pass the medium $\tau_{\text{had, vis}}$ ID (see Table 5.9). This particular anti- $\tau_{\text{had, vis}}$ ID region is used because the use of looser anti- $\tau_{\text{had, vis}}$ ID regions results in a mismodeling of the low $m_{\text{MMC}}^{\tau\tau}$ region. All other signal region selection criteria remain the same.
- N_{Tight} is a subset of N_{Loose} and refers to events passing the tight selection. In this case, the tight selection requires two tight τ_{had} candidates to pass the tight tau identification, keeping all other signal region selection criteria the same.
- N_{Real} refers to events passing the loose criteria with two real τ_{had} candidates.

¹² The matrix method can be applied to cases with mixtures of backgrounds. In the $\tau_{\text{had}}\tau_{\text{had}}$ case a 2-D matrix is used since the fake- τ background consists almost purely of QCD multijet. If there were an admixture of processes contributing to the fake- τ background, such as in the $\tau_{\text{lep}}\tau_{\text{had}}$ channel with a mixture of W +jets and multijet, a 4-D matrix would be better.

- N_{Fake} refers to events passing the loose criteria with two fake τ_{had} candidates.
- Efficiency, e , is the signal efficiency, defined as the fraction of events with two real tau leptons passing the tight selection over those that pass the loose selection.
- Misidentification probability, f , is the fraction of events with two fake τ_{had} candidates passing the tight selection over those that pass the loose selection.

Since the efficiency and misidentification probability can be measured experimentally, the unknown fake- τ shape and normalization can be solved as the events containing two fake τ_{had} candidates in the tight region:

$$f \cdot N_{\text{Fake}} = \frac{f}{e - f} (eN_{\text{Loose}} - N_{\text{Tight}}). \quad (5.14)$$

The efficiency is measured in the $Z \rightarrow \tau\tau$ simulated sample as

$$e = \frac{n_{\text{Tight}}^{Z \rightarrow \tau\tau}}{n_{\text{Medium}}^{Z \rightarrow \tau\tau}}. \quad (5.15)$$

The misidentification probability is determined from a control region. In this analysis, the SS control region in data is used:

$$f = \frac{n_{\text{Tight}}^{\text{Same-Sign Data}}}{n_{\text{Medium}}^{\text{Same-Sign Data}}} \quad (5.16)$$

This assumes that the efficiencies are similar throughout the whole signal region. Here, a misidentification probability is used instead of a fake factor to ensure correct use of the tau ID scale factors. The tau ID scale factors should be applied to events that pass a minimum selection and not to events required to fail a certain $\tau_{\text{had, vis}}$ ID working point.

This MM so far assumes that the misidentification probabilities are independent of event kinematics. To address this, the method can be separated, or binned, based on, e.g., the number of tracks. Table 5.12 shows the misidentification probability depending on the number of tracks, and Figure 5.22 shows the $m_{\text{MMC}}^{\tau\tau}$ distribution where the templates are further separated by the number of τ_{had} tracks. Since there is no strong improvement in the modeling performance, inclusive misidentification probabilities and efficiencies are used.

Control Region	Misidentification Probability	Efficiency	r_Z
Inclusive	$0.555^{+0.00841}_{-0.00843}$	$0.864^{+0.00309}_{-0.00313}$	0.773 ± 0.0135
τ_1 1p	$0.581^{+0.00804}_{-0.00807}$	$0.883^{+0.00344}_{-0.00350}$	0.746 ± 0.0105
τ_1 3p	$0.475^{+0.0155}_{-0.0155}$	$0.784^{+0.00801}_{-0.00812}$	

Table 5.12: Misidentification probabilities and efficiencies in the matrix method using a loose tau region where the leading- p_T tau passes tight and the subleading- p_T tau passes medium. The uncertainties on the misidentification probabilities and efficiencies take into account the fact that they are not calculated from statistically independent regions.

There are several advantages of the MM compared to the OS-nOS method:

- In the MM, the normalization of the fake- τ background does not have to be fitted.

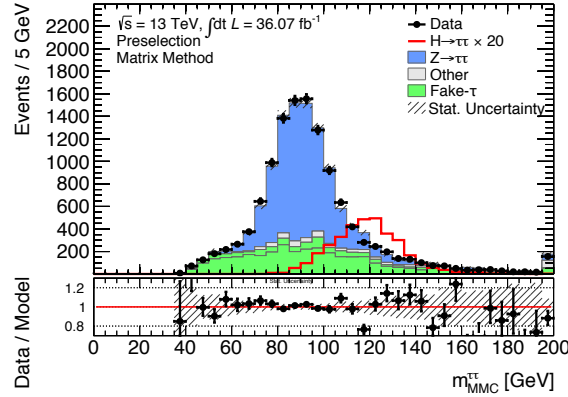


Figure 5.22: The $m_{\text{MMC}}^{\tau\tau}$ observable using the matrix method with fake- τ templates selected based on the number of τ_{had} tracks.

- The only reliance on simulation comes from the calculation of the efficiency.
- The shapes for the tight and loose templates are taken from OS data, and there is no subtraction of real- τ contamination from these templates.
- There is a weaker dependence on the SS control region since the MM uses only one number from the region (the misidentification probability) as opposed to extracting the $m_{\text{MMC}}^{\tau\tau}$ shape from the nOS control region in the OS-nOS method.

To take care of the $Z \rightarrow \tau\tau$ normalization and the possible problems with MC scale factors, the $Z \rightarrow \tau\tau$ normalization is also floated in this MM, as it is in the OS-nOS method. Figure 5.26 shows a comparison of the fake- τ background templates from the OS-nOS method and the MM. The MM shows a better agreement with data, in particular, for the ΔR and $\Delta\phi$ distributions. It reduces the low ΔR and $\Delta\phi$ disagreement from about 20% to about 10% (c.f. Figures 5.19(d) and 5.23(b)).

5.7.2.7 Systematic uncertainties on the matrix method background estimation

Systematic uncertainties on the MM arise due to the following assumptions:

- The efficiency is measured from a finite simulated $Z \rightarrow \tau\tau$ sample, which is corrected by $\tau_{\text{had, vis}}$ ID scale factors.
- The MM assumes that the misidentification probability is universal for all jets. However, the misidentification probability is measured in SS data, which has a different q/g composition than the OS data.

For the efficiency, two systematic uncertainties are assigned for the statistical and systematic uncertainties. The event yields in the tight and loose regions are varied by ± 1 standard deviation of their statistical uncertainties for the uncertainty on the $Z \rightarrow \tau\tau$ efficiency, henceforth referred to as the MM $Z \rightarrow \tau\tau$ efficiency stat. unc. For the systematic shape uncertainty on the efficiency, henceforth referred to as the MM $Z \rightarrow \tau\tau$ efficiency sys. unc., the $\tau_{\text{had, vis}}$ ID scale factors are varied by $\pm 1\sigma$. One advantage of using a misidentification probability instead of a fake

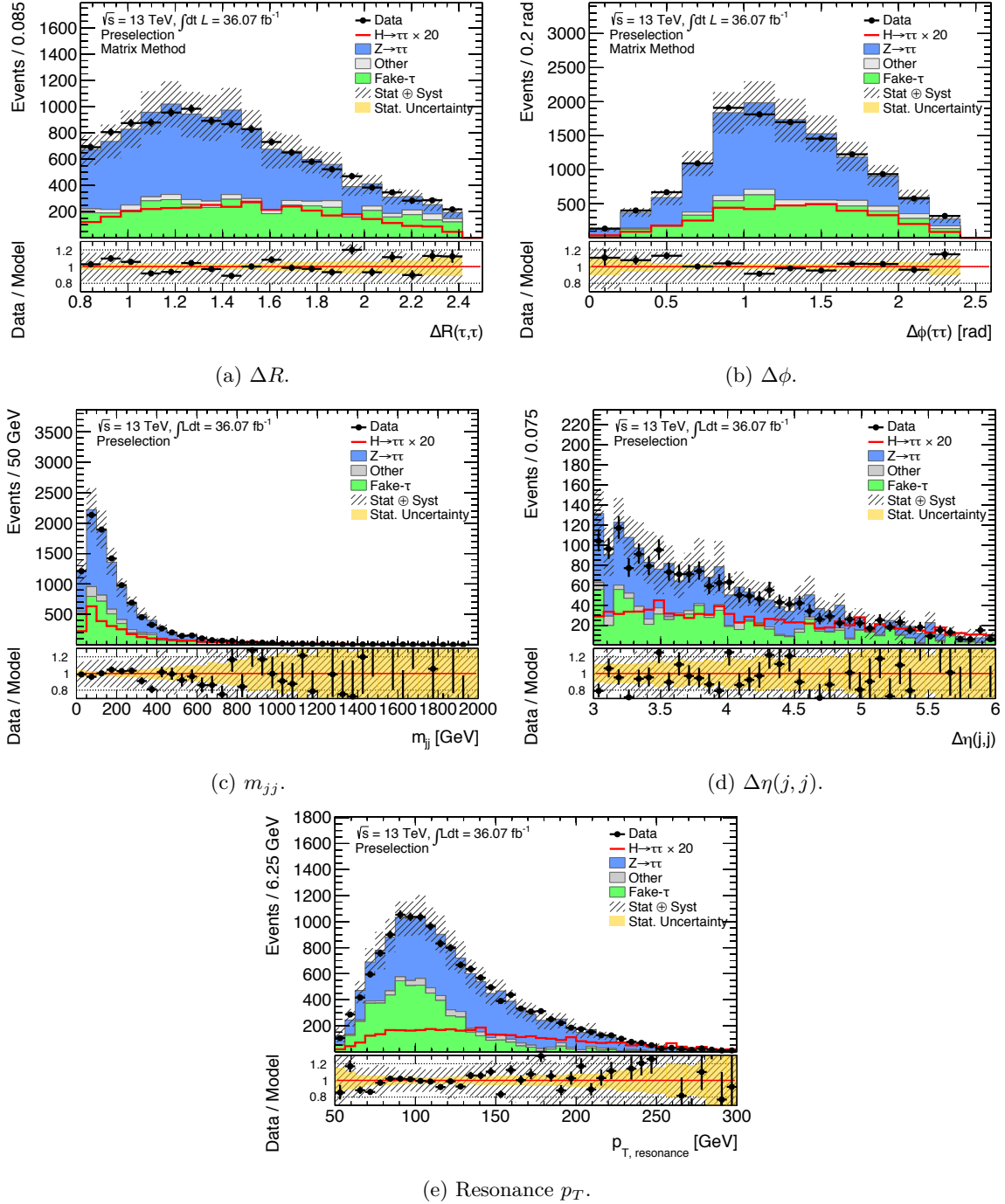


Figure 5.23: Matrix method background modeling. The systematic uncertainties include all uncertainties described later in Section 5.8 except for those concerning the fake- τ background estimation.

factor in the matrix method is that the $\tau_{\text{had, vis}}$ ID scale factors partially cancel out in the loose-to-tight efficiency ratio. However, this also means that varying the scale factors by $\pm 1\sigma$ can yield an underestimated systematic uncertainty. (One way to address this would be to include the numerator (tight) and denominator (loose) values separately with an anti-correlated

factor in the fit.) The statistical uncertainty addressing the measurement of the efficiency from a $Z \rightarrow \tau\tau$ sample of limited size is also taken into account by varying the total number of $Z \rightarrow \tau\tau$ events in the loose and tight regions by $\pm 1\sigma$ of their statistical uncertainty. Figure 5.24 shows variations in the systematic and statistical uncertainties and that the efficiency is statistically dominated (shown as an example for the high-statistics Boosted Loose category). The variation in the event yield from each efficiency systematic uncertainty is shown in Table 5.13.

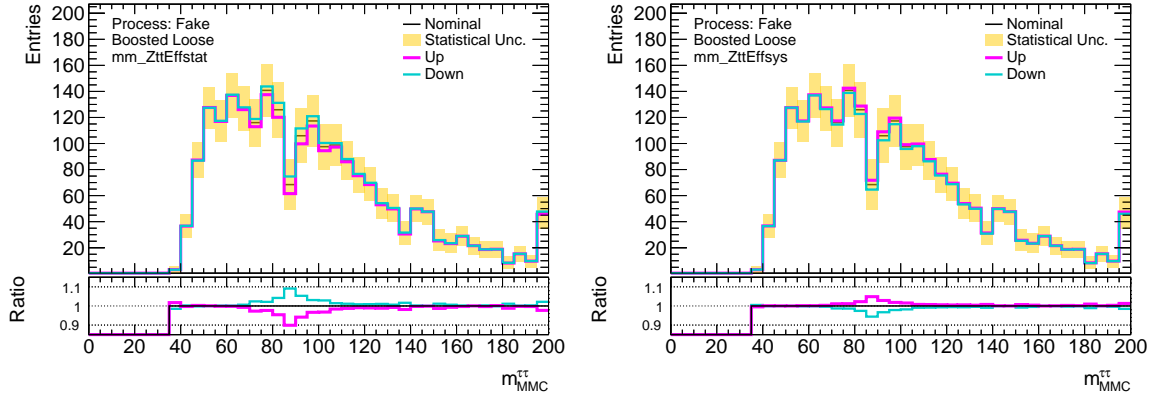


Figure 5.24: Statistical (left) and systematic (right) uncertainties on the $Z \rightarrow \tau\tau$ efficiency. The red (blue) lines show the up (down) systematic uncertainties, and the shaded yellow bands show the systematic uncertainties.

The systematic uncertainties on the misidentification probability, henceforth referred to as the MM W control region stat./sys. unc., address the differences between the SS data from which the misidentification probability is measured and the OS data to which the misidentification probability is applied.¹³ The misidentification probability depends on the q/g jet composition. The heavy flavor content also affects the misidentification probability since the $\tau_{\text{had, vis}}$ ID classifies jets from heavy and light quarks differently. Heavy flavor jets, for example, contain particles with longer lifetimes, and this affects the track-based variables of the $\tau_{\text{had, vis}}$ ID. The particle multiplicity is also higher for heavy flavor quarks.

Therefore, misidentification probabilities from a more quark-like $W + \text{jets}$ control region are measured to account for the fact that the OS region is more quark-like than the SS region. The $W + \text{jets}$ region from the $H \rightarrow \tau_{\text{lep}}\tau_{\text{had}}$ channel is used since it is statistically powerful. The MM W control region stat. unc. addresses the statistical uncertainty arising from the finite sample size of the $W + \text{jets}$ region, while the MM W control region sys. unc. addresses the difference in the misidentification probability between the $W + \text{jets}$ and the SS region. The same τ_{had} selection is used for the τ_{had} candidate. For the trigger, however, the tau+lepton trigger (TLT) is applied instead of the single tau trigger since the latter is heavily prescaled. That is, due to the high event rate, prescaled triggers allow only a certain percentage of events by randomly allowing events to pass the trigger. Figure 5.25 shows systematic uncertainties from the $W + \text{jet}$ misidentification probability with the TLT. The percentage variation is shown in Table 5.13. Since the trigger used for the misidentification probability systematic uncertainties is different, the estimated systematic band is extremely large and should be constrained in the final fit.

¹³ One advantage of measuring the misidentification probability from a control region in data instead of from simulation is that the misidentification probability will not depend on the details of jet fragmentation and the underlying event model.

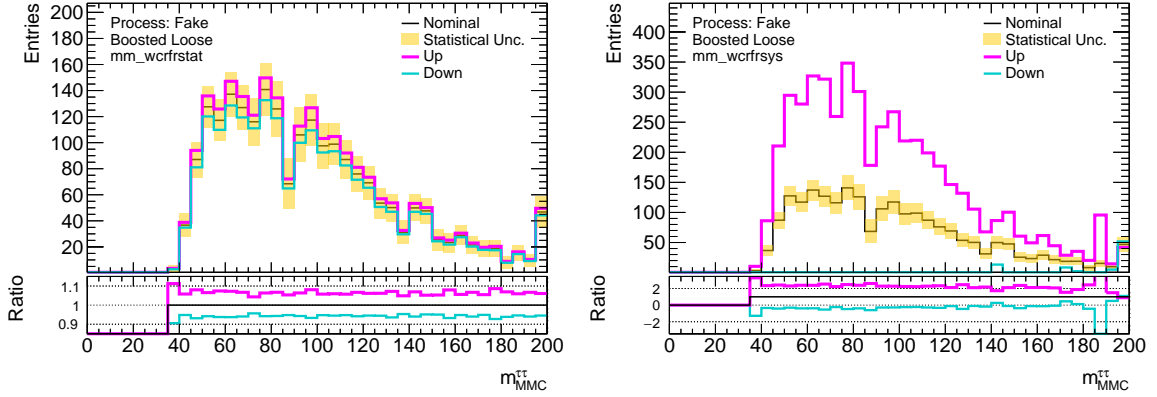


Figure 5.25: Statistical (left) and systematic (right) uncertainties on the misidentification probability. The bottom ratio plots for the statistical (left) and systematic (right) uncertainties show different ranges due to the large differences in variation.

	Boosted		VBF							
			High ΔR				Low ΔR			
	Tight	Loose	Tight	Loose	Loose	Loose	-1 σ	+1 σ		
	-1 σ	+1 σ	-1 σ	+1 σ	-1 σ	+1 σ	-1 σ	+1 σ	-1 σ	+1 σ
MM $Z \rightarrow \tau\tau$ efficiency stat. unc.	-0.97	0.9	-0.58	0.54	0.0	0.0	-0.61	0.57	-0.57	0.55
MM $Z \rightarrow \tau\tau$ efficiency sys. unc.	-0.69	0.6	-0.42	0.37	0.0	0.0	0.0	0.0	-0.39	0.34
MM W control region stat. unc.	-0.42	0.45	-1.73	1.88	-2.39	2.6	-1.56	1.62	-0.85	0.93
MM W control region sys. unc.	-1.55	1.55	-13.54	13.54	-31.44	31.44	-7.72	7.72	-0.58	1.03

Table 5.13: Relative impact of the matrix method systematic uncertainties compared to the total number of fake- τ background events at the prefit level (%).

5.8 Systematic Uncertainties

With the background estimation method described, the following section now discusses systematic uncertainties arising from the experimental methods used, in addition to those from the background modeling described in the previous section. They are used in the final fit validation, where the performance of the OS-nOS and matrix method background estimate methods are compared.

The prescription of systematic uncertainties is analysis-specific and addresses assumptions and possible mis-measurements made in estimating the expected templates and event yields. The systematic uncertainties prescribed are either shape or event yield uncertainties (previously defined in Section 5.7.2.3). They are included in the final fit as nuisance parameters (NPs), as detailed in Section 5.9. These uncertainties are separate from the statistical uncertainties arising from the finite number of expected events in each histogram bin. A complete list of systematic uncertainties can be found in Appendix I, and an example for the boosted loose category is shown in Table 5.14.

5.8.1 Experimental uncertainties

The experimental uncertainties are grouped into the following categories:

Nuisance Parameter	Signal		Background	
	+1 σ	-1 σ	+1 σ	-1 σ
BR($H \rightarrow \tau\tau$)	5.7	-5.7	0.00	0.00
Forward JVT	0.2	-0.2	0.00	0.00
JER	-0.3	0.3	0.04	-0.04
JES (Effective NP 1)	0.8	-2.54	1.8	-1.7
JES (Effective NP 2)	1.95	-1.73	0.58	-0.13
JES (Effective NP 3)	-0.04	0.59	0.00	0.00
JES (Effective NP 4)	0.45	0.08	0.00	0.00
JES (Effective NP 5)	0.54	0.00	0.28	-0.35
JES (Effective NP 6)	0.54	0.00	0.08	-0.16
JES (Inter- $ \eta $ Calibration, Model)	0.73	-1.57	0.56	-0.39
JES (Inter- $ \eta $ Calibration, Nonclosure)	0.00	0.00	0.00	0.00
JES (Inter- $ \eta $ Calibration, Stat.)	-0.07	-0.07	0.28	-0.37
JES (Flavor composition)	1.94	-4.38	1.84	-1.91
JES (Flavor response)	-1.75	1.68	-0.71	1.38
JES (PU Offset μ)	0.1	-0.04	0.32	-0.26
JES (PU Offset NPV)	0.87	-0.93	0.18	-0.18
JES (PU p_T term)	0.54	-0.01	0.51	-0.51
JES (PU ρ)	1.53	-1.08	1.03	-2.24
JVT	0.00	0.00	0.00	0.00
MET Soft track (Parallel resolution)	0.02	-0.02	0.76	-0.76
MET Soft track (Perpendicular resolution)	-0.17	0.17	0.66	-0.66
MET Soft track (Scale)	0.81	-0.14	0.73	0.22
PRW Data SF	-6.63	3.74	-2.6	2.09
Tau Eff. (e -OLR, true e)	0.00	0.00	0.00	0.00
Tau Eff. (e -OLR, true τ_{had})	1.97	-1.95	1.28	-1.26
Tau Eff. (ID, high- p_T)	0.00	0.00	0.00	0.00
Tau Eff. (ID, total)	12.77	-12	7.5	-7.06
Tau Eff. (Reco, high- p_T)	0.00	0.00	0.00	0.00
Tau Eff. (Reco, total)	6.66	-6.45	4.45	-4.31
Tau Eff. (2015 Trigger, data, stat.)	0.05	-0.14	0.00	0.00
Tau Eff. (2016 Trigger, data, stat.)	2.9	-3.63	1.85	-2.22
Tau Eff. (2015 Trigger, MC, stat.)	0.06	-0.08	0.00	0.00
Tau Eff. (2016 Trigger, MC, stat.)	2.33	-3	1.47	-1.8
Tau Eff. (2015 Trigger, sys.)	0.00	0.00	0.00	0.00
Tau Eff. (2016 Trigger, sys.)	2.09	-2.28	1.41	-1.56
TES (Detector)	-1.9	2.32	-1.82	1.95
TES (In situ)	1.2	-2.18	3.46	-4.33
TES (Model)	0.17	0.4	0.25	-0.16
UE (gg)	4.58	-4.58	0.00	0.00
UE (qq)	0.73	-0.73	0.00	0.00
Luminosity	2.9	-2.9	0.17	-0.17
NLO EWK Higgs	0.29	-0.29	0.00	0.00
QCD scale (VH)	0.37	-0.35	0.00	0.00
QCD scale (ggH m_{12})	-5.35	6.11	0.00	0.00
QCD scale (ggH ptH m_{01})	24.44	-18.33	0.00	0.00
QCD scale (qqH)	0.06	-0.08	0.00	0.00
Theory $Z \rightarrow \tau\tau$ CKK	0.00	0.00	-14.07	14.07
Theory $Z \rightarrow \tau\tau$ Factorization	0.00	0.00	-1.37	1.37
Theory $Z \rightarrow \tau\tau$ QSF	0.00	0.00	3.42	-3.42
Theory $Z \rightarrow \tau\tau$ Renormalization	0.00	0.00	0.00	0.00
EWK $Z \rightarrow \tau\tau$ proportion	0.00	0.00	0.21	-0.21
Fake- τ contamination	0.00	0.00	-1.61	1.61
Fake- τ extrapolation	0.00	0.00	5.53	-5.53
Higgs PDF (gg)	5.73	-5.27	0.00	0.00
Higgs PDF (gg , Acceptance)	1.43	-1.18	0.00	0.00
Higgs PDF (qq)	0.61	-0.66	0.00	0.00
Higgs PDF (qq , Acceptance)	0.13	-0.12	0.00	0.00

Table 5.14: Relative impact of the nuisance parameters compared to the total number of events in percentage, shown for the Boosted Loose category at the prefit level. See Appendix I for the other signal categories.

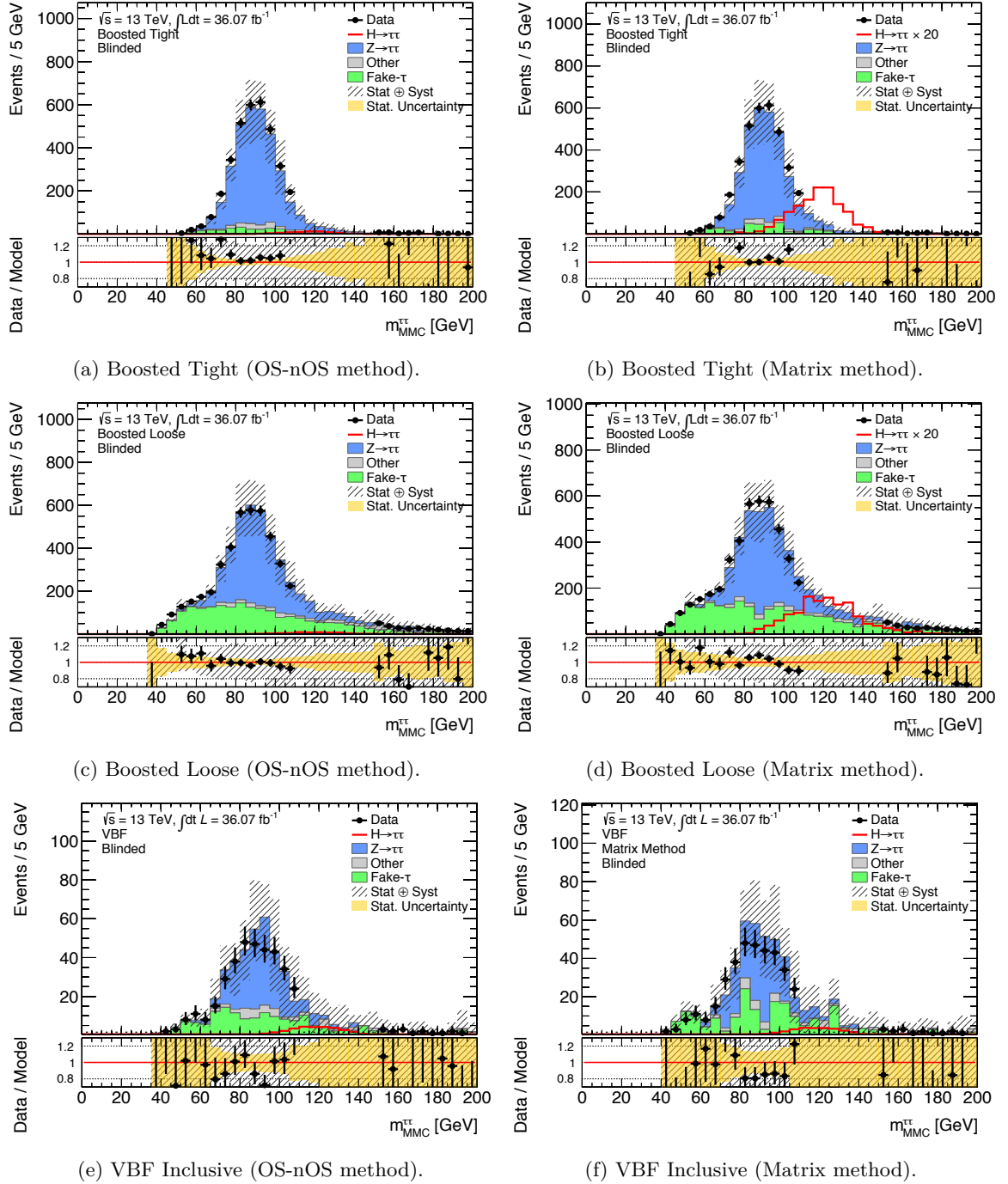


Figure 5.26: Comparison of the OS-nOS (left) and matrix method (right) background modeling for the $m_{\text{MMC}}^{\tau\tau}$ observable. For the VBF region, only the inclusive category is shown due to the small sample size in the exclusive VBF categories.

- Uncertainties on the tau energy scale and the efficiencies of the tau reconstruction, $\tau_{\text{had, vis}}$ ID tau trigger, and electron overlap removal (OLR).
- Uncertainties on the jet energy resolution (JER) and scale (JES) measurement and the

\cancel{E}_T measurement.

- Uncertainties on the background estimation.
- Uncertainties on the pileup reweighting.
- Uncertainty on the luminosity measurement.

The $\pm 1\sigma$ prefit impact for each systematic uncertainty is shown in Appendix I.

5.8.1.1 Tau reconstruction, identification, and trigger

Tau-related scale factors correct the tau energy reconstruction efficiency and the differences in efficiencies between simulation and data. They were previously described in Section 4.4.3. They are applied as specified by the recommendations from the tau trigger group and ATLAS Tau Combined Performance Group [107–110, 115]. This section describes the uncertainties on the scale factors (described previously in Section 4.4.2) that are included as NPs in the final fit (described in Section 5.9).

Measurement of the τ_{had} energy scale (TES) The TES uncertainty is composed of several parts [109]:

- TES (In situ): Addresses the uncertainty on the α shift factor (see Equation 4.6 of Section 4.4.1) and uncertainties that come from background modeling, tau energy resolution, and muon performance.
- TES (Detector): Addresses the uncertainty on the detector geometry and response correction in the TES calibration is evaluated using an alternative shower model from GEANT4 [131]. The uncertainty from the shower model is significant in the central regions of the detector.
- TES (Model): Addresses the uncertainties on the model, including the underlying event and pileup subtraction. It is evaluated by comparing the calibration in alternative simulated samples and shifting the resolution of the calibrated energies.

Measurement of the tau reconstruction and electron overlap removal efficiencies The tau reconstruction efficiency is the fraction of hadronically decaying tau leptons that are reconstructed as τ_{had} candidates and is measured separately for 1- and 3-prong tau leptons. The systematic uncertainties on these efficiencies are measured by varying the amount inner detector material and pileup. The probability of an electron that can be classified as both a τ_{had} candidate and an electron ($< 2.5\%$) differs in simulation and data. Scale factors are measured to correct these differences, and the uncertainties on these factors amount to about 5% [109].

Measurement of the tau trigger and $\tau_{\text{had, vis}}$ ID efficiencies The $\tau_{\text{had, vis}}$ ID scale factors correct the offline $\tau_{\text{had, vis}}$ ID efficiencies in simulation to align them with those observed in data. Efficiency measurements for $\tau_{\text{had, vis}}$ ID are performed using $Z \rightarrow \tau_{\text{lep}}\tau_{\text{had}}$ tag-and-probe data, where events are selected using a lepton (tag) and a τ_{had} candidate (probe). The efficiencies are extracted from the number of reconstructed τ_{had} candidates before and after $\tau_{\text{had, vis}}$ ID. The uncertainties on these factors are measured by varying the amount of detector material, the

calorimeter performance, the underlying event for the signal template, and the shower model. The trigger efficiency measurement is performed in the same way as for the $\tau_{\text{had, vis}}$ ID but is instead measured with respect to offline τ_{had} candidates.

5.8.1.2 Jet and MET (\cancel{E}_T) measurements

The JES calibration scales the reconstructed jet energy to the truth jet energy. Uncertainties on these JES scale factors are described in [105] and listed in Appendix I.

The uncertainty on the JER, described in Section 4.2, is included as a single parameter using a fully correlated scheme that encapsulates mismodeling effects. The public $H \rightarrow \tau\tau$ result in [4, 126] has since changed to an 11-NP decomposition of the single JER NP scheme, obtained from a principle component analysis (PCA), which is a statistical procedure that identifies a number of uncorrelated variables, known as principle components, from a set of observations of possibly correlated variables (each of which take on numerical values in a large dataset) [146]. This scheme is preferred since it provides a more accurate parametrization of the difference between data and simulation for the JER.

Uncertainties on the \cancel{E}_T resolution and scale are also taken into account by varying the soft track term [147]. The soft track term improves the robustness against pileup by including tracks that were measured but not associated to a hard object (c.f. Equation 4.5). The MET Soft track (Parallel resolution) and MET Soft track (Perpendicular resolution) NPs account for uncertainties on the \cancel{E}_T resolution in the parallel and perpendicular directions. The MET Soft track (Scale) NP accounts for uncertainties on the \cancel{E}_T scale.

5.8.1.3 Pileup re-weighting

Uncertainties on the pileup re-weighting arise from the re-weighting of the simulated samples according to the observed pileup profile from the 2015 and 2016 datasets. A correction factor of $\frac{1}{1.16}$ is applied to the number of interactions per bunch crossing in the simulated samples. The 1σ uncertainty is $^{+0.07}_{-0.16}$.

5.8.1.4 Background estimation

Systematic uncertainties concerning the background model for the fake- τ background are described in Sections 5.7.2.3 and 5.7.2.7 for the OS-nOS method and the matrix method, respectively. Systematic uncertainties for the $Z \rightarrow \tau\tau$ background estimation are a mixture of theory and experiment uncertainties. They are described in this section.

Systematic uncertainties on the $Z \rightarrow \tau\tau$ background estimation Theory uncertainties are derived from the SHERPA $Z \rightarrow \tau\tau$ samples. They address uncertainties from:

- The combination of the QCD matrix element and parton showers using the CKKW jet-to-parton matching procedure [148].
- Renormalization (see Section 2.1.2.2).
- Factorization (see Section 2.1.2.3).
- The running QCD coupling constants at each leg of the parton branch, which affects the scale dependence of the parton shower evolution.

The variation of the factorization and renormalization scales account for uncertainties from higher order corrections that are missing. Uncertainties on the underlying event are evaluated using a sample with a different setup for multiple interactions and are found to be negligible. The strategy for uncertainties on the parton showering in June 2017 was still under development. One way to address this would be to compare the SHERPA $Z \rightarrow \tau\tau$ sample with a sample from a generator with a different showering model, e.g., MADGRAPH+PYTHIA8. However, complications arise since this largely duplicates the built-in SHERPA theory uncertainties.

The $Z \rightarrow \tau\tau$ theory systematic uncertainties do not impact the $m_{\text{MMC}}^{\tau\tau}$ shape significantly and mainly change the overall event yield. The number of additional jets, the most difficult feature to model, is within the theory uncertainties.

5.8.1.5 Measurement of the integrated luminosity

The uncertainty on the integrated luminosity for the 2015 and 2016 combined dataset is determined from the calibration of the luminosity scale from $x - y$ beam separation scans, which was performed separately in 2015 and 2016.

5.8.2 Theoretical uncertainties

The theoretical uncertainties address the following:

- Uncertainty on the $H \rightarrow \tau\tau$ branching fraction.
- Uncertainty on the Higgs boson production cross section, especially given the L1 jet requirement. These uncertainties are provided by the Higgs boson cross section working group [149].
- Uncertainties on the electroweak fraction of the Z production.
- Uncertainties on experimental input parameters, such as PDFs and α_S .
- Uncertainties on matrix element calculations.
- Uncertainties on the underlying event and hadronization (the nonperturbative part of the SM calculation).

Each uncertainty is listed and described in Appendix I. The $\pm 1\sigma$ prefit impact for each systematic uncertainty is shown in Appendix I.3.

5.9 Fit model and signal extraction

A robust statistical model is constructed in the $H \rightarrow \tau\tau$ search to measure the compatibility of the observed data with the models built for the "background-plus-signal" or "background-only" hypotheses. If the deviation of the background-only hypothesis from the data is significant enough, it is rejected in favor of the hypothesis that the SM $H \rightarrow \tau\tau$ signal is present in data. This significance is quantified by measuring the incompatibility between the background-only hypothesis and data. There are two significances considered: expected and observed. In order to avoid potential biases in the analysis, the expected significance is first measured in Asimov data (described later in Section 5.9.3). Once the analysis methods are finalized, the observed significance is measured in the observed un-blinded data.

5.9.1 The likelihood function

In the $H \rightarrow \tau\tau$ measurement, the agreement between the data and two possible hypotheses is quantified. The two hypotheses are

- The null hypothesis, H_0 : The background-only hypothesis.
- The alternate hypothesis, H_1 : The signal-plus-background hypothesis.

To determine the level of agreement for the background-only hypothesis, the fit model is built with the signal strength, μ , as the continuous parameter of interest (POI). The signal strength is the ratio between the fitted $H \rightarrow \tau\tau$ yield and the expected SM $H \rightarrow \tau\tau$ yield (previously presented in Equation 5.1).

The probability model is a Marked Poisson Model describing the probability of obtaining n events where each event e has a discriminant variable value x_e .

$$P_{\text{Marked Poisson Model}} = \text{Pois}(n|\mu S + B) \prod_{e=1}^n \frac{\mu S f_S(x_e) + B f_B(x_e)}{\mu S + B}, \quad (5.17)$$

where S and B are the expected signal and background yields, $f_{S,B}$ are the signal and background probability density functions describing the $m_{\text{MMC}}^{\tau\tau}$ shape. They are defined such that $\int f_{S,B}(x)dx = 1$, and $\text{Pois}(n|\mu s + b)$ is the Poisson probability of observing n events when the expected number of events is $\mu s + b$. In this case, the discriminant variable is $x = m_{\text{MMC}}^{\tau\tau}$ because it provides good discrimination between the $H \rightarrow \tau\tau$ signal and the background processes and because it is sensitive to the Higgs boson mass.

The set of nuisance parameters (NPs), α , for statistical and systematic uncertainties on the event yield and/or the $m_{\text{MMC}}^{\tau\tau}$ shape is included with a Gaussian constraint for each parameter p ($G(a_p|\alpha_p, \sigma_p)$) such that Equation 5.17 becomes

$$P = P_{\text{Marked Poisson Model}} \prod_p G(a_p|\alpha_p, \sigma_p), \quad (5.18)$$

where the constraint describing an auxiliary measurement, a_p , for a nuisance parameter, $\alpha_p \in \alpha$, with an uncertainty of σ_p on the auxiliary measurement, is included as a univariate Gaussian distribution:

$$G(a_p|\alpha_p, \sigma_p) = \frac{1}{\sqrt{2\pi\sigma_p^2}} \exp\left(-\frac{(a_p - \alpha_p)^2}{2\sigma_p^2}\right). \quad (5.19)$$

In this equation, $a_p = 1$ is the nominal value and α_p is allowed to float in the fit with respect to a_p . For cases where negative values can occur, the Gaussian constraint is modified as a log-normal distribution.

For use in the statistical interpretation in this binned analysis, which uses histograms, the probability model in Equation 5.17 can be written as a product of Poisson distributions over each bin, $\text{bin} \in \text{bins}$, per channel, $c \in \text{channel}$. The set of parameters in this model is $\alpha = \{\mu, \alpha_p, \phi_p, \gamma_p\}$, where

- $\mathbb{S} = \{\alpha_p\}$ is the set of parameters related to the systematic uncertainties based on auxiliary measurements or theoretical calculations. Event yield NPs that do not alter the shape are parametrized normalization factors (factor around 1).

- $\mathbb{N} = \{\phi_p\}$ is the set of unconstrained normalization factors for the $Z \rightarrow \tau\tau$ and fake- τ backgrounds. They are determined in the fit to the $m_{\text{MMC}}^{\tau\tau}$ distribution and are given the prefit normalization as the starting value.
- $\mathbf{\Gamma} = \{\gamma_p\}$ is the set of bin-by-bin scale factors for the statistical uncertainties on the expected number of events in each bin \in bins

Then, the probability density function for obtaining n_{cb} events in bin of channel c is

$$\mathcal{P}(n_{cb}, a_p | \phi_p, \alpha_p, \gamma_b) = \prod_{c \in \text{channels}} \prod_{\text{bin} \in \text{bins}} \text{Pois}(n_{cb} | v_{cb}) G(L_0 | \lambda, \Delta_L) \prod_{p \in \mathbb{S}} f_p(a_p | \alpha_p), \quad (5.20)$$

where

- $f_p(a_p | \alpha_p)$ is the pdf for the constraint on each nuisance parameter, α_p , described previously in Section 5.8 and listed in Appendix I.2.
- $G(L_0 | \lambda, \Delta_L)$ is the Gaussian probability for the integrated luminosity, L_0 , given the true integrated luminosity, λ , and the measurement uncertainty, Δ_L .

To determine the best-fit values of the parameters for a certain hypothesis of μ , the principle of maximum likelihood principle is used. The likelihood function is defined as

$$L(\mu, \alpha) = P(n_{cb}, a_p | \mu, \phi_p, \alpha_p, \gamma_p) \quad (5.21)$$

and measures the support provided by the data given the possible value of the model's parameters, θ . The statistical description of the data is determined by the maximum likelihood estimator (MLE), which is the set of parameter values, $\hat{\theta}$, that maximizes the likelihood. The maximization, or minimization of $-\log L(\theta)$ (NLL), is performed with MINUIT [150].

The statistical model described in Equation 5.20 is built using HISTFACTORY [151]. It takes a ROOWORKSPACE as input. This ROOWORKSPACE is constructed using a WORKSPACE BUILDER package, which creates probability density functions (pdfs) for each sample and channel as binned histograms of the expected $m_{\text{MMC}}^{\tau\tau}$ distributions. The binning of each $m_{\text{MMC}}^{\tau\tau}$ distribution per category is optimized for the highest signal sensitivity and is listed in Table I.1.

5.9.2 Hypothesis testing

A test statistic is constructed to compare the goodness of fit for the H_0 and H_1 hypotheses:

$$q_\mu = -2 \ln(\lambda(\mu)) = -2 \ln \left(\frac{L(\mu, \hat{\theta})}{L(\hat{\mu}, \hat{\theta})} \right), \quad (5.22)$$

where μ is the value being tested, $\hat{\theta}$ is the set of parameters that maximize the likelihood for the test value of μ , and $\hat{\mu}$ and $\hat{\theta}$ are the values that maximize the likelihood. Since the signal strength, μ , is non-negative, the following test statistic is defined

$$q_0 = \begin{cases} -2 \ln \lambda(\mu = 0) & \hat{\mu} \geq 0, \\ 0 & \hat{\mu} < 0, \end{cases} \quad (5.23)$$

where the case for $\hat{\mu} \geq 0$ measures the lack of agreement between H_0 and the data. If a signal is observed, $\mu > 0$, then this lack of agreement increases. To quantify this disagreement, the p -value is defined:

$$p_0 = \int_{q_0, \text{ obs}}^{\infty} f(q_0 | \mu = 0) dq_0, \quad (5.24)$$

which tells the probability of obtaining results at least (or more) extreme in future experiments, given that H_0 is true. In particle physics, the p -value is converted into a significance, Z ,

$$Z = \Phi^{-1}(1 - p), \quad (5.25)$$

defined such that the p -value is the upper-tail probability for a Gaussian distributed variable to be found Z standard deviations from its mean (see Figure 5.27). Here, Φ is the quantile (or inverse of the cumulative distribution) of the standard Gaussian. In a particle physics search, a *discovery* is claimed if the null hypothesis is rejected at the $Z = 5\sigma$ significance level, corresponding to a p -value of $p = 2.87 \times 10^{-7}$ or a probability of about 1 in 3.5 million. It is considered *evidence* of a signal if it is rejected with a significance of at least $Z = 3\sigma$, corresponding to $p = 1.3 \times 10^{-3}$. In the case where no signal is observed, the threshold for excluding the signal-plus-background hypothesis is $p \geq 0.05$, corresponding to $Z = 1.64\sigma$, or a 95% confidence level.

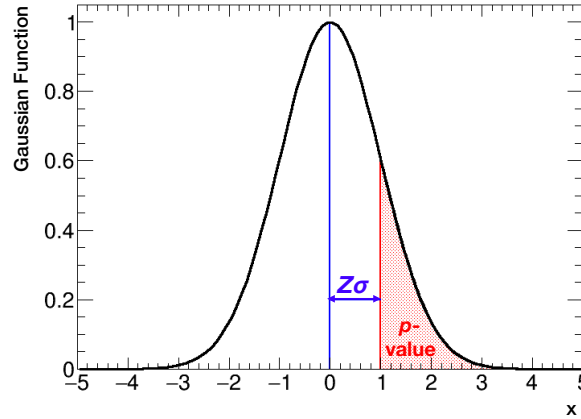


Figure 5.27: The relationship between the p -value and the significance, Z .

5.9.3 Expected sensitivity

Before fitting to the observed data, expected sensitivity studies are first performed on Asimov data to study the stability of the fit behavior and to determine the expected sensitivity. Asimov data can be used to obtain the median significance that would be obtained from performing many toy experiments (c.f. Wald's and Wilk's Theorems) [152]. A stable fit model should yield a result similar to the input that was used to build the Asimov dataset.

The advantages of using the Asimov dataset is that it is a representative dataset where the statistical fluctuations typically seen in observed data are suppressed. It allows q_μ , described in Equation 5.22 to be evaluated without using toy models, and it allows for the measurement of the expected sensitivity for different hypotheses, such as different values of μ .

For each NP in the fit model, an NLL profile is used to study its constraints and pulls. The

NLL profile is calculated by fixing that particular NP to its best fit value¹⁴ and performing fits to the other NPs. A stable fit should yield the same input NP value used to build the Asimov dataset, i.e., a no pulls ($\min(\text{NLL}) \approx 0$), with a similar postfit uncertainty on the NP. An NP is constrained if the postfit uncertainty on the NP is $< \pm 1\sigma$. For the parameter of interest, the NLL curve shows the significance. A value of $2 \cdot \Delta\text{NLL} = 1$ corresponds to the 68% confidence level (1σ) while a value of $2 \cdot \Delta\text{NLL} = 4$ corresponds to the 95% confidence level (2σ):

$$N\sigma \text{ corresponds to } 2 \cdot \Delta\text{NLL} = N^2 \quad (5.26)$$

Furthermore, to provide well-behaved NPs and assist the fit stability, all NPs in the fit model are subject to symmetrization, pruning, and smoothing in the Workspace Builder. Symmetrization takes care of NPs with one-sided variations. If both \pm variations of a bin are one-sided, it takes the larger of the two and symmetrizes the variation to both sides. To address the large statistical noise in the $\pm 1\sigma$ shape variations, the pruning removes negligible NPs to simplify the fit model and avoid fit instabilities without reducing sensitivity. In order to remove noisy shapes without removing genuine shape variations, an NP is pruned if it is considered to be negligible.¹⁵ Finally, variations are smoothed using the smoothing method from ROOT [153].

In addition, bins with zero predicted events are problematic in the fit model due the calculation of the uncertainty on zero expected events. Therefore, fixes are performed on each such bin, b , where the fixed bin value, n'_b , and error, $\sigma_{n'_b}$, for each distribution are set to:

$$n'_b = \frac{\sum_{b \in \text{bins}} w_b}{\sum_{b \in \text{bins}} n_b}, \quad \sigma_{n'_b} = \frac{\sum_{b \in \text{bins}} w_b^2}{\sum_{b \in \text{bins}} n_b}, \quad (5.27)$$

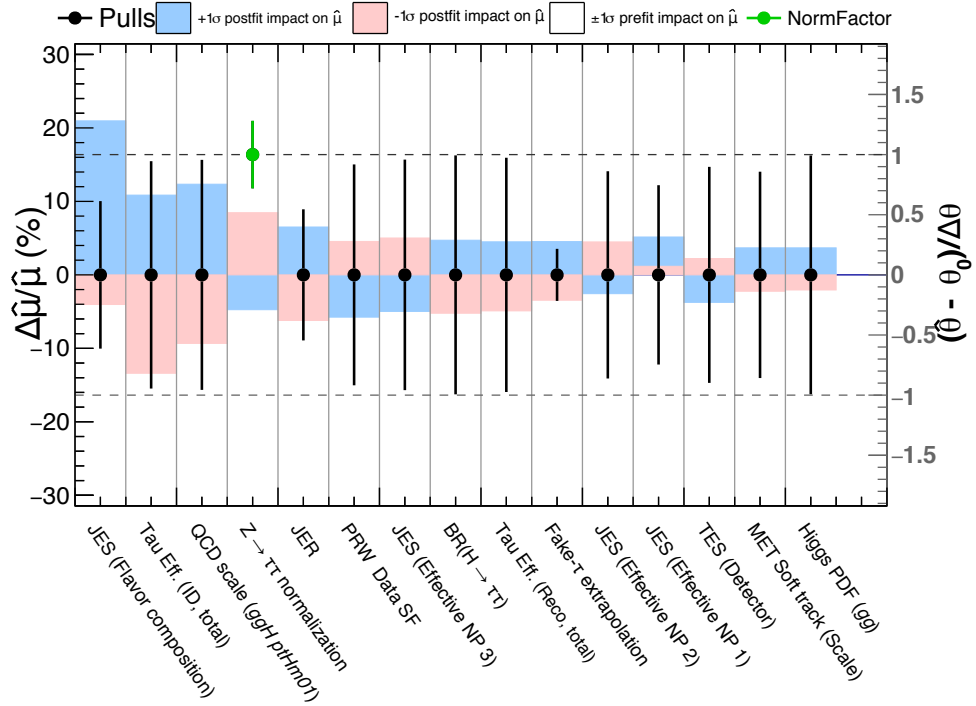
where w_b is the sum of weights in each bin.

For the fit to Asimov data built with a signal strength of $\mu = 1$, the postfit signal strength is shown in Table 5.15. The analysis is dominated by its systematic uncertainties. Running the Asimov fit without systematic uncertainties yields a signal strength of $\mu = 1.00 \pm 0.286$ and a p -value of 0.000189, corresponding to a significance of 3.55σ . (See also Table 5.15 for the breakdown of the uncertainty on μ from statistical, systematic, experimental, and theory uncertainties.) The p -value is 0.00764, which corresponds to an expected significance of 2.43σ . Figure 5.28(a) shows the ranking of the NPs based on their postfit impact on μ . The postfit impact on μ of an NP, θ , is calculated by fixing the NP to the $\pm 1\sigma$ uncertainty on its postfit value, $\hat{\theta} \pm 1\sigma$, and repeating the fit.

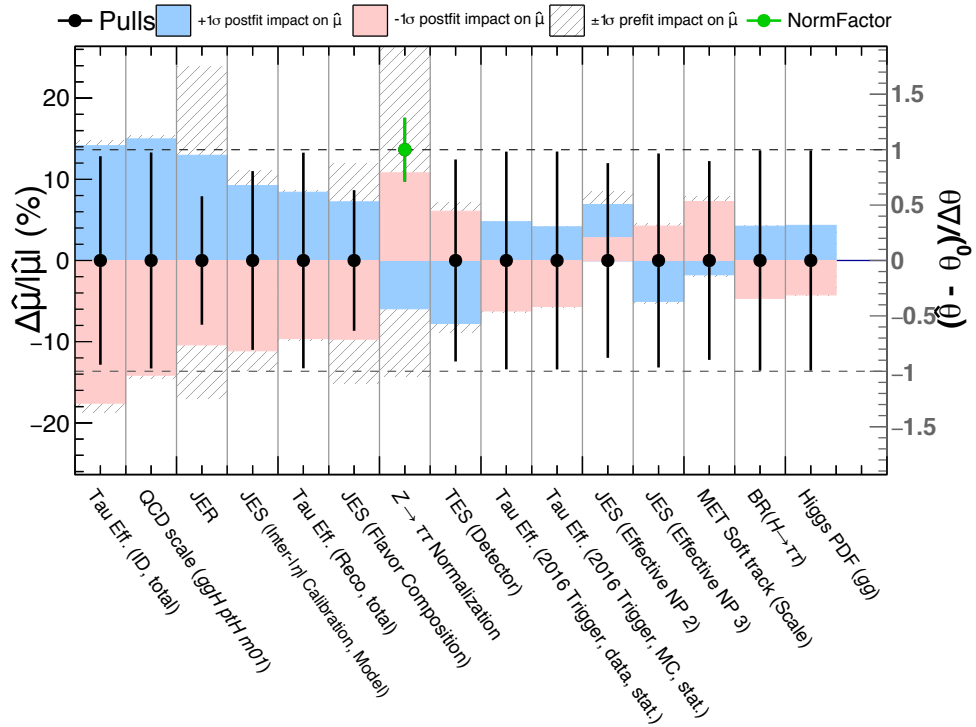
The Asimov fit shows that all highly ranked NPs, except the JER, JES (Flavor Composition), and the fake- τ extrapolation (Boost) NPs, are well behaved with no significant pulls or constraints. Concerning the $\sim 50\%$ constraint on the JER NP, implying that the width of the resolution is smaller than expected, individual Asimov fits to each signal category shows that the pull on the JER is driven by the Boosted categories. Since the Boosted category requires at least one

¹⁴ The value for which the $-\text{NLL}$ is at its minimum.

¹⁵ An NP is pruned if the statistical uncertainty on the integral if a histogram is larger than 0.1 or if $\chi^2(\pm 1\sigma \text{ variation, nominal variation}) < 0.1$. Normalization NPs on a sample are also pruned away if the $\pm 1\sigma$ variation is less than 0.5% or if it is smaller than the total statistical uncertainty on the sample. In addition, shape systematic uncertainties on a background contribution are pruned if the maximum of the variation significance over all bins, $b \in \text{bins}$, is less than 0.1, i.e., $\max(|u_b - d_b|/\sigma_b^{\text{total}}) < 0.1$, where u_b and d_b are the up/down variations in bin b and σ_b^{total} is the statistical uncertainty on the background in bin b .



(a) OS-nOS method



(b) Matrix method.

Figure 5.28: The ranking of NPs according to their postfit impact on μ (filled blue and red bands), i.e., $\Delta\hat{\mu}/|\hat{\mu}|$, calculated by fixing that NP to the $\pm 1\sigma$ uncertainty on its postfit value and repeating the fit. Performed on Asimov data (top) and observed data (bottom). The pulls (black dots) with the postfit uncertainties on the NPs (black lines with respect to the black dots) are also shown. Normalization factors are shown in green, where a value of 1 means that the postfit normalization matches the prefit normalization.

additional jet, a variation of the JER directly impacts the \cancel{E}_T and shifts it to higher values. Higher values of \cancel{E}_T lead to a shift of the $m_{\text{MMC}}^{\tau\tau}$ to higher values. The $H \rightarrow \tau\tau$ analysis in [4] has since moved to an 11-NP JER scheme to address this issue.

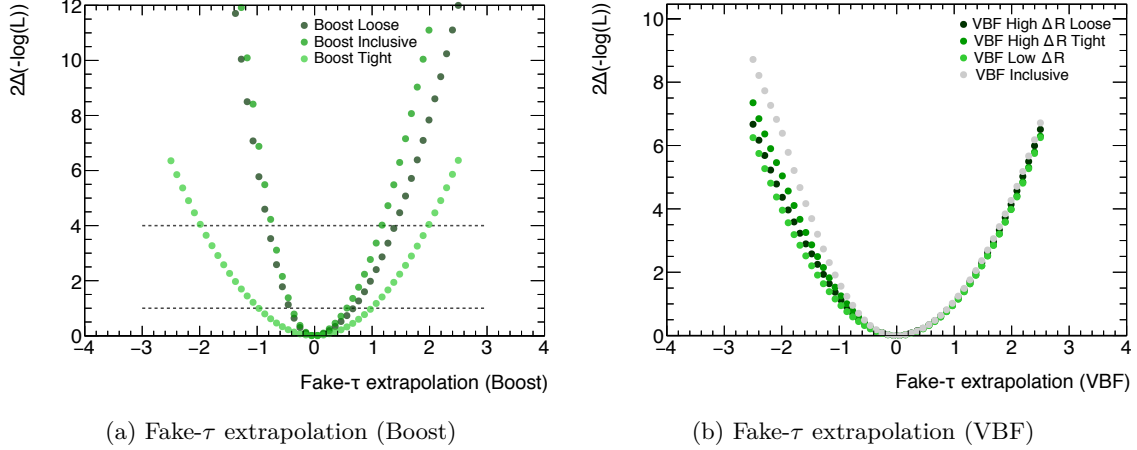


Figure 5.29: NLL profiles of the fake- τ extrapolation systematic shown separately for each Boosted (left) and VBF (right) signal category.

The NLL profiles for the fake- τ extrapolation systematic uncertainties are also shown as an example in Figure 5.29 since they are new systematic uncertainties that have not been used in any previous $H \rightarrow \tau_{\text{had}}\tau_{\text{had}}$ analyses and also because the fake- τ extrapolation systematic uncertainty is significantly constrained in the Asimov fit. When the NLL profile is not a symmetric parabola with a minimum at the best fit NP value and uncertainties of $\pm 1\sigma$, it can be studied by scanning the NLL profile for separate categories, as shown in Figure 5.29(a). The NLL profile in the exclusive boosted categories shows that the constraint on the systematic uncertainty is driven by the boosted tight category and becomes more constrained in the inclusive boosted category since it has more events with which to constrain it.

The postfit normalization factors are close to 1, which confirms that the prefit normalizations obtained from the $\Delta\eta$ fit at preselection (see Figure 5.18) and Table 5.8) describe the $m_{\text{MMC}}^{\tau\tau}$ distributions in the VBF and Boosted categories well. Studies performed with a dedicated normalization factor for the VBF category and for the Boosted category for the final fit show that the sensitivity is similar when using only one normalization factor (a fitted μ of $\hat{\mu} = 1.00 \pm 0.455934$ with sensitivity of 2.45 compared to $\hat{\mu} = 1.00 \pm 0.43705$ with a sensitivity of 2.42).

It also shows that the NPs related to the background estimation, especially the fake- τ extrapolation systematic for the boosted category, fake- τ extrapolation (Boost), and the normalization factors for the $Z \rightarrow \tau\tau$ background, the fake- τ background in the VBF categories, and the fake- τ background in the Boosted categories, which are highly variable at the prefit level are well behaved at the postfit level, when including all other NPs. The fitting of the normalization factors may have been assisted by the NPs that also affect the $Z \rightarrow \tau\tau$ normalization (which is inversely correlated with the fake- τ normalization), especially the highly ranked NP concerning $\tau_{\text{had, vis}}$ ID efficiency.

5.9.3.1 Matrix method results on Asimov data

The results of the final fit performed with the matrix method are shown in Table 5.15. The expected significance is lower than that of the OS-nOS method. Figure 5.28(b) shows the pulls of the NPs and the ranking of the NPs based on their postfit impact on μ . It shows that, compared with OS-nOS model, the systematic uncertainties from the fake- τ background estimation for the matrix method are not as highly ranked. In addition, the only highly constrained NP is the misidentification probability systematic uncertainty from the W +jets control region (hh_mm_wcrsys), which is not shown in Figure 5.28(b) since it is not highly ranked. These problematic misidentification probabilities from the W + jets control region are expected to be highly constrained, as they overestimated the variation from the nominal misidentification probability.

Since the expected sensitivity is higher for the OS-nOS method than for the matrix method, the final unblinded results are performed using the former.¹⁶ The matrix method is nevertheless a key new development in validating that the nOS control region is a competent model for the fake- τ background. Furthermore, it can be used to re-evaluate the existing systematic uncertainties prescribed for the OS-nOS method. It is already used to determine the anti- $\tau_{\text{had, vis}}$ ID region used for the fake- τ extrapolation systematic uncertainty in the OS-nOS method. Before the development of the matrix method, the loosest possible anti- $\tau_{\text{had, vis}}$ ID region was used, which has been seen to be less signal-like.

Moreover, the systematic uncertainties for the OS-nOS method can be re-evaluated by replacing the fake- τ extrapolation systematic uncertainty with the nominal fake- τ shape template from the matrix method. Then, the OS/nOS shape ratio from the anti- $\tau_{\text{had, vis}}$ ID region be used to reweight the nominal $m_{\text{MMC}}^{\tau\tau}$ distribution from the OS-nOS method. In this dissertation preliminary studies performed with the $m_{\text{MMC}}^{\tau\tau}$ distribution reweighted by the fake- τ extrapolation ratio show that the signal sensitivity improves by about 5%.

5.10 Results

With the statistical model validated, the following section presents the results of the $H \rightarrow \tau_{\text{had}}\tau_{\text{had}}$ search on observed data. The observed signal strength is $\mu_{\text{observed}} = 0.62_{-0.40}^{+0.44}$. (See Table 5.15 for the breakdown of the uncertainty on μ .) The observed p -value is 0.0639, which corresponds to a significance of 1.52. The NLL profiles of μ in each signal category are shown in Figure 5.30, where it can be seen that the VBF categories have the highest sensitivity.

Figure 5.31 shows the postfit $m_{\text{MMC}}^{\tau\tau}$ distributions, and Table 5.16 shows the postfit event yields. Figure 5.32 shows the NP ranking, where it can be seen that the sensitivity of the $H \rightarrow \tau\tau$ analysis shown here strongly depends on the $Z \rightarrow \tau\tau$ background normalization, the fake- τ background estimation, and the modeling of the underlying jet. The binning of the $m_{\text{MMC}}^{\tau\tau}$ distribution also has a large effect on the observed signal strength. With an unoptimized binning, the fitted μ can be as low as 0.14 ± 0.43 (c.f. Table I.1 for the optimized binning configuration). The gain in the binning of the $m_{\text{MMC}}^{\tau\tau}$ distribution comes, for example, from splitting the VBF low ΔR binning into two bins as (100,120,140) GeV instead of using a single large bin from 110 to 200 GeV. This allows the fit to more signal and reduce the fake- τ background.

Further investigations should be conducted on several of the auxiliary measurements used for

¹⁶ The systematic uncertainties on the misidentification probabilities used in the matrix method calculated from a W + jets control region also still require some work.

Data Fake- τ Estimation Method	Asimov				Observed	
	OS-nOS		Matrix Method		OS-nOS	
Postfit μ	1.00		1.00		0.62	
Total Uncertainty	0.46	-0.42	0.63	-0.51	0.44	0.40
Statistical Uncertainty	0.24	-0.23	0.25	-0.25	0.25	-0.24
Systematic Uncertainty	0.40	-0.35	0.58	-0.45	0.36	-0.31
Experimental Uncertainty	0.37	-0.33	0.58	-0.45	0.34	-0.31
Theory Uncertainty	0.15	-0.08	0.25	-0.07	0.12	-0.06
p -value	0.00764		0.0207		0.0639	
Significance	2.43		2.04		1.52	

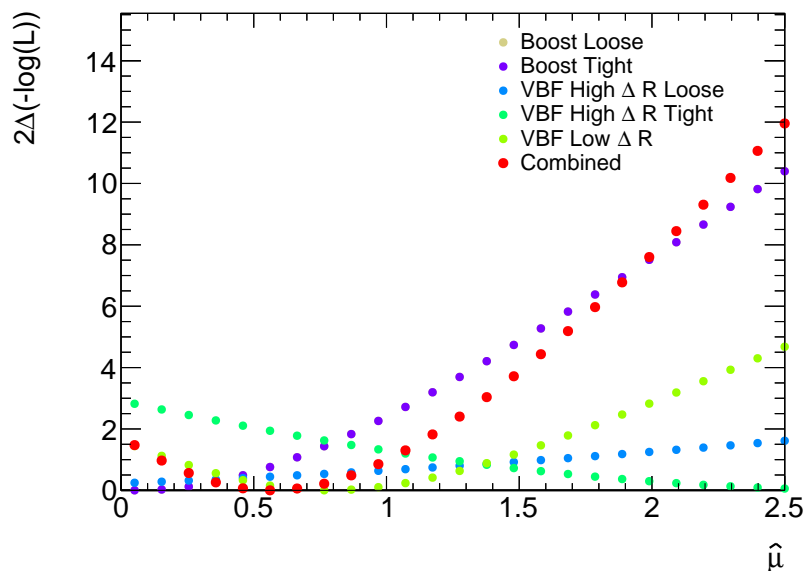
Table 5.15: Expected and observed results in the $H \rightarrow \tau\tau$ analysis.

Figure 5.30: NLL profiles of the POI for the combined signal categories.

the systematic uncertainties. For example, given the significant deviation of the prefit $Z \rightarrow \tau\tau$ background from that of the MC prediction, the results suggest that the $\tau_{\text{had, vis}}$ ID scale factors should be investigated. The measurement in [4] also sees a significant deviation from the $Z \rightarrow \tau\tau$ event yield predicted in MC. The JES (Flavor composition) NP should also be investigated given its high and asymmetric postfit impact on μ , as it is the highest ranked NP. An NLL profile scans of this NP is shown to be a symmetric parabola that is constrained. Given the high ranking, constraint, and pull of the fake- τ extrapolation systematic uncertainty, it is worthwhile to reevaluate the fake- τ background uncertainties and use the fake- τ shape from the matrix method as the fake- τ shape systematic uncertainty instead, as discussed in Section 5.9.3.1. The NP ranking supports this, especially since the pull in the positive direction implies that the fit wants to make the fake- τ background shape more like the OS shape.

There is a large pull on the jet energy resolution (JER) NP, and if it were not pulled in the

Process	Boost		VBF					
	Loose	Tight	High ΔR	Loose	High ΔR	Tight	Low ΔR	
ggH	26.24 ± 18.07	30.10 ± 21.02	0.69 ± 0.50		1.26 ± 0.94		2.43 ± 1.73	
VBF	5.15 ± 3.56	5.87 ± 4.07	0.85 ± 0.58		3.76 ± 2.56		6.06 ± 4.19	
WH	2.22 ± 1.59	1.57 ± 1.08	–		–		0.29 ± 0.20	
ZH	1.01 ± 0.71	2.53 ± 1.79	–		–		0.12 ± 0.09	
$t\bar{t}H$	0.02 ± 0.02	0.04 ± 0.03	–		0.00 ± 0.00		0.00 ± 0.00	
$Z \rightarrow \tau\tau$	2886.30 ± 129.90	3224.20 ± 136.47	44.29 ± 6.00		81.66 ± 9.54		129.50 ± 11.02	
Fake- τ	1657.88 ± 134.17	224.58 ± 65.07	51.19 ± 5.59		88.56 ± 8.75		19.45 ± 5.74	
Other	266.23 ± 28.85	118.55 ± 22.61	5.07 ± 1.09		9.19 ± 1.93		5.50 ± 3.42	
$S + B$	4845.05 ± 77.05	3607.43 ± 91.35	102.09 ± 7.68		184.44 ± 11.11		163.34 ± 10.00	
Data	4832.00 ± 69.51	3625.00 ± 60.21	100.00 ± 10.00		187.00 ± 13.67		158.00 ± 12.57	

Table 5.16: Postfit event yields and their total uncertainties. The fitted signal-plus-background yield is denoted as $S + B$.

positive direction by so much, the NP ranking plot shows that the postfit μ could be almost 20% smaller. This makes sense since a widening of the energy resolution means the energy resolution of the $H \rightarrow \tau\tau$ mass peak would also be wider, and the expected number of events for $\mu = 1$ can be lower due to the wider shape of the expected Higgs boson peak. Figure 5.32 implies that if the JER were not pulled by about 50% in the positive direction, the fitted μ would be smaller.

The observed result presented in this dissertation is compatible with the recent $H \rightarrow \tau\tau$ result from the ATLAS Collaboration presented in [4], which obtains a $H \rightarrow \tau_{\text{had}}\tau_{\text{had}}$ significance of 2.4250, with a μ of $0.73^{+0.41}_{-0.34}$. See Table 5.17 for the observed results from ATLAS and CMS in Run-I and Run-II. There are several ways the analysis presented in this dissertation could be improved to achieve a higher signal sensitivity, such as reweighting the nominal fake- τ template by its extrapolation systematic uncertainty. It is clear that there is a background process in the OS region that is not present in the SS or nOS region. The measurement presented in [4] does not completely address this since it reweights the $m_{\text{MMC}}^{\tau\tau}$ distribution obtained from the nOS control region using another observable. It would be interesting to identify the origin of this missing background. For example, simulated samples of hypothesized background processes can be generated and included in the $H \rightarrow \tau_{\text{had}}\tau_{\text{had}}$ fit model.

Run-I		Run-II		
ATLAS and CMS combined	ATLAS	CMS	ATLAS	Presented result
$H \rightarrow \tau\tau$	$H \rightarrow \tau_{\text{had}}\tau_{\text{had}}$	$H \rightarrow \tau_{\text{had}}\tau_{\text{had}}$	$H \rightarrow \tau_{\text{had}}\tau_{\text{had}}$	$H \rightarrow \tau_{\text{had}}\tau_{\text{had}}$
$1.11^{+0.24}_{-0.22}$	$1.2^{+0.7}_{-0.6}$	$1.36^{+0.40}_{-0.35}$	$0.71^{+0.39}_{-0.34}$	$0.62^{+0.44}_{-0.40}$

Table 5.17: The presented result and the observed $H \rightarrow \tau\tau$ results from Run-I and Run-II analyses by the ATLAS and CMS collaborations [1, 4, 87].

5.11 Conclusion

The observation of the Higgs boson decaying to two τ_{had} candidates is an essential measurement in probing the coupling of the Higgs boson to fermions. The analysis presented in this chapter is performed on 36.07 fb^{-1} of data collected at the ATLAS detector in 2015 and 2016 at a center-of-mass energy of $\sqrt{s} = 13 \text{ TeV}$. The signal selection is optimized for highly boosted Higgs bosons from the ggH and VBF production processes.

In the signal extraction, the main irreducible background contribution from the QCD $Z \rightarrow \tau\tau$ process is modeled using simulation, and the main reducible background from multijet production can be modeled using two different background methods developed in this dissertation. The signal is extracted by comparing the expected signal and background $m_{\text{MMC}}^{\tau\tau}$ distributions to the observed $m_{\text{MMC}}^{\tau\tau}$ distribution in data. An excess of signal events beyond the expected background yield is measured with an observed significance of 1.52σ and an expected significance of 2.42σ . The measured signal strength relative to that predicted by the Standard Model is $\mu = 0.62_{-0.24}^{+0.25}(\text{stat})_{-0.31}^{+0.36}(\text{syst}) = 0.62_{-0.40}^{+0.44}$ and is consistent with the Standard Model prediction.

The measured signal strength is similar to the cut-based result from the Run-I analysis of $\mu = 1.2 \pm 0.4(\text{stat})_{-0.4}^{+0.5}(\text{syst}) = 1.2_{-0.6}^{+0.7}$ and the public result using multivariate methods of $\mu = 2.0_{-0.7}^{+0.9}$ (c.f. Figure 5.3) [1, 154]. It is also consistent with the result measured in the recent $H \rightarrow \tau\tau$ analysis presented by the ATLAS Collaboration, which presents a $H \rightarrow \tau_{\text{had}}\tau_{\text{had}}$ signal strength of $\mu = 0.71 \pm_{-0.34}^{+0.39}$ [4]. The major differences between the two measurements are that [4] uses updated systematic uncertainties, especially for the JER, a different background estimation method, and a newer version of the data processing. In comparison to the $H \rightarrow \tau\tau$ $H \rightarrow \tau\tau$ analysis from the CMS Collaboration, which shows an observed sensitivity of over 5σ in all $H \rightarrow \tau\tau$ channels with $\mu = 1.09_{-0.26}^{+0.27}$ ($\mu = 1.36_{-0.35}^{+0.40}$ in the $H \rightarrow \tau_{\text{had}}\tau_{\text{had}}$ channel only), the CMS measurement profits from the additional 0-jet category, from which several systematic uncertainties can be constrained [87]. The $H \rightarrow \tau\tau$ $H \rightarrow \tau\tau$ analysis at ATLAS cannot use this category due to the L1 jet requirement in the tau trigger.

This analysis is not only vital in confirming the Standard Model predictions but is also a preparation for Higgs CP measurements in the $H \rightarrow \tau_{\text{had}}\tau_{\text{had}}$ channel. The methods developed in this analysis are used as a basis for the Higgs CP measurement, and a cross section measurement from the $H \rightarrow \tau_{\text{had}}\tau_{\text{had}}$ analysis can be used as input for the Higgs boson signal strength when performing a CP measurement.

In conclusion, this chapter presents a measurement of the signal strength in the $H \rightarrow \tau_{\text{had}}\tau_{\text{had}}$ using the Run-I analysis as a starting point and with new methods developed for Run-II. The analysis presented here shows that the methods used in the $H \rightarrow \tau\tau$ analysis in Run-I are not sufficient in describing the new Run-II dataset. The methods presented in this dissertation address the mismodeling of the $m_{\text{MMC}}^{\tau\tau}$ distribution, seen earlier in the Run-I analysis, by using the anti- $\tau_{\text{had, vis}}$ ID region both in the prescription of systematic uncertainties and in the determination of the nominal fake- τ background template. This region is a sizable signal-like control region in data that has not been used in the $H \rightarrow \tau\tau$ $H \rightarrow \tau\tau$ analysis before and is a first step in new opportunities to be explored.

The future for the $H \rightarrow \tau\tau$ analysis is to include the additional integrated luminosity of 46.9 fb^{-1} from 2017 that is reconstructed with an improved release of the ATLAS reconstruction algorithm and to explicitly measure the $H \rightarrow \tau\tau$ coupling instead of only the signal strength, μ . Combined with the data already taken from Run-I, ATLAS can perform precise measurements of the $H \rightarrow \tau\tau$ signal strength and cross section, as well as its properties.

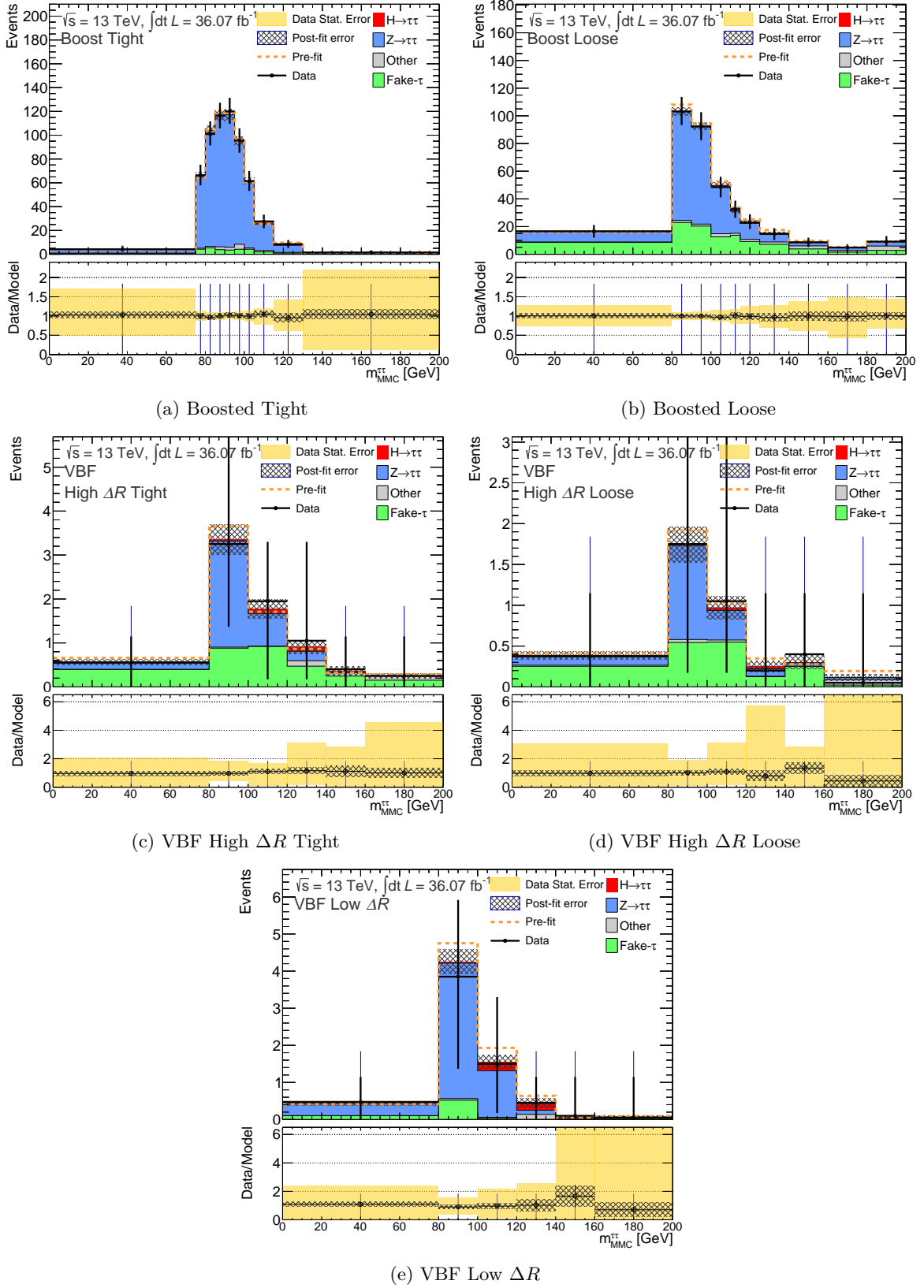


Figure 5.31: The prefit (orange) and postfit $m_{\text{MMC}}^{\tau\tau}$ distributions after the fit to observed data. The binning used in the final fit to the $m_{\text{MMC}}^{\tau\tau}$ observable is listed in Table I.1.

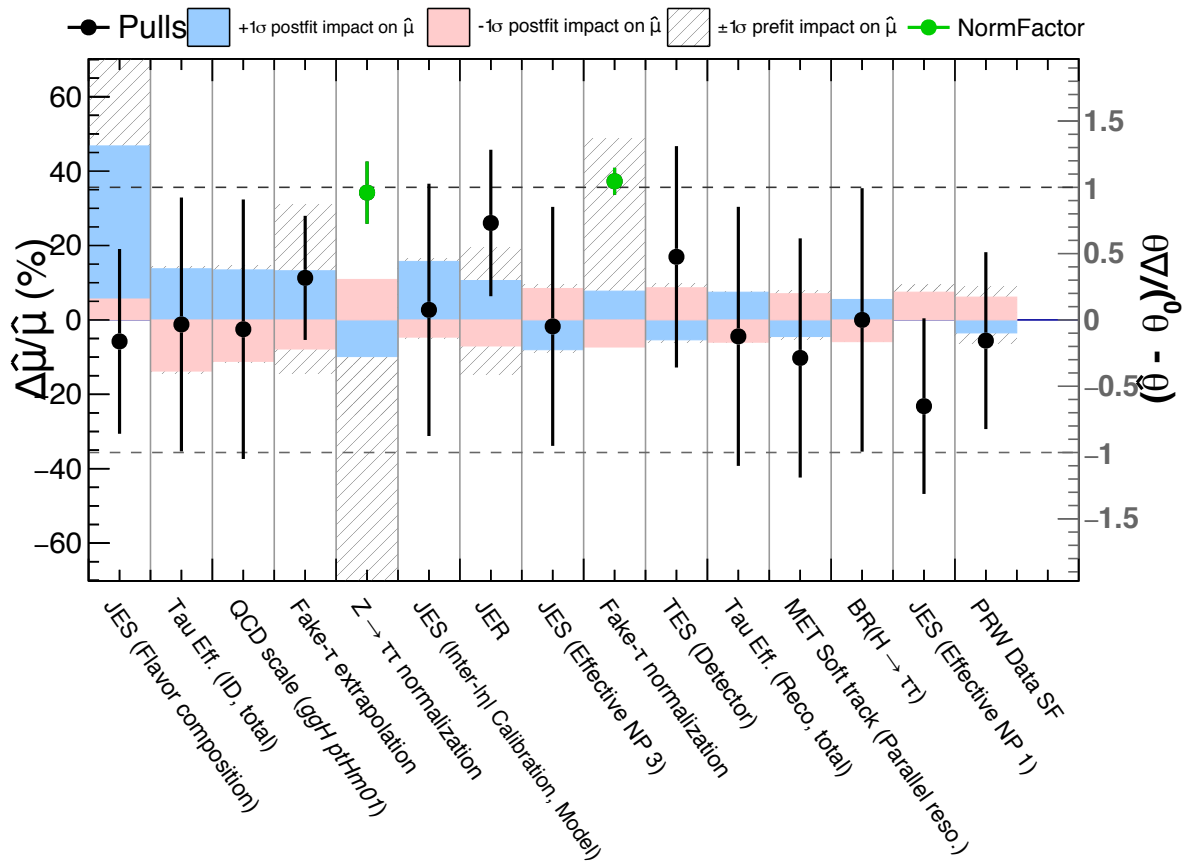


Figure 5.32: Ranking of NPs based on their postfit impact on $\hat{\mu}$ (filled blue and red bands) for observed data using the OS-nOS method. (See Figure 5.28 for further details on the interpretation of the figure.)

Higgs CP analysis in the $H \rightarrow \tau_{\text{had}}\tau_{\text{had}}$ channel

The discovery of the Higgs boson by the ATLAS and CMS collaborations in 2012 has been an important first step in understanding the nature of electroweak symmetry breaking. Subsequent studies of the Higgs boson spin, parity, and coupling properties are vital in confirming whether the Higgs boson observed at the LHC is compatible with the SM Higgs boson.

This chapter presents an analysis of the \mathcal{CP} properties of the Higgs boson in the $H \rightarrow \tau_{\text{had}}\tau_{\text{had}}$ channel. As previously discussed in Section 2.3, the $H \rightarrow \tau_{\text{had}}\tau_{\text{had}}$ decay mode is the most promising for studies of \mathcal{CP} mixing in the Higgs sector since the tau leptons contain unique information on Higgs \mathcal{CP} properties and the tau spin is experimentally observable at the LHC.¹ With the integrated luminosity of the 2016–2017 Run-II dataset, it is not expected for this analysis to be sensitive to Higgs \mathcal{CP} mixing. Nevertheless, it is a basis for future Higgs \mathcal{CP} measurements with more data, and studies are performed in this dissertation to identify hindrances to the analysis and possible improvements.

In this chapter, Section 6.1 describes the \mathcal{CP} sensitive observables for each di-tau decay mode. Then, Section 6.2 explains the relevant signal and background processes in the $H \rightarrow \tau_{\text{had}}\tau_{\text{had}}$ decay channel for the Higgs \mathcal{CP} analysis. Section 6.3 lists the data and simulated samples used for the analysis. Section 6.4 outlines the selection of physics objects and events that targets the $H \rightarrow \tau_{\text{had}}\tau_{\text{had}}$ signal signature. Section 6.5 discusses the modeling of signal and background contributions. Section 6.6 details the uncertainties considered in the final statistical interpretation, discussed in Section 6.7. Section 6.8 presents studies of the limitations in the \mathcal{CP} sensitivity and a sensitivity projection given more luminosity. Given the limitations identified in the sensitivity projection, Section 6.9 delineates studies to include decay modes with additional pions using machine learning studies. Finally, the results are reported in Section 6.10.

6.1 \mathcal{CP} -sensitive observables

Tau leptons from a scalar, pseudoscalar, or \mathcal{CP} -mixed Higgs boson exhibit certain angular correlations in which Higgs \mathcal{CP} properties are encoded. For the Higgs decay to a $\tau^+\tau^-$ pair, these \mathcal{CP} properties are encoded in the transverse spin components of the di-tau pair:

$$d\Gamma \propto 1 - s_z^- s_z^+ + \cos(2\phi_\tau)(s_\perp^- \cdot s_\perp^+) + \sin(2\phi_\tau) \left((s_\perp^- \times s_\perp^+) \cdot \hat{k}^- \right), \quad (6.1)$$

¹ The other two fermionic decays involving the b quark and the top quark are complicated. The extraction of the b quark polarization state is difficult due to depolarization effects in the fragmentation process, and top quarks decay before fragmentation, thus destroying their spin information.

where \hat{k}^- is the normalized momentum of the τ^- lepton in the rest frame of the Higgs boson, \hat{s}^\pm are the unit spin vectors of the τ^\pm leptons in their respective rest frames, and s_\perp^\pm and s_z^\pm are the transverse and longitudinal components of \hat{s}^\pm with respect to \hat{k}^- , respectively. The hadronic decay channel of the tau lepton is especially relevant for Higgs CP studies because the kinematics of the decay products of the tau lepton have preferred emission directions in the rest frame of the Higgs boson, and these decay products can be reconstructed with the new substructure algorithm previously discussed in Section 4.5.

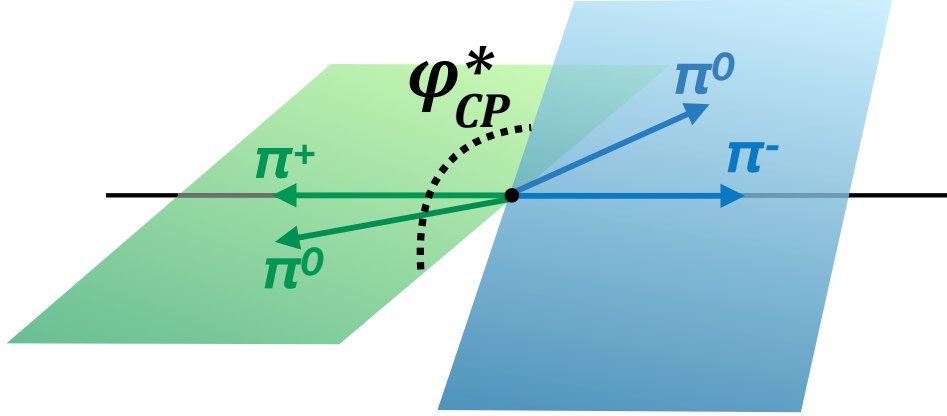


Figure 6.1: Schematic of acoplanarity angle between the tau decay planes, φ_{CP}^* , shown, as an example, for the $\rho\rho$ (1p1n-1p1n) decay mode.

The $\tau^+\tau^-$ spin correlation can be inferred from the angle between the tau decay planes, or the acoplanarity angle (see Figure 6.1). This CP sensitive acoplanarity angle is reconstructed differently depending on each tau decay mode since the associated visible decay products must be used to reconstruct the tau decay planes. The construction of this observable developed in [69, 155, 156] uses the new decay mode classification. The tau decay modes considered in this analysis are the 1p0n and 1p1n modes (refer to Table 4.3 previously defining the decay mode nomenclature). Methods for 1pXn decay modes with more than one pion (ρa_1 , $a_1 a_1$) are discussed in Section 6.9. In these cases, a machine-learning algorithm is better suited, given the many possible angles and tau decay planes, in addition to the correct assignment of the pions in the a_1 decay chain.

6.1.1 Impact parameter method

Since the tau flight direction is not known due to the presence of neutrinos, the tau spin direction in the $\tau \rightarrow \pi\nu_\tau$ case is instead evaluated using the impact parameter (or IP, previously discussed in Section 4.4.2) of each τ_{had} candidate [69]. The component of the pion momentum vector, \vec{p}_\pm^* , perpendicular to the τ_{had} momentum vector, \vec{k}_\pm , is affected by the transverse spin component of the tau lepton, and the impact parameter is a handle on this (see Figure 6.2). In the $\tau \rightarrow \pi\nu_\tau$ decay, the impact parameter is defined as the shortest path between the primary vertex and the pion momentum vector extended in the direction of the tau decay point. The 4-vector of the normalized impact parameter for each τ^\pm in the laboratory frame is denoted as $n_\pm^\mu = (0, \vec{n}_\pm)$.²

² A 4-vector is used instead of a 3-vector since the mass component of 0 for each τ^\pm in the laboratory frame changes after boosting into a different frame.

In the zero-momentum frame (ZMF) of the $\pi^+\pi^-$ pair, it is

$$n_{\pm}^{*\mu} = (n_{0\pm}^*, \vec{n}_{\pm}^*), \quad (6.2)$$

where $n_{0\pm}^*$ is from the boost into the ZMF since its prior value was 0 in for each τ^{\pm} in the laboratory frame, \vec{n}_{\pm}^* is composed of its perpendicular and parallel components, $\hat{n}_{\perp}^{*\pm}$ and $\hat{n}_{\parallel}^{*\pm}$, respectively, with respect to \vec{p}_{\pm}^* . Thus, \vec{n}_{\pm}^* can be expressed as $\vec{n}_{\pm}^* = r_{\perp}^{\pm} \hat{n}_{\perp}^{*\pm} + r_{\parallel}^{\pm} \hat{n}_{\parallel}^{*\pm}$, where r_{\perp}^{\pm} and r_{\parallel}^{\pm} are constants.

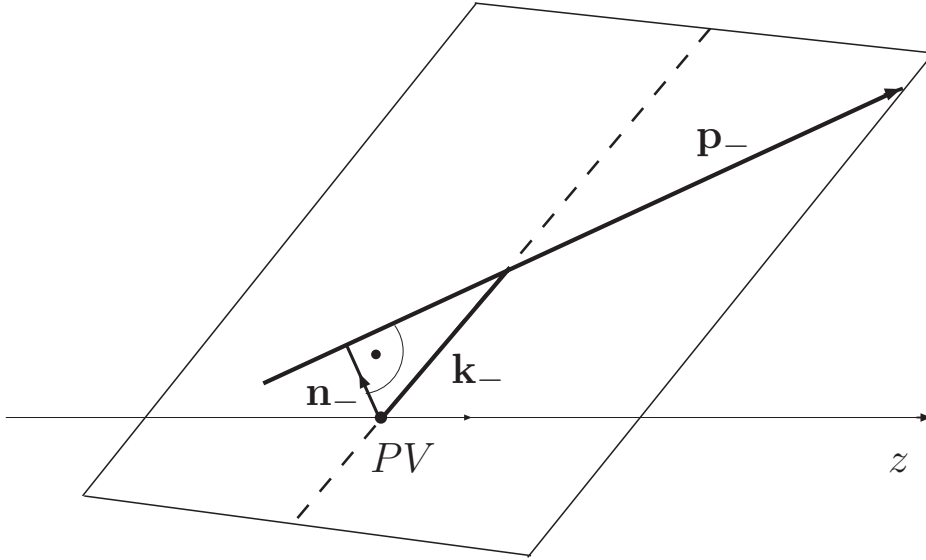


Figure 6.2: Schematic of the τ_{had} decay plane with the impact parameter vector, \vec{n}_- (see Equation 6.2). The τ_{had} momentum vector is k_- , the primary vertex of the tau is PV , and the pion momentum vector is p_- . Taken from [69].

The variable φ^* can be used to distinguish between CP -odd and CP -even Higgs bosons and is expressed as

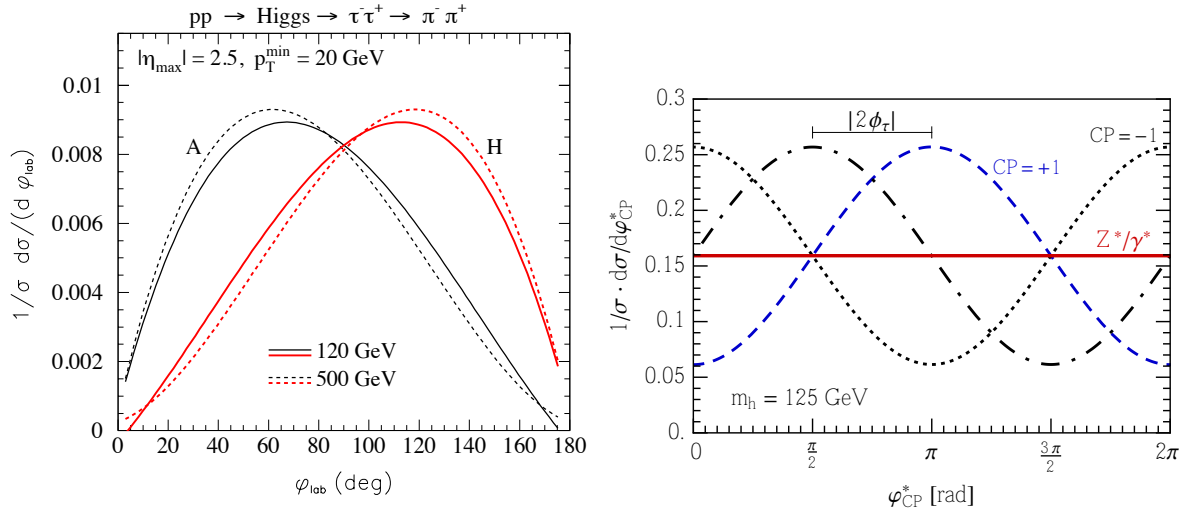
$$\varphi^* = \arccos(\hat{n}_{\perp}^{*+} \cdot \hat{n}_{\perp}^{*-}). \quad (6.3)$$

The observable φ^* can be extended to define a variable φ_{CP}^* that is also sensitive to ϕ_{τ} for CP -odd and CP -even mixtures. Using the triple-odd correlation, O_{CP}^* , where \hat{p}_-^* is the normalized π^- momentum, φ_{CP}^* is defined as

$$\varphi_{CP}^* = \begin{cases} \varphi^* & \text{for } O_{CP}^* \geq 0 \\ 2\pi - \varphi^* & \text{for } O_{CP}^* < 0 \end{cases}, \quad \text{with } O_{CP}^* = \hat{p}_-^* \cdot (\hat{n}_{\perp}^{*+} \times \hat{n}_{\perp}^{*-}). \quad (6.4)$$

Figure 6.3 shows the observables φ_{CP}^* , φ_{CP}^* , and the phase differences for a CP -even, CP -odd, and a CP -mixed ($\phi_{\tau} = -\frac{\pi}{4}$) Higgs boson.

The sensitivity of the φ_{CP}^* method to the CP mixing angle, ϕ_{τ} , depends on the reconstruction of the impact parameter vector, especially the direction of its z -component (c.f. Figure 4.1) [157]. The cases where the impact parameters are small or of similar order of magnitude as the uncertainty on the PV degrade the sensitivity of the φ_{CP}^* method. They can be identified based



(a) φ_{CP} for a purely \mathcal{CP} -even and \mathcal{CP} -odd Higgs boson at 120 and 500 GeV [69]. (b) φ_{CP}^* for a \mathcal{CP} -even, \mathcal{CP} -odd, and a \mathcal{CP} -mixed ($\phi_\tau = -\frac{\pi}{4}$) Higgs boson [65].

Figure 6.3: The φ_{CP} and φ_{CP}^* distributions from the IP method.

on the significance of the track impact parameter in the transverse plane:

$$d_0^{\text{sig}} = \frac{d_0}{\sigma(d_0)}, \quad (6.5)$$

where d_0 is the track impact parameter and $\sigma(d_0)$ is its uncertainty. Using d_0^{sig} , the \mathcal{CP} sensitivity of φ_{CP}^* is highest when splitting according to

$$\varphi_{CP}^* = \begin{cases} \varphi_{CP}^*, \text{ low sensitivity} & \text{for } |d_0^{\text{sig}}|(\tau_0 \text{ or } \tau_1) \leq 1.4 \\ \varphi_{CP}^*, \text{ high sensitivity} & \text{for } |d_0^{\text{sig}}|(\tau_0, \tau_1) > 1.4 \end{cases}, \quad (6.6)$$

where the low sensitivity events are kept to retain the statistical power [158]. The optimization of this splitting is performed using the \mathcal{CP} sensitivity estimate described later in Section 6.7.

6.1.2 ρ method

An analogous φ_{CP}^* observable for the $\tau \rightarrow \rho\nu_\tau$ decay is explained in this section. The method for ρ decays was first presented by Desch et al. [64]. Further work in [65] prescribe an extension of the IP method for ρ decays.

In the case of tau decays via the $\rho^\pm(769)$ resonance, i.e., $\tau^\pm \rightarrow \rho^\pm (\rightarrow \pi^\pm \pi^0) \nu_\tau$, the tau decay planes can be defined using the charged and neutral 4-momenta for the charged and neutral components (q_\pm^μ and $q_\pm^{\mu 0}$, respectively, where they are boosted into the rest frame of the $\rho^\pm \rho^\mp$ resonance). In the case where both τ_{had} candidates decay via the ρ resonance, the triple-odd correlation and φ_{CP}^* , analogous to Equation 6.4 for the IP method case, are defined as

$$\varphi_{CP}^{*'} = \begin{cases} \varphi & \text{for } O_{CP}^* \geq 0 \\ 2\pi - \varphi & \text{for } O_{CP}^* < 0 \end{cases}, \quad \text{with } O_{CP}^* = \hat{q}^- \cdot (\hat{q}_\perp^{0+} \times \hat{q}_\perp^{0-}), \quad (6.7)$$

where \hat{q} is the unit vector of the three-momentum vector in q^μ .

For the ρ case, the $\varphi^{*'}_{CP}$ variable is not sensitive to ϕ_τ unless the asymmetry between the energies of the π^\pm and π^0 (Upsilon, Y) is taken into account, yielding the φ^*_{CP} observable for the ρ method:

$$\varphi^*_{CP} = \begin{cases} \varphi^{*'} & Y_{\rho^+}Y_{\rho^-} \geq 0 \\ 2\pi - \varphi^{*'} & Y_{\rho^+}Y_{\rho^-} < 0 \end{cases}, \text{ with } Y_{\rho^\pm} = \frac{E_{\pi^\pm} - E_{\pi^0}}{E_{\pi^\pm} + E_{\pi^0}} = \frac{2p_T^{\text{track}} - p_T^\tau}{p_T^\tau}. \quad (6.8)$$

The Y_ρ definition used in this analysis is the p_T -based Y_ρ in Equation 6.8. The sensitivity of φ^*_{CP} is higher for events with $|Y_{\rho^+}Y_{\rho^-}|$ values that are not around zero since it is less likely that the sign is wrong. An optimization of this splitting, performed using \mathcal{CP} sensitivity estimate described in Section 6.7, yields the following low- and high-sensitivity categorization:

$$\varphi^*_{CP} = \begin{cases} \varphi^*_{CP, \text{ low sensitivity}} & \text{for } |Y_{\rho^+}Y_{\rho^-}| < 0.2 \\ \varphi^*_{CP, \text{ high sensitivity}} & \text{for } |Y_{\rho^+}Y_{\rho^-}| \geq 0.2 \end{cases}, \quad (6.9)$$

As in the IP method, the low sensitivity events are kept to retain their statistical power.

6.1.3 Combined IP ρ method

The IP and ρ methods (discussed in Section 6.1.1 and 6.1.2) can be combined to reconstruct the angle between the tau decay planes for $h \rightarrow \tau^\pm \tau^\mp \rightarrow \pi^\pm \rho^\mp + 2\nu_\tau$ events. Events with this decay mode combination will henceforth be referred to as 1p0n-1p1n or IP ρ events. In these cases, φ^*_{CP} is defined in the $\pi^\pm \rho^\mp$ rest frame as

$$\varphi^*_{CP} = \arccos(\hat{q}_\perp^{0+} \cdot \hat{n}_\perp^{0-}), \text{ with } O_{CP}^* = \hat{q}_- \cdot (\hat{q}_\perp^+ \times \hat{n}_\perp^-). \quad (6.10)$$

The separation is performed similarly using the triple-odd correlation and Y analogously to Equations 6.4 and 6.8. The separation power is further enhanced by splitting according to d_0^{sig} and $|Y_{\rho^+}Y_{\rho^-}|$:

$$\varphi^*_{CP} = \begin{cases} \varphi^*_{CP, \text{ low sensitivity}} & \text{for } d_0^{\text{sig}} \leq 1.4 \text{ or } |Y_{\rho^+}Y_{\rho^-}| < 0.3 \\ \varphi^*_{CP, \text{ high sensitivity}} & \text{for } d_0^{\text{sig}} > 1.4 \text{ and } |Y_{\rho^+}Y_{\rho^-}| \geq 0.3 \end{cases}, \quad (6.11)$$

6.2 Signal and background processes

The background processes in the Higgs \mathcal{CP} analysis are the same as in the $H \rightarrow \tau\tau$ analysis, with the main contributions coming from the QCD $Z \rightarrow \tau\tau$ +jets and fake- τ backgrounds. They were previously described in Section 5.3, with the Feynman diagrams shown in Figure 5.4. The signal processes, on the other hand, are the $H \rightarrow \tau\tau$ process for different possible \mathcal{CP} mixing angles. Only the VBF and ggH Higgs boson production processes are considered since the VH and $t\bar{t}H$ processes contribute minimally to this analysis. The angles available in the samples used for this analysis (discussed in Section 6.3) range from $\phi_\tau = -80^\circ$ to $\phi_\tau = 90^\circ$ in steps of 10° , where $\phi_\tau = 0^\circ$ is the SM hypothesis of a purely \mathcal{CP} -even Higgs boson. The modulation in the φ^*_{CP} observable at reconstruction level for the signal templates with different \mathcal{CP} hypotheses is shown in Figure 6.4.

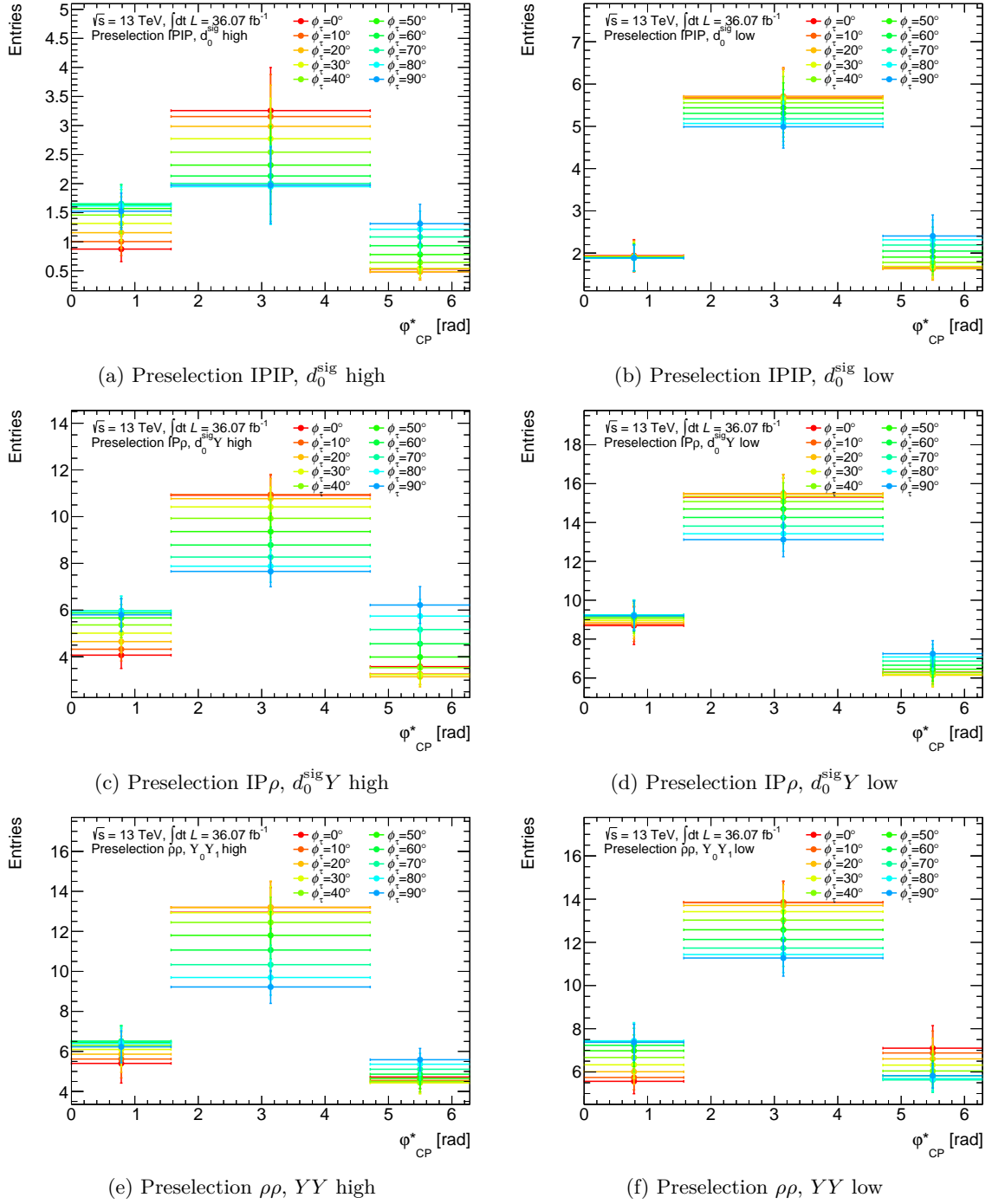


Figure 6.4: The CP mixing signal templates at the preselection level, shown as an example from $\phi_\tau = 0^\circ$ to $\phi_\tau = 90^\circ$ in 10° steps. The error bars show only the statistical uncertainty.

6.3 Data and simulated samples

The same data and background samples are used in the Higgs CP analysis as in the $H \rightarrow \tau\tau$ analysis. They were previously described in Section 5.4. The modeling of transverse tau spin

correlations for the $Z \rightarrow \tau\tau$ background was found to perform best for the same background sample from SHERPA 2.2 as is used in the $H \rightarrow \tau\tau$ analysis.

The signal samples are obtained from unpolarized ggH and VBF samples, where the CP states are simulated by a weight from TAUSPINNER [159]. The TAUSPINNER weights are computed using the true kinematics of the tau decay. The respective weight for each CP mixing angle is applied on each event of the unpolarized sample. These unpolarized samples are simulated with POWHEG interfaced with PYTHIA 8 and use the CT10 PDF parametrization [136]. The SM Higgs boson template is obtained from the unpolarized sample for the $\phi_\tau = 0^\circ$ hypothesis, as opposed to the standard SM Higgs boson samples used in the $H \rightarrow \tau\tau$ analysis, where the tau spin correlations are computed by PYTHIA (see Section 5.4.2). This avoids differences between TAUSPINNER and PYTHIA. Since the same unpolarized sample is used to build each hypothesis, the final sensitivity estimate suffers less from statistical fluctuations. The cross sections for the unpolarized signal samples are shown in Table E.1, the same table where the cross sections for the background samples were previously listed.

For the machine-learning studies in Section 6.9 for the ρa_1 and $a_1 a_1$ modes, samples containing generator-level information are simulated using PYTHIA 8.2 [160]. Ten million events are generated per decay mode, each for a purely CP -even and a purely CP -odd Higgs boson.

6.4 Event selection and categorization

The same preselection requirements are used in the Higgs CP analysis as in the $H \rightarrow \tau\tau$ analysis, with a few minor differences that are detailed in this section. Only events in the Higgs boson signal region ($100 < m_{\text{MMC}}^{\tau\tau} < 150$ GeV) are selected. This avoids the low- $m_{\text{MMC}}^{\tau\tau}$ mismodeling discussed in Section 5.7.2.4. As opposed to the $H \rightarrow \tau\tau$ analysis which fits to the $m_{\text{MMC}}^{\tau\tau}$ distribution, events outside of this region are not strictly needed to fit the φ_{CP}^* observables. Moreover, the medium-tight $\tau_{\text{had, vis}}$ ID working point is used, instead of the tight-tight selection since the former does not impact the sensitivity and the additional events are essential.

Events are then categorized into Boosted and VBF categories, as in the $H \rightarrow \tau\tau$ analysis (c.f. Section 5.6.3f). The same Boosted categories are used in the Higgs CP analysis, but all VBF categories are merged into one VBF category due to the limited number of events.³ After this, further categorization is performed by decay mode since the φ_{CP}^* discriminant variables used for the sensitivity estimate are constructed differently for each decay mode combination. Because the φ_{CP}^* observable is so far only calculated for IPIP, $IP\rho$, and $\rho\rho$ events, only these decay modes are used in the Higgs CP analysis. The selection on the Higgs boson signal region and the 1p0n/1p1n events removes about 60% of signal events and 85% of data events.

Decay mode	Low sensitivity	High sensitivity
IPIP	$ d_0^{\text{sig}} (\tau_0) < 1.4$ or $ d_0^{\text{sig}} (\tau_1) < 1.4$	$ d_0^{\text{sig}} (\tau_0 \text{ and } \tau_1) < 1.4$
$IP\rho$	$ d_0^{\text{sig}} (\tau_{\text{IP}}) \leq 1.4$ or $Y(\tau_\rho) < 0.3$	$ d_0^{\text{sig}} (\tau_{\text{IP}}) > 1.4$ and $Y(\tau_\rho) \geq 0.3$
$\rho\rho$	$ Y \cdot Y \geq 0.3$	$ Y \cdot Y < 0.3$

Table 6.1: Low- and high- CP sensitivity categorization by decay mode, each for the VBF Inclusive, Boosted Tight, and Boosted Loose categories.

³ Future studies can be performed to optimize the categorization according to the CP sensitivity instead of the POI, μ , from the $H \rightarrow \tau\tau$ analysis.

After categorizing by decay mode, the final categorization is optimized according to the sensitivity in separating between a purely \mathcal{CP} -even and a purely \mathcal{CP} -odd Higgs boson. The IPIP, $\text{IP}\rho$, and $\rho\rho$ events are categorized into low- and high-sensitivity regions according to Equations 6.6, 6.9, and 6.11. The categorization by decay mode is summarized in Table 6.1. The resulting categories and their expected yields are shown in Table 6.2. For cases where the categorization results in zero expected events for a background process, the respective low- and high- \mathcal{CP} sensitivity categories are merged. This affects the low- and high-sensitivity regions for the VBF IPIP and VBF $\text{IP}\rho$ categories.

6.5 Background model

In this section, the background estimation strategy is discussed. First, the estimation of the main irreducible background from the QCD $Z \rightarrow \tau\tau$ +jets process is presented, followed by the estimation of the main reducible background from the fake- τ process. All other backgrounds are estimated from simulation, as is done in the $H \rightarrow \tau\tau$ analysis. A summary is shown in Table 6.3.

6.5.1 Estimation of the $Z \rightarrow \tau\tau$ background

The QCD $Z \rightarrow \tau\tau$ + jets background is the main irreducible background. It is crucial to correctly model the transverse tau spin correlations in this background since a mismodeling can lead to nontrivial φ_{CP}^* distributions and mimic a \mathcal{CP} -mixed signal. The spin correlations of the tau pair from a Z boson are different from those of the Higgs boson since the tau leptons can be longitudinally polarized to some degree due to the parity violating couplings of the Z (c.f. Table 2.7).⁴

The φ_{CP}^* distribution of the $Z \rightarrow \tau\tau$ background is expected to be a uniform distribution when integrated over the entire phase space [65]. It can deviate from a uniform distribution if the phase space is restricted. For example, the φ_{CP}^* distribution is not uniform if a π^\pm in the IPIP method is restricted to being coplanar or perpendicular to the tau production plane. The angle between the charged product and the τ_{had} production plane for the IP and ρ decay modes is sensitive to this feature:

$$\cos(\alpha_-, \text{IP}) = \left| \frac{\hat{e}_z \times \hat{p}_{\pi^-}}{|\hat{e}_z \times \hat{p}_{\pi^-}|} \cdot \frac{\hat{n}_\perp^- \times \hat{p}_{\pi^-}}{|\hat{n}_\perp^- \times \hat{p}_{\pi^-}|} \right| \quad \cos(\alpha_-, \rho) = \left| \frac{\hat{e}_z \times \hat{p}_{\rho^-}}{|\hat{e}_z \times \hat{p}_{\rho^-}|} \cdot \frac{\hat{p}_{\pi^-} \times \hat{p}_{\rho^-}}{|\hat{p}_{\pi^-} \times \hat{p}_{\rho^-}|} \right|, \quad (6.12)$$

where \hat{p}_{π^\pm} and \hat{p}_{ρ^\pm} are the normalized momenta of the π^\pm and ρ^\pm in the laboratory frame, respectively. The normal component of the π^\pm track impact parameter is \hat{n}_\perp^- , and \hat{e}_z points along the direction of one of the proton beams. A value of $\alpha_- < \frac{\pi}{4}$ means the charged decay product is parallel to the tau production plane, while a value of $\alpha_- \geq \frac{\pi}{4}$ means it is perpendicular.

The α_- observable is used to investigate the size and modeling of the transverse tau spin correlations and to compare the modeling of the transverse spin correlations in different generators in restricted phase spaces. Figure 6.5 shows the φ_{CP}^* distribution where it is expected to be sinusoidal in restricted phase spaces and where it is consistent with being uniform without restrictions. The generator level distributions are also compared with those from [158], separately

⁴ These longitudinal tau polarizations from tau pair production in an $H \rightarrow \tau\tau$ decay, on the other hand, are small, even when taking higher order electroweak corrections into account.

Category		Fake- τ	Other	$Z \rightarrow \tau\tau$	VBF $H \rightarrow \tau\tau$	ggH	Data	
Preselection		$24\,219.6 \pm 223.7$	$1\,073.4 \pm 35.8$	$12\,208.5 \pm 115.0$	61.3 ± 0.4	196.4 ± 2.8	$21\,846.0 \pm 147.8$	
$70 < m_{\text{MMC}}^{\tau\tau} < 140$ GeV		$8\,265.4 \pm 127.4$	340.4 ± 20.8	$2\,836.6 \pm 65.5$	51.5 ± 0.4	160.9 ± 2.5	$6\,205.0 \pm 78.8$	
1p0n/1p1n		$1\,637.9 \pm 54.4$	154.6 ± 13.1	$1\,413.7 \pm 45.5$	23.8 ± 0.2	74.0 ± 1.7	$3\,087.0 \pm 55.6$	
VBF	IPIP	6.7 ± 3.3	0.4 ± 0.3	5.1 ± 2.06	0.8 ± 0.0447	4.03 ± 0.104	30 ± 5.49	
	$\text{IP}\rho$	41.7 ± 8.35	3.4 ± 1.16	29.3 ± 3.86	5.1 ± 0.141	2.5 ± 0.282	61 ± 7.78	
	$\rho\rho$	Y_+Y_- high	6.7 ± 3.3	1.7 ± 1.7	6.9 ± 1.8	2 ± 0.1	1.1 ± 0.3	18 ± 4.2
		Y_+Y_- low	18.3 ± 5.5	2 ± 0.8	11.6 ± 2.3	2.4 ± 0.1	1.5 ± 0.2	27 ± 5.2
Boost	IPIP	d_0^{sig} high	1.7 ± 1.7	0.2 ± 0.1	18.3 ± 2.9	0.2 ± 0.03	1.0 ± 0.2	32 ± 5.7
		d_0^{sig} low	3.3 ± 2.4	4.0 ± 1.4	52.9 ± 4.8	0.3 ± 0.03	2.9 ± 0.3	56 ± 7.5
Tight	$\text{IP}\rho$	d_0^{sig} high	11.7 ± 4.4	5.0 ± 1.5	75 ± 6.2	1.1 ± 0.1	4.9 ± 0.4	89 ± 9.4
		d_0^{sig} low	30.0 ± 7.1	11.4 ± 2.8	132.9 ± 7.2	1.8 ± 0.1	8.6 ± 0.5	185 ± 13.6
	$\rho\rho$	Y_+Y_- high	11.7 ± 4.4	3.9 ± 3.1	89.1 ± 6.3	1.1 ± 0.1	5.9 ± 0.5	122 ± 11
		Y_+Y_- low	40.0 ± 8.2	10.3 ± 2.9	94.6 ± 6.8	1.4 ± 0.1	7.7 ± 0.5	145 ± 12
Boost	IPIP	d_0^{sig} high	6.7 ± 3.3	0.9 ± 0.4	11.4 ± 5.5	0.1 ± 0.02	0.9 ± 0.2	35 ± 5.9
		d_0^{sig} low	28.3 ± 6.9	5.9 ± 2.9	62.3 ± 8.5	0.3 ± 0.03	1.6 ± 0.3	84 ± 9.2
	$\text{IP}\rho$	$d_0^{\text{sig}}Y$ high	46.6 ± 8.8	7.1 ± 2.3	78.3 ± 7.5	0.56 ± 0.04	4.1 ± 0.4	132 ± 11.5
		$d_0^{\text{sig}}Y$ low	151.5 ± 15.9	16.5 ± 6.5	147.6 ± 10.1	1.3 ± 0.1	7.0 ± 0.5	339 ± 18.4
Loose	$\rho\rho$	Y_+Y_- high	89.9 ± 12.2	23.3 ± 8.6	97.6 ± 8.6	0.6 ± 0.04	4.9 ± 0.4	202 ± 14.2
		Y_+Y_- low	163.2 ± 16.5	17 ± 5.3	114.5 ± 20.2	1.0 ± 0.1	5.4 ± 0.4	269 ± 16.4

Table 6.2: Expected event yields for background, signal, and data samples in the Higgs \mathcal{CP} analysis. In cases where a background is expected to have no events, the low- and high- \mathcal{CP} sensitivity categories are merged. Thus, the low- and high-sensitivity for the VBF IPIP and VBF $\text{IP}\rho$ categories are merged. The expected $t\bar{t}H$ and VH event yields are negligible and are not considered in this analysis.

for events with 0, 1, or 2 additional partons in the final state, and are found to be consistent within the statistical uncertainties [158]. The SHERPA $Z \rightarrow \tau\tau$ sample models the φ_{CP}^* observable in these different phase spaces well and is therefore used for the $Z \rightarrow \tau\tau$ background, as previously mentioned in Section 6.3.

The SHERPA $Z \rightarrow \tau\tau$ sample is used to validate the modeling of important observables and to determine the $Z \rightarrow \tau\tau$ normalization, as will be later described in Section 6.5.2. However, in the final CP sensitivity estimate, the $Z \rightarrow \tau\tau$ template is taken from data. The shape of the $Z \rightarrow \tau\tau$ background from MC is replaced with $Z \rightarrow \tau\tau$ events from data in the Z -peak region ($70 < m_{\text{MMC}}^{\tau\tau} < 100$ GeV) with the fake- τ and other backgrounds subtracted. Figure 6.6 shows the agreement of the shapes from the Z -peak region and the Higgs boson signal region in MC. (The comparison is not made between MC and data due to differences introduced by reconstruction effects of the φ_{CP}^* observable.) The differences in shapes are covered within 1σ of the statistical uncertainties in every category except the $\rho\rho$ high category. However, in this category, it is only the center bin deviates by less than 2σ , which is not a significant difference. Based on these results, the $Z \rightarrow \tau\tau$ background template is modeled using data in the Z -peak region. The determination of the normalization of this data-driven $Z \rightarrow \tau\tau$ background is scaled to a fit from data using the MC template and is discussed in the next section.

This method has the advantage of not reusing the MC $Z \rightarrow \tau\tau$ sample that is used for the derivation of substructure-related *in-situ* systematic uncertainties, such as those described in Section 6.6. It also avoids MC-associated uncertainties. However, the disadvantage is that the $Z \rightarrow \tau\tau$ peak is not used to constrain MC uncertainties in the final fit.

6.5.2 Estimation of the fake- τ background

The φ_{CP}^* distribution for the fake- τ background is expected to be uniform because the multijet production in the fake- τ background is random. It is important to verify this and compare with a control region in data. Unlike in the $H \rightarrow \tau\tau$ analysis, the nOS control region in data cannot be used in the Higgs CP analysis for the fake- τ background template. This is because a categorization is performed by tau decay mode in order to construct the φ_{CP}^* observables. Therefore, the track requirement cannot be reverted. Other control regions where a signal region selection is reverted also have the problem of containing different π^\pm and π^0 multiplicities. Therefore, the SS control region per decay mode category is used in an "OS-SS" method analogous to the "OS-nOS" method in the $H \rightarrow \tau\tau$ analysis.

The fake- τ background template is estimated according to the steps below, with elaboration

Process	Template	Prefit normalization	Final fit normalization
Fake- τ	SS Control Region	Fit to $m_{\text{MMC}}^{\tau\tau}$ ($70 < m_{\text{MMC}}^{\tau\tau} < 140$ GeV)	Floated (unconstrained)
QCD $Z \rightarrow \tau\tau$	Data in the $70 < m_{\text{MMC}}^{\tau\tau} < 100$ GeV region with expected fake- τ and other backgrounds subtracted	Fit to $m_{\text{MMC}}^{\tau\tau}$ ($70 < m_{\text{MMC}}^{\tau\tau} < 140$ GeV)	Fixed
Other	MC	MC cross section	Fixed

Table 6.3: Summary of the Higgs CP background strategy.

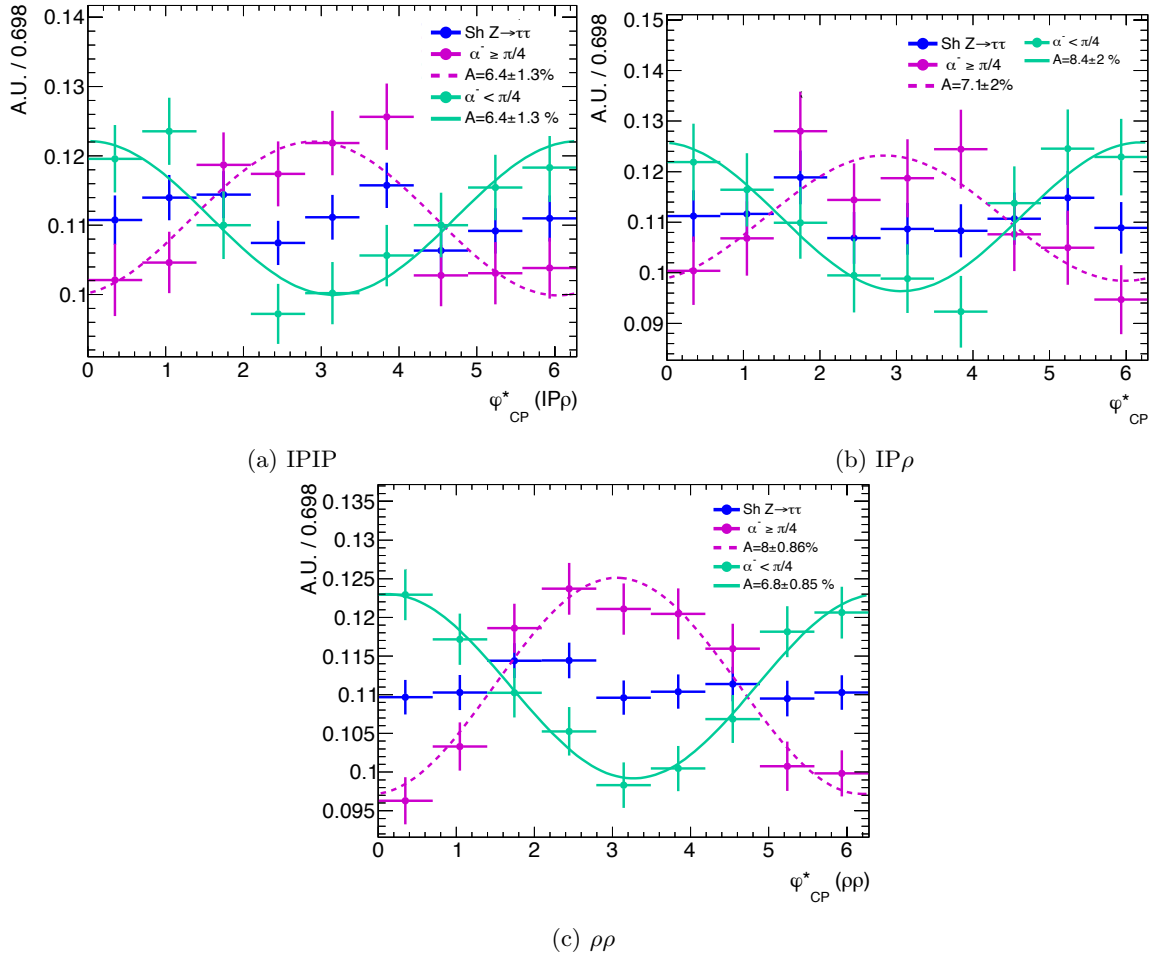


Figure 6.5: Generator-level φ_{CP}^* distributions of the simulated SHERPA 2.2 $Z \rightarrow \tau\tau$ sample for the inclusive phase space and the $\alpha_- \geq \pi$ and $\alpha_- < \pi$ regions. Only minimal selection has been applied using generator-level quantities: $p_{T, \text{vis}} > 20$ GeV, $|\eta_{\tau, \text{vis}}| < 2.5$, and $m_{\tau\tau} > 80$ GeV. Taken from [158].

on each step following this list:

1. Template from the SS control region in data.
2. Contamination of real- τ events subtracted from the SS template.
3. Validation of the uniform shape of the fake- τ background template.
4. Normalization of the pre-fit fake- τ background template performed in a template fit to the $70 < m_{\text{MMC}}^{\tau\tau} < 140$ GeV range of the $m_{\text{MMC}}^{\tau\tau}$ distribution in data (c.f. Equation 5.11, Table 6.3, and Section 5.7.2.1.)

Validation of the use of the SS region is performed using the same procedure as that used in the $H \rightarrow \tau\tau$ analysis. The contamination from real- τ backgrounds is checked and found to be about 1% to 10% depending on decay mode, as shown in Figure 6.7. The contamination is subtracted to obtain the nominal fake- τ shape, as is done in the $H \rightarrow \tau\tau$ analysis.

The fake- τ background template obtained from the SS region is consistent with that of a uniform distribution, as shown in Figure 6.8. The fitted uniform distributions are within the

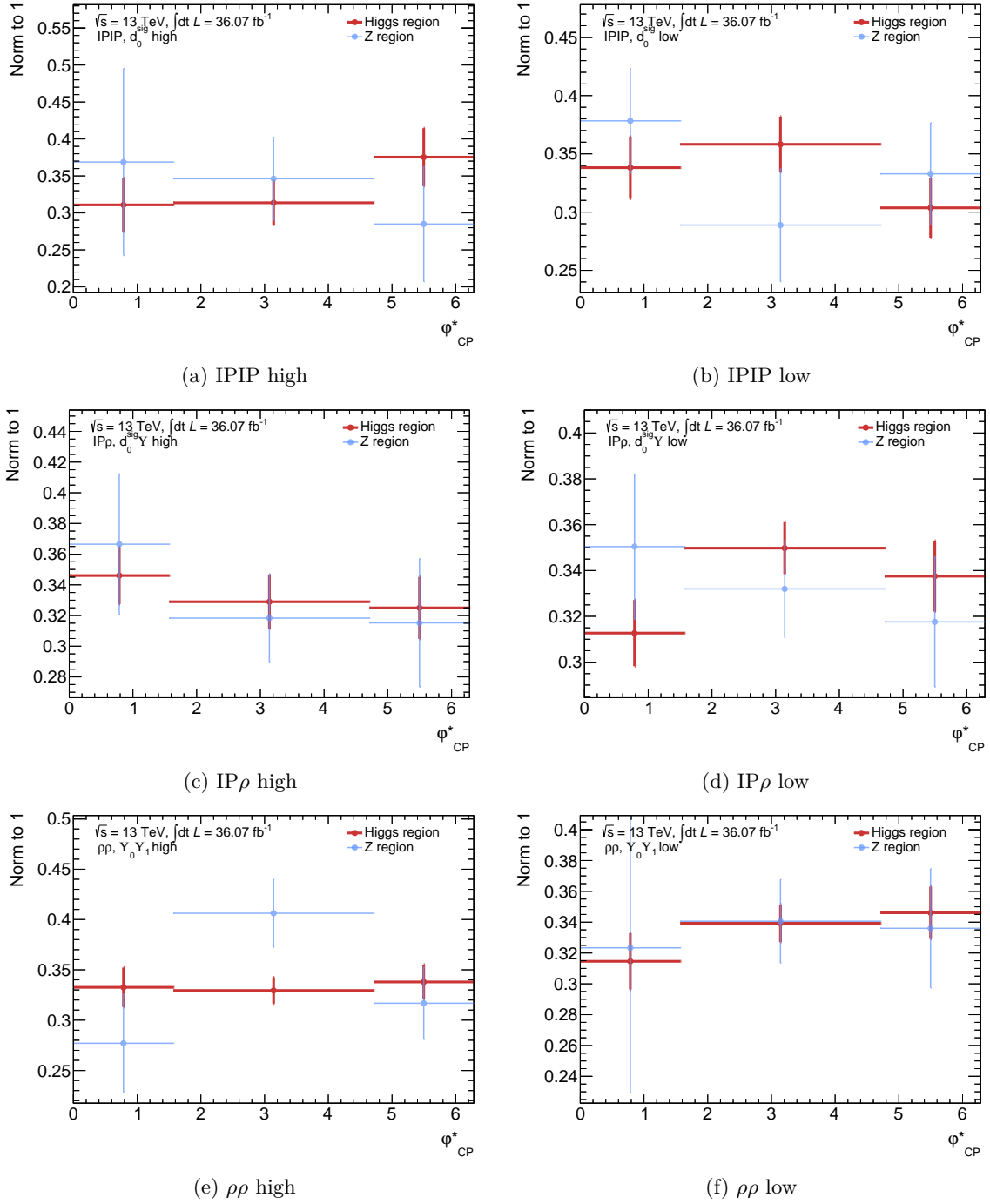


Figure 6.6: Comparison of $Z \rightarrow \tau\tau$ shapes in the Z region ($70 < m_{\text{MMC}}^{\tau\tau} < 100 \text{ GeV}$) and the Higgs boson region ($100 < m_{\text{MMC}}^{\tau\tau} < 140 \text{ GeV}$) for MC at the preselection level.

statistical uncertainties on the SS template, and the χ^2/ndf values for the fits of the SS template to a uniform distribution are reasonable. In addition, the deviations from a uniform distribution are within 1σ of the statistical uncertainty for every bin except for the 0 to $\pi/4$ bin in the $\rho\rho$ $Y_+ Y_-$ high category. However, the difference is less than 2σ of the statistical uncertainty, and

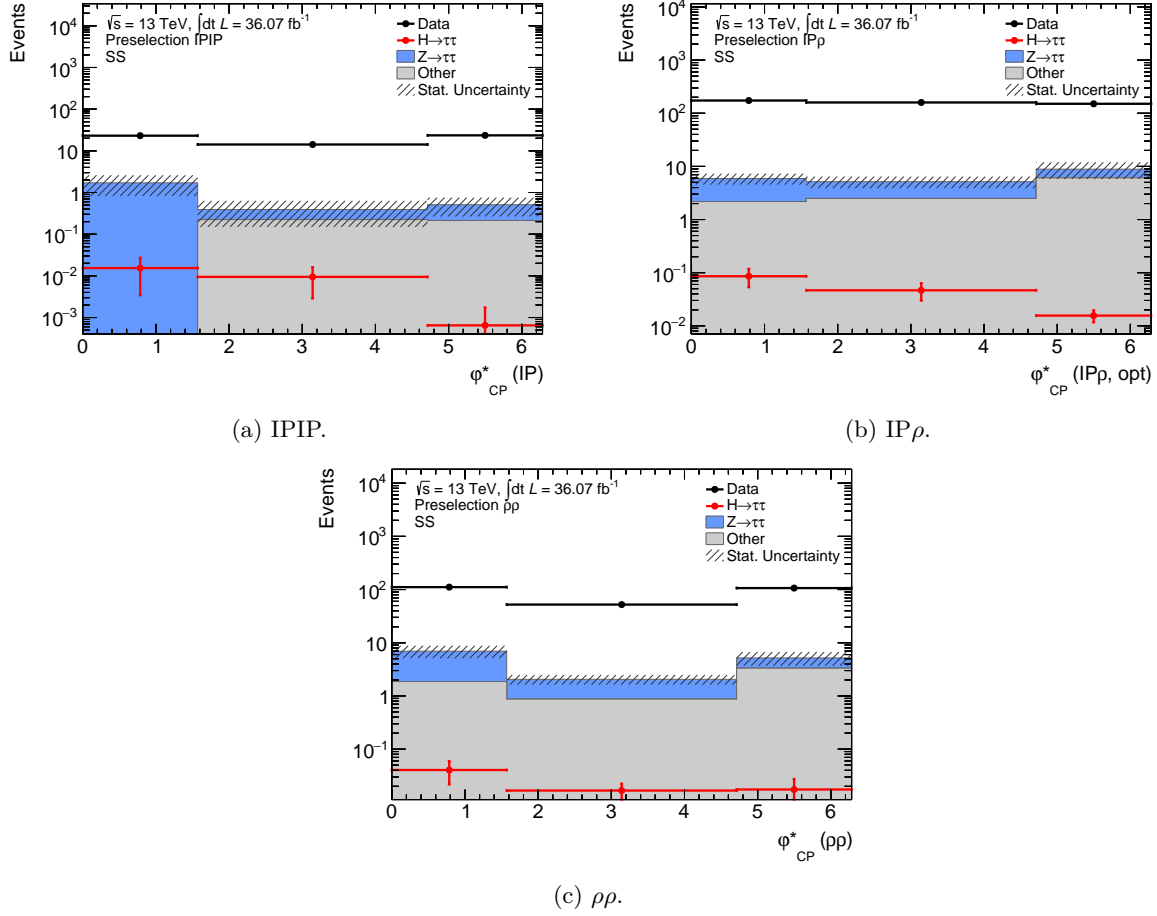


Figure 6.7: Contamination from real- τ backgrounds in the SS control region for each decay mode at preselection.

is, thus, not a significant enough feature. A validation is also performed in the anti- $\tau_{\text{had, vis}}$ ID region enriched with fake- τ candidates, which suffers from less MC contamination to compare the shapes in the OS and SS regions. Figure 6.9 shows the compatibility of the fake- τ shape in the anti- $\tau_{\text{had, vis}}$ ID region in the OS and SS regions. Based on these results, the \mathcal{CP} sensitivity estimates are performed on both the SS fake- τ background template and the uniform background template normalized to the expected fake- τ event yield. Appropriate systematic uncertainties on both methods are described in Section 6.6.

The normalization of the MC $Z \rightarrow \tau\tau$ and data-driven fake- τ backgrounds, r_Z and r_{QCD} , respectively, are obtained from a template fit to $m_{\text{MMC}}^{\tau\tau}$ in OS data at the preselection level. Moreover, it is performed in an extended $70 < m_{\text{MMC}}^{\tau\tau} < 140$ GeV range (called the QCD fit region). The template fit procedure was previously described in Section 5.7.2.1 for the $H \rightarrow \tau\tau$ analysis (see Equation 5.11). The differences in the \mathcal{CP} analysis are the definition of the preselection criteria, the discriminant used ($m_{\text{MMC}}^{\tau\tau}$ instead of $\Delta\eta$), and the SS control region instead of the nOS control region. (A summary was previously shown in Table 6.3.) In addition, the fit is performed separately for each decay mode as the r_Z and r_{QCD} factors are dependent on the decay mode. They are not performed per VBF and Boosted category since these fits are unstable due to the limited statistics. Table 6.4 shows the background

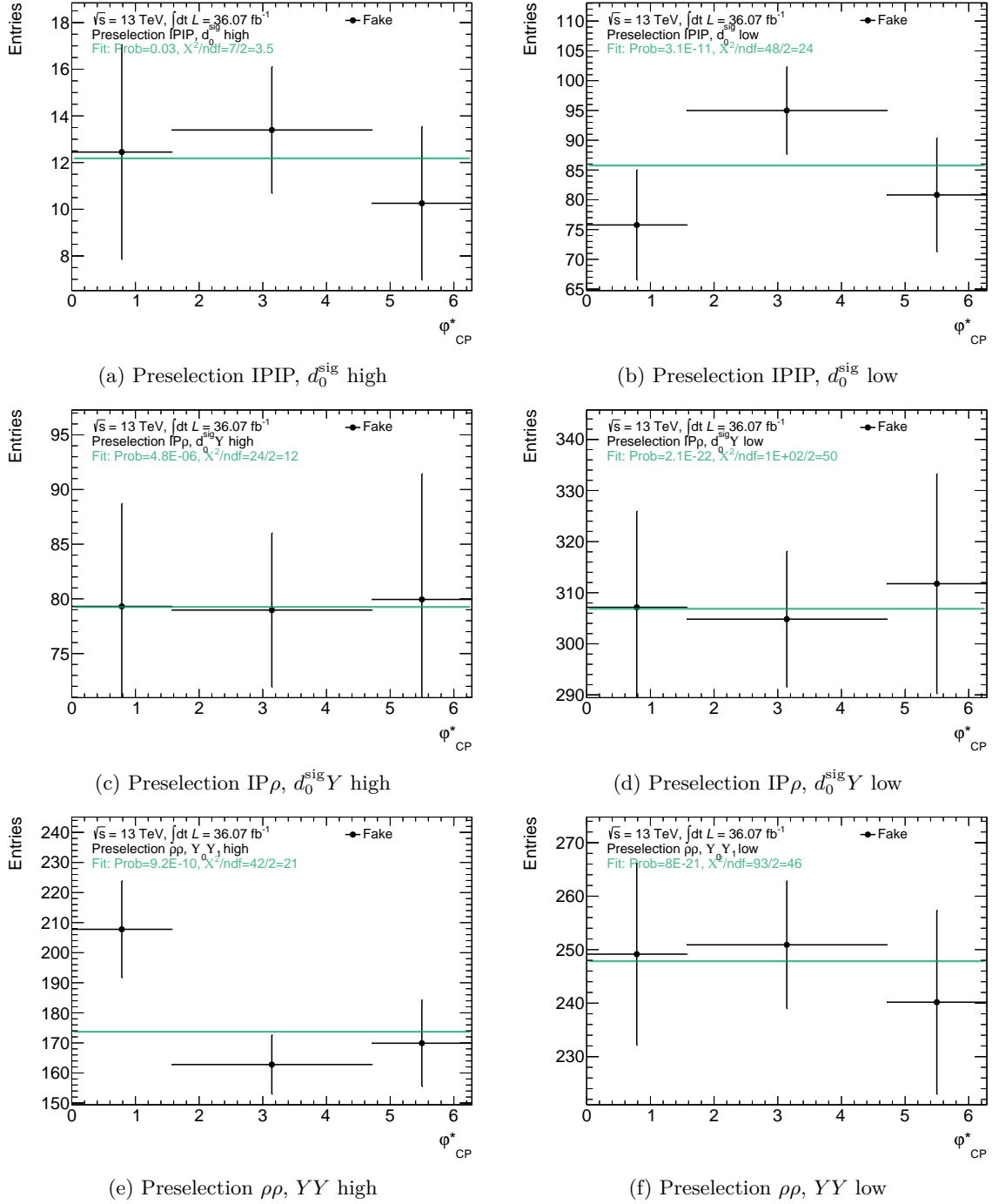


Figure 6.8: Compatibility of the SS fake- τ shape from data with a uniform distribution. The error bars show the statistical uncertainties only.

normalization values for each decay mode, and Figure 6.10 shows the $m_{\text{MMC}}^{\tau\tau}$ distribution after the background normalization. Figure 6.11 shows the φ_{CP}^* observable for each decay mode at preselection. (See Appendix K for each signal category.)

The r_{QCD} factor obtained from the template fit is used as a starting value for the fake- τ

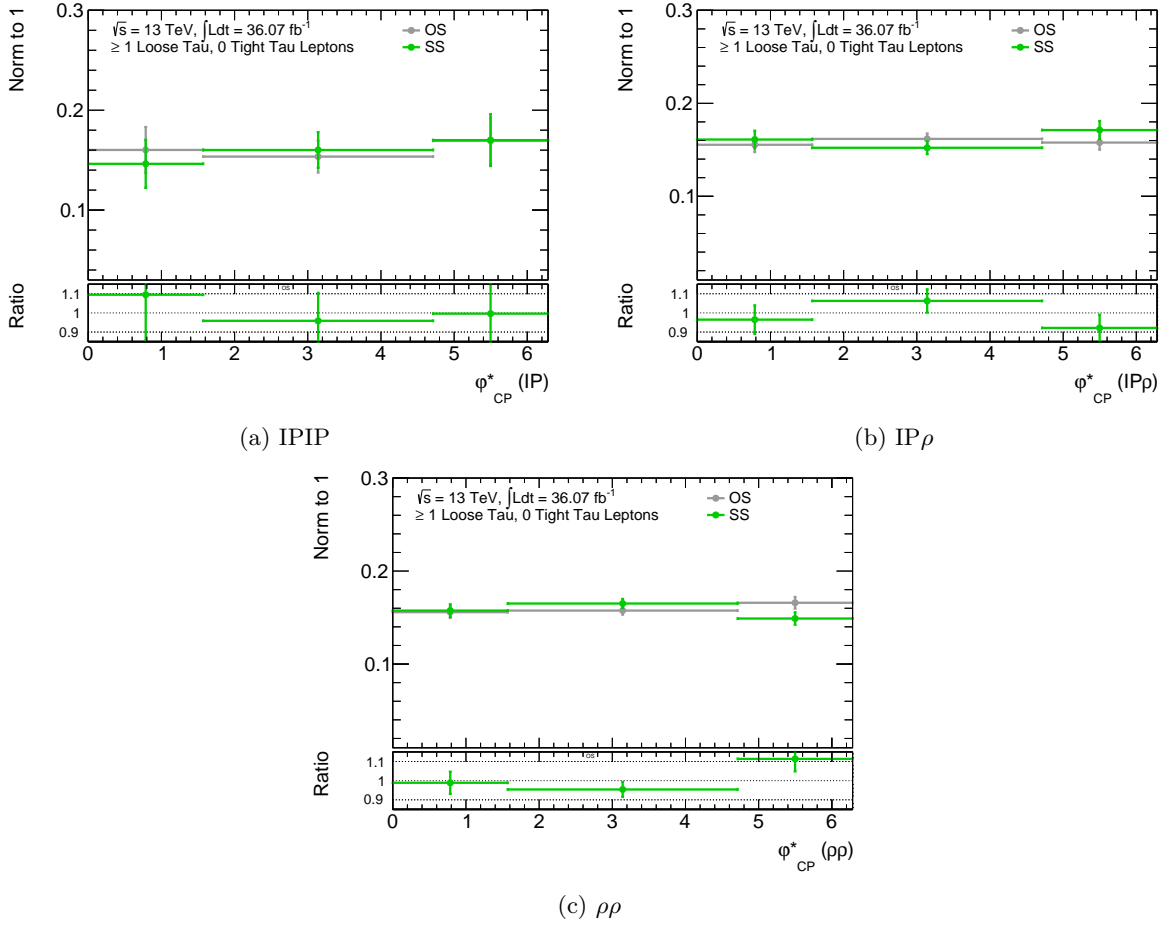


Figure 6.9: The fake- τ background shapes in OS and SS events of the anti- $\tau_{\text{had, vis}}$ ID region at preselection level.

Fit parameter	IPIP Method	$IP\rho$ Method	$\rho\rho$ Method
r_{QCD}	1.35 ± 0.235	1.77 ± 0.00425	1.47 ± 0.0990
r_Z	0.98 ± 0.0860	0.89 ± 0.0223	1.03 ± 0.0443

Table 6.4: Normalization factors after the prefit background estimation (c.f. Figure 6.10).

normalization in the final fit for the \mathcal{CP} sensitivity estimate, described later in Section 6.7. Unlike the $H \rightarrow \tau\tau$ analysis, however, the $Z \rightarrow \tau\tau$ normalization is fixed in the final fit. This is because the φ_{CP}^* observable is used as the discriminant in the final fit, and the $Z \rightarrow \tau\tau$ and fake- τ backgrounds exhibit uniform φ_{CP}^* shapes. Only the fake- τ normalization is allowed to vary in the fit (using the prefit r_{QCD} result as the starting value) to account, for example, for the extrapolation of the normalization from preselection to each signal region.

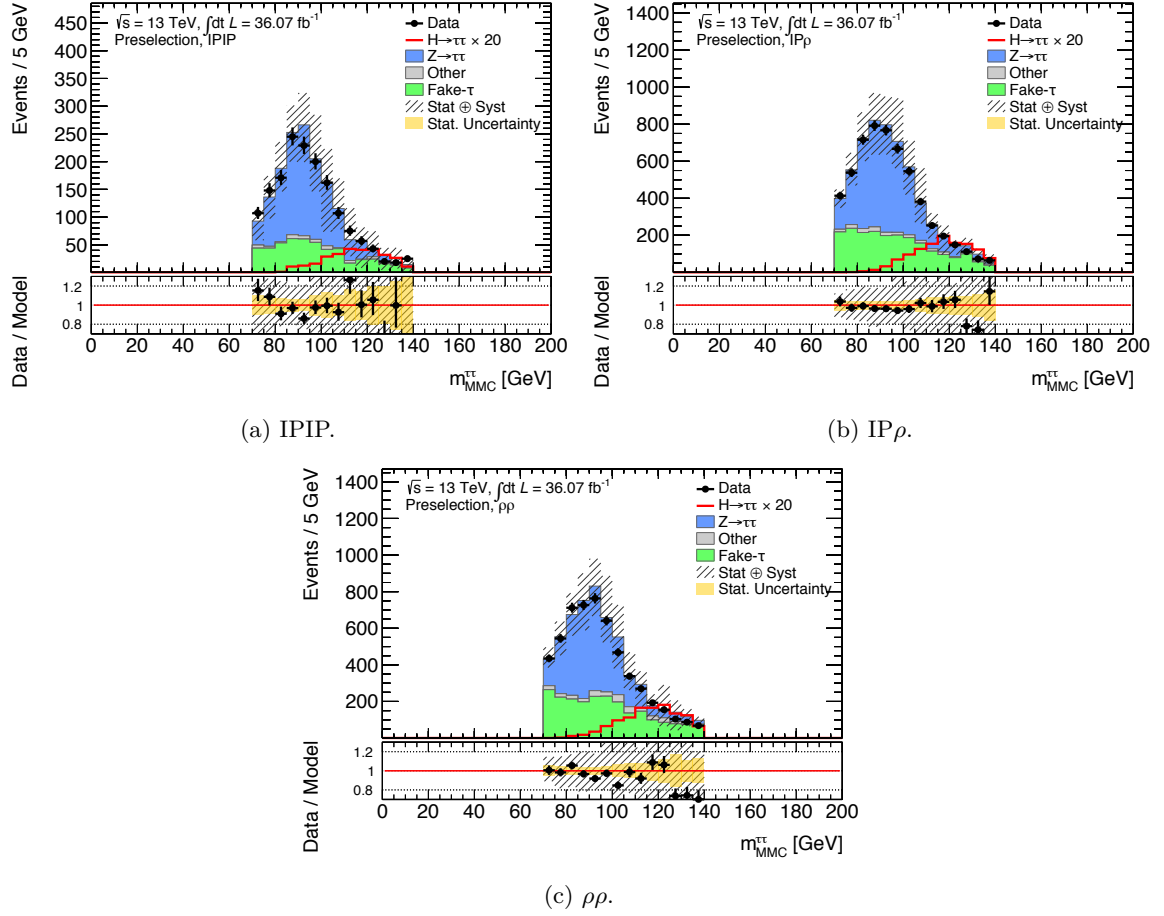


Figure 6.10: Prefit background estimation using a fit to $m_{\text{MMC}}^{\tau\tau}$ in the $70 < m_{\text{MMC}}^{\tau\tau} < 140$ GeV region for each decay mode. See Table 6.4 for the r_{QCD} and r_Z values.

6.5.3 Background model validation

The background model is validated at the preselection level and in the signal categories. In the signal categories, the modeling of the φ_{CP}^* observable is checked in the $70 < m_{\text{MMC}}^{\tau\tau} < 100$ GeV region only, i.e., blinded in the Higgs boson signal region. The blinded φ_{CP}^* distributions and the distributions of important observables used to define the Higgs CP signal regions ($|d_0^{\text{sig}}|$, Y , and $|YY|$) are shown in Appendix K. The figures show that the expected distributions of the observables are consistent with the observed data within the uncertainties. The expected event yields in each signal category are listed in Table 6.2.

6.6 Systematic uncertainties

The same systematic uncertainties from the $H \rightarrow \tau\tau$ analysis are used in the Higgs CP analysis (see Section 5.8), with the background estimation uncertainties adapted for the CP analysis. Additional systematic uncertainties for the use of substructure reconstruction must be derived and are still under investigation. In this section, the systematic uncertainties from the fake- τ and $Z \rightarrow \tau\tau$ background estimation methods are first described. Then, sources of uncertainties

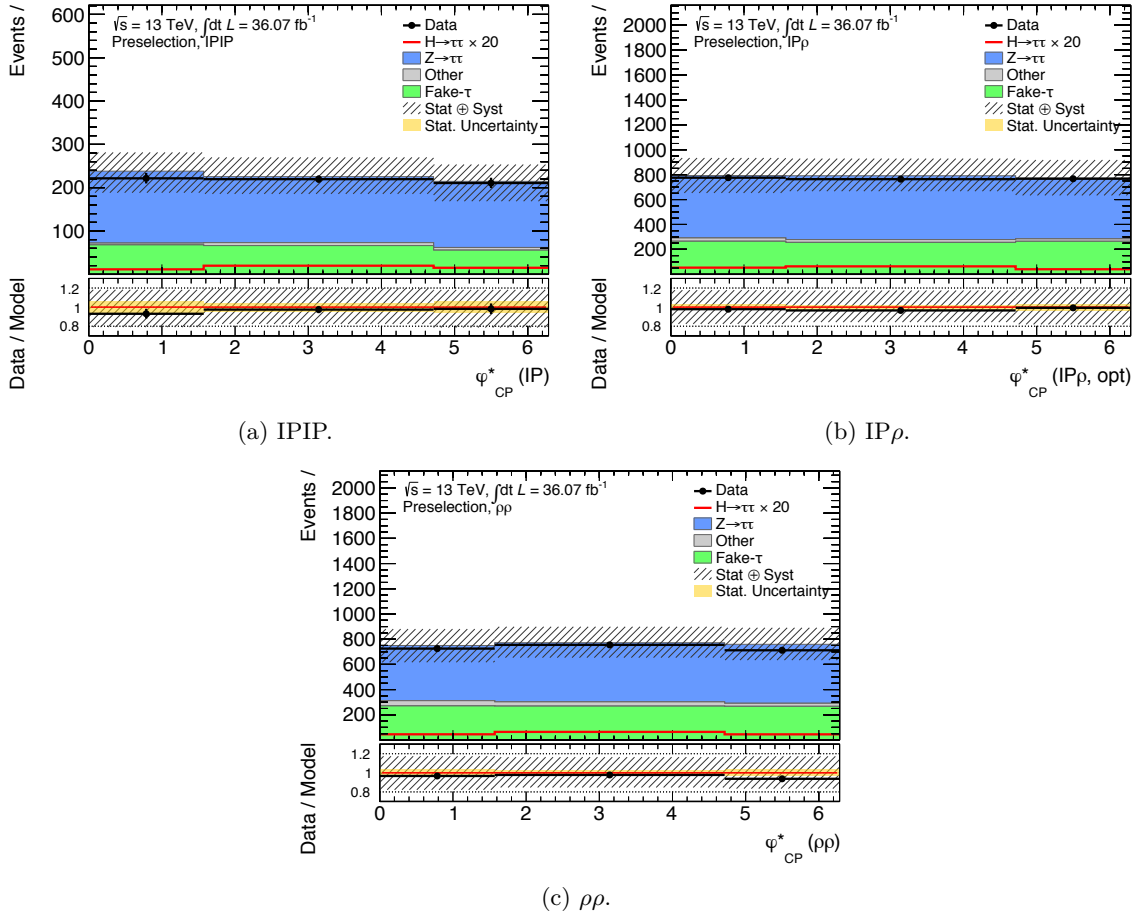


Figure 6.11: Modeling of the φ_{CP}^* distribution in the HCP analysis for the $70 < m_{MMC}^{\tau\tau} < 100$ GeV region, i.e., blinded in the $100 < m_{MMC}^{\tau\tau} < 140$ GeV region. See Appendix K for the distributions in each signal category.

from the substructure reconstruction are identified. The profit impact from the systematic uncertainties for each signal category is listed in Appendix L.2 for the $\phi_\tau = 0^\circ$ case as an example.

6.6.1 Systematic uncertainties on the fake- τ background estimation

The fake- τ background systematic uncertainties on the OS-nOS method are adapted for the OS-SS method used in the CP analysis. The fake- τ extrapolation systematic uncertainty is evaluated for each φ_{CP}^* observable, as it was for the $m_{MMC}^{\tau\tau}$ observable in the $H \rightarrow \tau\tau$ analysis. Figure 6.12 shows the ratio between the fake- τ background templates in the OS and SS regions at different levels of anti- $\tau_{had, vis}$ ID. Since the $\frac{OS}{SS}$ shapes are compatible for the different anti- $\tau_{had, vis}$ ID levels, the loosest anti- $\tau_{had, vis}$ ID region, requiring at least one loose τ_{had} candidate and no tight τ_{had} candidates, is used for the Fake- τ extrapolation systematic. This anti- $\tau_{had, vis}$ ID level is used because the CP analysis is more statistically dominated than the $H \rightarrow \tau\tau$ analysis, and the CP analysis is not affected by the mismodeling of the low $m_{MMC}^{\tau\tau}$ region.

For the uniform fake- τ background method, systematic uncertainties on the uniform distribu-

tion method are derived allowing each bin to vary by the difference observed in the anti- $\tau_{\text{had, vis}}$ ID region. This allows for bin-by-bin fluctuations to account for possible deviations from a uniform distribution instead of an overall template scaling. Currently, it is implemented as one NP per bin across all categories. When there is more data, this treatment can be made more detailed with an NP allowing each bin in each category to vary.

6.6.2 Systematic uncertainties on the $Z \rightarrow \tau\tau$ background estimation

Since the $Z \rightarrow \tau\tau$ background is taken from the Z -peak region in the data, a shape systematic uncertainty is included for the difference between the $Z \rightarrow \tau\tau$ templates in the Z region and the Higgs boson region (see Figure 6.6). In addition, since the fake- τ and other backgrounds are subtracted from the Z region in data, a shape systematic uncertainty is included for possible errors in subtraction. This systematic uncertainty allows the $Z \rightarrow \tau\tau$ shape to vary by the $\pm 1\sigma$ statistical uncertainty on the total fake- τ and other background subtracted in each bin.

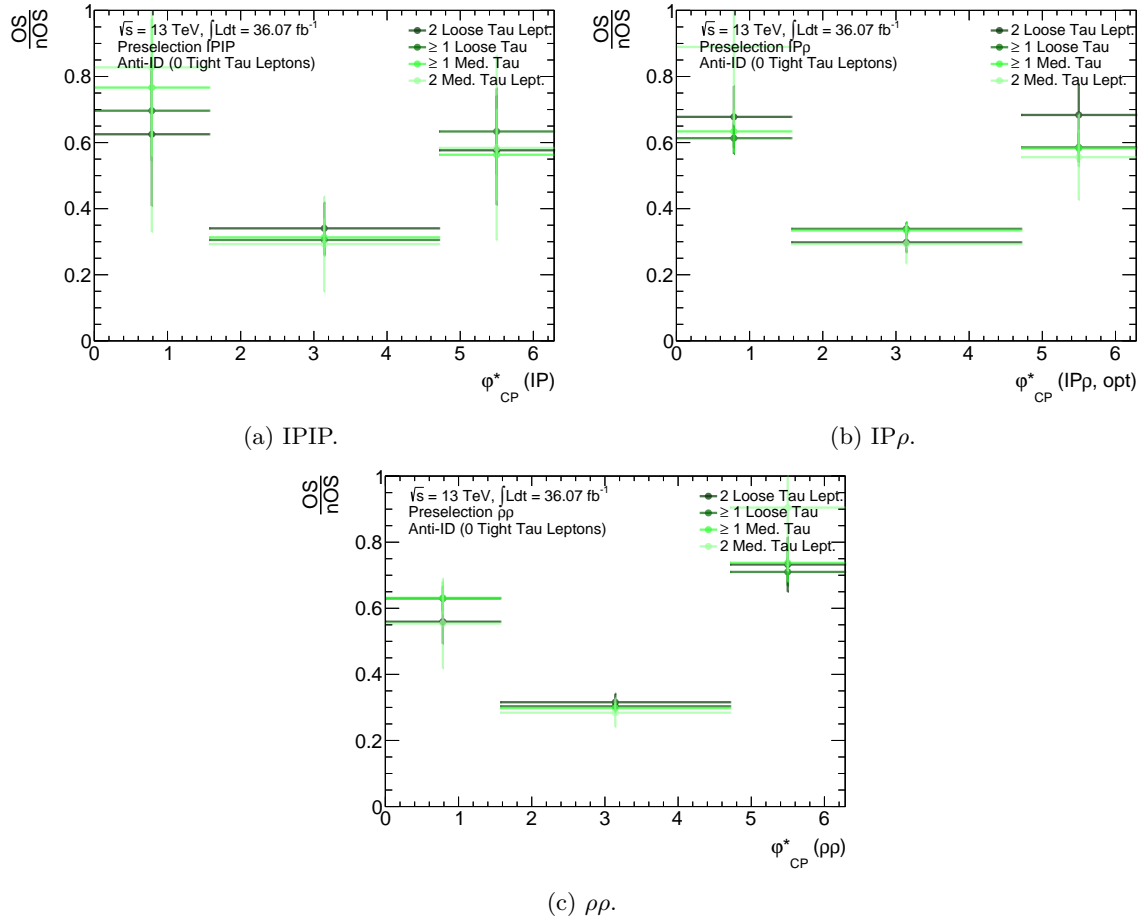


Figure 6.12: φ_{CP}^* shape comparisons in the anti- $\tau_{\text{had, vis}}$ ID region for each decay mode at the preselection level.

6.6.3 Systematic uncertainties from the substructure reconstruction

The largest source of uncertainties is expected to stem from the systematic uncertainties concerning the use of substructure algorithm in the CP analysis to reconstruct the neutral pions.⁵ The uncertainties that need to be addressed come from many different effects, including:

- Track reconstruction effects that can mismodel the impact parameter reconstruction for the IP method.
- Effects from tau decay mode misclassification (c.f. Figure 4.15(b)) that alter, for example, the expected yields of signal and background events, the composition of signal and background contribution, and the relative amplitude of the φ_{CP}^* observable. In addition, misreconstructed decay modes could potentially alter the expected uniform background template of the φ_{CP}^* observable and mimic a signal.
- Effects from the finite 4-momentum resolution of each pion reconstructed by the substructure algorithm (c.f. Figure 4.14).
- Effects from object/event selection requirements for the signal regions of the Higgs CP analysis, especially the differences of these requirements at reconstruction level compared to the generator level. The most significant effects on the relative amplitude of φ_{CP}^* come from:
 - The \cancel{E}_T and p_T selection, which affect the individual pion resolution: with increasing \cancel{E}_T there is a greater degradation in the relative amplitude since the neutrinos carry away more energy, resulting in a greater difference between the visible τ_{had} frame and the true τ_{had} frame. The principle is the same with increasing p_T , where the reconstructed visible τ_{had} frame becomes closer to the true τ_{had} frame [158].
 - The YY observable: Values of $|YY|$ closer to 0 correspond to a smaller relative amplitude since resolution effects from YY are more likely to result in false sign flips (see Equation 6.7).
- Differences in the acceptance of events into the signal categories between the MC and reconstruction.
- Substructure-dependent differences in reconstruction for MC and observed data samples from using the tau trigger and $\tau_{\text{had, vis}}$ ID.

On top of this, these effects can be correlated in a complicated way.

To start to address the effects, systematic uncertainties on the π^0 reconstruction can be derived from a smearing of the π^0 4-momentum. In addition, systematic uncertainties on the differences in performance between simulation and reconstruction of the substructure algorithm can be derived from a calibration of the φ_{CP}^* distribution using the MC $Z \rightarrow \tau\tau$ sample. This is one of the motivating factors for replacing the MC $Z \rightarrow \tau\tau$ background with $Z \rightarrow \tau\tau$ events from data in the background model. The most important reconstruction effects are estimated to be from the frame reconstruction for the Y_+Y_- calculation, the neutral pion angular reconstruction, and the decay mode classification [142].

⁵ The charged pions are reconstructed from tracks, which have good momentum resolution.

6.7 Fit model and sensitivity estimate

The parameter of interest (POI) of the CP analysis, the CP mixing angle (ϕ_τ), is measured using the same template fit procedure as in the $H \rightarrow \tau\tau$ analysis, described previously in Section 5.9. Instead of using the $m_{\text{MMC}}^{\tau\tau}$ observable as the final discriminant, however, the CP analysis uses the φ_{CP}^* observable. The template fit is performed for different CP mixing angle hypotheses, from $\phi_\tau = -80^\circ$ to $\phi_\tau = 90^\circ$ in steps of 10° , as discussed previously in Section 6.2.

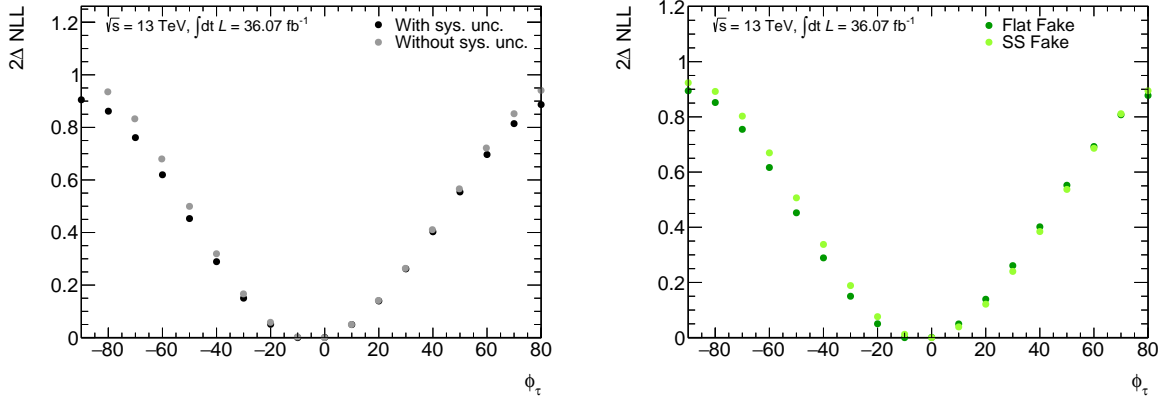
A fit model for each CP mixing hypothesis is built according to Equation 5.20, analogous to the single fit model for the SM Higgs boson in the $H \rightarrow \tau\tau$ analysis. In each fit model, the background model remains the same, while the signal template for the respective CP mixing angle is used. The signal normalization is either fixed to the SM prediction (μ fixed) or allowed to float (μ fitted) such that the analysis is model independent. (The fits for these two cases are performed in separate measurements.) A binned maximum likelihood fit is performed for each hypothesis to measure their ΔNLL values. Each fit is validated, and an example of the NP pulls and rankings is shown in Figure 6.14 for the $\phi_\tau = 0^\circ$ hypothesis with Asimov data.

The CP sensitivity estimate is obtained by computing the difference between the minimum NLL value and the NLL values for the other CP angle hypothesis. The expected CP sensitivity estimate performed on Asimov data is shown in Figure 6.13(a) with and without systematic uncertainties for the case where μ is allowed to be fitted.⁶ The fit is stable and yields the same $\phi_\tau = 0^\circ$ mixing angle that was used to build the Asimov data. Since the $2\Delta\text{NLL}$ value between the purely CP -odd and hypothesis for CP -odd mixing is less than one, the analysis is not expected to exclude the CP -odd hypothesis at even the 68% confidence level (c.f. Equation 5.26). In addition, it shows that the systematic uncertainties have minimal impact on the sensitivity and that the current analysis is statistically dominated, although this conclusion is incomplete since the systematic uncertainties addressing the substructure reconstruction are not yet available. The sensitivity estimates comparing the SS fake- τ template and the uniform fake- τ template are shown in Figure 6.13(b). Since the fit to Asimov data is shown to be stable and performs similarly with the uniform fake- τ template, the analysis presented in this dissertation is finalized to use the uniform distribution for the fake- τ background, with appropriate systematic uncertainties, instead of using the SS template that contains additional statistical fluctuations. It also uses data from the Z -peak region for the $Z \rightarrow \tau\tau$ background. In future analyses, the sensitivity estimate can be improved by interpolating between the 10° angle points to determine the mixing angle at the minimum NLL value more precisely.

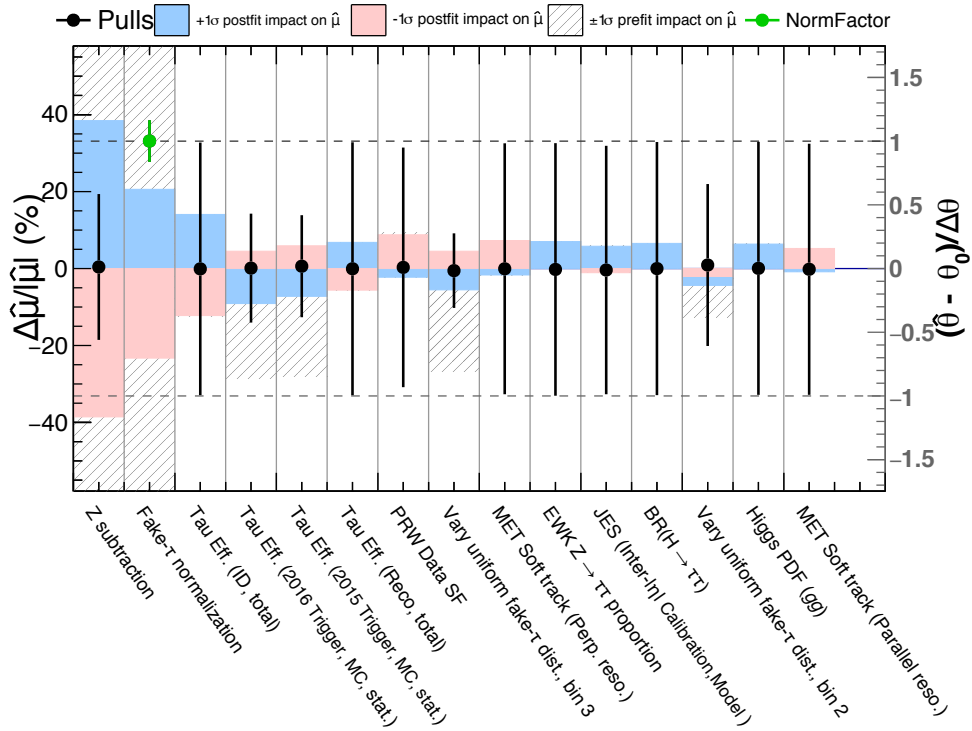
6.7.1 Toy experiments

Although the fit to Asimov data is stable, the small sample size suggests that the Higgs CP analysis is within the limit in which the asymptotic distributions of the test statistics derived using the results of Wilks and Wald are valid (i.e., the asymptotic limit) [152]. In order to be properly validated, the fit is repeated many times with toy experiments in which the data are built by randomly sampling from a Poissonian or Gaussian distribution around the expected value for each bin of the φ_{CP}^* discriminant variable. The values from which the toy experiments sample take into account systematic uncertainties by first randomly sampling a value from a Poissonian or Gaussian around each NP. Figure 6.15 shows an example of the cumulative best fit ϕ_τ result from 1000 toy experiments, which are randomly sampled from the background-

⁶ The fit where μ is fixed to the SM prediction shows similar sensitivity.



(a) Sensitivity with and without systematic uncertainties.

(b) Sensitivity estimate with uniform vs SS fake- τ background.Figure 6.13: Expected \mathcal{CP} sensitivity for different configurations of the final fit: with and without systematic uncertainties (left) and with the uniform vs. SS fake template (right).Figure 6.14: The ranking of NPs for the Asimov fit according to their postfit impact on μ (filled blue and red bands), i.e., $\Delta\hat{\mu}/|\hat{\mu}|$, calculated by fixing that NP to the $\pm 1\sigma$ uncertainty on its postfit value and repeating the fit (c.f. Section 5.9.3). Shown as an example for the $\phi_\tau = 0^\circ$ hypothesis. The pulls (black dots) with the postfit uncertainties on the NPs (black lines with respect to the black dots) are also shown. Normalization factors are shown in green, where a value of 1 means that the postfit normalization matches the prefit normalization.

plus-signal $\phi_\tau = 0^\circ$ hypothesis as an example. These 1000 toy experiments are generated for each background-plus-signal hypothesis ($\phi_\tau \in \{-80, 90\}$ in 10° steps). About 9% of the toy

experiments show NLL curves with double minima when μ is fixed, and about 15% of the toy experiments exhibit double minima when μ is fitted. The remainder of the fits are otherwise stable. The cumulative results are fitted using a Gaussian distribution

$$\text{Gaus}(\phi_\tau) = ae^{-\frac{(\phi_\tau - b)^2}{2c^2}}, \quad (6.13)$$

with a best fit ϕ_τ of $b = 2.5 \pm 0.6$ and a width of $c = 18.3 \pm 0.7$ for the case where μ is fixed (see Figure 6.15(a)). For the case where μ is floated, the best fit ϕ_τ is $b = -1.0 \pm 0.9$ with a width of $c = 27.5 \pm 0.9$ (see Figure 6.15(b)). The core of the distribution is consistent with a Gaussian distribution. The deviation from a Gaussian distribution may be because the determination of the best fit ϕ_τ is not performed with an interpolation between mixing angles. The deviations could also, in general, be caused by the fact that the toy datasets are samples from a statistically limited distribution and may suffer from the statistical fluctuations.

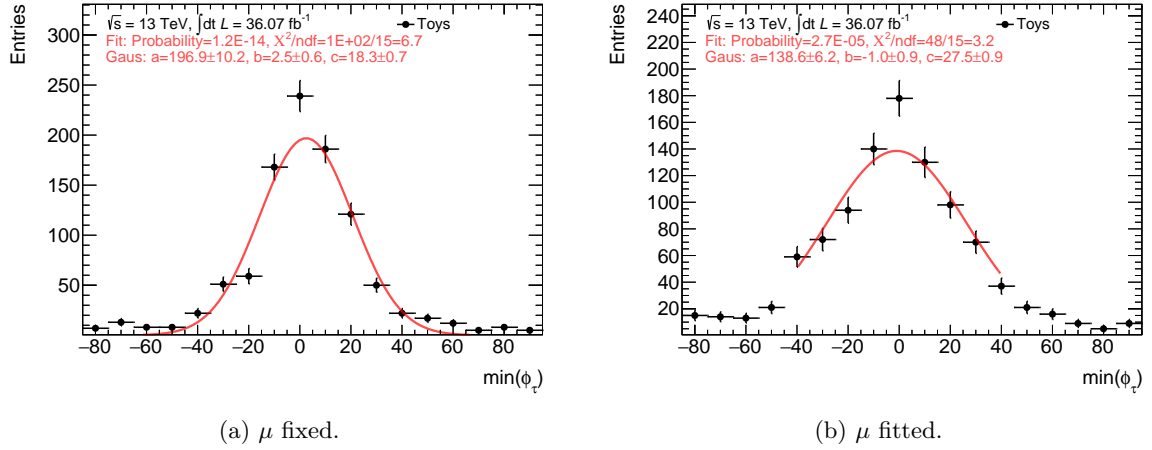


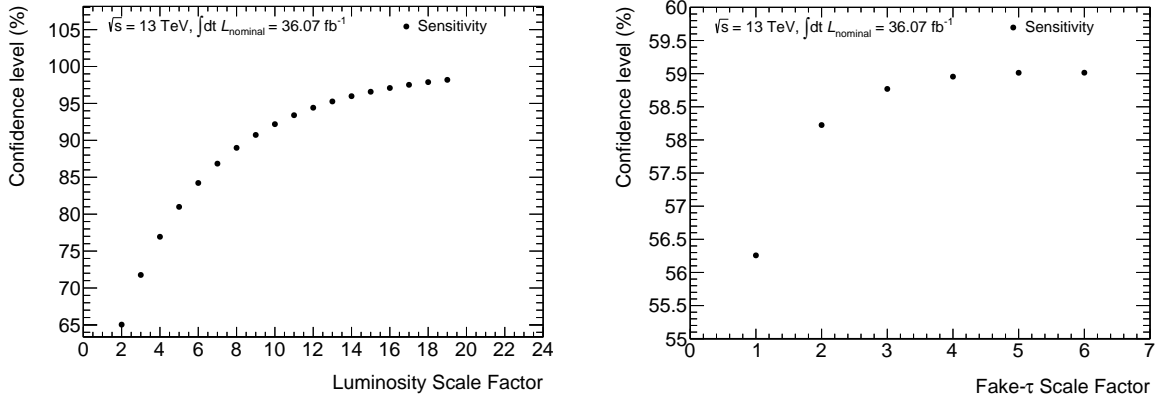
Figure 6.15: Results of the toy experiments from randomly sampling around the background-plus-signal model for the $\phi_\tau = 0^\circ$ hypothesis.

6.8 Sensitivity projection

Given the low sensitivity of the analysis with the finalized setup, a sensitivity projection is performed before fitting to observed data to identify the impediments of the analysis and possible improvements. If the sensitivity is hindered by the limited integrated luminosity, the amount of additional integrated luminosity needed to exclude, for example, the purely CP -odd case at the 95% confidence level can be quantified. If hindrances come from the size of the background or signal samples, more statistically powerful samples or control regions can be investigated.

With the current setup and integrated luminosity, not even the purely CP -odd hypothesis can be excluded at the 68% confidence level, let alone any CP mixing hypotheses. To determine the amount of additional luminosity needed to at least exclude the CP -odd hypothesis at a certain confidence level, a luminosity extrapolation is performed. For these studies, the Asimov data, as well as the signal and background templates, are scaled up by a scale factor, N . Additionally, the systematic uncertainties are not taken into account since the analysis is statistically limited, and the uncertainties are, in any case, not yet fully developed. Figure 6.16(a) shows that about

13 times more integrated luminosity is needed to exclude the CP -odd hypothesis at the 95% confidence level (corresponding to $2\Delta\text{NLL}=4$ as previously presented in Equation 5.26).



(a) Luminosity projection showing that the CP -odd hypothesis can be excluded at 95% CL when about 13 times the current integrated luminosity is achieved. (b) Sensitivity projection when the sample size of the respective template increases by a given scan factor.

Figure 6.16: Projection of the Higgs CP sensitivity estimate when the sizes of the data, signal, and fake- τ samples are extrapolated to higher luminosity. The y -axes show the confidence level (CL) for which the CP -odd hypothesis can be excluded, i.e., $2\Delta\text{NLL}$ ($\phi_\tau = 0^\circ, \phi_\tau = 90^\circ$) (c.f. Equation 5.26).

It is also interesting to see how much the sizes of the background and/or signal samples impact the CP sensitivity estimate with the current integrated luminosity. For example, the simulated samples from which the MC templates are derived can be increased by producing more simulated events. In the case of the data-driven fake- τ background template where the SS control region is used, the sample size for the fake- τ template can be increased by, for example, using a larger control region. Instead of taking only SS events from the Higgs boson mass region, a larger mass region can be used since the CP properties of the fake- τ background are expected to be random in the inclusive regions as well. To study this, the statistical uncertainties on the expected data are kept constant while the background templates are scaled up by a scale factor, N , i.e., the statistical uncertainties on each template are scaled down by \sqrt{N} . Figure 6.16(b) shows an example of the increase in CP sensitivity when the statistical uncertainties on the SS fake- τ background template are scaled down (for the case where the SS control region is used instead of the uniform fake- τ template). It shows that that the sensitivity is not dominated by the lack of statistics. The maximum obtainable sensitivity with the current integrated luminosity begins to asymptote. Even at this asymptote, the CP -odd hypothesis cannot be excluded at the 68% confidence level. Similar asymptotic behavior is seen when scaling the statistical uncertainties on the signal and the $Z \rightarrow \tau\tau$ background samples down.

For the purposes of distinguishing between the purely CP -odd and CP -even cases, the periodicity of the φ_{CP}^* observable can be changed from $0^\circ - 360^\circ$ to $0^\circ - 180^\circ$, resulting in a 2-bin φ_{CP}^* observable and thereby doubling the sample size. With the current data sample, fits to the 2-bin observable are unstable. However, this observable can, in principle, be used in combination with the output from multivariate studies presented in the next section.

6.9 Addition of a_1 decay modes with machine learning

In the Higgs CP analysis, a significant fraction of the available events is unused in cases where the tau decays into more than two visible decay products. In principle, it only utilizes 6.7% of the $H \rightarrow \tau\tau$ events (1p0n-1p0n, 1p0n-1p10n, and 1p1n-1p1n events). Given the luminosity projection result in Section 6.8, further studies are performed in this dissertation to increase the amount of usable events by adding a_1 decay modes. In principle, including events where at least one of the τ_{had} candidates decays via the 3p0n mode can add 7.0% (c.f. Table 2.6). The $a_1^\pm \rightarrow \pi^\pm\pi^\pm\pi^\mp$ decay mode is considered since the $a_1^\pm \rightarrow \pi^\pm\pi^0\pi^0$ decay mode suffers from poor reconstruction due to the additional neutral pions. Building a CP sensitive observable for the ρa_1 (1p1n-3p0n) and $a_1 a_1$ (3p0n-3p0n) cases can, in principle, add an additional 4.6% and 8% of the lost events, respectively. The caveat is that events where the τ_{had} candidate decays via the a_1 , such as the ρa_1 and $a_1 a_1$ decay modes, have a lower Higgs CP sensitivity. This is because the mass of the ρ is much smaller than the tau mass, as discussed in Section 2.2.1. The helicity of the ρ is, therefore, better defined than that of the a_1 . In addition, a decay plane for the tau candidate(s) that decayed via the a_1 needs to be reconstructed from the three final state pions.

Moreover, since there are multiple pions in the final state for these decay modes, it is necessary to identify which pions came from the corresponding ρ and/or a_1 decay chains. In this section, it is shown that the acoplanarity angle between the ρ and/or a_1 decay planes reconstructed using rudimentary kinematic variables achieves an additional separation of about 1% to 2% better than random guessing between the CP -odd and CP -even states. Using a machine learning method, this additional separation can be improved by about 5 to 10%. These machine-learning studies are performed for the simplest case of distinguishing between a purely CP -even and CP -odd Higgs boson. Distinguishing CP mixing states are not considered since the luminosity projection studies in Section 6.8 show that there is not enough sensitivity to achieve even the simplest case. Moreover, the output from the machine-learning method can be used to build a 2-bin distribution for distinguishing only the CP -even and CP -odd states, analogous to the 2-bin φ_{CP}^* observable discussed in Section 6.8. In this way, it can be included with the φ_{CP}^* observable for the 1p0n and 1p1n decay modes.⁷ The machine-learning method is trained and tested on generator-level samples and then applied on the reconstruction level. This is done because the sizes of the generator-level samples are larger and because tracks are known to be reconstructed with a high resolution.

6.9.1 The ρa_1 method

In the ρa_1 case, there are four different possibilities for building an observable analogous to φ_{CP}^* for the acoplanarity angle. A schematic of some of the possible angles/planes is shown in Figure 6.17. A machine-learning method can be used to better identify the pions that most likely came from the corresponding ρ and a_1 decay chains. To determine the most likely assignment of pions, the 4-vectors of each visible decay product (π^\pm and π^0) are first boosted into the $\tau_{\text{vis}}^\pm - \tau_{\text{vis}}^\mp$ rest frame. The tau decay plane for the τ_{had} candidate that decays to a $\pi^\pm\pi^0$ pair is defined as the plane spanned by their 3-vectors: $\vec{v}_{\pi^\pm} \times \vec{v}_{\pi^0}$.

For the τ_{had} candidate that decays via the a_1 , two oppositely-charged pions of the three charged pions ($a_1 \rightarrow \pi^\pm\pi_1^\mp\pi_2^\mp$) can be combined to form the ρ resonance from the a_1 , assuming the a_1 has decayed via the ρ resonance. Since it is not known which of the two oppositely-charged

⁷ Alternatively, machine-learning studies can be performed as a regression problem, where a continuous output is produced.

pions came from the ρ resonance, both possible pairings are considered. The a_1 plane is the plane spanned by the $\rho\pi^\pm$ pair $(\vec{v}_\rho \times \vec{v}_{\pi_{1,2}^\mp})$. Angles from using the ρ plane of the ρ from the a_1 decay are also \mathcal{CP} sensitive. Therefore, the $(\vec{v}_{\pi^\pm} \times \vec{v}_{\pi_{1,2}^\mp})$ pair is also considered.

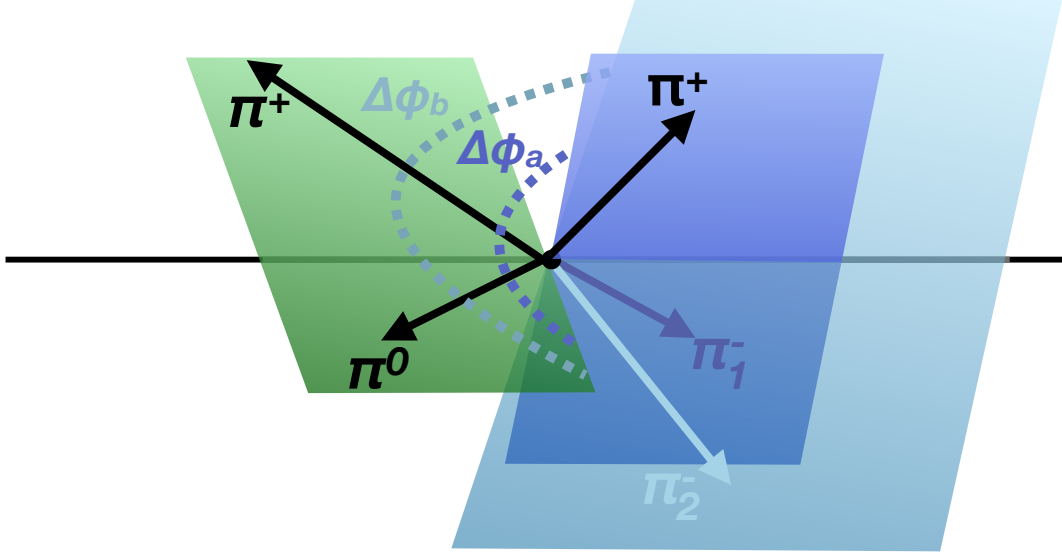


Figure 6.17: Schematic of $\Delta\phi$ angles between the plane spanned by the $\pi^\pm\pi^\mp$ decay products from the $\tau \rightarrow (\rho \rightarrow)\pi^\pm\pi^\mp$ decay and example planes spanned by two of the three decay products from the $\tau \rightarrow (a_1 \rightarrow)\pi^\pm\pi_1^\mp\pi_2^\mp$ decay. Shown in the $\tau_{\text{vis}}^\pm\tau_{\text{vis}}^\mp$ rest frame.

For the calculation of the $\Delta\phi$ angle between the two tau decay planes, one plane is designated the reference frame to which the angles for all other planes are measured. Therefore, the ϕ of the $\vec{v}_{\pi^\mp} \times \vec{v}_{\pi^\pm}$ plane for the ρ decay mode is, by definition and without loss of generality, 0. The $\Delta\phi$ angle formed from the a_1 plane (written in a lighter color to differentiate the two τ_{had} candidates) is then calculated with respect to this ρ plane, yielding four possible angles:

1. $\Delta\phi(\vec{v}_{\pi^\pm} \times \vec{v}_{\pi^0}, \vec{v}_\rho \times \vec{v}_{\pi_1^\mp})$
2. $\Delta\phi(\vec{v}_{\pi^\pm} \times \vec{v}_{\pi^0}, \vec{v}_\rho \times \vec{v}_{\pi_2^\mp})$
3. $\Delta\phi(\vec{v}_{\pi^\pm} \times \vec{v}_{\pi^0}, \vec{v}_{\pi_1^\mp} \times \vec{v}_{\pi^0})$
4. $\Delta\phi(\vec{v}_{\pi^\pm} \times \vec{v}_{\pi^0}, \vec{v}_{\pi_2^\mp} \times \vec{v}_{\pi^0})$

These angles are hereafter called either $\varphi_{\rho a_1}^*$ or φ_{CP}^* . Analogous to Y in Equation 6.8, the Y variables for the ρ^0 case and the a_1 case, which includes a mass correction term, are

$$y_{\rho^0} = \frac{E_{\pi^\pm} - E_{\pi^\mp}}{E_{\pi^\pm} + E_{\pi^\mp}}, \quad y_{a_1} = \frac{\frac{E_\rho}{N} - \frac{E_{\pi^\pm}}{1-N}}{\frac{E_\rho}{N} + \frac{E_{\pi^\pm}}{1-N}}, \quad (6.14)$$

where $N = \frac{m_{a_1}^2 - m_{\pi^\pm}^2 + m_\rho^2}{2m_{a_1}^2}$ [66]. The $\Delta\phi$ angles are then separated using these Y variables, analogously to Equation 6.7.

6.9.2 The $a_1 a_1$ method

For the $a_1 a_1$ method, combinatorics yield 16 possible angles for the four possible decay planes of the a_1^\pm and a_1^\mp each. A schematic of some of the possible planes and the $\Delta\phi$ angles between them is shown in Figure 6.18.

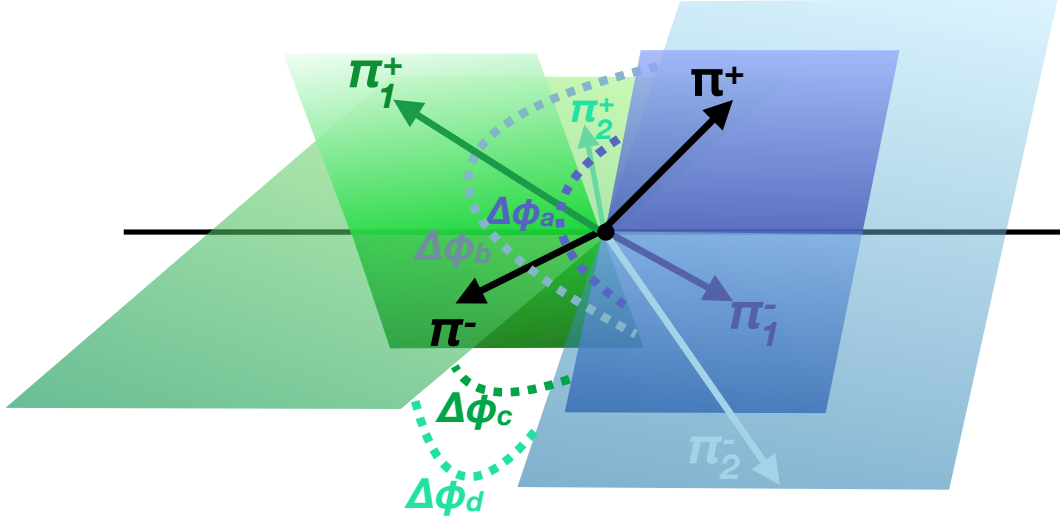


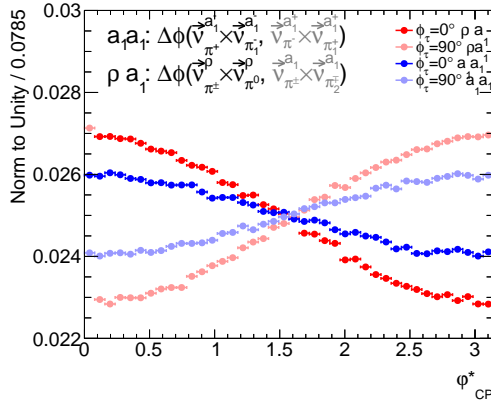
Figure 6.18: Schematic of $\Delta\phi$ angles between example planes spanned by two of the three decay products from the $\tau \rightarrow (a_1 \rightarrow)\pi^\pm\pi_1^\mp\pi_2^\mp$ decays. Shown in the $\tau_{\text{vis}}^\pm\tau_{\text{vis}}^\mp$ rest frame.

The tau decay planes can be formed in the same way as for the a_1 plane in the ρa_1 method. To reconstruct the angle between the tau decay planes, the four vectors of each visible decay product are boosted into the rest frame of the $\tau_{\text{vis}}^\pm - \tau_{\text{vis}}^\mp$ pair. The $\Delta\phi$ angles are calculated with respect to one of the possible planes, which is designated the reference frame. Therefore, the ϕ of the $\vec{v}_{\pi^\mp} \times \vec{v}_{\pi^\pm}$ plane for the ρ decay mode is, by definition and without loss of generality, 0. The angles between the possible tau decay planes are:

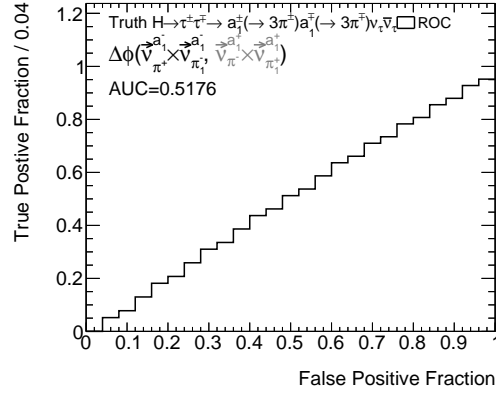
- | | |
|--|---|
| 1. $\Delta\phi\left(\vec{v}_{\rho\rightarrow\pi^+\pi_1^-} \times \vec{v}_{\pi_2^-}, \vec{v}_{\rho\rightarrow\pi^-\pi_1^+} \times \vec{v}_{\pi_2^\mp}\right)$ | 9. $\Delta\phi\left(\vec{v}_{\pi^+} \times \vec{v}_{\pi_1^-}, \vec{v}_{\rho\rightarrow\pi^-\pi_1^+} \times \vec{v}_{\pi_2^+}\right)$ |
| 2. $\Delta\phi\left(\vec{v}_{\rho\rightarrow\pi^+\pi_1^-} \times \vec{v}_{\pi_2^-}, \vec{v}_{\rho\rightarrow\pi^-\pi_2^+} \times \vec{v}_{\pi_1^\mp}\right)$ | 10. $\Delta\phi\left(\vec{v}_{\pi^+} \times \vec{v}_{\pi_1^-}, \vec{v}_{\rho\rightarrow\pi^-\pi_2^+} \times \vec{v}_{\pi_1^+}\right)$ |
| 3. $\Delta\phi\left(\vec{v}_{\rho\rightarrow\pi^+\pi_1^-} \times \vec{v}_{\pi_2^-}, \vec{v}_{\pi^-} \times \vec{v}_{\pi_1^+}\right)$ | 11. $\Delta\phi\left(\vec{v}_{\pi^+} \times \vec{v}_{\pi_1^-}, \vec{v}_{\pi^-} \times \vec{v}_{\pi_1^+}\right)$ |
| 4. $\Delta\phi\left(\vec{v}_{\rho\rightarrow\pi^+\pi_1^-} \times \vec{v}_{\pi_2^-}, \vec{v}_{\pi^-} \times \vec{v}_{\pi_2^+}\right)$ | 12. $\Delta\phi\left(\vec{v}_{\pi^+} \times \vec{v}_{\pi_1^-}, \vec{v}_{\pi^-} \times \vec{v}_{\pi_2^+}\right)$ |
| 5. $\Delta\phi\left(\vec{v}_{\rho\rightarrow\pi^+\pi_2^-} \times \vec{v}_{\pi_1^-}, \vec{v}_{\rho\rightarrow\pi^-\pi_1^+} \times \vec{v}_{\pi_2^\mp}\right)$ | 13. $\Delta\phi\left(\vec{v}_{\pi^+} \times \vec{v}_{\pi_2^-}, \vec{v}_{\rho\rightarrow\pi^-\pi_1^+} \times \vec{v}_{\pi_2^+}\right)$ |
| 6. $\Delta\phi\left(\vec{v}_{\rho\rightarrow\pi^+\pi_2^-} \times \vec{v}_{\pi_1^-}, \vec{v}_{\rho\rightarrow\pi^-\pi_2^+} \times \vec{v}_{\pi_1^\mp}\right)$ | 14. $\Delta\phi\left(\vec{v}_{\pi^+} \times \vec{v}_{\pi_2^-}, \vec{v}_{\rho\rightarrow\pi^-\pi_2^+} \times \vec{v}_{\pi_1^+}\right)$ |
| 7. $\Delta\phi\left(\vec{v}_{\rho\rightarrow\pi^+\pi_2^-} \times \vec{v}_{\pi_1^-}, \vec{v}_{\pi^-} \times \vec{v}_{\pi_1^+}\right)$ | 15. $\Delta\phi\left(\vec{v}_{\pi^+} \times \vec{v}_{\pi_2^-}, \vec{v}_{\pi^-} \times \vec{v}_{\pi_1^+}\right)$ |
| 8. $\Delta\phi\left(\vec{v}_{\rho\rightarrow\pi^+\pi_2^-} \times \vec{v}_{\pi_1^-}, \vec{v}_{\pi^-} \times \vec{v}_{\pi_2^+}\right)$ | 16. $\Delta\phi\left(\vec{v}_{\pi^+} \times \vec{v}_{\pi_2^-}, \vec{v}_{\pi^-} \times \vec{v}_{\pi_2^+}\right)$ |

The \mathcal{CP} sensitivity of these $\Delta\phi$ angles is preliminarily quantified using a receiver operator characteristic curve (ROC), previously described in Section 4.5.4. This is done to study

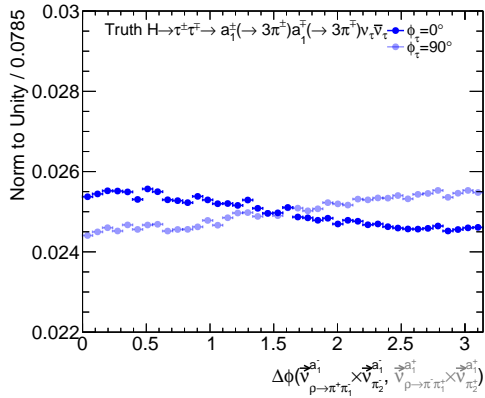
the behavior before resorting to MVA methods, so exhaustive methods for the calculation of uncertainties on these quantities are not pursued. In the case of the $\Delta\phi$ distributions, it is calculated using the cumulative distribution functions from the distributions shown in Figures 6.19(a) and 6.19(c). The area under the ROC (AUC) for the angle between the two ρ decay planes is larger than that for two a_1 decay planes. (An AUC of 0.5 is equivalent to random guessing.)



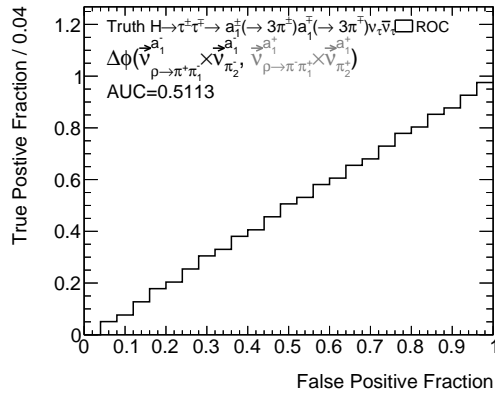
(a) Comparison of one of the angles between the ρ and a_1 decay planes for the ρa_1 decay mode (red) and ρ^\pm and ρ^\mp decay planes for the $a_1 a_1$ decay mode (blue).



(b) ROC curve showing the sensitivity of one of the angles between the two possible ρ planes for the $a_1 a_1$ decay mode, corresponding to cumulative distribution functions built from the blue distributions in Figure 6.19(a).



(c) Angle between the a_1 decay planes for the $a_1 a_1$ mode.



(d) ROC curve showing the sensitivity of the angle between the a_1 decay planes.

Figure 6.19: Angles between the two tau decay planes for the $a_1 a_1$ mode at generator level.

6.9.3 Boosted decision trees for the ρa_1 and $a_1 a_1$ decay modes

Boosted decision trees (BDTs) are trained to combine the information encoded in multiple input variables into one variable that predicts the \mathcal{CP} state. Studies have been performed using neural networks to predict the \mathcal{CP} mixing state but have not investigated the use of Boosted Decision or Regression Trees (BRTs), which can be more easily trained and used with the data formats from ATLAS [66]. These studies have also taken the most complex case of a regression problem

to predict CP mixing and have also not investigated whether BDTs/BRTs can perform as well as neural networks.

Since the goal in this chapter is to distinguish between two states (purely CP -even and CP -odd), this machine learning study is a classification problem as opposed to a regression problem. Therefore, instead of predicting a continuous variable using BRTs, the problem can be simplified to predict categorical variables, where BDTs are trained on signal (CP -odd) and background (CP -even) events. The final output of the BDT, a BDT score which represents the underlying model⁸ as a single value, can be used to build a two-bin variable analogous to φ_{CP}^* , where events that pass a BDT score threshold fall into the CP -odd bin, and background events below the BDT threshold fall in the CP -even bin. In this manner, the BDT score output can be combined with the φ_{CP}^* variables that can also be binned into two bins and where the periodicity is changed from $0^\circ - 360^\circ$ to $0^\circ - 360^\circ$ in order to decrease the statistical uncertainty on each bin of the distribution.

The BDT training/testing and hyperparameter tuning are performed using XGBOOST, which is an implementation of gradient boosted decision trees, a technique described later in this paragraph [161]. The figure of merit is the AUC, the same as for where the CP sensitivity was measured for the non-BDT case in Sections 6.9.1 and 6.9.2. To determine the model, an objective function is optimized and contains two terms as functions of the parameter(s), θ : one for the training loss, $L(\theta)$, which measures how well the model fits the training data, and one for regularization, $\Omega(\theta)$, which measures the complexity of the model and is optimized to avoid overfitting [162]:

$$\text{obj}(\theta) = L(\theta) + \Omega(\theta). \quad (6.15)$$

The loss function used is the logistic loss function [161]. The model is created using tree boosting in order to combine many simple trees instead of a single complicated tree, which is more prone to overtraining. In this case, the algorithm optimizes for such a narrow region of phase space that the training and test results are not similar. In gradient boosting, the cost function is optimized via a procedure called gradient descent, which adds a tree to the model that reduces the loss, i.e., follows the gradient.

The sets of variables used as BDT inputs are

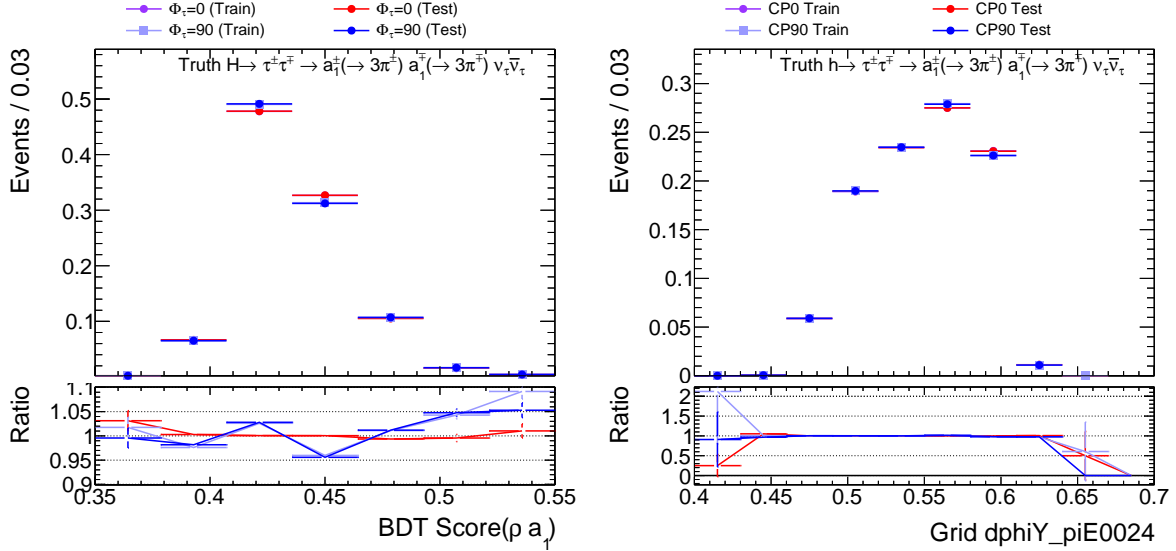
- The acoplanarity angles discussed in Sections 6.9.1 and 6.9.2.
- Y .
- Invariant masses of the pion pairs (and triplets for the a_1 case).
- 4-momentum vector(s) of each pion.

The performance of the optimized BDTs for the ρa_1 and $a_1 a_1$ decay modes at generator level are shown in Figure 6.20. The classifier correctly classifies the ρa_1 decay modes 59.5% of the time and the $a_1 a_1$ decay modes 55.8% of the time. The performance at reconstruction level is shown, as an example, for the $a_1 a_1$ decay mode since they are trained completely on track information, which is known to be well-modeled. This is confirmed in the BDT response shown in Figure 6.21(b), where the BDT response is defined as

$$\text{BDT Response} = \text{BDT}_{\text{matched}} - \text{BDT}_{\text{reco}}, \quad (6.16)$$

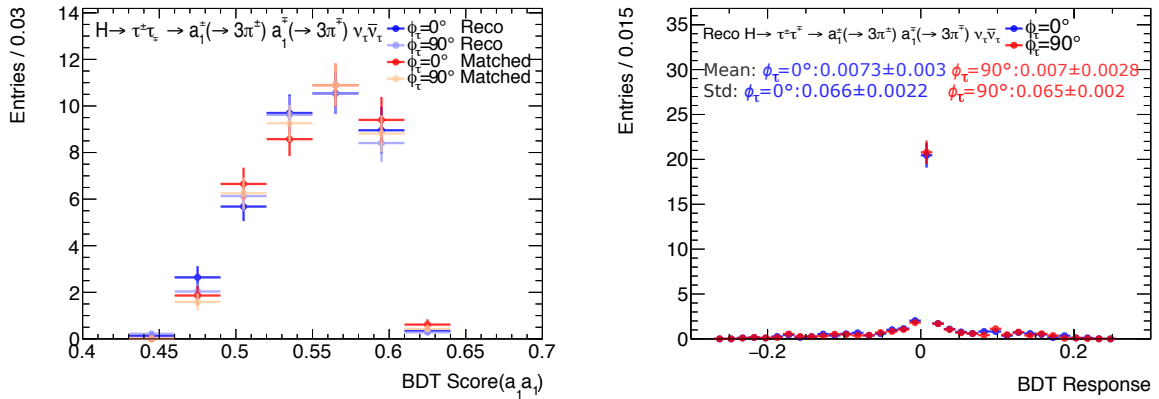
⁸ In supervised learning, the model is the mathematical structure for how the output prediction is made using the input variables.

Here, $\text{BDT}_{\text{matched}}$ is the BDT output computed using MC generator information and BDT_{reco} is the output computed using reconstructed quantities. The BDT response is not defined as a relative percentage since there are cases where the $\text{BDT}_{\text{matched}} - \text{BDT}_{\text{reco}}$ difference is the same order of magnitude of the actual BDT score, which would cause unnecessary outliers in the distribution. The BDT response is narrow with a standard deviation width of about 0.06.



(a) BDT Score distribution for the training and testing truth samples. (b) BDT Score distribution for the training and testing truth samples.

Figure 6.20: BDT Score distribution for the generated (training and testing) samples shown for the ρa_1 mode (left) and the $a_1 a_1$ mode (right).



(a) BDT Score distribution for the reconstructed and truth-matched samples.

(b) BDT Response for the $a_1 a_1$ method.

Figure 6.21: The BDT performance at reconstruction level for the $a_1 a_1$ decay.

In principle, the BDT score output can be used to build a 2-bin observable to be used with a 2-bin φ_{CP}^* observable for the 1p0n and 1p1n decay modes. Although the performance is similar to that obtained by neural network studies in [66], no additional time is spent on including these

decay modes in this dissertation, given the low separation power seen in the machine learning results.

6.10 Results

The observed CP sensitivity of the Higgs CP analysis is measured using unblinded data and is shown in Figure 6.22. It is presented for the case where the normalization of the ϕ_τ hypothesis is fitted in order to be model independent (μ fitted) and where the normalization is fixed to its prediction (μ fixed). For the former case, the fitted μ of $\hat{\mu} = 0.705 \pm 0.834$ for the $\phi_\tau = 0^\circ$ fit is smaller than the prediction ($\mu = 1$), which explains why the fixed μ case has a higher sensitivity. In future analyses, the signal strength, μ , can be fixed to that measured in the $H \rightarrow \tau\tau$ analysis instead of being fitted simultaneously with the Higgs CP mixing angle.

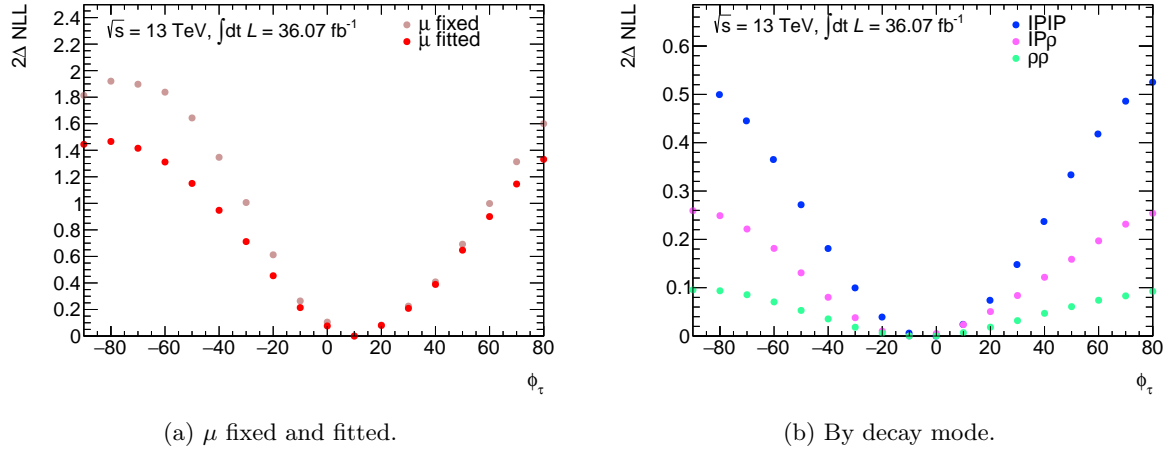


Figure 6.22: Unblinded CP sensitivity measurement.

		Confidence level (%)
ATLAS	μ fitted	99.97
CMS	μ fitted	99.84
Presented results	μ fixed	83.54
	μ fitted	77.38

Table 6.5: The exclusion level of the purely CP -odd Higgs boson hypothesis ($J^P = 0^-$) when testing against the SM Higgs boson prediction (purely even, $J^P = 0^+$): confidence levels presented in this dissertation (c.f. Figure 6.22 and Equation 5.26), listed with the results from the ATLAS and CMS Collaborations in the bosonic decay channels of the Higgs boson ($H \rightarrow ZZ^* \rightarrow 4\ell$ and $H \rightarrow WW^* \rightarrow \ell\nu\ell\nu$) [57, 163].

The observed sensitivity is similar to the expected sensitivity and found to be $2 \cdot \Delta\text{NLL}(\phi_\tau = 0^\circ, \phi_\tau = 90^\circ) \approx 0.5$ higher because the fit to observed data scales the background down more than it does the signal. This can be seen when comparing the fitted postfit yields in Table 6.6 with the expected prefit yields in Table 6.2.

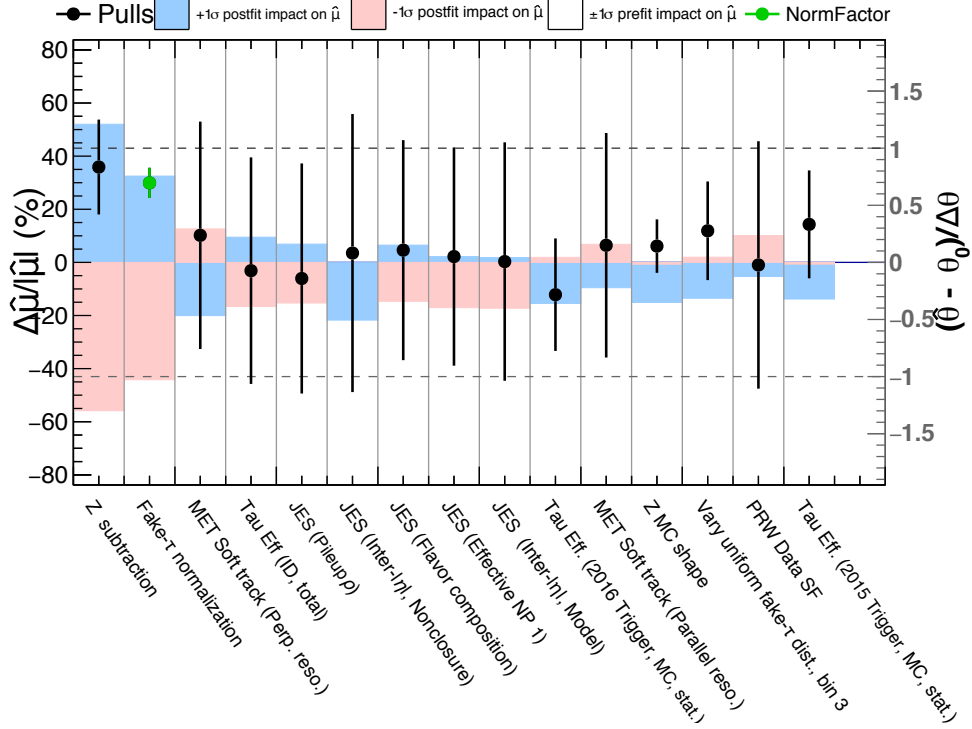


Figure 6.23: The ranking of NPs for the unblinded fit according to their postfit impact on μ (filled blue and red bands), i.e., $\Delta\hat{\mu}/|\hat{\mu}|$. The pulls (black dots) with the postfit uncertainties on the NPs (black lines with respect to the black dots) are also shown. Presented as an example for the $\phi_\tau = 0^\circ$ hypothesis. Normalization factors are shown in green, where a value of 1 means that the postfit normalization matches the prefit normalization.

The best-fit ϕ_τ is 10° with an uncertainty of $\sigma_{\text{stat}} = 18.3^\circ \pm 0.7^\circ$ for a fixed μ ($\sigma_{\text{stat}} = 27.5^\circ \pm 0.9^\circ$ for a fitted μ) from the toy experiments presented in Section 6.7.1.⁹ It is consistent with the expected CP mixing angle of $\phi_\tau = 0^\circ$ within the uncertainties. The corresponding results from the ATLAS and CMS Collaborations are listed in Table 6.5. The postfit distributions are shown for the $\phi_\tau = 0^\circ$ case, as an example, in Figures 6.24–6.26. The NP ranking and pulls are shown for $\phi_\tau = 0^\circ$ in Figure 6.23. The most highly ranked NPs are the NPs that affect the $Z \rightarrow \tau\tau$ shape and the NPs that affect the $Z \rightarrow \tau\tau$ and fake- τ background normalizations. A 1σ variation of the NP related to the $Z \rightarrow \tau\tau$ template taken from data can result in a 40% change in the normalization of the $H \rightarrow \tau\tau$ signal. Performing the CP measurement by decay mode, it can be seen that the IPIP mode has the highest sensitivity, followed by the $IP\rho$ decay mode (c.f. Figure 6.22(b)).

6.11 Conclusion

The measurement of the Higgs CP mixing angle in the $H \rightarrow \tau_{\text{had}}\tau_{\text{had}}$ decay channel is essential since tau leptons contain unique information on Higgs CP mixing properties. The analysis presented in this chapter is performed on 36.07 fb^{-1} of data collected with the ATLAS detector

⁹ This assumes that the uncertainties from the toy experiment are similar at each mixing angle. Further toy experiments can be performed for each mixing angle to verify this.

			$H \rightarrow \tau\tau$	$Z \rightarrow \tau\tau$	Other	Fake- τ	$S + B$	Data
VBF	IPIP		1.9 ± 2.1	17.4 ± 4.2	0.7 ± 0.6	7.1 ± 3.7	27.1 ± 4.7	30 ± 5.5
	IP ρ		4.5 ± 4.8	33.8 ± 5.0	3.0 ± 0.6	26.6 ± 4.9	67.9 ± 6.5	61 ± 7.8
	$\rho\rho$	Y_+Y_- high	1.9 ± 2.0	9.9 ± 2.4	3.1 ± 0.7	4.0 ± 1.1	18.8 ± 2.9	18 ± 4.2
		Y_+Y_- low	2.2 ± 2.3	13.4 ± 2.3	1.7 ± 0.8	13.7 ± 3.1	31.0 ± 4.0	27 ± 5.2
Boost	IPIP	d_0^{sig} high	1.9 ± 2.1	22.7 ± 2.5	0.2 ± 0.1	1.2 ± 0.5	26.1 ± 2.8	32 ± 5.7
		d_0^{sig} low	2.1 ± 2.3	55.5 ± 5.5	4.2 ± 0.8	1.7 ± 0.8	63.5 ± 5.7	56 ± 7.5
Tight	IP ρ	$d_0^{\text{sig}}Y$ high	5.4 ± 5.7	78.7 ± 5.1	4.8 ± 1.3	5.7 ± 2.0	94.5 ± 6.1	89 ± 9.4
		$d_0^{\text{sig}}Y$ low	8.3 ± 8.9	139.8 ± 7.2	13.3 ± 2.2	20.7 ± 3.6	182.1 ± 9.1	185 ± 13.6
	$\rho\rho$	Y_+Y_- high	6.6 ± 7.1	97.2 ± 6.7	6.8 ± 1.0	8.3 ± 3.0	118.9 ± 7.5	122 ± 11.0
Y_+Y_- low		7.0 ± 7.5	99.6 ± 5.9	12.7 ± 3.6	27.8 ± 5.6	147.1 ± 8.1	145 ± 12.0	
Boost	IPIP	d_0^{sig} high	0.7 ± 0.8	17.1 ± 3.0	1.2 ± 0.4	6.2 ± 1.7	25.1 ± 3.4	35 ± 5.9
		d_0^{sig} low	2.8 ± 3.1	66.5 ± 6.1	6.3 ± 1.4	18.1 ± 4.0	93.6 ± 7.3	84 ± 9.2
Loose	IP ρ	$d_0^{\text{sig}}Y$ high	3.8 ± 4.1	89.9 ± 7.8	7.4 ± 2.0	31.5 ± 7.2	132.6 ± 8.4	132 ± 11.5
		$d_0^{\text{sig}}Y$ low	7.0 ± 7.8	170.6 ± 12.2	23.6 ± 10.9	126.9 ± 20.2	328.1 ± 16.0	339 ± 18.4
Loose	$\rho\rho$	Y_+Y_- high	5.4 ± 5.9	111.0 ± 9.4	21.4 ± 6.9	66.8 ± 11.0	204.6 ± 11.5	202 ± 14.2
		Y_+Y_- low	6.1 ± 6.7	127.4 ± 10.2	21.3 ± 4.9	119.2 ± 17.5	273.9 ± 14.2	269 ± 16.4

Table 6.6: Postfit event yields and their total uncertainties for the $\phi_\tau = 0^\circ$ case. The fitted signal-plus-background yield is denoted as $S + B$.

in 2015 and 2016 at a center-of-mass energy of $\sqrt{s} = 13$ TeV. Given the limited sample size, this analysis is not yet expected to be sensitive to Higgs CP mixing. Rather, the analysis serves as a preparation and basis for future Higgs CP analyses.

In the signal extraction, the main irreducible background from the QCD $Z \rightarrow \tau\tau$ +jets process is modeled using a data-driven method, and the main reducible fake- τ background from multijet production is modeled using a uniform background template with appropriate systematic uncertainties. The Higgs CP sensitivity is extracted by comparing the expected signal and background φ_{CP}^* distributions to the observed φ_{CP}^* distribution in data for different degrees of Higgs CP mixing. Studies are performed in this dissertation to validate the signal extraction fit with toy experiments and to identify the main hindrance of the analysis, which is confirmed to be the limited integrated luminosity.

A best-fit CP mixing angle, given the samples generated at 10° steps, is 10° with an uncertainty of $18.3^\circ \pm 0.7^\circ$ for the case where the Higgs boson cross section is fixed to the SM prediction and an uncertainty of $27.5^\circ \pm 0.9^\circ$ where it is fitted. It is consistent with the SM prediction of $\phi_\tau = 0^\circ$ and the results from the bosonic decay channels (c.f. Table 6.5) [164]. The future for this $H \rightarrow \tau_{\text{had}}\tau_{\text{had}}$ CP analysis is to include the additional integrated luminosity of 46.9 fb^{-1} from 2017 and to develop systematic uncertainties associated with the use of the tau particle flow reconstruction.

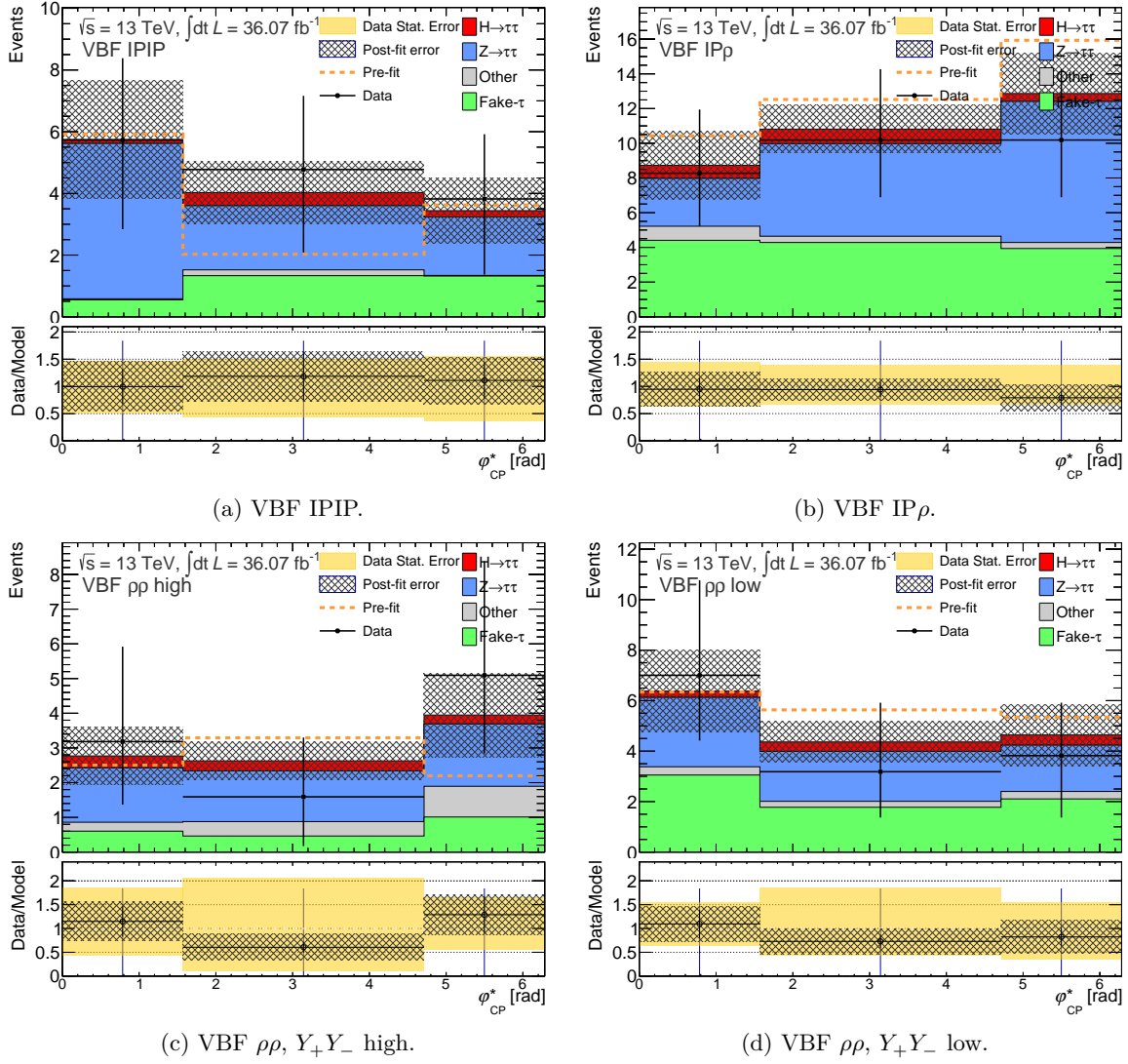


Figure 6.24: The prefit (orange) and postfit φ_{CP}^* distributions for the inclusive **VBF** category for the $\phi_\tau = 0^\circ$ case.

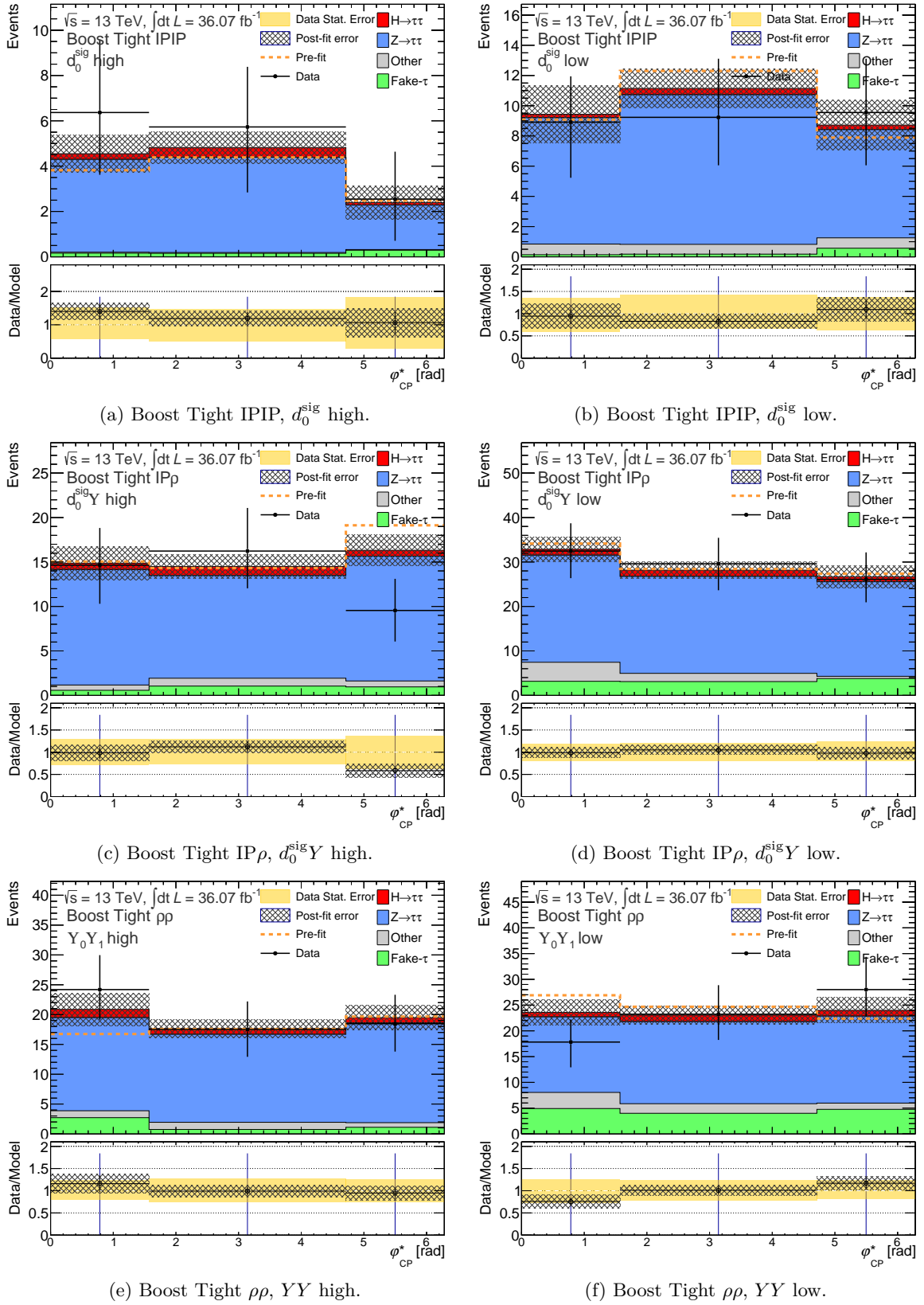


Figure 6.25: The prefit (orange) and postfit φ_{CP}^* distributions for the **Boost Tight** category for the $\phi_\tau = 0^\circ$ case.

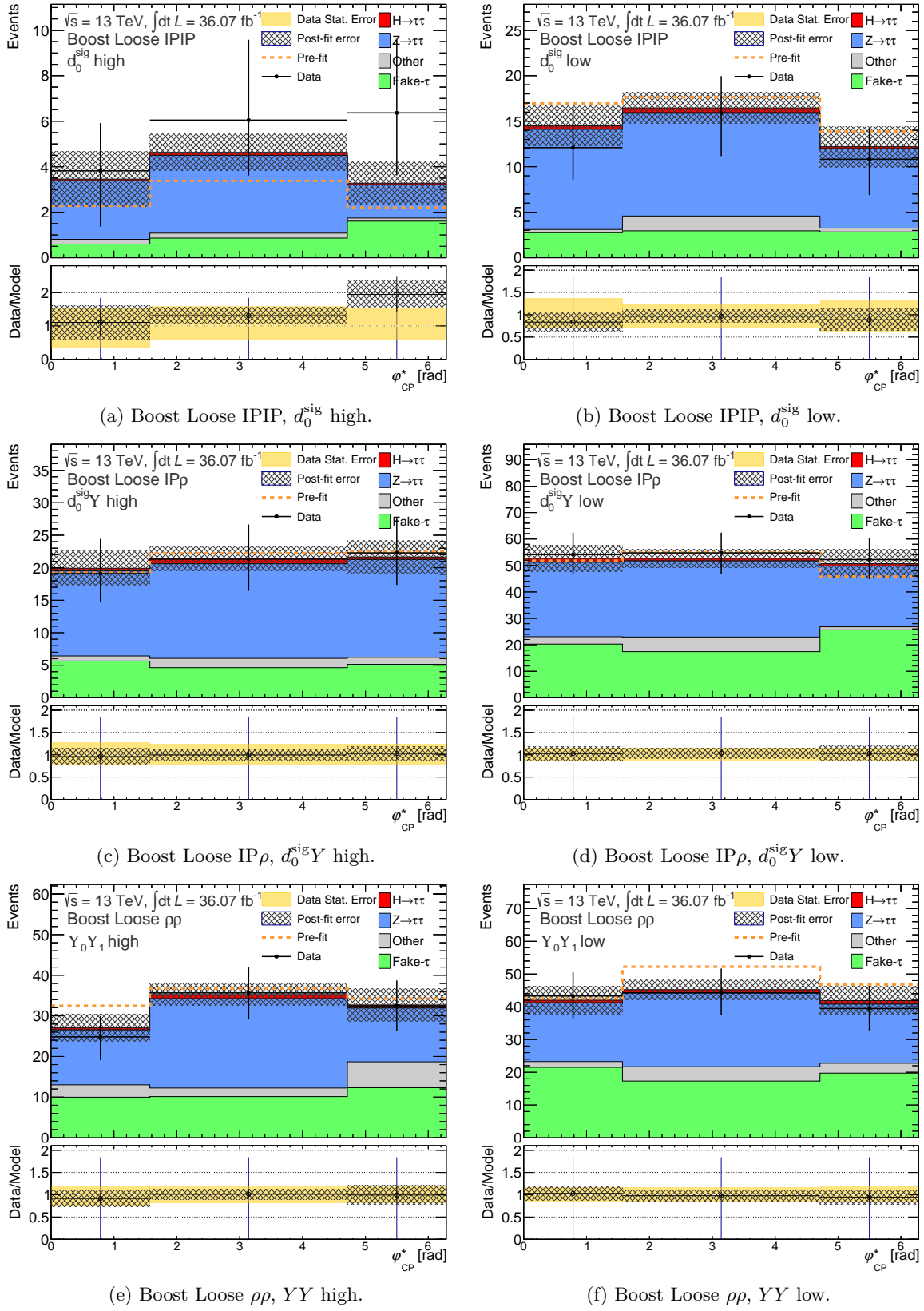


Figure 6.26: The prefit (orange) and postfit φ_{CP}^* distributions for the **Boost Loose** category for the $\phi_\tau = 0^\circ$ case.

Conclusion

Analyses of Higgs boson decays to a pair of tau leptons are essential in probing the coupling of the Higgs boson to fermions. The $H \rightarrow \tau\tau$ analysis presented in this dissertation is performed on 36.07 fb^{-1} of data collected at the ATLAS detector from 2015 to 2016 at $\sqrt{s} = 13 \text{ TeV}$. The Higgs boson signal is extracted by comparing the expected signal and background reconstructed di-tau invariant mass distributions to the observed distribution in data. To optimize the selection of signal events, the main production processes (via gluon-gluon fusion and vector boson fusion) that produce highly boosted Higgs bosons are targeted. Even after this optimization, this decay channel suffers from the overwhelming fake- τ background from multijet production at the LHC that must be well-modeled. The modeling of this background is improved and validated with the methods developed in this dissertation. An excess of signal events beyond the expected background yield is measured with an observed significance of 1.52σ . The measured signal strength relative to that predicted by the Standard Model is $\mu = 0.62_{-0.24}^{+0.25}(\text{stat})_{-0.31}^{+0.36}(\text{sys}) = 0.62_{-0.40}^{+0.44}$ and is consistent with the Standard Model prediction. The sensitivity depends on modeling of the underlying high- p_T jet required by the tau trigger and the background estimation.

This analysis is not only vital in confirming the Standard Model predictions but is also a preparation for Higgs \mathcal{CP} measurements in the $H \rightarrow \tau_{\text{had}}\tau_{\text{had}}$ channel. This analysis is a basis for the Higgs \mathcal{CP} measurement. The measurement of the Higgs \mathcal{CP} mixing angle in the $H \rightarrow \tau_{\text{had}}\tau_{\text{had}}$ decay channel is essential since tau lepton kinematics contain unique information on the Higgs \mathcal{CP} mixing properties. These properties are encoded in the transverse tau spin correlations, which can be inferred from the acoplanarity angle between the tau decay planes. The reconstruction of this angle requires a reliable tau decay mode classification and a robust reconstruction of each visible tau decay product. These goals are accomplished with the tau particle flow algorithm, to which the work in this dissertation contributed.

Given the relatively small sample size of selected data events, this Higgs \mathcal{CP} analysis is not yet expected to be sensitive to Higgs \mathcal{CP} mixing but is, rather, intended as a basis for future Higgs \mathcal{CP} analyses. A best-fit \mathcal{CP} mixing angle to the observed data is $\phi_\tau = 10^\circ$ with an uncertainty of $18.3^\circ \pm 0.7^\circ$ for the case where the Higgs boson cross section is fixed to the Standard Model prediction and an uncertainty of $27.5^\circ \pm 0.9^\circ$ where it is fitted. It is consistent with the Standard Model prediction of $\phi_\tau = 0^\circ$ and the measurements from the bosonic decay channels. The dominant limitation of the analysis derives from the limited integrated luminosity. In addition, additional systematic uncertainties need to be derived for the Higgs \mathcal{CP} analysis for the use of the tau particle flow reconstruction. The next step for these analyses is to include the additional integrated luminosity of 46.9 fb^{-1} from 2017.

Bibliography

- [1] ATLAS and CMS Collaborations, *Measurements of the Higgs boson production and decay rates and constraints on its couplings from a combined ATLAS and CMS analysis of the LHC pp collision data at $\sqrt{s} = 7$ and 8 TeV*, Journal of High Energy Physics (2016) 45, ISSN: 1029-8479.
- [2] T. Ullrich, B. Wyslouch and J. W. Harris, *Proceedings of XXIII International Conference on Ultrarelativistic Nucleus-Nucleus Collisions*, Nuclear Physics A **904-905** (2013) IFC, The Quark Matter 2012, ISSN: 0375-9474.
- [3] CMS and LHCb Collaborations, *Observation of the rare $B_s^0 \rightarrow \mu^+ \mu^-$ decay from the combined analysis of CMS and LHCb data*, Nature **522** (2015) 68, Letter, ISSN: 0028-0836.
- [4] ATLAS Collaboration, *Cross-section measurement of Higgs bosons that decay to a pair of tau leptons in proton-proton collisions at $\sqrt{s} = 13$ TeV with the ATLAS detector*, tech. rep. ATL-COM-PHYS-2018-264, Publication in preparation.: CERN, 2018.
- [5] ATLAS Collaboration, *Observation of Higgs boson production in association with a top quark pair at the LHC with the ATLAS detector*, 2018, arXiv: 1806.00425 [hep-ex].
- [6] ATLAS Collaboration, *Evidence for the $H \rightarrow b\bar{b}$ decay with the ATLAS detector*, JHEP **12** (2017) 024, arXiv: 1708.03299 [hep-ex].
- [7] A. Einstein, *Die Grundlage der allgemeinen Relativitätstheorie*, vol. 49, Annalen der Physik IV, 1916.
- [8] E. Noether, *Invariante Variationsprobleme*, Nachr. D. Koenig. Gesellsch. D. Wiss. Zu Göttingen, Math-phys. Klasse. **2** (1918) 235.
- [9] W. Heisenberg, *Über den Bau der Atomkerne. I*, Zeitschrift für Physik **77** (1932) 1, ISSN: 0044-3328.
- [10] A. Pich, *The Standard model of electroweak interactions*, (2008) 1, [1(2007)], arXiv: 0705.4264 [hep-ph].
- [11] M. Thomsen, *Modern Particle Physics*, Cambridge University Press, 2013, ISBN: 9781107034266.
- [12] F. Halzen and A. D. Martin, *Quarks and Leptons: An Introductory Course in Modern Particle Physics*, Wiley, 1984, ISBN: 9780471887416.
- [13] A. Djouadi, *The Anatomy of electro-weak symmetry breaking. I: The Higgs boson in the standard model*, Phys. Rept. **457** (2008) 1, arXiv: hep-ph/0503172 [hep-ph].
- [14] V. A. Bednyakov, N. D. Giokaris and A. V. Bednyakov, *On Higgs mass generation mechanism in the Standard Model*, Phys. Part. Nucl. **39** (2008) 13, arXiv: hep-ph/0703280 [HEP-PH].

- [15] H. E. Logan, *TASI 2013 lectures on Higgs physics within and beyond the Standard Model*, 2014, eprint: arXiv:1406.1786.
- [16] C. Patrignani et al., *Review of Particle Physics*, Chin. Phys. **C40** (2016) 100001.
- [17] S. Bethke, *Experimental tests of asymptotic freedom*, Progress in Particle and Nuclear Physics **58** (2007) 351, ISSN: 0146-6410.
- [18] W. Bietenholz, *Hadron Physics from Lattice QCD*, Int. J. Mod. Phys. **E25** (2016) 1642008, arXiv: 1605.08103 [hep-ph].
- [19] J. C. Collins, D. E. Soper and G. F. Sterman, *Factorization of Hard Processes in QCD*, Adv. Ser. Direct. High Energy Phys. **5** (1989) 1, arXiv: hep-ph/0409313 [hep-ph].
- [20] A. D. Martin et al., *Parton distributions for the LHC*, The European Physical Journal C **63** (2009) 189, ISSN: 1434-6052.
- [21] S. L. Glashow, *Partial-symmetries of weak interactions*, Nuclear Physics **22** (1961) 579, ISSN: 0029-5582.
- [22] S. Weinberg, *Conceptual Foundations of the Unified Theory of Weak and Electromagnetic Interactions*, Rev.Mod.Phys. **52** (1980) 515.
- [23] C. S. Wu et al., *Experimental Test of Parity Conservation in Beta Decay*, Phys. Rev. **105** (4 1957) 1413.
- [24] A. Kleppe, “Helicity and chirality”, <http://www.nbi.dk/kleppe/random/chir/ch/ch.html>.
- [25] E. C. G. Sudarshan and R. E. Marshak, *The Nature of the Four-Fermion Interaction*, (1957) v, Proc. Conf. on Mesons and Newly Discovered Particles, Padua-Venice (Conf. held in Sept 1957).
- [26] R. P. Feynman and M. Gell-Mann, *Theory of the Fermi Interaction*, Phys. Rev. **109** (1 1958) 193.
- [27] Nobel Media AB, *The Nobel Prize in Physics 1984*.
- [28] F. Englert and R. Brout, *Broken Symmetry and the Mass of Gauge Vector Mesons*, Phys. Rev. Lett. **13** (9 1964) 321.
- [29] G. S. Guralnik, C. R. Hagen and T. W. B. Kibble, *Global Conservation Laws and Massless Particles*, Phys. Rev. Lett. **13** (20 1964) 585.
- [30] P. W. Higgs, *Broken symmetries, massless particles and gauge fields*, Physics Letters **12** (1964) 132, ISSN: 0031-9163.
- [31] P. W. Higgs, *Broken Symmetries and the Masses of Gauge Bosons*, Phys. Rev. Lett. **13** (16 1964) 508.
- [32] P. W. Higgs, *Spontaneous Symmetry Breakdown without Massless Bosons*, Phys. Rev. **145** (4 1966) 1156.
- [33] J. Goldstone, A. Salam and S. Weinberg, *Broken Symmetries*, Phys. Rev. **127** (3 1962) 965.
- [34] N. Cabibbo, *Unitary Symmetry and Leptonic Decays*, Phys. Rev. Lett. **10** (12 1963) 531.

-
- [35] M. Kobayashi and T. Maskawa,
CP-Violation in the Renormalizable Theory of Weak Interaction,
Progress of Theoretical Physics **49** (1973) 652, eprint: /oup/backfile/content_public/journal/ptp/49/2/10.1143/ptp.49.652/2/49-2-652.pdf.
- [36] D. de Florian et al.,
Handbook of LHC Higgs Cross Sections: 4. Deciphering the Nature of the Higgs Sector,
(2016), arXiv: 1610.07922 [hep-ph].
- [37] S. Dawson, *Radiative corrections to Higgs boson production*,
Nuclear Physics B **359** (1991) 283, ISSN: 0550-3213.
- [38] S. Marzani et al.,
Higgs production via gluon-gluon fusion with finite top mass beyond next-to-leading order,
Nuclear Physics B **800** (2008) 127, ISSN: 0550-3213.
- [39] A. Djouadi, M. Spira and P. Zerwas,
Production of Higgs bosons in proton colliders. QCD corrections,
Physics Letters B **264** (1991) 440, ISSN: 0370-2693.
- [40] R. V. Harlander and W. B. Kilgore,
Next-to-Next-to-Leading Order Higgs Production at Hadron Colliders,
Phys. Rev. Lett. **88** (2002) 201801, arXiv: hep-ph/0201206 [hep-ph].
- [41] R. D. Ball et al., *Higgs production in gluon fusion beyond NNLO*,
Nucl. Phys. **B874** (2013) 746, arXiv: 1303.3590 [hep-ph].
- [42] G. Degrossi and F. Maltoni,
Two-loop electroweak corrections to Higgs production at hadron colliders,
Physics Letters B **600** (2004) 255, ISSN: 0370-2693.
- [43] M. Grazzini and H. Sargsyan,
Heavy-quark mass effects in Higgs boson production at the LHC, JHEP **09** (2013) 129,
arXiv: 1306.4581 [hep-ph].
- [44] The LHC Higgs Cross Section Working Group et al.,
Handbook of LHC Higgs Cross Sections: 3. Higgs Properties, (2013),
eprint: arXiv:1307.1347.
- [45] J. R. Andersen et al.,
Loop induced interference effects in Higgs Boson plus two jet production at the LHC,
Journal of High Energy Physics **2008** (2008) 057.
- [46] M. Ciccolini, A. Denner and S. Dittmaier, *Strong and electroweak corrections to the production of Higgs+2jets via weak interactions at the LHC*,
Phys. Rev. Lett. **99** (2007) 161803, arXiv: 0707.0381 [hep-ph].
- [47] P. Bolzoni et al., *Higgs production via vector-boson fusion at NNLO in QCD*,
Phys. Rev. Lett. **105** (2010) 011801, arXiv: 1003.4451 [hep-ph].
- [48] P. Bolzoni et al., *Higgs production at NNLO in QCD: the VBF channel*,
Nucl. Phys. Proc. Suppl. **205-206** (2010) 314, arXiv: 1006.2323 [hep-ph].
- [49] G. Ferrera, M. Grazzini and F. Tramontano, *Associated WH production at hadron colliders: a fully exclusive QCD calculation at NNLO*,
Phys. Rev. Lett. **107** (2011) 152003, arXiv: 1107.1164 [hep-ph].

- [50] M. L. Ciccolini, S. Dittmaier and M. Krämer, *Electroweak Radiative Corrections to Associated WH and ZH Production at Hadron Colliders*, Phys. Rev. **D68** (2003) 073003, arXiv: hep-ph/0306234 [hep-ph].
- [51] W. Beenakker et al., *Higgs Radiation off Top Quarks at the Tevatron and the LHC*, Phys. Rev. Lett. **87** (2001) 201805, arXiv: hep-ph/0107081 [hep-ph].
- [52] ATLAS and CMS Collaborations, *Combined Measurement of the Higgs Boson Mass in pp Collisions at $\sqrt{s} = 7$ and 8 TeV with the ATLAS and CMS Experiments*, Phys. Rev. Lett. **114** (2015) 191803, arXiv: 1503.07589 [hep-ex].
- [53] ATLAS Collaboration, *Measurements of the Higgs boson production and decay rates and coupling strengths using pp collision data at $\sqrt{s} = 7$ and 8 TeV in the ATLAS experiment*, (2015), eprint: arXiv:1507.04548.
- [54] W. Bernreuther, *CP violation and baryogenesis*, Lect. Notes Phys. **591** (2002) 237, [,237(2002)], arXiv: hep-ph/0205279 [hep-ph].
- [55] Z. Maki, M. Nakagawa and S. Sakata, *Remarks on the Unified Model of Elementary Particles*, Progress of Theoretical Physics **28** (1962) 870, eprint: /oup/backfile/content_public/journal/ptp/28/5/10.1143/ptp.28.870/2/28-5-870.pdf.
- [56] ATLAS Collaboration, *Evidence for the spin-0 nature of the Higgs boson using ATLAS data*, Phys. Lett. **B726** (2013) 120, arXiv: 1307.1432 [hep-ex].
- [57] ATLAS Collaboration, *Study of the spin and parity of the Higgs boson in diboson decays with the ATLAS detector*, The European Physical Journal C **75** (2015) 476, ISSN: 1434-6052.
- [58] Nobel Media AB, *The Nobel Prize in Physics 1995*.
- [59] A. Stahl, *Physics with Tau Leptons*, Springer, 2000.
- [60] T. Nattermann, K. Desch, P. Wienemann, and C. Zender, *Measuring tau-polarisation in neutralino2 decays at the LHC*, J. High Energy Phys. **04** (2008) 057. 16 p.
- [61] Z. Czczyula and M. Dam, *Search for New Physics in Tau-pair Events in ATLAS at the LHC*, Presented on 27 Aug 2009, Doctoral dissertation, 2009.
- [62] A. Rouge, *Tau decays as polarization analysers*, (1991) 213.
- [63] T. Pierzchala et al., *Spin effects in tau-lepton pair production at LHC*, Acta Phys. Polon. **B32** (2001) 1277, arXiv: hep-ph/0101311 [hep-ph].
- [64] K. Desch et al., *Probing the CP nature of the Higgs boson at linear colliders with spin correlations; the case of mixed scalar-pseudoscalar couplings*, Physics Letters B **579** (2004) 157, ISSN: 0370-2693.
- [65] S. Berge, W. Bernreuther and S. Kirchner, *Determination of the Higgs CP mixing angle in the tau decay channels at the LHC including the Drell-Yan background*, Eur. Phys. J. **C74** (2014) 3164, arXiv: 1408.0798 [hep-ph].

-
- [66] R. Jozefowicz, E. Richter-Was and Z. Was, *Potential for optimizing Higgs boson CP measurement in H to tau tau decay at LHC and ML techniques*, Phys. Rev. **D94** (2016) 093001, arXiv: 1608.02609 [hep-ph].
- [67] S. Berge, *Probing Higgs sector CP violation in the tau decay channels at the LHC*, Seminar über Teilchenphysik at Universität Bonn, 2014.
- [68] M. Krämer et al., *Prospects of measuring the parity of Higgs particles*, Zeitschrift für Physik C Particles and Fields **64** (1994) 21, ISSN: 1431-5858.
- [69] S. Berge and W. Bernreuther, *Determining the CP parity of Higgs bosons at the LHC in the τ to 1-prong decay channels*, Physics Letters B **671** (2009) 470, ISSN: 0370-2693.
- [70] M. Worek, *Higgs CP from H/A \rightarrow tau tau decay*, Acta Phys. Polon. **B34** (2003) 4549, arXiv: hep-ph/0305082 [hep-ph].
- [71] S. Jadach, J. H. Kuehn and Z. Was, *TAUOLA - a library of Monte Carlo programs to simulate decays of polarized τ leptons*, Computer Physics Communications **64** (1991) 275, ISSN: 0010-4655.
- [72] The Planck Collaboration, *Planck 2013 results. I. Overview of products and scientific results*, Astron. Astrophys. **571** (2014) A1, arXiv: 1303.5062 [astro-ph.CO].
- [73] J. M. Pendlebury et al., *A Revised Experimental Upper Limit on the Electric Dipole Moment of the Neutron*, (2015), eprint: arXiv:1509.04411.
- [74] S. F. King, *Models of neutrino mass, mixing and CP violation*, Journal of Physics G: Nuclear and Particle Physics **42** (2015) 123001.
- [75] C. S. Hill, *Lecture 4 - Beyond the Standard Model (SUSY)*, 2008.
- [76] M. Holthausen, K. S. Lim and M. Lindner, *Planck Scale Boundary Conditions and the Higgs Mass*, JHEP **02** (2012) 037, arXiv: 1112.2415 [hep-ph].
- [77] C. Csaki, *The Minimal Supersymmetric Standard Model (MSSM)*, Mod. Phys. Lett. **A11** (1996) 599, arXiv: hep-ph/9606414 [hep-ph].
- [78] G. Busoni, *Large Extra Dimensions at LHC Run 2*, 2016, eprint: arXiv:1602.00516.
- [79] ATLAS Collaboration, *The ATLAS Experiment at the CERN Large Hadron Collider*, JINST **3** (2008) S08003.
- [80] R. Garoby, *Upgrade Issues for the CERN Accelerator Complex*, (2008), Conf. Proc.C0806233.
- [81] R. Bruce et al., *LHC Run 2: Results and challenges*, (2016) MOAM5P50. 7 p.
- [82] ATLAS Collaboration, *Luminosity Public Results*, <https://twiki.cern.ch/twiki/bin/view/AtlasPublic/LuminosityPublicResults>.
- [83] ATLAS Collaboration, *Luminosity Public Results Run2*, <https://twiki.cern.ch/twiki/bin/view/AtlasPublic/LuminosityPublicResultsRun2>.
- [84] Andreas Hoecker, *The LHC Run-2 and Future Prospects*, European School of High-Energy Physics, Skeikampen, Norway, 2016.

- [85] ATLAS Collaboration, *Measurement of the Inelastic Proton-Proton Cross Section at $\sqrt{s} = 13$ TeV with the ATLAS Detector at the LHC*, Phys. Rev. Lett. **117** (2016) 182002, arXiv: 1606.02625 [hep-ex].
- [86] T. Gleisberg et al., *Event generation with SHERPA 1.1*, JHEP **02** (2009) 007, arXiv: 0811.4622 [hep-ph].
- [87] CMS Collaboration, *Observation of the Higgs boson decay to a pair of τ leptons with the CMS detector*, Phys. Lett. B **779** (2017) 283.
- [88] ATLAS Collaboration, *The Run-2 ATLAS Trigger System*, Journal of Physics: Conference Series **762** (2016) 012003.
- [89] ATLAS Outreach, *ATLAS Fact Sheet : To raise awareness of the ATLAS detector and collaboration on the LHC*, ATLAS-Brochure-2010-002-Eng, 2010.
- [90] M. Capeans et al., *ATLAS Insertable B-Layer Technical Design Report*, tech. rep. CERN-LHCC-2010-013. ATLAS-TDR-19, 2010.
- [91] M. Backhaus, *The upgraded Pixel Detector of the ATLAS Experiment for Run 2 at the Large Hadron Collider*, Nuclear Instruments and Methods in Physics Research Section A: Accelerators, Spectrometers, Detectors and Associated Equipment **831** (2016) 65, Proceedings of the 10th International Hiroshima Symposium on the Development and Application of Semiconductor Tracking Detectors, ISSN: 0168-9002.
- [92] B. T. Winter, *Measurement of Tau Polarisation in $Z/\gamma^* \rightarrow \tau\tau$ Decays in Proton-Proton Collisions at ATLAS*, Doctoral dissertation: Universität Bonn, 2018.
- [93] ATLAS Collaboration, *Measurement of the inclusive isolated prompt photon cross section in pp collisions at $\sqrt{s} = 7$ TeV with the ATLAS detector*, Phys. Rev. D **83** (2011) 052005.
- [94] ATLAS Collaboration, *Reconstruction of hadronic decay products of tau leptons with the ATLAS experiment*, The European Physical Journal C **76** (2016) 295, ISSN: 1434-6052.
- [95] S. P. Y. Yuen, *Improving the Reconstruction of Neutral Pions in Tau Decays Using the Strip Layer of the ATLAS Electromagnetic Calorimeter*, CERN-THESIS-2013-465, Master thesis: Universität Bonn, 2013.
- [96] W. Lampl et al., *Calorimeter Clustering Algorithms: Description and Performance*, tech. rep. ATL-LARG-PUB-2008-002. ATL-COM-LARG-2008-003, CERN, 2008.
- [97] P. Giovannini and the ATLAS Liquid Argon Calorimeter Group, *Local hadron calibration with ATLAS*, Journal of Physics: Conference Series **293** (2011) 012057.
- [98] Sven Menke, *Hadron Calibration*, MPI/HEC Meeting, 2009.
- [99] ATLAS Collaboration, *Performance of the ATLAS Trigger System in 2015*, Eur. Phys. J. **C77** (2017) 317, arXiv: 1611.09661 [hep-ex].
- [100] T. Cornelissen et al., *Single Track Performance of the Inner Detector New Track Reconstruction (NEWT)*, tech. rep. ATL-INDET-PUB-2008-002. ATL-COM-INDET-2008-004, CERN, 2008.

-
- [101] ATLAS Collaboration, *Performance of primary vertex reconstruction in proton-proton collisions at $\sqrt{s} = 7$ TeV in the ATLAS experiment*, tech. rep. ATLAS-CONF-2010-069, CERN, 2010.
- [102] ATLAS Collaboration, *Impact Parameter Resolution*, 2015, eprint: IDTR-2015-007/.
- [103] M. Cacciari, G. P. Salam and G. Soyez, *The anti- k_T jet clustering algorithm*, Journal of High Energy Physics **2008** (2008) 063.
- [104] ATLAS Collaboration, *Jet Calibration and Systematic Uncertainties for Jets Reconstructed in the ATLAS Detector at $\sqrt{s} = 13$ TeV*, tech. rep. ATL-PHYS-PUB-2015-015, CERN, 2015.
- [105] ATLAS Collaboration, *Jet energy scale measurements and their systematic uncertainties in proton-proton collisions at $\sqrt{s} = 13$ TeV with the ATLAS detector*, Phys. Rev. **D96** (2017) 072002, arXiv: 1703.09665 [hep-ex].
- [106] *Data-driven determination of the energy scale and resolution of jets reconstructed in the ATLAS calorimeters using dijet and multijet events at $\sqrt{s} = 8$ TeV*, tech. rep. ATLAS-CONF-2015-017, CERN, 2015.
- [107] ATLAS Collaboration, *Commissioning of the reconstruction of hadronic tau lepton decays in ATLAS using pp collisions at $\sqrt{s} = 13$ TeV*, tech. rep. ATL-PHYS-PUB-2015-025, CERN, 2015.
- [108] ATLAS Collaboration, *Identification and energy calibration of hadronically decaying tau leptons with the ATLAS experiment in pp collisions at $\sqrt{s} = 8$ TeV*, Eur. Phys. J. **C75** (2015) 303, arXiv: 1412.7086 [hep-ex].
- [109] ATLAS Collaboration, *Reconstruction, Energy Calibration, and Identification of Hadronically Decaying Tau Leptons in the ATLAS Experiment for Run-2 of the LHC*, tech. rep. ATL-PHYS-PUB-2015-045, CERN, 2015.
- [110] ATLAS Collaboration, *Measurement of the tau lepton reconstruction and identification performance in the ATLAS experiment using pp collisions at $\sqrt{s} = 13$ TeV*, tech. rep. ATLAS-CONF-2017-029, CERN, 2017.
- [111] ATLAS Collaboration, *Tagging and suppression of pileup jets with the ATLAS detector*, tech. rep. ATLAS-CONF-2014-018, CERN, 2014.
- [112] Y. Freund and R. E. Schapire, *A Decision-Theoretic Generalization of On-Line Learning and an Application to Boosting*, Journal of Computer and System Sciences **55** (1997) 119, ISSN: 0022-0000.
- [113] ATLAS Collaboration, *Electron efficiency measurements with the ATLAS detector using 2012 LHC proton-proton collision data*, Eur. Phys. J. **C77** (2017) 195, arXiv: 1612.01456 [hep-ex].
- [114] ATLAS Collaboration, *Identification of the Hadronic Decays of Tau Leptons in 2012 Data with the ATLAS Detector*, tech. rep. ATLAS-CONF-2013-064, CERN, 2013.
- [115] ATLAS Collaboration, *The ATLAS Tau Trigger in Run 2*, tech. rep. ATLAS-CONF-2017-061, CERN, 2017.
- [116] ATLAS Collaboration, *Performance of the Reconstruction and Identification of Hadronic Tau Decays with ATLAS*, tech. rep. ATLAS-CONF-2011-152, CERN, 2011.

- [117] T. Sjostrand, S. Mrenna and P. Z. Skands, *A Brief Introduction to PYTHIA 8.1*, Comput.Phys.Commun. **178** (2008) 852, arXiv: 0710.3820 [hep-ph].
- [118] P. M. Nadolsky et al., *Implications of CTEQ global analysis for collider observables*, Phys. Rev. **D78** (2008) 013004, arXiv: 0802.0007 [hep-ph].
- [119] ATLAS Collaboration, *Summary of ATLAS Pythia 8 tunes*, tech. rep. ATL-PHYS-PUB-2012-003, CERN, 2012.
- [120] M. L. Mangano et al., *ALPGEN, a generator for hard multiparton processes in hadronic collisions*, JHEP **07** (2003) 001, arXiv: hep-ph/0206293 [hep-ph].
- [121] P. Z. Skands, *Tuning Monte Carlo Generators: The Perugia Tunes*, Phys. Rev. **D82** (2010) 074018, arXiv: 1005.3457 [hep-ph].
- [122] B. T. Winter, *Reconstruction of neutral pions in hadronic tau lepton decays in the ATLAS detector*, Master thesis: Universität Bonn, 2012.
- [123] M. K. Ayoub, *Search of the Standard Model Higgs boson decaying into two lepton taus with the Run2 data of ATLAS detector in LHC*, Doctoral dissertation: Université Paris-Saclay, 2016.
- [124] V. Scharf, *Neutral Pion Subshower Reconstruction in Hadronic Tau Lepton Decays at the ATLAS experiment*, Master thesis: Ruprecht-Karls-Universität Heidelberg, 2009.
- [125] ATLAS Collaboration, *Reconstruction of hadronic decay products of tau leptons with the ATLAS experiment*, tech. rep. ATL-COM-PHYS-2015-245, CERN, 2015.
- [126] ATLAS Collaboration, *Measurement of the $H \rightarrow \tau^+\tau^-$ cross-section in 13 TeV Collisions with the ATLAS detector*, tech. rep., Internal note: CERN, 2018.
- [127] ATLAS Collaboration, *Study of the spin and parity of the Higgs boson in diboson decays with the ATLAS detector*, Eur. Phys. J. **C75** (2015) 476, [Erratum: Eur. Phys. J.C76,no.3,152(2016)], arXiv: 1506.05669 [hep-ex].
- [128] ATLAS Collaboration, *Evidence for the Higgs-boson Yukawa coupling to tau leptons with the ATLAS detector*, Journal of High Energy Physics **2015** (2015) 117, ISSN: 1029-8479.
- [129] N. Metropolis and S. Ulam, *The Monte Carlo Method*, Journal of the American Statistical Association **44** (1949) 335, ISSN: 01621459.
- [130] ATLAS Collaboration, *The ATLAS Simulation Infrastructure*, Eur. Phys. J. **C70** (2010) 823, arXiv: 1005.4568 [physics.ins-det].
- [131] S. Agostinelli et al., *GEANT4: A Simulation toolkit*, Nucl. Instrum. Meth. **A506** (2003) 250.
- [132] S. Alioli et al., *A general framework for implementing NLO calculations in shower Monte Carlo programs: the POWHEG BOX*, JHEP **06** (2010) 043, arXiv: 1002.2581 [hep-ph].

-
- [133] J. Alwall et al., *The automated computation of tree-level and next-to-leading order differential cross sections, and their matching to parton shower simulations*, JHEP **07** (2014) 079, arXiv: 1405.0301 [hep-ph].
- [134] M. Bahr et al., *Herwig++ Physics and Manual*, Eur. Phys. J. **C58** (2008) 639, arXiv: 0803.0883 [hep-ph].
- [135] J. Bellm et al., *Herwig 7.0/Herwig++ 3.0 release note*, Eur. Phys. J. **C76** (2016) 196, arXiv: 1512.01178 [hep-ph].
- [136] H.-L. Lai et al., *New parton distributions for collider physics*, Phys. Rev. **D82** (2010) 074024, arXiv: 1007.2241 [hep-ph].
- [137] ATLAS Collaboration, *Measurement of the Z/γ^* boson transverse momentum distribution in pp collisions at $\sqrt{s} = 7$ TeV with the ATLAS detector*, JHEP **09** (2014) 145, arXiv: 1406.3660 [hep-ex].
- [138] ATLAS Collaboration, *ATLAS Run 1 Pythia8 tunes*, tech. rep. ATL-PHYS-PUB-2014-021, CERN, 2014.
- [139] R. D. Ball et al., *Parton distributions for the LHC Run II*, JHEP **04** (2015) 040, arXiv: 1410.8849 [hep-ph].
- [140] T. Sjostrand, S. Mrenna and P. Skands, *PYTHIA 6.4 Physics and Manual*, JHEP **05** (2006) 026, arXiv: hep-ph/0603175 [hep-ph].
- [141] M. Pitt, *Search for the Standard Model Higgs boson in the $H \rightarrow \tau\tau$ channel with the ATLAS detector*, tech. rep. ATL-PHYS-PROC-2013-141, CERN, 2013.
- [142] M. Hübner, *Effects of tau decay product reconstruction in a Higgs CP analysis with the ATLAS experiment*, Master thesis: Universität Bonn, 2016.
- [143] G. Punzi, *Sensitivity of searches for new signals and its optimization*, [,79(2003)], 2003, arXiv: physics/0308063 [physics].
- [144] ATLAS Collaboration, *Forward Jet Vertex Tagging: A new technique for the identification and rejection of forward pileup jets*, tech. rep. ATL-PHYS-PUB-2015-034, CERN, 2015.
- [145] ATLAS Collaboration, *Measurement of the Mis-identification Probability of τ Leptons from Hadronic Jets and from Electrons*, tech. rep. ATLAS-CONF-2011-113, CERN, 2011.
- [146] K. Pearson, *LIII. On lines and planes of closest fit to systems of points in space*, The London, Edinburgh, and Dublin Philosophical Magazine and Journal of Science **2** (1901) 559, eprint: <https://doi.org/10.1080/14786440109462720>.
- [147] ATLAS Collaboration, *Performance of missing transverse momentum reconstruction with the ATLAS detector using proton-proton collisions at $\sqrt{s} = 13$ TeV*, 2018, arXiv: 1802.08168 [hep-ex].
- [148] S. Hoeche et al., *Matching Parton Showers and Matrix Elements*, 2006, eprint: arXiv:hep-ph/0602031.
- [149] The LHC Higgs Cross Section Working Group et al., *Handbook of LHC Higgs Cross Sections: 3. Higgs Properties*, (2013), eprint: arXiv:1307.1347.

- [150] M. Fischler and D. Sachs, *An Object-Oriented Minimization Package for HEP*, eConf **C0303241** (2003) MOLT004, arXiv: hep-ph/0306054 [hep-ph].
- [151] K. Cranmer et al., *HistFactory: A tool for creating statistical models for use with RooFit and RooStats*, CERN-OPEN-2012-016 (2012).
- [152] G. Cowan et al., *Asymptotic formulae for likelihood-based tests of new physics*, Eur. Phys. J. **C71** (2011) 1554, [Erratum: Eur. Phys. J. **C73**,2501(2013)], arXiv: 1007.1727 [physics.data-an].
- [153] R. Brun and F. Rademakers, *ROOT: An object oriented data analysis framework*, Nucl. Instrum. Meth. **A389** (1997) 81.
- [154] D. Zanzi, H. Kroha and S. Kortner, *Search for the Standard Model Higgs Boson in Hadronic $\tau^+\tau^-$ Decays with the ATLAS Detector*, CERN-THESIS-2014-085, 2014.
- [155] S. Berge et al., *How to pin down the CP quantum numbers of a Higgs boson in its tau decays at the LHC*, Phys. Rev. **D84** (2011) 116003, arXiv: 1108.0670 [hep-ph].
- [156] S. Berge, W. Bernreuther and S. Kirchner, *Determination of the Higgs CP mixing angle in the tau decay channels at the LHC including the Drell-Yan background*, Eur. Phys. J. **C74** (2014) 3164, arXiv: 1408.0798 [hep-ph].
- [157] C. Callenberg, *Feasibility to measure Higgs boson CP properties in $H \rightarrow \tau\tau$ decays at ATLAS using the impact parameters of the charged hadronic τ decay products*, Master thesis: Universität Bonn, 2015.
- [158] ATLAS Collaboration, *Test for CP invariance in Higgs Boson Decays to Tau Leptons with the ATLAS Detector*, Internal note in progress.
- [159] Z. Czynzula, T. Przedzinski and Z. Was, *TauSpinner program for studies on spin effect in tau production at the LHC*, The European Physical Journal C **72** (2012) 1988, ISSN: 1434-6052.
- [160] T. Sjöstrand et al., *An Introduction to PYTHIA 8.2*, Comput. Phys. Commun. **191** (2015) 159, arXiv: 1410.3012 [hep-ph].
- [161] T. Chen and C. Guestrin, *XGBoost: A Scalable Tree Boosting System*, KDD '16 (2016) 785.
- [162] T. Hastie, R. Tibshirani and J. Friedman, *The elements of statistical learning: data mining, inference and prediction*, 2nd ed., Springer, 2009.
- [163] ATLAS Collaboration, *Constraints on the spin-parity and anomalous HVV couplings of the Higgs boson in proton collisions at 7 and 8 TeV*, Phys. Rev. D **92** (1 2015) 012004.
- [164] ATLAS Collaboration, *Measurement of the Higgs boson coupling properties in the $H \rightarrow ZZ^* \rightarrow 4\ell$ decay channel at $\sqrt{s} = 13$ TeV with the ATLAS detector*, JHEP **03** (2018) 095, arXiv: 1712.02304 [hep-ex].

Relevant algebra of the unitary group $U(n)$ and special unitary group $SU(n)$

$SU(n)$ are the special unitary groups of degree n with $n \times n$ matrices, U , that obey $U^\dagger U = 1$ and $\det(U) = 1$. The Lie algebra of these groups has the commutation relation

$$[T_a, T_b] = i f_{abc} T_c \quad (\text{A.1})$$

for the generators, T , of the group with structure constant f_{abc} .

The $SU(2) \otimes U(1)$ group of the electroweak theory has three generators, T_a , that form the $SU(2)$ algebra, and a generator, Y , for the $U(1)$ algebra, with

$$[T_a, T_b] = i f_{abc} T_c, \quad [T_a, Y] = 0. \quad (\text{A.2})$$

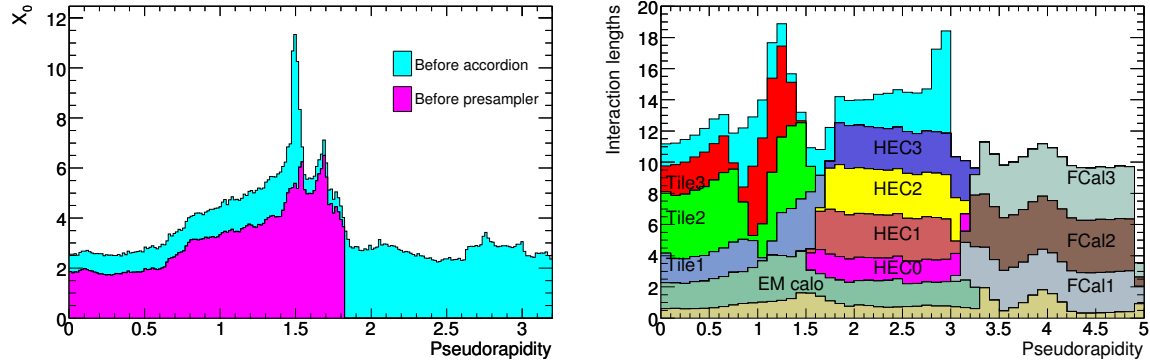
Relevant Properties of the ATLAS Detector

B.1 Segmentation of the Calorimeters at ATLAS

	Longitudinal Segmentation	Coverage in $ \eta $	Lateral Segmentation: Granularity ($\Delta\eta \times \Delta\phi$)
Electromagnetic Calorimeter (Barrel)	Presampler	$ \eta < 1.52$	0.025×0.1
	1st layer (strip layer)	$\eta < 1.40$	$0.025/8 \times 0.1$
	2nd layer	$1.40 < \eta < 1.475$	0.025×0.025
		$ \eta < 1.40$	0.025×0.025
		$1.40 < \eta < 1.475$	0.075×0.025
	3rd layer	$ \eta < 1.35$	0.050×0.025
Electromagnetic Calorimeter (Endcap)	Presampler	$1.5 < \eta < 1.8$	0.025×0.1
	1st layer (strip layer)	$1.375 < \eta < 1.425$	0.025×0.1
		$1.5 < \eta < 1.8$	$0.025/8 \times 0.1$
		$1.8 < \eta < 2.0$	0.004×0.1
		$2.0 < \eta < 2.5$	0.006×0.1
		$2.5 < \eta < 3.2$	0.1×0.1
	2nd layer	$1.375 < \eta < 2.5$	0.025×0.025
		$2.5 < \eta < 3.2$	0.1×0.1
	3rd layer	$1.5 < \eta < 2.5$	0.5×0.025

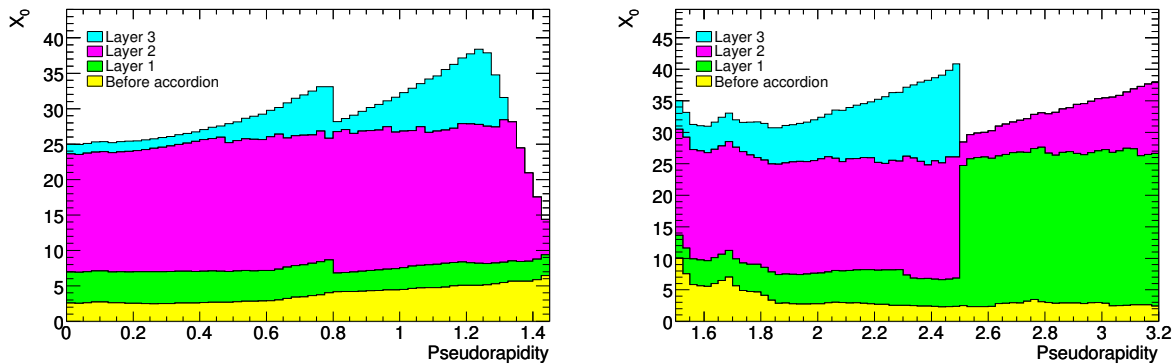
Table B.1: Segmentation of the ATLAS electromagnetic calorimeter. The strip layer is shown in red, except for the crack region, which is shown in gray. [79].

B.2 Amount of Material in the ATLAS Detector



(a) Amount of material, before the presampler and the ECAL accordion vs. Pseudorapidity [79]. (b) Amount of material in front of each subcomponent of the detector from the ECAL outward vs. Pseudorapidity [79].

Figure B.1: Amount of material before each subcomponent of the detector.



(a) Amount of material of each layer of the ECAL (barrel) vs. Pseudorapidity [79]. (b) Amount of material, in units of radiation length, of each layer of the ECAL (end cap) vs. Pseudorapidity [79].

Figure B.2: Length of each layer of the electromagnetic calorimeter.

Variables Used for the π^0 -ID

	Symbol	Description
Abs	FIRST ETA	Absolute value of the pseudorapidity of the cluster
	SECONDR	Second moment in distance to the shower axis
	CENTERLAMBDAhelped	Distance of the shower center from the calorimeter front face measured along the shower axis
	ENGFRACEM	Fraction of energy in EM calorimeter accordion (For this case: Ecal1 and Ecal2)
	ENGFRACCORE	Sum of the energy fractions in the most energetic cells per sampling
log	SECOND ENG DENS	$\log \langle (E/V)^2 \rangle$ Logarithm of the second moment in energy density
	$\frac{E_{core}}{E_{Ecal1}}$	Energy in three innermost Ecal1 cells normalized to the total energy in Ecal1
	AsymmetryWRTTrack	Asymmetry of energy distribution in Ecal1 with respect to the track
	NPosCellsEM1	Number of cells with positive energy in Ecal1
	NPosCells EM2	Number of cells with positive energy in Ecal2
	$\langle \eta^2 \rangle_{Ecal1}$	Second moment in pseudorapidity in Ecal1
	$\langle \eta^2 \rangle_{Ecal2}$	Second moment in pseudorapidity in Ecal2

Table C.1: Variables used to identify π^0 clusters in the π^0 -ID BDT.

Properties of the simulated single π^\pm sample used for developments of the tau particle flow algorithm

Properties of the simulated single π^\pm samples from PYTHIA 8.1 used for the development of the cluster-based π^\pm subtraction and discussed in Section 4.5.3.1 [117] are shown in this section.

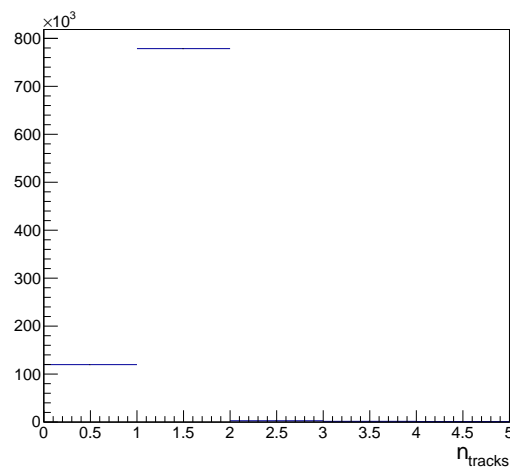


Figure D.1: Number of reconstructed tracks per event in the single π^\pm sample.

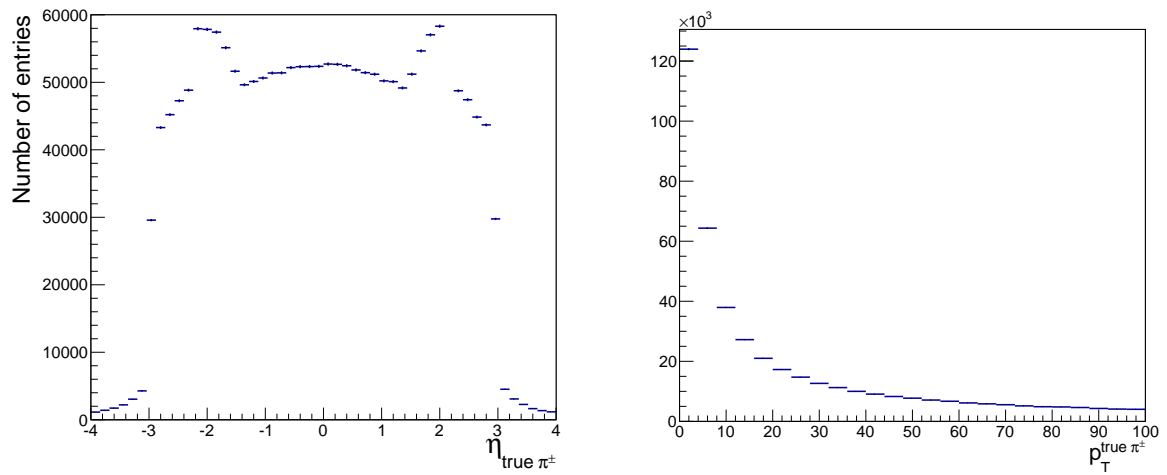


Figure D.2: The η (left) and p_T (right) spectra of the true charged pions in the single π^\pm sample.

Cross section values of background and signal processes in the $H \rightarrow \tau\tau$ analyses

Process	Dataset Name	σ [pb]	k -Fact.	Eff.
VBF	PoPy8 CT10AZNLOCTEQ6L1 VBFH125 tautauhh	0.24	0.98	0.42
ggH	PoPy8 CT10AZNLO WmH125J MINLO muvmuWWlvqq	1.91	1.45	0.42
$t\bar{t}H$	aMcAtNloHppEG UE5 C6L1 CT10ME ttH125 H2tau dilep	0.05	1.00	0.06
	aMcAtNloHppEG UE5 C6L1 CT10ME ttH125 H2tau semilep	0.46	1.00	0.03
	aMcAtNloHppEG UE5 C6L1 CT10ME ttH125 H2tau allhad	0.46	1.00	0.03
WH	Pythia8 A14NNPDF23LO WH125 inc	1.10	1.25	1.00
ZH	Pythia8 A14NNPDF23LO ZH125 inc	0.60	1.45	1.00
VBF (CP)	PowhegPythia8 VBFH125 tautauhh unpol	0.24	1.00	0.42
ggH (CP)	PowhegPythia8 ggH125 tautauhh unpol	3.05	1.00	0.42
QCD	Sherpa221 NN30NNLO Ztt Mll10 40MaxHtptv0 70BVeto	2417.90	0.98	0.97
$Z \rightarrow \tau\tau$	Sherpa221 NN30NNLO Ztt Mll10 40MaxHtptv0 70BFilt	2414.20	0.98	0.03
	Sherpa221 NN30NNLO Ztt Mll10 40MaxHtptv70 280BVeto	50.37	0.98	0.89
	Sherpa221 NN30NNLO Ztt Mll10 40MaxHtptv70 280BFilt	50.44	0.98	0.11
	Sherpa221 NN30NNLO Ztt Mll10 40MaxHtptv280ECMS BVeto	3.28	0.98	0.85
	Sherpa221 NN30NNLO Ztt Mll10 40MaxHtptv280ECMS BFil.	3.28	0.98	0.14
	Sherpa221 NNPDF30NNLO Ztt MaxHtptv0 70 h30h20	1982.20	1.00	0.06
	Sherpa221 NNPDF30NNLO Ztt MaxHtptv70 140 h30h20	110.49	1.00	0.09
	Sherpa221 NNPDF30NNLO Ztt MaxHtptv140 280 h30h20	40.69	1.00	0.11
	Sherpa221 NNPDF30NNLO Ztt MaxHtptv280 500CVetoBVeto	8.55	0.98	0.56
	Sherpa221 NNPDF30NNLO Ztt MaxHtptv280 500CFiltBVeto	8.67	0.98	0.26
	Sherpa221 NNPDF30NNLO Ztt MaxHtptv280 500BFilt	8.68	0.98	0.17
	Sherpa221 NNPDF30NNLO Ztt MaxHtptv500 1000	1.81	0.98	1.00
	Sherpa221 NNPDF30NNLO Ztt MaxHtptv1000ECMS	0.15	0.98	1.00
EWK	Sherpa CT10 Ztautau2JetsEW1JetQCD15GeV40	2.5413	1	1.00
$Z \rightarrow \tau\tau$				
$Z \rightarrow \ell\ell$	Sherpa CT10 Znunu2JetsEW1JetQCD15GeV	13.59	1.00	1.00
	Sherpa CT10 Zee2JetsEW1JetQCD15GeV40	2.55	1.00	1.00
	Sherpa CT10 Zmumu2JetsEW1JetQCD15GeV40	2.54	1.00	1.00
W +jets	Wenu Np0	13939.00	1.20	1.00
	Wenu Np1	1894.00	1.20	1.00
	Wenu Np2	642.66	1.20	1.00
	Wenu Np3	179.18	1.20	1.00
	Wenu Np4	70.79	1.20	1.00
	Wmunu Np0	13935.00	1.20	1.00

Appendix E Cross section values of background and signal processes in the $H \rightarrow \tau\tau$ analyses

Process	Dataset Name	σ [pb]	k -Fact.	Eff.
	Wmunu Np1	1 893.30	1.20	1.00
	Wmunu Np2	642.70	1.20	1.00
	Wmunu Np3	179.19	1.20	1.00
	Wmunu Np4	70.76	1.20	1.00
	Wtaunu Np0	13 920.00	1.20	1.00
	Wtaunu Np1	1 891.90	1.20	1.00
	Wtaunu Np2	641.87	1.20	1.00
	Wtaunu Np3	179.21	1.20	1.00
	Wtaunu Np4	71.01	1.20	1.00
Top	PowhegPythia P2012 ttbar hdamp172p5 nonallhad	696.11	1.19	0.54
	PowhegPythia P2012 ttbar hdamp172p5 allhad	695.99	1.20	0.46
	PowhegPythia P2012 singletop tchan lept top	43.74	1.01	1.00
	PowhegPythia P2012 singletop tchan lept top	25.78	1.02	1.00
	PowhegPythia P2012 Wt inclusive top	34.01	1.05	1.00
	PowhegPythia P2012 Wt inclusive antitop	33.99	1.05	1.00
	PowhegPythia P2012 Wt dilepton top	3.58	1.05	1.00
Diboson	Sherpa CT10 WplvWmqq SHv21 improved	24.89	0.91	1.00
	Sherpa CT10 WlvZqq SHv21 improved	11.49	0.91	1.00
	Sherpa CT10 WqqZll SHv21 improved	3.42	0.91	1.00
	Sherpa CT10 WqqZvv SHv21 improved	6.78	0.91	1.00
	Sherpa CT10 ZqqZll SHv21 improved	16.45	0.91	0.14
	Sherpa CT10 ZqqZvv SHv21 improved	16.43	0.91	0.28

Table E.1: Cross section values of background and signal processes at $\sqrt{s} = 13$ TeV. The signal assumes a Higgs boson mass of 125 GeV. The k -factor (k -fact.) describes the difference between the leading and higher-order cross sections (see Equation 2.46), and the efficiency (eff.) describes the detection efficiency. See Table 5.1 for a summary of the generators, PDF parametrization, and UE tunes for the simulated samples.

Changes to the $H \rightarrow \tau_{\text{had}}\tau_{\text{had}}$ preselection in Run-II

Several preselection criteria were changed with respect to those used in Run-I [128]. They are summarized in Table F.1. The kinematic selections were tightened in response to the higher center-of-mass energy. Also, the $\tau_{\text{had, vis}}$ ID working points were tightened to decrease the impact from mismodeling of the fake- τ background at low $m_{\text{MMC}}^{\tau\tau}$ and also to avoid the ambiguity in the application of the tight $\tau_{\text{had, vis}}$ ID scale factor in the use of a tight-medium working point. The tightening of the $\tau_{\text{had, vis}}$ ID does not weaken the expected sensitivity of the analysis.

In addition to the change in tau ID requirement, the isolation requirement used in Run-1 was removed. This required the τ_{had} lepton to have 1 or 3 tracks within a cone of $\Delta R < 0.6$ around the tau axis, i.e., no additional tracks, e.g., from pileup, in the annulus of $0.4 < \Delta R < 0.6$ around the tau axis. This altered the definition of the tau such that it was no longer similar to the tau objects used to measure tau ID scale factor corrections. Removal of the anti-isolation requirement does not make a difference in the quality of the background model with respect to data, and it avoids the necessity to measure analysis-specific tau identification scale factors. One side effect is that the removal of this anti- isolation requirement increases the amount of contamination since the $Z \rightarrow \tau\tau$ process is expected to contain more events that would fail the isolation requirement. However, the contamination is still minimal at about 15%.

Run-I	Run-II
No L1 jet requirement in trigger	L1 jet required in trigger
$p_{T,\tau_0} > 35$ GeV	$p_{T,\tau_0} > 40$ GeV
$p_{T,\tau_1} > 25$ GeV	$p_{T,\tau_1} > 30$ GeV
$0.6 < \Delta R < 2.5$	$0.8 < \Delta R < 2.4$
$\tau_{\text{had, vis}}$ ID: Tight-Medium	$\tau_{\text{had, vis}}$ ID: Tight-Tight
Isolation ($n_{\text{tracks}} = 0$ in) the $0.4 < \Delta R < 0.6$ annulus around the τ_{had} axis	No isolation requirement

Table F.1: Changes to the $H \rightarrow \tau\tau$ preselection in Run-II compared to Run-I [128].

Composition of the SS and nOS control regions

The following section shows the composition of the SS and nOS control regions. The errors on the relative event yields include statistical uncertainties only. In the nOS control region, about 57% of fake- τ events and 88% of $Z \rightarrow \tau\tau$ contamination events contain at least one τ_{had} lepton with exactly two prongs.

		nOS Control Region			$Z \rightarrow \tau\tau$		
$\tau_1 \backslash \tau_0$		1p	2p	3p	1p	2p	3p
1p		28.0 ± 1.1	22.6 ± 0.9	6.5 ± 0.4	5.9 ± 1.0	32.3 ± 3.4	3.1 ± 0.7
2p		19.9 ± 0.8	4.4 ± 0.3	4.7 ± 0.3	33.8 ± 3.7	1.9 ± 0.6	12.7 ± 1.7
3p		6.7 ± 0.4	5.5 ± 0.3	1.7 ± 0.2	2.3 ± 0.5	7.1 ± 1.0	0.8 ± 0.3

Table G.1: Track composition of the nOS control region at preselection level in percentage.

Validation of the Background Modeling in the $H \rightarrow \tau\tau$ analysis

The distributions of important observables used to define the signal categories are shown in this section. They use the OS-nOS background estimate method. The systematic errors include all uncertainties described in Section 5.8 except for those concerning the fake- τ background estimation.

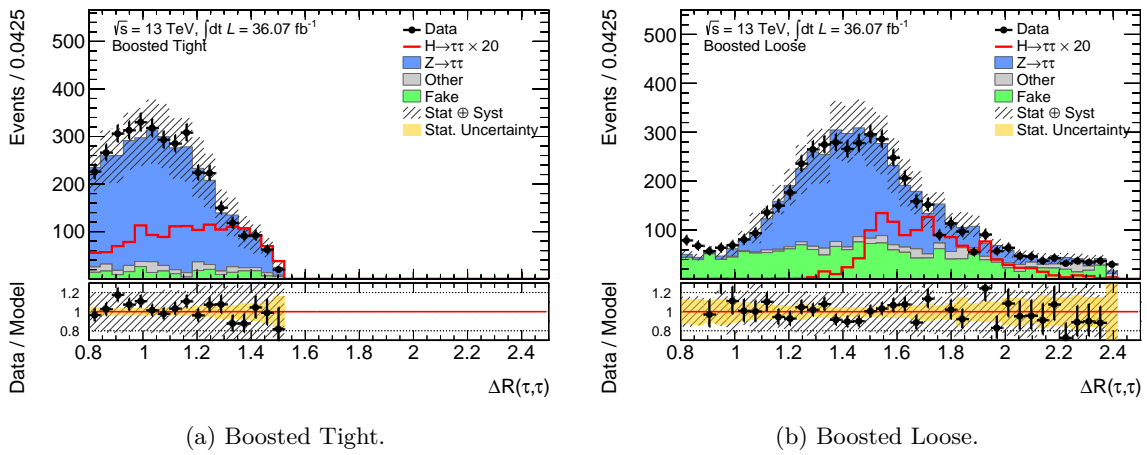


Figure H.1: Validation of the OS-nOS background modeling for the ΔR observable.

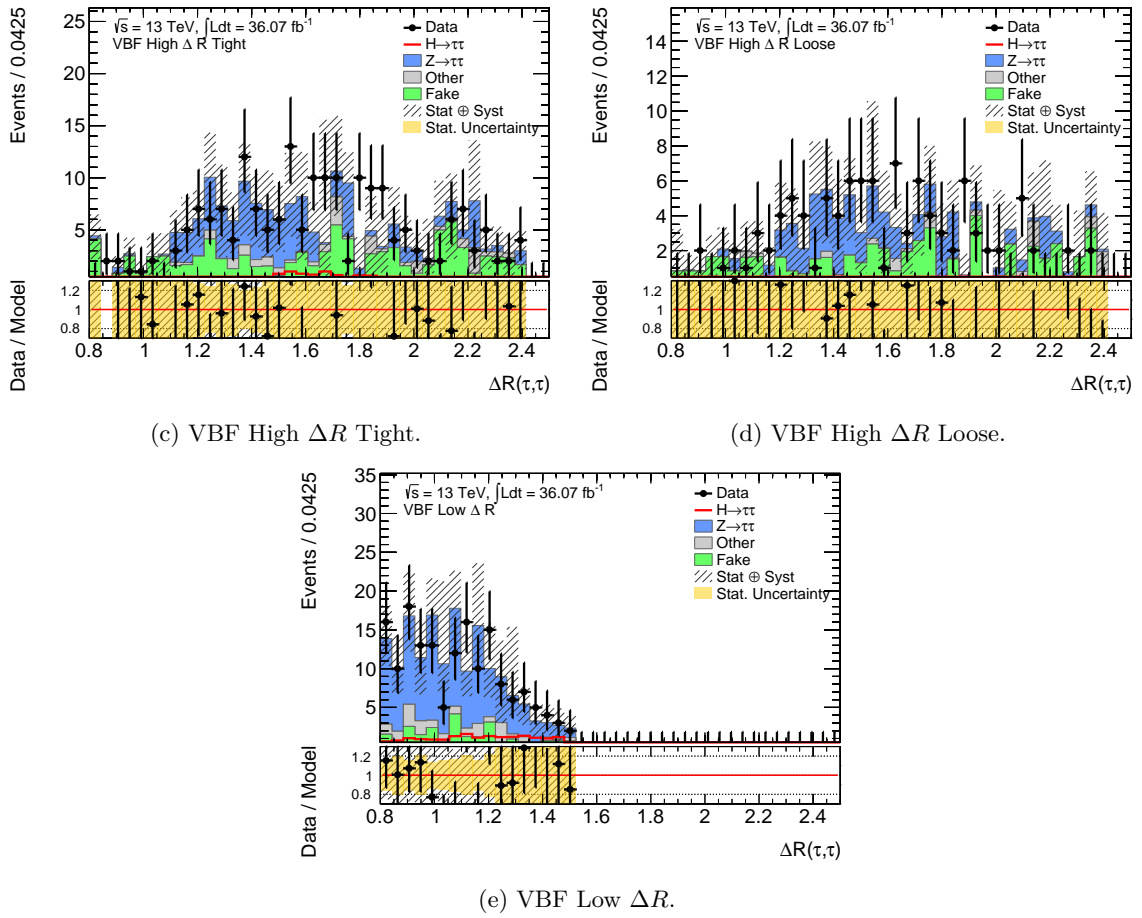


Figure H.1: Validation of the OS-nOS background modeling for the ΔR observable.

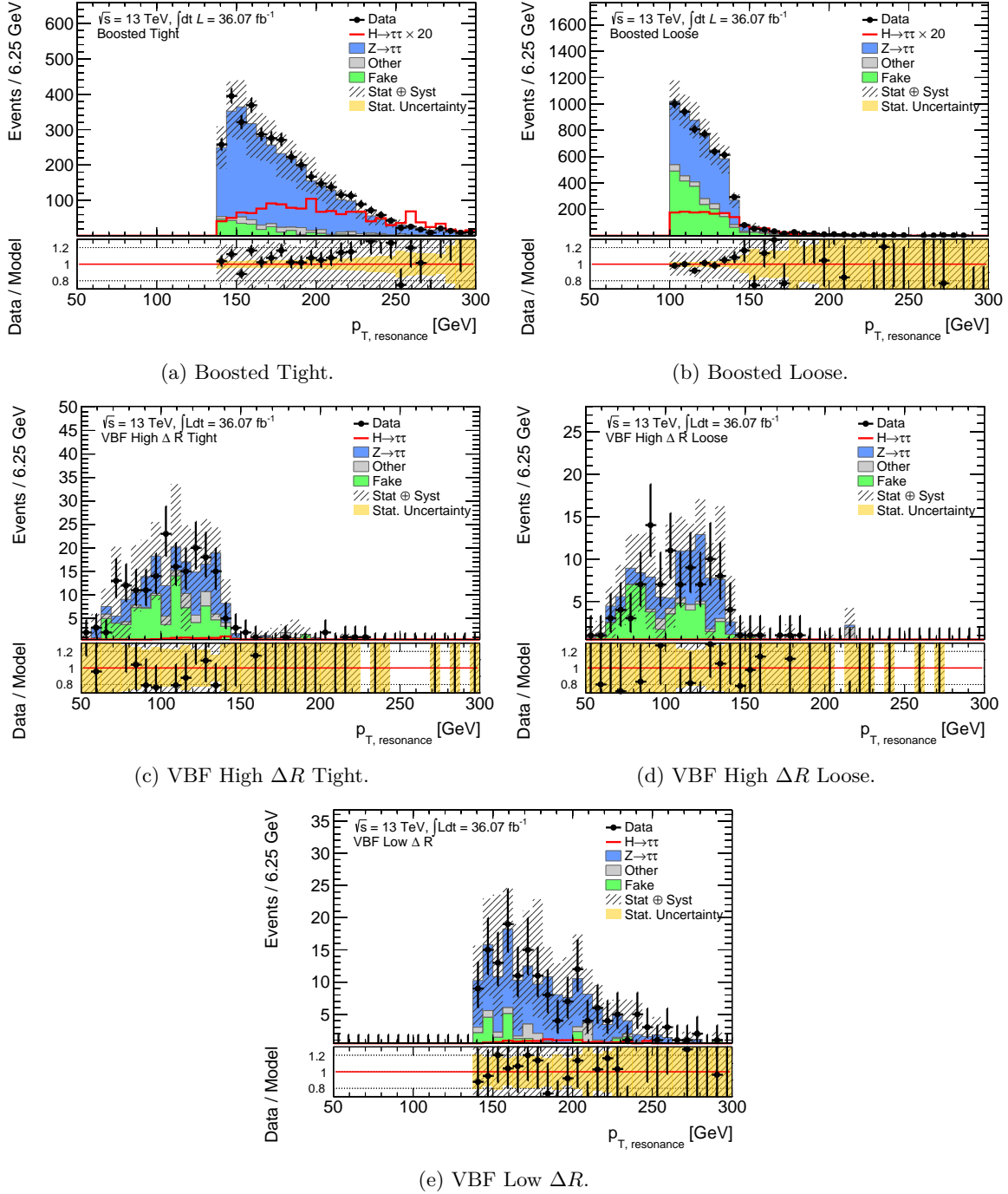
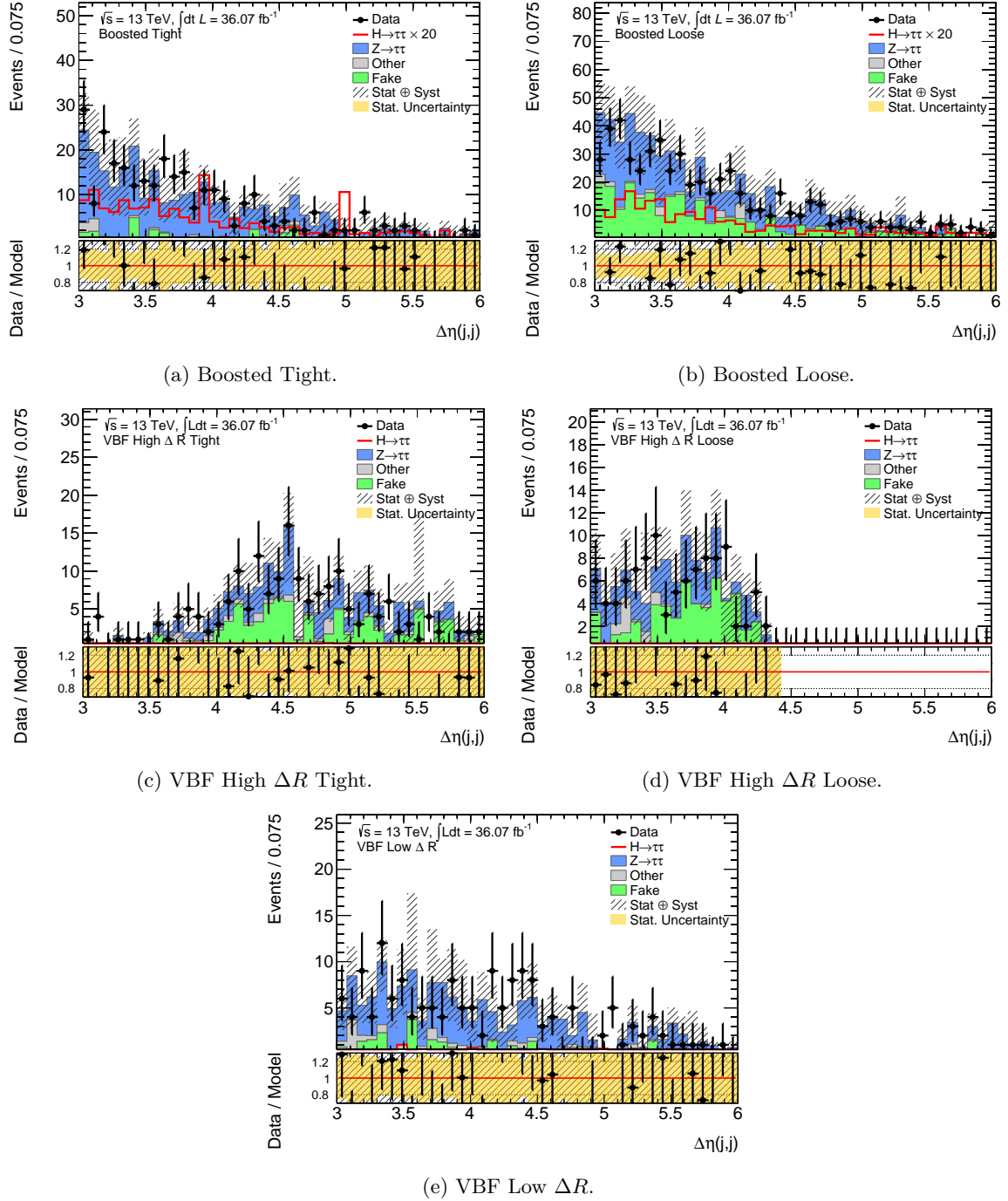


Figure H.2: Validation of the OS-nOS background modeling for the p_T of the di-tau resonance.


 Figure H.3: Validation of the OS-nOS background modeling for the $\Delta\eta(j,j)$ observable.

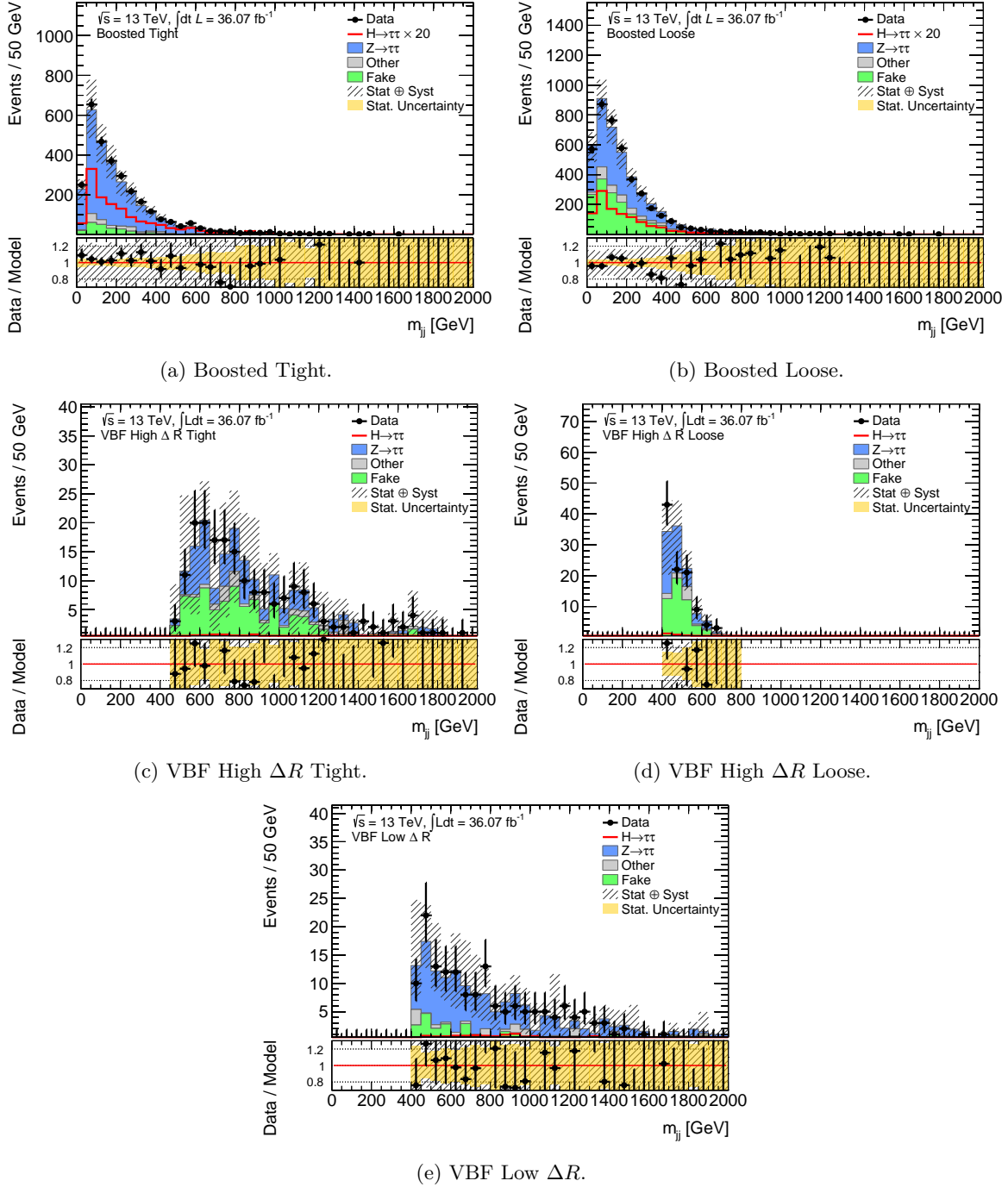


Figure H.4: Validation of the OS-nOS background modeling for the m_{jj} observable.

Supplemental information on the final fit to the $m_{\text{MMC}}^{\tau\tau}$ distribution in the couplings analysis

The following section provides details on the statistical model presented in Section 5.9. The binning used in the final fit to the $m_{\text{MMC}}^{\tau\tau}$ observable is listed in Table I.1. A list of each NP with its notation and corresponding meaning is given in this section, and the prefit impact from each NP is shown in Section I.3.

I.1 Binning of the $m_{\text{MMC}}^{\tau\tau}$ discriminant in the statistical interpretation

Category	$m_{\text{MMC}}^{\tau\tau}$ Binning
Boost Tight	0, 75, 80, 85, 90, 95, 100, 105, 115, 130, 200
Boost Loose	0, 80, 90, 100, 110, 115, 125, 140, 160, 180, 200
VBF High ΔR Tight	0, 80, 100, 120, 140, 160, 200
VBF High ΔR Loose	0, 80, 100, 120, 140, 160, 200
VBF Low ΔR	0, 80, 100, 120, 140, 160, 200

Table I.1: Binning of the $m_{\text{MMC}}^{\tau\tau}$ distribution used in the final fit.

I.2 Definitions of nuisance parameters

BR($H \rightarrow \tau\tau$): Event yield NP on the $H \rightarrow \tau\tau$ branching ratio.

Forward JVT: Event yield and shape NP for efficiency uncertainties of the forward jet vertex tagger (fJVT).

JER: Event yield NP addressing the uncertainty on the jet energy resolution.

JES (Effective NP 1-6): Event yield and shape NPs, broken down into individual effective NPs, addressing the uncertainty on the JES.

- JES (Inter- $|\eta|$ Calibration, Model):** Event yield and shape NP addressing the uncertainty on the JES related to the η intercalibration.
- JES (Inter- $|\eta|$ Calibration, Nonclosure):** Event yield and shape NP addressing the nonclosure for the JES η intercalibration binning.
- JES (Inter- $|\eta|$ Calibration, Stat.):** Event yield and shape NP addressing the nonclosure for the statistical uncertainty on the JES η intercalibration.
- JES (Flavor composition):** Event yield and shape NP addressing the uncertainty on the JES related to the difference in flavor composition (quark- vs. gluon- initiated jets).
- JES (Flavor Response):** Event yield and shape NP addressing the uncertainty on the JES related to the differences in detector response for the differences flavor compositions.
- JES (PU Offset μ):** Event yield and shape NP addressing the potential MC mismodeling of μ in the JES calibration.
- JES (PU Offset NPV):** Event yield and shape NP addressing the potential MC mismodeling of the number of reconstructed primary vertices, N_{PV} , in the JES calibration.
- JES (PU p_T term):** Event yield and shape NP addressing the potential MC mismodeling of the residual p_T dependence in the JES calibration.
- JES (PU ρ):** Event yield and shape NP addressing the potential MC mismodeling of the per-event p_T density modeling, or ρ topology, in the JES calibration.
- JVT:** Event yield and shape NP for efficiency uncertainties of the jet vertex tagger (JVT).
- MET Soft track (Parallel resolution):** Event yield and shape NP addressing the uncertainty on the \cancel{E}_T resolution.
- MET Soft track (Perpendicular resolution):** Event yield and shape NP addressing the uncertainty on the \cancel{E}_T resolution.
- MET Soft track (Scale):** Event yield and shape NP addressing the uncertainties on the \cancel{E}_T scale.
- PRW Data SF:** Event yield and shape NP addressing the pileup reweighting.
- Tau Eff. (e-OLR, true e):** Event yield and shape NP addressing the uncertainty on the electron veto efficiency for a true electron.
- Tau Eff. (e-OLR, true τ_{had}):** Event yield and shape NP addressing the uncertainty on the electron veto efficiency for a true τ_{had} lepton.
- Tau Eff. (ID, high- p_T):** Event yield and shape NP for efficiency uncertainties from $\tau_{had, vis}$ ID

at high- p_T .

Tau Eff. (ID, total): Event yield and shape NP for efficiency uncertainties from $\tau_{\text{had, vis}}$ ID (total).

Tau Eff. (Reco, high- p_T): Event yield and shape NP addressing the uncertainty on the τ_{had} reconstruction efficiency at high- p_T .

Tau Eff. (Reco, total): Event yield and shape NP addressing the uncertainty on the τ_{had} reconstruction efficiency.

Tau Eff. (2015 Trigger, data, stat.): Event yield and shape NP addressing the statistical uncertainty on the data in the 2015 τ_{had} trigger efficiency measurement.

Tau Eff. (2016 Trigger, data, stat.): Event yield and shape NP addressing the statistical uncertainty on the data in the 2016 τ_{had} trigger efficiency measurement.

Tau Eff. (2015 Trigger, MC, stat.): Event yield and shape NP addressing the statistical uncertainty on the MC in the 2015 τ_{had} trigger efficiency measurement.

Tau Eff. (2016 Trigger, MC, stat.): Event yield and shape NP addressing the statistical uncertainty on the MC in the 2016 τ_{had} trigger efficiency measurement.

Tau Eff. (2015 Trigger, sys.): Event yield and shape NP addressing the uncertainty on the τ_{had} trigger efficiency measurement in 2015 data.

Tau Eff. (2016 Trigger, sys.): Event yield and shape NP addressing the uncertainty on the τ_{had} trigger efficiency measurement in 2016 data.

TES (Detector): Event yield and shape NP for uncertainties on the TES measurement from the detector response.

TES (In situ): Event yield and shape NP for the measurement of the shifts in energy related to the *in-situ* based TES measurement.

TES (Model): Event yield and shape NP for uncertainties on the TES measurement from the simulation model.

UE (gg): Event yield NP addressing the uncertainty on the underlying event (UE) of the cross sections of the gg signal processes.

UE (qq): Event yield NP addressing the uncertainty on the underlying event (UE) of the cross sections of the qq signal processes.

Luminosity: Event yield NP addressing the uncertainty on the measurement of the integrated luminosity.

- NLO EWK Higgs:** Event yield NP addressing the uncertainty on the NLO calculations of the electroweak production of the Higgs.
- QCD scale (VH):** Event yield NP addressing the uncertainty on the VH cross section.
- QCD scale (ggH m12):** Event yield NP addressing QCD scale uncertainty on $H + > 1$ jet events in the ggH production process.
- QCD scale (ggH ptH m01):** Event yield NP addressing QCD scale uncertainty on $H + < 2$ jets events in the ggH production process.
- QCD scale (qqH):** Event yield NP addressing the uncertainty on the VBF cross section.
- Theory $Z \rightarrow \tau\tau$ CKK:** Event yield and shape NP addressing the CKKW parton-jet matching procedure for the $Z \rightarrow \tau\tau$ background.
- Theory $Z \rightarrow \tau\tau$ Factorization:** Event yield and shape NP addressing the factorization in the simulated $Z \rightarrow \tau\tau$ background.
- Theory $Z \rightarrow \tau\tau$ QSF:** Event yield and shape NP addressing the running QCD coupling constants at each leg of the parton branch in the simulated $Z \rightarrow \tau\tau$ background.
- Theory $Z \rightarrow \tau\tau$ Renormalization:** Event yield and shape NP addressing the renormalization in the simulated $Z \rightarrow \tau\tau$ background.
- EWK $Z \rightarrow \tau\tau$ proportion:** Event yield NP addressing the uncertainty of the proportion of the $Z \rightarrow \tau\tau$ background from the EWK production process.
- Fake- τ contamination:** Event yield and shape NP for the subtraction of non-fake- τ backgrounds from the nOS fake- τ template.
- Fake- τ extrapolation:** Event yield and shape NP for differences between the OS and nOS control region used for the fake- τ background.
- Higgs PDF (gg):** Event yield NP for the cross section of the signal processes from gg production processes (ggH).
- Higgs PDF (gg , Acceptance):** Event yield NP for the acceptance of signal events into the signal categories due to the uncertainty on the cross section of the signal processes from gg production processes (ggH).
- Higgs PDF (qq):** Event yield NP for the cross section of the signal processes from qq production processes (VBF, VH).
- Higgs PDF (qq , Acceptance):** Event yield NP for the acceptance of signal events into the signal categories due to the uncertainty on the cross section of the signal processes from qq production processes (VBF, VH).

I.3 Prefit impact of each nuisance parameter in each signal category

Nuisance Parameter	Signal		Background	
	+1 σ	-1 σ	+1 σ	-1 σ
BR($H \rightarrow \tau\tau$)	5.7	-5.7	0.00	0.00
Forward JVT	0.00	0.00	0.00	0.00
JER	-3.91	3.91	-3.24	3.24
JES (Effective NP 1)	4.53	-8.12	6.15	-7.53
JES (Effective NP 2)	-0.02	0.45	-0.34	-1.36
JES (Effective NP 3)	-0.87	0.23	-1.06	0.54
JES (Effective NP 4)	0.84	0.00	0.00	0.00
JES (Effective NP 5)	-0.81	0.84	-0.6	0.76
JES (Effective NP 6)	0.00	0.00	-0.54	0.45
JES (Inter- $ \eta $ Calibration, Model)	2.59	-2.69	6.38	-8.25
JES (Inter- $ \eta $ Calibration, Nonclosure)	-0.73	0.03	0.00	0.00
JES (Inter- $ \eta $ Calibration, Stat.)	0.75	-3.37	0.00	-0.89
JES (Flavor composition)	7.33	-10.21	6.41	-9.24
JES (Flavor Response)	-5.24	3.23	-0.93	0.01
JES (PU Offset μ)	0.00	0.00	2.72	-4.77
JES (PU Offset NPV)	2.7	-2.65	0.13	0.23
JES (PU p_T term)	2.48	-2.46	0.03	-0.06
JES (PU ρ)	-2.94	1.92	3.49	-3.94
JVT	0.00	0.00	0.00	0.00
MET Soft track (Parallel resolution)	0.59	-0.59	1.62	-1.62
MET Soft track (Perpendicular resolution)	-0.69	0.69	1.29	-1.29
MET Soft track (Scale)	0.39	-0.39	0.51	-0.44
PRW Data SF	-3.27	3.64	-2.81	3.36
Tau Eff. (e -OLR, true e)	0.00	0.00	0.07	-0.07
Tau Eff. (e -OLR, true τ_{had})	1.99	-1.97	1.08	-1.07
Tau Eff. (ID, high- p_T)	0.00	0.00	0.00	0.00
Tau Eff. (ID, total)	12.78	-12.01	5.96	-5.63
Tau Eff. (Reco, high- p_T)	0.00	0.00	0.00	0.00
Tau Eff. (Reco, total)	6.73	-6.51	3.7	-3.58
Tau Eff. (2015 Trigger, data, stat.)	0.00	0.00	0.00	0.00
Tau Eff. (2016 Trigger, data, stat.)	2.75	-3.44	1.53	-1.84
Tau Eff. (2015 Trigger, MC, stat.)	0.00	0.00	0.00	0.00
Tau Eff. (2016 Trigger, MC, stat.)	2.32	-2.94	1.19	-1.47
Tau Eff. (2015 Trigger, sys.)	0.00	0.00	0.00	0.00
Tau Eff. (2016 Trigger, sys.)	2.01	-2.24	1.19	-1.3
TES (Detector)	-6.52	2.23	-1.86	1.68
TES (In situ)	-2.43	-1.16	1.72	-0.72
TES (Model)	0.29	-0.39	0.00	0.00
UE (gg)	0.46	-0.46	0.00	0.00
UE (qq)	4.34	-4.34	0.00	0.00
Luminosity	2.9	-2.9	0.21	-0.21
NLO EWK Higgs	1.08	-1.08	0.00	0.00
QCD scale (VH)	0.00	0.00	0.00	0.00
QCD scale (ggH $m12$)	11.9	-9.15	0.00	0.00
QCD scale (ggH ptH $m01$)	0.00	0.00	0.00	0.00
QCD scale (qqH)	0.54	-0.43	0.00	0.00
Theory $Z \rightarrow \tau\tau$ CKK	0.00	0.00	-12.25	12.25
Theory $Z \rightarrow \tau\tau$ Factorization	0.00	0.00	-1	1
Theory $Z \rightarrow \tau\tau$ QSF	0.00	0.00	2.81	-2.81
Theory $Z \rightarrow \tau\tau$ Renormalization	0.00	0.00	0.7	-0.7
EWK $Z \rightarrow \tau\tau$ proportion	0.00	0.00	0.29	-0.29
Fake- τ contamination	0.00	0.00	-4.58	4.58
Fake- τ extrapolation	0.00	0.00	3.35	-3.35
Higgs PDF (gg)	3.43	-3.16	0.00	0.00
Higgs PDF (gg , Acceptance)	1.25	-1.06	0.00	0.00
Higgs PDF (qq)	1.41	-1.52	0.00	0.00
Higgs PDF (qq , Acceptance)	1.17	-1	0.00	0.00

Table I.2: Relative impact of the nuisance parameters on the total number of events shown for the **VBF High ΔR Loose** category (%).

Appendix I Supplemental information on the final fit to the $m_{MMC}^{\tau\tau}$ distribution in the couplings analysis

Nuisance Parameter	Signal		Background	
	+1 σ	-1 σ	+1 σ	-1 σ
BR($H \rightarrow \tau\tau$)	5.7	-5.7	0.00	0.00
Forward JVT	0.00	0.00	0.00	0.00
JER	-0.12	0.12	-8.96	8.96
JES (Effective NP 1)	3.56	-3.81	8.88	-1.99
JES (Effective NP 2)	0.3	-0.86	1.78	-1.08
JES (Effective NP 3)	0.00	0.00	-2.66	2.39
JES (Effective NP 4)	-0.34	0.08	1.99	-0.86
JES (Effective NP 5)	1.74	-1.41	0.00	0.00
JES (Effective NP 6)	0.00	0.00	0.00	0.00
JES (Inter- $ \eta $ Calibration, Model)	2.18	-3.02	3.29	-0.27
JES (Inter- $ \eta $ Calibration, Nonclosure)	-0.92	2.41	-0.45	0.16
JES (Inter- $ \eta $ Calibration, Stat.)	1.55	-2.72	0.51	-0.49
JES (Flavor composition)	7.19	-7.08	9.23	-4.32
JES (Flavor Response)	-4.1	4.92	3.22	-2.48
JES (PU Offset μ)	2.07	-1.37	1.85	-1.59
JES (PU Offset NPV)	2.01	-1.84	-0.17	-0.1
JES (PU p_T term)	0.00	0.00	1.05	1.15
JES (PU ρ)	4.68	-3.58	1.66	-1.64
JVT	0.00	0.00	0.00	0.00
MET Soft track (Parallel resolution)	0.52	-0.52	1.36	-1.36
MET Soft track (Perpendicular resolution)	-0.35	0.35	-3.53	3.46
MET Soft track (Scale)	1.14	-1.15	0.3	-1.75
PRW Data SF	-6.05	4.83	-2.28	2.31
Tau Eff. (e -OLR)	0.00	0.00	0.00	0.00
Tau Eff. (e -OLR, true τ_{had})	2.01	-1.99	1.09	-1.08
Tau Eff. (ID, high- p_T)	0.00	0.00	0.00	0.00
Tau Eff. (ID, total)	12.74	-11.98	6.85	-6.45
Tau Eff. (Reco, high- p_T)	0.00	0.00	0.00	0.00
Tau Eff. (Reco, total)	6.78	-6.57	3.87	-3.74
Tau Eff. (2015 Trigger, data, stat.)	0.00	0.00	0.00	0.00
Tau Eff. (2016 Trigger, data, stat.)	2.77	-3.47	1.59	-1.88
Tau Eff. (2015 Trigger, MC, stat.)	0.00	0.00	0.00	0.00
Tau Eff. (2016 Trigger, MC, stat.)	2.3	-2.97	1.22	-1.47
Tau Eff. (2015 Trigger, sys.)	0.00	0.00	0.00	0.00
Tau Eff. (2016 Trigger, sys.)	1.97	-2.15	1.32	-1.46
TES (Detector)	-0.56	1.87	-1.97	1.32
TES (In situ)	3.79	-3.98	3.09	-6.58
TES (Model)	0.34	0.22	-0.2	0.21
UE (gg)	0.27	-0.27	0.00	0.00
UE (qq)	5.85	-5.85	0.00	0.00
Luminosity	2.9	-2.9	0.15	-0.15
NLO EWK Higgs	1.46	-1.46	0.00	0.00
QCD scale (VH)	0.00	0.00	0.00	0.00
QCD scale (ggH $m12$)	6.97	-5.36	0.00	0.00
QCD scale (ggH ptH $m01$)	0.00	0.00	0.00	0.00
QCD scale (qqH)	0.73	-0.59	0.00	0.00
Theory $Z \rightarrow \tau\tau$ CKK	0.00	0.00	-12.04	12.05
Theory $Z \rightarrow \tau\tau$ Factorization	0.00	0.00	-1.63	1.63
Theory $Z \rightarrow \tau\tau$ QSF	0.00	0.00	2.21	-2.21
Theory $Z \rightarrow \tau\tau$ Renormalization	0.00	0.00	0.00	0.00
EWK $Z \rightarrow \tau\tau$ proportion	0.00	0.00	1.17	-1.17
Fake- τ contamination	0.00	0.00	-2.72	2.72
Fake- τ extrapolation	0.00	0.00	0.31	-1.69
Higgs PDF (gg)	2.01	-1.85	0.00	0.00
Higgs PDF (gg , Acceptance)	0.73	-0.62	0.00	0.00
Higgs PDF (qq)	1.9	-2.05	0.00	0.00
Higgs PDF (qq , Acceptance)	1.57	-1.36	0.00	0.00

Table I.3: Relative impact of the nuisance parameters on the total number of events shown for the **VBF High ΔR Tight** category (%).

I.3 Prefit impact of each nuisance parameter in each signal category

Nuisance Parameter	Signal		Background	
	+1 σ	-1 σ	+1 σ	-1 σ
BR($H \rightarrow \tau\tau$)	5.7	-5.7	0.00	0.00
Forward JVT	0.00	0.00	0.00	0.00
JER	-2.23	2.23	2.34	-2.34
JES (Effective NP 1)	4.85	-7.51	8.82	-9.85
JES (Effective NP 2)	-0.26	-0.25	1.18	-0.06
JES (Effective NP 3)	-1.1	1.39	-1.52	2.41
JES (Effective NP 4)	-1.9	1.9	0.00	0.00
JES (Effective NP 5)	0.00	0.00	0.00	0.00
JES (Effective NP 6)	0.00	0.00	0.00	0.00
JES (Inter- $ \eta $ Calibration, Model)	4.99	-4.69	8.84	-8.68
JES (Inter- $ \eta $ Calibration, Nonclosure)	0.06	-0.06	-2.06	3.1
JES (Inter- $ \eta $ Calibration, Stat.)	0.81	-1.15	4.54	-0.82
JES (Flavor composition)	5.58	-5.77	22.39	-9.46
JES (Flavor Response)	-2.08	2.14	-2.23	4.83
JES (PU Offset μ)	0.35	-0.78	4.14	-4.82
JES (PU Offset NPV)	0.37	-0.97	-0.26	-0.64
JES (PU p_T term)	0.00	0.00	-1.34	1.55
JES (PU ρ)	0.43	-1.33	4.09	-1.5
JVT	0.00	0.00	-0.02	0.02
MET Soft track (Parallel resolution)	0.61	-0.61	-0.19	0.19
MET Soft track (Perpendicular resolution)	0.06	-0.07	1.37	-1.37
MET Soft track (Scale)	1.4	-0.93	0.00	0.00
PRW Data SF	-4.78	3.22	-3.89	3.3
Tau Eff. (e -OLR)	0.00	0.00	-0.01	0.01
Tau Eff. (e -OLR, true τ_{had})	2.31	-2.28	1.8	-1.78
Tau Eff. (ID, high- p_T)	0.00	0.00	0.00	0.00
Tau Eff. (ID, total)	12.77	-12	10.64	-10
Tau Eff. (reco, high- p_T)	0.00	0.00	0.00	0.00
Tau Eff. (Reco, total)	6.05	-5.88	5.37	-5.2
Tau Eff. (2015 Trigger, data, stat.)	0.14	-0.35	0.00	0.01
Tau Eff. (2016 Trigger, data, stat.)	3.09	-4.35	2.31	-3.1
Tau Eff. (2015 Trigger, MC, stat.)	0.00	0.00	0.00	0.00
Tau Eff. (2016 Trigger, MC, stat.)	2.6	-4.43	1.87	-2.77
Tau Eff. (2015 Trigger, sys.)	0.00	0.00	0.00	0.00
Tau Eff. (2016 Trigger, sys.)	1.48	-1.73	1.61	-1.77
TES (Detector)	-1.17	2.04	-1.99	2.01
TES (In situ)	0.47	-1.02	3.26	-3.33
TES (Model)	-0.66	-0.29	0.03	-0.66
UE (gg)	0.29	-0.29	0.00	0.00
UE (qq)	5.28	-5.28	0.00	0.00
Luminosity	2.9	-2.9	0.12	-0.12
NLO EWK Higgs	1.32	-1.32	0.00	0.00
QCD scale (VH)	0.04	-0.04	0.00	0.00
QCD scale (ggH $m12$)	7.67	-5.9	0.00	0.00
QCD scale (ggH ptH $m01$)	0.00	0.00	0.00	0.00
QCD scale (qqH)	0.66	-0.53	0.00	0.00
Theory $Z \rightarrow \tau\tau$ CKK	0.00	0.00	-21.55	21.55
Theory $Z \rightarrow \tau\tau$ Factorization	0.00	0.00	-1.25	1.25
Theory $Z \rightarrow \tau\tau$ QSF	0.00	0.00	3.9	-3.9
Theory $Z \rightarrow \tau\tau$ Renormalization	0.00	0.00	1.17	-1.17
EWK $Z \rightarrow \tau\tau$ proportion	0.00	0.00	1.9	-1.9
Fake- τ contamination	0.00	0.00	-2.77	9.27
Fake- τ extrapolation	0.00	0.00	-1.47	1.63
Higgs PDF (gg)	2.21	-2.04	0.00	0.00
Higgs PDF (gg , Acceptance)	0.8	-0.68	0.00	0.00
Higgs PDF (qq)	1.83	-1.97	0.00	0.00
Higgs PDF (qq , Acceptance)	1.42	-1.22	0.00	0.00

Table I.4: Relative impact of the nuisance parameters on the total number of events shown for the **VBF Low ΔR** category (%).

Appendix I Supplemental information on the final fit to the $m_{MMC}^{\tau\tau}$ distribution in the couplings analysis

Nuisance Parameter	Signal		Background	
	+1 σ	-1 σ	+1 σ	-1 σ
BR($H \rightarrow \tau\tau$)	5.7	-5.7	0.00	0.00
Forward JVT	0.00	0.00	0.00	0.00
JER	-2.6	2.6	-0.39	0.39
JES (Effective NP 1)	-1.4	1.04	3.53	-3.13
JES (Effective NP 2)	-0.84	-1.03	1.26	-1.84
JES (Effective NP 3)	0.00	0.00	-1.13	1.04
JES (Effective NP 4)	0.00	0.00	0.00	0.00
JES (Effective NP 5)	0.00	0.00	0.00	0.00
JES (Effective NP 6)	0.00	0.00	0.00	0.00
JES (Inter- $ \eta $ Calibration, Model)	-1.24	-0.06	1.93	-2.02
JES (Inter- $ \eta $ Calibration, Nonclosure)	0.00	0.00	0.00	0.00
JES (Inter- $ \eta $ Calibration, Stat.)	0.00	-0.68	0.89	-1.31
JES (Flavor composition)	1.93	-1.91	3.36	-4.19
JES (Flavor Response)	-0.98	0.8	-1.79	1.95
JES (PU Offset μ)	0.00	0.00	0.00	0.00
JES (PU Offset NPV)	0.00	0.00	0.00	0.00
JES (PU p_T term)	0.00	0.00	0.00	0.01
JES (PU ρ)	0.07	-0.76	1.53	-2.03
JVT	0.00	0.00	0.00	0.00
MET Soft track (Parallel resolution)	-0.04	0.04	-0.25	0.25
MET Soft track (Perpendicular resolution)	0.81	-0.81	-0.14	0.14
MET Soft track (Scale)	0.24	0.38	0.47	-0.02
PRW Data SF	-3.1	1.16	-4.11	2.47
Tau Eff. (e -OLR)	0.00	0.00	0.00	0.00
Tau Eff. (e -OLR, true τ_{had})	2.27	-2.25	1.9	-1.88
Tau Eff. (ID, high- p_T)	0.00	0.00	0.00	0.00
Tau Eff. (ID, total)	12.76	-11.99	11.03	-10.38
Tau Eff. (reco, high- p_T)	0.00	0.00	0.00	0.00
Tau Eff. (Reco, total)	6	-5.82	5.67	-5.49
Tau Eff. (2015 Trigger, data, stat.)	0.00	0.00	-0.04	0.07
Tau Eff. (2016 Trigger, data, stat.)	2.95	-4.27	2.38	-3.17
Tau Eff. (2015 Trigger, MC, stat.)	0.00	0.00	0.00	0.00
Tau Eff. (2016 Trigger, MC, stat.)	2.51	-4.36	1.94	-2.85
Tau Eff. (2015 Trigger, sys.)	0.00	0.00	0.00	0.00
Tau Eff. (2016 Trigger, sys.)	1.47	-1.7	1.55	-1.76
TES (Detector)	-1.88	1.13	-2.11	1.73
TES (In situ)	1.42	-0.91	2.58	-2.88
TES (Model)	0.00	0.00	0.48	0.21
UE (gg)	4.47	-4.47	0.00	0.00
UE (qq)	0.71	-0.71	0.00	0.00
Luminosity	2.9	-2.9	0.1	-0.1
NLO EWK Higgs	0.28	-0.28	0.00	0.00
QCD scale (VH)	0.46	-0.44	0.00	0.00
QCD scale (ggH $m12$)	-5.22	5.96	0.00	0.00
QCD scale (ggH ptH $m01$)	23.86	-17.89	0.00	0.00
QCD scale (qqH)	0.06	-0.08	0.00	0.00
Theory $Z \rightarrow \tau\tau$ CKK	0.00	0.00	-25.16	25.16
Theory $Z \rightarrow \tau\tau$ Factorization	0.00	0.00	-1.1	1.1
Theory $Z \rightarrow \tau\tau$ QSF	0.00	0.00	4.52	-4.52
Theory $Z \rightarrow \tau\tau$ Renormalization	0.00	0.00	2.53	-2.53
EWK $Z \rightarrow \tau\tau$ proportion	0.00	0.00	0.46	-0.46
Fake- τ contamination	0.00	0.00	-1.32	1.36
Fake- τ extrapolation	0.00	0.00	0.81	-0.66
Higgs PDF (gg)	5.6	-5.15	0.00	0.00
Higgs PDF (gg , Acceptance)	1.39	-1.15	0.00	0.00
Higgs PDF (qq)	0.66	-0.71	0.00	0.00
Higgs PDF (qq , Acceptance)	0.13	-0.12	0.00	0.00

Table I.5: Relative impact of the nuisance parameters on the total number of events shown for the **Boosted Tight** category (%).

Studies concerning the flavor composition of the jet energy scale nuisance parameter in the couplings analysis

The postfit impact on the signal strength of the nuisance parameter for the flavor composition of the jet energy scale (JES Flav Comp) is not centered around 0 in the unblinded fit for the coupling analysis. This feature appears only in combination with the JER, JES (Effective NP 1) and JES (Inter- $|\eta|$ Calibration, Model) NPs, as shown in Figure J.1, which are correlated in a complicated way (see Figure J.2). The prefit event yield is symmetric around 0, as shown in Appendix I, but the prefit impact is one-sided when evaluated with the other NPs in this group.

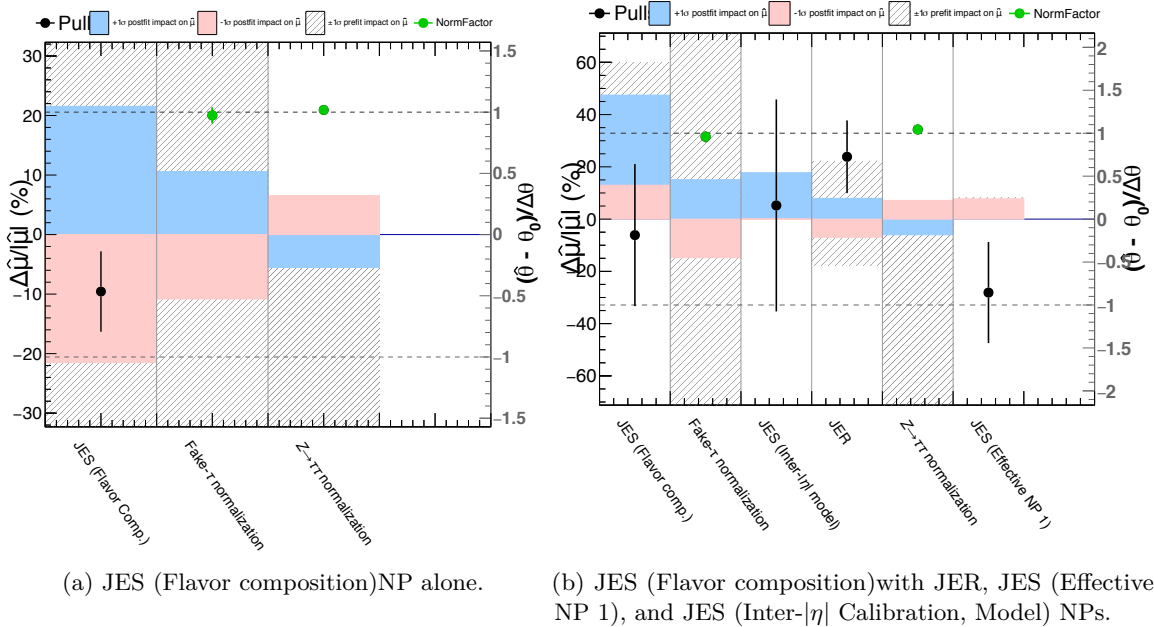


Figure J.1: Postfit impact on μ from selected jet NPs.

This behavior comes from the VBF low ΔR category that has limited statistics (see Figure 5.31). The variations of these NPs, especially in the $140 < m_{\text{MMC}}^{\tau\tau} < 160$ GeV bin, need to be symmetrized in the VBF low ΔR category. The feature disappears when the final fit is performed without

this category, as shown in Figure J.3.

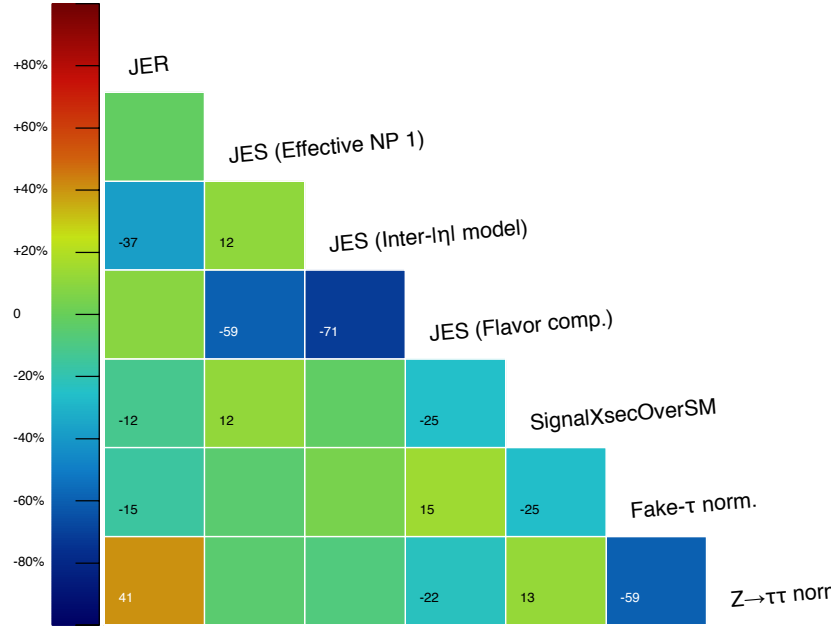


Figure J.2: Correlation matrix for selected jet NPs.

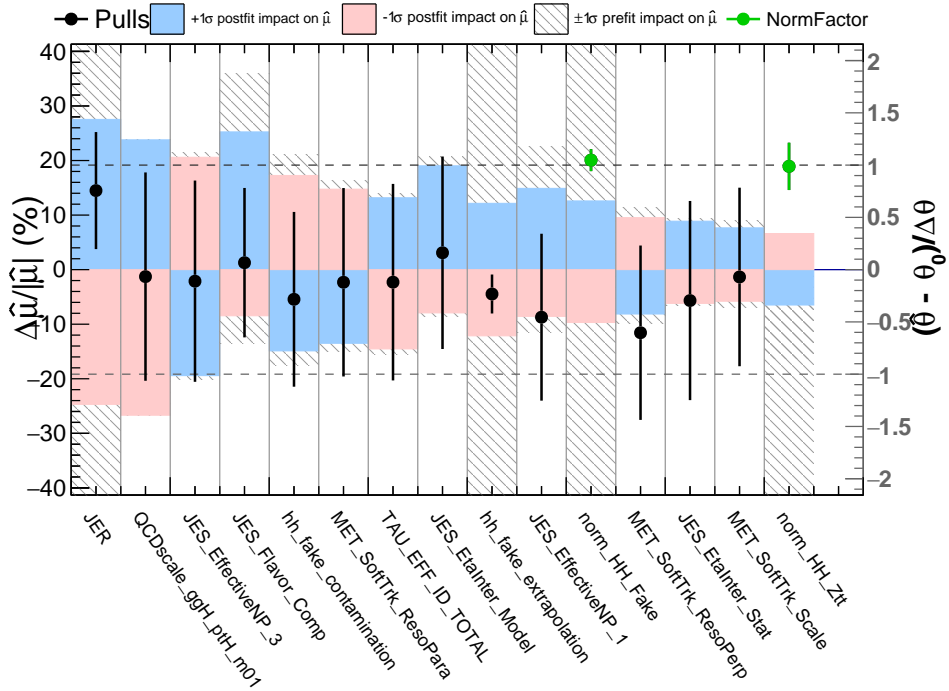
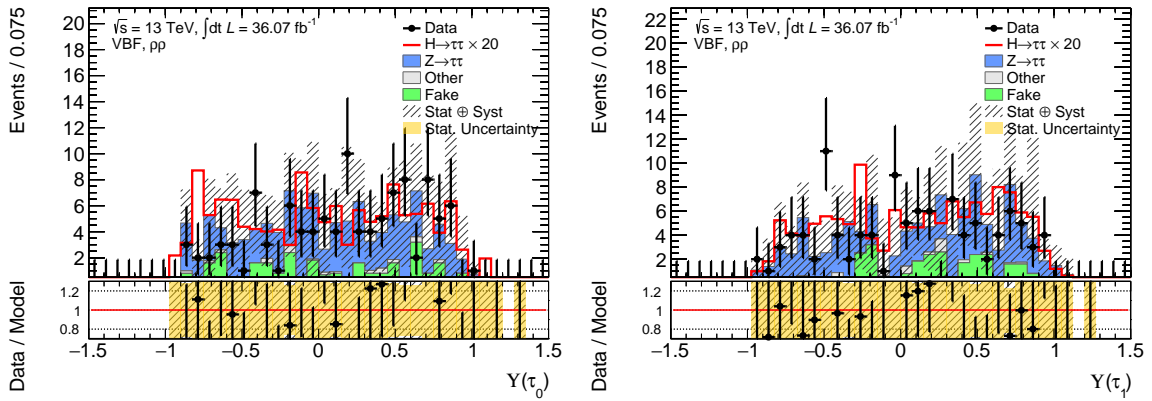


Figure J.3: NP ranking and postfit impact on μ without the VBF low ΔR category.

Validation of the Background Modeling in the Higgs CP analysis

The section shows the distributions of important observables used to define the signal categories. The systematic errors include all uncertainties described in Section 6.6 except for those concerning the fake- τ background estimation.

K.1 VBF category



(a) $\rho\rho, Y(\tau_0)$

(b) $\rho\rho, Y(\tau_1)$

Figure K.1: Modeling of the Y distribution in the VBF category.

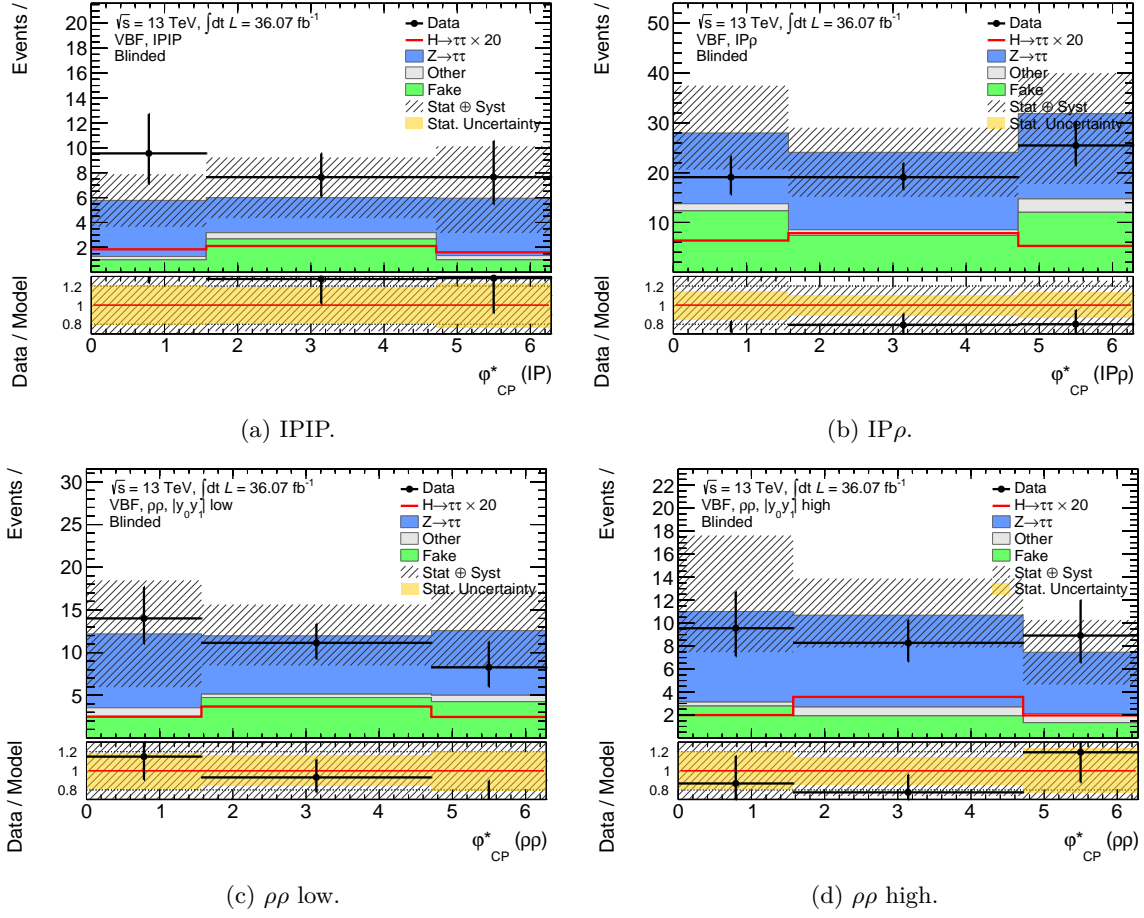
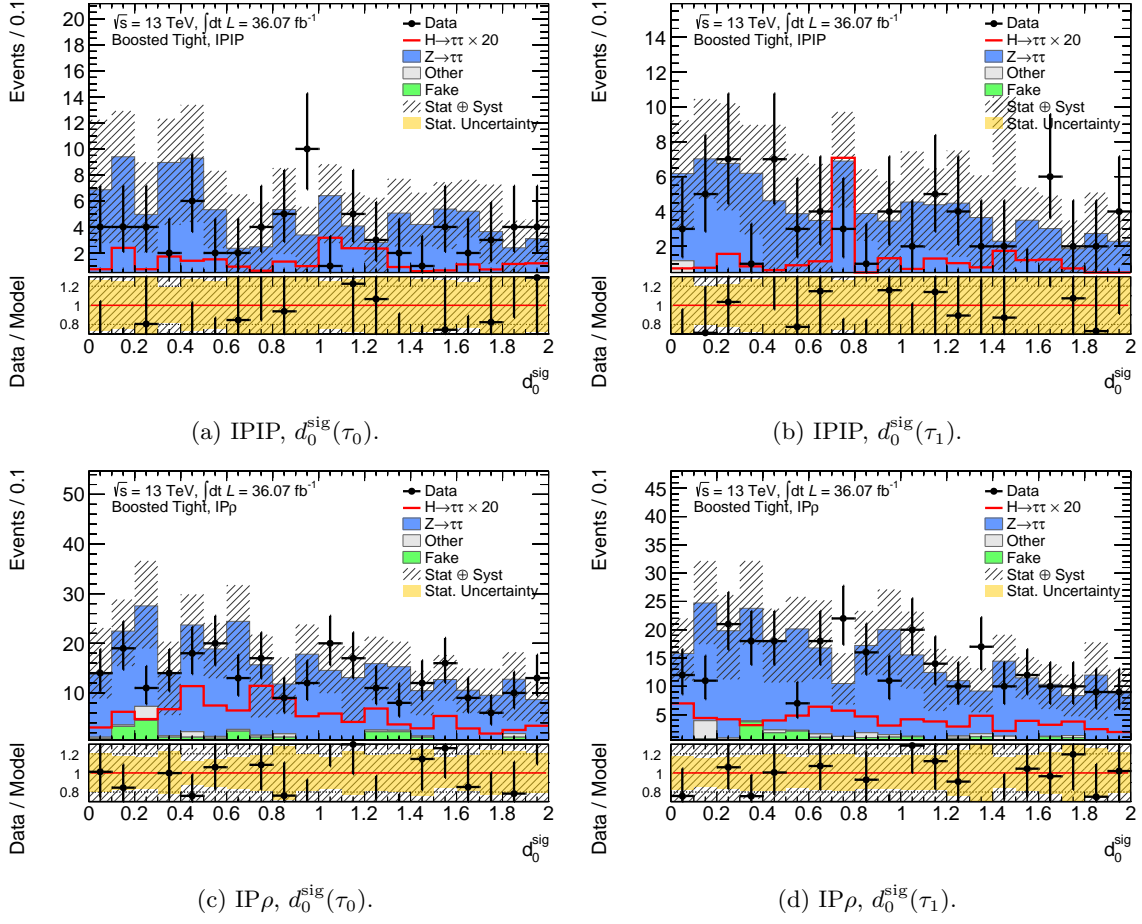


Figure K.2: Modeling of the φ_{CP}^* distribution in the HCP analysis for the $70 < m_{MM}^{\tau\tau} < 100$ GeV region, i.e., blinded in the $100 < m_{MM}^{\tau\tau} < 140$ GeV region, for the VBF category.

K.2 Boosted tight category

Figure K.3: Modeling of the d_0^{sig} observable in the Boosted Tight category.

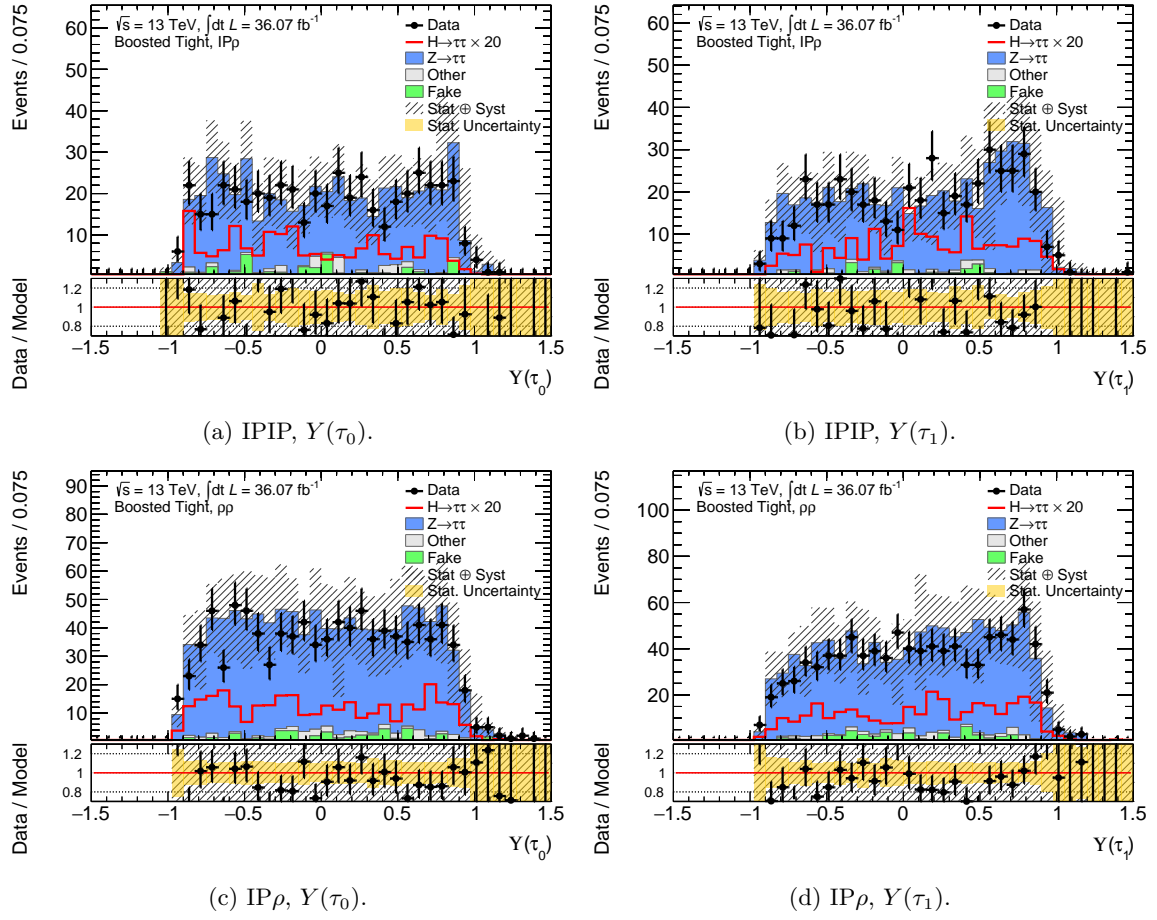


Figure K.4: Modeling of the Y distribution in the Boosted Tight category.

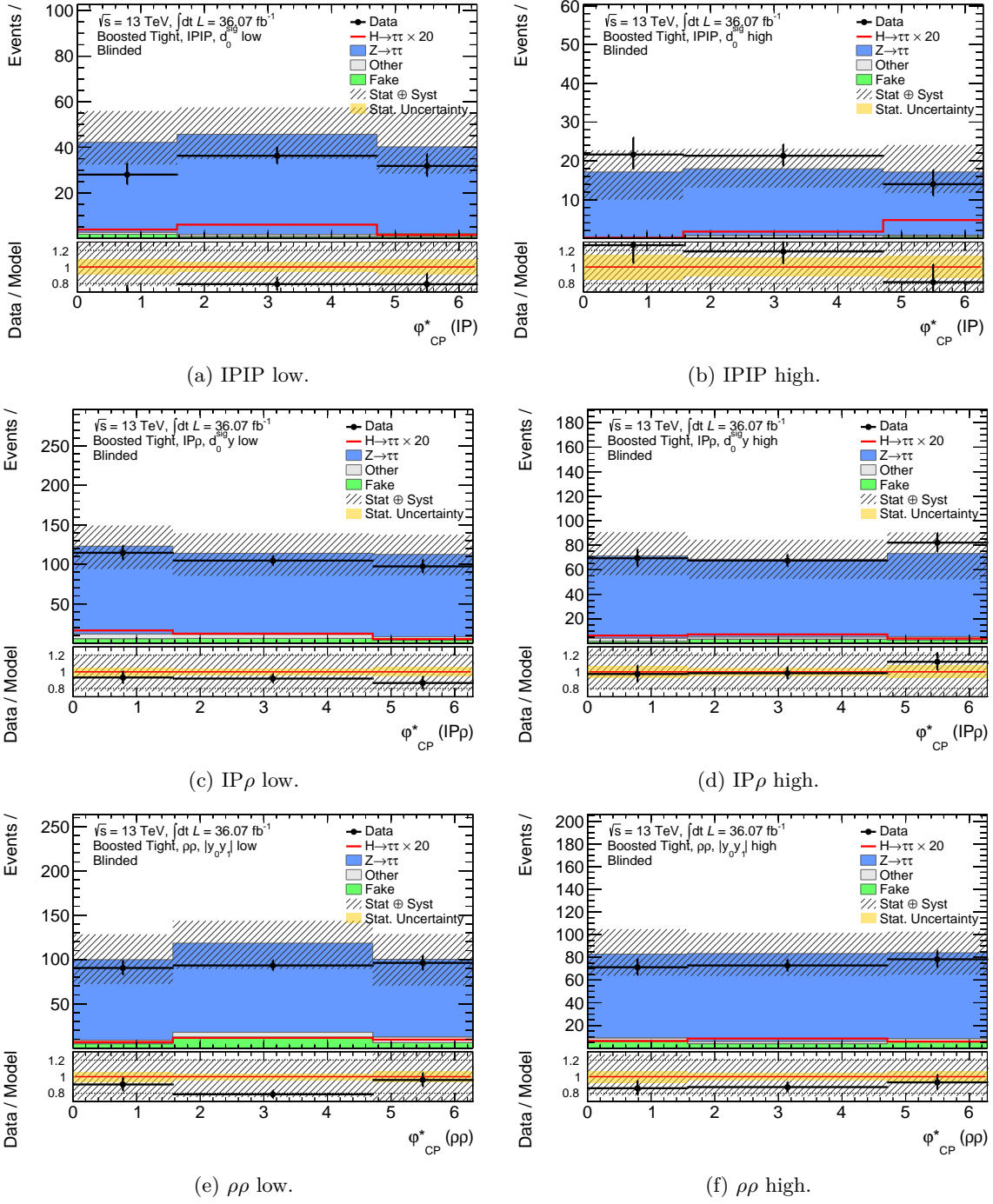


Figure K.5: Modeling of the φ_{CP}^* distribution in the HCP analysis for the $70 < m_{MM}^{\tau\tau} < 100$ GeV region, i.e., blinded in the $100 < m_{MM}^{\tau\tau} < 140$ GeV region, for the Boosted tight category.

K.3 Boosted loose category

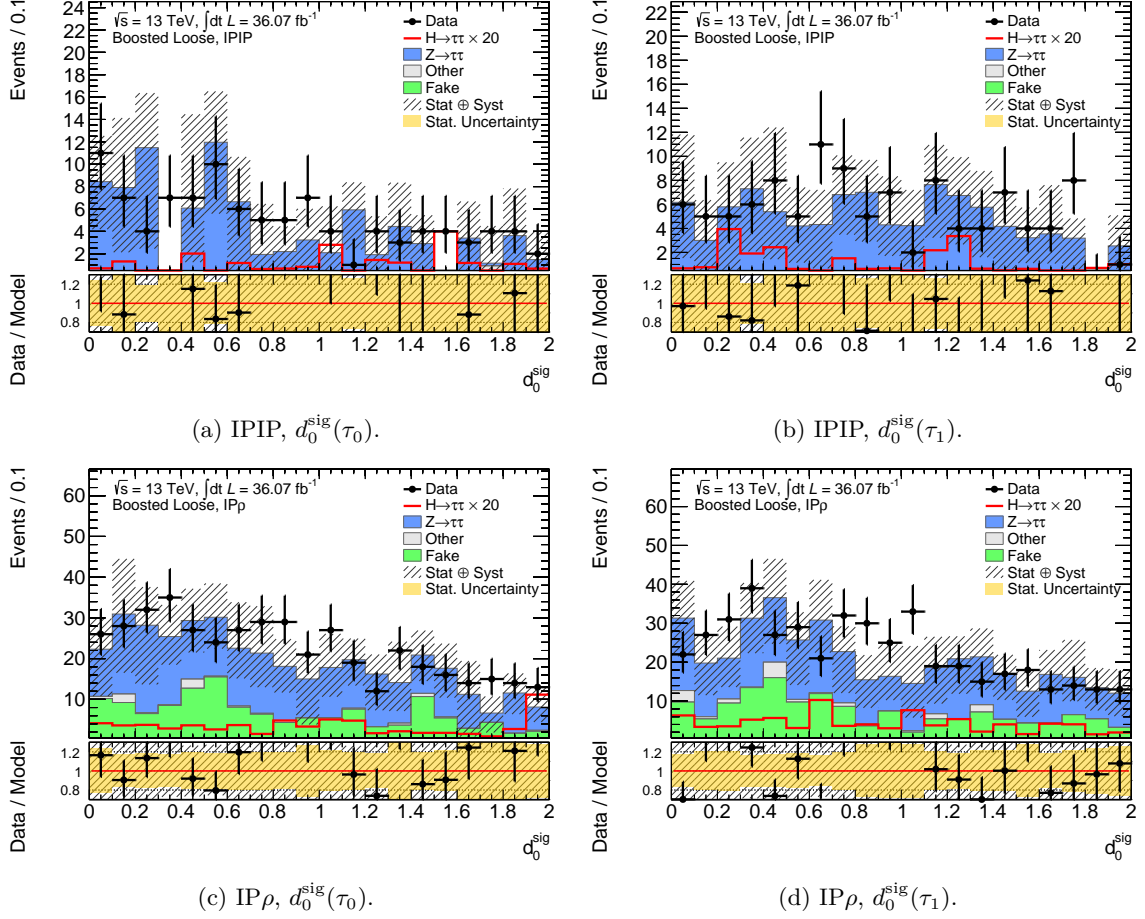
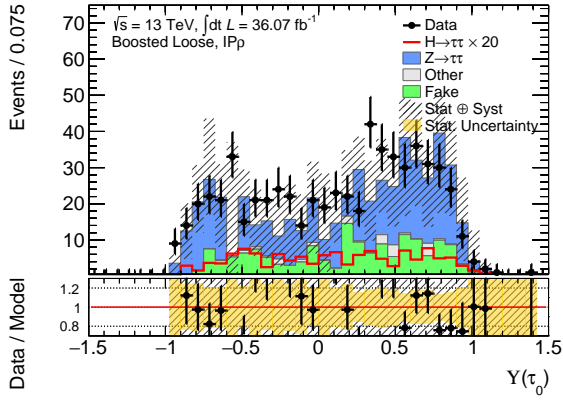
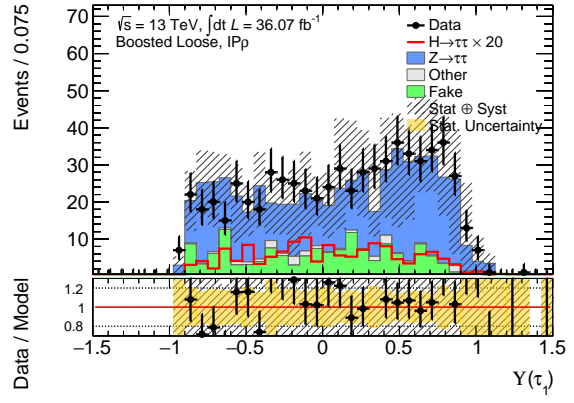


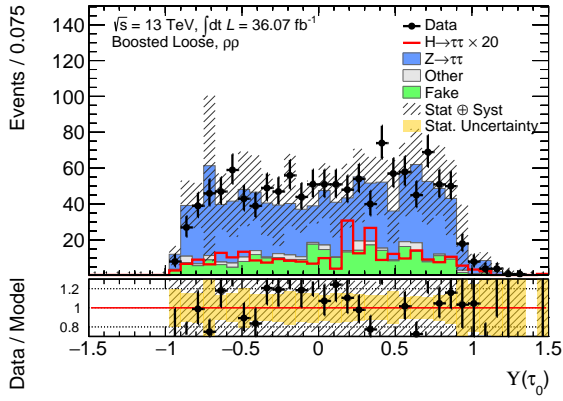
Figure K.6: Modeling of the d_0^{sig} observable in the Boosted Loose category.



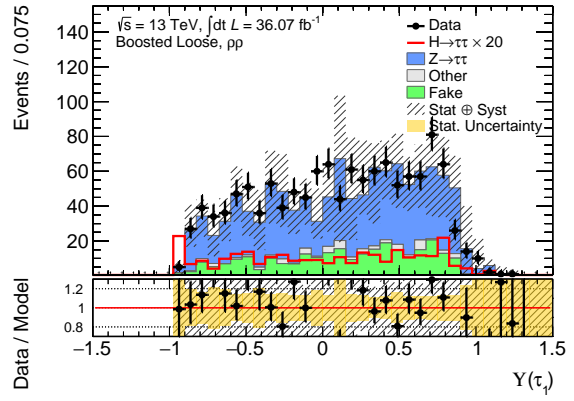
(a) IPIP, $Y(\tau_0)$.



(b) IPIP, $Y(\tau_1)$.



(c) IP ρ , $Y(\tau_0)$.



(d) IP ρ , $Y(\tau_1)$.

Figure K.7: Modeling of the Y distribution in the Boosted Loose category.

Appendix K Validation of the Background Modeling in the Higgs CP analysis

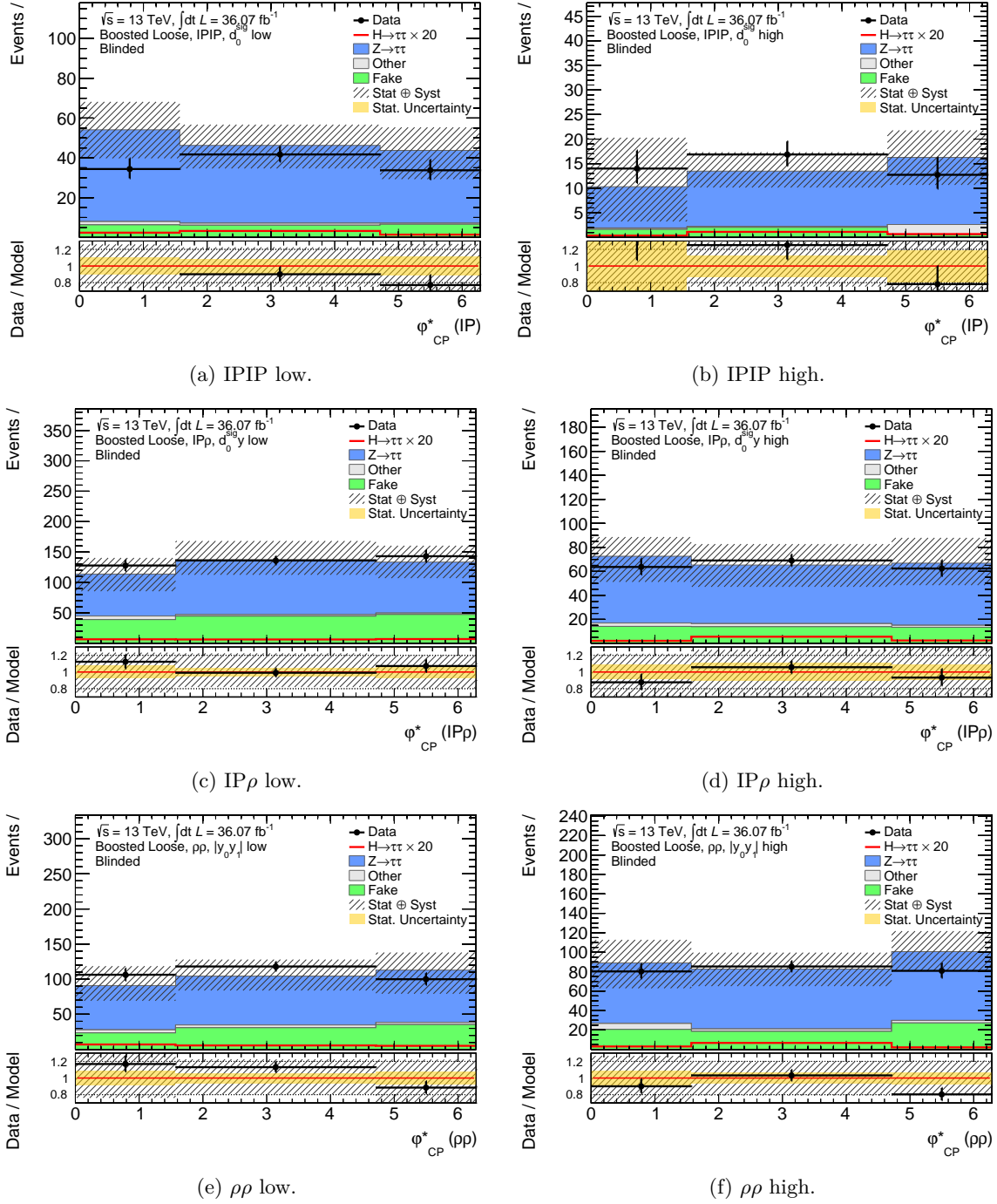


Figure K.8: Modeling of the φ_{CP}^* distribution in the HCP analysis for the $70 < m_{MMC}^{\tau\tau} < 100$ GeV region, i.e., blinded in the $100 < m_{MMC}^{\tau\tau} < 140$ GeV region, for the Boosted loose category.

Supplemental information on the final fit to the φ_{CP}^* observables in the Higgs CP analysis

The following section provides details on the statistical model presented in Section 6.7. The list of NPs specific to the Higgs CP analysis can be found in Appendix L, and the prefit impact from each NP is shown in Appendix L.2 for the $\phi_\tau = 0$ case as an example.

L.1 Definitions of nuisance parameters specific to the Higgs CP analysis

This section defines the CP analysis-specific NPs. The full list of the standard NPs can be found in Section I.2.

Z subtraction: Shape and event yield NP for the subtraction of fake- τ and other backgrounds from the $Z \rightarrow \tau\tau$ shape taken from data in the Z mass region.

Z MC shape: Shape and event yield NP for the MC difference between the $Z \rightarrow \tau\tau$ background shape in the Higgs and Z peak regions.

Vary uniform fake- τ distribution, bin 1: Shape and event yield NP allowing the first bin of the fake- τ background contribution to the φ_{CP}^* observable to differ from a flat line by the OS/SS difference seen in the anti- $\tau_{\text{had, vis}}$ ID region.

Vary uniform fake- τ distribution, bin 2: Shape and event yield NP allowing the second bin of the fake- τ background contribution to the φ_{CP}^* observable to differ from a flat line by the OS/SS difference seen in the anti- $\tau_{\text{had, vis}}$ ID region.

Vary uniform fake- τ distribution, bin 3: Shape and event yield NP allowing the third bin of the fake- τ background contribution to the φ_{CP}^* observable to differ from a flat line by the OS/SS difference seen in the anti- $\tau_{\text{had, vis}}$ ID region.

L.2 Prefit impact of each nuisance parameter in each Higgs CP signal category

Nuisance Parameter	Signal		Background	
	+1 σ	-1 σ	+1 σ	-1 σ
BR($H \rightarrow \tau\tau$)	5.7	-5.7	0.00	0.00
Forward JVT	0.00	0.00	0.00	0.00
JER	4.52	-4.52	0.25	-0.25
JES (Effective NP 1)	1.74	-1.86	0.88	0.00
JES (Effective NP 2)	0.00	0.00	0.00	0.00
JES (Effective NP 3)	-2.89	2.89	0.00	0.00
JES (Effective NP 4)	0.00	0.00	0.00	0.00
JES (Effective NP 5)	0.00	0.00	0.00	0.00
JES (Effective NP 6)	3.86	-0.41	0.00	0.00
JES (Inter- $ \eta $ Calibration, Model)	5.31	-3.58	0.00	0.00
JES (Inter- $ \eta $ Calibration, Nonclosure)	3.7	-1.26	0.00	0.00
JES (Inter- $ \eta $ Calibration, Stat.)	3.2	-0.18	0.00	0.00
JES (Flavor composition)	5.74	-4.58	0.88	0.00
JES (Flavor Response)	0.00	0.00	0.00	0.00
JES (PU Offset μ)	3.06	0.21	0.00	0.00
JES (PU Offset NPV)	3.16	-1.36	0.00	0.00
JES (PU p_T term)	4.76	-0.79	0.88	0.00
JES (PU ρ)	0.00	0.00	0.00	0.00
ATLAS_JVT	0.00	0.00	0.00	0.00
MET Soft track (Parallel resolution)	4.27	-4.27	0.00	0.00
MET Soft track (Perpendicular resolution)	1.64	-1.64	0.00	0.00
MET Soft track (Scale)	0.00	0.00	0.00	0.00
PRW Data SF	-3.49	0.56	-0.03	0.02
Tau Eff. (e -OLR, true e)	0.00	0.00	0.00	0.00
Tau Eff. (e -OLR, true τ_{had})	2.97	-2.92	0.00	0.00
Tau Eff. (ID, high- p_T)	0.00	0.00	0.00	0.00
Tau Eff. (ID, total)	11.9	-11.24	0.03	-0.03
Tau Eff. (Reco, high- p_T)	0.00	0.00	0.00	0.00
Tau Eff. (Reco, total)	6.83	-6.6	0.02	-0.02
Tau Eff. (2015 Trigger, data, stat.)	0.00	0.00	0.00	0.00
Tau Eff. (2016 Trigger, data, stat.)	1.94	-2.78	0.00	0.00
Tau Eff. (2015 Trigger, MC, stat.)	0.00	0.00	0.9	-0.9
Tau Eff. (2016 Trigger, MC, stat.)	1.52	-2.47	0.87	-0.87
Tau Eff. (2015 Trigger, syst.)	0.00	0.00	0.00	0.00
Tau Eff. (2016 Trigger, syst.)	1.62	-1.87	0.00	0.00
TES (Detector)	-4.87	5.7	0.00	0.00
TES (In situ)	0.00	0.00	0.00	0.00
TES (Model)	0.00	0.00	0.00	0.00
UE (gg)	0.00	0.00	0.00	0.00
UE (qq)	5.01	-5.01	0.00	0.00
Luminosity	2.9	-2.9	0.00	0.00
NLO EW Higgs	1.25	-1.25	0.00	0.00
QCD scale (ggH m_{12})	9.72	-7.48	0.00	0.00
EWK $Z \rightarrow \tau\tau$ proportion	0.00	0.00	0.22	-0.22
Vary uniform fake- τ distribution, bin 1	0.00	0.00	20.71	-7.45
Z subtraction	0.00	0.00	0.00	0.00
Vary uniform fake- τ distribution, bin 1	0.00	0.00	8.62	-8.62
Vary uniform fake- τ distribution, bin 2	0.00	0.00	-20.45	20.45

L.2 Prefit impact of each nuisance parameter in each Higgs CP signal category

Nuisance Parameter	Signal		Background	
	+1 σ	-1 σ	+1 σ	-1 σ
Vary uniform fake- τ distribution, bin 3	0.00	0.00	17.47	-17.47
Higgs PDF (gg)	2.8	-2.58	0.00	0.00
Higgs PDF (gg , Acceptance)	1.02	-0.87	0.00	0.00
Higgs PDF (qq)	1.63	-1.75	0.00	0.00
Higgs PDF (qq , Acceptance)	1.35	-1.16	0.00	0.00

Table L.1: Relative impact of the nuisance parameters compared to the total number of events in percentage, shown for the **VBF IPIP** category.

Appendix L Supplemental information on the final fit to the φ_{CP}^* observables in the Higgs CP analysis

Nuisance Parameter	Signal		Background	
	+1 σ	-1 σ	+1 σ	-1 σ
BR($H \rightarrow \tau\tau$)	5.7	-5.7	0.00	0.00
Forward JVT	0.00	0.00	0.00	0.00
JER	-3.32	3.32	-0.07	0.07
JES (Effective NP 1)	2.41	-5.67	0.21	-0.02
JES (Effective NP 2)	0.00	0.00	0.00	0.00
JES (Effective NP 3)	0.00	0.00	0.00	0.00
JES (Effective NP 4)	0.00	0.00	0.00	0.00
JES (Effective NP 5)	0.00	0.00	0.00	0.00
JES (Effective NP 6)	0.00	0.00	0.00	0.00
JES (Inter- $ \eta $ Calibration, Model)	2.22	-4.44	0.17	0.00
JES (Inter- $ \eta $ Calibration, Nonclosure)	0.00	0.00	0.00	0.00
JES (Inter- $ \eta $ Calibration, Stat.)	2.46	-1.7	0.00	0.00
JES (Flavor composition)	4.91	-7.33	0.2	-0.02
JES (Flavor Response)	-2.38	1.86	0.00	0.17
JES (PU Offset μ)	-0.59	1.53	0.00	0.00
JES (PU Offset NPV)	0.00	0.00	0.00	0.00
JES (PU p_T term)	-0.62	1.25	0.00	0.00
JES (PU ρ)	2.75	-1.91	0.00	0.00
ATLAS_JVT	0.00	0.00	0.00	0.00
MET Soft track (Parallel resolution)	0.00	0.00	0.00	0.00
MET Soft track (Perpendicular resolution)	-1.35	1.35	0.00	0.00
MET Soft track (Scale)	0.00	0.00	0.00	0.00
PRW Data SF	-5.84	4.85	0.05	-0.18
Tau Eff. (e -OLR, true e)	0.00	0.00	0.02	-0.02
Tau Eff. (e -OLR, true τ_{had})	2.73	-2.69	0.03	-0.03
Tau Eff. (ID, high- p_T)	0.00	0.00	0.00	0.00
Tau Eff. (ID, total)	11.9	-11.24	0.13	-0.12
Tau Eff. (Reco, high- p_T)	0.00	0.00	0.00	0.00
Tau Eff. (Reco, total)	6.99	-6.76	0.08	-0.08
Tau Eff. (2015 Trigger, data, stat.)	0.00	0.00	0.00	0.00
Tau Eff. (2016 Trigger, data, stat.)	1.94	-2.71	0.02	-0.03
Tau Eff. (2015 Trigger, MC, stat.)	0.00	0.00	-17.73	17.73
Tau Eff. (2016 Trigger, MC, stat.)	1.54	-2.35	-17.76	17.76
Tau Eff. (2015 Trigger, syst.)	0.00	0.00	0.00	0.00
Tau Eff. (2016 Trigger, syst.)	1.63	-1.93	0.02	-0.02
TES (Detector)	-3.04	2.97	0.00	0.00
TES (In situ)	1.92	-4.67	0.00	0.00
TES (Model)	0.18	-1.1	0.00	0.00
UE (gg)	0.00	0.00	0.00	0.00
UE (qq)	5.14	-5.14	0.00	0.00
Luminosity	2.9	-2.9	0.04	-0.04
NLO EW Higgs	1.28	-1.28	0.00	0.00
QCD scale (ggH m_{12})	9.31	-7.16	0.00	0.00
EWK $Z \rightarrow \tau\tau$ proportion	0.00	0.00	0.12	-0.12
Z MC shape	0.00	0.00	27.64	-10.84
Z subtraction	0.00	0.00	9.81	-6.48
Vary uniform fake- τ distribution, bin 1	0.00	0.00	-6.56	6.56
Vary uniform fake- τ distribution, bin 2	0.00	0.00	10.54	-10.54
Vary uniform fake- τ distribution, bin 3	0.00	0.00	1.49	-12.18
Higgs PDF (gg)	2.68	-2.47	0.00	0.00
Higgs PDF (gg , Acceptance)	0.00	0.00	0.00	0.00
Higgs PDF (qq)	1.67	-1.8	0.00	0.00
Higgs PDF (qq , Acceptance)	1.38	-1.19	0.00	0.00

Table L.2: Relative impact of the nuisance parameters compared to the total number of events in percentage, shown for the **VBF $IP\rho$** category.

L.2 Prefit impact of each nuisance parameter in each Higgs CP signal category

Nuisance Parameter	Signal		Background	
	+1 σ	-1 σ	+1 σ	-1 σ
BR($H \rightarrow \tau\tau$)	5.7	-5.7	0.00	0.00
Forward JVT	0.00	0.00	0.00	0.00
JER	0.00	0.00	-3.28	3.28
JES (Effective NP 1)	0.00	0.00	0.00	0.00
JES (Effective NP 2)	-1.36	1.3	0.00	0.00
JES (Effective NP 3)	-0.94	0.94	0.00	0.00
JES (Effective NP 4)	0.00	0.00	0.00	0.00
JES (Effective NP 5)	-1.99	1.99	0.00	0.00
JES (Effective NP 6)	0.00	0.00	0.00	0.00
JES (Inter- $ \eta $ Calibration, Model)	6.03	-6.03	0.00	0.00
JES (Inter- $ \eta $ Calibration, Nonclosure)	0.00	0.00	0.00	0.00
JES (Inter- $ \eta $ Calibration, Stat.)	2.03	-2.56	0.00	0.00
JES (Flavor composition)	6.17	-4.84	-0.46	-0.06
JES (Flavor Response)	0.00	0.00	0.00	0.00
JES (PU Offset μ)	0.00	0.00	0.06	0.00
JES (PU Offset NPV)	0.00	0.00	0.00	0.00
JES (PU p_T term)	0.00	0.00	0.00	0.00
JES (PU ρ)	0.00	0.00	0.00	0.00
ATLAS_JVT	0.00	0.00	0.00	0.00
MET Soft track (Parallel resolution)	0.00	0.00	0.00	0.00
MET Soft track (Perpendicular resolution)	1.91	-1.91	0.00	0.00
MET Soft track (Scale)	1	0.4	0.00	0.00
PRW Data SF	-4.67	2.31	-0.09	0.15
Tau Eff. (e -OLR, true e)	0.00	0.00	0.06	-0.06
Tau Eff. (e -OLR, true τ_{had})	2.74	-2.7	0.06	-0.06
Tau Eff. (ID, high- p_T)	0.00	0.00	0.00	0.00
Tau Eff. (ID, total)	11.9	-11.24	0.27	-0.26
Tau Eff. (Reco, high- p_T)	0.00	0.00	0.00	0.00
Tau Eff. (Reco, total)	6.86	-6.63	0.17	-0.16
Tau Eff. (2015 Trigger, data, stat.)	0.00	0.00	0.00	0.00
UE (gg) Tau Eff. (2016 Trigger, data, stat.)	2.01	-2.9	0.05	-0.07
Tau Eff. (2015 Trigger, MC, stat.)	0.00	0.00	0.00	0.00
Tau Eff. (2016 Trigger, MC, stat.)	1.56	-2.61	-23.2	23.19
Tau Eff. (2015 Trigger, syst.)	0.00	0.00	0.00	0.00
Tau Eff. (2016 Trigger, syst.)	1.67	-1.97	0.00	0.00
TES (Detector)	-8.85	6.33	-0.51	0.00
TES (In situ)	-2.64	-4.96	0.00	0.00
TES (Model)	0.00	0.00	0.00	-0.4
UE (gg)	0.00	0.00	0.00	0.00
UE (qq)	5.91	-5.91	0.00	0.00
Luminosity	2.9	-2.9	0.09	-0.09
NLO EW Higgs	1.48	-1.48	0.00	0.00
QCD scale (ggH m_{12})	6.79	-5.23	0.00	0.00
EWK $Z \rightarrow \tau\tau$ proportion	0.00	0.00	0.63	-0.63
Z MC shape	0.00	0.00	0.00	0.00
Z subtraction	0.00	0.00	0.00	0.00
Vary uniform fake- τ distribution, bin 1	0.00	0.00	0.00	0.00
Vary uniform fake- τ distribution, bin 2	0.00	0.00	-12.88	12.88
Vary uniform fake- τ distribution, bin 3	0.00	0.00	13.99	-13.02
Higgs PDF (gg)	1.96	-1.8	0.00	0.00
Higgs PDF (gg , Acceptance)	0.00	0.00	0.00	0.00
Higgs PDF (qq)	1.92	-2.07	0.00	0.00
Higgs PDF (qq , Acceptance)	1.59	-1.37	0.00	0.00

Table L.3: Relative impact of the nuisance parameters compared to the total number of events in percentage, shown for the **VBF $\rho\rho$, high Y_+Y_-** category.

Appendix L Supplemental information on the final fit to the φ_{CP}^* observables in the Higgs CP analysis

Nuisance Parameter	Signal		Background	
	+1 σ	-1 σ	+1 σ	-1 σ
BR($H \rightarrow \tau\tau$)	5.7	-5.7	0.00	0.00
Forward JVT	0.00	0.00	0.00	0.00
JER	2.37	-2.37	1.57	-1.57
JES (Effective NP 1)	9.1	-7.01	0.04	-0.39
JES (Effective NP 2)	2.97	-2.98	0.00	0.00
JES (Effective NP 3)	0.00	0.00	2.19	0.00
JES (Effective NP 4)	0.00	0.00	0.00	0.00
JES (Effective NP 5)	0.00	0.00	0.00	-0.39
JES (Effective NP 6)	0.00	0.00	0.00	0.00
JES (Inter- $ \eta $ Calibration, Model)	4.46	-0.56	0.04	-0.39
JES (Inter- $ \eta $ Calibration, Nonclosure)	0.00	0.00	0.00	0.00
JES (Inter- $ \eta $ Calibration, Stat.)	3.35	-3.49	0.00	0.00
JES (Flavor composition)	9.21	-5.13	0.04	-0.8
JES (Flavor Response)	-3.61	3.33	0.00	0.00
JES (PU Offset μ)	2.11	-3.9	0.00	-0.39
JES (PU Offset NPV)	0.00	0.00	0.00	-0.39
JES (PU p_T term)	0.00	0.00	-0.39	0.00
JES (PU ρ)	4.7	-4.7	0.00	0.00
ATLAS_JVT	0.00	0.00	0.00	0.00
MET Soft track (Parallel resolution)	1.33	-1.33	0.00	0.00
MET Soft track (Perpendicular resolution)	2.61	-2.61	0.00	0.00
MET Soft track (Scale)	2.71	-2.71	0.00	0.00
PRW Data SF	-5.05	4.67	0.00	0.00
Tau Eff. (e -OLR, true e)	0.00	0.00	0.07	-0.07
Tau Eff. (e -OLR, true τ_{had})	2.88	-2.84	0.04	-0.04
Tau Eff. (ID, high- p_T)	0.00	0.00	0.00	0.00
Tau Eff. (ID, total)	11.9	-11.24	0.18	-0.18
Tau Eff. (Reco, high- p_T)	0.00	0.00	0.00	0.00
Tau Eff. (Reco, total)	7.03	-6.8	0.11	-0.11
Tau Eff. (2015 Trigger, data, stat.)	0.00	0.00	0.00	0.00
Tau Eff. (2016 Trigger, data, stat.)	1.81	-2.55	0.04	-0.05
Tau Eff. (2015 Trigger, MC, stat.)	0.00	0.00	0.00	0.00
Tau Eff. (2016 Trigger, MC, stat.)	1.43	-2.21	-11.92	11.91
Tau Eff. (2015 Trigger, syst.)	0.00	0.00	0.00	0.00
Tau Eff. (2016 Trigger, syst.)	1.52	-1.78	0.02	-0.03
TES (Detector)	4.96	-4.96	0.36	-0.39
TES (In situ)	8.12	-7.53	1.04	0.04
TES (Model)	1.71	-3.94	0.00	-0.39
UE (gg)	0.00	0.00	0.00	0.00
UE (qq)	4.96	-4.96	0.00	0.00
Luminosity	2.9	-2.9	0.06	-0.06
NLO EW Higgs	1.24	-1.24	0.00	0.00
QCD scale (ggH m_{12})	9.88	-7.6	0.00	0.00
EWK $Z \rightarrow \tau\tau$ proportion	0.00	0.00	0.11	-0.11
Z MC shape	0.00	0.00	0.00	5.9
Z subtraction	0.00	0.00	21.56	-13.83
Vary uniform fake- τ distribution, bin 1	0.00	0.00	-3.43	3.43
Vary uniform fake- τ distribution, bin 2	0.00	0.00	-8.12	8.12
Vary uniform fake- τ distribution, bin 3	0.00	0.00	16.28	-16.28
Higgs PDF (gg)	2.85	-2.62	0.00	0.00
Higgs PDF (gg , Acceptance)	1.04	-0.88	0.00	0.00
Higgs PDF (qq)	1.61	-1.74	0.00	0.00
Higgs PDF (qq , Acceptance)	1.33	-1.15	0.00	0.00

Table L.4: Relative impact of the nuisance parameters compared to the total number of events in percentage, shown for the **VBF $\rho\rho$, low $Y_+ Y_-$** category.

L.2 Prefit impact of each nuisance parameter in each Higgs CP signal category

Nuisance Parameter	Signal		Background	
	+1 σ	-1 σ	+1 σ	-1 σ
BR($H \rightarrow \tau\tau$)	5.7	-5.7	0.00	0.00
Forward JVT	0.00	0.00	0.00	0.00
JER	9.33	-9.33	0.4	-0.4
JES (Effective NP 1)	2.31	-3.54	0.24	-0.13
JES (Effective NP 2)	4.3	-3.63	0.00	0.00
JES (Effective NP 3)	-1.23	0.67	0.00	0.04
JES (Effective NP 4)	0.00	0.00	0.00	0.00
JES (Effective NP 5)	0.00	0.00	0.00	0.00
JES (Effective NP 6)	0.00	0.00	0.00	0.00
JES (Inter- $ \eta $ Calibration, Model)	0.00	0.00	0.00	0.00
JES (Inter- $ \eta $ Calibration, Nonclosure)	0.00	0.00	0.00	0.00
JES (Inter- $ \eta $ Calibration, Stat.)	2.23	-2.78	0.1	0.01
JES (Flavor composition)	7.59	-8.72	0.19	-0.12
JES (Flavor Response)	-3.21	1.26	0.00	0.00
JES (PU Offset μ)	-2.51	2.29	0.13	-0.01
JES (PU Offset NPV)	-2.55	2.55	0.00	0.00
JES (PU p_T term)	0.00	0.00	0.04	-0.04
JES (PU ρ)	0.00	0.00	0.13	-0.03
ATLAS_JVT	0.00	0.00	0.00	0.00
MET Soft track (Parallel resolution)	3.47	-3.47	0.00	0.00
MET Soft track (Perpendicular resolution)	5.03	-5.03	0.04	-0.04
MET Soft track (Scale)	0.00	0.00	-0.06	-0.06
PRW Data SF	9.18	-5.2	0.00	0.00
Tau Eff. (e -OLR, true e)	0.00	0.00	0.00	0.00
Tau Eff. (e -OLR, true τ_{had})	2.53	-2.5	0.03	-0.03
Tau Eff. (ID, high- p_T)	0.00	0.00	0.00	0.00
Tau Eff. (ID, total)	11.9	-11.24	0.13	-0.13
Tau Eff. (Reco, high- p_T)	0.00	0.00	0.00	0.00
Tau Eff. (Reco, total)	7.79	-7.5	0.09	-0.08
Tau Eff. (2015 Trigger, data, stat.)	0.00	0.00	0.00	0.00
Tau Eff. (2016 Trigger, data, stat.)	2.08	-2.59	0.03	-0.04
Tau Eff. (2015 Trigger, MC, stat.)	0.00	0.00	0.00	0.00
Tau Eff. (2016 Trigger, MC, stat.)	1.4	-1.74	-4.36	4.36
Tau Eff. (2015 Trigger, syst.)	0.00	0.00	0.00	0.00
Tau Eff. (2016 Trigger, syst.)	2.12	-2.34	0.03	-0.03
TES (Detector)	-2.19	2.75	0.00	0.00
TES (In situ)	0.00	0.00	0.17	-0.14
TES (Model)	0.00	0.00	0.01	-0.07
UE (gg)	5.28	-5.28	0.00	0.00
UE (qq)	0.00	0.00	0.00	0.00
Luminosity	2.9	-2.9	0.06	-0.06
NLO EW Higgs	0.00	0.00	0.00	0.00
QCD scale (ggH m_{12})	-6.16	7.04	0.00	0.00
EWK $Z \rightarrow \tau\tau$ proportion	0.00	0.00	0.1	-0.1
Z MC shape	0.00	0.00	0.00	-0.99
Z subtraction	0.00	0.00	7.38	-7.38
Vary uniform fake- τ distribution, bin 1	0.00	0.00	3.75	-3.75
Vary uniform fake- τ distribution, bin 2	0.00	0.00	-0.65	2.52
Vary uniform fake- τ distribution, bin 3	0.00	0.00	1.17	-13.42
Higgs PDF (gg)	6.6	-6.07	0.00	0.00
Higgs PDF (gg , Acceptance)	1.64	-1.36	0.00	0.00
Higgs PDF (qq)	0.00	0.00	0.00	0.00
Higgs PDF (qq , Acceptance)	0.00	0.00	0.00	0.00

Table L.5: Relative impact of the nuisance parameters compared to the total number of events in percentage, shown for the **Boost Loose IPiP, low d_0^{sig}** category.

Appendix L Supplemental information on the final fit to the φ_{CP}^* observables in the Higgs CP analysis

Nuisance Parameter	Signal		Background	
	+1 σ	-1 σ	+1 σ	-1 σ
BR($H \rightarrow \tau\tau$)	5.7	-5.7	0.00	0.00
Forward JVT	0.00	0.00	0.00	0.00
JER	-1.7	1.7	0.2	-0.2
JES (Effective NP 1)	-1.16	16.22	0.44	-0.38
JES (Effective NP 2)	-11.18	10.56	0.00	0.00
JES (Effective NP 3)	13.32	-13.32	0.00	0.07
JES (Effective NP 4)	-11.27	13.32	0.07	0.00
JES (Effective NP 5)	0.00	0.00	0.00	0.00
JES (Effective NP 6)	0.00	15.54	0.00	0.00
JES (Inter- $ \eta $ Calibration, Model)	-1.65	31.75	0.00	0.00
JES (Inter- $ \eta $ Calibration, Nonclosure)	13.32	2.05	0.00	0.07
JES (Inter- $ \eta $ Calibration, Stat.)	1.9	13.6	0.00	0.00
JES (Flavor composition)	-1.16	23.39	0.37	-0.38
JES (Flavor Response)	15.35	-2.53	0.00	0.00
JES (PU Offset μ)	-0.38	15.89	0.00	0.00
JES (PU Offset NPV)	-0.79	13.31	0.00	0.00
JES (PU p_T term)	13.61	2.05	0.07	0.00
JES (PU ρ)	1.82	11.04	0.00	0.00
ATLAS_JVT	0.00	0.00	0.00	0.00
MET Soft track (Parallel resolution)	0.00	0.00	0.00	0.00
MET Soft track (Perpendicular resolution)	12.96	-12.96	0.05	-0.05
MET Soft track (Scale)	15.36	-15.54	0.00	0.00
PRW Data SF	0.00	0.00	0.00	0.00
Tau Eff. (e -OLR, true e)	0.00	0.00	0.00	0.00
Tau Eff. (e -OLR, true τ_{had})	2.6	-2.57	0.04	-0.04
Tau Eff. (ID, high- p_T)	0.00	0.00	0.00	0.00
Tau Eff. (ID, total)	11.9	-11.24	0.18	-0.17
Tau Eff. (Reco, high- p_T)	0.00	0.00	0.00	0.00
Tau Eff. (Reco, total)	7.53	-7.26	0.12	-0.12
Tau Eff. (2015 Trigger, data, stat.)	0.00	0.00	0.00	0.00
Tau Eff. (2016 Trigger, data, stat.)	2.09	-2.57	0.03	-0.04
Tau Eff. (2015 Trigger, MC, stat.)	0.00	0.00	0.00	0.00
Tau Eff. (2016 Trigger, MC, stat.)	1.41	-1.77	-0.01	0.01
Tau Eff. (2015 Trigger, syst.)	0.00	0.00	0.00	0.00
Tau Eff. (2016 Trigger, syst.)	1.85	-2.26	0.04	-0.04
TES (Detector)	-12.54	12.8	0.07	0.00
TES (In situ)	-6.69	6.69	0.07	0.00
TES (Model)	0.00	0.00	0.00	0.00
UE (gg)	4.26	-4.26	0.00	0.00
UE (qq)	1.45	-1.45	0.00	0.00
Luminosity	2.9	-2.9	0.04	-0.04
NLO EW Higgs	0.00	0.00	0.00	0.00
QCD scale (ggH m_{12})	-4.97	5.68	0.00	0.00
EWK $Z \rightarrow \tau\tau$ proportion	0.00	0.00	0.09	-0.09
Z MC shape	0.00	0.00	0.00	0.00
Z subtraction	0.00	0.00	20.29	-19.1
Vary uniform fake- τ distribution, bin 1	0.00	0.00	3.57	-3.57
Vary uniform fake- τ distribution, bin 2	0.00	0.00	-11.05	11.05
Vary uniform fake- τ distribution, bin 3	0.00	0.00	14.97	-14.97
Higgs PDF (gg)	5.33	-4.9	0.00	0.00
Higgs PDF (gg , Acceptance)	1.33	-1.1	0.00	0.00
Higgs PDF (qq)	0.00	0.00	0.00	0.00
Higgs PDF (qq , Acceptance)	0.00	0.00	0.00	0.00

Table L.6: Relative impact of the nuisance parameters compared to the total number of events in percentage, shown for the **Boost Loose IPIP, high d_0^{sig}** category.

L.2 Prefit impact of each nuisance parameter in each Higgs CP signal category

Nuisance Parameter	Signal		Background	
	+1 σ	-1 σ	+1 σ	-1 σ
BR($H \rightarrow \tau\tau$)	5.7	-5.7	0.00	0.00
Forward JVT	0.00	0.00	0.00	0.00
JER	7.55	-7.55	-0.46	0.46
JES (Effective NP 1)	0.79	0.93	0.51	-0.55
JES (Effective NP 2)	3.18	-4.04	-0.11	-0.09
JES (Effective NP 3)	-3.06	2.81	-0.41	0.41
JES (Effective NP 4)	3.56	-3.56	0.00	0.00
JES (Effective NP 5)	0.00	0.00	0.00	0.00
JES (Effective NP 6)	-1.59	2.05	0.00	0.00
JES (Inter- $ \eta $ Calibration, Model)	-4.87	4.87	0.00	0.00
JES (Inter- $ \eta $ Calibration, Nonclosure)	0.00	0.00	0.12	-0.04
JES (Inter- $ \eta $ Calibration, Stat.)	-0.48	2.03	0.4	-0.4
JES (Flavor composition)	-0.22	0.22	0.12	-0.66
JES (Flavor Response)	0.00	0.00	-0.11	-0.09
JES (PU Offset μ)	0.65	0.58	0.00	0.00
JES (PU Offset NPV)	0.11	0.68	0.12	0.03
JES (PU p_T term)	3.78	-4.07	-0.24	0.24
JES (PU ρ)	-1.27	1.44	0.15	-0.15
ATLAS_JVT	0.00	0.00	0.00	0.00
MET Soft track (Parallel resolution)	7.88	-7.88	0.33	-0.33
MET Soft track (Perpendicular resolution)	1.83	-1.83	0.28	-0.28
MET Soft track (Scale)	0.00	0.00	0.00	0.00
PRW Data SF	-3.19	1.15	0.00	0.00
Tau Eff. (e -OLR, true e)	0.00	0.00	0.00	0.00
Tau Eff. (e -OLR, true τ_{had})	2.6	-2.57	0.04	-0.04
Tau Eff. (ID, high- p_T)	0.00	0.00	0.00	0.00
Tau Eff. (ID, total)	11.9	-11.24	0.18	-0.17
Tau Eff. (Reco, high- p_T)	0.00	0.00	0.00	0.00
Tau Eff. (Reco, total)	7.37	-7.12	0.11	-0.11
Tau Eff. (2015 Trigger, data, stat.)	0.00	0.00	0.00	0.00
Tau Eff. (2016 Trigger, data, stat.)	1.91	-2.49	0.03	-0.04
Tau Eff. (2015 Trigger, MC, stat.)	0.00	0.00	0.00	0.00
Tau Eff. (2016 Trigger, MC, stat.)	1.47	-1.93	-1.66	1.66
Tau Eff. (2015 Trigger, syst.)	0.00	0.00	0.00	0.00
Tau Eff. (2016 Trigger, syst.)	1.83	-2.13	0.03	-0.04
TES (Detector)	0.55	6.02	0.00	0.00
TES (In situ)	0.00	0.00	0.57	-0.43
TES (Model)	4.06	-4.06	0.00	0.00
UE (gg)	5.29	-5.29	0.00	0.00
UE (qq)	0.00	0.00	0.00	0.00
Luminosity	2.9	-2.9	0.07	-0.07
NLO EW Higgs	0.00	0.00	0.00	0.00
QCD scale (ggH m_{12})	-6.17	7.06	0.00	0.00
EWK $Z \rightarrow \tau\tau$ proportion	0.00	0.00	0.00	0.00
Z MC shape	0.00	0.00	0.00	0.00
Z subtraction	0.00	0.00	4.55	-4.55
Vary uniform fake- τ distribution, bin 1	0.00	0.00	-1.53	1.53
Vary uniform fake- τ distribution, bin 2	0.00	0.00	1.81	-3.08
Vary uniform fake- τ distribution, bin 3	0.00	0.00	14.55	-14.55
Higgs PDF (gg)	6.62	-6.09	0.00	0.00
Higgs PDF (gg , Acceptance)	1.65	-1.36	0.00	0.00
Higgs PDF (qq)	0.00	0.00	0.00	0.00
Higgs PDF (qq , Acceptance)	0.00	0.00	0.00	0.00

Table L.7: Relative impact of the nuisance parameters compared to the total number of events in percentage, shown for the **Boost Loose IP ρ , low d_0^{sig} Y** category.

Appendix L Supplemental information on the final fit to the φ_{CP}^* observables in the Higgs CP analysis

Nuisance Parameter	Signal		Background	
	+1 σ	-1 σ	+1 σ	-1 σ
BR($H \rightarrow \tau\tau$)	5.7	-5.7	0.00	0.00
Forward JVT	0.00	0.00	0.00	0.00
JER	7.38	-7.38	-1.76	1.76
JES (Effective NP 1)	5.86	-4.79	0.3	-0.2
JES (Effective NP 2)	4.31	-4.31	0.00	0.00
JES (Effective NP 3)	0.00	0.00	0.00	0.00
JES (Effective NP 4)	0.00	0.00	0.00	0.00
JES (Effective NP 5)	0.00	0.00	-0.02	0.16
JES (Effective NP 6)	0.00	0.00	-0.21	0.08
JES (Inter- $ \eta $ Calibration, Model)	4.13	-3.29	0.00	-0.04
JES (Inter- $ \eta $ Calibration, Nonclosure)	-1.55	0.58	0.00	0.00
JES (Inter- $ \eta $ Calibration, Stat.)	1.88	-1.37	0.00	0.00
JES (Flavor composition)	7.61	-2.97	0.34	-0.22
JES (Flavor Response)	-4.2	5.08	-0.19	0.18
JES (PU Offset μ)	2.65	-2.37	0.01	0.1
JES (PU Offset NPV)	1.24	-3.6	0.09	-0.21
JES (PU p_T term)	0.00	0.00	-0.05	0.18
JES (PU ρ)	5.41	-4.95	0.14	-0.04
ATLAS_JVT	0.00	0.00	0.00	0.00
MET Soft track (Parallel resolution)	6.38	-6.38	0.00	0.00
MET Soft track (Perpendicular resolution)	2.2	-2.2	0.1	-0.1
MET Soft track (Scale)	-1.19	2.16	0.00	0.00
PRW Data SF	0.00	0.00	-0.34	0.25
Tau Eff. (e -OLR, true e)	0.00	0.00	0.00	0.00
Tau Eff. (e -OLR, true τ_{had})	2.53	-2.5	0.05	-0.05
Tau Eff. (ID, high- p_T)	0.00	0.00	0.00	0.00
Tau Eff. (ID, total)	11.9	-11.24	0.21	-0.2
Tau Eff. (Reco, high- p_T)	0.00	0.00	0.00	0.00
Tau Eff. (Reco, total)	7.43	-7.17	0.13	-0.13
Tau Eff. (2015 Trigger, data, stat.)	0.00	0.00	0.00	0.00
Tau Eff. (2016 Trigger, data, stat.)	2.11	-2.63	0.04	-0.04
Tau Eff. (2015 Trigger, MC, stat.)	0.00	0.00	0.00	0.00
Tau Eff. (2016 Trigger, MC, stat.)	1.52	-1.89	-4.4	4.4
Tau Eff. (2015 Trigger, syst.)	0.00	0.00	0.00	0.00
Tau Eff. (2016 Trigger, syst.)	2.02	-2.35	0.03	-0.04
TES (Detector)	-1.84	2.2	0.1	0.03
TES (In situ)	7.36	-4.54	0.00	0.00
TES (Model)	0.00	0.00	0.04	-0.29
UE (gg)	5.22	-5.22	0.00	0.00
UE (qq)	0.00	0.00	0.00	0.00
Luminosity	2.9	-2.9	0.07	-0.07
NLO EW Higgs	0.00	0.00	0.00	0.00
QCD scale (ggH m_{12})	-6.09	6.96	0.00	0.00
EWK $Z \rightarrow \tau\tau$ proportion	0.00	0.00	0.06	-0.06
Z MC shape	0.00	0.00	2.49	-1.74
Z subtraction	0.00	0.00	8.06	-8.06
Vary uniform fake- τ distribution, bin 1	0.00	0.00	-2.71	2.71
Vary uniform fake- τ distribution, bin 2	0.00	0.00	2.44	-1.93
Vary uniform fake- τ distribution, bin 3	0.00	0.00	0.41	-12.14
Higgs PDF (gg)	6.53	-6	0.00	0.00
Higgs PDF (gg , Acceptance)	1.63	-1.34	0.00	0.00
Higgs PDF (qq)	0.00	0.00	0.00	0.00
Higgs PDF (qq , Acceptance)	0.00	0.00	0.00	0.00

Table L.8: Relative impact of the nuisance parameters compared to the total number of events in percentage, shown for the **Boost Loose IP ρ , high d_0^{sig} Y** category.

L.2 Prefit impact of each nuisance parameter in each Higgs CP signal category

Nuisance Parameter	Signal		Background	
	+1 σ	-1 σ	+1 σ	-1 σ
BR($H \rightarrow \tau\tau$)	5.7	-5.7	0.00	0.00
Forward JVT	0.00	0.00	0.00	0.00
JER	1.01	-1.01	-0.04	0.04
JES (Effective NP 1)	0.00	0.00	0.29	-0.19
JES (Effective NP 2)	0.00	0.00	0.00	0.00
JES (Effective NP 3)	-0.26	-0.88	0.00	0.00
JES (Effective NP 4)	-1.04	1.7	0.04	-0.11
JES (Effective NP 5)	0.00	0.00	0.00	0.00
JES (Effective NP 6)	-2.39	1.9	0.00	0.00
JES (Inter- $ \eta $ Calibration, Model)	0.00	0.00	0.00	0.00
JES (Inter- $ \eta $ Calibration, Nonclosure)	0.00	0.00	-0.03	0.00
JES (Inter- $ \eta $ Calibration, Stat.)	0.00	0.00	0.00	0.00
JES (Flavor composition)	0.00	0.00	0.00	0.00
JES (Flavor Response)	0.00	0.00	-0.18	0.05
JES (PU Offset μ)	-1.27	2.2	0.17	-0.17
JES (PU Offset NPV)	3.33	-4.33	0.00	0.00
JES (PU p_T term)	0.69	-1.09	-0.08	0.17
JES (PU ρ)	0.09	1.49	0.08	-0.07
ATLAS_JVT	0.00	0.00	0.00	0.00
MET Soft track (Parallel resolution)	2.05	-2.05	0.00	0.00
MET Soft track (Perpendicular resolution)	-2.26	2.26	-0.06	0.06
MET Soft track (Scale)	0.00	0.00	0.00	0.00
PRW Data SF	0.00	0.00	-0.47	0.36
Tau Eff. (e -OLR, true e)	0.00	0.00	0.07	-0.07
Tau Eff. (e -OLR, true τ_{had})	2.6	-2.57	0.05	-0.05
Tau Eff. (ID, high- p_T)	0.00	0.00	0.00	0.00
Tau Eff. (ID, total)	11.9	-11.24	0.23	-0.22
Tau Eff. (Reco, high- p_T)	0.00	0.00	0.00	0.00
Tau Eff. (Reco, total)	7.34	-7.09	0.14	-0.14
Tau Eff. (2015 Trigger, data, stat.)	0.00	0.00	0.00	0.00
Tau Eff. (2016 Trigger, data, stat.)	1.97	-2.54	0.04	-0.05
Tau Eff. (2015 Trigger, MC, stat.)	0.00	0.00	0.00	0.00
Tau Eff. (2016 Trigger, MC, stat.)	1.51	-1.93	-3.43	3.42
Tau Eff. (2015 Trigger, syst.)	0.00	0.00	0.00	0.00
Tau Eff. (2016 Trigger, syst.)	1.86	-2.14	0.03	-0.04
TES (Detector)	0.00	0.00	-0.3	0.08
TES (In situ)	6.92	-11.35	-0.13	0.15
TES (Model)	2.13	-1.58	0.00	0.00
UE (gg)	5.36	-5.36	0.00	0.00
UE (qq)	0.00	0.00	0.00	0.00
Luminosity	2.9	-2.9	0.08	-0.08
NLO EW Higgs	0.00	0.00	0.00	0.00
QCD scale (ggH m_{12})	-6.25	7.14	0.00	0.00
EWK $Z \rightarrow \tau\tau$ proportion	0.00	0.00	0.03	-0.03
Z MC shape	0.00	0.00	-2.93	1.96
Z subtraction	0.00	0.00	4.33	-4.33
Vary uniform fake- τ distribution, bin 1	0.00	0.00	0.00	0.00
Vary uniform fake- τ distribution, bin 2	0.00	0.00	-3.51	0.09
Vary uniform fake- τ distribution, bin 3	0.00	0.00	3.43	-15.42
Higgs PDF (gg)	6.7	-6.16	0.00	0.00
Higgs PDF (gg , Acceptance)	1.67	-1.38	0.00	0.00
Higgs PDF (qq)	0.00	0.00	0.00	0.00
Higgs PDF (qq , Acceptance)	0.00	0.00	0.00	0.00

Table L.9: Relative impact of the nuisance parameters compared to the total number of events in percentage, shown for the **Boost Loose $\rho\rho$, low Y_+Y_-** category.

Appendix L Supplemental information on the final fit to the φ_{CP}^* observables in the Higgs CP analysis

Nuisance Parameter	Signal		Background	
	+1 σ	-1 σ	+1 σ	-1 σ
BR($H \rightarrow \tau\tau$)	5.7	-5.7	0.00	0.00
Forward JVT	0.00	0.00	0.66	-0.66
JER	-12.47	12.47	0.07	-0.07
JES (Effective NP 1)	10.93	-10.93	0.09	-0.03
JES (Effective NP 2)	0.00	0.00	0.00	0.00
JES (Effective NP 3)	0.00	0.00	0.00	0.00
JES (Effective NP 4)	0.00	0.00	0.00	0.00
JES (Effective NP 5)	0.00	0.00	-0.05	0.06
JES (Effective NP 6)	0.00	0.00	-0.26	0.26
JES (Inter- $ \eta $ Calibration, Model)	0.00	0.00	-0.9	0.9
JES (Inter- $ \eta $ Calibration, Nonclosure)	0.00	0.00	0.00	0.00
JES (Inter- $ \eta $ Calibration, Stat.)	0.00	0.00	0.00	0.00
JES (Flavor composition)	6.75	-7.61	0.00	0.00
JES (Flavor Response)	0.00	0.00	0.00	0.00
JES (PU Offset μ)	0.00	0.00	0.00	0.00
JES (PU Offset NPV)	0.00	0.00	0.00	-0.04
JES (PU p_T term)	0.00	0.00	0.37	-0.07
JES (PU ρ)	0.00	0.00	0.00	0.00
ATLAS_JVT	0.00	0.00	0.00	0.00
MET Soft track (Parallel resolution)	0.00	0.00	-0.21	0.21
MET Soft track (Perpendicular resolution)	0.00	0.00	0.24	-0.24
MET Soft track (Scale)	0.00	0.00	0.37	-0.37
PRW Data SF	6.09	-5.71	0.38	-0.89
Tau Eff. (e -OLR, true e)	0.00	0.00	0.00	0.00
Tau Eff. (e -OLR, true τ_{had})	2.54	-2.51	0.05	-0.05
Tau Eff. (ID, high- p_T)	0.00	0.00	0.00	0.00
Tau Eff. (ID, total)	11.9	-11.24	0.26	-0.26
Tau Eff. (Reco, high- p_T)	0.00	0.00	0.00	0.00
Tau Eff. (Reco, total)	7.4	-7.15	0.16	-0.16
Tau Eff. (2015 Trigger, data, stat.)	0.00	0.00	0.00	0.00
Tau Eff. (2016 Trigger, data, stat.)	2.15	-2.83	0.07	-0.08
Tau Eff. (2015 Trigger, MC, stat.)	0.00	0.00	-11.43	11.43
Tau Eff. (2016 Trigger, MC, stat.)	1.57	-2.07	-1.65	1.64
Tau Eff. (2015 Trigger, syst.)	0.00	0.00	0.00	0.00
Tau Eff. (2016 Trigger, syst.)	2.13	-2.36	0.07	-0.07
TES (Detector)	0.00	0.00	0.00	0.00
TES (In situ)	14.44	-14.44	0.46	-0.54
TES (Model)	6.96	-6.96	0.14	-0.44
UE (gg)	5.33	-5.33	0.00	0.00
UE (qq)	0.00	0.00	0.00	0.00
Luminosity	2.9	-2.9	0.12	-0.12
NLO EW Higgs	0.00	0.00	0.00	0.00
QCD scale (ggH m_{12})	-6.21	7.1	0.00	0.00
EWK $Z \rightarrow \tau\tau$ proportion	0.00	0.00	0.05	-0.05
Z MC shape	0.00	0.00	-0.19	0.00
Z subtraction	0.00	0.00	5.27	-5.27
Vary uniform fake- τ distribution, bin 1	0.00	0.00	-5.15	5.15
Vary uniform fake- τ distribution, bin 2	0.00	0.00	-7.23	7.23
Vary uniform fake- τ distribution, bin 3	0.00	0.00	3.12	-14.61
Higgs PDF (gg)	6.66	-6.13	0.00	0.00
Higgs PDF (gg , Acceptance)	1.66	-1.37	0.00	0.00
Higgs PDF (qq)	0.00	0.00	0.00	0.00
Higgs PDF (qq , Acceptance)	0.00	0.00	0.00	0.00

Table L.10: Relative impact of the nuisance parameters compared to the total number of events in percentage, shown for the **Boost Loose $\rho\rho$, high $Y_+ Y_-$** category.

L.2 Prefit impact of each nuisance parameter in each Higgs CP signal category

Nuisance Parameter	Signal		Background	
	+1 σ	-1 σ	+1 σ	-1 σ
BR($H \rightarrow \tau\tau$)	5.7	-5.7	0.00	0.00
Forward JVT	0.00	0.00	0.00	0.00
JER	2.77	-2.77	0.63	-0.63
JES (Effective NP 1)	3.61	-4.25	0.00	0.00
JES (Effective NP 2)	0.00	0.00	0.00	0.00
JES (Effective NP 3)	0.00	0.00	0.00	0.00
JES (Effective NP 4)	0.42	-2.92	0.4	-0.4
JES (Effective NP 5)	0.00	0.00	0.00	0.00
JES (Effective NP 6)	3.12	-3.12	0.00	0.00
JES (Inter- $ \eta $ Calibration, Model)	-0.39	2.17	0.00	0.00
JES (Inter- $ \eta $ Calibration, Nonclosure)	1.18	-1.05	0.00	-0.38
JES (Inter- $ \eta $ Calibration, Stat.)	3.42	-3.88	0.00	0.00
JES (Flavor composition)	3.35	-4.77	0.00	0.00
JES (Flavor Response)	0.00	0.00	0.00	0.00
JES (PU Offset μ)	0.00	0.00	0.00	0.00
JES (PU Offset NPV)	0.00	0.00	0.00	0.00
JES (PU p_T term)	0.00	0.00	0.00	0.00
JES (PU ρ)	-0.47	0.19	0.01	-0.45
ATLAS_JVT	0.00	0.00	0.00	0.00
MET Soft track (Parallel resolution)	-3.02	3.02	0.00	0.00
MET Soft track (Perpendicular resolution)	-1.39	1.39	-0.47	0.47
MET Soft track (Scale)	0.00	0.00	0.00	0.00
PRW Data SF	2.06	-3.14	-0.26	0.15
Tau Eff. (e -OLR, true e)	0.00	0.00	0.06	-0.06
Tau Eff. (e -OLR, true τ_{had})	3.04	-3	0.1	-0.1
Tau Eff. (ID, high- p_T)	0.00	0.00	0.00	0.00
Tau Eff. (ID, total)	11.9	-11.24	0.33	-0.32
Tau Eff. (Reco, high- p_T)	0.00	0.00	0.00	0.00
Tau Eff. (Reco, total)	6.68	-6.47	0.2	-0.2
Tau Eff. (2015 Trigger, data, stat.)	0.00	0.00	0.04	-0.06
Tau Eff. (2016 Trigger, data, stat.)	2.13	-3.26	0.06	-0.08
Tau Eff. (2015 Trigger, MC, stat.)	0.00	0.00	4.1	-4.1
Tau Eff. (2016 Trigger, MC, stat.)	1.62	-3.12	-8.77	8.75
Tau Eff. (2015 Trigger, syst.)	0.00	0.00	0.00	0.00
Tau Eff. (2016 Trigger, syst.)	1.64	-1.85	0.00	0.00
TES (Detector)	-1.82	3.88	0.00	0.00
TES (In situ)	0.00	0.00	0.00	0.00
TES (Model)	1.41	-2.02	0.00	0.00
UE (gg)	5	-5	0.00	0.00
UE (qq)	0.00	0.00	0.00	0.00
Luminosity	2.9	-2.9	0.12	-0.12
NLO EW Higgs	0.00	0.00	0.00	0.00
QCD scale (ggH m_{12})	-5.83	6.67	0.00	0.00
EWK $Z \rightarrow \tau\tau$ proportion	0.00	0.00	0.33	-0.33
Z MC shape	0.00	0.00	0.00	0.00
Z subtraction	0.00	0.00	11.42	-11.42
Vary uniform fake- τ distribution, bin 1	0.00	0.00	3.1	-3.1
Vary uniform fake- τ distribution, bin 2	0.00	0.00	-4.68	4.68
Vary uniform fake- τ distribution, bin 3	0.00	0.00	2.02	-3.54
Higgs PDF (gg)	6.25	-5.75	0.00	0.00
Higgs PDF (gg , Acceptance)	1.56	-1.29	0.00	0.00
Higgs PDF (qq)	0.00	0.00	0.00	0.00
Higgs PDF (qq , Acceptance)	0.00	0.00	0.00	0.00

Table L.11: Relative impact of the nuisance parameters compared to the total number of events in percentage, shown for the **Boost Tight IPIP, low d_0^{sig}** category.

Appendix L Supplemental information on the final fit to the φ_{CP}^* observables in the Higgs CP analysis

Nuisance Parameter	Signal		Background	
	+1 σ	-1 σ	+1 σ	-1 σ
BR($H \rightarrow \tau\tau$)	5.7	-5.7	0.00	0.00
Forward JVT	0.00	0.00	0.00	0.00
JER	1.48	-1.48	0.33	-0.33
JES (Effective NP 1)	5.25	-4.24	-0.08	-0.32
JES (Effective NP 2)	2.37	-4.19	0.05	-0.09
JES (Effective NP 3)	0.00	0.00	-0.08	0.12
JES (Effective NP 4)	2.12	0.16	-0.35	0.07
JES (Effective NP 5)	0.00	0.00	0.00	0.00
JES (Effective NP 6)	0.00	0.00	0.00	0.00
JES (Inter- $ \eta $ Calibration, Model)	0.00	0.00	0.00	0.00
JES (Inter- $ \eta $ Calibration, Nonclosure)	-5.11	1.76	-0.22	0.00
JES (Inter- $ \eta $ Calibration, Stat.)	0.00	0.00	0.00	0.00
JES (Flavor composition)	0.00	0.00	-0.17	-0.22
JES (Flavor Response)	0.00	0.00	-0.33	0.07
JES (PU Offset μ)	5.71	-6.02	0.00	0.00
JES (PU Offset NPV)	0.00	0.00	0.00	0.00
JES (PU p_T term)	-3.46	2.58	-0.23	-0.05
JES (PU ρ)	5.19	-5.19	0.00	0.00
ATLAS_JVT	0.00	0.00	0.00	0.00
MET Soft track (Parallel resolution)	0.00	0.00	-0.5	0.5
MET Soft track (Perpendicular resolution)	-1.1	1.1	-0.21	0.21
MET Soft track (Scale)	2.28	-0.21	-0.6	0.31
PRW Data SF	-5.69	4.26	-0.21	0.07
Tau Eff. (e -OLR, true e)	0.00	0.00	0.00	0.00
Tau Eff. (e -OLR, true τ_{had})	2.86	-2.82	0.06	-0.06
Tau Eff. (ID, high- p_T)	0.00	0.00	0.00	0.00
Tau Eff. (ID, total)	11.9	-11.23	0.22	-0.22
Tau Eff. (Reco, high- p_T)	0.00	0.00	0.00	0.00
Tau Eff. (Reco, total)	6.72	-6.51	0.12	-0.12
Tau Eff. (2015 Trigger, data, stat.)	0.00	0.00	0.00	0.00
Tau Eff. (2016 Trigger, data, stat.)	1.89	-2.84	0.05	-0.06
Tau Eff. (2015 Trigger, MC, stat.)	0.00	0.00	8.03	-8.03
Tau Eff. (2016 Trigger, MC, stat.)	1.5	-2.74	-8.1	8.08
Tau Eff. (2015 Trigger, syst.)	0.00	0.00	0.00	0.00
Tau Eff. (2016 Trigger, syst.)	1.48	-1.77	0.00	0.00
TES (Detector)	0.00	0.00	0.00	0.00
TES (In situ)	-0.33	-0.04	0.33	-0.58
TES (Model)	1.08	-0.23	0.04	-0.33
UE (gg)	5.19	-5.19	0.00	0.00
UE (qq)	0.00	0.00	0.00	0.00
Luminosity	2.9	-2.9	0.08	-0.08
NLO EW Higgs	0.00	0.00	0.00	0.00
QCD scale (ggH m_{12})	-6.05	6.92	0.00	0.00
EWK $Z \rightarrow \tau\tau$ proportion	0.00	0.00	0.54	-0.54
Z MC shape	0.00	0.00	0.00	6.68
Z subtraction	0.00	0.00	8.71	-8.71
Vary uniform fake- τ distribution, bin 1	0.00	0.00	-4.1	4.1
Vary uniform fake- τ distribution, bin 2	0.00	0.00	4.47	-4.47
Vary uniform fake- τ distribution, bin 3	0.00	0.00	0.02	-4.63
Higgs PDF (gg)	6.48	-5.97	0.00	0.00
Higgs PDF (gg , Acceptance)	1.62	-1.34	0.00	0.00
Higgs PDF (qq)	0.00	0.00	0.00	0.00
Higgs PDF (qq , Acceptance)	0.00	0.00	0.00	0.00

Table L.12: Relative impact of the nuisance parameters compared to the total number of events in percentage, shown for the **Boost Tight IPIP, high d_0^{sig}** category.

L.2 Prefit impact of each nuisance parameter in each Higgs CP signal category

Nuisance Parameter	Signal		Background	
	+1 σ	-1 σ	+1 σ	-1 σ
BR($H \rightarrow \tau\tau$)	5.7	-5.7	0.00	0.00
Forward JVT	0.00	0.00	0.00	0.00
JER	-2.52	2.52	0.49	-0.49
JES (Effective NP 1)	3.79	-3.99	-0.14	0.03
JES (Effective NP 2)	0.00	0.00	0.00	0.00
JES (Effective NP 3)	3.63	-2.91	0.00	0.00
JES (Effective NP 4)	-1.81	1.25	0.00	0.00
JES (Effective NP 5)	0.00	0.00	0.00	0.00
JES (Effective NP 6)	-1.21	1.24	-0.2	0.21
JES (Inter- $ \eta $ Calibration, Model)	0.00	0.00	0.21	-0.04
JES (Inter- $ \eta $ Calibration, Nonclosure)	0.00	0.00	0.00	0.00
JES (Inter- $ \eta $ Calibration, Stat.)	-1.32	1.32	0.00	0.00
JES (Flavor composition)	6.16	-6.1	0.27	-0.38
JES (Flavor Response)	0.23	-1.55	-0.1	0.09
JES (PU Offset μ)	-3.33	2.62	-0.21	0.21
JES (PU Offset NPV)	0.00	0.00	0.00	0.00
JES (PU p_T term)	2	-2.47	0.00	0.00
JES (PU ρ)	3.32	-3.39	0.00	0.00
ATLAS_JVT	0.00	0.00	0.00	0.00
MET Soft track (Parallel resolution)	-1.76	1.76	-0.15	0.15
MET Soft track (Perpendicular resolution)	0.00	0.00	-0.16	0.16
MET Soft track (Scale)	0.00	0.00	0.00	0.00
PRW Data SF	-10.5	12.82	-0.1	0.07
Tau Eff. (e -OLR, true e)	0.00	0.00	0.00	0.00
Tau Eff. (e -OLR, true τ_{had})	2.91	-2.87	0.06	-0.06
Tau Eff. (ID, high- p_T)	0.00	0.00	0.00	0.00
Tau Eff. (ID, total)	11.9	-11.23	0.27	-0.26
Tau Eff. (Reco, high- p_T)	0.00	0.00	0.00	0.00
Tau Eff. (Reco, total)	6.59	-6.38	0.15	-0.15
Tau Eff. (2015 Trigger, data, stat.)	0.00	0.00	0.00	0.00
Tau Eff. (2016 Trigger, data, stat.)	1.86	-2.81	0.05	-0.08
Tau Eff. (2015 Trigger, MC, stat.)	0.00	0.00	-4.68	4.68
Tau Eff. (2016 Trigger, MC, stat.)	1.52	-2.62	-8.19	8.17
Tau Eff. (2015 Trigger, syst.)	0.00	0.00	0.00	0.00
Tau Eff. (2016 Trigger, syst.)	1.43	-1.63	0.00	0.00
TES (Detector)	-2.59	-0.26	0.09	-0.09
TES (In situ)	-5.14	3	0.09	-0.04
TES (Model)	0.00	0.00	0.16	-0.25
UE (gg)	5.2	-5.2	0.00	0.00
UE (qq)	0.00	0.00	0.00	0.00
Luminosity	2.9	-2.9	0.11	-0.11
NLO EW Higgs	0.00	0.00	0.00	0.00
QCD scale (ggH m_{12})	-6.06	6.93	0.00	0.00
EWK $Z \rightarrow \tau\tau$ proportion	0.00	0.00	0.43	-0.43
Z MC shape	0.00	0.00	0.61	0.00
Z subtraction	0.00	0.00	5.56	-5.56
Vary uniform fake- τ distribution, bin 1	0.00	0.00	-2.01	2.01
Vary uniform fake- τ distribution, bin 2	0.00	0.00	5.52	-5.52
Vary uniform fake- τ distribution, bin 3	0.00	0.00	7.51	-7.51
Higgs PDF (gg)	6.5	-5.98	0.00	0.00
Higgs PDF (gg , Acceptance)	1.62	-1.34	0.00	0.00
Higgs PDF (qq)	0.00	0.00	0.00	0.00
Higgs PDF (qq , Acceptance)	0.00	0.00	0.00	0.00

Table L.13: Relative impact of the nuisance parameters compared to the total number of events in percentage, shown for the **Boost Tight IP ρ , low d_0^{sig} Y** category.

Appendix L Supplemental information on the final fit to the φ_{CP}^* observables in the Higgs CP analysis

Nuisance Parameter	Signal		Background	
	+1 σ	-1 σ	+1 σ	-1 σ
BR($H \rightarrow \tau\tau$)	5.7	-5.7	0.00	0.00
Forward JVT	0.00	0.00	0.00	0.00
JER	1.48	-1.48	0.33	-0.33
JES (Effective NP 1)	5.25	-4.24	-0.08	-0.32
JES (Effective NP 2)	2.37	-4.19	0.05	-0.09
JES (Effective NP 3)	0.00	0.00	-0.08	0.12
JES (Effective NP 4)	2.12	0.16	-0.35	0.07
JES (Effective NP 5)	0.00	0.00	0.00	0.00
JES (Effective NP 6)	0.00	0.00	0.00	0.00
JES (Inter- $ \eta $ Calibration, Model)	0.00	0.00	0.00	0.00
JES (Inter- $ \eta $ Calibration, Nonclosure)	-5.11	1.76	-0.22	0.00
JES (Inter- $ \eta $ Calibration, Stat.)	0.00	0.00	0.00	0.00
JES (Flavor composition)	0.00	0.00	-0.17	-0.22
JES (Flavor Response)	0.00	0.00	-0.33	0.07
JES (PU Offset μ)	5.71	-6.02	0.00	0.00
JES (PU Offset NPV)	0.00	0.00	0.00	0.00
JES (PU p_T term)	-3.46	2.58	-0.23	-0.05
JES (PU ρ)	5.19	-5.19	0.00	0.00
ATLAS_JVT	0.00	0.00	0.00	0.00
MET Soft track (Parallel resolution)	0.00	0.00	-0.5	0.5
MET Soft track (Perpendicular resolution)	-1.1	1.1	-0.21	0.21
MET Soft track (Scale)	2.28	-0.21	-0.6	0.31
PRW Data SF	-5.69	4.26	-0.21	0.07
Tau Eff. (e -OLR, true e)	0.00	0.00	0.00	0.00
Tau Eff. (e -OLR, true τ_{had})	2.86	-2.82	0.06	-0.06
Tau Eff. (ID, high- p_T)	0.00	0.00	0.00	0.00
Tau Eff. (ID, total)	11.9	-11.23	0.22	-0.22
Tau Eff. (Reco, high- p_T)	0.00	0.00	0.00	0.00
Tau Eff. (Reco, total)	6.72	-6.51	0.12	-0.12
Tau Eff. (2015 Trigger, data, stat.)	0.00	0.00	0.00	0.00
Tau Eff. (2016 Trigger, data, stat.)	1.89	-2.84	0.05	-0.06
Tau Eff. (2015 Trigger, MC, stat.)	0.00	0.00	8.03	-8.03
Tau Eff. (2016 Trigger, MC, stat.)	1.5	-2.74	-8.1	8.08
Tau Eff. (2015 Trigger, syst.)	0.00	0.00	0.00	0.00
Tau Eff. (2016 Trigger, syst.)	1.48	-1.77	0.00	0.00
TES (Detector)	0.00	0.00	0.00	0.00
TES (In situ)	-0.33	-0.04	0.33	-0.58
TES (Model)	1.08	-0.23	0.04	-0.33
UE (gg)	5.19	-5.19	0.00	0.00
UE (qq)	0.00	0.00	0.00	0.00
Luminosity	2.9	-2.9	0.08	-0.08
NLO EW Higgs	0.00	0.00	0.00	0.00
QCD scale (ggH m_{12})	-6.05	6.92	0.00	0.00
EWK $Z \rightarrow \tau\tau$ proportion	0.00	0.00	0.54	-0.54
Z MC shape	0.00	0.00	0.00	6.68
Z subtraction	0.00	0.00	8.71	-8.71
Vary uniform fake- τ distribution, bin 1	0.00	0.00	-4.1	4.1
Vary uniform fake- τ distribution, bin 2	0.00	0.00	4.47	-4.47
Vary uniform fake- τ distribution, bin 3	0.00	0.00	0.02	-4.63
Higgs PDF (gg)	6.48	-5.97	0.00	0.00
Higgs PDF (gg , Acceptance)	1.62	-1.34	0.00	0.00
Higgs PDF (qq)	0.00	0.00	0.00	0.00
Higgs PDF (qq , Acceptance)	0.00	0.00	0.00	0.00

Table L.14: Relative impact of the nuisance parameters compared to the total number of events in percentage, shown for the **Boost Tight IP ρ , high d_0^{sig} Y** category.

L.2 Prefit impact of each nuisance parameter in each Higgs CP signal category

Nuisance Parameter	Signal		Background	
	+1 σ	-1 σ	+1 σ	-1 σ
BR($H \rightarrow \tau\tau$)	5.7	-5.7	0.00	0.00
Forward JVT	0.00	0.00	0.00	0.00
JER	-5.6	5.6	0.59	-0.59
JES (Effective NP 1)	3.91	-2.48	0.82	0.09
JES (Effective NP 2)	5.02	-5.02	0.00	0.00
JES (Effective NP 3)	-4.53	4.33	0.00	0.00
JES (Effective NP 4)	0.00	0.00	-0.04	0.13
JES (Effective NP 5)	-1.94	2.68	0.16	-0.04
JES (Effective NP 6)	0.00	0.00	0.14	-0.06
JES (Inter- $ \eta $ Calibration, Model)	2.84	-2.84	0.1	0.05
JES (Inter- $ \eta $ Calibration, Nonclosure)	0.00	0.00	-0.1	0.02
JES (Inter- $ \eta $ Calibration, Stat.)	3.72	-3.93	0.09	0.00
JES (Flavor composition)	3.12	-3.28	-0.01	-0.07
JES (Flavor Response)	-5.8	5.6	-0.04	0.72
JES (PU Offset μ)	0.14	-0.48	0.00	0.00
JES (PU Offset NPV)	-1.44	-0.18	0.48	0.1
JES (PU p_T term)	0.00	0.00	0.13	-0.03
JES (PU ρ)	5.35	-5.51	0.74	-0.61
ATLAS_JVT	0.00	0.00	0.00	0.00
MET Soft track (Parallel resolution)	0.00	0.00	0.00	0.00
MET Soft track (Perpendicular resolution)	0.00	0.00	-0.48	0.48
MET Soft track (Scale)	5.75	-5.75	0.00	0.00
PRW Data SF	-10.4	7.98	-0.8	0.58
Tau Eff. (e -OLR, true e)	0.00	0.00	0.07	-0.07
Tau Eff. (e -OLR, true τ_{had})	2.91	-2.86	0.12	-0.12
Tau Eff. (ID, high- p_T)	0.00	0.00	0.00	0.00
Tau Eff. (ID, total)	11.9	-11.24	0.46	-0.45
Tau Eff. (Reco, high- p_T)	0.00	0.00	0.00	0.00
Tau Eff. (Reco, total)	6.49	-6.29	0.28	-0.27
Tau Eff. (2015 Trigger, data, stat.)	0.00	0.00	0.00	0.00
Tau Eff. (2016 Trigger, data, stat.)	2.02	-3.01	0.07	-0.09
Tau Eff. (2015 Trigger, MC, stat.)	0.00	0.00	-9.83	9.83
Tau Eff. (2016 Trigger, MC, stat.)	1.62	-2.86	-20.81	20.78
Tau Eff. (2015 Trigger, syst.)	0.00	0.00	0.00	0.00
Tau Eff. (2016 Trigger, syst.)	1.38	-1.64	0.06	-0.08
TES (Detector)	0.00	0.00	0.46	-0.46
TES (In situ)	7.91	-8.21	0.6	-1.17
TES (Model)	2.67	-0.29	0.06	-0.22
UE (gg)	5.28	-5.28	0.00	0.00
UE (qq)	0.00	0.00	0.00	0.00
Luminosity	2.9	-2.9	0.16	-0.16
NLO EW Higgs	0.00	0.00	0.00	0.00
QCD scale (ggH m_{12})	-6.15	7.03	0.00	0.00
EWK $Z \rightarrow \tau\tau$ proportion	0.00	0.00	0.22	-0.22
Z MC shape	0.00	0.00	-3.31	0.00
Z subtraction	0.00	0.00	8.14	-8.14
Vary uniform fake- τ distribution, bin 1	0.00	0.00	-5.55	5.55
Vary uniform fake- τ distribution, bin 2	0.00	0.00	-12	12
Vary uniform fake- τ distribution, bin 3	0.00	0.00	10.58	-10.58
Higgs PDF (gg)	6.59	-6.07	0.00	0.00
Higgs PDF (gg , Acceptance)	1.64	-1.36	0.00	0.00
Higgs PDF (qq)	0.00	0.00	0.00	0.00
Higgs PDF (qq , Acceptance)	0.00	0.00	0.00	0.00

Table L.15: Relative impact of the nuisance parameters compared to the total number of events in percentage, shown for the **Boost Tight $\rho\rho$, low $Y_+ Y_-$** category.

Appendix L Supplemental information on the final fit to the φ_{CP}^* observables in the Higgs CP analysis

Nuisance Parameter	Signal		Background	
	+1 σ	-1 σ	+1 σ	-1 σ
BR($H \rightarrow \tau\tau$)	5.70	-5.70	0.00	0.00
Forward JVT	0.00	0.00	0.00	0.00
JER	2.05	-2.05	0.58	-0.58
JES (Effective NP 1)	3.05	-3.6	0.00	0.00
JES (Effective NP 2)	0.00	0.00	-0.02	0.19
JES (Effective NP 3)	0.00	0.00	0.21	-0.04
JES (Effective NP 4)	0.00	0.00	0.01	0.21
JES (Effective NP 5)	0.00	0.00	0.00	0.00
JES (Effective NP 6)	0.00	0.00	0.00	0.00
JES (Inter- $ \eta $ Calibration, Model)	0.00	0.00	0.00	0.00
JES (Inter- $ \eta $ Calibration, Nonclosure)	-2.54	1.66	0.00	0.00
JES (Inter- $ \eta $ Calibration, Stat.)	0.00	0.00	-0.01	0.17
JES (Flavor composition)	2.69	-3.9	-0.06	-0.01
JES (Flavor Response)	-3.01	2.47	0.00	0.00
JES (PU Offset μ)	2.97	-1.44	0.00	0.00
JES (PU Offset NPV)	0.00	0.00	0.28	-0.1
JES (PU p_T term)	0.00	0.00	0.00	0.00
JES (PU ρ)	0.00	0.00	0.00	0.00
ATLAS_JVT	0.00	0.00	0.00	0.00
MET Soft track (Parallel resolution)	2.79	-2.79	-0.06	0.06
MET Soft track (Perpendicular resolution)	-1.17	1.17	-0.21	0.21
MET Soft track (Scale)	2.49	-0.68	-0.08	0.27
PRW Data SF	2.41	-1.04	-0.12	0.08
Tau Eff. (e -OLR, true e)	0.00	0.00	0.00	0.00
Tau Eff. (e -OLR, true τ_{had})	2.93	-2.89	0.07	-0.07
Tau Eff. (ID, high- p_T)	0.00	0.00	0.00	0.00
Tau Eff. (ID, total)	11.9	-11.24	0.31	-0.3
Tau Eff. (Reco, high- p_T)	0.00	0.00	0.00	0.00
Tau Eff. (Reco, total)	6.64	-6.43	0.18	-0.18
Tau Eff. (2015 Trigger, data, stat.)	0.00	0.00	0.00	0.00
Tau Eff. (2016 Trigger, data, stat.)	1.99	-3.03	0.05	-0.07
Tau Eff. (2015 Trigger, MC, stat.)	0.00	0.00	-0.01	0.01
Tau Eff. (2016 Trigger, MC, stat.)	1.54	-2.84	-4.59	4.57
Tau Eff. (2015 Trigger, syst.)	0.00	0.00	0.00	0.00
Tau Eff. (2016 Trigger, syst.)	1.49	-1.71	0.05	-0.06
TES (Detector)	-6.58	2.81	-0.23	0.09
TES (In situ)	-1.55	1.11	0.00	0.00
TES (Model)	-0.28	2.48	0.00	0.00
UE (gg)	5.29	-5.29	0.00	0.00
UE (qq)	0.00	0.00	0.00	0.00
Luminosity	2.9	-2.9	0.11	-0.11
NLO EW Higgs	0.00	0.00	0.00	0.00
QCD scale (ggH m_{12})	-6.17	7.05	0.00	0.00
EWK $Z \rightarrow \tau\tau$ proportion	0.00	0.00	0.21	-0.21
Z MC shape	0.00	0.00	2.60	0.00
Z subtraction	0.00	0.00	10.59	-10.59
Vary uniform fake- τ distribution, bin 1	0.00	0.00	-2.37	2.37
Vary uniform fake- τ distribution, bin 2	0.00	0.00	-2.17	2.17
Vary uniform fake- τ distribution, bin 3	0.00	0.00	0.09	-7.13
Higgs PDF (gg)	6.61	-6.08	0.00	0.00
Higgs PDF (gg , Acceptance)	1.65	-1.36	0.00	0.00
Higgs PDF (qq)	0.00	0.00	0.00	0.00
Higgs PDF (qq , Acceptance)	0.00	0.00	0.00	0.00

Table L.16: Relative impact of the nuisance parameters compared to the total number of events in percentage, shown for the **Boost Tight $\rho\rho$, high $Y_+ Y_-$** category.

List of Figures

2.1	Leading-order interaction vertices predicted by the SM before spontaneous symmetry breaking	7
2.2	Running strong coupling constant, α_S	8
2.3	Martin-Stirling-Thorne-Watt (MSTW) Parton distribution functions (PDFs) . .	10
2.4	The Higgs potential	14
2.5	Higgs boson interaction vertices	16
2.6	Feynman diagrams of the main Higgs boson production processes at the LHC.) .	19
2.7	Cross sections of the Higgs boson production processes	19
2.8	Feynman diagrams of the VBF production process	20
2.9	Branching ratios of the SM Higgs boson	21
2.10	The predicted mass dependence of the Higgs boson coupling	23
2.11	The preferred decay kinematics in the $\tau \rightarrow \pi\nu_\tau$ decay	25
2.12	Angular distributions of the visible tau decay products for different tau polarization states	27
2.13	The preferred decay kinematics in the $\tau^- \rightarrow \rho^- \bar{\nu}_\tau$ decay	28
2.14	Angular correlations of the tau decay products from $H, A \rightarrow \tau\tau$ decays	30
2.15	Schematic of the pion angles in the $\tau \rightarrow \pi\nu_\tau$ decay	31
2.16	Distribution of the acoplanarity angle between the tau decay planes for a scalar and pseudoscalar Higgs boson	31
2.17	The hierarchy problem	34
3.1	Schematic of the LHC accelerator complex	36
3.2	Ratio of the inclusive pp cross sections for selected physics processes at $\sqrt{s} = 8$ and 13 TeV	38
3.3	Schematic of a pp collision	39
3.4	Cut-away schematic of the ATLAS detector showing the principal subdetectors .	41
3.5	Schematic of the magnetic system	42
3.6	Schematic of each layer of the inner detector	43
3.7	Energy and transverse momentum resolutions in the ATLAS calorimeter and tracking systems	44
3.8	Cut-away schematic of the ATLAS calorimeter system	46
3.9	Schematic of a module of the ECAL barrel	47
3.10	Schematic of a hadronic shower and the types of energy detected/undetected by the HCAL	49
3.11	The L1 trigger tower	50
4.1	The transverse impact parameter resolution	52
4.2	Schematic of the tau isolation cone	55

4.3	Example of a discriminating variable used in the $\tau_{\text{had, vis}}$ ID	57
4.4	Tau reconstruction and identification efficiencies	59
4.5	Efficiencies of the tau trigger	60
4.6	Schematic of a hadronically decaying tau in the ATLAS detector	63
4.7	Schematic of the cluster level π^\pm subtraction.	64
4.8	Charged pion showers in <i>ECAL</i>	66
4.9	RMS of the p_T resolution for the $\tau_{\text{had-vis}}$ candidate after the different methods of subtraction in the simulated $Z \rightarrow \tau\tau$ sample with pileup.	67
4.11	Display of a τ_{had} decay from a $Z \rightarrow \tau\tau$ event in the strip layer	69
4.12	Photon hit reconstruction efficiency and share probability	70
4.13	Performance of the decay mode classification after the π^0 -ID and photon hit counting	70
4.14	Energy and spatial resolution of reconstructed neutral pions	71
4.15	Performance of the decay mode classification using BDT tests	72
4.16	Energy and spatial resolution of the reconstructed $\tau_{\text{had-vis}}$ candidate	73
4.17	Decay mode classification in $Z \rightarrow \tau\tau$ and $Z \rightarrow \mu\mu$ events	74
5.1	The best fit value of the Higgs boson signal strength in the Run-I searches	76
5.2	Final states and branching fractions of the $H \rightarrow \tau\tau$ decay channel.	77
5.3	The best fit value of the Higgs boson signal strength in the Run-I $H \rightarrow \tau\tau$ search	78
5.4	Example leading-order Feynman diagrams of the VBF and ggH signal processes with the corresponding main background processes below each diagram	81
5.5	Comparison of the di-tau mass reconstruction methods	84
5.6	Flow chart showing each step of the $H \rightarrow \tau\tau$ analysis	86
5.7	Background/signal admixture in each signal category of the $H \rightarrow \tau\tau$ analysis	91
5.8	Schematic of the differences in kinematic configurations between preselection and the categories.	92
5.9	The improvement in the $m_{\text{MMC}}^{\tau\tau}$ resolution going from preselection to the VBF and Boosted categories for the $H \rightarrow \tau\tau$ and $Z \rightarrow \tau\tau$ samples	92
5.10	Categorization of the VBF region into the low and high ΔR VBF categories, shown for the $H \rightarrow \tau\tau$, $Z \rightarrow \tau\tau$, and fake- τ background processes.	94
5.11	Categorization of the VBF High ΔR region into tight and loose categories, shown for the $H \rightarrow \tau\tau$, $Z \rightarrow \tau\tau$, and fake- τ background processes.	95
5.12	Categorization of the boosted region into the tight and loose boosted categories, shown for the $H \rightarrow \tau\tau$, $Z \rightarrow \tau\tau$, and fake- τ background processes.	96
5.13	$Z \rightarrow \tau\tau$ modeling of the number of jets at preselection	97
5.14	$Z \rightarrow \tau\tau$ modeling of the η of the subleading p_T jet at preselection	98
5.15	Comparison of the $m_{\text{MMC}}^{\tau\tau}$ modeling with the SS and nOS control regions	101
5.16	Comparison of the $m_{\text{MMC}}^{\tau\tau}$ distribution in the SS and nOS regions	101
5.17	Contamination from processes other than the fake- τ background in the nOS Control region	102
5.18	Pre-fit background estimation using a fit to $\Delta\eta(\tau, \tau)$	104
5.19	Validation of background modeling in the $H \rightarrow \tau\tau$ analysis	105
5.20	Comparison of the OS and nOS templates in the anti- $\tau_{\text{had, vis}}$ ID region at different $\tau_{\text{had, vis}}$ ID working points	108
5.21	Different configurations of the background model revealing an underestimate of the low $m_{\text{MMC}}^{\tau\tau}$ region	109

5.22	The $m_{\text{MMC}}^{\tau\tau}$ observable using the matrix method with fake- τ templates that are selected based on the number of τ_{had} tracks	113
5.23	Validation of background modeling in the $H \rightarrow \tau\tau$ analysis	114
5.24	Statistical and systematic uncertainties on the $Z \rightarrow \tau\tau$ efficiency	115
5.25	Statistical and systematic uncertainties on the misidentification probability.	116
5.26	Comparison of background estimation methods in the $H \rightarrow \tau\tau$ analysis	118
5.27	The relationship between the p -value and the significance, Z	124
5.28	Pulls and ranking of NPs based on their postfit impact on $\hat{\mu}$ for Asimov data	126
5.29	NLL profiles of the fake- τ extrapolation systematic uncertainties from the OS-nOS method	127
5.30	NLL profiles of the POI	129
5.31	Pre- and postfit $m_{\text{MMC}}^{\tau\tau}$ distributions	132
5.32	Pulls and ranking of NPs based on their postfit impact on $\hat{\mu}$ for the unblinded fit in the $H \rightarrow \tau\tau$ analysis	133
6.1	Schematic of the acoplanarity angle between the tau decay planes, φ_{CP}^*	136
6.2	Schematic of IP method	137
6.3	The φ_{CP} and φ_{CP}^* distributions from the IP method.	138
6.4	CP mixing signal templates at the preselection level	140
6.5	Generator-level φ_{CP}^* distributions of the simulated $Z \rightarrow \tau\tau$ sample in inclusive and restricted phase spaces	145
6.6	Comparison of $Z \rightarrow \tau\tau$ shapes in MC and data for the VBF categories	146
6.7	Contamination from real- τ backgrounds in the SS control region for each decay mode at preselection.	147
6.8	Compatibility of the SS fake- τ shape from data with a uniform distribution	148
6.9	The fake- τ background shapes in OS and SS events of the anti- $\tau_{\text{had, vis}}$ ID region at preselection level.	149
6.10	Higgs CP prefit background estimation using a fit to $m_{\text{MMC}}^{\tau\tau}$	150
6.11	Modeling of the φ_{CP}^* distribution in the Higgs CP analysis	151
6.12	φ_{CP}^* shape comparisons in the anti- $\tau_{\text{had, vis}}$ ID region	152
6.13	Expected CP sensitivity for different configurations of the final fit	155
6.14	NP ranking and pulls for the Asimov fit in the Higgs CP analysis	155
6.15	Toy experiments for fit validation in the Higgs CP analysis	156
6.16	Projection of the Higgs CP sensitivity estimate when the sizes of the data, signal, and fake- τ samples are extrapolated to higher luminosity	157
6.17	Schematic of $\Delta\phi$ angles between example planes from the ρa_1 decay	159
6.18	Schematic of $\Delta\phi$ angles between example planes from the $a_1 a_1$ decay	160
6.19	Angles between the two tau decay planes for the $a_1 a_1$ mode at generator level.	161
6.20	BDT Scores for the a_1 modes	163
6.21	The BDT performance at reconstruction level	163
6.22	Unblinded CP sensitivity measurement	164
6.23	NP ranking and pulls for the unblinded fit in the Higgs CP analysis	165
6.24	Pre- and postfit φ_{CP}^* distributions for the VBF category	167
6.25	Pre- and postfit φ_{CP}^* distributions for the Boost Tight category	168
6.26	Pre- and postfit φ_{CP}^* distributions for the Boosted Loose category	169
B.1	Amount of material before each subcomponent of the detector.	186

B.2	Length of each layer of the electromagnetic calorimeter.	186
D.1	Number of reconstructed tracks per event in the single π^\pm sample	189
D.2	The η and p_T spectra of the true charged pions in the single π^\pm sample	190
H.1	Validation of the OS-nOS background modeling for the ΔR observable.	197
H.1	Validation of the OS-nOS background modeling for the ΔR observable.	198
H.2	Validation of the OS-nOS background modeling for the p_T of the di-tau resonance.	199
H.3	Validation of the OS-nOS background modeling for the $\Delta\eta(j, j)$ observable.	200
H.4	Validation of the OS-nOS background modeling for the m_{jj} observable.	201
J.1	Postfit impact on μ from selected jet NPs.	211
J.2	Correlation matrix for selected jet NPs.	212
J.3	NP ranking and postfit impact on μ without the VBF low ΔR category.	212
K.1	Modeling of the Y distribution in the HCP analysis	213
K.2	Modeling of the φ_{CP}^* distribution in the VBF category	214
K.3	Modeling of the d_0^{sig} observable in the HCP analysis	215
K.4	Modeling of the Y distribution in the HCP analysis	216
K.5	Modeling of the φ_{CP}^* distribution in the HCP analysis in the Boosted tight category	217
K.6	Modeling of the d_0^{sig} observable in the Boosted Loose category	218
K.7	Modeling of the Y distribution in the Boosted Loose category	219
K.8	Modeling of the φ_{CP}^* distribution in the HCP analysis in the Boosted loose category	220

List of Tables

2.1	The fundamental forces and their properties	4
2.2	The fermions and their properties	5
2.3	The masses of the fermions	5
2.4	Vector and axial-vector couplings	14
2.5	Higgs boson production cross sections at the LHC	18
2.6	Decay modes and branching ratios of the tau lepton	25
2.7	Probability of the longitudinal polarization configurations of a tau lepton pair from different origins	30
3.1	LHC Parameters (2010-2017)	37
4.1	The tau trigger nomenclature and selection criteria	58
4.2	Summary of the generators, PDF parametrization, and UE tunes for the simulated samples used for the tau particle flow algorithm	61
4.3	The decay modes classified by the tau particle flow algorithm	62
4.4	Optimized selection requirements for an identified π^0 cluster	67
5.1	Summary of the generators, PDF parametrization, and UE tunes for the simulated samples in the $H \rightarrow \tau\tau$ analysis	82
5.2	Object selection.	88
5.3	Selection criteria for preselection and categories.	89
5.4	Expected event yield ($H \rightarrow \tau\tau$ analysis)	90
5.5	Summary of the $H \rightarrow \tau\tau$ background strategy	96
5.6	Selection requirements for the SS and nOS control regions	100
5.7	Contamination from signal and real- τ backgrounds in the SS and nOS control regions	102
5.8	The $H \rightarrow \tau\tau$ analysis prefit normalization factors	104
5.9	Selection requirements of the anti- $\tau_{\text{had, vis}}$ ID regions	107
5.10	Relative size of the nOS control region compared to the OS region in the anti- $\tau_{\text{had, vis}}$ ID regions	110
5.11	Projection of the maximum possible impact from fake factors	111
5.12	Misidentification probabilities and efficiencies in the matrix method	112
5.13	Relative impact of the matrix method systematic uncertainties compared to the total number of fake- τ background events at the prefit level	116
5.14	Relative impact of the nuisance parameters compared to the total number of events for the Boosted Loose category at the prefit level	117
5.15	Expected and observed results in the $H \rightarrow \tau\tau$ analysis	129
5.16	Postfit event yields and their total uncertainties in the $H \rightarrow \tau\tau$ analysis	130

5.17	Observed $H \rightarrow \tau\tau$ results from Run-I and Run-II analyses by the ATLAS and CMS collaborations	130
6.1	Low- and high- \mathcal{CP} sensitivity categorization by decay mode	141
6.2	Expected Higgs \mathcal{CP} event yield	143
6.3	Summary of the Higgs \mathcal{CP} background strategy.	144
6.4	Higgs \mathcal{CP} analysis prefit normalization factors	149
6.5	The exclusion level of the $J^P = 0^-$ Higgs boson hypothesis when tested against the SM $J^P = 0^+$ Higgs boson prediction	164
6.6	Postfit event yields of the Higgs \mathcal{CP} analysis	166
B.1	Segmentation of the ATLAS electromagnetic calorimeter	185
C.1	Variables used to identify π^0 clusters in the π^0 -ID BDT	187
E.1	Cross section values of background and signal processes at $\sqrt{s} = 13$ TeV	192
F.1	Changes in the $H \rightarrow \tau\tau$ preselection	193
G.1	Track composition of the nOS control region	195
I.1	Binning of the $m_{\text{MMC}}^{\tau\tau}$ distribution for in the final fit	203
I.2	Relative impact of the nuisance parameters on the total number of events for the VBF High ΔR Loose category	207
I.3	Relative impact of the nuisance parameters on the total number of events for the VBF High ΔR Tight category	208
I.4	Relative impact of the nuisance parameters on the total number of events for the VBF Low ΔR category	209
I.5	Relative impact of the nuisance parameters on the total number of events for the Boosted Tight category	210
L.1	Relative impact of the nuisance parameters on the total number of events for the VBF IPIP category	223
L.2	Relative impact of the nuisance parameters on the total number of events for the VBF IP ρ category	224
L.3	Relative impact of the nuisance parameters on the total number of events for the VBF $\rho\rho$, high Y_+Y_- category	225
L.4	Relative impact of the nuisance parameters on the total number of events for the VBF $\rho\rho$, low Y_+Y_- category	226
L.5	Relative impact of the nuisance parameters on the total number of events for the Boost Loose IPIP, low d_0^{sig} category	227
L.6	Relative impact of the nuisance parameters on the total number of events for the Boost Loose IPIP, high d_0^{sig} category	228
L.7	Relative impact of the nuisance parameters on the total number of events for the Boost Loose IP ρ , low $d_0^{\text{sig}}Y$ category	229
L.8	Relative impact of the nuisance parameters on the total number of events for the Boost Loose IP ρ , high $d_0^{\text{sig}}Y$ category	230
L.9	Relative impact of the nuisance parameters on the total number of events for the Boost Loose $\rho\rho$, low Y_+Y_- category	231

L.10	Relative impact of the nuisance parameters on the total number of events for the Boost Loose $\rho\rho$, high Y_+Y_- category	232
L.11	Relative impact of the nuisance parameters on the total number of events for the Boost Tight IPIP, low d_0^{sig} category	233
L.12	Relative impact of the nuisance parameters on the total number of events for the Boost Tight IPIP, high d_0^{sig} category	234
L.13	Relative impact of the nuisance parameters on the total number of events for the Boost Tight IP ρ , low $d_0^{\text{sig}}Y$ category	235
L.14	Relative impact of the nuisance parameters on the total number of events for the Boost Tight IP ρ , high $d_0^{\text{sig}}Y$ category	236
L.15	Relative impact of the nuisance parameters on the total number of events for the Boost Tight $\rho\rho$, low Y_+Y_- category	237
L.16	Relative impact of the nuisance parameters on the total number of events for the Boost Tight $\rho\rho$, high Y_+Y_- category	238

Acknowledgements

This dissertation would not have been possible without the support of many people.

To Jochen Dingfelder, I extend my sincere gratitude — for his continuous guidance and for making the work presented here possible.

To those I have had the privilege to work with, especially Benedict Winter, the German big brother I never had — as has been said by many before, how lucky am I to have something that makes saying goodbye so hard.

To Malte Wittwer, for his love, unfailing support, and uncanny ability to make me laugh during even the hardest times. Thank you for being my anchor during even the loftiest of endeavors.

And to my family, especially my parents, Philip and Christine Yuen, and my grandparents 袁石財, 孫見掌, 胡國通, 袁土妹, who, for the sake of their children and grandchildren, made something from nothing — I owe it all to you.